Universität Augsburg
Mathematisch-Naturwissenschaftlich-
Technische Fakultät

Synthesis, Characterisation and Structure-Property Relations of Silicate-analogous Tungstates, Sulfates, Sulfatotungstates and Borosulfates

Dissertation

zur Erlangung des akademischen Grades
Dr. rer. nat.

eingereicht an der
Mathematisch-Naturwissenschaftlich-Technischen Fakultät
der Universität Augsburg
von

Matthias Hämmer

Augsburg, März 2022

Erstgutachter:	Prof. Dr. Henning A. Höppe
Zweitgutachter:	Prof. Dr. Leo van Wüllen
Tag der mündlichen Prüfung:	01.06.2022

Für mein Selinchen und Mathilda.

Science is not truth. Science is finding the truth. When science changes its opinion, it didn't lie to you. It learned more.

(Gil Wernovsky)

Abstract

The immense structural variety of silicates is surpassed by the material class of silicate-analogous materials. In this thesis, silicate-analogous tungstates, sulfates, sulfatotungstates and borosulfates are investigated. Firstly, the two precursor compounds $Sr_3(C_6H_5O_7)_2 \cdot H_2O$ and $Ln[CO_3][OH]$ (Ln = La, Pr, Nd, Sm, Eu, Gd, Tb) are extensively studied and their suitability as precursors is demonstrated. For the latter, the discussion about the correct space group can finally be clarified with the help of powder SHG measurements. Structure-property relations were established for the pentasodium rare earth metal tetratungstates $Na_5M(WO_4)_4$ (M = Y, La-Nd, Sm-Lu, Bi) and the double tungstates $AM(WO_4)_2$ (A = Li, Na, K; M = Y, La, Pr, Tb, Bi) to the optical properties such as cross-relaxation and the thermal properties such as the trend of the decomposition temperature with the size of the rare earth ion. With $Cs_6[(WO_2)_2O(SO_4)_4]$, only the fifth sulfatotungstate is prepared and characterised. The anion exhibits - hitherto unknown - edge-sharing of sulfate tetrahedra and tungstate octahedra. In addition, six new compounds and crystal structures are described in the ternary and quaternary systems Sn-S-O, Bi-S-O and Bi-S-O-H. These serve as model systems to show - by comparison to quantum chemical calculations - that geometric calculations using the method of Balić-Žunić and Makovicky enable both qualitative and quantitative analyses of the stereochemical activity within a crystal structure. These distortions resulting from the lone pair effect can be described just as well as on the basis of elaborate calculations of the electron localisation function. Consequently, the geometric calculations represent a powerful tool for the analysis of new crystal structures. As the last silicate-analogous material class, the borosulfates are expanded by three new cations, seven new compounds and four new structure types. With $Bi_2[B_2(SO_4)_6]$, the first bismuth borosulfate is prepared and characterised. The further bismuth borosulfates $BiX[B(SO_4)_2]_4$ ($X = H_3O^+$, NO_2^+ and NH_4^+) have tectosilicate-analogous (3D) anionic substructures - a rarity in borosulfates with only one example, so far - and are the first borosulfates with two differently charged cations. In contrast to these compounds, in which the lone pair effect is quenched, the antimony cation in $(NH_4)Sb[B(SO_4)_2]_4$ shows stereochemical activity. $(NH_4)Sb[B(SO_4)_2]_4$ is also a tectosilicate-analogous borosulfate. All four tectosilicate-analogous borosulfates show high SHG activities comparable to the benchmark material KDP. Additionally, the transition metal borosulfates $Cd[B_2(SO_4)_4]$ and $Cu[B_2(SO_4)_4]$ are reported. The latter compound shows polymorphism with the anionic substructure of the two polymorphs differing in their dimensionalities for the first time in borosulfate chemistry.

Kurzzusammenfassung

Die enorme Strukturvielfalt der Silicate wird von der Materialklasse der silicatanalogen Materialien übertroffen. In dieser Arbeit werden silicatanaloge Wolframate, Sulfate, Sulfatowolframate und Borosulfate behandelt. Zunächst werden die zwei Vorläuferverbindungen Strontiumcitratmonohydrat $Sr_3(C_6H_5O_7)_2 \cdot H_2O$ und Seltenerdcarbonathydroxid $Ln[CO_3][OH]$ (Ln = La, Pr, Nd, Sm, Eu, Gd, Tb) ausgiebig untersucht und insbesondere ihre Eignung als Vorläuferverbindungen demonstriert. Für letztere wird die Diskussion über die korrekte Raumgruppe mithilfe von Pulver-SHG Messungen abschließend geklärt. Die Verbindungen mit großen Seltenerdionen bis zum Gadolinium kristallisieren in der zentrosymmetrischen Raumgruppe *Pnma* und alle Verbindungen ab dem Terbium in der nicht-zentrosymmetrischen Raumgruppe $P2_12_12_1$. Struktur-Eigenschaftsbeziehungen für die Pentanatriumseltenerdmetalltetrawolframate $Na_5M(WO_4)_4$ (M = Y, La-Nd, Sm-Lu, Bi) und die Doppelwolframate $AM(WO_4)_2$ (A = Li, Na, K; M = Y, La, Pr, Tb, Bi) zu den optischen Eigenschaften wie zum Beispiel der Cross-Relaxation und den thermischen Eigenschaften wie dem Verlauf der Zersetzungstemperatur mit der Größe des Seltenerdions werden aufgezeigt. Mit $Cs_6[(WO_2)_2O(SO_4)_4]$ wird erst das fünfte Sulfatowolframat synthetisiert und charakterisiert. Das Anion weist eine – bis dato unbekannte – Kantenverknüpfung von Sulfattetraedern und Wolframatoktaedern auf. Zudem werden in den ternären und quartären Systemen Sn-S-O, Bi-S-O und Bi-S-O-H insgesamt sechs neue Verbindungen und Kristallstrukturen beschrieben: $Sn(SO_4)_2$-I, $Sn(SO_4)_2$-II, $Sn_2(SO_4)_3$, $Bi_2(SO_4)_3$, $Bi(H_3O)(SO_4)_2$ und $Bi(HSO_4)_3$. Die letzten vier dienen als Modelsysteme, um – anhand des Vergleichs zu quantenchemischen Rechnungen – zu zeigen, dass geometrische Berechnungen nach der Methode von Balić-Žunić und Makovicky sowohl qualitative als auch quantitative Aussagen über die stereochemische Aktivität innerhalb einer Kristallstruktur treffen können. Diese Verzerrungen aufgrund des Lone Pair Effekts können damit ebenso gut beschrieben werden wie anhand aufwändiger Berechnungen der Elektronenlokalisierungsfunktion. Folglich stellen die geometrischen Rechnungen eine aufwandarme und doch aussagekräftige Möglichkeit der Analyse neuer Kristallstrukturen dar. Als letzte silicatanaloge Materialklasse werden die Borosulfate um drei neue Kationen, sieben neue Verbindungen und vier neue Kristallstrukturtypen erweitert. Das erste Bismutborosulfat $Bi_2[B_2(SO_4)_6]$ wird hergestellt und charakterisiert. Die weiteren Bismutborosulfate $BiX[B(SO_4)_2]_4$ (X = H_3O^+, NO_2^+ and NH_4^+) weisen tectosilicatanaloge (3D) anionische Substrukturen auf – bis dato eine Rarität bei Borosulfaten mit nur einem Beispiel – und sind die ersten Borosulfate mit zwei unterschiedlich geladenen Kationen. Im Gegensatz zu diesen Verbindungen, in denen der Lone Pair Effekt „verschwindet“, zeigt das Antimonkation

in $(NH_4)Sb[B(SO_4)_2]_4$ stereochemische Aktivität. $(NH_4)Sb[B(SO_4)_2]_4$ ist ebenfalls ein tectosilicatanaloges Borosulfat. Die Kristallstrukturbeziehung zum $Bi(NH_4)[B(SO_4)_2]_4$ kann mittels einer Gruppe-Untergruppe-Beziehung beschrieben werden. Alle vier tectosilicatanalogen Borosulfate zeigen hohe SHG-Aktivitäten in der Größenordnung des Benchmarkmaterials KDP. Außerdem werden die Übergangsmetallborosulfate $Cd[B_2(SO_4)_4]$ und $Cu[B_2(SO_4)_4]$ beschrieben. Letztere Verbindung zeigt zum ersten Mal in der Borosulfatchemie Polymorphie, bei der sich die anionische Substruktur der beiden Polymorphe in ihrer Dimensionalität unterscheidet.

List of Abbreviations

ATR	attenuated total reflection
a.u.	arbitrary units
CN	coordination number
CT	charge transfer
CTAB	cetyltrimethylammonium bromide ($[(C_{16}H_{33})N(CH_3)_3]Br$)
Δ	ligand field splitting energy
DFT	density functional theory
$\boldsymbol{\Delta_{octa}}$	deviation from octahedral symmetry in %
DOS	density of states
DSC	differential scanning calorimetry
DTA	differential thermal analysis
$\boldsymbol{\Delta_{tetra}}$	deviation from tetrahedral symmetry in %
DTG	derivative thermogravimetry
ECoN	effective coordination number
EDX	energy-dispersive X-ray spectroscopy
e.g.	exempli gratia
$\boldsymbol{E_g}$	bandgap energy
E_{JT}	Jahn-Teller energy
ELF	electron localisation function
emu	electromagnetic unit
$\boldsymbol{\epsilon}$	eccentricity
EtOH	ethanol
FT	Fourier transformation
FT-IR	Fourier transform infrared
i.e.	id est
IR	infrared
IR	ionic radii
IVCT	intervalence charge transfer
KDP	potassium dihydrogenphosphate (KH_2PO_4)
$\boldsymbol{\lambda}$	wavelength
LED	light-emitting diode
LMCT	ligand to metal charge transfer
M	molar mass in $\frac{g}{mol}$
$\boldsymbol{m}$	mass
MAPLE	Madelung Part of Lattice Energy

NIR	near infrared
NIST	National Institute of Standards and Technology
NLO	non-linear optical
pcWLED	phosphor converting white light emitting diode
PDOS	partial density of states
PJTE	pseudo Jahn-Teller effect
PTFE	polytetrafluoroethylene (“Teflon”)
PXRD	powder X-ray diffraction
$\boldsymbol{R_c}$	centroid deviation
RT	room temperature
SC-XRD	single-crystal X-ray diffraction
SEM	scanning electron microscopy
SHG	second harmonic generation
TG	thermogravimetry
TGA	thermogravimetric analysis
TPXRD	temperature-programmed powder X-ray diffraction
UV	ultraviolet
V	volume
VASP	Vienna ab initio simulation package
Vis	visible
vol.-%	percentage by volume
VSEPR	valence-shell electron pair repulsion
wt.-%	weight percent
XRD	X-ray diffraction
YAG	yttrium aluminium garnet ($Y_3Al_5O_{12}$)

Contents

1 Introduction and Motivation

1.1 Silicate-Analogous Materials

Natural occurring silicates[i] are the most abundant material on earth with the crust of the earth comprising of at least 90 wt.-% and 95 vol.-% silicates.[1] Their relative crustal abundance is shown in Figure 1.1.1.

The basic building unit of such silicates are SiO_4 tetrahedra - except for rare cases like the high pressure SiO_2 modification *stishovite*, which can be found in the lower mantle of the earth, comprising SiO_6 octahedra.[ii] The crystal structure of silicates can be described by the connection pattern of these tetrahedral building units connected with each other via common corners. For that, Friedrich Liebau's classification and nomenclature is used and later adapted, herein.[1] There are nesosilicates with non-condensed SiO_4 tetrahedra (0D), sorosilicates with spacial restricted groups of tetrahedra, often also called molecular anions (0D), cyclosilicates with rings of tetrahedra (0D), inosilicates with chains of tetrahedra (1D), phyllosilicates with anionic layers (2D) and tectosilicates with the SiO_4 tetrahedra forming a framework (3D). Examples are depicted in Figure 1.1.2. The Si:O ratio determines the topology of the anion. Ratios of 1:4, 1:3, 1:2.5 and 1:2 result in neso- or sorosilicates, cyclo- or inosilicates, phyllosilicates and tectosilicates, respectively. Consequently, silicates are not only the most abundant class of natural occurring inorganic compounds, but also the one with the greatest structural diversity. More than 1000 natural and several hundreds of synthetic silicates are known.[2]

The immense structural diversity can be even further increased by chemical partial or full substitution of the tetrahedral building unit TX_4 (T = Si; X = O for silicates). Such materials called "silicate-analogous" are in the centre of attention in this work. The most common ones are alumosilicates (T = Al, Si, X = O) occurring both naturally and synthetically. For nitridosilicates (T = Si; X = N), the structural diversity is further increased since nitrogen can be triply or even quadruply bridged and enable edge-sharing tetrahedra. Additional substitution variants - all substituting the central silicon atom completely - include tungstates (T = W; X = O), sulfates (T = S; X = O), borates (T = B; X = O) with more variable structures due to additional trigonal planar BO_3

[i] For this consideration, the binary oxide SiO_2 is included which is strictly speaking no silicate since this term only refers to anionic Si-O structures, more precisely to salts of silicic acid.

[ii] This rarity can be easily explained by electrostatic arguments since the average O-O distance is smaller in the octahedral than in the tetrahedral configuration and therefore, the electrostatic repulsion between adjacent oxygen anion is increased.[1]

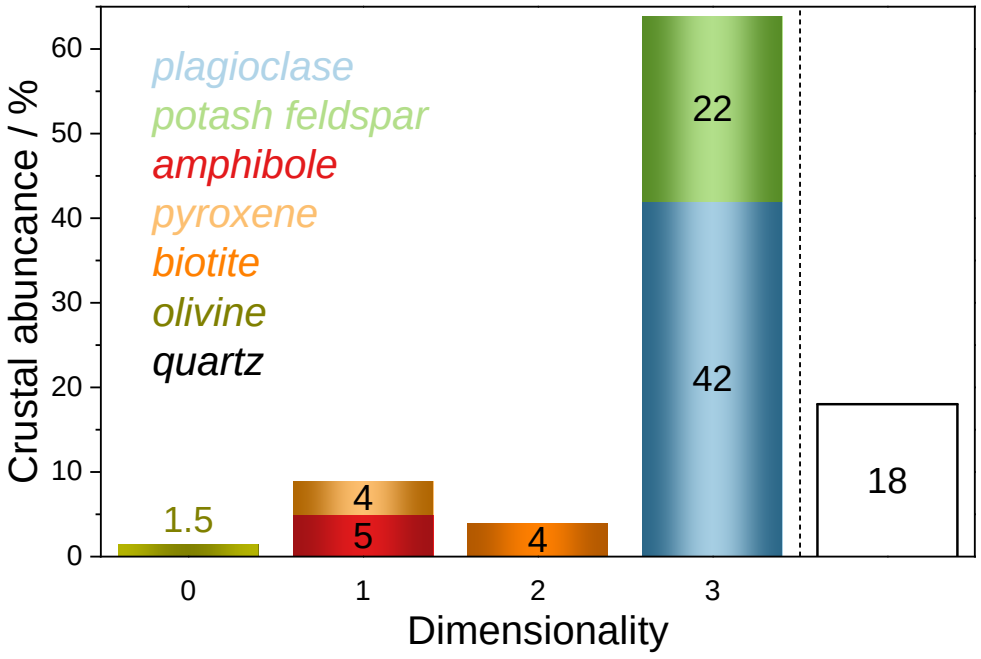

Fig. 1.1.1: Crustal abundance of the most important silicates after [3]: They are sorted by the dimensionality of their anion, i.e. *plagioclase* is a tectosilicate et cetera. *Quartz* (SiO_2) is listed separately since it is strictly speaking no silicate. Non-silicate minerals are neglected. The important ones are *magnetite* (Fe_3O_4) and *ilmentite* ($FeTiO_3$) with 2 vol.-%, and *apatite* ($Ca_5(PO_4)_3(OH, F, Cl)$) with 0.5 vol.-%. For all minerals, the respective sum formulae are given - where appropriate in the generalised form.[1,4–6] The substitution of Si^{4+} by Al^{3+} or others is omitted in the sum formulae for clarity. Only dominating cations are listed. The sum formulae are $Na_{1-x}Ca_xAl_{1+x}Si_{3-x}O_8$ for *plagioclase*, $KAlSi_3O_8$ for *potash feldspar*, $A_{0\ldots1}A'_2A''_5Si_8O_{22}X_2$ ($A = Na^+, K^+$; $A' = Ca^{2+}, Na^+, Mg^{2+}, Fe^{2+}, Mn^{2+}, Li^+$; $A'' = Mg^{2+}, Fe^{2+}, Mn^{2+}, Li^+$; $X = (OH)^-, F^-, Cl^-, O^{2-}$) for *amphibole*, $MM'Si_2O_6$ ($M = Mg^{2+}, Fe^{2+}, Mn^{2+}$; $M' = Mg^{2+}, Fe^{2+}, Mn^{2+}, Ca^{2+}$) for *pyroxene*, $K(Mg, Fe, Mn)_3AlSi_3O_{10}(F, OH)_2$ for *biotite* and $(Mg, Fe)_2SiO_4$ for *olivine*, respectively.

building units and the two double substituted material classes of borophosphates (T = B, P; X = O) and borosulfates (T = B, S; X = O).

All these silicate and silicate-analogous materials have a wide range of applications from the glass and ceramics industry over catalysts and molecular sieves to phosphors and other compounds with interesting optical properties. Many of these applications are based on the structural feature of the absence of an inversion centre for the fundamental tetrahedral building unit, i.e. fostering non-centrosymmetric coordination environments around emitting cations and thus promoting high luminescent probabilities or even non-linear optical properties if the whole crystal structure lacks inversion symmetry.[1,7–12]

In the following, the almost exclusively silicate-analogous material classes covered in this thesis are introduced.

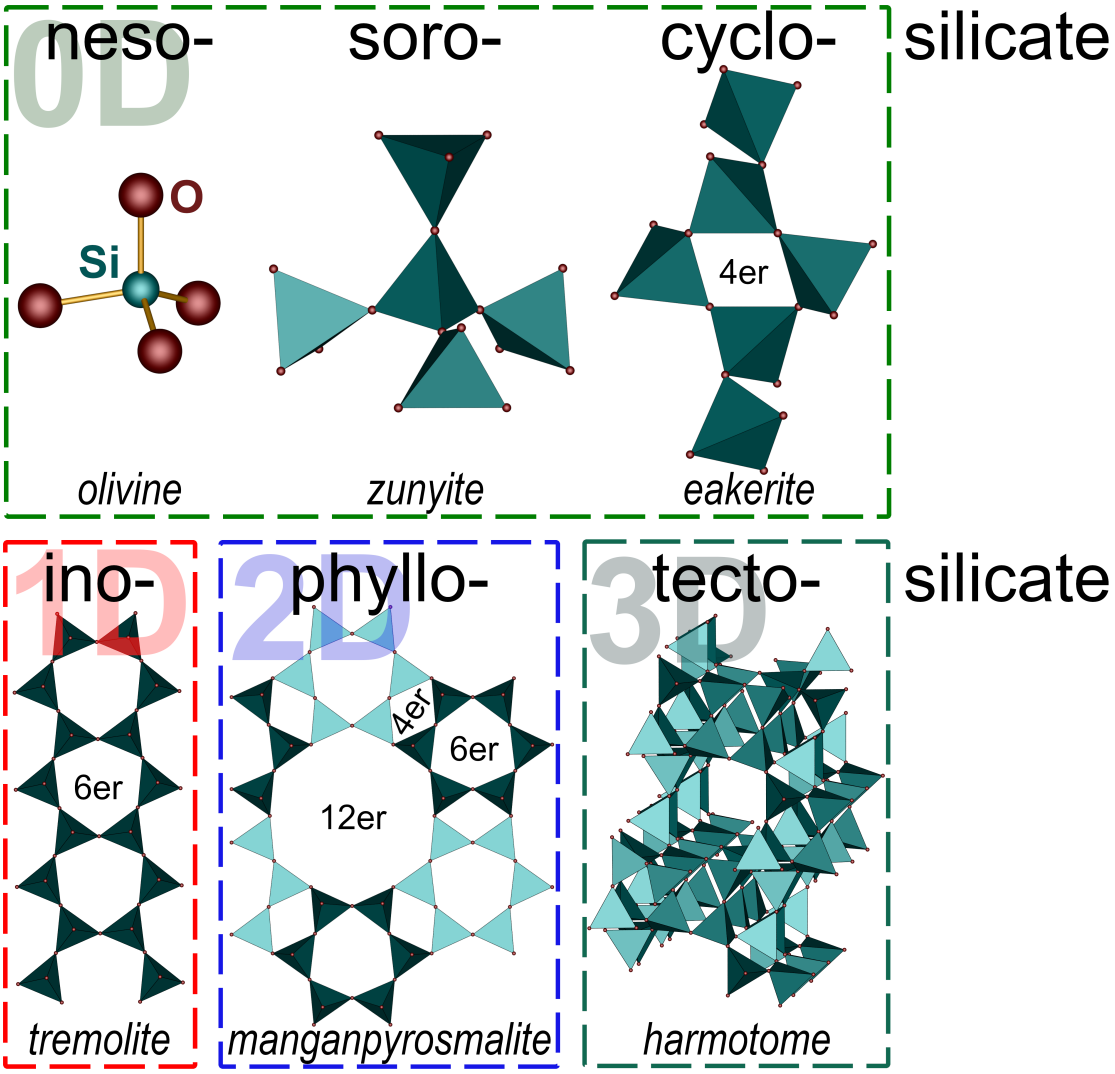

Fig. 1.1.2: Examples of silicate anions with all possible dimensionalities, i.e. neso-, soro-, cyclo-, ino-, phyllo- and tectosilicates. For non-zero dimensionalities, naturally only a characteristic excerpt of the anionic substructure is shown. Where applicable, the periodicity of the respective rings is labelled. Most commonly, the periodicity of these rings is described by the terms *vierer*, *sechser* and *zwölfer* ring using the German numeral and the suffix "er". Due to the lack of space in the graph it is abbreviated by the Arabic numeral. However, the long version is used in the following text. The respective sum formulae of the depicted silicates are Mg_2SiO_4 for *olivine*,[13] $Al_{13}Si_5O_{20}(OH)_9F_9Cl$ for *zunyite*,[14] $Ca_2SnAl_2Si_6O_{18}(OH)_2 \cdot 2\,H_2O$ for *eakerite*,[15] $Ca_2MgSi_8O_{22}(OH)_2$ for *tremolite*,[16] $(Mn, Fe)_{16}Si_{12}O_{30}(OH)_{17}Cl_3$ for *manganpyrosmalite*[17] and $Ba_2Al_4Si_{12}O_{32} \cdot 12\,H_2O$ for *harmotome*.[18]

1.2 Carbon-based Precursor Compounds

Not only in the context of so-called soft chemistry or chimie douce,[19] precursor materials are highly interesting. On the one hand, they can facilitate new - often less energy intensive - synthesis routes, e.g. at lower temperatures by enhanced diffusion. On the other hand, the synthesis of the final product is often possible by thermal decomposition of the precursor without any significant changes to size and shape, therefore, enabling the control of the morphology of the product. This is interesting since the size and shape of for example lanthanide based materials can influence their optical properties like emission spectra or quantum efficiencies.[20,21] Good precursors should be inexpensive, readily available, and defined and homogeneous in stoichiometry and composition.[20–24] In chapter 4, two types of carbon-based precursors are presented which both fulfil these requirements.

1.3 Tungstates

Tungstates are an extensively researched class of materials with reports dating back well into the 19th century.[25–27] They comprise frequently either nesosilicate-analogous WO_4 tetrahedra, WO_5 trigonal bipyramids, WO_6 octahedra or WO_7 pentagonal bipyramids as shown in Figure 1.3.1. WO_4 tetrahedra are always non-condensed due to the high charge of the central W^{6+} cation and the consequent electrostatic repulsion of adjacent cations. So far, the anion of $R_2(WO_4)_3$ (R = La, Ce, Nd, Eu, Dy)[28–32] comes the closest to a sorosilicate-analogous tungstate anion with a coordination that can be described as $4+1$. WO_6 octahedral building units are most commonly condensed and connected to each other via common corners or edges. Consequently, this leads to a significant flexibility in the structures adapted by tungstates and therefore, to a huge range of applications for this material class from laser host materials, photonics in general over sensors to phosphors.[33–39]
The most important naturally occurring minerals of this material class are *scheelite* ($CaWO_4$) and *wolframite* ($(Fe,Mn)WO_4$)[iii] - the two most important ores of tungsten.[40] They both crystallise in their own structure types which are also adapted by the double tungstates discussed in section 5.2. The respective unit cells are shown in Figure 1.3.2. Detailed structure descriptions are given in the following.
Despite of - or better on the shoulders of - past research, there are still gaps of knowledge in the material class of tungstates. Herein, such are filled for the highly related compound groups of pentasodium rare earth tetratungstates $Na_5M(WO_4)_4$ (M = La-Nd, Sm-Lu, Y, Bi) and alkali rare earth double tungstates $AM(WO_4)_2$ (A = Li, Na, K, M = Y, La, Pr, Tb, Bi) in chapter 5.

[iii] To be precise, *wolframite* does not describe a discrete mineral, but the solid solution series between *ferberite* $FeWO_4$ and *hübnerite* $MnWO_4$.

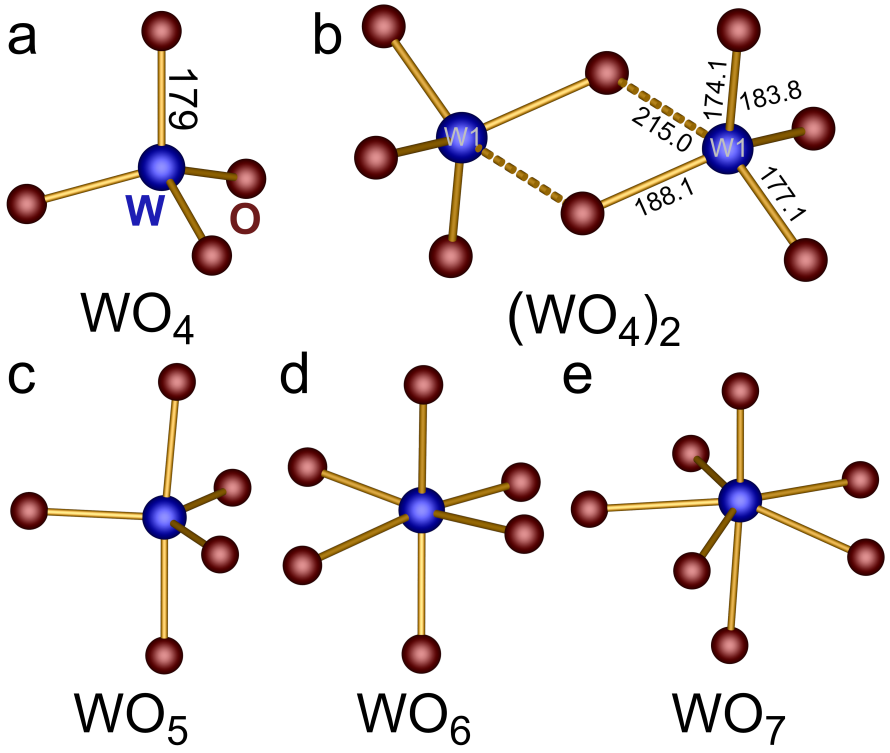

Fig. 1.3.1: Overview over common polyhedra found as part of the anionic substructure of tungstates; W-O distances are given in pm: (a) the WO_4 tetrahedral building unit (shown for $NaEu(WO_4)_2$ from the SC-XRD in section 5.1) can be classified as nesosilicate-analogous; (b) $Nd_2(WO_4)_3$[30] comes the closest to a sorosilicate-analogous tungstates; the WO_5 (c), WO_6 (d) and WO_7 (e) building units are shown for K_4WO_5,[41] $LiY(WO_4)_2$ (from the SC-XRD in section 5.2) and $WO(SO_4)_2$,[42] respectively.

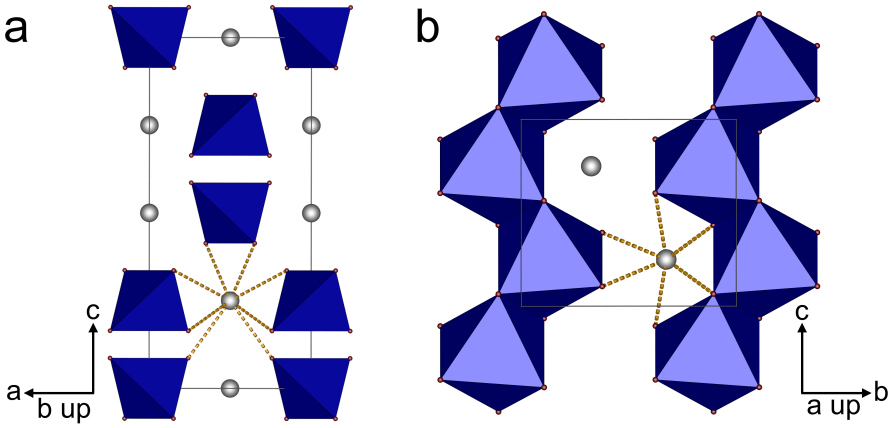

Fig. 1.3.2: Unit cells of (a) *scheelite* $CaWO_4$ comprising non-condensed WO_4 tetrahedra and CaO_8 dodecahedra (space group $I4_1/a$ (no. 88), a = 524 pm, c = 1138 pm)[43] and (b) *ferberite* $FeWO_4$ representing the *wolframite* structure type comprising zigzag-chains of edge sharing WO_6 octahedra and octahedrally coordinated iron (space group $P2/n$ (no. 13), a = 475 pm, b = 572 pm, c = 497 pm, $\beta = 90.2°$);[44,45] tungsten atoms blue, oxygen atoms red, calcium and iron atoms grey; a more detailed description of these structure types is given for isotypic $AM(WO_4)_2$ in chapter 5.

1.4 Sulfatotungstates

Herein, sulfatotungstates are defined as compounds comprising both sulfate and tungstate moieties as well as S-O-W bridges linking the two of them - excluding polyoxometalates also including S-O-W bridges.[46] They are a rather young and small material class. Namely, $K_8[W_2O_4(SO_4)_6]$,[47]$Rb_8[W_2O_4(SO_4)_6]$,,[48] $R_2[W_2O_3(SO_4)_6]$ (R = Sm, Eu, Gd, Ho)[49] and $WO(SO_4)_2$[42] are all compounds with known crystal structure so far - comprising only three different anion types (Figure 1.4.1). In chapter 6, a new member, $Cs_6[(WO_2)_2O(SO_4)_4]$, with an unprecedented anion is added to this material class.

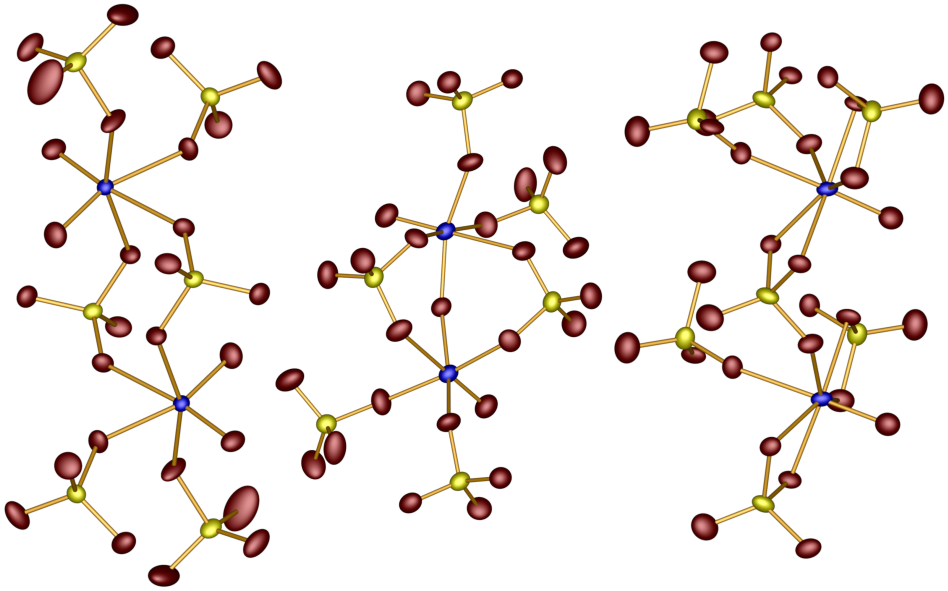

Fig. 1.4.1: Anions of $K_8[W_2O_4(SO_4)_6]$,[47] $Eu_2[W_2O_3(SO_4)_6]$[49] and $WO(SO_4)_2$[42] from left to right: In both $K_8[W_2O_4(SO_4)_6]$ and $Eu_2[W_2O_3(SO_4)_6]$, the anions comprising corner-sharing WO_6 octahedra and sulfate tetrahedra are non-condensed, while the anion of $WO(SO_4)_2$ formed by WO_7 polyhedra and sulfate tetrahedra sharing both edges and corners form a layer via common sulfates; only a section of this layer is depicted; tungsten blue, sulfur yellow, oxygen atoms red; all ellipsoids are shown at 80% probability.

The first sulfatotungstates originated from research on catalysts to oxidise SO_2 to SO_3 in the sulfuric acid production. There, transition metal oxides are dissolved in molten alkali pyrosulfates confirming that $K_2S_2O_7$ is able to dissolve not only WO_3 but also V_2O_5, Nb_2O_5, Ta_2O_5 and MoO_3.[50–54] For all sulfatotungstates, merely the crystal structure was determined and for $R_2[W_2O_3(SO_4)_6]$ (R = Sm, Eu, Gd, Ho) and $WO(SO_4)_2$ the thermal decomposition was investigated. No further characterisation was performed.

From an electrostatic point of view, it is fascinating that these condensed building units formed by polyhedra with central cations with the nominal charge +6 are stable in the solid state, even sharing edges in the case of $WO(SO_4)_2$ contradicting Pauling's third rule.[55]

1.5 Sulfates

The salts of sulfuric acid are called sulfates. Most commonly, their anion, tetrahedral SO_4^{2-}, can be described as nesosilicate-analogous (Figure 1.5.1a). However, there are also sorosilicate-analogous sulfates with the longest chain featuring six SO_4 tetrahedra (*sechser* chain) in $A_2[S_6O_{19}]$ (A = NH_4, Rb)[56] (Figure 1.5.1b). This is much shorter than for silicates with the "record" sorosilicate $Na_{24}Y_8[Si_{24}O_{72}]$[57] comprising a 24er chain. The reason for that - and for the fact that there are no reports on any sulfates with anions with dimensionalities larger than zero - can be found in the higher charge of S^{6+} hampering the stability of condensed anionic substructures.

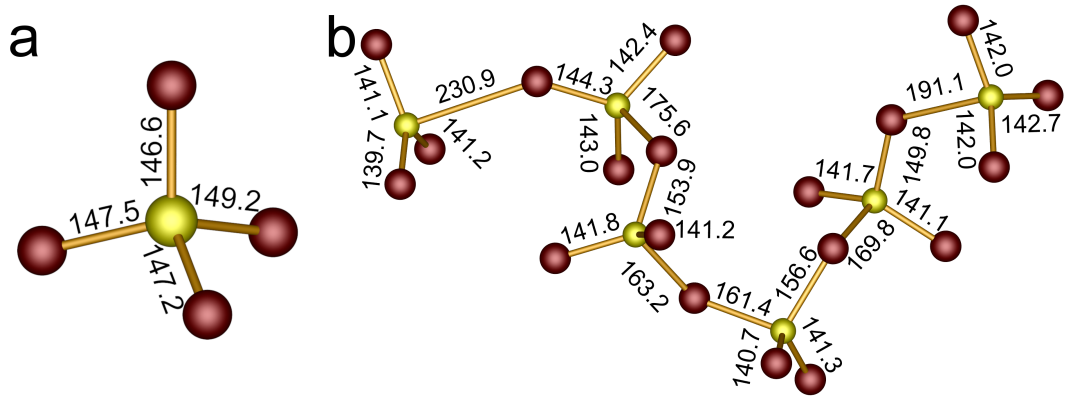

Fig. 1.5.1: Range of possible sulfate anions: in (a) the nesosilicate-analogous sulfate anion of $Bi_2(SO_4)_3$ (from the SC-XRD in section 7.2) and in (b) the sorosilicate-analogous *sechser* chain sulfate anion in $(NH_4)_2[S_6O_{19}]$[56] are shown together with the respective S-O distances in pm from SC-XRD data; oxygen atom red, sulfur atoms yellow.

Herein, yet unreported or not extensively studied sulfates of the cations tin and bismuth are presented. Both Sn^{2+} and Bi^{3+} are s^2 ions able to exhibit the lone pair effect. Thus, a short excursion covering the underlying chemistry is included here.

Jahn-Teller Effect, Pseudo Jahn-Teller Effect and Lone Pair Effect

The so-called theorem of structural instability states that the Jahn-Teller effect and the pseudo Jahn-Teller effect "are the only source of structural instability of polyatomic systems in the high-symmetry configuration."[58]
The Jahn-Teller theorem from 1937 states that any nonlinear system with an orbital degeneracy is electronically unstable and thus, distorts in such a way that the degeneracy is removed.[59,60] In the case of Cu^{2+} (d^9), this results in elongated octahedral coordination for the most part. Being based solely on symmetry arguments, the theorem does not state anything about the strength of the distortion. This appears to be governed by cooperative effects[61] between for example the Cu^{2+} cation and the anionic substructure or - in other words - by the total energy gain for the whole polyatomic system by the distortion introduced by the Jahn-Teller effect. This effect is discussed in more detail in

section 9.2. While this first effect is only present in systems with degenerate electronic states, the second effect exists in all polyatomic systems. The pseudo (or second-order) Jahn-Teller effect (PJTE) describes the extension of the original Jahn-Teller theorem onto systems with nondegenerate electronic states close in energy, i.e. pseudodegenerate ground and excited states.[58,62] In this case, the Jahn-Teller distortion does not vanish, but is modified and structural distortions are produced. Notably, there is no limit for the energy gap between the interacting ground and excited states. Nature tends to avoid degeneracy or pseudodegeneracy by symmetry breaking if there are degrees of freedom to do it. The PJTE distortion takes place if the energy gain by the additional covalent bonding is higher than energy loss due to the distortion away from the symmetric arrangement. It is produced by the interaction of occupied orbitals of one type of atom and unoccupied orbitals of another type of atoms. Since the related wave functions are orthogonal in the high symmetry configuration, distortion is necessary for this interaction to happen.[58]

In a less general way, the so-called lone pair effect, i.e. the stereochemical activity of ions with a s^2 electron configuration distorting the coordination environment of such ions away from symmetric arrangements, can be considered as a special form of the pseudo Jahn-Teller effect. There is a variety of semiempirical models to describe this effect with the most prominent one still being Gillespie's valence-shell electron pair repulsion (VSEPR) model[63–65] and its extension by Andersson and Galy.[66,67] Representing the classical view on the lone pair effect,[68] the VSEPR concept explains the local symmetry of the s^2 cation and the coordinating atoms by the repulsion of bonding and lone electron pairs. The latter is formed by the s^2 electrons of the cation. Thus, Bi^{3+} - for example - may occur in four different stereochemistries: distorted trigonal planar BiO_2E, distorted tetrahedral BiO_3E, distorted trigonal bipyramidal BiO_4E and distorted octahedral or square-bipyramidal BiO_5E with E representing an active lone pair.

The modern view on the lone pair effect could show that there is no such thing as a lone or non-bonding electron pair.[69–71] The stereochemical activity is governed by bond energy effects. The cation s states and the anion p states interact strongly giving rise to bonding and antibonding states. The latter interact with empty p states of the cation. This covalent interaction is stabilised - or in the sense of the PJTE caused - by the distortion away from a highly symmetric coordination environment, i.e. away from the centroid of the respective coordination polyhedron, and is usually accompanied by diverging bond lengths. The asymmetric electron density is formed by the antibonding part of this interactions, i.e. in the case of a bonding interaction with p-character - as often found for SnO_3 building units for example - the "lone pair" electron density cloud comprises the rear side of the p orbitals of the metal that are bond to the p orbitals of the anion on the front. The lone pair effect, i.e. the stereochemical activity can be either expressed or quenched. This depends on the energy gain by the respective distortion and the available degrees of freedom. Walsh et al. identify the relative energetic position of the ligand p states as one crucial parameter for the expression of stereoactivity.[70,72]

Accordingly, the larger the energetic gap between the metal s states and the ligand p states, the weaker the driving force for expression of the lone-pair effect. This follows a similar thought by Atanasov and Reinen who identified the overall chemical hardness as crucial parameter[69] – the harder the chemical moiety containing the s^2 ion, the stronger the expression. As a general trend, the stereochemical activity is less pronounced when going from the top to the bottom of the periodic table due to increasing relativistic stabilisation of the s electrons.[70]

In this work, the lone pair effect is assessed for compounds containing s^2 ions by the method of Balić-Žunić and Makovicky (section 3.6.2) and additional DFT and ELF calculations as detailed in sections 3.6.2 and 3.6.3.

1.6 Borosulfates

Borosulfates are a young, ever-expanding and fascinating class of silicate-analogous materials. Despite the first reports - both in 1962 - by Schott and Kibbel on "sulfatoborates" prepared by the reaction of metal sulfates, boric acid and oleum yielding various compounds and their sum formulae based on gravimetry and acidimetric titration, namely $A[B(SO_4)_2]$ (A = Li, Na, K, (NH_4), Rb, Cs, Ag, Tl), $A[B(SO_4)_2]_2$ (A = Mg, Ca, Sr, Ba, Pb, Mn, Co, Ni, Cu, Zn, Cd, Hg) and $A[B_2O(SO_4)_3]$ (A = Ca, Sr, Ba),[73] and by Gillespie and Robinson on white precipitates during their investigation on the super acid tetrahydrogensulfato boric acid $HB(HSO_4)_4$,[74] it took until 2012 for the first crystal structure to be determined for the borosulfate $K_5[B(SO_4)_4]$ by Höppe et al.[75] The structure comprises complex anions formed by central borate tetrahedron connected via common corners to four sulfate tetrahedra. This anion being structurally related to the mineral *zunyite* (Figure 1.1.2) already shows how borosulfates can be classified as silicate-analogous in two ways: On the one hand, their anions consist - except for rare cases[76,77] - of corner sharing borate and sulfate tetrahedra, solely. Both can be considered silicate-analogous individually. On the other hand, such structures can be understood by considering supertetrahedra TX_4 formed by a boron atom acting as centre T coordinated tetrahedrally by four SO_4 moieties X as frequently observed in the building unit $[B(SO_4)_4]^{5-}$. The $[B(SO_4)_4]^{5-}$ supertetrahedron is shown in Figure 1.6.1 in four different ways of viewing it. Consequently, the T:X ratio has the potential to determine the topology of the anion as well-known for silicates. However, these supertetrahedra are able to share edges resembling the connection pattern of SiS_4 tetrahedra in SiS_2 forming chains.[78] Thus, the topology is not strictly governed by the T:X ratio.

The first way, $K_5[B(SO_4)_4]$ can be considered sorosilicate-analogous, while it is classified as nesosilicate-analogous in the second way. It is helpful to discuss borosulfates in the second way due to the better comparability to other silicate-analogous compounds or even to silicates and the easier description for high dimensional structures.

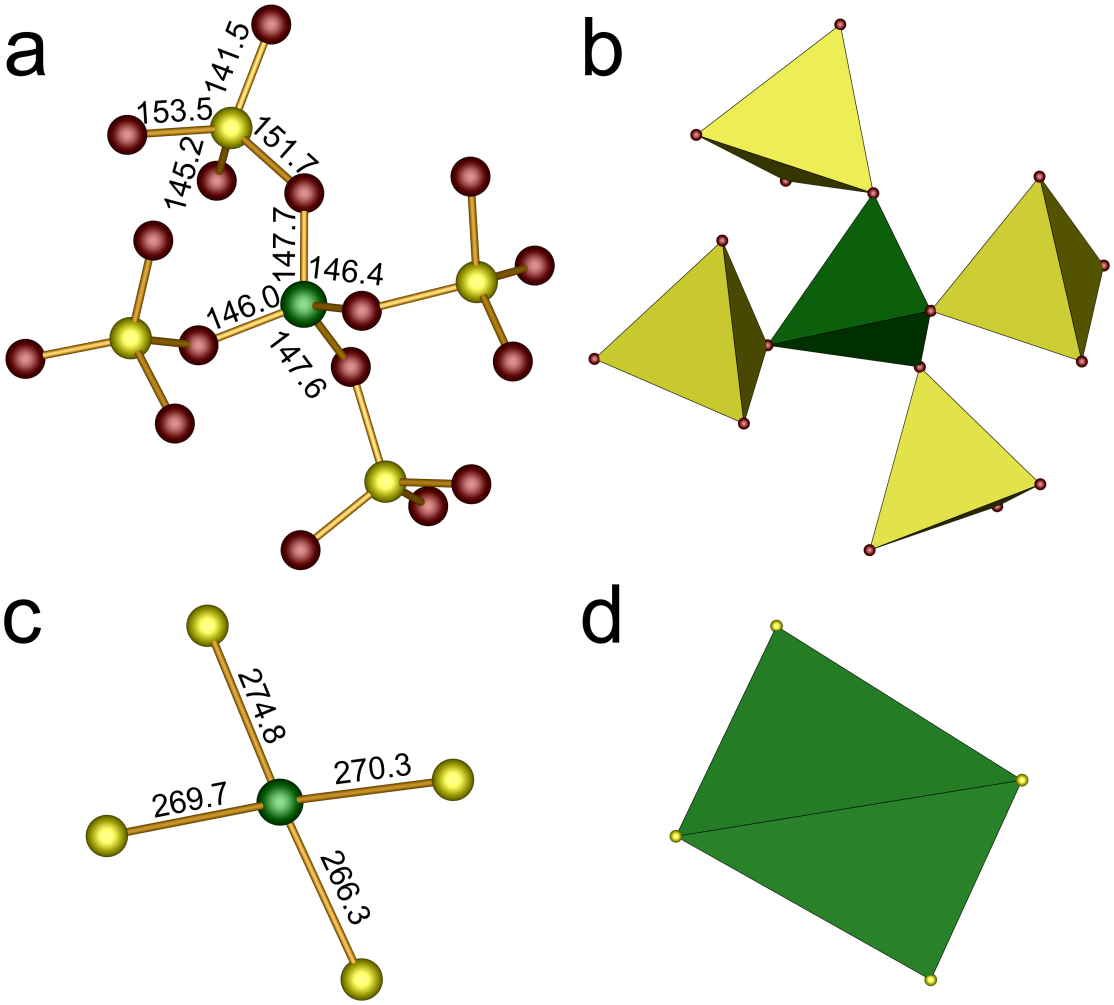

Fig. 1.6.1: Typical $[B(SO_4)_4]^{5-}$ supertetrahedron building unit of borosulfates shown for $Bi(H_3O)[B(SO_4)_2]_4$ (from SC-XRD discussed in section 8.2): In (a) and (b) the single borate and sulfate tetrahedra are shown; in (c) and (d) the oxygen atoms are neglected to emphasise the supertetrahedra; oxygen atoms red, sulfur atoms yellow, boron atoms green, respective polyhedra likewise, supertetrahedra light green; the distances are given in pm; note, that $Bi(H_3O)[B(SO_4)_2]_4$ comprises a tectosilicate-analogous anionic substructure explaining the larger S-O distance for one oxygen atom since this is connected to another borate tetrahedron.

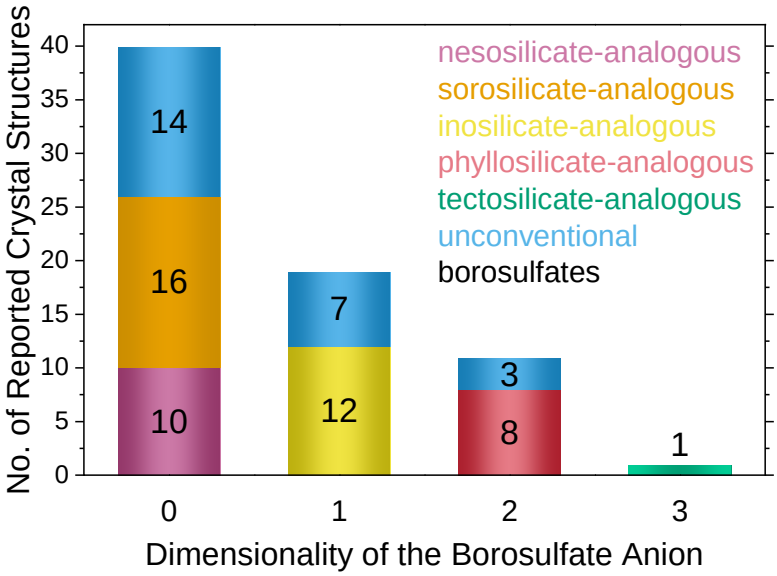

Fig. 1.6.2: Number of reported borosulfates shown with respect to the dimensionality of their borosulfate anion, i.e. the connection of supertetrahedra: The respective silicate-analogies are colour coded; unconventional borosulfates comprise either S-O-S or B-O-B, or trigonal planar BO_3 building units; the borosulfates presented in this work are excluded from this graph.

The majority of the compounds reported by Schott and Kibbel[iv] and Gillespie and Robinson[v] could be confirmed and their crystal structure could be determined. A more detailed account on the history of borosulfates can be found in [93, 94].

As of today, there are 72 borosulfates with reported crystal structures - excluding the compounds presented in chapters 8 and 9. Borosulfates can be classified by the dimensionality of the borosulfate anion, i.e. the connection of supertetrahedra, adapting Friedrich Liebau's classification of silicates introduced above. There are borosulfates with 0D anions like the nesosilicate-analogous $K_5[B(SO_4)_4]$[75] or the sorosilicate-analogous $R_2[B_2(SO_4)_6]$ (R =Y, La–Nd, Sm–Lu)[92,95] which can be also considered cyclosilicate-analogous by viewing the individual borate and sulfate tetrahedra, 1D anions like the inosilicate-analogous $(NH_4)_3[B(SO_4)_3]$,[85] 2D anions like the phyllosilicate-analogous α- and β-$M[B_2(SO_4)_4]$ (M = Mg, Co)[82,83,89] and 3D anions like the tectosilicate-analogous $Li[B(SO_4)_2]$.[79] In contrast to these so-called conventional borosulfates, there are also unconventional borosulfates comprising S-O-S or B-O-B bridges like $Sr[B_2(SO_4)_3(S_2O_7)]$[96] and $Mg_4[B_2O(SO_4)_6]$[82] violating Pauling's fourth[55] and Loewenstein's rules,[97] respectively. It was shown that the respective reactant governs the bond formation in borosulfates for the cations of barium and strontium.[86,96] Pure oleum promotes the

[iv] Namely, $Li[B(SO_4)_2]$,[79] $Na[B(SO_4)_2]$, $K[B(SO_4)_2]$, $(NH_4)[B(SO_4)_2]$,[80] $Ag[B(SO_4)_2]$,[81] $Mg[B_2(SO_4)_4]$,[82,83] $Ca[B_2(SO_4)_4]$,[84] $Sr[B_2(SO_4)_4]$,[85] $Ba[B_2(SO_4)_4]$,[86] $Pb[B_2(SO_4)_4]$,[87] $Mn[B_2(SO_4)_4]$,[88] $Co[B_2(SO_4)_4]$,[83,89] $Ni[B_2(SO_4)_4]$,[89] $Cu[B_2(SO_4)_4]$,[90] $Zn[B_2(SO_4)_4]$,[88] $Sr[B_2O(SO_4)_3]$,[91] $Ba[B_2O(SO_4)_3]$.[92]

[v] Namely, $K[B(SO_4)_2]$ and $(NH_4)[B(SO_4)_2]$.

formation of disulfate units, i.e. S-O-S bonds, a mixture of oleum and H_2SO_4 exclusively B-O-S bonds and pure H_2SO_4 B-O-B bonds within the respective borosulfates. Further unconventional borosulfates comprise BO_3 building units forming a Lewis acid–base adduct with a water molecule[76] or $^2_\infty[(BO_{3/2})_3(BO_{3/2}(SO_4)]^{2-}$ layers.[77]
As one can see from Figure 1.6.2, borosulfates with high dimensionalities appear to be rare. So far, $Li[B(SO_4)_2]$[79] is the only 3D representative. This might be related to the decreasing thermal[82,83,95] and therefore, global stability of borosulfates with increasing dimensionality. Moreover, charge balance can be easier achieved between high charged B^{3+} and S^{6+} cations with smaller dimensionality. Nevertheless, new tectosilicate-analogous borosulfates could be prepared and extensively characterised in chapter 8.

Additional introductions are given at the beginning of each chapter and section summarising relevant previous research and giving context for the respective work presented in the following.

1.7 Objective of This Thesis

The objective of this thesis is the advancement of fundamental knowledge in the material classes introduced above. It was aimed for the synthesis and characterisation - with special respect to the crystal structure - of new materials or not yet extensively investigated compounds in order to establish structure-property relations and to possibly manipulate them for the purpose of special optical properties. Such materials are applied in the field of lighting. There, huge advantages have been made in the last decades with the introduction of light emitting diodes (LEDs).[98,99] For almost all lighting applications, phosphor converted white LEDs (pcWLEDs) can be used nowadays. In these devices, one or multiple phosphors convert the blue or UV emission from the LED resulting in an overall white emission.[100] However, the technology is still emerging and the research for new phosphors - for example for special applications - is still needed.[101]
Another application are so-called SHG materials. These are compounds exhibiting the second-harmonic generation effect detailed in section 3.2.4, i.e. they have non-linear optical properties. This effect results in the doubling of laser wavelengths enabling the construction of efficient lasers in energy ranges where lasers commonly perform poorly.[102–104] The most prominent example is the green laser pointer. The state-of-the-art material KH_2PO_4 (KDP)[105] is well suited for the excitation with an 1064 nm Nd:YAG laser for the green emission at 532 nm. However, there is extensive research in this field ever-expanding the respective nonlinear optical response beyond the benchmark KDP and also enlarging the range of excitation wavelengths.[103,106–112]
For these purposes, all compound classes introduced above were investigated.
In chapter 4, two types of carbon-based precursors for silicate-analogous materials suited as hosts for Eu^{2+} and Eu^{3+} ions, respectively and therefore, interesting for phosphors are investigated. While with $Sr_3(C_6H_5O_7)_2 \cdot H_2O$ a hitherto unreported compound is

presented, ambiguity with respect to the crystal structure of the family $Ln[CO_3][OH]$ (Ln = La, Pr, Nd, Sm, Eu, Gd, Tb) is elucidated applying - among other techniques - SHG measurements for the unambiguous clarification of the respective crystal structures.
In chapter 5, rather "old" tungstates comprising anions formed by both alkali and rare earth metals excellently suited as phosphors due to the tungstate moiety acting as an antenna are revisited. For the first time, the group $Na_5M(WO_4)_4$ (M = Y, La-Nd, Sm-Lu, Bi) is systematically studied over the whole range of M^{3+} ions. The second compound group $AM(WO_4)_2$ (A = Li, Na, K) is closely related to the former. Besides the structural, thermal and magnetic ones, the optical properties of both were investigated with special interest on the energy transfer mechanisms within these compounds since they are highly relevant for their application as luminescent materials.
In chapter 6, a new member is added to the small class of sulfatotungstates exhibiting excellent potential for luminescent materials combining the weak coordinating sulfate moiety and the tungstate group acting as an antenna. So far, it was not shown if the latter is actually "working" in such materials.
In chapters 7 and 8, a deeper understanding of the ternary and quaternary systems of Sn-S-O, Bi-S-O and Bi-S-O-H is aimed as all systems are yet poorly studied. Such understanding might be interesting from a fundamental knowledge point of view but also with respect to the synthesis of more complicated systems like borosulfates where such sulfates might act as obstacle for the synthesis of the borosulfate compound. Moreover, as the sulfate moieties coordinate the stereochemical active cation in both sulfates and borosulfates, the influence of the lone pair effect and potential resulting distortions of the crystal structure are of interest. This influence should not be underestimated.[vi]
Besides the enhancement of the elemental diversity of borosulfates by the first-time introduction of Bi^{3+} and Sb^{3+} cations, chapter 8 answers the question whether two differently charged cations can be incorporated into one borosulfate. Additionally, a new structural motif is introduced in form of the tectosilicate-analogous anion increasing the number of three-dimensional borosulfates significantly. Moreover, these borosulfates show promising SHG activities.
Finally, insights on transition metal borosulfates are presented in chapter 9. This group exhibits polymorphism frequently, while such behaviour is very rare for all other borosulfates. It is possible for these polymorphs to differ in the dimensionality of their anion? Furthermore, transition metal borosulfates are suited to investigate the coordination behaviour of the borosulfate anion analysing their optical properties.

Consequently, the objectives of this thesis can be summarised as the establishment of structure-property relations of various silicate-analogous materials by synthesising them, determining their crystal structure and investigating their optical, magnetic and thermal properties.

[vi] For example, the thermoelectric properties of PbTe could only recently be fully understood taking into account the stereochemical activity - despite this material serving well in several space research programs for decades.[113]

2 Preparative Methods

2.1 Solid-State Synthesis

Solid-state synthesis - also referred to as ceramic method or shake'n'bake method - is the oldest, simplest and mostly used method for the preparation of inorganic solids.[114,115] Hereby, various powdered solids are mixed together - usually using an agate mortar and pestle for intensive grinding in order to increase the surface and contact area of the educts - frequently representing the elemental stoichiometry of the desired product. Subsequently, the mixture is heated for several hours to days at elevated temperatures. Relatively high temperatures and long duration are required to increase the intrinsically slow diffusion rates since the starting materials are even after extensive grinding very inhomogeneous on the atomic level. Diffusion occurs via lattice vacancies as demonstrated by the Kirkendall effect.[116] As a rule of thumb, at temperatures of two thirds of the melting point of at least one of the starting materials, a reasonable fast diffusion rate is achieved.[115] Such high temperatures require the used containers to both withstand them and to be inert enough to not take part in the reaction. Commonly, - and in this work - containers made from platinum, corundum, silica or porcelain are used. Further, various muffle and tube furnaces were used either at air or with controlled atmospheres, e.g. via nitrogen flow.
The obvious advantages of simple sample preparation, the abundance of available starting compounds and often good up-scaling are opposed by the disadvantages of huge energy requirements and the formation of merely thermodynamically stable products often including undesired side phases.

2.2 Crystal Growth via Precipitation from Melt

Single-crystals can often be grown from the melt via precipitation or recrystallisation.[114] Therefore, the sample is heated inside a platinum crucible above its melting point and after a certain holding time slowly cooled. A slow cooling rate ensures the formation of crystal with a small number of defects. In order to reduce the melting point of the heated sample, a so-called flux can be added. The flux being in the liquid or even gaseous state at the reaction temperature enhances the diffusion rate. This might be necessary due to a phase transition of the sample at temperatures below the melting point or due to practical reasons such as the temperature limits of the available furnaces. Flux syntheses are also possible as an enhancement of solid-state reactions by increasing diffusion rates

without the whole educt mixture melting during the heating cycle. Additionally, syntheses including the melting of the mixture of starting materials are possible inside sealed and evacuated silica glass ampoules if the mixture is not melting at air.

2.3 Molten Salt Synthesis

The molten salt synthesis can be viewed as a special case of flux synthesis. Here, the added compound - usually a water-soluble and low melting salt - is added in vast excess to increase diffusion rates by its melt enclosing the actual reactants. However, in contrast to the flux synthesis the molten salt is acting not only as solvent but also as reactant. After the heating cycle the molten salt can be dissolved leaving behind the desired product. Consequently, the required temperature and required time can be significantly reduced compared to solid-state reaction.[114] Additionally, single-crystals can be formed by this method without the need for further recrystallisation from the melt.[117]

2.4 Hydrothermal Synthesis

Hydrothermal syntheses imitate natural geological processes. Therefore, the reactants and water acting both as pressure-transmitting medium and solvent are placed inside PTFE-lines containers. These so-called autoclaves are sealed and heated in order to achieve high pressuresinside the reaction chamber. Heat can be applied by placing the autoclave in either a furnace or a compartment dryer in conventional hydrothermal synthesis, i.e. requiring in-diffusion of heat, or by microwave radiation in the case of the microwave-assisted hydrothermal method. While for the former the reaction times range in days, they are reduced by two or three orders of magnitude with usual reaction times of several minutes for the latter.[114,115,118] The conventional hydrothermal syntheses in this work were conducted using 30 ml PTFE pressure digestion vessels[119] and the microwave-assisted variation using a CEM Discover S microwave reactor and 10 ml borosilicate glass sample tubes. The advantages of hydrothermal synthesis are the rather low required temperatures, the ability to solve otherwise insoluble starting materials, the accessibility of non-thermodynamically stable products and the frequent formation of highly crystalline products even containing single-crystals.

2.5 Solvothermal Synthesis

Solvothermal syntheses are similar to hydrothermal syntheses using other solvent than water. In this work, sulfuric acid with various SO_3 contents was used as both solvent and reactant in the synthesis of various sulfates and borosulfates by filling the solid starting materials together with the solvent in silica glass ampoules, which were subsequently sealed using an oxyhydrogen flame under normal pressure. The ampoules were heated

inside a muffle furnace. Afterwards, they were cooled in liquid nitrogen and opened with a glass cutter. Using this synthesis method single-crystals can be obtained frequently.

2.6 Handling of Hygroscopic Products

Since various products - especially the ones prepared by the preceding solvothermal synthesis, i.e. all compounds in chapters 7 to 9 - are highly hygroscopic, these were handled with special care. Therefore, the opened ampoule was stored inside a nitrogen flushed Schlenk flask directly after opening. After warming to room temperature, excess sulfuric acid was removed by decantation and the product was washed three times with in total 6 ml dry acetonitrile CH_3CN (100%, VWR) inside a nitrogen flushed Schlenk line with a ceramic frit for vacuum filtration. The experimental setup is shown in Figure 2.6.1. Then, the product was transferred to an argon filled glovebox (MBraun UniLAB, typical values: < 0.1 ppm H_2O, < 0.1 ppm O_2) and stored there for further characterisation.

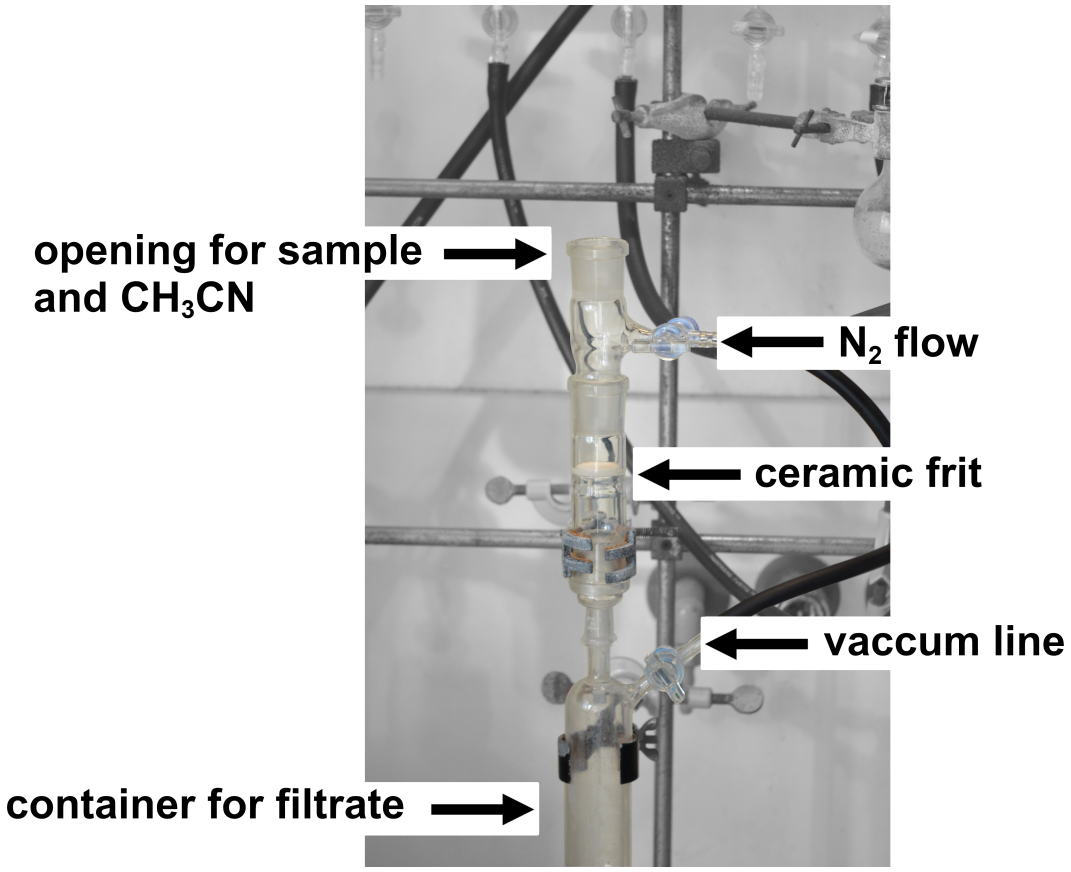

Fig. 2.6.1: Experimental setup for washing of the hygroscopic products with acetonitrile.

3 Analytical Methods

3.1 X-Ray Diffraction

X-ray diffraction (XRD) is presumably the most important analytical method in solid-state chemistry since it is used for both structural analysis via single-crystal XRD (SC-XRD) and phase analysis via powder XRD (PXRD) of crystalline solids.
All crystalline compounds possess a three-dimensional periodical lattice. XRD is based on the interaction of monochromatic electromagnetic radiation with energies in the range of 200 eV to 1 MeV with the electron clouds of the atoms in this periodic arrangement. X-rays are generated by focussing an electron beam onto an anode. A typical spectrum is shown in Figure 3.1.1. K_α radiation is focussed on the sample using a monochromator.

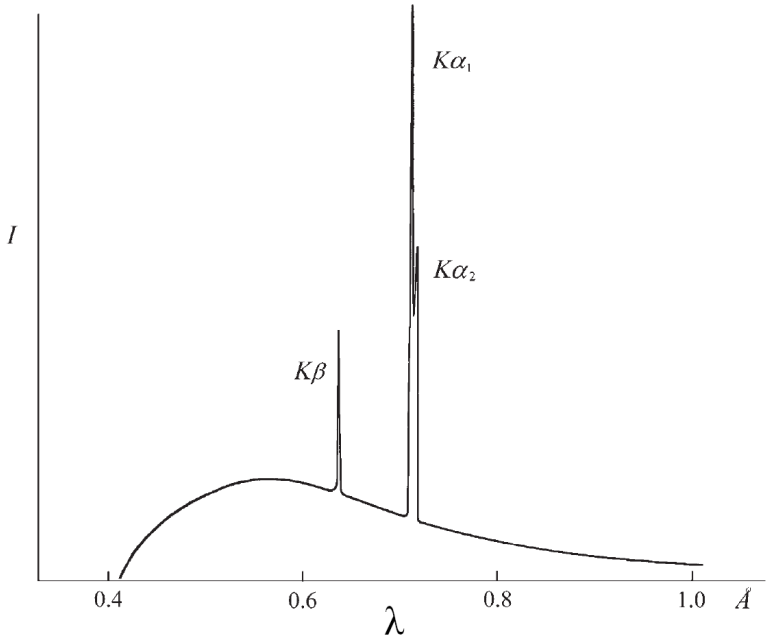

Fig. 3.1.1: X-ray spectrum of a Mo X-ray tube comprising both *Bremsstrahlung* and the characteristic *K* bands.[120]

Since the wavelength of these X-rays - copper ($\lambda_{\mathrm{Cu}-K_\alpha} = 1.54178\,\text{Å}$) and molybdenum radiation ($\lambda_{\mathrm{Mo}-K_\alpha} = 0.71073\,\text{Å}$) was used in this work - is in the order of the lattice constant of a crystal, elastic scattering occurs (Figure 3.1.2). The crystalline solid acts as a three-dimensional diffraction grating with destructive and constructive interference

taking place. The latter phenomenon, which occurs when the path difference equals an integer multiple of the wavelength, is described by Bragg's law:

$$2d\sin(\Theta) = n\lambda$$

d : distance of lattice planes, Θ :incident angle, n : integer, λ : wavelength.

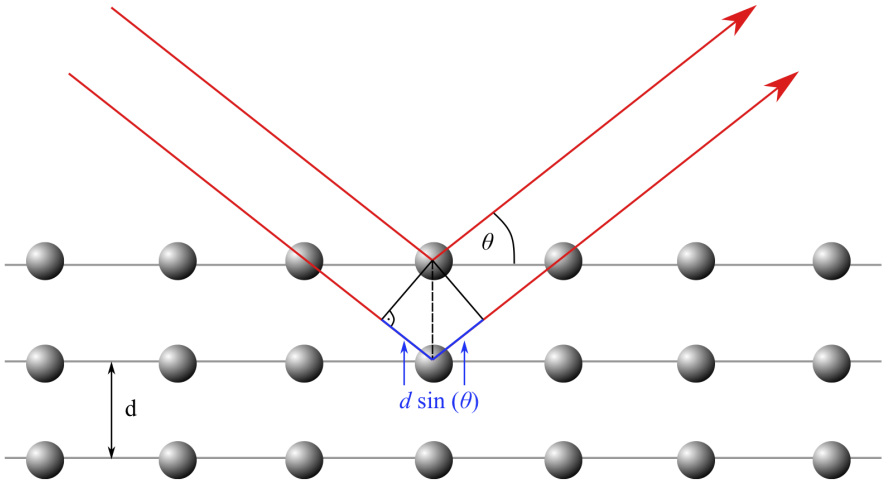

Fig. 3.1.2: Scattering of X-rays in a crystal and derivation of Bragg's law; taken from [121].

The distance d depends on the particular unit cell of the respective crystalline compound. An equivalent description of this phenomenon is the Laue condition.
The intensity of a reflex in a diffraction pattern I_{hkl} is proportional to the structure factor F_{hkl}:

$$I_{hkl} \propto F_{hkl}^2$$

The Miller indices hkl describe the respective lattice plane. The scattering potential depends on the number of electrons of the respective atom in the solid since XRD can be described as Thomson scattering of the X-ray with the electron cloud. Consequently, heavier atoms have larger contributions to the intensity I_{hkl}.[120,122]
In general, the intensity of the scattered X-ray is recorded with respect to the reflection position during a XRD experiment. In the following, single-crystal and powder XRD are detailed in particular.

Single-Crystal X-Ray Diffraction

Frequently, the crystal structure of novel crystalline compounds can be elucidated by SC-XRD. Therefore, a single-crystal with dimensions between 10 and 500 μm is irradiated by a focussed X-ray. The diffraction pattern, i.e. the intensity and location of the single reflections on the area detector, represents the Fourier transform of the crystal.[120,122] Thus, the phase information is lost. This phase problem[123] can be tackled by e.g. direct

methods,[124] the Patterson-Method[125] or intrinsic phasing[126] resulting in the extraction and refinement of a structure model for the respective crystal. The reliability of such crystal structure solutions is assessed by so-called residuals or R factors describing the deviation between the observed F_o and calculated F_c structure factors:

$$R_1 = \frac{\sum\limits_{hkl} || F_\mathrm{o} | - | F_\mathrm{c} ||}{\sum\limits_{hkl} | F_\mathrm{o} |}$$

$$wR_2 = \sqrt{\frac{\sum\limits_{hkl} w \left(F_\mathrm{o}^2 - F_\mathrm{c}^2\right)^2}{\sum\limits_{hkl} w \left(F_\mathrm{o}^2\right)^2}}$$

w : weighing factor.

For a satisfying structure refinement, R_1 and wR_2 should reach values below 5% and 15%, respectively.[120] A further relevant parameter is the goodness of fit S:

$$S = \sqrt{\frac{\sum\limits_{hkl} w \, || F_\mathrm{o} | - | F_\mathrm{c} ||^2}{m - n}}$$

m : number of reflections,

n : number of parameters.

For a correct structure model, the value of S should be close to unity. The denominator of the last equations points towards another relevant aspect of SC-XRD, namely the reflection to parameter ratio. It should always be above 10, preferably above 20. Otherwise, no reliable structure model might be found.

Suited single-crystals were selected using a Olympus SZX2-ILLT microscope with polarisation filter after dispersing the crystals in paraffin oil or LV CryoOil (MiTeGen) in the case of hygroscopic samples. The respective crystal was picked with a *MicroLoop* (MiTeGen) and investigated using a Bruker D8 Venture transmission diffractometer equipped with a Kappa four-circle goniometer, a molybdenum anode ($\lambda_{\mathrm{Mo}-K_\alpha} = 0.71073\,\text{Å}$) and a PHOTON 100 detector. The cryostream 700 plus cooling system (Oxford Cryosystems) enables the measurement between 100 K and 500 K using liquid nitrogen. The sample is cooled or heated by a nitrogen stream. This was used for hygroscopic crystals preventing moisture from affecting the sample. For the initial verification of the scattering properties, the quick determination of the unit cell, the measurement strategy based on this unit cell, the actual measurement, the indexing, the integration and the scaling the software APEX3 was applied.[127] The absorption correction was performed employing the multi-scan method.[128] The crystal structures were solved with direct methods within the SHELXS program[129] and refined by the full-matrix least squares technique within the SHELXTL program.[126] Where present, hydrogen atoms were refined using residual density of electrons for localisation and a reasonable restraint for the length of the

O–H bond.[130] If the displacement could not be reliably refined freely, fixed isotropic displacement parameters were assigned to hydrogen atoms equal to $1.2\,U_{eq}$ of the bonded carbon, nitrogen or oxygen atom within e.g. CH_2, NH_4 and OH groups and $1.5\,U_{eq}$ in crystal water molecules, respectively.

Powder X-Ray Diffraction

PXRD is used for qualitative and quantitative analysis of the composition of crystalline powders. In contrast to SC-XRD, a two-dimensional diffraction pattern is obtained recording the intensity of the diffracted radiation as a function of the diffraction angle 2Θ. Therefore, radiation from the X-ray source is filtered by a monochromator, scattered and partially reflected by the sample, which was ground before in order to gain randomly oriented and small crystallites and therefore, enough crystallites in any diffracting orientation to obtain a reproducible pattern. In general, the shape of the resulting pattern depends on the long and short range order of the investigated material. Amorphous solids only showing short range order with some statistically distributed interatomic distances yield a diffusive shaped amorphous halo, while crystalline solids exhibiting long range order yield diffraction pattern characteristic for each compound due to a limited number of interatomic distances fulfilling Bragg's law and therefore, resulting in sharp reflections.[122,131]

All PXRD patterns in this work were measured using a copper anode in either Bragg-Brentano setup as depicted in Figure 3.1.3 by reflection of the beam from the surface of a flat rotating sample in a Seifert 3003 TT instrument (Meteor 1D linear detector, Ni-Filter to suppress K_β radiation, X-ray tube operated at 40 kV and 40 mA, scan range: $5° < 2\Theta < 80°$, increment: 0.02°, 40 scans per data point, integration time: 200 s per degree, variable divergence slit) or Debye-Scherrer setup shown in Figure 3.1.4 with transmission geometry using a Bruker D8 Advance instrument (1D LynxEye detector, X-ray tube operated at 40 kV and 40 mA, scan range: $5° < 2\Theta < 80°$, increment: 0.02° and rotating Hilgenberg glass capillaries (outer diameter varying from 0.2 to 0.5 mm, wall thickness 0.01 mm) filled with the ground sample. The used capillary tubes were made of soda lime glass for room temperature measurements and quartz glass for temperature-programmed XRD (TPXRD) at elevated temperatures. For the latter, a furnace attachment was used enabling measurements up to 1000°C. Both the absorption by the capillary and by the furnace attachment result in a strong background at lower diffraction angles or between $12.5° < 2\Theta < 30°$, respectively. Naturally, the capillaries were filled inside an argon filled glovebox in the case of all hygroscopic samples.

Phase analysis is possible by a comparison to pattern calculated from structural data[i] or by Rietveld refinement.

[i] Most commonly obtained by SC-XRD.

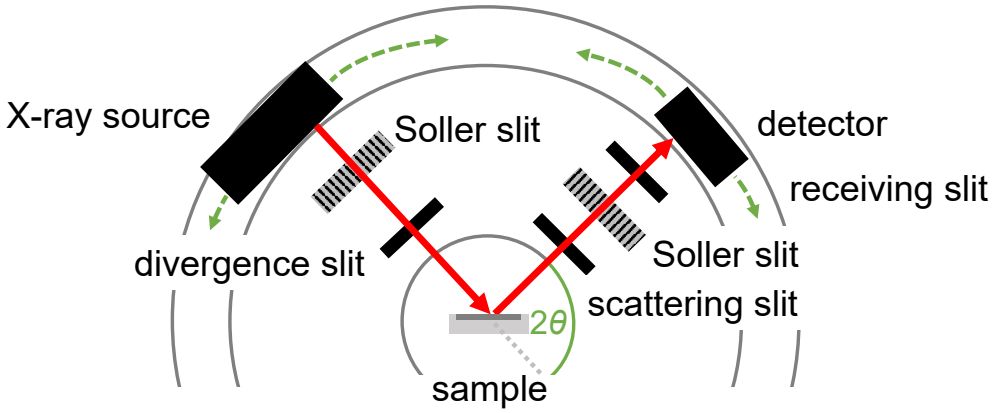

Fig. 3.1.3: Schematic representation of the Bragg-Brentano setup in PXRD measuring in reflection: During the measurement both the source and the detector are moved in order to scan the 2Θ range.

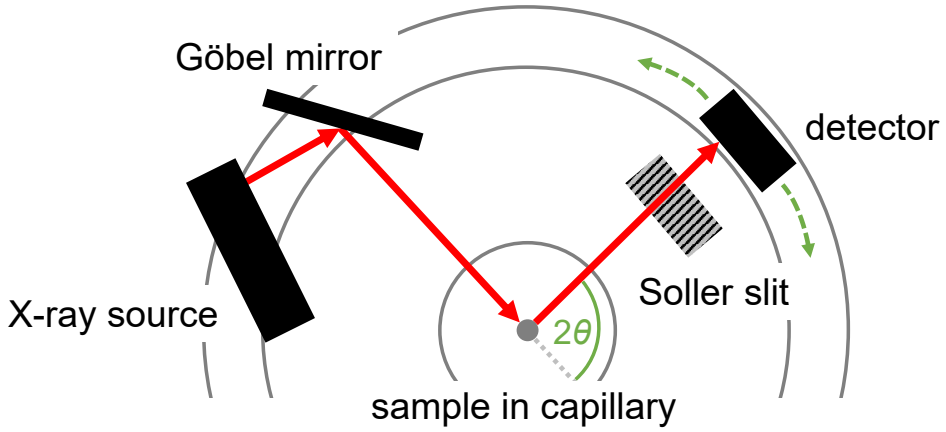

Fig. 3.1.4: Schematic representation of the Debye-Scherrer setup in PXRD measuring in transmission: During the measurement the detector is moved in order to scan the 2Θ range.

Rietveld Analysis

The Rietveld method[132–134] is a crystal structure analysis method for powder diffraction data based on a lest-square minimisation procedure.[120,131,135] It can be used for both the refinement of crystal structures starting from a reasonably close structural model and for quantitative phase analysis. The residual S_y

$$S_y = \sum_i w_i \left(y_{i,\mathrm{obs}} - y_{i,\mathrm{calc}}\right)^2$$

w_i : weighting coefficient at step i

$y_{i,\mathrm{obs}}$: observed intensity at step i

$y_{i,\mathrm{calc}}$: calculated intensity at step i

is minimised by the calculation of intensities for each data point i based on the structure factor $|F_K|^2$ values from the structural model adding up all contributions from neighbouring reflections and the background

$$y_{i,\mathrm{calc}} = s \sum_K p_K L_\Theta A_\Theta T_K E_K \Phi\left(2\Theta_i - 2\Theta_K\right) |F_K|^2 + y_{i,\mathrm{background}}$$

s : scaling factor

p_K : multiplicity factor

L_Θ : Lorentz polarisation factor

A_Θ : absorption correction

T_K : factor for preferred orientation

E_K : extinction correction

Φ : reflection profile

$y_{i,\mathrm{background}}$: background intensity at step i

K : Miller indices hkl for a Bragg reflection.

In general, each peak in a powder diffractogram can be described by five parameters: position, intensity, shape, width and asymmetry. The latter three are strongly influenced by the instrument. The fundamental parameter approach[136,137] can be used to discriminate between influences from the sample and the instrument. Therefore, the so-called instrumental resolution function was determined empirically from a set of fundamental parameters using a reference scan of silicon (NIST 640d). This allows the refinement of all non-sample related parameters, i.e. the influence from the hardware and the experimental conditions, since the crystallite size and the crystal structure of the standard sample is known. Subsequently, the obtained values for the instrumental parameters were used and no longer refined. Thus, less parameters are needed for the refinement and the wrong description of sample related influences by instrumental parameters can be avoided.

Tab. 3.1.1: Refinable parameters within the analysis of powder diffraction data[135]

Local[i]	Global
Atomic positions x_j, y_j and z_j	2Θ-Zero
Isotropic thermal parameters B_j	Instrumental profile
Occupation factor N_j	Profile asymmetry
Scaling factor s	Background
Sample-profile width parameters	Wavelength
Lattice parameters a, b, c, α, β and γ	Sample displacement
Individual anisotropic thermal parameters	Sample transparency
Preferred orientation	Absorption
Crystallite size and microstrain[ii]	
Extinction	

[i] These parameters are present and vary for each phase. [ii] Most commonly originating in point defects within the sample.

The least-square minimisation leads to the calculation of shifts of the parameters of the starting model improving the model. This process is iterative and repeated until a certain convergence criterion is met. The parameters can be divided into local and global ones as tabulated in Table 3.1.1. Due to the correlation of some parameters and false (local) minima, a careful stepwise refinement is necessary applying physically and chemically plausible constraints. Another pitfall is overparametrisation. The observation to parameter ratio should always be higher than three, better higher than five with the number of observed reflections as number of observations,[ii] not the number of steps in the measurement.[131]

To access the quality of the refinement, difference plots between the measured and calculated pattern as well as different residuals or R factors are employed. The chemical plausibility and the agreement of the observed and calculated profiles - as shown in Figure 3.1.5 for instance[iii] - are followed by the R_{Bragg} value in the importance of these aspects in order to judge the quality of the refinement:

$$R_{\mathrm{Bragg}} = \frac{\sum_K \mid \sqrt{I_{K,\mathrm{obs}}} - \sqrt{I_{K,\mathrm{calc}}} \mid}{\sum_K \sqrt{I_{K,\mathrm{obs}}}}$$

I_K is the intensity of reflection K at the end of the refinement. The R_{Bragg} value is calculated for each phase and a refinement can be considered plausible if its value is below 3%. Next, the profile residual R_{P}, the weighted profile residual R_{wp} and the goodness of fit (GOF) follow:

[ii] For the refinements herein, the number of Bragg positions refined with non-zero structure factors was taken from the refinement in TOPAS V.

[iii] M. Hämmer, H.A. Höppe, unpublished results, space group $I4_1/a$ (no. 88), $a = 520.734(4)$ pm, $c = 1127.67(1)$ pm, $R_{\mathrm{Bragg}} = 0.007$, $R_{\mathrm{wp}} = 0.019$, 116 observed reflections, 31 refined parameters.

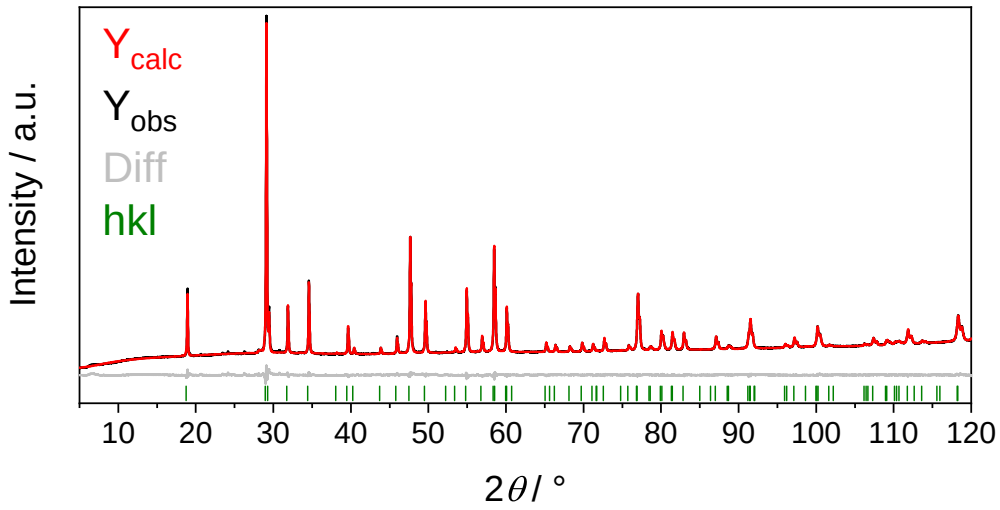

Fig. 3.1.5: Exemplary Rietveld refinement plot for $NaHo(WO_4)_2$: Both the observed (black) and calculated pattern (red) as well as the difference plot (grey) are shown. Below, the Bragg positions (green) of the reflexes hkl are indicated. This type of graphical representation of the Rietveld refinement is the easiest and most important way to judge the quality of the refinement.

$$R_\mathrm{p} = \frac{\sum_i \mid y_{i,\mathrm{obs}} - y_{i,\mathrm{calc}} \mid}{\sum_i w_i y_{i,\mathrm{obs}}}$$

$$R_\mathrm{wp} = \sqrt{\frac{\sum_i w_i \left(y_{i,\mathrm{obs}} - y_{i,\mathrm{calc}}\right)^2}{\sum_i w_i y_{i,\mathrm{obs}}^2}}$$

$$\mathrm{GOF} = \frac{R_\mathrm{wp}}{R_\mathrm{expected}} = \frac{\sum_i w_i \left(y_{i,\mathrm{obs}} - y_{i,\mathrm{calc}}\right)^2}{N-P} = \frac{S_y}{N-P}$$

N : number of measurement points

P : number of refined parameters

$$R_\mathrm{expected} = \sqrt{\frac{N-P}{\sum_i w_i y_{i,\mathrm{obs}}^2}}$$

Naturally, the residual should be as small as possible and the GOF close to unity. However, the chemical plausibility and the graphical agreement of observed and calculated patterns should always be given more weight than the residuals since the latter can also be small in the case of a poor refinement due to pure numerical reasons.

The quantitative analysis of multiphase mixtures is enabled by the relation of the scaling factors s_p obtained from the Rietveld refinement and the relative weight fractions w_p of phase p in a mixture of n phases:[138]

$$w_p = \frac{s_p Z_p M_p V_p}{\sum_{j=1}^{n} s_j Z_j M_j V_j}$$

Z : number of formula units per unit cell

M : mass of the formula unit

V : volume of the unit cell.

Despite Rietveld programs calculating the weight fraction with mathematical, but not chemical plausible standard deviations in the sub-percent region quantification errors in the order of 1 wt.-% can be expected.[131] Consequently, all values given in the following are rounded up.
In this work, analyses of PXRD data were performed using the Rietveld method along with indexing and Pawley fits as implemented in the program TOPAS V.[139] The structural models used as starting models for Rietveld analysis are stated in the respective chapters. Depending on the quality of data, the isotropic thermal parameters were constrained to one common value for all atoms, for each atom type or for all heavy or light atom, respectively, in order to minimise quantification errors. Likewise, the atomic positions were either refined for all atoms or the heavy atoms only. The parameters of hydrogen atoms were not refined. The background was modelled with a Chebyshev polynomial.

3.2 Spectroscopic Methods

All analytical methods based on the interaction of electromagnetic radiation and matter can be grouped under the term spectroscopy. Depending on the used wavelength λ or energy regime, i.e. the region in the electromagnetic spectrum depicted in Figure 3.2.1, various properties of the crystalline solids can be probed according to the different types of interaction of the atoms of the solid with the radiation. This interaction is plotted as a function of energy. Thus, this is in contrast to and excluding XRD (section 3.1).

3.2.1 Infrared Spectroscopy

Starting at low energies or high wavelength, infrared (IR) spectroscopy can investigate vibrations of molecules by the absorption of light in the infrared region ($800\,\mathrm{nm} < \lambda < 1\,\mathrm{mm}$). The intensity of the absorption is usually plotted inversely as transmission by passing a beam of IR light trough the sample as a function of the wavenumber $\tilde{\nu} = \frac{1}{\lambda}$ most commonly showed in a range of $4000 - 400\,\mathrm{cm}^{-1}$, i.e. with increasing energy from left to right. Functional groups possess characteristic absorption bands. Since the vibrational frequencies depend on bond strength, bond angles and the masses of the atoms, a variety of structural information can be extracted from IR spectra.[140,141] In general, vibrations involving heavier atoms are observed at lower energies, i.e. M-O vibrations with M being any of the metal cations in this work are located at or even below the low energy

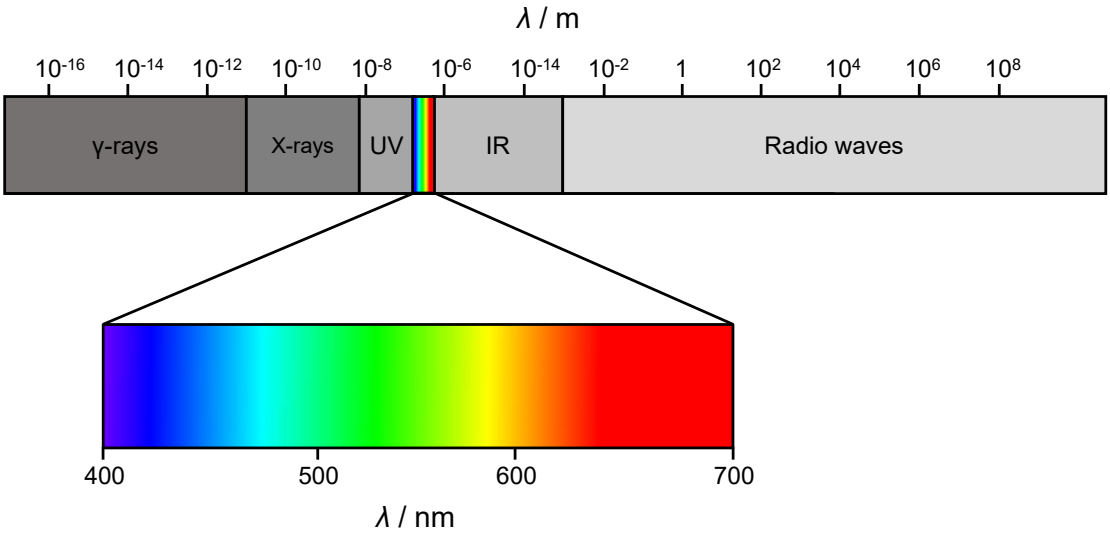

Fig. 3.2.1: Electromagnetic spectrum with enlarged visible region

end of the IR spectra. Stretching vibrations and bending vibrations represented as ν and δ,[iv] respectively, can be distinguished. These vibrations are IR active if the posses an alterable or induced dipole moment, i.e. if they are not symmetric to the centre of symmetry. The expected modes for a certain molecule or moiety can be assessed by group theory as conducted in section 4.2.

Nowadays, Fourier transform infrared (FT-IR) spectrometer with a Michelson interferometer and an ATR[v] unit are used almost exclusively for measurements of solid compounds in the mid-infrared region. The layout of such a spectrometer is schematically depicted in Figure 3.2.2. A interferogram, i.e. the intensity signal from the detector as a function of the change of the optical pathlength introduced by the shift of the movable mirror varying the interference between the beam reflected on the fixed mirror and the one reflected on the movable mirror, is measured. This is transformed via Fourier transformation into the transmission spectrum.

The attenuated total reflection (ATR) technique schematically shown in Figure 3.2.3 is applied for samples too strongly absorbing for standard transmission measurements. It utilises the physical effect of total reflection of light at the interface between two materials of different refractive indices. By the use of a diamond crystal with a large refractive index as internal reflection element, the evanescent IR wave is totally reflected multiple times while the sample absorbs parts of the radiation at each point of reflection. The resulting spectrum showing the interaction of the sample, i.e. the less dense medium, with the wave is equivalent to a measurement in classic transmission geometry. Further, the bands at the lower energy end of the measuring range are more intense in the case of

[iv] δ represents scissoring modes. Further bending modes are rocking ρ, wagging ω and twisting τ. However, only δ vibrations are relevant for the spectra displayed in this work.

[v] See below.

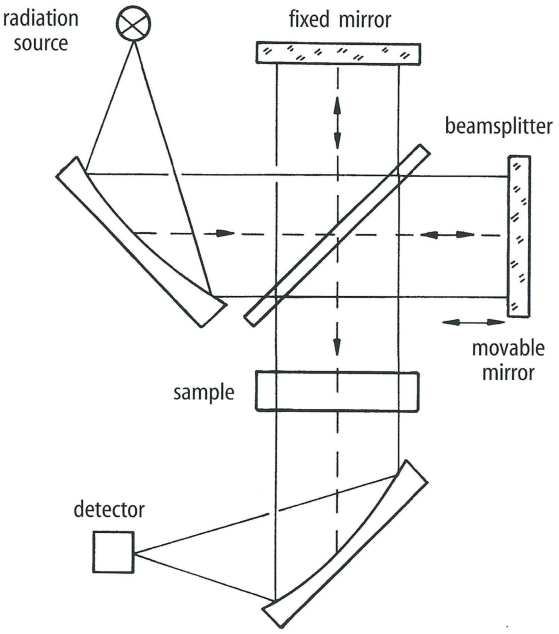

Fig. 3.2.2: Schematic layout of a Fourier transform infrared (FT-IR) spectrometer with a Michelson interferometer; taken from [142]

an ATR measurement due to the dependency of the penetration depth on the wavelength. This is advantageous since the majority of vibrations for inorganic compounds such as the ones studied in this work are observed there. In general, the use of FT-IR spectrometers and the ATR technique are widely popular due to better signal-to-noise ratios, faster measurements and the ability to measure any substance including powders independently of their transmission behaviour.[142]

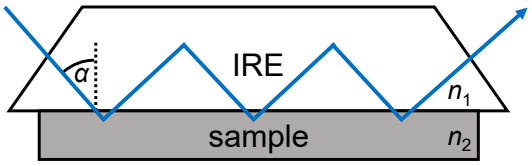

Fig. 3.2.3: Schematic representation of the total internal reflection within the ATR unit: n_1: refractive index of the internal reflection element (IRE), n_2: refractive index of the sample, $n_1 > n_2$, α: angle of incidence; this angle must exceed the critical angle Θ_c for internal total reflection: $\Theta_c = \sin^{-1}\left(\frac{n_2}{n_1}\right)$.

The IR spectra in this work were measured using a Bruker Equinox 55 FT-IR spectrometer with a platinum ATR unit and recording a background spectrum before measuring the respective sample. The measurement is carried out over the range of $4000 - 400\,\mathrm{cm}^{-1}$ at a resolution of $2\,\mathrm{cm}^{-1}$, with 32 scans per sample with the program OPUS. The spectra were analysed by comparison to both experimental and theoretical data on related compounds from literature.

3.2.2 UV-Vis-NIR Spectroscopy

In optical spectroscopy or UV-Vis-NIR spectroscopy, the probed range of the electromagnetic spectrum includes the UV (200-400 nm), the visible regime (400-800 nm) and the near infrared (NIR, 800-1500 nm). Absorption in this energy range leads to the excitation of valence electrons from the ground state to excited states. This is shown in the Jablonski diagram in Figure 3.2.4 in blue.[143–145] The solids in this work are investigated by diffusive reflectance spectroscopy. In doing so, the relative reflection is measured with respect to the wavelength comparing the intensities of the reflected radiation and the irradiated light by the use of a white standard. The measurement setup is sketched in Figure 3.2.5. These spectra yield insights into whether the studied substance is transparent at a given wavelength, the samples optical band gap as well as the absorption or excitation bands of the sample.
If the requirement that the sample consists of randomly orientated and isotropically distributed crystallites that are much smaller than the thickness of the complete sample is fulfilled - this was ensured by grinding the samples prior to the measurement -, the Kubelka-Munk equation[vi]

$$\frac{K}{S} = \frac{(1-R)^2}{2R},$$

with R being the measured reflection, K the absorption coefficient and S the backscattering coefficient, can be used to convert the reflection spectra to the corresponding absorption spectra. Consequently, $\frac{K}{S}$ can be plotted with respect to the wavelength instead of R.[146–149] Further, these results can be used for the calculation of Tauc plots.[149,150] The Tauc method is based on the equation

$$(\alpha\,\hbar\nu)^{\frac{1}{\gamma}} = B(\hbar\nu - E_\mathrm{G})$$

with α being the (energy dependent) absorption coefficient, $\hbar$ the Planck constant, ν the frequency of the photon, E_G the band gap and B a constant. γ is depending on the nature of the transition either $\frac{1}{2}$ for direct or 2 for indirect band gaps. Tauc plots can be prepared by the substitution of $\frac{K}{S}$ for α showing a step increase of absorption with increasing energy. Then, the (optical) band gap E_G can be estimated by the linear fit of this increase and its intersection with the zero-absorption line (linear fit of non-absorbing part of the spectrum).[149]
In this work, UV-Vis spectra were recorded as diffuse reflection spectra at room temperature with a Varian Cary 300 Scan UV-Vis spectrophotometer using an Ulbricht sphere detector and deuterium arc lamp (UV) / tungsten-halogen lamp (Vis) light sources (scan range: 200-800 nm, increment 1 nm, scan rate: 120 nm min^{-1}). For the compounds investigated in section 9.2, diffuse reflectance UV-Vis-NIR spectra were recorded at room temperature on a PerkinElmer λ 750s spectrometer equipped with a Labsphere

[vi] The Kubelka-Munk equation is valid in this form only for non-transparent layers with infinite thickness. In the case of fine ground powders, this is achieved with a sample thickness of a few mm.

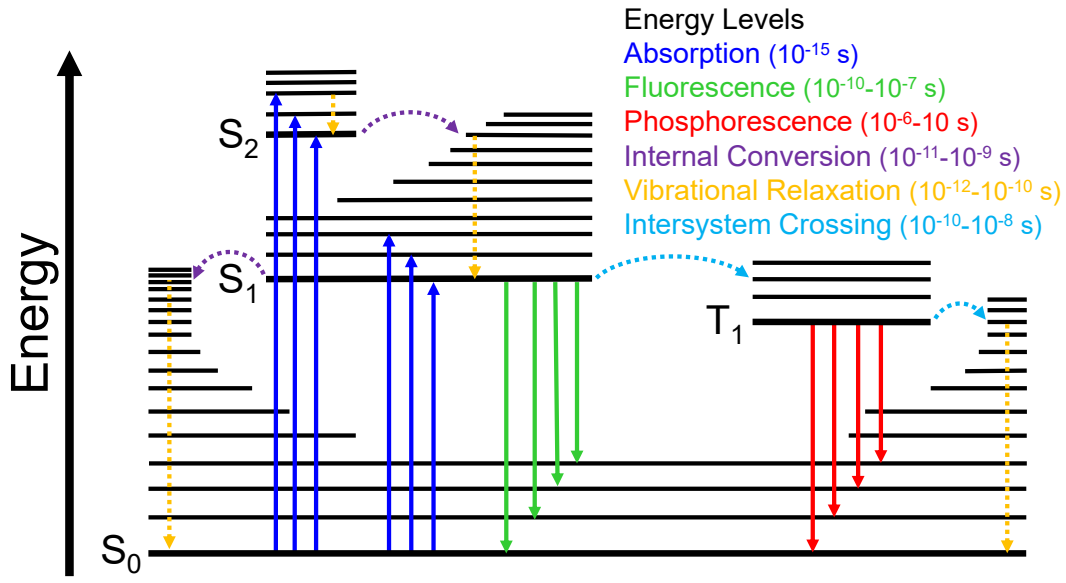

Fig. 3.2.4: Jablonski Diagram (Perrin-Jablonski Diagram): Arbitrary energy levels of the ground state S_0, the singlet excited states S_1 and S_2 as well as the excited triplet state T_1 are shown; starting with the absorption various processes occur on the way of the electron back to the ground state resulting in the radiative fluorescence or phosphorescence as well as the non-radiative vibrational relaxation; special energy levels for specific compounds or ions are discussed with the respective compounds in the following sketching them in similar fashion.

60 mm RSA ASSY integrating sphere with a $0° \, d^{-1}$ measuring geometry (scan range: 200-1500 nm, increment 1 nm, scan rate: 120 nm min^{-1}). Labsphere Spectralon SRS-99 was used as the white standard. Artefacts due to the changes of light sources or detectors during the measurements were corrected manually, where possible.
In the case of hygroscopic samples, the sample holder was filled and tightly closed inside the argon filled glovebox. Additionally, IR spectra were recorded after each measurement in order to assess the possible degradation by hydrolysis on the basis of the presence (or absence) of respective vibrations stemming from water. Consequently, only the spectra were analysed after whose measurements no indication for degradation by hydrolysis were found.

3.2.3 Fluorescence Spectroscopy

Subsequent to the absorption or excitation probed by UV-Vis spectroscopy, further processes occur in the sample as depicted in the Jablonski diagram in Figure 3.2.4 that can be investigated by fluorescence spectroscopy.[144,145] An excited electron can return to the ground state via radiationless vibrational relaxation or via radiating fluorescence with the excited and ground state having the same spin orientation or phosphorescence from an excited triplet state reached by intersystem crossing. The latter is spin-forbidden and therefore, much slower than fluorescence. The respective time scales are given in

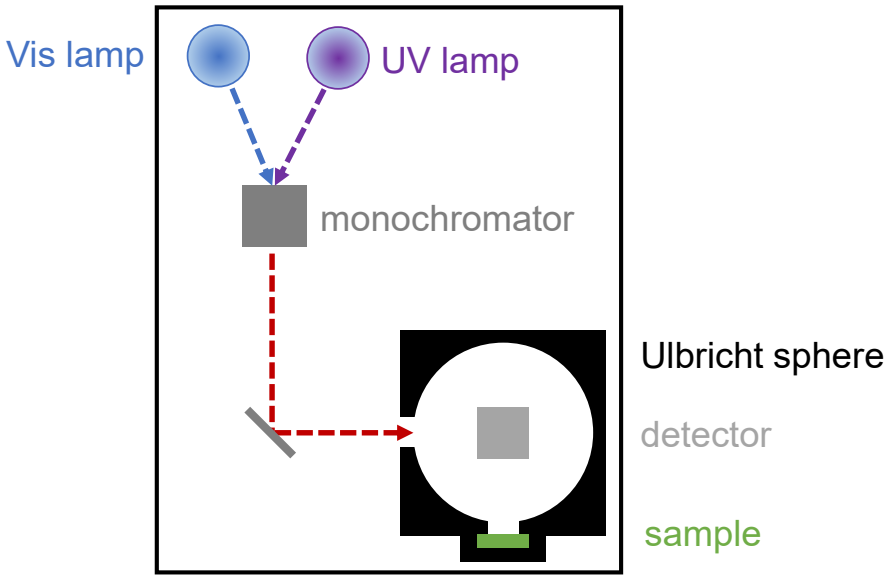

Fig. 3.2.5: Schematic setup used for UV-Vis spectroscopy with the diffusive reflectance accessory including an integrating (Ulbricht) sphere with an integrated detector: Upon irradiation with a wavelength defined by the monochromator the reflection by the sample is measured inside the sphere relatively to the intensity of the baseline measurement using a white standard.

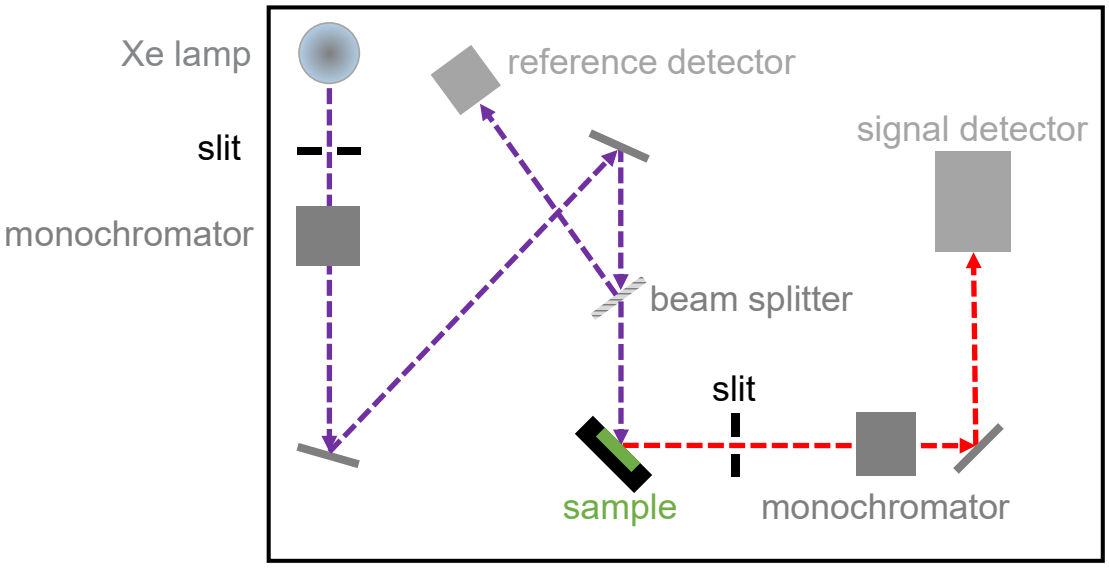

Fig. 3.2.6: Schematic setup used for fluorescence spectroscopy.

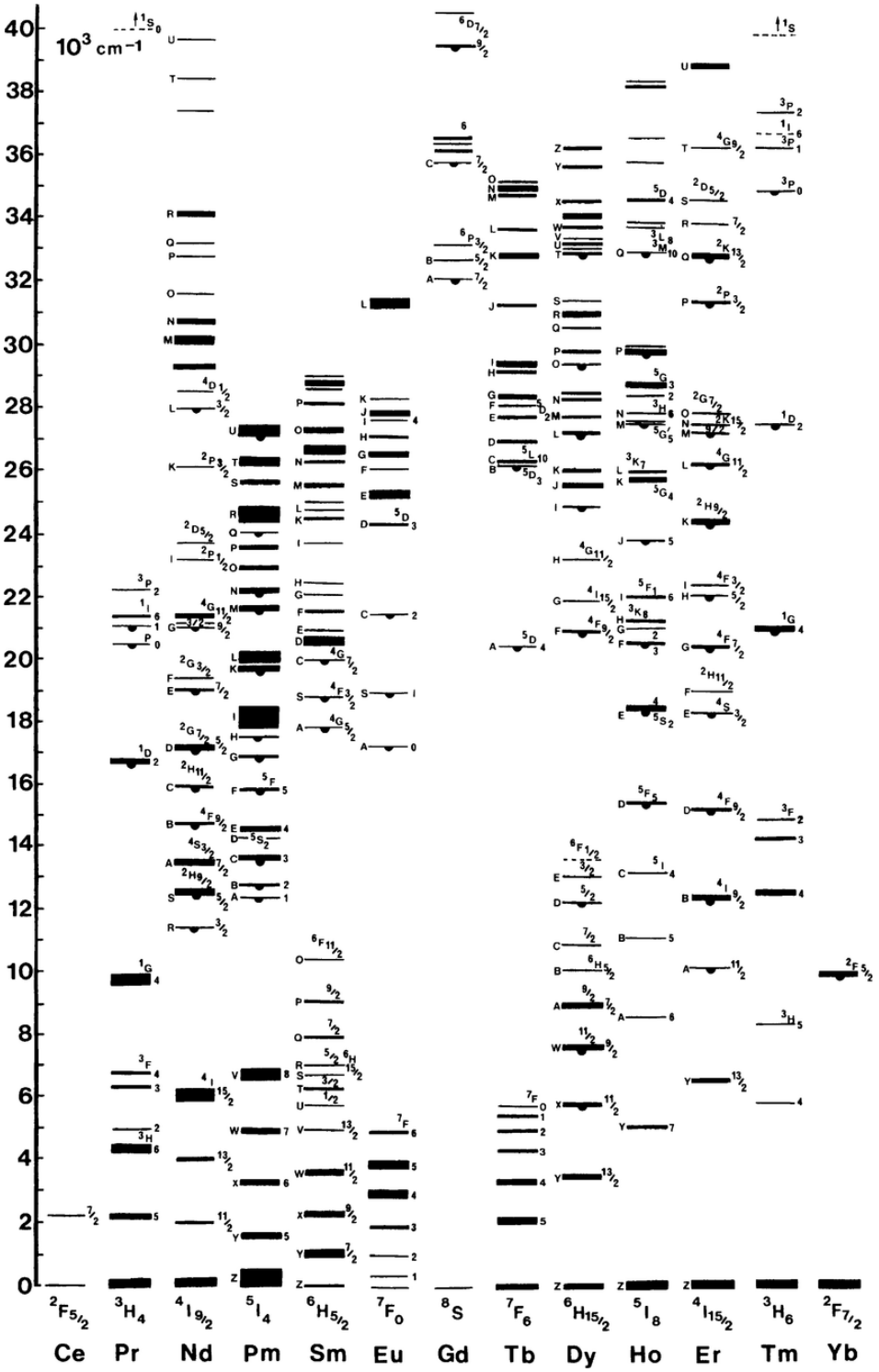

Fig. 3.2.7: Dieke diagram taken from[151] showing the energy levels of free trivalent lanthanide ions: Broader lines indicate the existence of multiple vibrational states; small circles indicate that emission from these levels can be observed.

Figure 3.2.4. In both cases of luminescence, the emission wavelength is larger than the excitation wavelength due to relaxation processes. This phenomenon is called Stokes-shift. The existence of various vibrational states explains the observation of excitation and emission bands instead of lines.

Trivalent lanthanide cations are very prominent emitters or activators with characteristic line emissions due to 4f-4f transitions. These transitions are only weakly influenced by the host lattice due to strong shielding by the $5s^2$ and $5p^6$ orbitals. Thus, the energies of these transitions can be displayed generally in the Dieke diagram in Figure 3.2.7.[151] For the detailed analysis, the data reported by Carnall et al. was used.[152–157] Further transitions frequently observed in fluorescence spectroscopy are d-d transitions involving transition metals and charge-transfer transitions. Both result in emission and excitation bands broader than the narrow lines characteristic for f-f transitions. Detailed discussion of all these transitions is given for the respective compounds in the following.

In fluorescence spectroscopy, two separate spectra are recorded, namely excitation and emission spectra. The former is measured by varying the excitation wavelength λ_{ex} while keeping the emission wavelength λ_{em} at a constant value, and vice versa for the latter. Consequently, spectra labelled with a distinct excitation wavelength are emission spectra and vice versa.

Those solid-state excitation and emission spectra were recorded on a Horiba FluoroMax-4 fluorescence spectrometer equipped with a xenon discharge lamp scanning a range from 200 to 800 nm. The excitation spectra were corrected with respect to the lamp intensity.[vii] Low temperature measurements were performed with a liquid nitrogen dewar assembly within the same device. For this, the sample was filled into a small glass tube which was subsequently evacuated and closed with a hose and a clamp. This is necessary to prevent oxygen from air from condensation resulting in the scattering of light distorting the measurement. In the case of hygroscopic samples, the low temperature apparatus was used exclusively. The sample was filled into the glass tube inside the argon filled glovebox. Room temperature measurements were performed with an argon filled tube. The procedure for low temperature measurements was identical to the one for the non-hygroscopic samples.[viii]

[vii] In the rare cases, in which this was not possible due to the small signal-to-noise ratio hampering the correction, this is stated explicitly in the following.

[viii] Additionally, a Edinburgh Instruments FLS920 Fluorescence spectrometer was used to investigate the luminescent properties in the range from 200 to 1500 nm. These measurements showed that there is no emission for $Cu[B_2(SO_4)_4]$ (section 9.2). The sample was prepared inside the glovebox. Due to the lack of an appropriate setup, the powder was placed onto the middle of a microscope slide, silicone paste (KORASILON, Kurt Obermeier GmbH & Co. KG) was applied around it, a second slide was placed on top and the two slides were fixated firmly using adhesive tape. As detailed below, the hydrolysis of $Cu[B_2(SO_4)_4]$ could be easily observed due to the accompanied colour change. Accordingly, this setup was able to store the sample airtight for over one hour. This was also confirmed by subsequent FT-IR spectroscopy.

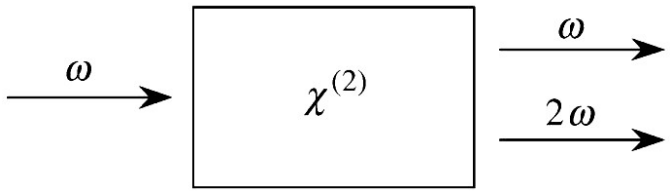

Fig. 3.2.8: Schematic representation of second harmonic generation taken from [158]

3.2.4 Second Harmonic Generation Measurement

Second harmonic generation (SHG) is a nonlinear optical (NLO) phenomenon.[158] It is nonlinear in the sense that the response of a material system to an applied optical field is nonlinear with respect to the strength of the optical field. SHG was discovered by Franken et al. in 1961.[102] In this process, sketched in Figure 3.2.8, the incident radiation at frequency ω is converted to radiation with the second-harmonic frequency 2ω by a quantum-mechanical process destroying two photons of frequency ω and creating one photon of frequency 2ω. The most prominent application of this effect is the green laser pointer - as already mentioned at page 12.
The prime requirement for SHG is a non-zero second-order susceptibility $\chi^{(2)}$. This is only the case in noncentrosymmetric crystals. In turn, the phenomenon of SHG can be use to confirm noncentrosymmetric crystal structures. Full evaluation of the NLO properties of a given material is only possible using large and defectless single-crystals often requiring extensive synthesis optimisation. However, Kurtz and Perry developed the powder SHG method.[159] It is commonly used as the first step to estimate the nonlinear optical properties of new materials or to detect the absence of an inversion centre in crystal structures.[160] The particle size can be expected to influence the SHG signal in such experiments for particle sizes smaller than the average coherence length. This is the case for all samples studied in this work. The coherence length depends on the materials' refractive indices at the frequencies ω and 2ω. For particle sizes larger than this length, the discrimination between phase-matchable and non phase-matchable is possible.[159]
The SHG measurements were conducted and analysed by Dr. Lkhamsuren Bayarjargal at Goethe-Universität Frankfurt am Main. The measurement setup is detailed in [161]. A Q-switched Nd:YAG laser (Impex-hightech, 1064-Q-HP, 1064 nm, 5-6 ns, 2 kHz) provided the fundamental pump wave. With a harmonic separator, a short-pass filter, and interference filter, the fundamental infrared light was separated from the generated second harmonic. The generated SHG signal at 532 nm was collected using a photomultiplier (R2949, Hamamatsu) and an oscilloscope (Tektronix). Non-hygroscopic sample were fixated on transparent non-SHG active tape, while the hygroscopic sample were measured inside the Hilgenberg glass capillaries also used for PXRD. SHG signals from five to eight different areas of the sample were measured to check the homogeneity of the sample. The average values of these different areas are presented. On each position 640 pulses were measured and averaged. The measured intensities were corrected by subtracting

background signals collected between the pulses. Non-centrosymmetric Al_2O_3, quartz, the benchmark material KDP and - in the case of hygroscopic samples - empty Hilgenberg glass capillaries were used as reference materials.

3.2.5 Energy-dispersive X-ray Spectroscopy

For the investigation of the elemental composition of the synthesised compounds, energy-dispersive X-ray spectroscopy (EDX) was applied. In this method, a beam of high energy electrons hits the surface of the sample creating an electron hole by removing one electron from an inner shell. The hole is filled by an electron of higher energy releasing the excess energy in form of an X-ray photon. This X-ray is characteristic for each chemical element. Both the energy and number of these is measured above the sample. Consequently, the relative elemental composition of the sample can be analysed. Usually, the amount of counts is plotted with respect to the energy. Due to overlapping emission lines, the accuracy of this methods decreases with lighter elements with the detection limited at the element boron.[162,163]
The measurements were performed by Dr. Romy Ettlinger (Universität Augsburg) using a Philips XL 30 FEG scanning electron microscope (SEM) equipped with an EDAX SiLi detector averaging three measurements. The samples were prepared as a thin powder film on a carbon pad.

3.2.6 Mößbauer Spectroscopy

In 1961, Rudolf Mößbauer was awarded the Nobel price in physics for his discovery and quantum-chemical explanation of the phenomenon of recoilless nuclear resonance absorption and emission, the Mößbauer effect.[164–166]
This effect is applied in Mößbauer spectroscopy.[167,168] In the experiment schematised in Figure 3.2.9, a γ-ray capable to excite the studied nuclei is radiated onto the probed sample. The energy of the γ-ray E_γ is modulated using the Doppler effect

$$E_\gamma = E_0(1 - \frac{v}{c})$$

E_0 : Energy at rest; v : Doppler velocity; c : speed of light

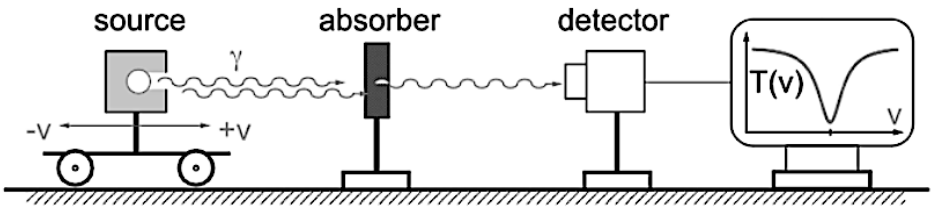

Fig. 3.2.9: Schema of the experimental setup of Mößbauer Spectroscopy: the studied sample is placed in the position of the absorber; taken from [167].

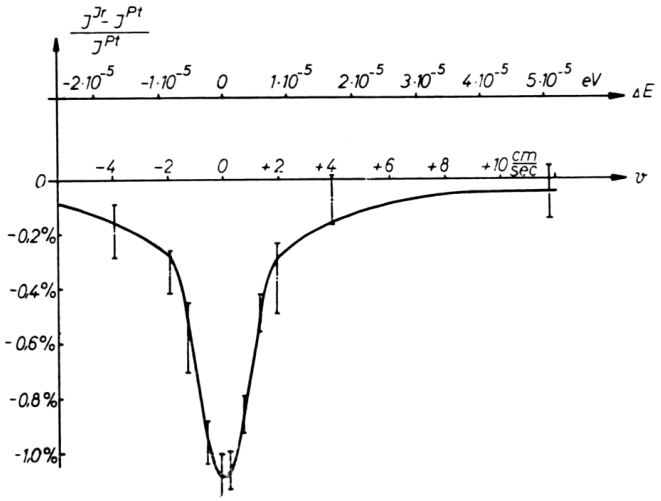

Fig. 3.2.10: The first - and original - ^{191}Ir Mößbauer spectrum of an iridium sheet taken from [166]: on top of the Doppler velocity the energy difference is plotted as abscissa emphasising the modulation of the energy of the γ-ray by the movement.

by moving source and sample relatively to each other at controlled velocities. The γ-rays transmitted by the sample when the excited nuclei relax to the ground state are detected and recorded in the form of relative transmission as a function of the Doppler velocity yielding the Mößbauer spectrum. The first of its kind is shown as an example in Figure 3.2.10. The velocity is defined as positive for movement of source and sample towards each other and negative vice versa. The spectra show minimum relative transmission due to maximum resonance at relative velocities, i.e. energies at which emission and absorption overlap. The Mößbauer effect is only observed for the recoil-free fraction of nuclear resonance based on zero-phonon-processes. This fraction vanishes for liquids and gases due to the large mean square displacement of the nuclei. However, the effect is detectable not only in crystalline samples but also in amorphous solids and frozen solutions. By interpretation of relative position (isomer shift δ), shape (line width Γ) and splitting (electric quadrupole splitting ΔE_{Q}) of the Mößbauer spectrum[ix] information about the oxidation state, the spin state and the local environment including symmetry and bonding properties of the studied nuclei can be obtained. In the case of mixed-valence compounds, the ratio, i.e. of Sn^{2+} and Sn^{4+} in $Sn_2(SO_4)_3$ as detailed in section 7.1 can be estimated from the area of the respective features in the Mößbauer spectrum.[169] Despite the Mößbauer effect being observed for over 40 elements, its application remains limited to 15-20 elements due to the lack of corresponding sources and physical reasons limiting the accessible energy range.
The ^{151}Eu and ^{119}Sn Mößbauer spectroscopic investigations were conducted and analysed by Steffen Klenner in the group of Prof. Rainer Pöttgen at Westfälische Wilhelms-

[ix] Magnetic hyperfine splitting is neglected from the consideration since no significant influence was observed for all studied compounds in this work.

Universität Münster. For the former, the 21.53 keV transition of a ^{151}Sm:EuF$_3$ source (55 MBq, 1% of the total source activity) and for the latter, a Ca^{119m}SnO$_3$ source were used. The samples were cooled to 6 K in a continuous flow He-cryostat system (JanisResearch Co LLC) and to 78 K in a standard liquid nitrogen bath cryostat, respectively. The Mößbauer sources were kept at room temperature. The samples were enclosed in small PMMA containers at an optimised thickness.[170] The data was fitted using the WinNormos for Igor6 program package.[171]

3.3 Microscopy

Scanning Electron Microscopy

Immediately before the EDX measurements (section 3.2.5), SEM pictures were taken. In this method, the surface of the sample is scanned in a raster scan pattern with a focused beam of electrons and the signals produced by the sample are recorded. Thus, a resolution of approximately 10 nm can be achieved.[162]

Light Microscopy

In order to investigate the morphology of the synthesised samples, standard light microscopy was applied using an Olympus IX70 Microscope with a Abrio CRi CCD camera. The sample was either spread on a microscope slide with or without the respective oil used for the SC-XRD or it was observed directly through the walls of the silica-glass ampoule in the cases of a solvothermal synthesis.

3.4 Magnetic Properties

The magnetic properties of the studied compounds were investigated in order to confirm the respective oxidation states and to elucidate further interaction or phenomena within the samples. The magnetic behaviour depends on the existence of centres with magnetic moments.[172,173] Compounds with closed electron shells, i.e. every material - however, other phenomena may occur much stronger - exhibit induced magnetic moments upon exposure to an external magnetic field. This phenomenon is called diamagnetism. If already existing magnetic moments within the sample are aligned to an external magnetic field, it is called paramagnetism for this interaction dependent on the external field, only. For the case that the alignment depends also on interactions within the sample, e.g. cooperative effects, the phenomena ferro-, antiferro- and ferrimagnetism may occur. In ferromagnetism, the magnetic moments align parallel to each other, while they align antiparallel in antiferromagnetism as well as ferrimagnetism. The latter two can be distinguished by their magnetisation in absence of an external field. In antiferromagnets, the magnetic moments compensate each other resulting in no permanent magnetisation, while ferrimagnets exhibit permanent magnetisation due to magnetic moments of a

certain direction predominating. Further, ferromagnetic materials show permanent magnetisation, too.

The most important quantity for these behaviours is the magnetic susceptibility χ defined as the proportionality factor between magnetisation M, i.e. the sum of all atomic magnetic moments μ per volume, and the external magnetic field H:

$$\chi = \frac{M}{H}.$$

For diamagnetic materials, χ is below zero, while for all other it is positive. The temperature dependence of χ allows insights in the magnetic behaviour.[x] Metallic material show temperature independent magnetic susceptibilities, i.e. Pauli paramagnetism. In non-metallic materials, i.e. all inorganic salts treated in this work, Curie paramagnetism can be frequently observed. It follows the Curie law

$$\chi = \frac{C}{T}$$

with C being the Curie constant that can be extracted from fits on plots of the inverse susceptibility χ^{-1}. More generally, the susceptibility of a paramagnetic material can be described by the Curie-Weiss law

$$\chi = \frac{C}{T - \Theta}$$

with Θ as the Weiss constant. The latter can be extracted by the intersection of the χ^{-1} fit with the abscissa. Positive values of Θ indicated ferromagnetic interactions and negative values ferrimagnetic interactions.

Both Curie law and Curie-Weiss law are not valid a very low temperature or very high magnetic fields due to saturation magnetisation.

Another interesting quantity is the effective magnetic moment μ_{eff} usually given in Bohr magnetons μ_{B} and compared to calculated values. μ_{eff} can also be calculated from measurement of the magnetic susceptibility by the equation

$$\mu_{\text{eff}} = \sqrt{\frac{3k_{\text{B}}C}{N_{\text{A}}\mu_0}}\mu_{\text{B}}$$

with the Boltzmann constant k_{B}, the Avogadro constant N_{A} and the vaccuum permeability μ_0. This equation is valid for compounds obeying the Curie law and an approximation for compounds obeying the Curie-Weiss law with small values of Θ. The theoretical μ_{eff} values can be calculated based on the electron configuration of the respective ion. For rare earth ions, the approximation of free ions is valid due to the 4f orbital being strongly shielded by the 5s and 5p orbitals and thus, only weakly interacting with the ligands.

[x] Due to diamagnetic contributions, the recorded susceptibilities have to be corrected according to $\chi_{\text{mol}} = \chi_{\text{para}} + \chi_{\text{dia}}$ with $\chi_{\text{dia}} < 0$. The following discussion is valid for these corrected values.

Consequently, the effective magnetic moment is given by

$$\mu_{\text{eff}} = g\sqrt{J(J+1)}\mu_{\text{B}}$$

with the total momentum J and the Landé factor

$$g = 1 + \frac{J(J+1) + S(S+1) - L(L+1)}{2J(J+1)}$$

with the total spin S and the total angular momentum L.
For 3d metal ions, the approximation of free ions cannot be applied. They exhibit strong interaction with the ligand field. Thus, the influence of the angular momentum can be neglected and the calculation of μ_{eff} is simplified in the spin-only scenario:

$$\mu_{\text{eff}} = 2\sqrt{S(S+1)}\mu_{\text{B}}.$$

Another contribution to the magnetic susceptibility relevant for compounds containing ions with electron configurations close to half filled shells is van Vleck paramagnetism.[174,175] The most prominent examples are Eu^{3+} and Sm^{3+} compounds. They feature temperature independent susceptibilities below a certain temperature because excited states contribute to it due to the proximity of ground and excited states. The paramagnetic susceptibility can be expressed according to the van Vleck theory as

$$\chi_{\text{para}}\left(\text{free } Eu^{3+}\right) = \frac{N\mu_{\text{B}}^2}{Z}\left(\frac{A}{3\lambda}\right) + n\left(\frac{C}{T}\right) + \chi_0.$$

The expressions of A and Z contain the contributions of the respective ground states found in the literature.[175] In order to describe the contributions of impurities,[xi] a C/T and a χ_0 term can be added to the equation. The coupling constant λ describes the Russell-Saunders or LS coupling. It is equivalent to the energy difference between e.g. the $^7F_0$ and $^7F_1$ states for Eu^{3+} via the equation:

$$E_J - E_{J-1} = \lambda J.$$

The measurements of the magnetic properties were conducted and analysed by PD Dr. Oliver Janka and Judith Bönnighausen in the group of Prof. Rainer Pöttgen at Westfälische Wilhelms-Universität Münster. The powdered samples were packed into polyethylene (PE) capsules - in the case of hygroscopic compounds this was done inside an argon filled drybox - and attached to the sample holder rod of a Vibrating Sample Magnetometer (VSM) for measuring the magnetisation $M(T,H)$ in a Quantum Design Physical Property Measurement System (PPMS). The samples were investigated in the temperature range of 2.5-300 K with applied external magnetic fields up to 80 kOe. The

[xi] Diamagnetic impurities and - in the case of Eu^{3+} - traces of Eu^{2+}.

recorded susceptibilities were corrected for the diamagnetic contributions, calculated from the increments tabulated in [176].

3.5 Thermal Analyses

Thermal analysis methods investigate the behaviour, the properties or the change of properties of a given sample with temperature. Possible processes include thermal decomposition, phase transition, melting, evaporation et cetera.[177]

Thermogravimetric Analysis

In thermogravimetric analysis, the mass change of a sample is recorded while it is exposed to a controlled temperature program. Most commonly, a constant heating ramp is applied. Thus, the mass loss can be plotted as a function of temperature with the measurement being highly dependent on the used heating rate, sample mass and type of crucible. The measurement is carried out in a closed system with controlled atmosphere - usually rinsing the sample chamber with inert gases. Alternatively, the results can be plotted in the form of the derivative of the original signal $\frac{\partial m}{\partial T}$ against temperature. This is called derivative thermogravimetry (DTG) and can add insights in the case of overlapping steps in the TG curve.
TGA was performed with a NETZSCH STA 409 PC Luxx thermobalance under nitrogen atmosphere with $70\,\mathrm{ml\,min^{-1}}$ flow in alumina crucibles (heating rate: $10\,\mathrm{K\,min^{-1}}$). The respective maximum temperature was held for 30 min before cooling to room temperature with $20\,\mathrm{K\,min^{-1}}$. For all samples, no mass change was observed upon cooling. Thus, the results upon heating are analysed and discussed, only. The residues of the investigated sample were investigated by PXRD. However, due to the high temperatures they were baked into the crucibles after the analyses several times, thus, hampering the PXRD. In these cases, the samples were additionally heat treated in furnaces. Details are discussed with the respective compounds in the following.
Naturally, mass losses are only detected where a volatile component is lost. Reactions taking place without mass loss can be analysed by the next two methods.

Differential Thermal Analysis

In both differential thermal analysis (DTA) and differential scanning calorimetry (DSC) discussed subsequently, information about the thermal changes inside a sample is obtained by heating (or cooling) it alongside a reference. Two identical measurement sensors are used: one for the sample and one for the reference. The difference in the signal is recorded with respect to the temperature. Both sample and reference are placed in a closed system with controlled atmosphere and a controlled temperature program is applied. In DTA, the difference in temperature is measured when providing the same energy to both in the

form of heat. The temperatures at the sample and at the reference differ in the case of endothermic or exothermic events within the sample.
DTA was performed simultaneously to TGA using a special setup in the NETZSCH STA 409 PC Luxx thermobalance under nitrogen atmosphere with 70 ml min^{-1} flow in alumina crucibles (heating rate: 10 K min^{-1}).

Differential Scanning Calorimetry

The general principle of DSC is the same as for DTA. The former can be regarded to be the more modern version of the latter. In heat flow DSC, the difference in heat flux between sample and reference is measured, i.e. the energy required to keep both at the same temperature. Again, this signal differs during endothermic or exothermic events.
DSC was either measured using a TA Instruments DSC 2920 in a 50 ml min^{-1} nitrogen flow using NETZSCH standard aluminium pans with pierced lids with a heating rate of 5 K min^{-1} or simultaneously to TGA using another special setup in the NETZSCH STA 409 PC Luxx thermobalance under nitrogen atmosphere with 50 ml min^{-1} flow in platinum crucibles with lids on corundum beds (heating rate: 10 K min^{-1}).

3.6 Calculation Methods

3.6.1 MAPLE Concept

The calculation of the lattice energy E_L in this work are based on the MAPLE concept (**MA**delung **P**art of **L**attice **E**nergy)[178,179] and are performed to confirm the electrostatic consistency of the studied compounds. Following the Born-Haber cycle, the Madelung part of the lattice energy E_M, the polarisation energy E_Pol, the repulsion energy E_Rep and the covalent energy E_Cov amount to the total lattice energy:

$$E_\mathrm{L} = E_\mathrm{M} + E_\mathrm{Pol} + E_\mathrm{Rep} + E_\mathrm{Cov} + E_\mathrm{Corr}$$

In general, the correction term E_Corr is added to take the difference between experimental and calculated lattice energies into account. The term for the Madelung part consists of the Madelung constant A considering the sum of all attractive and repulsive interactions in the crystal lattice and the Coulomb energy E_C considering the potential energy between a cation and an anion in distance d_0:

$$E_\mathrm{M} = AE_\mathrm{C} = AN_\mathrm{A}\frac{z^+z^-e^2}{4\pi\epsilon_0 d_0}$$

N_A : Avogadro constant, z^+ : charge of cation, z^- : charge of anion,
e : elementary charge, ϵ_0 : dielectric constant in vacuum.

Partial Madelung factors are calculated based on the charge, the position and the ionic radius of the individual ions and summed up in order to estimate the total MAPLE

value of the studied compound. By comparing this value with the sum of the MAPLE values of well characterised reference compounds, the electrostatic consistency of a new compound can be confirmed. If the deviation between both MAPLE values is below the empirical benchmark of 1%, electrostatic consistency can be expected. In the case of strongly differing bonding situations in the studied and the reference compounds higher deviations may occur.
The calculations were performed using the program MAPLE.[180]
Additionally, the effective coordination number ECoN[181] was calculated for each ion using the same program by the sum of the contributions from each ligand. On the one hand, the ECoN values can be used to confirm the coordination numbers assigned during the structure determination[xii] and on the other hand, the comparison of similar coordination environments is possible by comparison of the respective ECoN values.

3.6.2 Polyhedra and Centroid Deviation

For the analysis of the experimental data from the crystal structure determinations, the method of Balić-Žunić and Makovicky is used.[182,183] This numerical method is based on least-squares fitting of all ligands enclosing spheres to determine the centroid or the best centre of a defined polyhedron. This is shown schematically in Figure 3.6.1. A first measure of disorder or stereochemical influence is the distance of the central atom of the polyhedron from the centroid denoted R_c. To compare this value independently from different bond lengths stemming from different coordination numbers, the eccentricity ϵ can be used. It is calculated by division of the centroid deviation by the radius of the enclosing sphere.[182,184] This value was used to assess the lone pair effect for various compounds in literature.[184–189]
Secondly, the distortion of a coordination polyhedron can be assessed as a global measure by this method. Therefore, the volume ratio of an ideal or maximum-volume polyhedron within the enclosing sphere centred by the centroid and the real, i.e. experimental polyhedron is calculated and the distortion percentage v is given by the following equation:

$$v = \frac{V_i - V_r}{V_i} \times 100$$

V_i : volume of ideal polyhedron

V_r : volume of real polyhedron

The calculation of this distortion is easiest for tetrahedra and octahedra, but not limited to them. For the case of tetrahedra, regular tetrahedra exhibit a deviation below 1%.[190]
Alternative approaches were presented by Cumby and Attfield based on enclosing ellipsoids[191] and Stoiber and Niewa.[192] The latter is very similar to the method

[xii] The coordination number is confirmed by the number of ligands with ECoN values above 0.05.

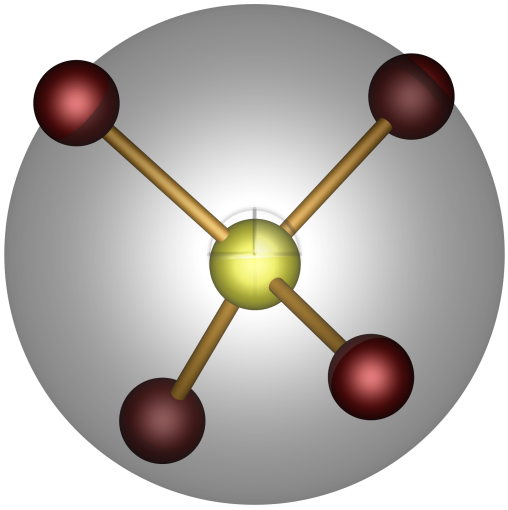

Fig. 3.6.1: Schematic representation of the enclosing sphere (grey) around a sulfate tetrahedron (sulfur yellow, oxygen red) and the centroid (semitransparent sphere with octant)

detailed above and based on the centre of gravity of the experimental polyhedron and the distance of the real ligands to the vertices of the ideal polyhedron.

3.6.3 Quantum Chemical Calculations

In order to access the structures and properties of chemical compounds by quantum chemical methods, the Schrödinger equation has to be solved.

$$H\Psi = E\Psi$$

H : Hamiltonian, Ψ : wave function, E : energy

For multiple atom systems, this is only possible by approximation and often requires immense computational power. In the case of crystalline solids, the density functional theory (DFT) is most frequently used. It is based on the Hohenberg-Kohn theorem.[193] Structure optimisation is achieved by iterative minimisation of atomic forces. In this work, this method is applied to quantify and compare the total energy of various crystal structures. Further, the electron localisation function (ELF) is used in order to investigate the lone pair activity of various compounds and related electron cloud. Therefore, the three-dimensional probability of presence of two electrons with same spin at a given location for the valence electrons w is calculated.[194,195] According to the Pauli principle, these electrons are part of two different electron pairs. The ELF is given by

$$\mathrm{ELF} = \frac{1}{1 + (c - w)^2}$$

with the arbitrary constant c defined in such way that ELF = 0.5 for a homogeneous electron gas. The ELF adapts values between 0 and 1. High values indicate the presence of an electron pair.[196] For example, high electron localisation can be found in the case of the covalent C-C bonds in diamond between two carbon atoms.[195] Another example is the asymmetric electron density around ns^2 cations with expressed lone pair effects. The DFT calculations in this work were performed and analysed by Jakoah Brgoch, University of Houston and Florian Pielnhofer, Universität Regensburg using the Vienna ab initio Simulation Package (VASP)[197,198] (these calculations employed a plane-wave basis set with projector-augment-wave (PAW) pseudopotentials[199] and the exchange and correlation were described using the Perdew-Burke-Ernzerhof (PBE) functional) and a linear combination of Gaussian-type functions (LCGTF) scheme as implemented in CRYSTAL17[200,201] (spin polarized (open shell) calculations were performed using the PBE[202] xc-functional with D3 dispersion correction[203–205]), respectively.

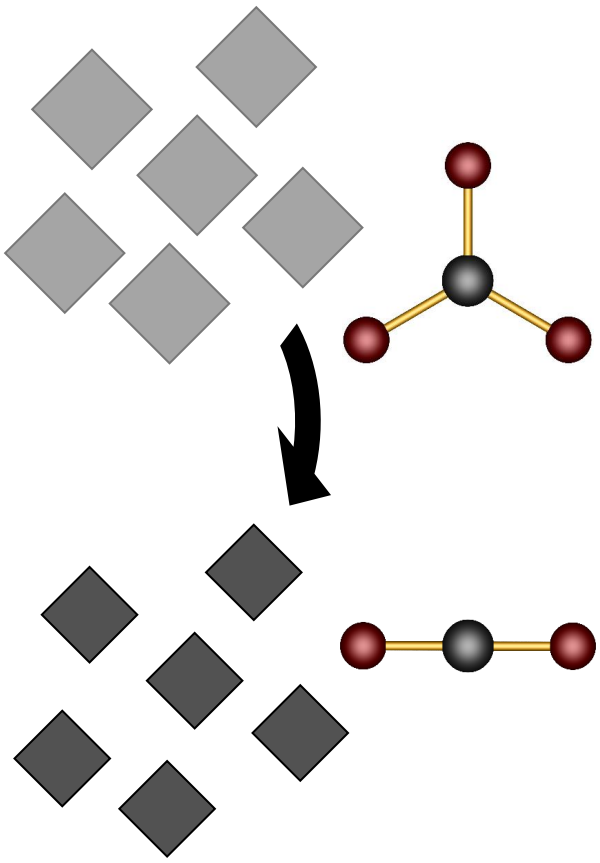

PRECURSORS

4 Carbon-based Precursor Compounds

In the context of silicate-analogous materials detailed in the introduction, cheap and readily available precursors are attractive if the morphology of the precursor is passed on to the final product or if they facilitate new synthesis routes - for example at significantly lower temperature.[20,22–24]

The results presented in the following sections were published partly in the journals *Zeitschrift für anorganische und allgemeine Chemie*[206] and *Zeitschrift für Naturforschung B*,[207] respectively.

4.1 $Sr_3(C_6H_5O_7)_2 \cdot H_2O$

The alkaline earth metal citrate hydrates can be used as precursors, i.e. alkaline metal source, for various oxidic compounds.[208,209] Surprisingly, only a small number of crystal structures has been reported so far for the alkaline earth metal citrates and citrate hydrates.[209–213] Regarding respective strontium compounds, $Sr_3(C_6H_5O_7)_2 \cdot 5\,H_2O$ is the only one with known crystal structure.[211] Moreover, $Sr_3(C_6H_5O_7)_2 \cdot 3.5H_2O$ was reported with the water content being determined by thermogravimetry, only.[208]

Consequently, the strontium citrate monohydrate $Sr_3(C_6H_5O_7)_2 \cdot H_2O$ has hitherto not been reported. According to the experiments detailed in the following it is only accessibly by hydrothermal conditions. The employed microwave-assisted hydrothermal method provides significant advantages such as straightforward preparation, mild reaction conditions, low cost and foremost short duration of syntheses.[214,215]

Frequently, silicate-analogous strontium compounds are capable of substitution of Sr^{2+} by Eu^{2+} ions due to the ions' similar ionic radii of 136 pm and 135 pm, respectively,[216] and the equal charge. Thus, they are suited as hosts for luminescent Eu^{2+} materials, i.e. phosphors for white LED applications.[217,218] $Sr_3(C_6H_5O_7)_2 \cdot H_2O$ could be a promising precursor for the synthesis of such phosphors.

This section contains the first report on $Sr_3(C_6H_5O_7)_2 \cdot H_2O$ and its crystal structure. PXRD, IR spectroscopy and TGA were applied to elucidate its decomposition behaviour as precursor material. For comparison and due to the lack of reported results, $Sr_3(C_6H_5O_7)_2 \cdot 5\,H_2O$ was prepared and investigated by the same methods – again with special interest on the compounds' suitability as precursors. Finally, both precursors are compared to the standard strontium source $SrCO_3$ by the preparation of $SrWO_4$ via solid-state reaction as a proof of principle.

Syntheses

$Sr_3(C_6H_5O_7)_2 \cdot H_2O$ was prepared via a microwave-assisted hydrothermal process. Firstly, 0.2 mmol $Sr(NO_3)_2$ (Fluka, > 99%) and 0.2 mmol citric acid $C_6H_8O_7$ (Bernd Kraft, > 99%) were dissolved in 1 ml deionised H_2O. The solution was filled in a borosilicate glass sample tube (10 ml) after stirring for 30 min (pH = 4). The tube was sealed, placed in a microwave reactor (CEM, Discover S) and heated to 130°C at 80 W for 60 min. After cooling to room temperature, the product was separated and washed by centrifugation at 4000 rpm for 10 min two times with deionised water and once with ethanol. Subsequently, the product was dried in a compartment dryer at 65°C for 24 h. $Sr_3(C_6H_5O_7)_2 \cdot H_2O$ was obtained as a homogeneous colourless and phase-pure powder (Figure 4.1.1 and Table A.1.1) including plate-like single-crystals, depicted in the SEM image in Figure 4.1.2, with a yield of 11% with respect to the employed strontium amount. EDX spectroscopy was used to determine the elemental composition (Figure A.1.1) revealing the presence of solely strontium, carbon and oxygen. The Sr to C ratio yielded 0.34 ± 0.05 and the Sr to O ratio 0.22 ± 0.03, which is in relatively good agreement with the calculated ratios of 0.25 and 0.20, respectively. The deviations can be explained by the decreased accuracy of EDX spectroscopy for low atomic number elements such as carbon and oxygen.

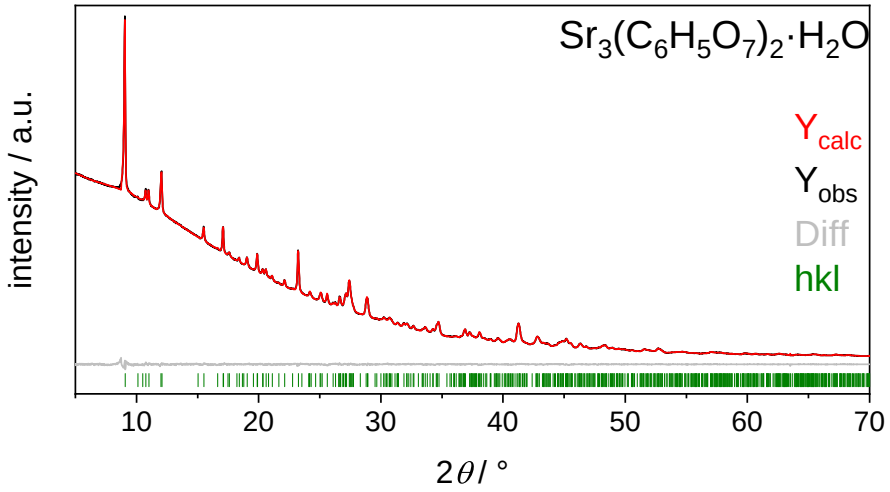

Fig. 4.1.1: Rietveld-Refinement of $Sr_3(C_6H_5O_7)_2 \cdot H_2O$; further details can be found in Table A.1.1.

For comparison, $Sr_3(C_6H_5O_7)_2 \cdot 5\,H_2O$ was synthesised via precipitation from an aqueous solution of 2.05 mmol $SrCl_2 \cdot 6\,H_2O$ (Merck, > 99%) and 1.37 mmol $Na_3C_6H_5O_7 \cdot 2\,H_2O$ (Aldrich, > 99%) dissolved in 50 ml deionised H_2O. After stirring at 100°C for 30 min the resulting precipitate was vacuum-filtered along with washing with additional 50 ml H_2O, then 50 ml Ethanol and finally dried at ambient conditions. $Sr_3(C_6H_5O_7)_2 \cdot 5\,H_2O$ was obtained as a colourless and phase-pure powder (Figure A.1.2) with a yield of 79% with respect to the employed strontium amount.

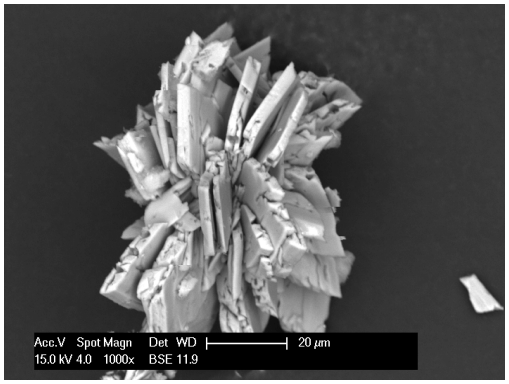

Fig. 4.1.2: SEM image of as prepared $Sr_3(C_6H_5O_7)_2 \cdot H_2O$.

Further, $Sr_3(C_6H_5O_7)_2 \cdot 5\,H_2O$ was dehydrated at 160°C in a corundum crucible inside a tube furnace with $90\,ml\,min^{-1}$ nitrogen flow for 12 h with heating ramps of $80\,K\,h^{-1}$ yielding a colourless powder which showed no crystalline order in the powder X-ray diffractogram (Figure A.1.3). Consequently, only the FT-IR spectrum of this sample was used for further discussion.

Crystal Structure

$Sr_3(C_6H_5O_7)_2 \cdot H_2O$

$Sr_3(C_6H_5O_7)_2 \cdot H_2O$ crystallises in the triclinic crystal system with space group $P\bar{1}$ and two formula units per unit cell. Details of the structure determination are displayed in Table 4.1.1 and the unit cell is shown in Figure 4.1.3.
The three strontium atoms occupying three lattice sites Sr(1), Sr(2) and Sr(3) are coordinated by eight, nine and ten oxygen atoms, respectively. The coordination numbers are confirmed by calculations based on the MAPLE concept (Madelung Part of Lattice Energy).[178–181] The coordination environments of Sr(1), Sr(2) and Sr(3) are depicted in Figure 4.1.4. The Sr(1)O8, Sr(2)O9 and Sr(3)O10 polyhedra are connected via either three or two common oxygen atoms, respectively. Hence, a network is formed. Due to the orientational disorder of one ligand discussed in the following, Sr(3) is disordered over two lattice sites with occupation factors of 83.0(2)% and 17.0(2)%, respectively. All Sr–O distances are reasonably close to the sum of ionic radii (Table 4.1.2) implying an ionic citrate–strontium bonding. By the citrate groups, Sr(1) is coordinated by two bidentate and four monodentate carboxylate groups, Sr(2) is coordinated by seven monodentate carboxylate groups and two hydroxyl groups, and Sr(3) is coordinated by three bidentate and three monodentate carboxylate groups as well as one hydroxyl group in both the majority and the minority variant (Figure A.1.4). The crystal water molecule does not coordinate directly to any strontium atom.
There are two different citrate groups both in trans/trans conformation, one of these shows oriental disorder. There, the substituents at the C-3 atom, i.e. the hydroxyl and

Tab. 4.1.1: Crystal data and structure refinement of $Sr_3(C_6H_5O_7)_2 \cdot H_2O$ determined from SC-XRD; the respective standard deviations are given in parentheses.

CSD-No.	1986186
M / g mol^{-1}	659.08
Crystal size / mm^3	0.08 × 0.04 × 0.02
Temperature / K	287(2)
Space group	$P\bar{1}$ (No. 2)
a / pm	1005.72(4)
b / pm	1015.06(5)
c / pm	1085.31(5)
α / °	89.642(2)
β / °	67.156(2)
γ / °	62.367(2)
Volume / 10^6 pm^3	883.85(7)
Z	2
ρ_{calcd} / g cm^3	2.476
Absorption coefficient μ / mm$^{\smile 1}$	9.1
F (000) / e	636
Radiation; wavelength λ / Å	Mo-K_α; 0.71073
Diffractometer	Bruker D8 Venture
Θ range / °	2.318-24.799
Absorption correction	multi-scan
Transmission (min; max)	0.6014; 0.7453
Index range $h \mid k \mid l$	±11 | ±11 | ±12
Reflections collected	30895
Independent reflections	3040
Obs. reflections [$I > 2\sigma(I)$]	2659
Refined parameters / restraints	353 / 47
R_{int}	0.059
R_1	0.039
wR_2	0.066
GOF	1.054
Residual electron density (max; min) / e^-Å^{-3}	1.16; -0.88

carboxyl groups, change their positions in approximately one fifth of all cases as shown in Figure 4.1.5. This disorder also causes a respective disorder of one strontium atom (Sr(3)). The conformation of the citrate anions in this work is in line with reports on alkali metal citrates with this conformation appearing for larger cations.[219] In the first citrate group, each of the three carboxylate groups coordinate one strontium bidentate and two strontium monodentate. In the majority disorder variant of the second citrate group, one carboxylate group coordinates one strontium bidentate and two further strontium atoms monodentate, the second carboxylate group coordinates one strontium bidentate and one monodentate and the third carboxylate group coordinates two strontium atoms monodentate. In the minority variant, two carboxylate groups are coordinating one strontium atom bidentate and two strontium atoms monodentate each, while the third carboxylate group coordinates two strontium atoms monodentate. Consequently, there is no non-coordinating oxygen atom in both citrate groups including the disordered variants.

The bond lengths and interatomic angles within the citrate groups depicted in Table 4.1.2 agree well with reports on other citrates and citric acid.[219,220] Within the carboxylate

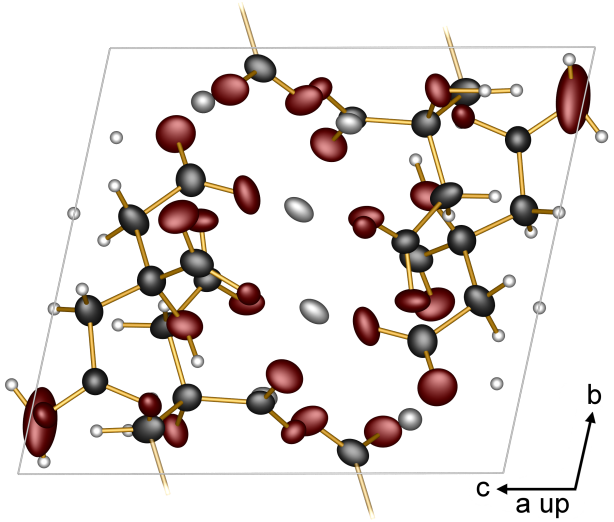

Fig. 4.1.3: Perspective view of the unit cell of $Sr_3(C_6H_5O_7)_2 \cdot H_2O$; the strontium atoms are shown in light grey, oxygen in red, carbon in black and hydrogen in white; the displacement ellipsoids are set to 60% probability and hydrogen atoms are shown as simple spheres; only the majority component is shown for the sake of clarity.

groups, the bond lengths are within the sum of ionic radii of 130 pm[216] implying a covalent bond, alongside with O–C–O angles larger than 120° due to the charge.

The two citrate groups differ in the conformation of hydrogen bonds shown in Figure A.1.5, too. The hydroxyl group of the first citrate group forms a hydrogen bond to the crystal water molecule, while the second exhibits intramolecular hydrogen bonds between the hydroxyl group and two carboxylate groups in the majority variant. The shorter distance to one carboxylate group is due to the respective oxygen atom being coordinated by two strontium atoms versus the oxygen atom of the other carboxylate group being bridging three strontium atoms. Further, intermolecular hydrogen bonds from the hydroxyl group to one methylene group of the first citrate group alongside with two hydrogen bonds of

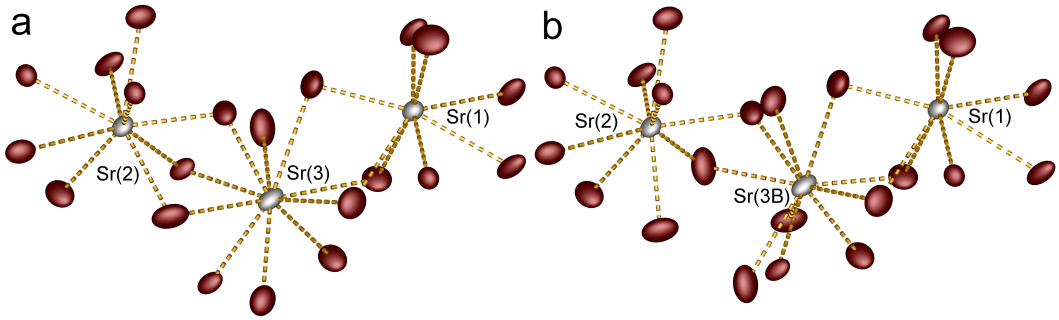

Fig. 4.1.4: Coordination environments of the Sr^{2+} cations in $Sr_3(C_6H_5O_7)_2 \cdot H_2O$; the strontium atoms are shown in light grey, oxygen in red; the displacement ellipsoids are set to 60% probability; in (a) the majority components of the orientational disorder and in (b) the minority components are shown.

Tab. 4.1.2: Selected interatomic distances (in pm) and angles (in °) in $Sr_3(C_6H_5O_7)_2 \cdot H_2O$; the respective standard deviations are given in parentheses.

Sr(1)-O	247(1)-291(6)
Sr(2)-O	247(5)-298.2(4)
Sr(3)-O[i]	249.7(4)-278.0(5)
Sr(3B)-O[ii]	243.9(5)-279.2(5)
$\sum$ IR (Sr(1)-O)[216][iii]	261-264
$\sum$ IR (Sr(2)-O)[216][iii]	266-269
$\sum$ IR (Sr(3)-O)[216][iii]	271-274
C-O_C[iv]	119(2)-128.0(8)
O-C-O	122.4(5)-125.9(7)
C-O_H[v]	137(2)-145.5(6)
C-C	152(2)-154(2)

[i] Majority component; [ii] Minority component; [iii] Range of ionic radii sums due to oxygen with CN = 2, 3 and 4; [iv] O_C = oxygen as part of carboxylate group; [v] O_H = oxygen as part of hydroxide group.

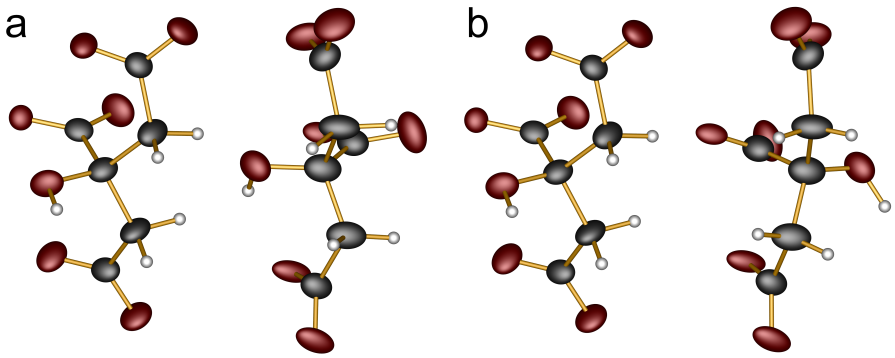

Fig. 4.1.5: The two different citrate anions in $Sr_3(C_6H_5O_7)_2 \cdot H_2O$: (a) shows the majority variant and (b) the minority variant differing in the orientation of the hydroxyl group of the citrate group on the right side; carbon is shown in black, oxygen in red and hydrogen in white; the displacement ellipsoids are set to 60% probability and hydrogen atoms are shown as simple spheres.

carboxylate groups with the crystal water molecule are formed in the majority variant. The minority component forms hydrogen bonds to the crystal water, only. However, the hydroxyl group is involved in the coordination of the strontium atoms. Presumably due to the difference in hydrogen bonding, the hydroxyl group and the central carboxylate group lie in the same plane in the first citrate molecule, only.

Consequently, the citrate groups form their own network connected via hydrogen bonds. The complete crystal structure is constructed by the two interpenetrating Sr–O and citrate–water frameworks.

$Sr_3(C_6H_5O_7)_2 \cdot 5\,H_2O$

The crystal structure of $Sr_3(C_6H_5O_7)_2 \cdot 5\,H_2O$ was reported by Zacharias and Glusker in 1993.[211] Here, there are also three strontium sites coordinated by 8, 9 or 10 oxygen atoms. The resulting Sr(1)O9, Sr(2)O8, Sr(3)O10 polyhedra are connected either via two or three oxygen atoms forming chains. The Sr-O distances of 250 to 278 pm are slightly smaller than the ones found in $Sr_3(C_6H_5O_7)_2 \cdot H_2O$. The major difference between both structures are the coordinating crystal water molecules in $Sr_3(C_6H_5O_7)_2 \cdot 5\,H_2O$. Sr(1) is coordinated by two bidentate and two monodentate carboxylate groups as well as twice by crystal water and by one hydroxyl group. Sr(2) is coordinated by six monodentate carboxylate groups and two crystal water molecules, whereas Sr(3) is coordinated by two bidentate and two monodentate carboxylate groups as well as one hydroxyl group and three crystal water molecules. Consequently, both citrate groups have two bidentate and one monodentate carboxylate group with one oxygen atom not coordinating any strontium atom. This oxygen atom is coordinated by hydrogen bonds towards the crystal water molecules. Via hydrogen bonds, the two citrate groups form chains that are connected towards layers via further hydrogen bonding with the crystal water molecules. Similarly, the Sr-O chains form a Sr-O-water network via hydrogen bonds.
To conclude, $Sr_3(C_6H_5O_7)_2 \cdot H_2O$ consists of interpenetrating Sr–O and citrate–water networks, whereas the network of $Sr_3(C_6H_5O_7)_2 \cdot 5\,H_2O$ is formed by the combination of Sr-O chains and citrate chains connected by hydrogen bonding via the crystal water molecules.

Infrared Spectroscopy

Infrared spectroscopy was performed on $Sr_3(C_6H_5O_7)_2 \cdot H_2O$ and $Sr_3(C_6H_5O_7)_2 \cdot 5\,H_2O$ powders as well as on dehydrated $Sr_3(C_6H_5O_7)_2 \cdot 5\,H_2O$. The spectra shown in Figure 4.1.6 fit to published reports for similar compounds.[141,221–224] The presence or absence of crystal water is shown by the OH stretching vibration around 3400 cm^{-1}. Consequently, the dehydrated $Sr_3(C_6H_5O_7)_2 \cdot 5\,H_2O$ can be treated as $Sr_3(C_6H_5O_7)_2$ with a broad weak ν(OH) band remaining between 3400 cm^{-1} and 3200 cm^{-1} due to hydrogen bonds within the compound. The spectra are dominated by asymmetric carboxylate stretching modes around 1550 cm^{-1} and the symmetric carboxylate stretching modes between 1450 and 1400 cm^{-1}. The COH bending vibrations appear around 1080 cm^{-1} in all three spectra. This confirms the formation of $Sr_3(C_6H_5O_7)_2$ instead of $Sr_3(C_6H_3O_6)_2$ after the dehydration together with the ν(OH) bands around 520 cm^{-1}. CH_2 bending modes appear between 1330 and 1260 cm^{-1} and around 850 and 750 cm^{-1}. The weak C–C bending vibrations are located around 2950 and 1700 cm^{-1} with the former overlapping with C–H stretching modes. In $Sr_3(C_6H_5O_7)_2 \cdot 5\,H_2O$, the additional band around 1200 cm^{-1} is assigned to the additional bending mode within the carboxylate group due to one oxygen atom within the carboxylate group not coordinating a strontium cation. The Sr–O vibrations appear below wavenumbers of 450 cm^{-1} with more intensity

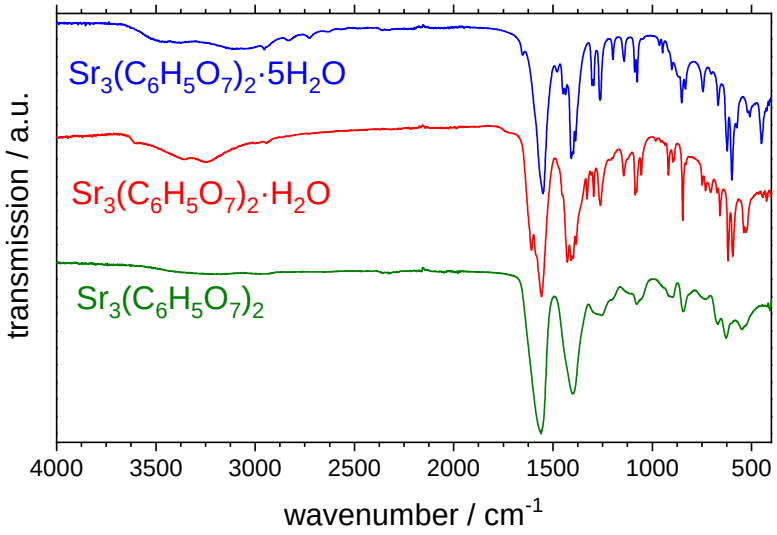

Fig. 4.1.6: Infrared spectra of $Sr_3(C_6H_5O_7)_2 \cdot H_2O$, $Sr_3(C_6H_5O_7)_2 \cdot 5\,H_2O$ and dehydrated $Sr_3(C_6H_5O_7)_2 \cdot 5\,H_2O$ labelled $Sr_3(C_6H_5O_7)_2$.

in $Sr_3(C_6H_5O_7)_2 \cdot 5\,H_2O$ than in $Sr_3(C_6H_5O_7)_2 \cdot H_2O$ due to the shorter Sr–O distances shifting the band above $400\,cm^{-1}$ and thus, in the measured range.

Thermal Decomposition

The thermal decompositions of both $Sr_3(C_6H_5O_7)_2 \cdot H_2O$ and $Sr_3(C_6H_5O_7)_2 \cdot 5\,H_2O$, were investigated by thermal analysis. For the monohydrate, the TG curve shows three plateaus (Figure 4.1.7). Firstly, one molecule H_2O is lost around 150°C. Between 300°C and 560°C two steps overlap. Here, presumably the reactions from strontium citrate to strontium aconitate, $Sr_3(C_6H_3O_6)_2$, followed by the decomposition of $Sr_3(C_6H_3O_6)_2$ to $SrCO_3$ occur. The last step between 700 and 880°C agrees well with the decomposition of $SrCO_3$ to strontium oxide. The mass losses during the decomposition match well with the expected values of the suggested intermediates (Table A.1.2) and are in agreement with earlier reports on other alkaline earth citrate hydrates.[209,225–227] Importantly, the first mass loss confirms the composition of the title compound as monohydrate.

The decomposition of the pentahydrate, $Sr_3(C_6H_5O_7)_2 \cdot 5\,H_2O$, follows a very similar sequence at almost the same temperatures (Figure 4.1.7 and Table A.1.3). There is no indication of the intermediate formation of the monohydrate during the first dehydration step. The formation of anhydrous $Sr_3(C_6H_5O_7)_2$ agrees well with the FT-IR spectrum of dehydrated $Sr_3(C_6H_5O_7)_2 \cdot 5\,H_2O$ discussed above (Figure 4.1.6). In contrast to $Sr_3(C_6H_5O_7)_2 \cdot H_2O$, the step towards strontium aconitate forms a distinct plateau. Furthermore, the mass losses for the formation of $SrCO_3$ and SrO deviate stronger from the calculated values than for $Sr_3(C_6H_5O_7)_2 \cdot H_2O$. This might be due to incomplete decomposition of $Sr_3(C_6H_3O_6)_2$ as reported for respective calcium and barium citrate

hydrates[226,228] or residual amorphous carbon. The formation of SrO is confirmed by powder X-ray diffraction (Figure A.1.6) after heating a sample of $Sr_3(C_6H_5O_7)_2 \cdot 5\,H_2O$ at 1200°C in a corundum crucible inside a muffle furnace for 10 h with heating ramps of $200\,K\,h^{-1}$. Interestingly, $Sr(OH)_2$ as final product is a conceivable explanation of the experimentally observed mass loss. But this is in disagreement with literature reporting its decomposition and the formation of SrO above 700°C[229] and our powder X-ray diffraction results – so it is chemically highly improbable.

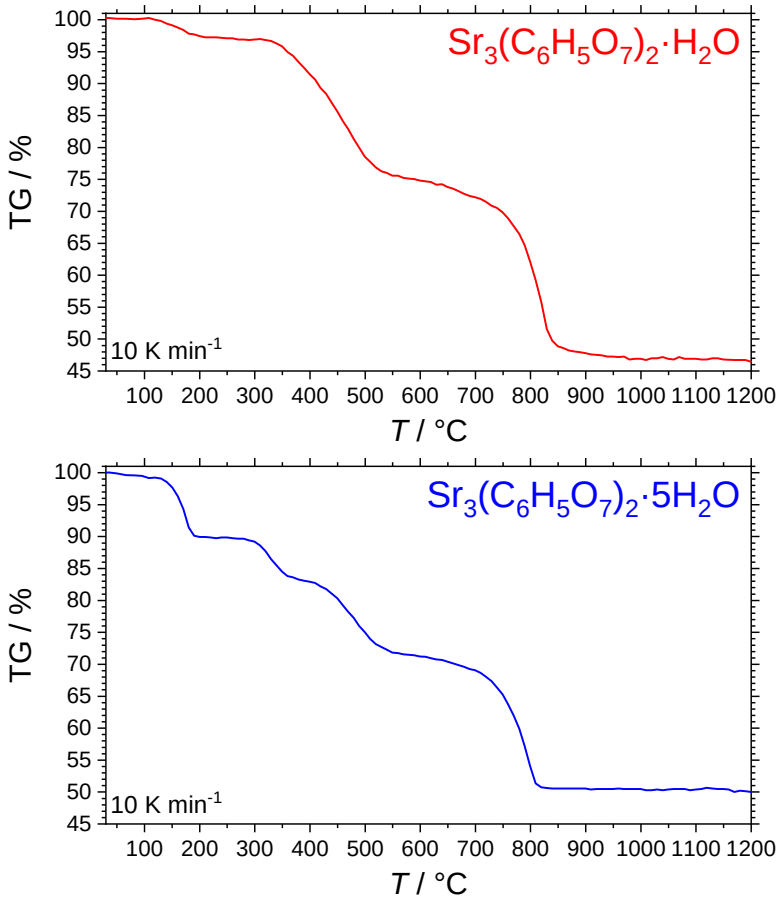

Fig. 4.1.7: Thermal analysis of $Sr_3(C_6H_5O_7)_2 \cdot H_2O$ (top) and $Sr_3(C_6H_5O_7)_2 \cdot 5\,H_2O$ (bottom): the thermogravimetric (TG) curve is shown versus temperature T.

Proof of Principle

Strontium tungstate $SrWO_4$ crystallises in the *scheelite* structure type[230,231] which is also the most important structure type of the double tungstates discussed in chapter 5. It is reported to be both a phosphor and a promising host material for phosphors.[232–234] Here, it was chosen as a simple example for the proof of principle. Therefore, $SrWO_4$ was prepared via solid-state reaction from the precursors ammonium paratungstate

tetrahydrate $(NH_4)_{10}[H_2W_{12}O_{42}] \cdot 4\,H_2O$ (Alfa Aesar, > 99.9%) and $Sr_3(C_6H_5O_7)_2 \cdot H_2O$, $Sr_3(C_6H_5O_7)_2 \cdot 5\,H_2O$ (both prepared as detailed above) or $SrCO_3$ (Aldrich, > 96%), respectively. The latter was chosen as a typical strontium educt.
Stochiometric amounts of the educts were ground, filled in corundum crucibles and successively heated for 24 h at 500, 600 and 700°C with heating and cooling ramps of $200\,K\,h^{-1}$. The resulting PXRD patterns are shown in Figure 4.1.8 showing the successful synthesis of $SrWO_4$. $(NH_4)_{10}[H_2W_{12}O_{42}] \cdot 4\,H_2O$ decomposes to WO_3 between 400 and 500°C.[235,236] Consequently, WO_3 is present as a side phase with its fraction decreasing with synthesis temperature. After the 500°C heating step, traces of $SrCO_3$ can be found in the PXRD. In contrast to that, both strontium citrate precursors are readily decomposed and not present in the PXRD demonstrating their suitability as precursors. This can best be seen by the diffractogram of the synthesis with $Sr_3(C_6H_5O_7)_2 \cdot 5\,H_2O$ (b, blue) after 500°C. Here, the final product is almost phase pure compared to highly mixed sample for the conventional educt $SrCO_3$ (c, blue).

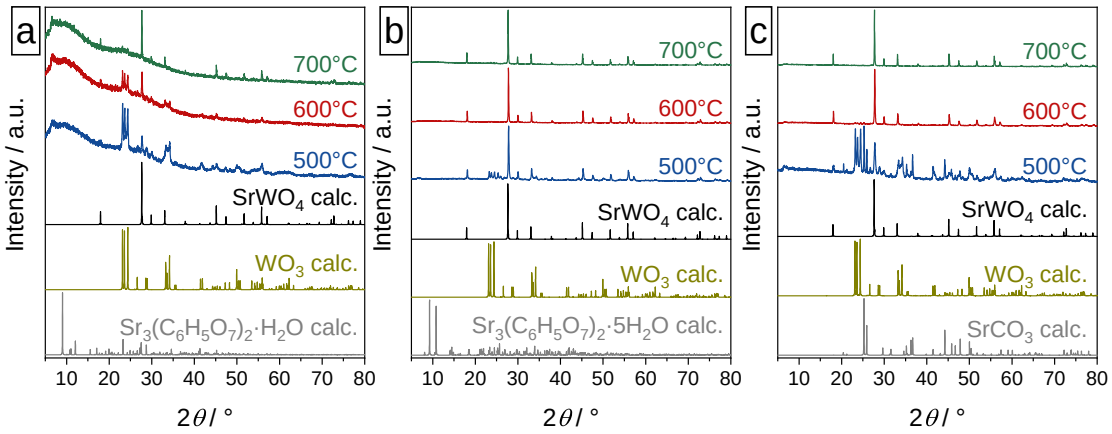

Fig. 4.1.8: PXRD patterns of the three $SrWO_4$ samples prepared from the precursors ammonium paratungstate tetrahydrate $(NH_4)_{10}[H_2W_{12}O_{42}] \cdot 4\,H_2O$ and $Sr_3(C_6H_5O_7)_2 \cdot H_2O$ (a), $Sr_3(C_6H_5O_7)_2 \cdot 5\,H_2O$ (b) or $SrCO_3$ (c), respectively. The experimental patterns are compared to calculated ones for $Sr_3(C_6H_5O_7)_2 \cdot H_2O$ from the SC-XRD, $Sr_3(C_6H_5O_7)_2 \cdot 5\,H_2O$,[211] $SrCO_3$,[237] WO_3[238] and $SrWO_4$;[231] the samples were successively heated for 2h h at the stated temperatures; the signal to noise ratio is worse for (a) due to a smaller total sample amount.

Consequently, both $Sr_3(C_6H_5O_7)_2 \cdot H_2O$ and $Sr_3(C_6H_5O_7)_2 \cdot 5\,H_2O$ are promising precursor materials for strontium compounds and - as discussed above - also for Eu^{2+} phosphors. Furthermore, $SrWO_4$:Eu^{3+} phosphors were reported in literature,[233] i.e. substituting Sr^{2+} by Eu^{3+} instead of Eu^{2+}. However, the material class presented in the following appears to be a better suited precursor for such applications.

4.2 *Ln*[CO_3][OH] (*Ln* = La, Pr, Nd, Sm, Eu, Gd, Tb)

Not only for Eu^{3+} phosphors, but for luminescent materials comprising trivalent rare earth cations in general, the rare earth carbonate hydroxides *Ln*[CO_3][OH] are a highly interesting class of materials with promising applications as host materials for phosphors,[239,240] catalysts,[241] magnetic-cooling materials,[242] and precursors for both rare earth carbonate dioxides and rare earth oxides and further synthesis.[20,240,243–247] The rare earth carbonate dioxides $Ln_2[CO_3]O_2$ can be used also as catalysts or catalyst support,[248] as host materials for luminescent applications[239,240] and as precursors for further syntheses.[243,249] The pure rare earth oxides Ln_2O_3 are well known as host materials for phosphors.[101]

In general, rare earth carbonate hydroxides occur in three modifications: A hexagonal modification crystallising in space group $P\bar{6}$ (no. 174) , an orthorhombic modification and a tetragonal modification crystallising in space group $P4_2/nmc$ (no. 137) existing only for Tm and Yb.[20,250–254] The orthorhombic polymorph is reported in space group *Pnma* (no. 62) for the large rare earth ions Pr, Nd and Sm and in space group $P2_12_12_1$ (no. 19) for the rare earth ions smaller than Sm (Eu, Gd, Tb, Dy, Ho, Er, Tm and Y).[20,250,252,254–256] Nevertheless, space group *Pnma* is also reported for Gd[CO_3][OH][242,257] showing disagreement with the exact structure of the orthorhombic modification. This issue is addressed in the following investigating the non-linear optical properties in addition to the redetermination of the crystal structures.

Several syntheses for rare earth carbonate hydroxides are reported in literature via homogeneous precipitation,[20,240,244] hydrothermal methods[20,239,241,246,247,250,253] solvothermal methods,[258] and thermolysis.[243]

In nature, the mineral *ancylite* $La_2O(CO_3)_2 \cdot H_2O$ crystallises in space group *Pnma* (no. 62).[259] It is the only rare earth oxycarbonate hydrate for which the crystal structure has been solved.[20,259] Dal Negro et al. solved the structure using a single-crystal from geological origin.[259] In the following, it will be shown that this compound is isotypic with orthorhombic La[CO_3][OH].[250]

In this section, the hydrothermal synthesis of orthorhombic *Ln*[CO_3][OH] (*Ln* = La, Pr, Nd, Sm, Eu, Gd) using CO_2 from air as carbonate source is presented. This process is likely to resemble the pathway followed in nature to form minerals such as *ancylite* or *kozoite* giving further insight into the formation of these minerals.[259–261]

The crystal structures of Pr[CO_3][OH], Eu[CO_3][OH], Gd[CO_3][OH] and Tb[CO_3][OH] are redetermined localising also the hydrogen atoms, and the first report on the structure of orthorhombic La[CO_3][OH] based on single-crystal XRD data is given. The structures are elucidated with a special focus on the presence or absence of inversion symmetry, as this point was under discussion in the literature. Further, the use of the materials as precursors for $Ln_2[CO_3]O_2$ and Ln_2O_3 is demonstrated accompanied by optical and thermal characterisation.

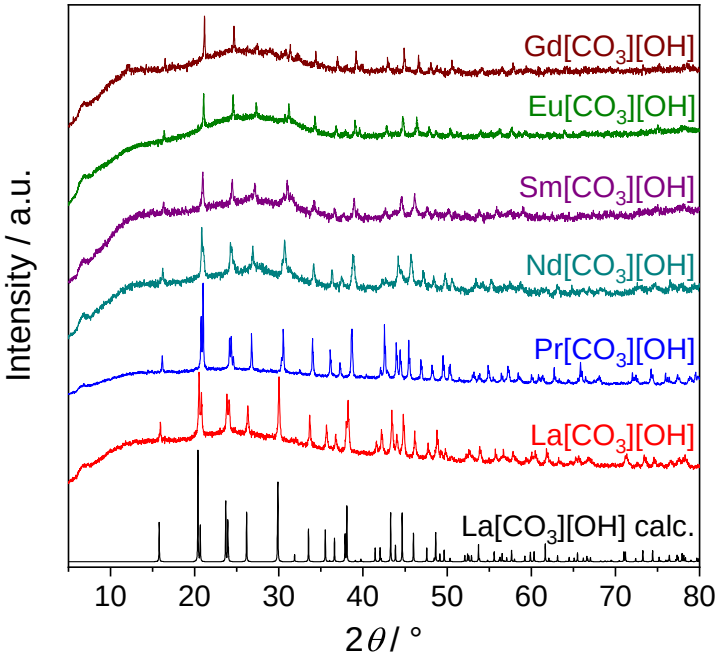

Fig. 4.2.1: PXRD patterns of *Ln*[CO$_3$][OH] (*Ln* = La, Pr, Nd, Sm, Eu, Gd) compared to a pattern calculated from single-crystal data of La[CO$_3$][OH] showing phase purity: With decreasing ionic radii due to the lanthanide contraction the double reflexes around $2\Theta = 20.5°$ and 24° are shifted closer to each other and eventually become no longer distinguishable for Eu[CO$_3$][OH] and Gd[CO$_3$][OH]; at the same time, the two reflexes around $2\Theta = 30°$ are drifted apart.

Syntheses

Phase-pure samples of *Ln*[CO$_3$][OH] (*Ln* = La, Pr, Nd, Sm, Eu, Gd) (Figure 4.2.1) were obtained via a facile hydrothermal process starting from aqueous solutions of 1 mmol *Ln*(NO$_3$)$_3 \cdot x$H$_2$O[i] in 20 ml H$_2$O. 0.5 mmol Cetyltrimethylammonium bromide (CTAB, Fluka) were added. It is well known to serve as a templating agent.[20,22] In literature, comparable syntheses using among others CO(NH$_2$)$_2$, Na$_2$CO$_3$, NaHCO$_3$, (NH$_4$)$_2$CO$_3$ as carbonate sources have been reported.[20,246] CO$_2$ is expected to act as carbonate source in the solvothermal synthesis of hexagonal La[CO$_3$][OH] in an ionic liquid-water mixture.[258] Accordingly, the first intended hydrothermal synthesis using only CO$_2$ from ambient air as carbonate source is reported here and further it is demonstrated, how easily these compounds are formed.

After stirring for 20 min at 70°C, the solution (pH = 5) was transferred into 30 ml PTFE pressure digestion vessels,[119] which were heated in a compartment dryer at 180°C for five days. After the vessels naturally cooled to room temperature, the precipitates were

[i] Namely, La(NO$_3$)$_3 \cdot 6$ H$_2$O, Nd(NO$_3$)$_3 \cdot 6$ H$_2$O, Pr(NO$_3$)$_3 \cdot 6$ H$_2$O (all from Strem Chemicals, Inc.), Eu(NO$_3$)$_3 \cdot 5$ H$_2$O, Sm(NO$_3$)$_3 \cdot 6$ H$_2$O (both from Alfa Aesar), Gd(NO$_3$)$_3 \cdot x$H$_2$O (Chempur) and Ce(NO$_3$)$_3 \cdot 5$ H$_2$O (Merck) were used.

separated and washed by centrifugation at 4000 rpm for 10 min with deionised water three times and subsequently dried in a compartment dryer at 65°C for 24 h.
All syntheses yielded homogeneous, coarsely crystalline products. The CTAB apparently has an influence on particle sizes and shape distributions (Figure A.2.1). For *Ln* = Nd, Sm, Eu and Gd, an additional heating step at 350°C for 10 h in corundum crucibles (heating ramps 200 K h^{-1}) was necessary to decompose residual CTAB and an unknown side product. The presence of these side phases was shown by infrared spectroscopy (Figure A.2.2), their decomposition around 350°C could be followed by DSC measurements (Figure A.2.3); this thermal behaviour of CTAB is well known.[262] The DSC measurements of Eu[CO_3][OH] and Gd[CO_3][OH] revealed an extra endothermic peak at 350°C corresponding to the decomposition of the side phases. This peak is not present for La[CO_3][OH] and Pr[CO_3][OH].
Further, the *Ln*[CO_3][OH] (*Ln* = La, Pr, Eu, Gd) samples were investigated by EDX. The expected molar ratio of the respective rare earth element and oxygen and the experimental results shown in Table 4.2.1 match well. The simultaneously taken SEM pictures show the crystallinity of the compound (Figure 4.2.2).

Tab. 4.2.1: EDX results for *Ln*[CO_3][OH] (*Ln* = La, Pr, Eu, Gd) comparing the ratio of *Ln* to O to the stoichiometric value of 0.25; the respective standard deviations are given in parentheses.

Sample	EDX result
La[CO_3][OH]	0.19(5)
Pr[CO_3][OH]	0.18(3)
Eu[CO_3][OH]	0.27(6)
Gd[CO_3][OH]	0.26(6)

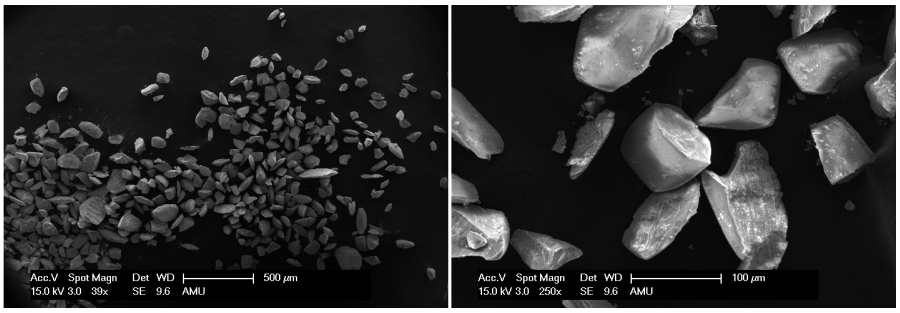

Fig. 4.2.2: SEM pictures of as prepared La[CO_3][OH] taken simultaneously to the EDX measurement.

Surprisingly, - at first - the use of $Ce(NO_3)_3 \cdot 5\,H_2O$ yielded phase-pure CeO_2 single-crystals (Figure A.2.4). Similar syntheses also using CTAB as templating ligand are known in the literature.[263] The reason for this behaviour can be found in the high stability of CeO_2 at low oxygen partial pressures.[264]
Notable, analogous syntheses with the smaller rare earth ions such as terbium did not yield phase-pure powders. Thus, Tb[CO_3][OH] was prepared using urea $CO(NH_2)_2$

instead of solely CO_2 from air as carbonate source.[ii] Similarly to the syntheses above, 1 mmol $Tb(NO_3)_3 \cdot 5\,H_2O$ (99.9%, Aldrich) and 0.5 mmol CTAB were dissolved in 20 ml H_2O by stirring for 20 min at 70°C. Then, 0.5 mmol urea were added to the clear solution which was stirred for another 30 min (pH = 5) before transfer into 30 ml PTFE pressure digestion vessels,[119] which were heated in a compartment dryer at 180°C for five days. After the vessels naturally cooled to room temperature, the precipitates were separated and washed by vacuum filtration with 200 ml H_2O and 100 ml ethanol and subsequently dried in a compartment dryer at 65°C for 24 h. Tb[CO_3][OH] was obtained in the form of a phase-pure powder containing single-crystals (Figure A.2.5).

Crystal Structures

Ln[CO_3][OH] (*Ln* = La, Pr, Eu, Gd)

All four compounds crystallise isotypically with *kozoite* in the orthorhombic crystal system with space group *Pnma* and four formula units per unit cell (Table 4.2.2). Due to ambiguity in literature, Eu[CO_3][OH] was additionally solved and refined in space group $P2_12_12_1$. This aspect is discussed below.

Five carbonate and two hydroxide groups are coordinated to the respective Ln^{3+} ion. Two carbonate groups act as monodentate and three as bidentate ligands. Thus, the Ln^{3+} ions are coordinated by ten oxygen atoms (Figure 4.2.3). The Ln^{3+} cation and the OH^- anions form $^1_\infty[(OH)Ln_{2/2}]^{2+}$ zigzag chains along [100] linked by carbonate anions.[250] The hydroxide anions are oriented towards the resulting channels between the chains (Figure 4.2.4). Each carbonate group acts as a bidentate ligand to three Ln^{3+} ions and as a monodentate ligand to two other Ln^{3+} ions. Consequently, the carbon atom is coordinated by three oxygen atoms in the first and surrounded by five Ln^{3+} ions in the second coordination sphere.

The Ln^{3+} cations are situated on Wyckoff site 4*c* with the *Ln*–O distances ranging from 240 to 278 pm (La[CO_3][OH]), 236 to 276 pm (Pr[CO_3][OH]), 230 to 275 pm (Eu[CO_3][OH]), and 230 to 276 pm (Gd[CO_3][OH]) (Table 4.2.3). These values are reasonably close to the sum of the respective ionic radii (Table 4.2.3).[216] The distances between adjacent Ln^{3+} ions are decreasing, following the lanthanide contraction, and the *Ln*–O distances follow the same trend. The bond lengths within the carbonate ions are below the sum of the ionic radii of 130 pm[216] implying a covalent bond. The O-C-O angles are close to 120°. Gd[CO_3][OH] has the largest deviation due to the increased repulsion between adjacent carbonate groups, since their distance is decreasing with the lanthanide contraction.

The electrostatic reasonability of the crystal structures was confirmed by calculations based on the MAPLE concept. The MAPLE values of La[CO_3][OH], Pr[CO_3][OH], Eu[CO_3][OH] and Gd[CO_3][OH] were calculated and compared to the sum of the respective chemically comparable rare earth oxides, ice and a hypothetical CO_2 derived from

[ii] This synthesis works also for Dy[CO_3][OH], Ho[CO_3][OH] and Er[CO_3][OH]. These results are not shown here.

Tab. 4.2.2: Crystal data and structure refinements of La[CO$_3$][OH], Pr[CO$_3$][OH], Eu[CO$_3$][OH] and Gd[CO$_3$][OH]; the respective standard deviations are given in parentheses.

	La[CO$_3$][OH]	Pr[CO$_3$][OH]	Eu[CO$_3$][OH]	Eu[CO$_3$][OH]	Gd[CO$_3$][OH]
CSD-No.	1862162	1862163	1862164		1862165
M / g mol^{-1}	215.93	217.93	228.98	228.98	234.27
Crystal size / mm^3	0.02 × 0.06 × 0.06	0.04 × 0.06 × 0.10	0.05 × 0.05 × 0.13	0.05 × 0.05 × 0.13	0.03 × 0.04 × 0.06
Temperature / K			300(2)		
Space group	*Pnma* (No. 62)	*Pnma* (No. 62)	*Pnma* (No. 62)	$P2_12_12_1$ (No. 19)	*Pnma* (No. 62)
a / pm	741.06(5)	727.55 (4)	710.40(4)	710.40(4)	706.9(7)
b / pm	505.02(3)	499.18(3)	489.40(3)	489.40(3)	487.4(5)
c / pm	859.01(6)	852.07(5)	845.77(5)	845.77(5)	846.4(9)
Volume / 10^6 pm^3	321.48(4)	309.45(3)	294.05(3)	294.05(3)	291.7(5)
Z			4		
ρ_{calcd} / g cm^3	4.46	4.68	5.17	5.17	5.34
Absorption coefficient μ / mm^{-1}	13.1	15.6	21.1	21.1	22.6
F (000) / e	384	392	408	408	412
Radiation; wavelength λ / Å			Mo-K_α; 0.71073		
Diffractometer			Bruker D8 Venture		
Absorption correction			multi-scan		
Transmission (min; max)	0.5936; 0.7461	0.6578; 0.7474	0.5307; 0.7503	0.5307; 0.7503	0.5815; 0.7465
Index range h | k | l	±10 | −6/7 | ±12	−10/12 | ±8 | −13/14	±15 | ±10 | −15/18	±15 | ±10 | −15/18	±9 | ±6 | ±11
Θ range / °	3.631-30.964	3.682-35.988	3.746-49.967	3.746-49.967	3.755-29.917
Reflections collected	3558	6776	8923	9324	3121
Independent reflections	563	801	1649	3076	465
R_{int}	0.032	0.047	0.031	0.029	0.073
Obs. reflections [$I > 2\sigma(I)$]	492	676	1478	2600	386
Refined parameters / restraints	38 / 1	38 / 1	38 / 1	61 / 1	38 / 1
R_1 (all data)	0.024	0.030	0.029	0.029	0.041
wR_2 (all data)	0.037	0.041	0.050	0.044	0.052
GOF	1.12	1.09	1.35	1.09	1.08
Flack x parameter	–	-	-	0.59(5) (refined as an inversion twin)	–
Residual electron density (max; min) / e^-Å^{-3}	1.35; -0.96	1.74; -1.22	2.77; -2.25	2.54; -1.37	1.26; -1.28

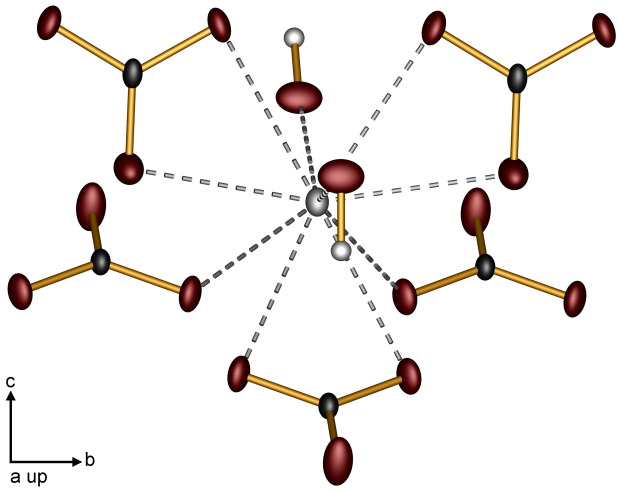

Fig. 4.2.3: Coordination of the Ln^{3+} cation in *Ln*[CO$_3$][OH] in space group $Pnma$ (grey: *Ln*, black: C, white: H, red: O); displacement ellipsoids are set to 75% probability; the data of La[CO$_3$][OH] was used for this figure.

Tab. 4.2.3: Selected interatomic distances (in pm) and angles (in °) in La[CO$_3$][OH], Pr[CO$_3$][OH], Eu[CO$_3$][OH] and Gd[CO$_3$][OH]; the respective standard deviations are given in parentheses.

	La[CO$_3$][OH]	Pr[CO$_3$][OH]	Eu[CO$_3$][OH]	Gd[CO$_3$][OH]
Ln-O$_C$ [i]	258.13(8)-278.0(2)	255.06(7)-275.5(2)	250.30(5)-274.89(17)	249.7(3)-275.8(5)
Ln-O$_H$ [ii]	240.9(3)-242.7(3)	236.2(3)-237.2(3)	230.4(2)-231.0(2)	229.8(7)-230.4(7)
$\sum$ IR (Ln-O) [216,265] [iii]	263; 265	259.2; 261.2	253.2; 255.2	250.8; 252.8
Ln-Ln	396.85(4)	390.45(4)	382.89(3)	381.54(34)
C-O	126.5(5)-129.4(3)	126.7(5)-129.1(3)	126.9(3)-128.6(2)	124.4(12)-129.3(7)
C-C	388.67(63)	382.73(61)	376.61(40)	374.82(119)
O-C-O	119.3(4)-120.31(18)	119.7(3)-120.05(17)	119.3(2)-120.29(12)	117.7(8)-121.1(4)
O-Ln-O	49.28(9)-94.45(5)	49.19(8)-94.84(5)	49.64(6)-95.08(4)	49.43(17)-94.83(11)

[i] O$_C$ = oxygen as part of the carbonate group; [ii] O$_H$ = oxygen as part of the hydroxide group;
[iii] Different sums of ionic radii due to oxygen with both CN = 3 and 4.

the difference of $CaCO_3$ and CaO – an approach also employed recently for other oxides, in which the respective crystal structure comprises only molecules.[266] For $CaCO_3$, the aragonite structure was chosen since there the carbonate group shows C_s symmetry being close to the C_{2v} symmetry of the carbonate groups in the present compounds.[141] The deviation is well below 1% for all four structures, which is the empirical benchmark for electrostatic consistency (Table A.2.1). The MAPLE values for Eu[CO$_3$][OH] in space groups $Pnma$ and $P2_12_12_1$ do not differ significantly (Table A.2.2).

There are two main aspects under discussion regarding "$LnCO_4H$", a chemical and a crystallographic one.

Firstly, the crystal structure of La[CO$_3$][OH] ($Pnma$, $Z = 4$) appears to be isostructural to *ancylite* $La_2O(CO_3)_2 \cdot H_2O$ ($Pnma$, $Z = 2$). My data suggest that they are actually isotypic. The only difference is the presence of OH^- anions or H_2O molecules besides O^{2-} ions; from a chemical point of view the latter discrimination is only reasonable if

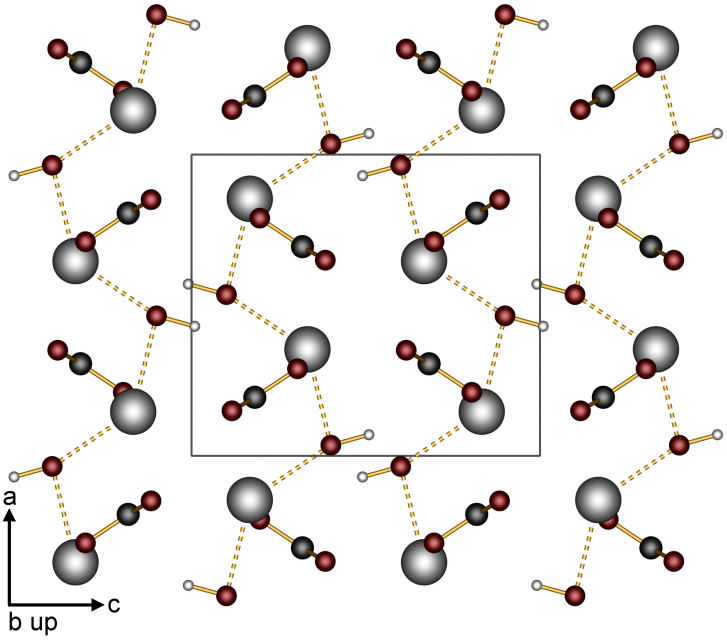

Fig. 4.2.4: $^{1}_{\infty}[(OH)Ln_{2/2}]^{2+}$ zigzag chains along [100] with OH^- anions oriented towards the resulting channels in *Ln*[CO_3][OH] (grey: *Ln*, black: C, white: H, red: O); the data of La[CO_3][OH] was used for this figure.

both oxygen atoms find themselves in different chemical environments, otherwise a simple acid base reaction yielding hydroxide ions can take place. Both the chemical environment and the electrostatic calculations suggest the presence of two hydroxide ions instead of water molecules besides oxide ions. A similar behaviour is reported for Gd[CO_3][OH] and $Gd_2O(CO_3)_2 \cdot H_2O$.[242] The structure model presented by dal Negro et al. contains only crystal water and no oxide;[259] this disagrees with an overall electrostatically neutral formula. Additionally, the assumption that the structure is that of a hydrate is not in agreement with the high thermal stability of the material (section 4.2). The first decomposition step takes place above 400°C.[20,244–246] For crystal water, a loss at lower temperatures is expected.[267] Therefore, it can be concluded that the structure is indeed a carbonate hydroxide. The same presumably holds true for the relationship of the minerals *kozoite* Nd[CO_3][OH] and La[CO_3][OH], and *calcioancylite* $CeCa(CO_3)_2(OH) \cdot H_2O$ with their respective carbonate hydroxides.[260,261,268] Consequently, all reported syntheses for $Ln_2O(CO_3)_2 \cdot H_2O$ using the analogy to *ancylite* can be taken as routes to orthorhombic *Ln*[CO_3][OH] compounds.[20,242,244]

The second aspect of the discussion regarding the proper structure model is the presence or absence of an inversion centre, i. e. space group $P2_12_12_1$ versus *Pnma*. Tahara et al. reported Eu[CO_3][OH] in $P2_12_12_1$,[250] while herein the structure refinement in space group *Pnma* was possible without any peculiarities. Both solutions differ in the lack of centrosymmetry of space group $P2_12_12_1$ resulting in a postulated change of the coordination sphere of the Eu^{3+} ion and a decrease of the coordination number from ten to

nine. This is not really justified by a close look on the interatomic distances and MAPLE calculations (Tables 4.2.3, A.2.2 and A.2.3). Three carbonate groups are monodentate ligands and only two are bidentate ligands in this described solution, because the carbonate group lost its symmetry from C_{2v} to C_s.[141,240,269] This modification is explained by the increased repulsion between the CO_3^{2-} anions due to the smaller ionic radius of Eu^{3+} following the lanthanide contraction.[250] This structure in space group $P2_12_12_1$ was first reported for Y[CO$_3$][OH].[255] The refinement of the single-crystal X-ray data implies unambiguously a centrosymmetry due to similar residuals (Table 4.2.2). Possible explanations are a centrosymmetric space group or an inversion twin. The space group *Pnma* was confirmed using the program PLATON.[270] Non-centrosymmetric crystal structures necessarily show non-linear optical properties – normally proven by recording the SHG intensity. The powder SHG method was used (section 3.2.4). Table 4.2.4 shows the intensity of the SHG signals in comparison to the quartz reference. In the cases of both Pr[CO$_3$][OH] and Eu[CO$_3$][OH], no respective signal could be detected in very careful measurements. Thus, both structures are centrosymmetric, i.e. the correct structure model is the one with space group *Pnma*.

Tab. 4.2.4: SHG results for Pr[CO$_3$][OH] and Eu[CO$_3$][OH] powders compared to reference materials; the standard deviations are given in parentheses.

Sample	SHG intensity / mV	$\frac{I_{SHG}}{I_{Quartz}}$
Quartz	57.1(31.3)	1
Al_2O_3	0.02(0.02)	0
KH_2PO_4 (KDP)	1142.7(249.5)	20
ZnO	245.0(26.6)	4.3
Pr[CO$_3$][OH]	0.06(0.03)	0
Eu[CO$_3$][OH]	0.02(0.02)	0

The same consideration holds for Gd[CO$_3$][OH]. Structure determinations have been reported in both *Pnma* and $P2_12_12_1$.[242,250,257] Using the new data, the structure could only reliably be solved and refined in space group *Pnma* (Table 4.2.2).

Tb[CO$_3$][OH]

The prior discussion showed that both Eu[CO$_3$][OH] and Gd[CO$_3$][OH] crystallise in the centrosymmetric space group *Pnma* - in contrast to earlier reports by Tahara et al. on the transition between the centrosymmetric and the non-centrosymmetric crystal structures of *Ln*[CO$_3$][OH] due to the increased repulsion between adjacent carbonate groups with decreasing *Ln*-O distances following the lanthanide contraction[250] placing it between samarium and europium. Consequently, the question arises whether gadolinium is the smallest lanthanide ion for which this structure type is adopted. Dixey and Saines report the crystal structure of Tb[CO$_3$][OH] in space group $P2_12_12_1$ based on both single-crystal XRD at 168 K and powder neutron diffraction at 100 K[256] -

Tab. 4.2.5: Crystal data and structure refinements of Tb[CO$_3$][OH]; the respective standard deviations are given in parentheses; both structures in $P2_12_12_1$ were refined as an inversion twin.

Temperature / K	150	320	320
M / g mol^{-1}		235.94	
Crystal size / mm^3		0.06 × 0.04 × 0.03	
Space group	$P2_12_12_1$ (No. 19)	$Pnma$ (No. 62)	$P2_12_12_1$ (No. 19)
a / pm	701.26(2)	702.40(5)	702.40(5)
b / pm	484.84(1)	485.70(4)	485.70(4)
c / pm	843.90(2)	846.05(6)	846.05(6)
Volume / 10^6 pm^3	286.93(1)	288.63(4)	288.63(4)
Z		4	
ρ_{calcd} / g cm^3	5.46	5.43	5.43
Absorption coefficient μ / mm$^{\check{}}$1	24.5	24.3	24.3
$F(000)$ / e	416	416	416
Radiation; wavelength λ / Å		Mo-K_α; 0.71073	
Diffractometer		Bruker D8 Venture	
Absorption correction		multi-scan	
Transmission (min; max)	0.5735; 0.7532	0.5563; 0.7531	0.5563; 0.7531
Index range h | k | l	±9 | ±13 | ±16	±9 | ±6 | ±11	±9 | ±6 | ±11
Θ range / °	3.78-44.99	3.77-29.97	3.77-29.97
Reflections collected	12410	4422	4744
Independent reflections	2354	455	830
R_{int}	0.041	0.040	0.039
Obs. reflections [$I > 2\sigma(I)$]	2217	450	803
Refined parameters / restraints	61 / 1	38 / 1	61 / 1
R_1 (all data)	0.018	0.024	0.015
wR_2 (all data)	0.035	0.067	0.034
GOF	1.02	1.599	1.099
Flack x parameter	0.45(3)	-	0.52(5)
Residual electron density (max; min) / e^- Å^{-3}	2.39; -1.19	2.60; -1.33	1.26; -0.98

confirming the structure determination by Tahara et al. at room temperature.[250] As expected for the ionic radii of the respective rare earth cation as decisive variable, space group $P2_12_12_1$ was also confirmed using neutron data for *Ln*[CO$_3$][OH] (*Ln* = Dy, Er, Ho).[256] The crystal structure of Tb[CO$_3$][OH] was redetermined at both 150 K and 320 K using the same crystal (Table 4.2.5). At 150 K, the structure could only reliably be solved in space group $P2_12_12_1$. At 320 K, a reasonable structure solution in $Pnma$ was possible. However, an additional measurement by the powder SHG method could confirm the non-centrosymmetric space group at room temperature by a non-zero SHG signal (Table 4.2.6). Consequently, the data measured at 320 K was revisited yielding an improved structure solution in $P2_12_12_1$ (Table 4.2.5). The main

Tab. 4.2.6: SHG results for Tb[CO$_3$][OH] powders compared to reference materials; the standard deviations are given in parentheses.

Sample	SHG intensity / mV	$\frac{I_{SHG}}{I_{Quartz}}$
Quartz	12.3(2.8)	1
Al_2O_3	0.1(0.1)	0
Tb[CO$_3$][OH]	9.0(8.2)	0.7

features of this - non-centrosymmetric crystal structures were already described during the discussion on Eu[CO$_3$][OH] above. There is one additional oxygen site due to the loss of centrosymmetry reducing the symmetry of the carbonate group from C_{2v} to C_s.[iii] In literature, this is followed by a reduction of the coordination number of terbium from ten to nine. However, MAPLE calculations confirming the electrostatic plausibility (Table A.2.4) yielded effective coordination numbers indicating coordination number ten for the structure in $P2_12_12_1$ - as already discussed for Eu[CO$_3$][OH] above. A wider range of terbium oxygen distances (Tb-O$_C$ = 227.2(3) − 228.4(4), Tb-O$_H$ = 247.9(4) − 284.6(5), sum of ionic radii: 250.1 − 252.1 pm,[265] compare to Table 4.2.3) can be realised in the less symmetric structure minimising electrostatic repulsion.

To summarise, the results show that the transition between the centrosymmetric (*Pnma*) and the non-centrosymmetric ($P2_12_12_1$) crystal structures of *Ln*[CO$_3$][OH] is located between gadolinium and terbium.

Optical Properties

Infrared Spectroscopy

The FT-IR spectra of the phase pure powders *Ln*[CO$_3$][OH] (*Ln* = La, Pr, Nd, Sm, Eu, Gd) shown in Figure 4.2.5 fit to structural units of the determined structures and to reports in literature for related systems.[239–241]

The OH stretching and bending vibrations appear around 3440 cm^{-1}, between 1680 and 1630 cm^{-1} and around 1320 cm^{-1}.[239,240,245] In agreement with the O–H···O distance derived from single-crystal structure determination, the second mode is shifted from La[CO$_3$][OH] to Gd[CO$_3$][OH] to higher wavenumbers.[130,141] The products are free of the starting material CTAB since the expected absorption bands ν_{as} (C−CH$_2$) and ν_s (C−CH$_2$) at 2920 and 2850 cm^{-1} are absent.[22] The bands between 1500 and 600 cm^{-1} can be assigned to coordinated CO_3^{2-}. The four normal modes can be found at 1090 − 1070 cm^{-1} (ν_1), 850 − 840 cm^{-1} (ν_2), 1500 − 1480 cm^{-1} and 1440 − 1420 cm^{-1} (ν_3), and 725 cm^{-1} and 700 − 690 cm^{-1} (ν_4).[239,240,245] The splitting of the degenerated modes ν_3 and ν_4 is caused by the symmetry reduction from D_3 to C_{2v} or C_s from the free to the coordinated carbonate anion (Figure 4.2.6).[141,239,240,245,269] For Eu[CO$_3$][OH], a discrimination between both possible space groups *Pnma* and $P2_12_12_1$ corresponding to point group C_{2v} and C_s for the carbonate anion is not possible based on the IR spectrum since six IR-active bands are expected for both symmetries compared to only three for both higher symmetries D_{3h} and D_3. Additionally, the CO_3^{2-} deformation band is present between 825 and 795 cm^{-1}.[240] Around 470 and 400 cm^{-1} the respective *Ln*-O vibrations occur.[22,271] A detailed assignment of the bands can be found in Table A.2.5.

[iii] The O-C-O angles of 119.0(4) to 120.7(5)° are close to the expected 120° for the carbonate group despite the symmetry reduction.

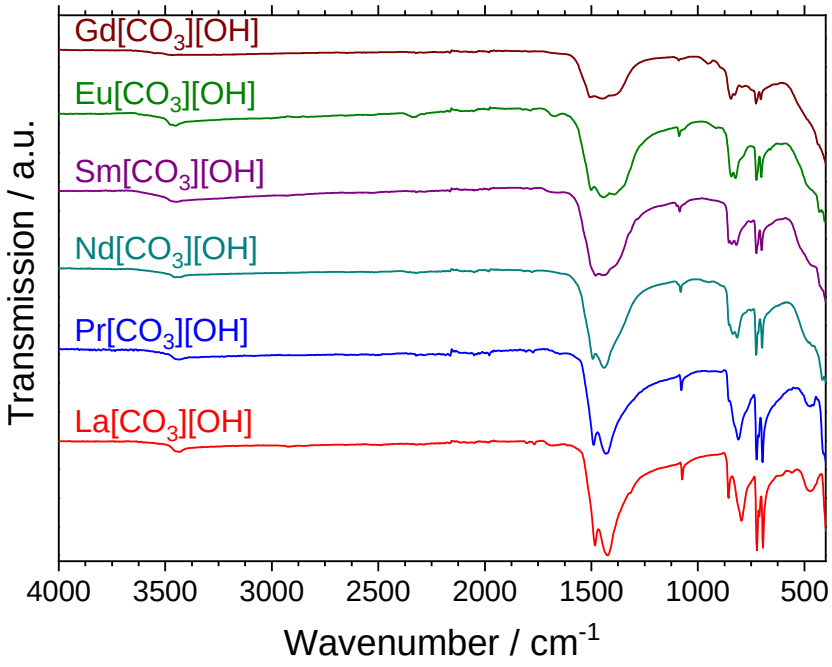

Fig. 4.2.5: Infrared spectra of *Ln*[CO$_3$][OH] (*Ln* = La, Pr, Nd, Sm, Eu, Gd).

UV-Vis Spectroscopy

The powder reflectance spectra of *Ln*[CO$_3$][OH] (*Ln* = La, Pr, Eu, Gd) depicted in Figure 4.2.7 show the expected electronic transitions for Pr^{3+} and Eu^{3+}. The absorption maxima at 440, 448, 465, 485 and 580 nm correspond to the $^3H_4 \rightarrow {}^3P_2$, $^1I_6$, $^3P_1$, $^3P_0$ and $^1D_2$ transitions of Pr^{3+}, respectively.[154] The characteristic transitions for Eu^{3+}, $^7F_0 \rightarrow {}^5L_6$, $^5D_2$ and $^5D_1$, result in the reflexion minima at 395, 466 and 534 nm, respectively.[157] As expected, no such transitions are observed within the range of measurement for La^{3+}. Below 300 nm the fundamental absorption of band gap of the samples governed by the carbonate ion is rising.[272] With increasing distance of the CO_3^{2-} from the rare earth ion - as already discussed above with Table 4.2.3 - the onset

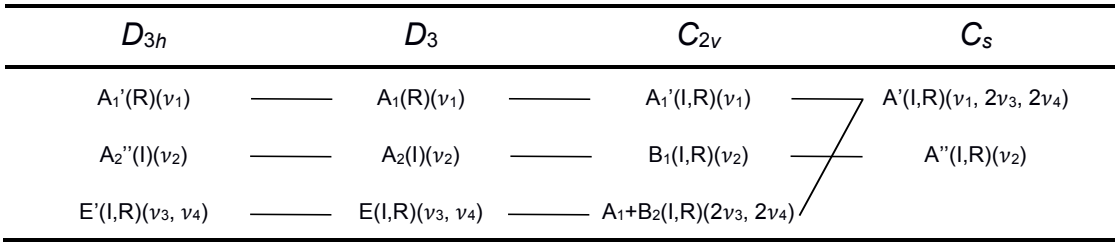

Fig. 4.2.6: Correlation scheme for D_{3h}, D_3, C_{2v}, C_s for the CO_3^{2-} ion: I: infrared active; R: Raman active; ν_1: symmetric C-O stretching; ν_2: CO_3 out-of-plane deformation; ν_3: asymmetric C-O stretching; ν_4: CO_3 in-plane deformation mode.

of the absorption is shifted to lower wavelengths. This absorption is overlapping the transitions for Gd^{3+}. Consequently, the ${}^8S_{\frac{7}{2}} \rightarrow {}^6I_{\frac{7}{2}}$ and ${}^8S_{\frac{7}{2}} \rightarrow {}^6P_{\frac{7}{2}}$ transitions expected at around 310 and 280 nm could not be observed.[153]

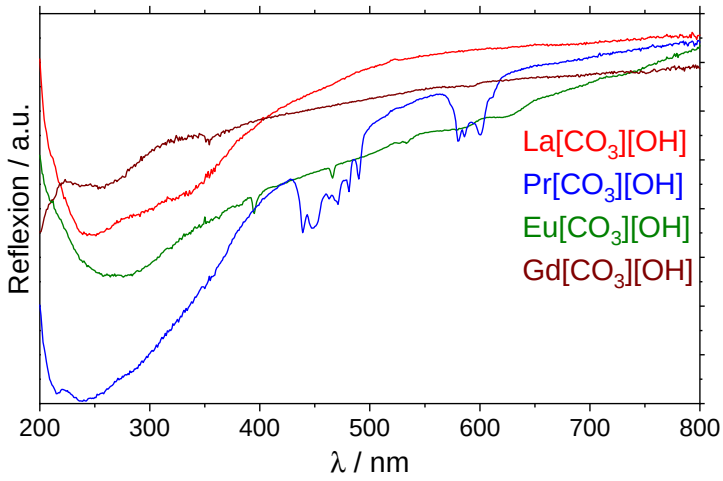

Fig. 4.2.7: UV-Vis spectra of La[CO$_3$][OH], Pr[CO$_3$][OH], Eu[CO$_3$][OH] and Gd[CO$_3$][OH].

Thermal Analyses

The compounds *Ln*[CO$_3$][OH] are well known as precursors for the preparation of *Ln*$_2$[CO$_3$]O$_2$ and *Ln*$_2$O$_3$ compounds. The thermolysis properties were investigated using thermal analysis. For all compounds, a two-step process was observed (Figure 4.2.8) according to the reaction equations:

$$Ln[CO_3][OH] \longrightarrow Ln_2[CO_3]O_2 + CO_2 + H_2O \quad \text{(I)}$$

$$Ln_2[CO_3]O_2 \longrightarrow Ln_2O_3 + CO_2 \quad \text{(II)}$$

The DTG curves reveal the temperatures at which the first and second reaction step take place as noted in Figure 4.2.8. The mass losses during these decompositions match well with the expected values from the reaction equation (Table A.2.6). For both La[CO$_3$][OH] and Pr[CO$_3$][OH], the mass losses are slightly higher than expected for the release of one CO_2 and one H_2O molecule due to residues decomposing at low temperatures. Only for Eu[CO$_3$][OH], the experimental value is lower than the theoretical one. This is presumably due to the post-synthesis heating step of the sample in order to remove side phases. During this step the decomposition of Eu[CO$_3$][OH] has already begun. For the second step, all samples match the expected values. For Gd[CO$_3$][OH], a non-heat-treated sample was used showing a mass loss of 3.8 wt.-% at 300°C due to the decomposition of the side phases. The further decomposition steps appear to overlap each other. However,

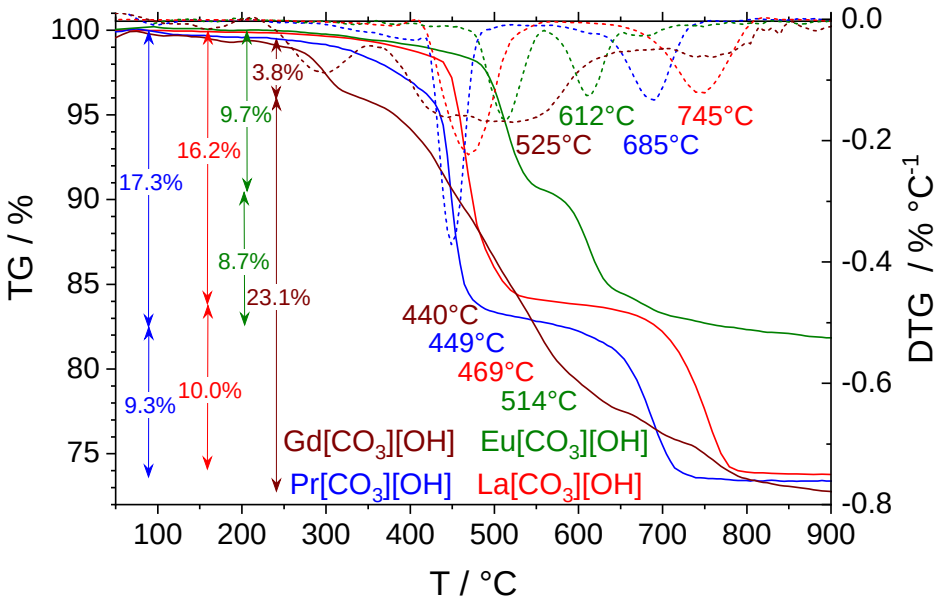

Fig. 4.2.8: Thermal analyses of La[CO$_3$][OH], Pr[CO$_3$][OH], Eu[CO$_3$][OH], and Gd[CO$_3$][OH]: Both the mass loss (TG in %, solid lines) and the first derivative of the mass loss with temperature (DTG in % C^{-1}, dotted lines) are given; further, the temperatures, at which the two-step process takes place, and the respective mass losses for these are noted inside the graph.

the overall mass loss fits to the decomposition of Gd[CO$_3$][OH] to Gd$_2$O$_3$. For all four samples, the phase transitions are confirmed by TPXRD (Figures A.2.6 to A.2.9). Additional DSC measurements support the transition temperatures taken from the DTG curves with endothermic peaks at similar temperatures for the first decomposition step (Figure A.2.3).

Moreover, another requirement for the possible use of the compounds as precursors is the passing on of the morphology of the precursors to the final products. This behaviour could be observed for the presented compounds as can be seen in the microscope pictures in Figures A.2.10 to A.2.12. The *Ln*[CO$_3$][OH] samples consist of single-crystals and their shape is inherited by the polycrystalline *Ln*$_2$[CO$_3$]O$_2$ and *Ln*$_2$O$_3$ products accompanied by a size reduction due to the release of gaseous CO$_2$ and H$_2$O. Consequently, the hydrothermally synthesised rare earth carbonate hydroxides *Ln*[CO$_3$][OH] are suited precursors for Ln^{3+} materials in general. In particular, they can also be used as precursors for the alkali rare earth metal double tungstates,[247] which are part of the next chapter.

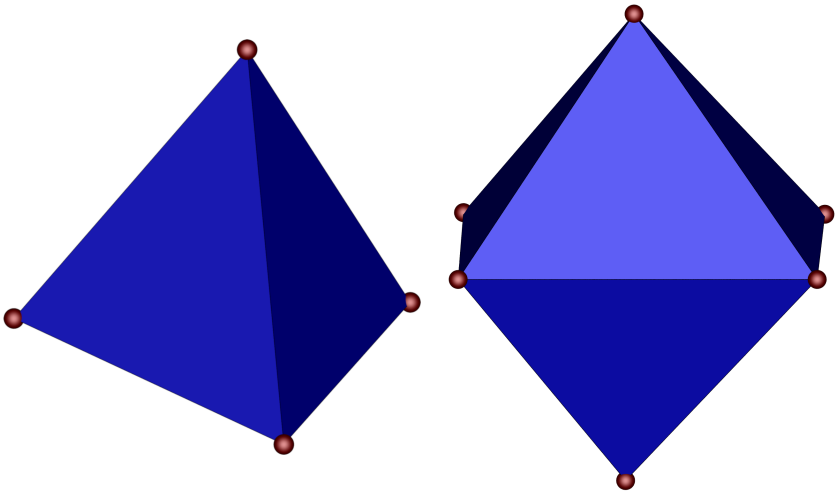

TUNGSTATES

5 Tungstates Containing Alkali and Rare Earth Metal Cations

Tungstates are capable of forming WO_4 tetrahedra and can therefore be classified as silicate-analogous materials. Tungstates containing alkali metal cations together with rare earth metal cations[i] were already investigated in the 19th century[25] followed by intense research on the alkali rare earth metal double tungstates in the 1970s.[273–275] During the latter period, the closely related group of $Na_5M(WO_4)_4$ compounds were investigated, too.[273,276,277]

The results presented in section 5.1 were published in the journal *Dalton Transactions*.[278] The ones in section 5.2 originate in part from the master theses of Katja Kreß[279] and Vivien Wessels[121] as well as the bachelor thesis of Florian Becker.[280]

5.1 $Na_5M(WO_4)_4$ (M = Y, La-Nd, Sm-Lu, Bi)

The first systematic report on pentasodium rare earth metal tetratungstates $Na_5M(WO_4)_4$ dates back over 70 years.[230] The $Na_5M(WO_4)_4$ representations crystallise isomorphous across the lanthanide series closely related to *scheelite* in space group $I4_1/a$ (no. 88) with the tungstate forming tetrahedral WO_4^{2-} units.[276,277,281–284] $Na_5M(WO_4)_4$ is reported to be a promising phosphor material both as a host or as an 100% phosphor because of its high chemical and thermal stability, low synthesis temperatures and its lack of concentration quenching.[283,285–287] Such phosphors may be of importance for the development of efficient luminescent devices like white LEDs or lamps.[101,288] Moreover, an important feature of tungstate phosphors is the antenna effect for which the tungstate acts as an efficient sensitiser transferring energy onto the activator. A ligand to metal charge transfer (LMCT) of O^{2-}-W^{6+} can frequently be excited by UV radiation subsequently enhancing forbidden f-f transition emissions of the rare earth ions via energy transfer.[39,117,289,290] Through the absorption of photons within the WO_4^{2-} group electrons from the 2p states of O^{2-} are excited to 5d states of W^{6+}, e.g. from the ground state W^{6+}-O^{2-} to the excited state W^{5+}-O^{-}.[289,291]

[i] or Bi^{3+} cations behaving very similar to the rare earth metal cations

$Na_5M(WO_4)_4$ melts simultaneously with the decomposition of the material[273,286,292,293] according to the reaction equation

$$Na_5M(WO_4)_4 \longrightarrow 2\,Na_2WO_4 + Na M(WO_4)_2.$$

The competition between $Na_5M(WO_4)_4$ and $NaM(WO_4)_2$ – both crystallising in space group type $I4_1/a$[273,294–296] – is also responsible for the observation that there are no sound reports on $A_5M(WO_4)_4$ with A = Li or K.[276,297]
In this section, the whole range of $Na_5M(WO_4)_4$ (M = La-Nd, Sm-Lu, Y, Bi) was prepared via flux syntheses significantly improving the purity of the obtained phosphor compared to solid-state syntheses reported in literature.[283,287,297] SC-XRD and Rietveld analysis were applied for crystal structure determination for the purpose of the first systematic comparison over the whole range of rare earth ions. The crystal structure discussion is supported by electrostatic calculations. Further, the crystallographic relationship between $Na_5M(WO_4)_4$ and $NaM(WO_4)_2$ is examined in detail in order to find a group-subgroup relation according to the Bärnighausen formalism.[298,299] Thereafter, the thermal decomposition is investigated searching for a trend throughout the rare earth ions. Moreover, the $Na_5M(WO_4)_4$ compounds are investigated by Infrared, UV-Vis, fluorescence and ^{151}Eu Mößbauer spectroscopy with special interest on their properties as phosphors and on the energy transfer mechanism from the LMCT O^{2-}-W^{6+} to the M^{3+} activator as well as for their magnetic properties in order to clarify the interaction of neighbouring M^{3+} ions. Additionally, solid solutions of $Na_5Y_{1-x}Eu_x(WO_4)_4$ and $Na_5Y_{1-x}Tb_x(WO_4)_4$ are addressed using both Rietveld analysis and fluorescence spectroscopy.

Syntheses

La_2O_3 (99,99%), Ho_2O_3 (99.9%), Er_2O_3 (99.9%), Yb_2O_3 (99.9%) (all from Auer-Remy), CeO_2 (99.99%, MaTecK), Pr_6O_{11} (99.9%), Nd_2O_3 (99.9%), $Na_2WO_4 \cdot 2\,H_2O$ (99%, all from Merck), Sm_2O_3 (99.9%, MC Industrial Chemical), Eu_2O_3 (99.99%), Tb_4O_7 (99.9%), Dy_2O_3 (99.99%), Tm_2O_3 (99.9%), Lu_2O_3 (99.9%, all from Chempur), Gd_2O_3 (99.99%, Fluka), Bi_2O_3 (99.5%, Riedel-de Haën), Y_2O_3 (99.99%), WO_3 (99.8%, both from Alfa Aesar) and Na_2CO_3 (99%, AppliChem) were used as starting materials without further purification and were handled in air. The respective purities are given in parentheses.
Polycrystalline samples of $Na_5M(WO_4)_4$ (M = La-Nd, Sm-Lu, Y, Bi) were prepared via flux syntheses with 500% excess of the educt $Na_2WO_4 \cdot 2\,H_2O$ following the reaction equation

$$\frac{1}{2}\,Na_2CO_3 + \frac{1}{2}\,M_2O_3 + 2\,WO_3 + 2\,Na_2WO_4 \cdot 2\,H_2O \longrightarrow Na_5M(WO_4)_4 + \frac{1}{2}\,CO_2$$

and the according equations for CeO_2, Pr_6O_{11}, Tb_4O_7. The ground powders were transferred into corundum crucibles and heated at 600°C for 90 h in air inside a muffle furnace with heating ramps of 200 Kh^{-1}. Subsequently, the obtained powders were

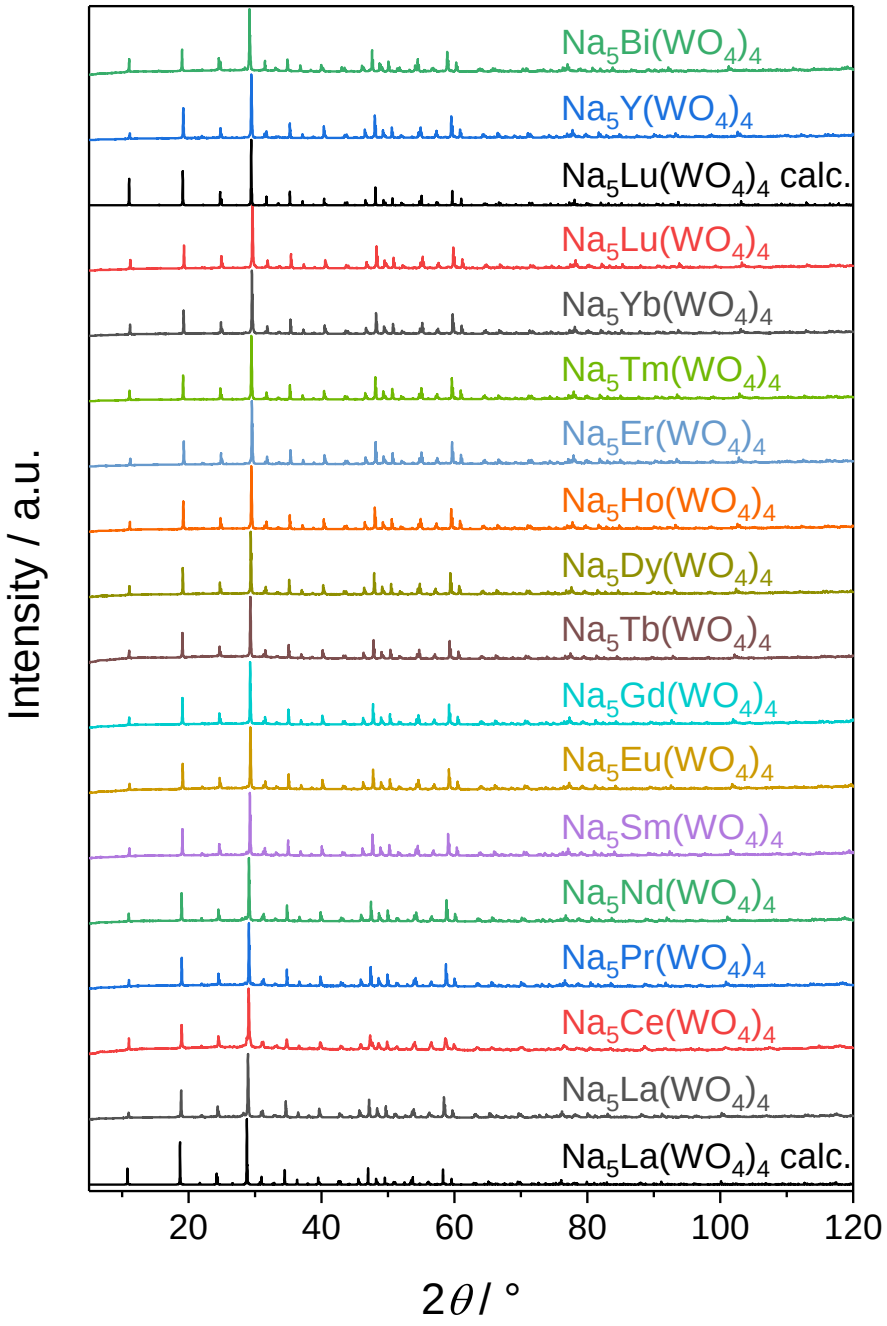

Fig. 5.1.1: PXRD patterns of polycrystalline $Na_5M(WO_4)_4$ (M = La-Nd, Sm-Lu, Y, Bi) compared to patterns calculated from the results of the Rietveld refinement of $Na_5La(WO_4)_4$ and $Na_5Lu(WO_4)_4$.

dissolved in 50 ml hot deionized water (200°C) under constant magnetic stirring (500 rpm) for 1 h, vacuum-filtrated along with washing with additional 50 ml of H_2O and dried in a compartment dryer at 65°C for 24 h. The excess facilitates the formation of $Na_5M(WO_4)_4$ over the competitive $NaM(WO_4)_2$ while leftover Na_2WO_4 is water soluble[284,300,301] and consequently, washed out during the further synthesis process. All samples were checked by PXRD for phase purity (Figure 5.1.1). A side phase of $NaM(WO_4)_2$ of e.g. 2 wt.-% $NaEu(WO_4)_2$ in $Na_5Eu(WO_4)_4$ could be found by Rietveld refinement (Figure B.1.1). The formation of this side phase is apparently significantly suppressed as solid-state syntheses at the same temperature of 600°C (Synthesis **A1**) as well as at 700°C (Synthesis **A2**) yield major $NaEu(WO_4)_2$ side phase amounts of 17 wt.-% and 16 wt.-% according to Rietveld refinements, respectively (Figure B.1.2). For synthesis **A1**, stoichiometric amounts of the educts according to the reaction equation

$$\frac{1}{2}\,Eu_2O_3 + 1.5\,WO_3 + 2.5\,Na_2WO_4 \cdot 2\,H_2O \longrightarrow Na_5Eu(WO_4)_4$$

reported by Chiu et al.[297] were ground and heated inside a muffle furnace in corundum crucibles at 600°C for 6 h in air with heating ramps of 200 Kh^{-1}. For synthesis **A2**, the educts according to the reaction equation

$$2.5\,Na_2CO_3 + \frac{1}{2}\,Eu_2O_3 + 4\,WO_3 + 2.5\,Na_2WO_4 \cdot 2\,H_2O \longrightarrow Na_5Eu(WO_4)_4 + 2.5\,CO_2$$

reported by Huang et al.[283] were weighed in stoichiometric ratios, ground and transferred into corundum crucibles, which were heated at 700°C for 6 h in air inside a muffle furnace with heating ramps of 200 Kh^{-1}. Subsequently, the same washing steps were carried out as for the flux synthesis in both cases. The choice of starting materials, i.e. choosing Na_2CO_3 or Na_2WO_4 as sodium source, is expected to play only a minor rule since van Vliet and Blasse report the synthesis of $Na_5Gd(WO_4)_4$ with the temperature program of **A1** and the educts of **A2**.[287]

Starting from the polycrystalline samples single-crystals of $Na_5M(WO_4)_4$ (M = Ce, Pr, Nd, Sm, Eu, Gd, Tb, Ho, Tm, Yb, Bi) were obtained via recrystallisation from the melt heating the respective polycrystalline powders in platinum crucibles inside a muffle furnace at 800°C for 10 h with a heating ramp of 200 Kh^{-1} and cooling to 400°C with a ramp of 5 Kh^{-1} and subsequently to room temperature with a ramp of 200 Kh^{-1}. Consequently, single-crystal X-ray structure determinations on $Na_5M(WO_4)_4$ (M = Ce-Nd, Sm-Tb, Ho, Tm, Yb, Bi) (Tables 5.1.1, B.1.1 and B.1.2) were performed along with Rietveld refinements of $Na_5M(WO_4)_4$ (M = La, Pr, Sm…Lu, Y) (Tables B.1.3 and B.1.4 and figures B.1.3 and B.1.4).

Samples of $Na_5Y_{1-x}Eu_x(WO_4)_4$ (x = 0.01, 0.05, 0.1, 0.5) and $Na_5Y_{1-y}Tb_y(WO_4)_4$ (y = 0.01, 0.02, 0.05, 0.5) were synthesised identically in order to study the fluorescent properties. For solid solutions of $Na_5Y(WO_4)_4$ and $Na_5Eu(WO_4)_4$ or $Na_5Tb(WO_4)_4$, respectively, a temperature dependent miscibility gap could be identified. Consequently,

single-crystals of $Na_5Y_{0.5}Eu_{0.5}(WO_4)_4$ and $Na_5Y_{0.5}Tb_{0.5}(WO_4)_4$ were grown from the melt starting from the polycrystalline powders and single-crystal X-ray structure determination was performed aside with Rietveld refinements. Additionally, $Na_5Y_{0.5}Eu_{0.5}(WO_4)_4$ samples were prepared via the two different solid-state syntheses **A1** and **A2** and analysed by Rietveld analysis while the closing of the miscibility gap was investigated by TPXRD on $Na_5Y_{0.5}Eu_{0.5}(WO_4)_4$ prepared by the flux synthesis.
Furthermore, phase pure polycrystalline $NaEu(WO_4)_2$ (Figure B.1.5) was synthesised via solid-state reaction according to the reaction equation

$$Na_2CO_3 + Eu_2O_3 + 4\,WO_3 \longrightarrow 2\,NaEu(WO_4)_2 + CO_2$$

weighing and subsequently grinding stoichiometric amounts of the educts with a surplus of 10% Na_2CO_3 due to losses caused by the evaporation of CO_2, heating the mixture inside a muffle furnace in a corundum crucible at 800°C for 10 h in air with heating ramps of $200\,Kh^{-1}$. Starting from this, single-crystals were grown from the melt in a platinum crucible inside a muffle furnace in air at 1000°C for 10 h with a heating ramp of $200\,Kh^{-1}$ and cooling to 400°C with a ramp of $5\,Kh^{-1}$ and subsequently to room temperature with a ramp of $200\,Kh^{-1}$. Single-crystal X-ray structure determination was performed enabling an adequate comparison of the concurring and crystallographically closely related structures of $NaEu(WO_4)_2$ and $Na_5Eu(WO_4)_4$ (Table 5.1.1).

Crystal Structures

$NaEu(WO_4)_2$

$NaEu(WO_4)_2$ adopts the *scheelite* structure type ($CaWO_4$) in space group $I4_1/a$ (no. 88) with one half of the Ca^{2+} positions occupied by Na^+ and the remaining ones by Eu^{3+}.[273,294–296] The refinement of single-crystal XRD data yielded a mixed occupation of 51.8(2)% Na and 48.2(2)% Eu in our structure model over the same 4*b* site. Details are displayed in Table 5.1.1. The tungsten atom on Wyckoff position 4*a* is coordinated by four oxygen atoms forming non-condensed WO_4 tetrahedra which are connected via corners to distorted [(Na/Eu)O_8] dodecahedra with four oxygen atoms coordinating with a distance of 245.7(2) pm and the other four with a distance of 247.7(2) pm (Table B.1.5 and figure B.1.6). These values are reasonably close to the sum of the respective ionic radii (248 pm).[216] The same holds for the W-O distance of 179.0(2) pm (sum of ionic radii: 178 pm).[216] The [(Na/Eu)O_8] dodecahedra are connected to adjacent ones via edges. The cations Na^+/Eu^{3+} and W^{6+} form Na/Eu-W chains along the *c* axis (Figure 5.1.2). The WO_4 tetrahedra can be classified as regular with $\Delta_{tetr} = 0.53\%$.

$Na_5M(WO_4)_4$ (M = La-Nd, Sm-Lu, Y, Bi)

All compounds of the $Na_5M(WO_4)_4$ series crystallise in a *scheelite* related structure in space group $I4_1/a$ (no. 88).[273,276,277,285,295] Details of the structure determinations are

Tab. 5.1.1: Crystal data and structure refinements of $NaEu(WO_4)_2$ and $Na_5Eu(WO_4)_4$ determined from single-crystal data (the respective standard deviations are given in parentheses)

	$NaEu(WO_4)_2$	$Na_5Eu(WO_4)_4$
M / g mol^{-1}	670.65	1258.31
Crystal size / mm^3	0.04 × 0.04 × 0.03	0.10 × 0.06 × 0.03
Temperature / K	298(2)	301(2)
Space group	$I4_1/a$	$I4_1/a$
a / pm	526.24(1)	1149.98(4)
c / pm	1140.78(3)	1140.61(4)
Volume / 10^6 pm^3	316.07(3)	1508.40(12)
Z	2	4
ρ_{calcd} / g cm^{-3}	7.05	5.54
Absorption coefficient μ / mm^{-1}	46.2	34.7
$F(000)$ / e	572	2168
Radiation; wavelength λ / Å	Mo$K\alpha$; 0.71073	
Diffractometer	Bruker D8 Venture	
Absorption correction	Multi-scan	
Transmission (min; max)	0.6338; 0.7503	0.6001; 0.7483
Index range $h \mid k \mid l$	-9/19|-9/9|-21/21	-20/20|-15/20|-20/20
θ range / deg	4.265−41.863	2.515−39.996
Reflections collected	21433	16901
Independent reflections	546	2337
R_{int}	0.0284	0.0406
Obs. reflections ($I > 2\sigma(I)$)	472	2025
Refined parameters	16	60
R_1 (all data)	0.018	0.0258
wR_2 (all data)	0.034	0.0356
GOF	1.120	1.026
Residual electron density (max; min) / e^- Å^{-3}	2.08; -1.51	1.41; -1.18

displayed in tables 5.1.1 and B.1.1 to B.1.4 and figures B.1.1, B.1.3 and B.1.4. The unit cell depicted in Figure 5.1.7b comprises non-condensed WO_4 tetrahedra. They consist of four crystallographically distinct sites O1, O2, O3 and O4. Non-condensed MO_8 dodecahedra including two groups of crystallographically equivalent M-O distances of e.g. 240.3(2) pm and 240.7(2) pm for $Na_5Eu(WO_4)_4$ (sum of ionic radii 242.6 pm[216]) are located on the special position 4a on the $\bar{4}$ axis. WO_4 and MO_8 are connected via corners setting up a $^3_\infty[M(WO_4)_{4/2}]^{5-}$ network. The resulting cavities are filled with Na^+ located on two non-equivalent lattice sites. Distorted $Na(1)O_6$ trigonal prisms on special Wyckoff site 4b are surrounded by six WO_4 tetrahedra via shared corners; distorted $Na(2)O_4$ tetrahedra are coordinated by eight $Na(1)O_6$ and four WO_4. The respective cation environments are shown in Figure B.1.7. Along the c axis, infinite W-Na(1) and M-Na(2) chains are formed (Figure 5.1.3). However, WO_4 tetrahedra and NaO_6 trigonal prisms as well as MO_8 dodecahedra and NaO_4 tetrahedra are not condensed along the W-Na(1) and the M-Na(2) chain, respectively - but $Na(1)O_6$ is connected via edges to $Na(1)O_6$, MO_8 and via corners to WO_4 and $Na(2)O_4$. Thus, the interconnection of neighbouring alternative chains forms the network. Consequently, the coordination numbers of the oxygen anions are four (O1) and three (O2, O3, O4).

Comparing all determined crystal structures for $Na_5M(WO_4)_4$, the lattice parameters a and c decrease with the ionic radii of M^{3+} following the lanthanide contraction (Fig-

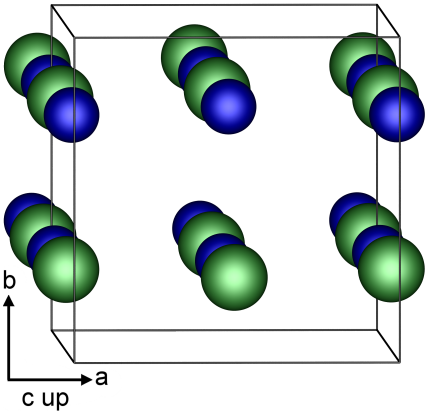

Fig. 5.1.2: Na/Eu-W chains along [001] in $NaEu(WO_4)_2$ displayed together with the unit cell (Na/Eu green, W blue).

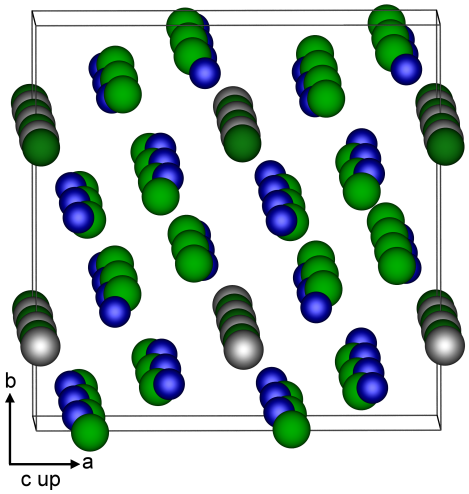

Fig. 5.1.3: W-Na(1) and M-Na(2) chains along [001] in $Na_5M(WO_4)_4$ displayed together with the unit cell (blue W, green Na(1), dark green Na(2), grey M).

ure 5.1.4). This affects both axes equally due to the pseudocubic nature of $Na_5M(WO_4)_4$ and the fact that the MO_8 dodecahedra adopt no special position towards the unit cell affecting both a and c evenly as a result of the lanthanide contraction shrinking the MO_8 dodecahedra. According to Figure 5.1.4, $Na_5Bi(WO_4)_4$ does not fit to the trend of the rare earth compounds. No peculiarities in both the first and the second coordination sphere of Bi^{3+} were found indicating an influence of the lone pair of Bi^{3+}. Further, the eccentricity $\epsilon = 0$. This is presumably due to the large Bi-Bi and Bi-O distances resulting in a quenched lone pair effect. Furthermore, Figure 5.1.4 shows the matching of the lattice parameters determined from SC-XRD and Rietveld data.

Tables B.1.6 to B.1.8 show selected interatomic distances and angles of $Na_5M(WO_4)_4$. Again, the M-M and M-O distances decrease following the lanthanide contraction with the values of the latter reasonably close to the sum of the respective ionic radii.[216] The same holds for the Na-O and W-O distances. Both Na(1)-O and Na(2)-O distance decrease with the lanthanide contraction.

The Δ_{tetr} results (Tables B.1.6 to B.1.8) show a linear increase in the deviation with decreasing ionic radius and lanthanide contraction in accordance with the report by Efremov et al. for $Na_5M(WO_4)_4$ (M = La, Tb, Lu).[277] However, the maximal deviation of 0.92% for $Na_5Yb(WO_4)_4$ is rather small. The tetrahedra can still be classified as regular. The increase in deviation is linked to the unit cell decrease and the M-O distance decrease following the lanthanide contraction, whereas the W-O distances do not differ considerably (Tables B.1.6 to B.1.8). In contrast, the $Na(2)O_4$ tetrahedra are not regular with deviations of 7-8%(Tables B.1.6 to B.1.8).

In literature, the lack of concentration quenching in $Na_5M(WO_4)_4$ was attributed to the

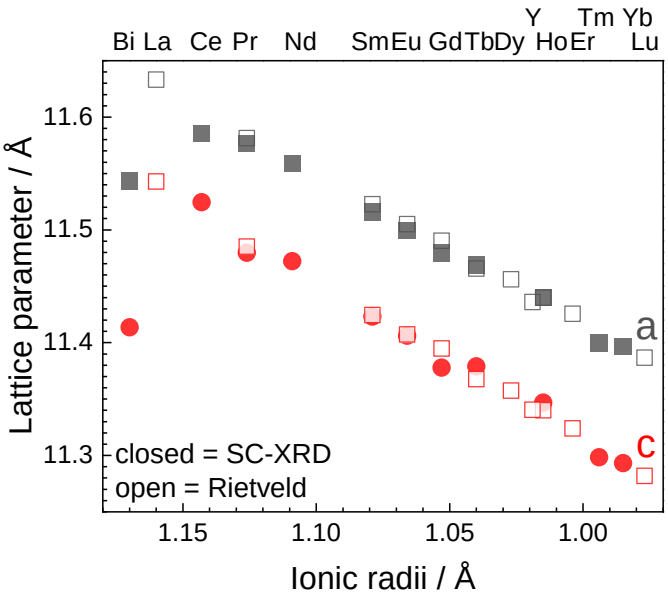

Fig. 5.1.4: The trend of the lattice parameters a and c with the ionic radii of M^{3+} in $Na_5M(WO_4)_4$: The open symbols indicate data from Rietveld refinement and the closed ones data from single-crystal XRD; the graph shows the homogeneous decrease of both lattice parameters with the lanthanide contraction; on the very left, $Na_5Bi(WO_4)_4$ does not follow the trend due to Bi^{3+} not being part of the lanthanide series.

special structure M-O-W-O-M with angles of M-O-W of 110° or 100°.[283,286,287] Our data show that the M-O-W angle lies in fact around 130° for all studied compounds leaving the large M-M distances of 635 to 649 pm (Tables B.1.6 to B.1.8) as an obvious reason preventing energy transfer between M^{3+} ions and consequently reducing concentration quenching. These large distances are realised via double M-O-W-O-M bridges depicted in Figure 5.1.5. For $NaEu(WO_4)_2$, a quite short distance of only 388 pm is found (Table B.1.5).

In summary, the crystal structures of $Na_5M(WO_4)_4$ determined by SC-XRD and Rietveld analysis of PXRD data are in agreement with the earlier reports in literature.[276,277,281–284] The first extensive reports of the structure are given for $Na_5Ce(WO_4)_4$, $Na_5Pr(WO_4)_4$, $Na_5Sm(WO_4)_4$, $Na_5Dy(WO_4)_4$, $Na_5Ho(WO_4)_4$, $Na_5Er(WO_4)_4$, $Na_5Tm(WO_4)_4$, $Na_5Yb(WO_4)_4$ and $Na_5Bi(WO_4)_4$. Furthermore, we reported the first structure determinations of $NaEu(WO_4)_2$ and $Na_5Eu(WO_4)_4$ from single-crystal data.

Electrostatic Calculations

The MAPLE values of $Na_5M(WO_4)_4$ (M = Pr, Sm, Eu, Tb, Ho, Yb, Bi) from single-crystal data and $Na_5M(WO_4)_4$ (M = La, Ho) from Rietveld data were calculated and compared to the sum of the respective chemically comparable rare earth oxides, sodium tungstate and tungsten trioxide (Table B.1.9). The deviations are well below 1% for all structures. The same holds true for $NaEu(WO_4)_2$. Here, the calculation was performed

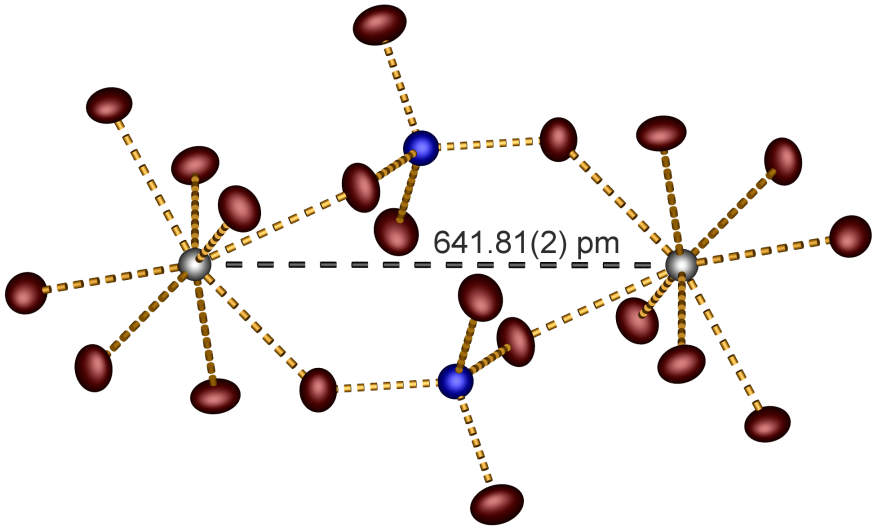

Fig. 5.1.5: The structural feature in $Na_5M(WO_4)_4$ (here M = Eu) showing the large Eu-Eu distances realised via Eu-O-W-O-Eu bridges; the ellipsoids of Eu^{3+} (grey), W^{6+} (blue) and oxygen (red) are shown at a 90% probability level.

in subgroup $I\bar{4}$ resolving the disorder of Na^+ and Eu^{3+}. Moreover, all coordination numbers were confirmed by the calculations.

Crystallographic Relationships

$NaM(WO_4)_2$ and $Na_5M(WO_4)_4$ are two closely related structures with the former being the decomposition product of the latter and both crystallising in the same space group type $I4_1/a$. For the sake of clarity and better understanding of this affinity, the systematic crystallographic relationship of $Na_5M(WO_4)_4$ to $NaM(WO_4)_2$ shown exemplarily on $Na_5Eu(WO_4)_4$ and $NaEu(WO_4)_2$ can be illustrated best by a group-subgroup relation scheme following the Bärnighausen formalism (Figure B.1.8).[298,299] The volume ratio suggests that $Na_5Eu(WO_4)_4$ essentially represents a five-fold superstructure of *scheelite* type $NaEu(WO_4)_2$. The lower symmetric $Na_5Eu(WO_4)_4$ can be derived by a symmetry reduction of $NaEu(WO_4)_2$ to the isomorphic subgroup $I4_1/a$ according to the transformation $\mathbf{a}+\mathbf{2b}$,$-\mathbf{2a}+\mathbf{b}$, $\mathbf{c}$. Isomorphic transitions of index 5 ($i5$) are rare.[302] Hence, the special Wyckoff positions $4a$ and $4b$ split into $4a$ and $16f$ and $4b$ and $16f$, respectively. The W^{6+} ion no longer occupies a special position, whereas Eu^{3+} is located on the $4a$ position and Na^+ occupies both the special position $4b$ and the general position $16f$. The Na^+ at $4b$ is tetrahedrally coordinated since its position is derived from tetrahedrally coordinated W^{6+}. The other Na^+ is coordinated by six oxygen atoms with the polyhedron derived from the dodecahedron of $NaEu(WO_4)_2$ via removal of two corners and the subsequent rearrangement of the oxygen atoms. The oxygen position itself splits as well leaving one of the five new positions vacant as expected since 20 Na,

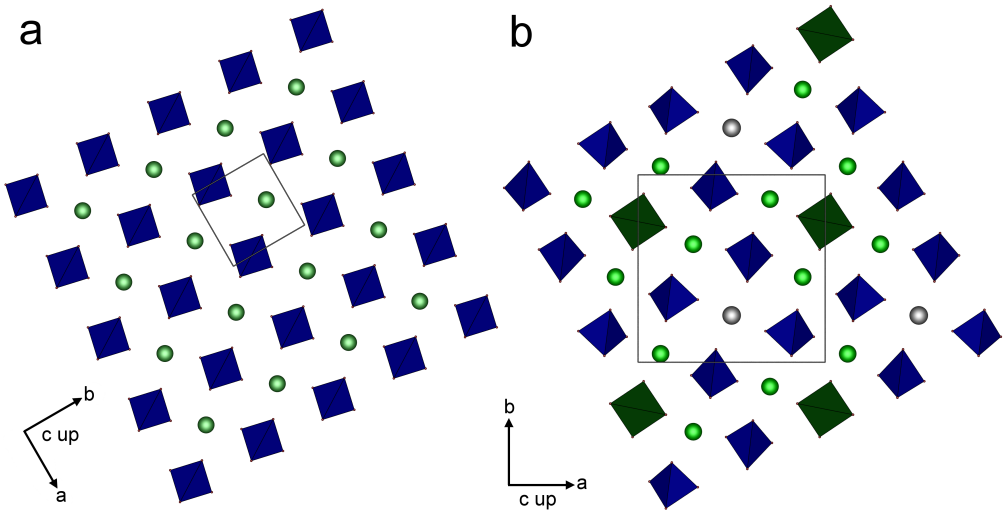

Fig. 5.1.6: Cation layer perpendicular to [001] in (a) $NaEu(WO_4)_2$ and (b) $Na_5Eu(WO_4)_4$: the unit cells are shown with a rotation of circa 60° in (a); blue tetrahedra represent WO_4, dark green ones NaO_4, the white spheres are shown for Eu^{3+}, green ones for Na^+ and pale green ones for disordered Na^+/Eu^{3+}.

4 Eu, 16 W and 64 O atoms were put onto 20 Na/Eu, 20 W and 80 O positions of the *scheelite* structure and there is less charge to be compensated by the oxygen anions.
Visually, the derivation of $Na_5Eu(WO_4)_4$ from $NaEu(WO_4)_2$ can be illustrated by the respective cation substructure shown in Figure 5.1.6.[273,295] Beside local distortion, the cations are distributed in the same way in both structures forming layers perpendicular to the c axis containing two types of series. $Na_5Eu(WO_4)_4$ is derived from $NaEu(WO_4)_2$ by replacing one fifth of the W^{6+} by Na^+ ions resulting in one NaO_4 alternating with four WO_4 along the tetrahedra series. Moreover, the disorder of Na^+ and Eu^{3+} vanishes and the former series of Na/Eu is replaced by alternations of four Na^+ and one Eu^{3+} ions. This results in minor changes in the cation positions already shown in Figure 5.1.3 and major changes in the anion substructure, even leading to one herein vacant oxygen position. This oxygen atom is now found in the second coordination sphere of the W^{6+} ions. While tungsten is surrounded by an oxygen tetrahedron in the first coordination sphere for both $NaEu(WO_4)_2$ and $Na_5Eu(WO_4)_4$ the tetrahedron is tetracapped in the second coordination sphere in the former and tricapped in the latter (Figure B.1.9). One should note, that the Eu^{3+} ions occupy a position coordinated by four $WO_4{}^{2-}$ anions. This can be expected to be governed by electrostatic reasons.
Furthermore, the crystal structure can elucidate the thermal behaviour of $Na_5Eu(WO_4)_4$. In the light of the decomposition of $Na_5Eu(WO_4)_4$ to $NaEu(WO_4)_2$ and Na_2WO_4, domains of both decomposition products may be found within the unit cell of $Na_5Eu(WO_4)_4$ (Figure 5.1.7). Consequently, one unit cell formally contains two parts of $NaEu(WO_4)_2$ (red rectangles) and four of Na_2WO_4 (grey rectangles) representing the stoichiometry of the decomposition products – such a behaviour is also known as *chemical twinning*.[303] While the domains of $NaEu(WO_4)_2$ include Na^+ and Eu^{3+} on defined positions, dis-

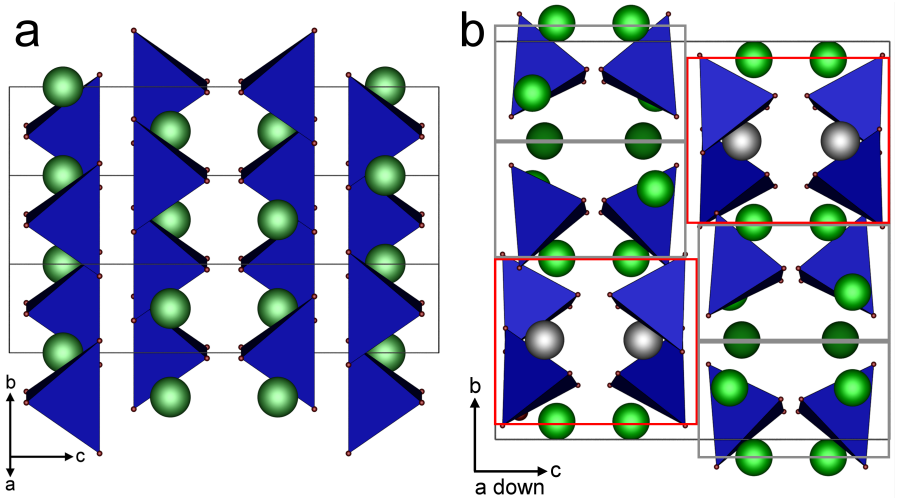

Fig. 5.1.7: Domain structure in the unit cell of $Na_5Eu(WO_4)_4$ (b) with $NaEu(WO_4)_2$ (red rectangles) and Na_2WO_4 (grey rectangles) resembling regions; (a) shows the unit cell of $NaEu(WO_4)_2$ rotated around the *c* axis for 63.4°: this view shows the similarity of the $NaEu(WO_4)_2$ unit cell (a) and the $NaEu(WO_4)_2$ related domain in $Na_5Eu(WO_4)_4$ (red rectangle in (b)).

order is introduced in $NaEu(WO_4)_2$ during crystallisation. In conclusion, the thermal decomposition of $Na_5Eu(WO_4)_4$ appears to be predetermined within its crystal structure.

Thermal Decomposition of $Na_5M(WO_4)_4$

The thermal decomposition of $Na_5M(WO_4)_4$ according to the reaction equation

$$Na_5M(WO_4)_4 \longrightarrow NaM(WO_4)_2 + 2\,Na_2WO_4$$

accompanied by simultaneous melting was investigated by DSC. The results in Figure B.1.10 show one endothermic peak for all measurements on $Na_5M(WO_4)_4$ (M = La, Pr, Eu, Gd, Tb, Ho, Yb, Lu, Bi). The maxima of the peaks were taken as decomposition temperatures T_D. Figure 5.1.8 shows the decomposition temperature against the ionic radii of the respective rare earth ions M^{3+}. For M = La, Eu, Lu and Bi, the values are in accordance with earlier reports.[273,286,292,293] There is a maximum in T_D around 754°C for $Na_5Ho(WO_4)_4$. Thus, T_D does not follow linearly the lanthanide contraction. Rather, the behaviour of T_D can be correlated to the difference of the ionic radii of M^{3+} and Na^+ in $Na_5M(WO_4)_4$ with CN = 8 and CN = 6, respectively. According to the earlier discussion of the crystal structure and the existence of domains, M^{3+} and Na^+ get disordered during the formation of $NaM(WO_4)_2$ due to thermodynamic reasons.[304] The energy benefit of this process scales with the difference of the ionic radii $|\,r\,(M) - r\,(\mathrm{Na})\,|$ in $Na_5M(WO_4)_4$. Consequently, maximal external energy in form of temperature is necessary for decomposition in the case of $Na_5Ho(WO_4)_4$ due to the minimal difference in the ionic radii (Figure 5.1.8). $Na_5Bi(WO_4)_4$ is decomposed while melting at 640°C.

The large difference cannot be explained by the ionic radii. It is presumably due to the the lack of f electrons in Bi^{3+}.

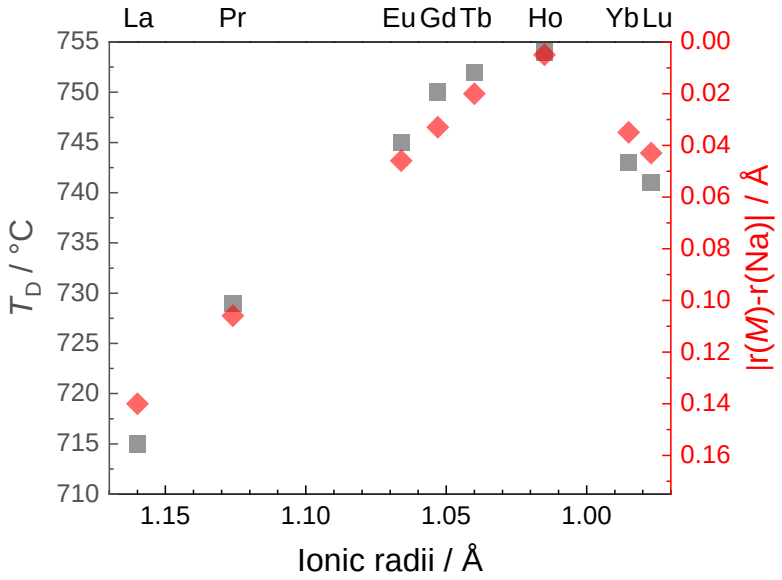

Fig. 5.1.8: Behaviour of the thermal decomposition temperature T_D of $Na_5M(WO_4)_4$ (grey) with the ionic radii of M^{3+} correlated to the difference of the ionic radii of M^{3+} with CN = 8 and Na^+ with CN = 6 (red)[216]

Miscibility Gap in $Na_5Y_{1-x}Eu_x(WO_4)_4$ and $Na_5Y_{1-y}Tb_y(WO_4)_4$

In contrast to earlier works,[284,285,292,297] the existence of a temperature dependent miscibility gap in both $Na_5Y_{1-x}Eu_x(WO_4)_4$ and $Na_5Y_{1-y}Tb_y(WO_4)_4$ could be demonstrated. Samples of the compositions $Na_5Y_{0.5}Eu_{0.5}(WO_4)_4$ and $Na_5Y_{0.5}Tb_{0.5}(WO_4)_4$ were prepared via flux syntheses at 600°C. Rietveld refinements displayed in Figures B.1.11 to B.1.13 showed the presence of two separated phases in $Na_5Y_{0.5}Eu_{0.5}(WO_4)_4$ and $Na_5Y_{0.5}Tb_{0.5}(WO_4)_4$, i.e. $Na_5Y(WO_4)_4$ versus $Na_5Eu(WO_4)_4$ and $Na_5Tb(WO_4)_4$ versus $Na_5Y(WO_4)_4$. Details are collected in Table B.1.10. Single-crystals were grown from the melt at 800°C for both samples. The single-crystal X-ray structure determinations yielded single-phased $Na_5Y_{0.49}Eu_{0.51}(WO_4)_4$ and $Na_5Y_{0.49}Tb_{0.51}(WO_4)_4$. Details can be found in Table B.1.11. Consequently, the miscibility gap could be closed via melting the compounds at 800°C. This was confirmed by Rietveld refinements (Table B.1.10 and figures B.1.14 to B.1.16) showing the three phases $Na_5Y_{0.5}Eu_{0.5}(WO_4)_4$, $NaY_{0.5}Eu_{0.5}(WO_4)_2$ and Na_2WO_4, and $Na_5Y_{0.5}Tb_{0.5}(WO_4)_4$, $NaY_{0.5}Tb_{0.5}(WO_4)_2$ and Na_2WO_4, respectively. Both sets of lattice parameters for $Na_5Y_{0.49}Eu_{0.51}(WO_4)_4$ determined by single-crystal XRD and Rietveld refinement agree with Vegard's law[305] yielding a mean Eu^{3+} content of 51.9±1.4% close to the result from SC-XRD of 51.2±0.3%. For $Na_5Y_{0.49}Tb_{0.51}(WO_4)_4$, the Tb^{3+} content derived from the lattice parameters determined

from Rietveld refinement according to Vegard's law[305] is 50±3% being close to the content from SC-XRD of 51.4±0.2%.

Additionally, two samples of the stoichiometry $Na_5Y_{0.5}Eu_{0.5}(WO_4)_4$ were synthesised via solid-state reactions **A1** and **A2** at 600°C and 700°C, respectively. According to Rietveld refinements of the respective PXRD pattern (Table B.1.10 and figures B.1.17 and B.1.18), synthesis **A1** yielded a two-phased product, while a single phase of $Na_5Y_{0.5}Eu_{0.5}(WO_4)_4$ was obtained by synthesis **A2**. In both cases, there is a considerable side phase of $NaY_{0.5}Eu_{0.5}(WO_4)_2$. It is worth noticing, that the side phase after synthesis **A1** is comprised of two separated phases $NaY(WO_4)_2$ and $NaEu(WO_4)_2$, too. Consequently, the miscibility gap in $Na_5Y_{1-x}Eu_x(WO_4)_4$ is temperature dependent since it is not related to the type of synthesis. The energy available during the synthesis at 600°C is sufficient to form $Na_5M(WO_4)_4$ but not for the M^{3+} ions to interchange. At 700°C synthesis temperature, there is no miscibility gap. Using TPXRD, the gap could be narrowed to 660°C-700°C (Figure B.1.19). This temperature provides sufficient activation energy for the interchange of the M^{3+} ions. The investigation of the 'width' of the miscibility gap in concentration is difficult due to the proximity of the reflections of $Na_5Y(WO_4)_4$ and $Na_5Eu(WO_4)_4$. The splitting of the dominant (321), (312) and (213) reflections around $2\theta = 29.5°$ was only unambiguously observed for $x = 0.5$ but not for $x = 0.1$.

Optical Properties of $Na_5M(WO_4)_4$

The infrared and UV-Vis spectra of $Na_5M(WO_4)_4$ can be found in the original paper.[278] Here, the focus lies on the fluorescence spectra of the phosphors $Na_5M(WO_4)_4$ (M = Pr, Sm, Eu, Tb, Tm) showing the characteristic excitation and emission of the f-f transitions. For the sake of better readability and clarity, most of the wavelength values are omitted.[ii] The emission can be excited both directly at the M^{3+} ion and using the O^{2-}-W^{6+} LMCT as an antenna. In general, an energy transfer from the O^{2-}-W^{6+} LMCT antenna towards the M^{3+} ion is possible via three different mechanisms: The first option is the Dexter mechanism relying on exchange interactions consequently requiring covalence between sensitiser and activator.[306] This mechanism is expected to be of little importance in $Na_5M(WO_4)_4$ due to the ionic nature. Secondly, the Förster mechanism assumes energy transfer via electric dipole transitions governed by the distance between sensitiser and activator.[307,308] In principle, this type of energy transfer is likely to occur in $Na_5M(WO_4)_4$ - in the light of the distances discussed earlier being smaller than the critical transfer distance.[287] The third possibility is the excitation of the activator via the luminescence emission of the sensitiser.[39] For $Na_5Gd(WO_4)_4$ having no relevant f-f transitions in the regime under discussion, a broad W^{6+}-O^{2-} LMCT emission centred at 470 nm is reported at 20 K,[287] while a broad emission around 460 nm could be observed for the $Na_5Y(WO_4)_4$ sample at 77 K (Figure B.1.20).

[ii] They can be found in Table B.1.12 including the assignment of each transition.

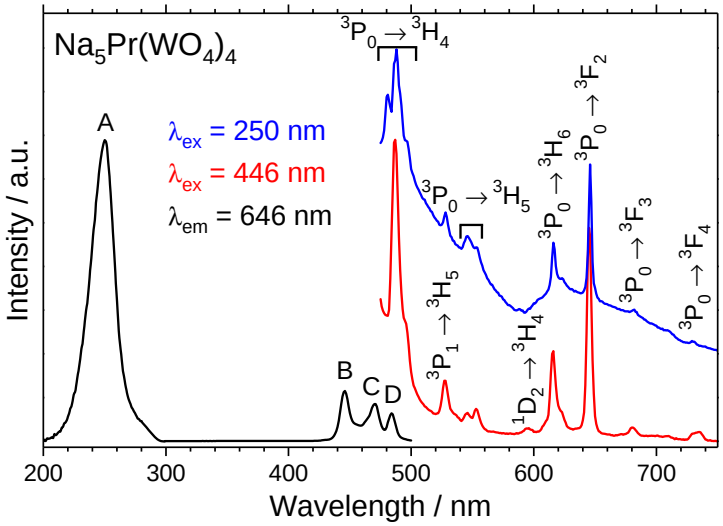

Fig. 5.1.9: Excitation and emission spectra of $Na_5Pr(WO_4)_4$: the assignment of the peaks can be found in Table B.1.12; the excitation spectra were corrected with respect to the lamp intensity.

$Na_5Pr(WO_4)_4$

$Na_5Pr(WO_4)_4$ exhibits the characteristic deep red emission of Pr^{3+} $({}^3P_0 \rightarrow {}^3H_2)$ accompanied by greenish-blue emission $({}^3P_0 \rightarrow {}^3H_4)$ for both excitation wavelengths shown in Figure 5.1.9.[309] This can be explained by the ability of the W^{6+}-O^{2-} LMCT emission to excite Pr^{3+}.[39,287,291] Consequently, an effective energy transfer from the $WO_4{}^{2-}$ group to the Pr^{3+} ion is possible. The excitation spectrum shows on the one hand the intensity of the LMCT excitation obviously being higher compared to excitation via the parity forbidden f-f transitions and on the other hand manifesting the energy transfer from $WO_4{}^{2-}$ group to Pr^{3+} in general. These properties are expected for all $Na_5M(WO_4)_4$ samples studied for their fluorescent properties. Moreover, Pr^{3+} doped titanates, orthovanadates and niobates show low-lying intervalence charge transfer (IVCT) states resulting in fast multi-phonon non-radiative relaxation process from $({}^3P_0 \rightarrow {}^1D_2)$ and consequently leading to a main emission around 600 nm $({}^1D_2 \rightarrow {}^3H_4)$. In distinct dissimilarity, tungstates show weak emission from the ${}^1D_2$ state only.[309–312] For $Na_5Pr(WO_4)_4$, only a very weak emission due to the ${}^1D_2 \rightarrow {}^3H_4$ transition was measured. The IVCT state in tungstates is located at higher energies.[311,312] The relaxations from ${}^3P_0$ to ${}^1D_2$ were correlated with both the Pr-W and the Pr-O distances taking into account both the first and the second coordination environments of the Pr^{3+} ions.[311] The large distances determined from single-crystal data of Pr-W around 386 pm and Pr-O around 246 pm are - in accordance to data reported in literature[311] - responsible for only weak non-radiative relaxation $({}^3P_0 \rightarrow {}^1D_2)$. Consequently, the emission of $Na_5Pr(WO_4)_4$ is dominated by transitions originating at the ${}^3P_0$ state at both excitations via the O^{2-}-W^{6+} LMCT antenna and the Pr^{3+} f-f transitions. The Pr^{3+} $4f^2 \rightarrow 4f^15d^1$ band is expected to be located at higher energies than the measured range due to the large praseodymium to oxygen distances.[312]

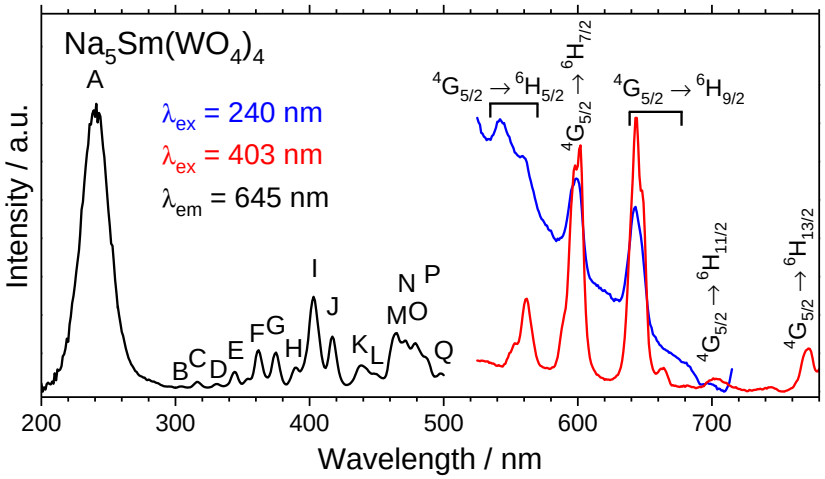

Fig. 5.1.10: Excitation and emission spectra of $Na_5Sm(WO_4)_4$: the assignment of the peaks can be found in Table B.1.12; the excitation spectra were corrected with respect to the lamp intensity.

$Na_5Sm(WO_4)_4$

The fluorescence emission spectra depicted in Figure 5.1.10 of the red phosphor $Na_5Sm(WO_4)_4$ gives further information on the local symmetry of the Sm^{3+} ion. Excited using either the Sm^{3+} f-f transitions or the O^{2-}-W^{6+} LMCT, two major emission peaks were observed ($^4G_{\frac{5}{2}} \rightarrow {}^6H_{\frac{7}{2}}$ and $^4G_{\frac{5}{2}} \rightarrow {}^6H_{\frac{9}{2}}$). The three major transitions of Sm^{3+} are $^4G_{\frac{5}{2}} \rightarrow {}^6H_{\frac{5}{2}}$,$^6H_{\frac{7}{2}}$ and $^6H_{\frac{9}{2}}$. The first is dominated by the magnetic dipole transition, the latter by electronic dipole transition, while $^4G_{\frac{5}{2}} \rightarrow {}^6H_{\frac{7}{2}}$ is partly of both magnetic and electric dipole nature. In accordance with the determined crystal structure, the highest intensity was observed for the $^4G_{\frac{5}{2}} \rightarrow {}^6H_{\frac{9}{2}}$ transition since the Sm^{3+} ion is located on a lattice site without inversion symmetry resulting in the hypersensibilisation of the electronic dipole transition $^4G_{\frac{5}{2}} \rightarrow {}^6H_{\frac{9}{2}}$.[313,314] Further, red emission is observed despite of the option to perform Sm^{3+}-Sm^{3+} ion pair cross-relaxation because of equidistant pairs of energy levels resulting in emission quenching at low concentrations of Sm^{3+}.[154,313,314] This is in accordance with the large Sm^{3+}-Sm^{3+} distances resulting in the special property of $Na_5M(WO_4)_4$ to show no concentration quenching as discussed above (Figure 5.1.5).

$Na_5Eu(WO_4)_4$

In the excitation spectrum of $Na_5Eu(WO_4)_4$, the broad peaks of the O^{2-}-W^{6+} LMCT and the O^{2-}-Eu^{3+} LMCT overlap.[315–319] Again, excitation using both the f-f transitions of Eu^{3+} and the LMCT is possible leading to the characteristic orange-red Eu^{3+} emission.[156,287,314,316] Due to the high site symmetry of Eu^{3+} the $^5D_0 \rightarrow {}^7F_1$ transition does not split and is thus in accordance with the determined crystal structure

of $Na_5Eu(WO_4)_4$.[316,320] The hypersensitivity of the $^5D_0 \rightarrow {}^7F_2$ transition is in agreement with earlier reports on $Na_5Eu(WO_4)_4$ and the lack of inversion symmetry at the europoium site.[283,292,316,320]

$Na_5Y_{1-x}Eu_x(WO_4)_4$

The fluorescence spectra of the solid solutions $Na_5Y_{1-x}Eu_x(WO_4)_4$ resemble the spectra of $Na_5Eu(WO_4)_4$ (Figure 5.1.11, Figure 5.1.12). The expected shift of the O^{2-}-Eu^{3+} LMCT bands with the decreased Eu-O distance with lower values of x towards higher energies in the excitation spectra[316–318] could be observed. Both O^{2-}-Eu^{3+} and O^{2-}-W^{6+} LMCT bands overlap. Hence, the relative intensity of the LMCT band to the f-f transitions in the excitation spectra is increasing with decreasing Eu^{3+} content since the overlap of both bands is increasing. This is exemplarily shown for $Na_5Eu(WO_4)_4$ and $Na_5Y_{0.95}Eu_{0.05}(WO_4)_4$ using Gaussian fits in Figure B.1.21. While the O^{2-}-W^{6+} LMCT band is located at 239 nm for both compounds there is a shift of the O^{2-}-Eu^{3+} LMCT band from 266.5 nm in $Na_5Eu(WO_4)_4$ to 260.5 nm in $Na_5Y_{0.95}Eu_{0.05}(WO_4)_4$. The former value is almost identical to the one reported for $Eu_2[B_2(SO_4)_6]$[112] indicating a weak coordination of Eu^{3+} in $Na_5Eu(WO_4)_4$. Both values are in the typical region for oxide coordinated europium compounds.[315]
In contrast to the ambiguous PXRD pattern of $Na_5Y_{0.9}Eu_{0.1}(WO_4)_4$ discussed earlier, the clear difference between the spectra of $Na_5Y_{0.9}Eu_{0.1}(WO_4)_4$ and $Na_5Eu(WO_4)_4$ indicates, that the former is an actual solid solution and not a phase mixture of $Na_5Y(WO_4)_4$ and $Na_5Eu(WO_4)_4$, giving further insight into the width of the miscibility gap.

$Na_5Tb(WO_4)_4$

$Na_5Tb(WO_4)_4$ emits green light due to the characteristic $^5D_4 \rightarrow {}^7F_J$ transitions of Tb^{3+} upon both excitation via the O^{2-}-W^{6+} LMCT, which overlays the Tb^{3+} f-d transitions, and the Tb^{3+} f-f transitions (Figure 5.1.13). The absence of a broad emission band between 450 nm and 500 nm due to the W^{6+}-O^{2-} LMCT emission while excited at the O^{2-}-W^{6+} LMCT indicates an effective energy transfer towards the Tb^{3+} ion.[287] As expected, there is no blue emission in $Na_5Tb(WO_4)_4$ due to Tb^{3+}-Tb^{3+} cross-relaxation.[145,285,321] This phenomenon will be discussed in detail along with the $Na_5Y_{1-y}Tb_y(WO_4)_4$ samples below. The excitation spectrum of $Na_5Tb(WO_4)_4$ shows a very high LMCT band, especially compared to the excitation spectrum of $Na_5Eu(WO_4)_4$. The intensity of the LMCT band is similar for $Na_5Pr(WO_4)_4$ and $Na_5Sm(WO_4)_4$. These findings are in accordance with literature on double tungstates[300,319] and can be explained by the better matching of the LMCT emission with the Pr^{3+}, Sm^{3+} and Tb^{3+} excitation spectra than with the Eu^{3+} excitation bands. There is only the $^7F_0 \rightarrow {}^5D_2$ transition accessible by the LMCT emission centred at 470 nm in $Na_5Eu(WO_4)_4$ (Figure 5.1.11), while multiple f-f transitions can be excited in $Na_5Pr(WO_4)_4$ (Figure 5.1.9) and $Na_5Sm(WO_4)_4$ (Figure 5.1.10). In $Na_5Tb(WO_4)_4$, the $^7F_6 \rightarrow {}^5D_4$ transition can be excited effectively (Figure 5.1.13).

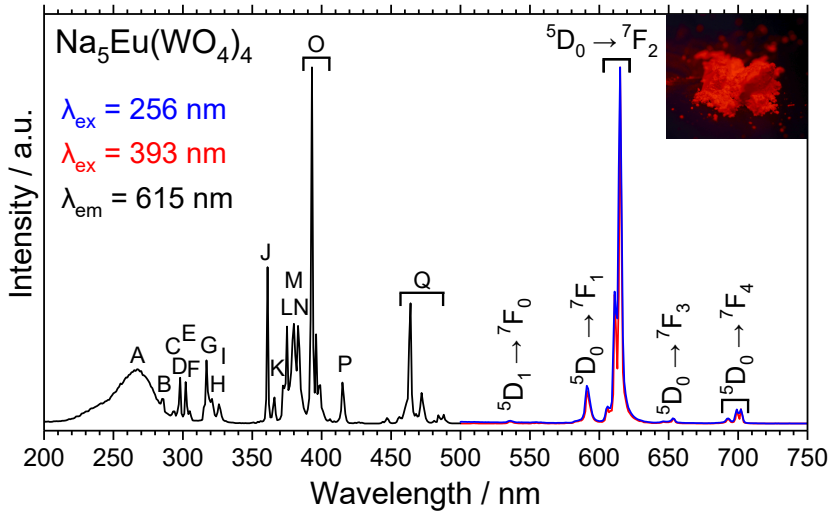

Fig. 5.1.11: Excitation and emission spectra of $Na_5Eu(WO_4)_4$: the assignment of the peaks can be found in Table B.1.12; the excitation spectra were corrected with respect to the lamp intensity; the inset shows a picture of $Na_5Eu(WO_4)_4$ powder under 254 nm UV radiation.

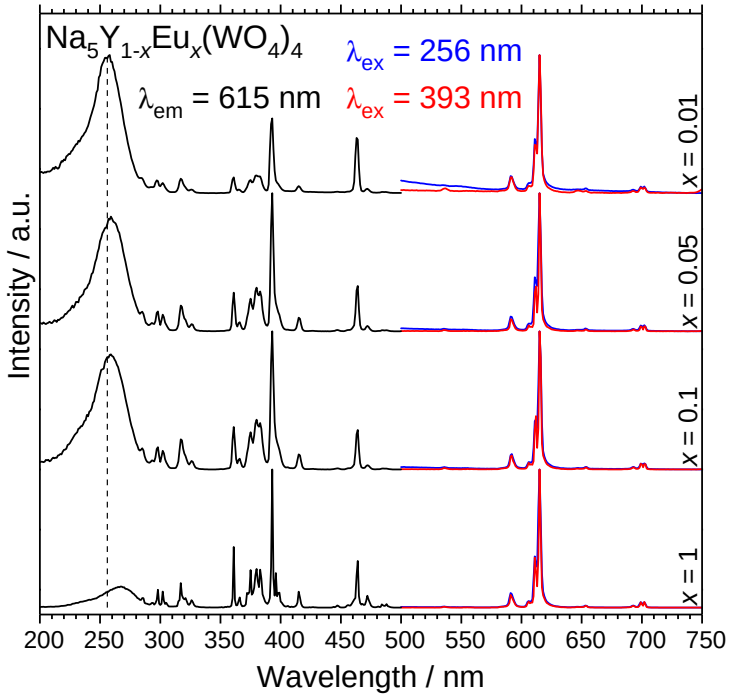

Fig. 5.1.12: Excitation and emission spectra of $Na_5Y_{1-x}Eu_x(WO_4)_4$ (x = 0.01, 0.05, 0.1, 1): The assignment of the peaks of $Na_5Eu(WO_4)_4$ ($x = 1$) can be found in Table B.1.12; there are no additional peaks for the three other samples; however, there is an increase in the intensity ratio of the broad LMCT band around 260 nm and the f-f transition excitation with its maximum at 393 nm $\left({}^7F_0 \rightarrow {}^5L_6\right)$ with decreasing x accompanied by a shift of the O^{2-}-Eu^{3+} LMCT band to lower wavelengths with decreasing x elucidated by the dotted line in the graph at 256 nm. The excitation spectra were corrected with respect to the lamp intensity; Gaussian fits of the excitation spectra for $x = 1$ and $x = 0.05$ can be found in Figure B.1.21.

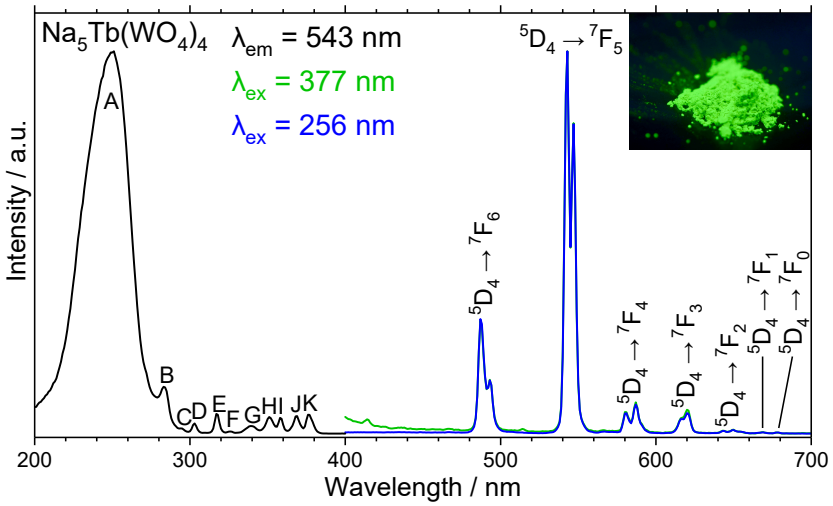

Fig. 5.1.13: Excitation and emission spectra of $Na_5Tb(WO_4)_4$: the assignment of the peaks can be found in Table B.1.12; the excitation spectra were corrected with respect to the lamp intensity; the inset shows a picture of $Na_5Tb(WO_4)_4$ powder under 254 nm UV radiation.

$Na_5Y_{1-y}Tb_y(WO_4)_4$

Compared to $Na_5Tb(WO_4)_4$, the $Na_5Y_{1-y}Tb_y(WO_4)_4$ samples show additional blue emission originating in the $^5D_3$ state increasing in intensity with lower Tb^{3+} content when excited at 377 nm (Figure 5.1.15). This can be explained by the less effective cross-relaxation process between an excited Tb^{3+} and an adjacent ground state Tb^{3+} ion

$$^5D_3(Tb^{3+}) + {}^7F_6(Tb^{3+}) \rightarrow {}^5D_4(Tb^{3+}) + {}^7F_0(Tb^{3+})$$

in low doped $Na_5Y_{1-y}Tb_y(WO_4)_4$ samples. The cross-relaxation depends on the distance of neighbouring Tb^{3+} ions and it is consequently minimised at low doping concentration.[145,285,321] Hence, the ratio of the Tb^{3+} emissions originating in the $^5D_3$ state to the ones from the $^5D_4$ state in decreasing with Tb^{3+} content (Figure 5.2.9). The presence of the blue Tb^{3+} emissions originating in the $^5D_3$ state up to doping concentrations of 5% in $Na_5Y_{1-y}Tb_y(WO_4)_4$ confirms a rather weak coordination behaviour for Tb^{3+}.[112,145] For comparison, no emission from the $^5D_3$ state was observed in $NaGd(WO_4)_2$:Tb^{3+} down to doping concentrations of 1%.[234] The dependency of this behaviour on the crystal structure is discussed in detail in the next section.
Further, the blue emission is absent when the phosphor is excited via the LMCT for all doping concentrations. The broad LMCT emission is able to excite Tb^{3+} to the $^5D_4$ state, only. The transferred energy is not sufficient to reach the $^5D_3$ state. The respective energy levels are sketched in Figure 5.1.14. Consequently, the blue emission originating from the latter is not present. The excitation spectra of $Na_5Y_{1-y}Tb_y(WO_4)_4$ (Figure B.1.22) resemble that of $Na_5Tb(WO_4)_4$, but they show a slight decrease of the ratio of LMCT to f-f transitions with increasing Tb^{3+} content presumably resulting from

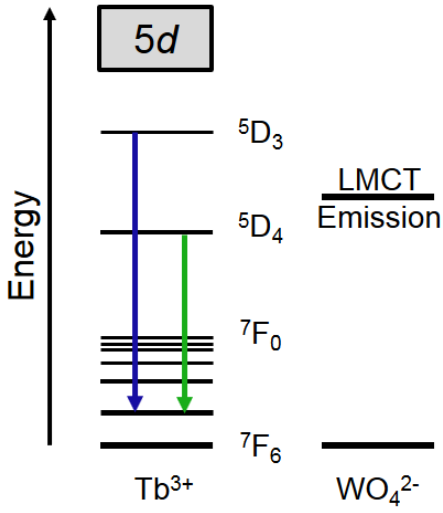

Fig. 5.1.14: Energy Levels of the Tb^{3+} f-states compared to the energy of the W^{6+}-O^{2-} LMCT: The transferred energy is sufficient to reach the green emitting $^5D_4$ state, only. Consequently, no blue emission originating in the $^5D_3$ state is observed when exciting the LMCT of the WO_4^{2-}.

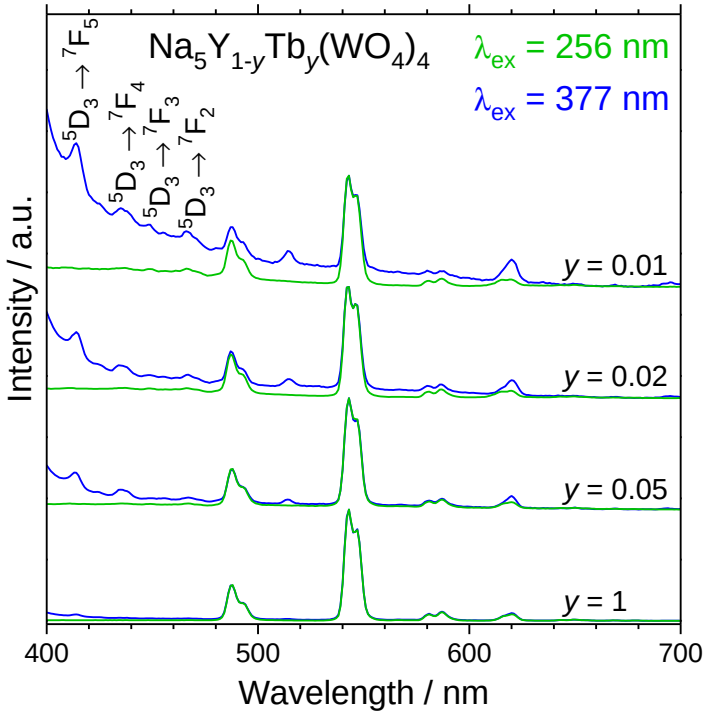

Fig. 5.1.15: Emission spectra of $Na_5Y_{1-y}Tb_y(WO_4)_4$ (y = 0.01, 0.02, 0.05, 1): the assignment of the peaks of $Na_5Tb(WO_4)_4$ ($y = 1$) can be found in Table B.1.12; there is an additional blue emission originating in the $^5D_3$ state of Tb^{3+} for low values for y; the respective transitions are indicated inside the graph.

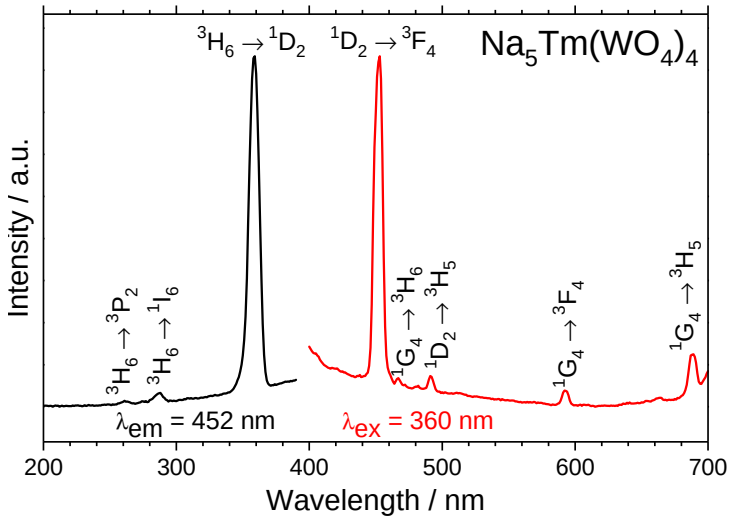

Fig. 5.1.16: Excitation and emission spectra of $Na_5Tm(WO_4)_4$: the assignment of the peaks can be found in Table B.1.12; the excitation spectra were corrected with respect to the lamp intensity.

the different overlap of the O^{2-}-W^{6+} LMCT and the Tb^{3+} f $\rightarrow$ d transitions due to the smaller Tb-O distances at lower doping concentrations.

Consequently, the absence of the blue emission when exciting at the $WO_4{}^{2-}$ antenna can be elucidated by an energy transfer from $WO_4{}^{2-}$ to Tb^{3+} via the luminescence emission of the W^{6+}-O^{2-} LMCT.[39] An energy transfer based on an electric dipole-dipole interaction as reported earlier[287] for the phosphor class appears to be merely of minor significance. In this case, the blue Tb^{3+} emission would not be absent when exciting at the $WO_4{}^{2-}$ antenna.

$Na_5Tm(WO_4)_4$

$Na_5Tm(WO_4)_4$ shows a sharp blue emitting line ($^1D_2 \rightarrow {}^3F_4$) (Figure 5.1.16). The emission can be excited primarily by the $^3D_6 \rightarrow {}^1D_2$ transition accompanied by the two weak transitions $^3H_6 \rightarrow {}^3P_2$ and $^3H_6 \rightarrow {}^1I_6$. Distinctly different from all other studied compounds there was no O^{2-}-W^{6+} LMCT excitation observed in $Na_5Tm(WO_4)_4$. This is in agreement with earlier results for $NaGd(WO_4)_2$:Tm^{3+}.[38,322] Apparently, there is no energy transfer from the $WO_4{}^{2-}$ antenna towards the Tm^{3+} ion. Both O^{2-}-W^{6+} LMCT excitation and W^{6+}-O^{2-} LMCT emission cannot be seen in Figure 5.1.16 since they are much weaker than the Tm^{3+} f-f transitions in the same regions of the spectrum.

Presumably, the energy transfer cannot take place due to the overlap of the emissions of Tm^{3+} ($^1D_2 \rightarrow {}^3F_4$) and the W^{6+}-O^{2-} LMCT. The energy transferred from the LMCT is not sufficient for Tm^{3+} to reach the $^1D_2$ state. In contrast, an energy transfer from the O^{2-}-W^{6+} LMCT to Tm^{3+} is reported in $CaWO_4$:Tm^{3+}[323] since there the W^{6+}-O^{2-} LMCT emission is located at higher energies compared to $Na_5Tm(WO_4)_4$.

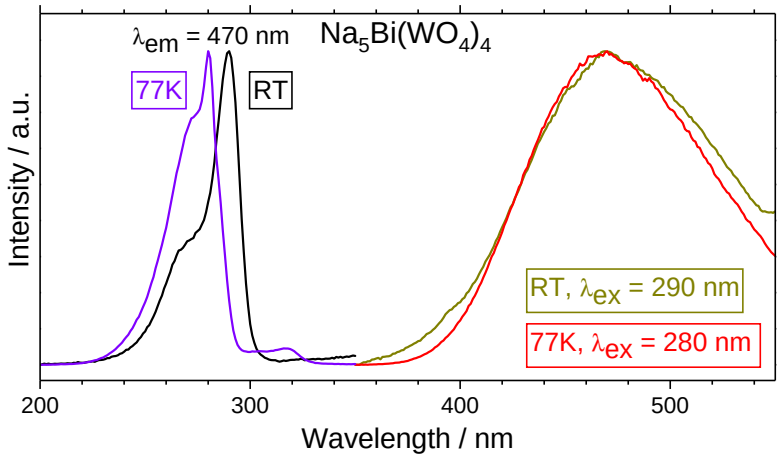

Fig. 5.1.17: Excitation and emission spectra of $Na_5Bi(WO_4)_4$ at both room temperature and 77 K: the assignment of the peaks can be found in Table B.1.12; please note that the excitation spectra are not corrected with respect to the lamp intensity; Gaussian fits of both excitation spectra can be found in Figure B.1.23.

$Na_5Bi(WO_4)_4$

The luminescent properties of $Na_5Bi(WO_4)_4$ were studied both at room temperature and at 77 K (Figure 5.1.17). The compound shows a broad blue emission due to the $^3P_1 \rightarrow {}^1S_0$ transition of Bi^{3+} at both temperatures. From the $6s^2$ ground state of Bi^{3+} ($^1S_0$) and the excited $6s6p$ states ($^3P_0$, $^3P_1$, $^3P_2$ and $^1P_1$ in sequence of increasing energy), the $^1S_0 \rightarrow {}^1P_1$ transition is parity and spin-allowed and the $^1S_0 \rightarrow {}^3P_1$ is partially allowed due to spin-orbit coupling. The other transitions are strictly forbidden. However, they may appear due to mixing enabled by low local symmetry.[315] Consequently, the $^1S_0 \rightarrow {}^1P_1$ and $^1S_0 \rightarrow {}^3P_1$ transitions emerge in the excitation spectra superimposed with the O^{2-}-W^{6+} LMCT band. Three transitions could be assigned using Gaussian fits for both excitation spectra (Figure B.1.23). At room temperature, the $^1S_0 \rightarrow {}^3P_1$ transition is centred at 290 nm, the $^1S_0 \rightarrow {}^1P_1$ at 275 nm and the O^{2-}-W^{6+} LMCT at 258 nm, while the bands occur at 281 nm, 273 nm and 250 nm at 77 K, respectively. Both the LMCT and the $^1S_0 \rightarrow {}^3P_1$ transition are shifted to smaller wavelengths at 77 K since more energy is necessary to surpass the respective threshold, because of temperature driven occupation of vibrational substates. The spin-allowed $^1S_0 \rightarrow {}^1P_1$ is not significantly affected by temperature. The absence of other transitions is in agreement with the structure determination resulting in the $4a$ Wyckoff site for Bi^{3+} with site symmetry $\bar{4}$. Further, the shift of the $^1S_0 \rightarrow {}^3P_1$ with temperature supports the conclusion of two different Bi^{3+} transitions instead of one transition with a doublet. The latter would require two independent Bi^{3+} sites.[324] According to the single-crystal XRD experiment, there is only one bismuth position in $Na_5Bi(WO_4)_4$. Since practicable fits were only possible using the non-corrected excitation spectra, the intensity of the LMCT can be expected to be underestimated in the results.

Conclusion of the Luminescence Properties

In conclusion, the discussed fluorescence emission and excitation spectra confirm that there is no apparent concentration quenching in $Na_5M(WO_4)_4$ in agreement with the large M-M distances (Figure 5.1.5). Moreover, all results indicate that the energy transfer from the sensitiser ${WO_4}^{2-}$ to the activator M^{3+} is governed by the luminescence emission of the W^{6+}-O^{2-} LMCT. Especially, the absence of blue emission in $Na_5Y_{1-y}Tb_y(WO_4)_4$ when excited via the O^{2-}-W^{6+} LMCT is not comprehensible by the other two mechanisms discussed earlier.[287,306–308]

Magnetic Properties of $Na_5M(WO_4)_4$

For $Na_5M(WO_4)_4$ (M = Ce, Pr, Sm, Eu, Tb, Tm, Yb, Bi), the temperature dependence of the magnetic susceptibility (χ) was measured at 10 kOe and is plotted along with their inverse susceptibility χ^{-1} in Figures 5.1.18 and B.1.24. The extracted magnetic data is summarised in Table 5.1.2. A more detailed discussion can be found in the original publication.[278] All samples, with the exception of $Na_5Bi(WO_4)_4$, show paramagnetism over the whole investigated temperature range. No onset of any magnetic interactions has been observed. This can be attributed to the large M-M distances in $Na_5M(WO_4)_4$ (Figure 5.1.5).

Tab. 5.1.2: Magnetic properties of $Na_5M(WO_4)_4$ (M = Ce, Pr, Sm, Eu, Tb, Tm, Yb, Bi): μ_{eff}, effective magnetic moment; μ_{calc}, calculated magnetic moment; Θ_p, paramagnetic Curie temperature; the respective standard deviations are given in parentheses.

M	μ_{eff} / μ_B	μ_{calc} / μ_B	Θ_p / K
Ce	2.38(1)	2.54	−103.6(1)
Pr	3.78(1)	3.58	−39.0(1)
Sm	0.61(1)	0.845	−0.3(1)
Eu	van Vleck, $\lambda = 612(10)$ K, $\chi_0 = 5.6(1) \times 10^{-3}$ emu mol^{-1}		
Gd	8.11(1)	7.94	+4.1(1)
Tb	9.77(1)	9.72	−0.8(1)
Tm	7.48(1)	7.56	−3.1(1)
Yb	4.71(1)	4.54	−43.6(1)
Bi	diamagnetic; χ (300 K) = $-190(1) \times 10^{-6}$ emu mol^{-1}		

The inverse susceptibility was fitted in the temperature range from 75-300 K using the modified Curie-Weiss law. The calculated effective magnetic moments are in line with the respective rare earth cations in the trivalent oxidation state. The inverse susceptibilities (χ^{-1} data) of $Na_5Ce(WO_4)_4$ and $Na_5Yb(WO_4)_4$ deviate from the linear behaviour due to crystal field effects.
$Na_5Sm(WO_4)_4$ and $Na_5Eu(WO_4)_4$ exhibit the typical van Vleck type paramagnetism (Figure 5.1.18).[174,175,320,325–331] For the former, it is caused by the close proximity of the excited $J = 7/2$ multiplet with respect the ground state $J = 5/2$ multiplet in the Sm^{3+} cations. The energy difference between these states is only about 1550 K, while the

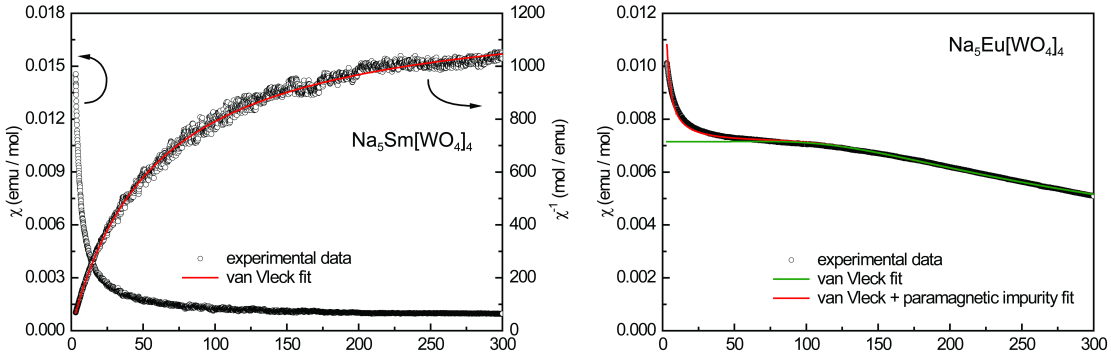

Fig. 5.1.18: Magnetic properties of $Na_5Sm(WO_4)_4$: (left) temperature dependence of the magnetic susceptibility (χ and χ^{-1} data) measured at 10 kOe along with the fit of the data (see text); magnetic properties of $Na_5Eu(WO_4)_4$: (right) temperature dependence of the magnetic susceptibility (χ data) measured at 10 kOe along with the fit of the data (see text).

respective other angular momentum levels are correspondingly higher. The energy barrier value $\Delta E = 1337\,\mathrm{K}$ was determined for the first time for any ionic compound via fitting using the Hamaker equation.[326] It is smaller than the ideal value of 1550 K, however, well in line with intermetallic $SmOs_4Sb_{12}$ ($\Delta E = 850\,\mathrm{K}$)[331] or $SmRh_4B_4$ ($\Delta E = 1080\,\mathrm{K}$).[326] Further fitting parameters and details on the Hamaker equation can be found in the original publication.[278]

For $Na_5Eu(WO_4)_4$, the result are in agreement with [320] and the fit applying van Vleck theory[174] yielded the coupling constant λ - equivalent to the energy difference between the $^7F_0$ and $^7F_1$ states as introduced on page 40 - with a value of 612 K slightly elevated compared to a free Eu^{3+} ion ($\lambda = 480\,\mathrm{K}$) or other ionic Eu^{3+} compounds in the literature (EuF_3:[175] $\lambda = 490\,\mathrm{K}$; $EuBO_3$:[175] $\lambda = 471\,\mathrm{K}$; $Eu_2Ta_2O_{7.1}N_{0.6}$:[332] $\lambda = 390(2)\,\mathrm{K}$; $Eu_2[B_2(SO_4)_6]$:[112] $\lambda = 589\,\mathrm{K}$). However, the energy difference calculated using the spectroscopic data discussed earlier, i.e. the energy values of the $^5D_1 \rightarrow {}^7F_0$ and $^5D_0 \rightarrow {}^7F_1$ transitions in the fluorescence spectrum (Figure 5.1.11) and the $^7F_0 \rightarrow {}^5D_1$ and $^5D_0$ bands in the UV-Vis spectrum,[278] of 555 K is in good agreement to the magnetic λ value of 612 K.

Finally, $Na_5Bi(WO_4)_4$ exhibits almost temperature independent diamagnetism (Figure B.1.24), in line with all atoms being close shell. Thus, the oxidation state +6 of tungsten with no unpaired electrons is confirmed.

^{151}Eu Mößbauer Spectroscopy

The ^{151}Eu Mößbauer spectrum of $Na_5Eu(WO_4)_4$ is shown in Figure 5.1.19. Only one spectral contribution with a line width of $\Gamma = 2.45(3)\,\mathrm{mm\,s^{-1}}$ at a typical isomer shift for trivalent europium at $\delta = +0.55(1)\,\mathrm{mm\,s^{-1}}$ can be observed. The Mößbauer spectroscopic results of the tungstate $KEu(WO_4)_2$ give an almost identical isomer shift for the trivalent

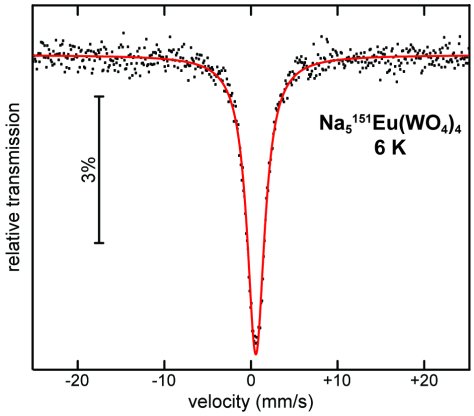

Fig. 5.1.19: Experimental (data points) and simulated (continuous line) ^{151}Eu Mößbauer spectra of $Na_5Eu(WO_4)_4$ measured at 6 K.

europium atoms in that compound.[333] Thus, the oxidation state +3 of europium is confirmed.

5.2 $AM(WO_4)_2$ (A = Li, Na, K; M = Y, La, Pr, Tb, Bi)

As discussed in the previous section, $Na_5M(WO_4)_4$ and $NaM(WO_4)_2$ are two highly related compound groups with the latter being the thermal decomposition product of the former and both being related via a group-subgroup relation. In this section, the view is widened to the double tungstates $AM(WO_4)_2$ in general, i.e. beyond only the alkali metal sodium.

For over 130 years, these double tungstates with the general formula $AM(WO_4)_2$ (A = alkali metal, M = trivalent metal) were investigated intensively.[25,230,273–275,334] Their applications range from phosphors due to their small concentration quenching over photonics including laser host materials to sensors.[34–38]

Herein, the consideration is limited to the compounds $AM(WO_4)_2$ with A = Li, Na, K and M = rare earth elements, i.e. lanthanides and yttrium as well as bismuth, excluding the compounds comprising the two alkali metals rubidium and caesium and the trivalent cations scandium and iron.[335,336] In general, the double tungstates $AM(WO_4)_2$ (A = Li, Na, K; M = Y, La-Nd, Sm-Lu, Bi) crystallise in four structure types. An overview is given in Figures 5.2.1 and B.2.1 and the respective units cells are shown in Figure 5.2.2. The most important structure type is *scheelite*. All three others can be considered distorted variants of *scheelite*. Detailed discussions are given below. For the lithium double tungstates exhibiting polymorphism, the low temperature form is referred to as $LiM(WO_4)_2$-I and the high temperature polymorph as $LiM(WO_4)_2$-II.

Moreover, the optical properties of the double tungstates are investigated extensively including the possible s-p fluorescence of ABi$(WO_4)_2$ and a study of the terbium to terbium cross-relaxation process and the energy transfer mechanisms in the four solid solutions $LiY_{1-x}Tb_x(WO_4)_2$-I, $LiY_{1-x}Tb_x(WO_4)_2$-II, $NaY_{1-x}Tb_x(WO_4)_2$ and $KY_{1-x}Tb_x(WO_4)_2$. Additionally, the optical properties are compared to the related compounds $Na_5M(WO_4)_4$ (M = Y, Bi, Tb) and respective solid solutions reported in the previous section.

Syntheses

All compounds in this section were synthesised by solid-state reactions following the reaction equation

$$A_2CO_3 + M_2O_3 + 4\,WO_3 \longrightarrow 2\,AM(WO_4)_2 + CO_2$$

and the respective modified equations when using Pr_6O_{11} and Tb_4O_7. Stoichiometric amounts of the educts M_2O_3[iii] and WO_3 as well as A_2CO_3[iv] with 10% excess[v] were

[iii] Bi_2O_3 (Riedel-de Haën, 99.5%), La_2O_3 (Auer-Remy, 99,99%), Pr_6O_{11} (Merck, 99.9%), Tb_4O_7 (Chempur, 99.9% and Y_2O_3 (Alfa Aesar, 99.99%)

[iv] Li_2CO_3 (Acros, 99.9%), Na_2CO_3 (AppliChem, 99%) and K_2CO_3 (Baker, 99%)

[v] This surplus was added due to losses caused by the evaporation of CO_2 and in order to suppress the formation of ternary tungstates such as Bi_2WO_6, $La_2W_2O_9$ or $Pr_2W_2O_9$ - to mention just a few of the side phases obtained during preliminary experiments prior to synthesis optimisation.

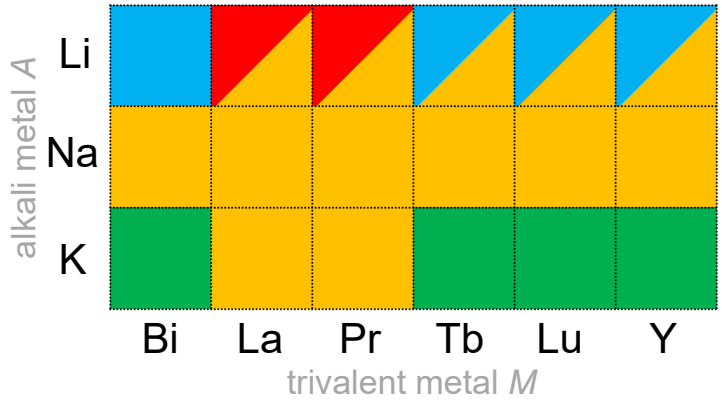

Fig. 5.2.1: Overview over the polymorphism of $AM(WO_4)_2$: The respective alkali metal A is given on the left and the respective trivalent metal M on the bottom; the colours represent different structure types with the colour code explained in Figure 5.2.2; for compounds adapting two structure types, the colour in the top left represents the low temperature polymorph - denoted by the suffix -I - and the colour on the bottom right the high temperature form - denoted with the suffix -II; an analogous overview over the whole range of lanthanides is given in Figure B.2.1.

ground together, filled in corundum crucibles and heated for 60 h at 720°C with 200 Kh^{-1} ramps in a muffle furnace - for all samples not denoted otherwise. For $LiPr(WO_4)_2$-II and $LiY(WO_4)_2$-II, the temperature was increased to 1000°C, respectively. $LiLa(WO_4)_2$-I and $LiPr(WO_4)_2$-I were prepared via flux syntheses according to

$$\frac{1}{2}\,Li_2WO_4 + \frac{1}{2}\,La_2O_3 + \frac{3}{2}\,WO_3 \longrightarrow LiLa(WO_4)_2$$

and the respectively modified equation for Pr_6O_{11} using stoichiometric amounts of La_2O_3, Pr_6O_{11} and WO_3, and 1000% excess of Li_2WO_4. The ground educts were heat treated inside a muffle furnace at 650°C for 10 h. Subsequently, all powders were dissolved in 50 ml hot deionized water (200°C) under constant magnetic stirring (500 rpm) for 1 h, vacuum-filtrated along with washing with additional 50 ml of H_2O and dried in a compartment dryer at 65°C for 24 h. Via this step, water soluble side phases like A_2WO_4 or $A_2W_2O_7$ were washed out. All samples were obtained in the form of colourless polycrystalline powders - except for pale yellow $ABi(WO_4)_2$ (A = Li, Na, K), brown $LiPr(WO_4)_2$-I and green $LiPr(WO_4)_2$-II. Phase-purity was confirmed by PXRD depicted in Figures B.2.2 to B.2.12 and Rietveld analysis (Figures B.2.13 and B.2.14).

Single-crystals were prepared via recrystallisation from the melt - analogously to $NaEu(WO_4)_2$ (page 79, after holding above the melting point for 10 h, cooling to 400°C with a ramp of 5 Kh^{-1}, then to room temperature with 200 Kh^{-1}). The temperature the sample was hold inside the platinum crucibles is summarised in Table 5.2.1. Single-crystals of $LiY(WO_4)_2$-I could not be prepared this way since the melting point is above the phase transition temperature of this compound. Consequently, single-crystals were obtained via flux synthesis mixing as-prepared $LiY(WO_4)_2$-I and $LiBO_2$ (Merck, 99%) in

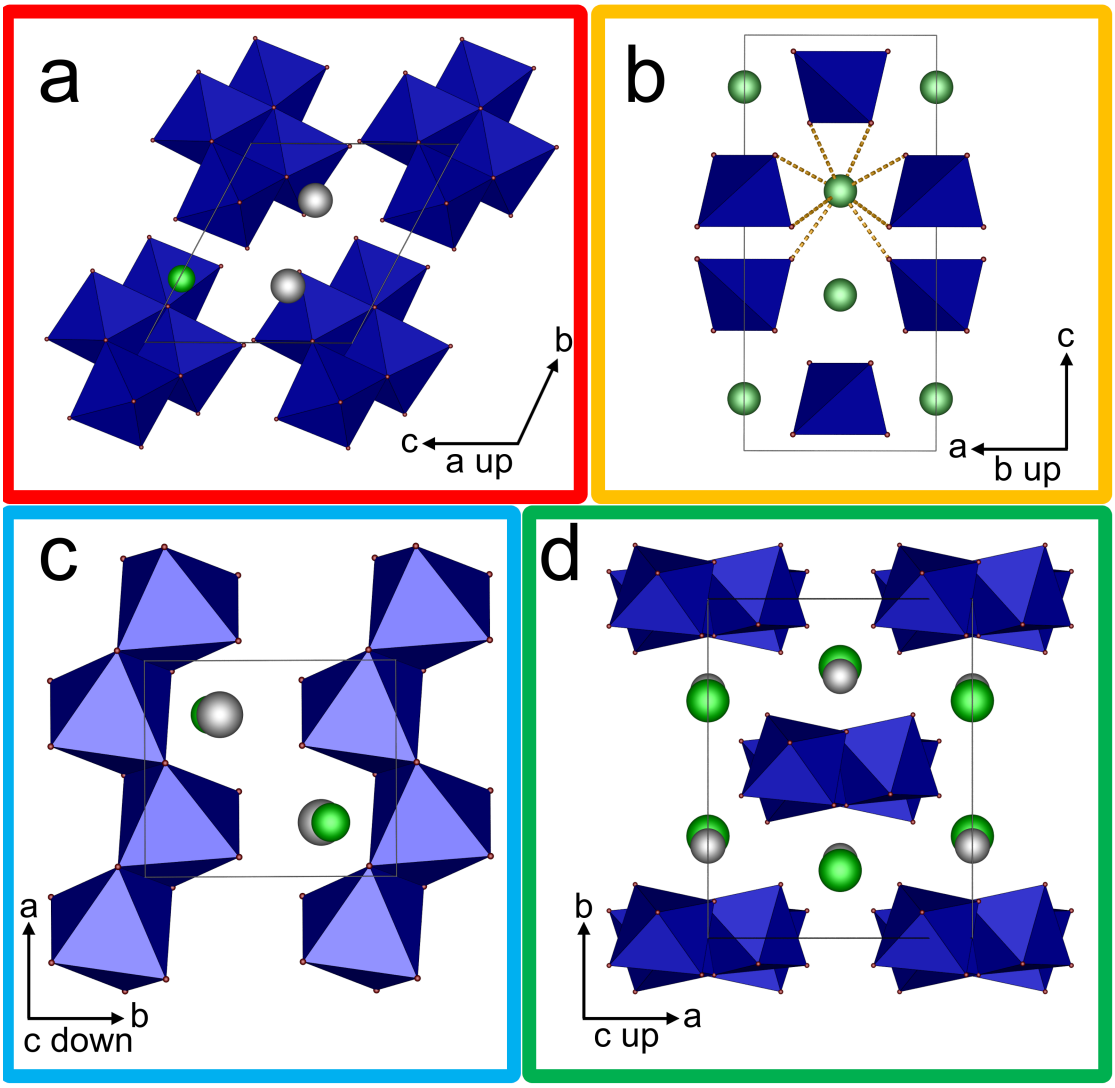

Fig. 5.2.2: Unit cells of the four structure types adapted by $AM(WO_4)_2$: (a) shows $LiPr(WO_4)_2$-I as an example for the $CuLa(WO_4)_2$ structure type; in (b) and (c) $LiY(WO_4)_2$-II and $LiY(WO_4)_2$-I are depicted crystallising in the *scheelite* and the *wolframite* structure type, respectively (see also Figure 1.3.2); in (d), the unit cell of $KY(WO_4)_2$ is shown representing the structure type of the same name related to *fergusonite*; tungstate polyhedra (WO_4 and WO_6) are shown in blue, oxygen atoms red, alkali metal atoms light green, rare earth metal atoms grey, disordered lithium and yttrium atoms in (b) are depicted in pale green.

a molar ratio of 1:1 by grinding. The mixture was heated in a platinum crucible inside a muffle furnace to 850°C. The temperature was hold for 10 h followed by cooling to 300°C with a ramp of 5 Kh^{-1}, then to room temperature with 200 Kh^{-1}.

Tab. 5.2.1: List of temperatures at which the respective $AM(WO_4)_2$ sample were hold inside platinum crucibles for 10 h prior to cooling for the recrystallisation from the melt.

Sample	T / °C
$LiBi(WO_4)_2$	800
$NaBi(WO_4)_2$	950
$KBi(WO_4)_2$	950
$LiLa(WO_4)_2$	1000
$KLa(WO_4)_2$	900
$LiPr(WO_4)_2$-II	950
$LiY(WO_4)_2$-II	1100
$NaY(WO_4)_2$	1100
$KY(WO_4)_2$	1300

Crystal Structures

The crystal structures discussed in the following were determined by single-crystal XRD or Rietveld refinement. The latter was used for the structures of $LiLa(WO_4)_2$-I and $LiPr(WO_4)_2$-I starting from the structural model for $LiPr(WO_4)_2$-I reported by Klevtsova et al.[275] The first extensive reports are given for $LiLa(WO_4)_2$-I, $LiPr(WO_4)_2$-II and $LiY(WO_4)_2$-II, while the first structure determinations from single-crystal data are reported for $LiBi(WO_4)_2$, $LiLa(WO_4)_2$-II and $LiY(WO_4)_2$-I. Moreover, the structures of $NaBi(WO_4)_2$, $KBi(WO_4)_2$, $KLa(WO_4)_2$, $LiPr(WO_4)_2$-I, $NaY(WO_4)_2$ and $KY(WO_4)_2$ were redetermined for the sake of comparison and clarification of ambiguities in literature. For example, there are contradicting reports on the structure types for $ABi(WO_4)_2$ (A = Li, Na, K).[274,337–339] This is evaluated in the following. Details on the structure determinations can be found in Figures B.2.13 and B.2.14 and Tables B.2.1 to B.2.3.

$CuLa(WO_4)_2$ Structure Type

$LiLa(WO_4)_2$-I and $LiPr(WO_4)_2$-I crystallise in the triclinic crystal system with space group $P\bar{1}$ (no. 2) and two formula units per unit cell (Figure 5.2.2a) in the $CuLa(WO_4)_2$ structure type.[340] Details on the structure determinations can be found in Table B.2.1. The anion consists of non-condensed $[W_4O_{16}]^{4-}$ building blocks formed by edge sharing WO_6 octahedra. As common for tungstates and due to the repulsion of adjacent W^{6+} cations, the tungsten atom is not located in the centre of these octahedra. There are two tungsten sites with Δ_{octa} of 17.2% and 1.6% and R_c of 34 pm and 26 pm, respectively.[vi] On the cationic side depicted in Figure B.2.15, the lithium and lanthanum

[vi] The calculations using the method of Balić-Žunić and Makovicky were carried out on $LiPr(WO_4)_2$-I.

or praseodymium atoms are coordinated by four and eight oxygen atoms, respectively. The (La/Pr)O_8 polyhedra form edge-sharing dimers which are in turn connected to two monodentate and two bidentate LiO_4 polyhedra[vii] resulting in cationic chains. Together with the $[W_4O_{16}]^{4-}$ building units, these form a network.

Scheelite Structure Type

$LiLa(WO_4)_2$-II, $LiPr(WO_4)_2$-II, $LiY(WO_4)_2$-II, $NaBi(WO_4)_2$, $NaY(WO_4)_2$ and $KLa(WO_4)_2$ crystallise in the *scheelite* structure type in the tetragonal crystal system with space group $I4_1/a$ (no. 88) and two formula units per unit cell (Figure 5.2.2b as well as Figures 1.3.2 and 5.1.2). The crystal structure was already described for $NaEu(WO_4)_2$ (page 79). Details on the structure determinations can be found in Tables B.2.2 and B.2.3. For $NaBi(WO_4)_2$, - very similar to related $Na_5Bi(WO_4)_4$ discussed on page 81 - no stereochemical influence due to the lone pair effect is observed with $\epsilon = 0$.

Wolframite Structure Type

$LiBi(WO_4)_2$ and $LiY(WO_4)_2$-I crystallise in the *wolframite* structure type in the monoclinic crystal system with space group $P2/n$ (no. 13) and two formula units per unit cell (Figure 5.2.2c). Details are found in Tables B.2.2 and B.2.3.The anion consists of zigzag-chains of edge-sharing WO_6 octahedra along [100]. In line with the discussion above, these octahedra can be considered distorted with Δ_{octa} of 3.2% and 8.7% and R_{c} of 28 pm and 28 pm for $LiBi(WO_4)_2$ and $LiY(WO_4)_2$-I, respectively. Again, the reason for these results can be found in the electrostatic repulsion of neighbouring W^{6+} cations. Both lithium and bismuth or yttrium atoms are located on distinct sites and coordinated by eight oxygen atoms (Figure B.2.16). The LiO_8 and (Bi/Y)O_8 dodecahedra are each connected both via edges to four of the opposite type resulting in layers in the *ab* plane. Further, they are each connected to four WO_6 octahedra resulting in a network formed by the stacking of the layers and the chains. Notably, the unit cell is enlarged for the double tungstate in contrast to the mineral *ferberite* (Figure 1.3.2b) approximately by the factor two via a doubled c unit cell parameter. This is due to the ordered introduction of two cation types A and M and contrary to the *scheelite* type double tungstates and their disorder of A and M atoms. Regarding the possible stereochemical activity of Bi^{3+} cations due to the lone pair effect, the comparison of the coordination environment of bismuth and yttrium is in order. The influence can be seen by the centroid deviation and eccentricity values of $R_c = 37$ pm and $\epsilon = 0.127$ and $R_c = 26$ pm and $\epsilon = 0.097$ for $LiBi(WO_4)_2$ and $LiY(WO_4)_2$-I, respectively. The values are also significant for the lone pair free $LiY(WO_4)_2$-I. This is due to the large electrostatic repulsion by the presence of highly charged W^{6+} cations. Nevertheless, the larger values for $LiBi(WO_4)_2$ indicate an expressed lone pair effect.

[vii] These LiO_4 building units can be described as highly distorted tetrahedra with $\Delta_{\mathrm{tetr}} = 22\%$ with the lithium atom located inside of one face of the tetrahedron. The coordination can also be described as 3+1.

$KY(WO_4)_2$ Structure Type

$KBi(WO_4)_2$ and $KY(WO_4)_2$ crystallise in the monoclinic crystal system with space group $C2/c$ (no. 15) and four formula units per unit cell (Figure 5.2.2d). Details can be found in Tables B.2.2 and B.2.3. The structure type is named after the second compound. The anion comprises double chains of WO_6 octahedra along [001]. Each octahedron is connected to two others via corners and one further via edges. Again, these octahedra can be considered distorted for electrostatic reasons with Δ_{octa} of 14.2% and 5.3% and R_{c} of 30 pm and 30 pm for $KBi(WO_4)_2$ and $KY(WO_4)_2$, respectively. Charge balance is achieved by K^+ and Bi^{3+} or Y^{3+} cations coordinated by twelve and eight oxygen atoms, respectively (Figure B.2.17). The $(Bi/Y)O_8$ distorted square antiprisms form chains along (101) via common edges. Each $(Bi/Y)O_8$ is connected to six monodentate WO_6 and two bidentate WO_6 resulting in a network. The openings in this network are filled by KO_{12} icosahedra.
In contrast to the previous structure type, the lone pair effect appears to be quenched in $KBi(WO_4)_2$. The eccentricities ϵ of 0.52 and 0.49 are very similar in $KBi(WO_4)_2$ and $KY(WO_4)_2$. Consequently, they can be expected to be caused - in both cases - by electrostatic repulsion only. There is no stereochemical activity in $KBi(WO_4)_2$.
The $KY(WO_4)_2$ structure type can be considered a distorted variant of the monoclinic or m-*fergusonite*[viii] structure as adapted by $YNbO_4$.[341] Therein, the cation comprises zigzag-chains of NbO_6 octahedra. Each NbO_6 is connected to two others via edges. The chains are connected by eightfold-coordinated Y^{3+} cations. In turn, the structure can be described as a network of edge-sharing YO_8 distorted square antiprisms with the NbO_6 chains running through it. Shifting the focus on $KBi(WO_4)_2$ and $KY(WO_4)_2$, the increased charge of W^{6+} compared to Nb^{5+} is compensated by the halfway substitution of the trivalent cation by monovalent potassium. Further, the larger charge leads to a straightened out chain of WO_6 octahedra forming double chains as detailed above. Consequently, differently sized voids are formed for the monovalent and trivalent cation to fill when stacking the WO_6 chains on top of each other. This leads to the KO_{12} polyhedra in the larger and the $(Bi/Y)O_8$ distorted square antiprisms in the smaller voids. The latter are connected to chains - in contrast to the YO_8 network in the m-*fergusonite* structure. Relevant structural features are compared in Figure B.2.18.

Crystallographic Relationships

All four structure types can be considered to be related to the parent *scheelite* structure type. The closest to the parent type come the compounds crystallising in this exact structure type with A^+ and M^{3+} cations disordered over the Ca^{2+} site. The $CuLa(WO_4)_2$ structure type adapted by $LiLa(WO_4)_2$-I and $LiPr(WO_4)_2$-I can be described as a highly distorted variant of the *scheelite* type.[274,275] The cationic substructure of the *scheelite*

[viii] The tetragonal *fergusonite* structure is isotypic to *scheelite* indicating the relationship of both structure types.

structure itself can be considered a two atom variant of the cationic substructure of *fluorite*. In the same way, the cationic substructure of the $CuLa(WO_4)_2$ structure type can be viewed as a distorted and ordered variant of this. The relationship is depicted in Figure B.2.19. The topology of the cation framework is similar, but the filling of the cation sites with different sized and charged cation types leads to structural deviations. These are especially pronounced in the anionic substructure and governed by electrostatic repulsion and ion size difference.

The relationship of the last two structure types, *wolframite* and m-*fergusonite*-related $KY(WO_4)_2$, can be understood by using results from high-pressure solid-state chemistry.[342,343] *Scheelite* oxides ABO_4, e.g. $CaWO_4$, show a pressure-induced and reversible phase transition to the *wolframite* structure, while *scheelite* fluorides ABF_4, e.g. $YLiF_4$, transform reversibly among pressure to the m-*fergusonite* structure. The differing transformation processes can be understood by the different covalency of the B to oxygen or fluorine bonds. In the oxides, this bond is more covalent. Thus, the BO_4 tetrahedra behave as rigid structural elements[ix] and the pressure is only affecting the AO_8 polyhedra. These are compressed resulting in increased cation repulsion. This repulsion is decreased when the structure relaxes into the *wolframite* type. Analogously, e.g. for $LiY(WO_4)_2$-I, the introduction of lithium and small rare earth cations lead to smaller cation distances destabilising the *scheelite* and favouring the *wolframite* structure type. On the other hand, the less covalent bond in the fluorides allows the B atoms to adapt to pressure by translative motion. Thus, these compounds relax into the m-*fergusonite* structure upon pressure. The situation in the $KY(WO_4)_2$ structure type can be viewed analogously. The large and hard potassium cations enlarge the unit cell and introduce more ionic interaction decreasing the covalency between tungsten and oxygen atoms. Further, the tendency of potassium to form large polyhedra - as evident from the KO_{12} building units in the final structure - introduces pressure-like sterical stress on the structure resulting in the relaxation in the m-*fergusonite*-related $KY(WO_4)_2$ structure type. This consideration is in line with DFT results from literature explaining the structural variety by the varying alkali metal oxygen distances.[304]

Consequently, the adapted structure types can be considered as a function of the average A^+ and M^{3+} cation size.[344][x] For values close to the size of Ca^{2+}, the *scheelite* structure type is adapted. This is the case for all sodium compounds. For the lithium compounds, temperature dependence is observed due to the larger size difference between Li^+ and M^{3+} leading to average cation sizes smaller than the one of Ca^{2+} and therefore, to the existence of $LiM(WO_4)_2$-I with ordered lithium and trivalent metal sites at low temperatures and the adaptation of the *scheelite* structure at high temperatures.[xi] Due to the different size of the trivalent cations and the respective space requirements, the compounds with large

[ix] Similar behaviour was already shown for the trend of interatomic distances in $Na_5M(WO_4)_4$ with the lanthanide contraction on page 81. The tungsten to oxygen distances are hardly affected.

[x] The term "size" refers to the ionic radii in this discussion.

[xi] Similar to the consideration on the thermal decomposition of $Na_5M(WO_4)_4$ (page 85), external energy in the form of temperature is necessary to introduce the Li^+/M^{3+} disorder.

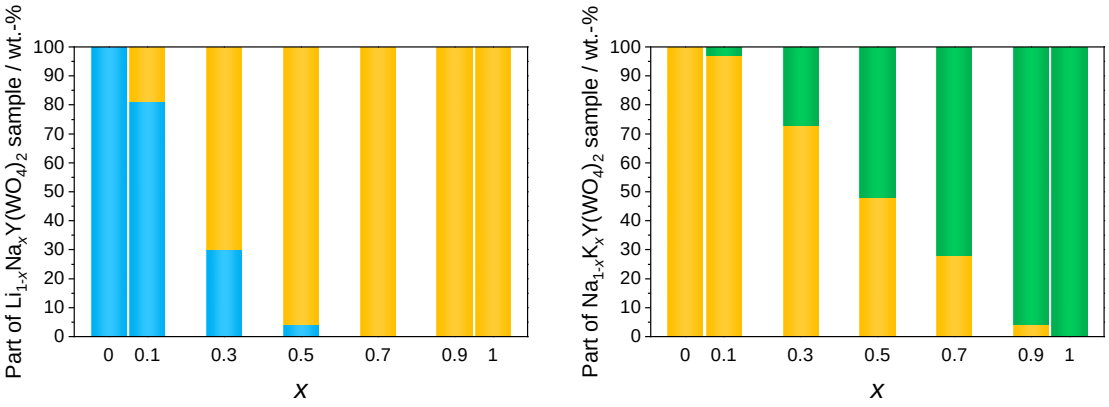

Fig. 5.2.3: Phase-composition of the solid solutions $Li_{1-x}Na_xY(WO_4)_2$ (left) and $Na_{1-x}K_xY(WO_4)_2$ (right) according to Rietveld analyses: The colour code is the same as in Figures 5.2.1 and 5.2.2, i.e. blue for the *wolframite*, yellow for the *scheelite* and green for the $KY(WO_4)_2$ structure type.

rare earth cations adapt the $CuLa(WO_4)_2$ structure, while the ones with smaller rare earth cations are stabilised in the *wolframite* structure. For the potassium representatives, the large size of K^+ dominates the adapted structure, pointing out that the stabilisation in the *scheelite* types is only possible below a certain threshold in the difference of the ionic radii of A^+ and M^{3+},[xii] beyond which the location of both cations on the same crystallographic site can no longer be realised due to electrostatic reasons.

Miscibility Studies

As discussed above, the average ionic radii of the A^+ and M^{3+} cations are decisive for the structure type adapted by the $AM(WO_4)_2$ double tungstates. This value can be changed gradually by the partial substitution of one alkali metal by another. Therefore, solid solution series $Li_{1-x}Na_xY(WO_4)_2$ and $Na_{1-x}K_xY(WO_4)_2$ were prepared and their composition was investigated by Rietveld analyses (Figure 5.2.3). More details on these refinements can be found in [279]. All samples were synthesised by solid-state reactions at 720°C, i.e. below the phase transition temperature from $LiY(WO_4)_2$-I to $LiY(WO_4)_2$-II. Thus, the first series comprises more precisely solid solutions of $LiY(WO_4)_2$-I and $NaY(WO_4)_2$.[xiii] Here, partial miscibility is observed. Considerable amounts of Li^+ cations can be incorporated into the *scheelite* type structure of $NaY(WO_4)_2$. Almost 50% lithium content is possible. This is not surprising due to existence of $LiY(WO_4)_2$-II isotypic to $NaY(WO_4)_2$. In turn, no sodium cations appear to be built into the *wolframite* type structure of $LiY(WO_4)_2$-I. On the contrary, no miscibility was observed for the second solid solution series of $NaY(WO_4)_2$ and $KY(WO_4)_2$. The phase composition follows the x value (Figure 5.2.3).

[xii] This value is around 40 pm.

[xiii] Complete miscibility can be expected for solid solutions of isotypic $LiY(WO_4)_2$-II and $NaY(WO_4)_2$. This was not investigated herein.

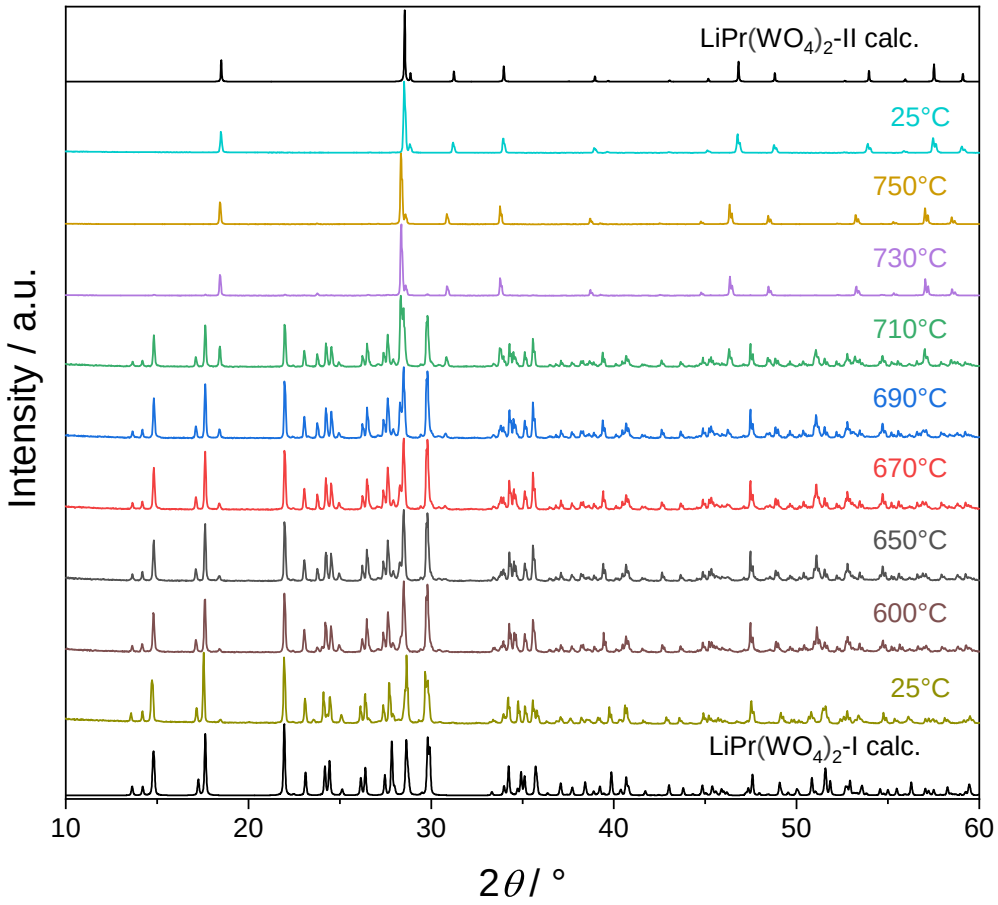

Fig. 5.2.4: TPXRD of $LiPr(WO_4)_2$-I showing the phase transition to $LiPr(WO_4)_2$-II: calculated patterns for both polymorphs are shown for comparison; the patterns follow the heating program chronically from bottom to top.

Thermal Properties

The phase transition from $LiPr(WO_4)_2$-I to $LiPr(WO_4)_2$-II was investigated by TPXRD depicted in Figure 5.2.4. The transition temperature can be located between 710 and 730°C. There a clear change of the pattern can be observed. These values agree with the result of 700 ± 15° by Klevtsova et al. from a DTA measurement.[275] However, $LiPr(WO_4)_2$-II appears to be present as side phase at temperatures as low as 650°C. Further, the phase transition from $LiY(WO_4)_2$-I to $LiY(WO_4)_2$-II was analysed by DSC. The data is shown in Figure B.2.20. There are two endothermic events at 910°C and 1049°C. The former represents the phase transition temperature in agreement with earlier reports locating it at 904°C.[345] The latter is the melting point of the compound - in good agreement with the literature value (1050°C).[344]

Optical Properties

The optical properties of the double tungstates were studied with special interest on their application as phosphors, i.e. predominantly by fluorescence spectroscopy.

Ligand to Metal Charge Transfer Luminescence

As already discussed in the previous section, tungstates feature the antenna effect based on the excitation via the O^{2-}-W^{6+} LMCT. In the absence of a suited activator, broad emission due to the W^{6+}-O^{2-} LMCT can frequently be observed (Figure B.1.20).[xiv] These emissions and respective excitations were recorded for $LiY(WO_4)_2$-I, $LiY(WO_4)_2$-II and $NaY(WO_4)_2$ by fluorescence spectroscopy shown in Figure 5.2.5. The intensities are high enough to be observed already at room temperature. The results for $LiY(WO_4)_2$-I and $NaY(WO_4)_2$ measured at 77 K show an increase in energy for the excitation bands and a decrease for the emission band compared to the measurements at room temperature. The former can be explained by the temperature driven occupation of vibrational substates.[xv] The latter is due to the weaker Jahn-Teller distortion at lower temperatures. This effect stabilises the ground state with respect to the excited state.[321,346] Its weakening reduces the energy gap between excited and ground state. Further, the excitation band is located at lower energies in $LiY(WO_4)_2$-I compared to $LiY(WO_4)_2$-II due to the larger number of oxygen ligands around tungsten atoms.[321]
No LMCT excitation and emission could be observed for $KY(WO_4)_2$. Presumably, non-radiative pathways are favoured due to the proximity of other WO_6 octahedra in the double chains. The behaviour of the $CuLa(WO_4)_2$ structure type double tungstates is discussed on the example of $LiPr(WO_4)_2$-I below.

Bi^{3+} Luminescence

Unambiguous luminescence due to s-p transitions of trivalent bismuth cations could only be observed for $KBi(WO_4)_2$ (Figure 5.2.6). Only the measurement at 77 K is discussed here since the emission is too weak at room temperature. In contrast to isotypic $KY(WO_4)_2$, a broad emission around 480 nm occurs. It can be excited at 300 and 350 nm. The former excitation band is only present as a shoulder on the second one. The shape of the excitation spectrum resembles the one already seen for $Na_5Bi(WO_4)_4$ (Figure 5.1.17). Consequently, and in line with the discussion above on page 95 emission occurs via the $^3P_1 \rightarrow {}^1S_0$ transition and excitation via the $^1S_0 \rightarrow {}^1P_1$ and $^1S_0 \rightarrow {}^3P_1$ transitions of Bi^{3+}. The s-p transitions are also present in the reflectance spectrum in Figure 5.2.6 in the form of broad absorptions overlapping the one from the LMCT located in the UV and reaching into the visible region - in line with the pale yellow powder.

[xiv] In more detail, the excitation from the $2p^6$ (O^{2-}) $5d^0$ (W^{6+}) ground state to the $2p^5$ (O^-) $5d^1$ (W^{5+}) excited state occurs via parity and spin-allowed $^1A_1 \rightarrow {}^1T_1$ transitions while the emission happens via the parity allowed, but spin-forbidden $^3T_1 \rightarrow {}^1A_1$ and $^3T_2 \rightarrow {}^1A_1$ transitions.[346]

[xv] This was already discussed for $Na_5Bi(WO_4)_4$ (page 95).

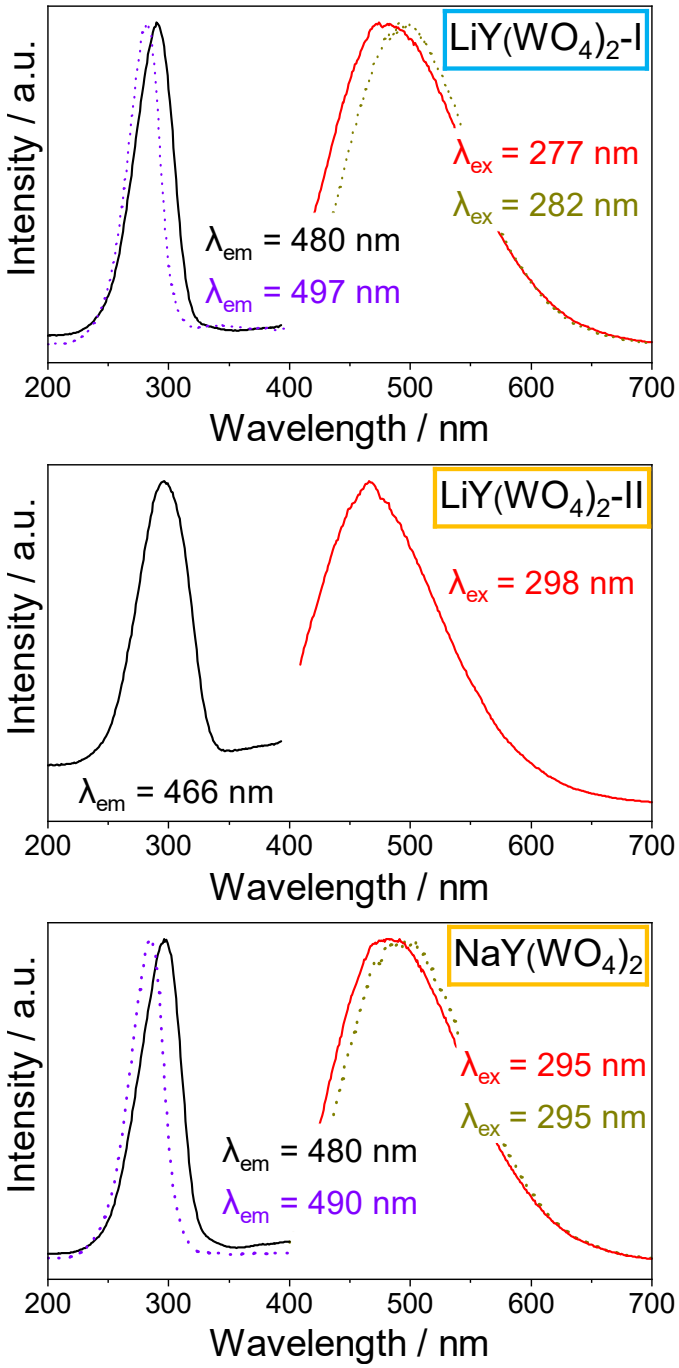

Fig. 5.2.5: Excitation and emission spectra of $LiY(WO_4)_2$-I, $LiY(WO_4)_2$-II and $NaY(WO_4)_2$ at both room temperature and 77K: The colour code for the box around the sum formulae is the same as in Figures 5.2.1 and 5.2.2, i.e. blue for the *wolframite* and yellow for the *scheelite* structure type; measurements at room temperature are shown as solid, the ones at 77K as dotted lines.

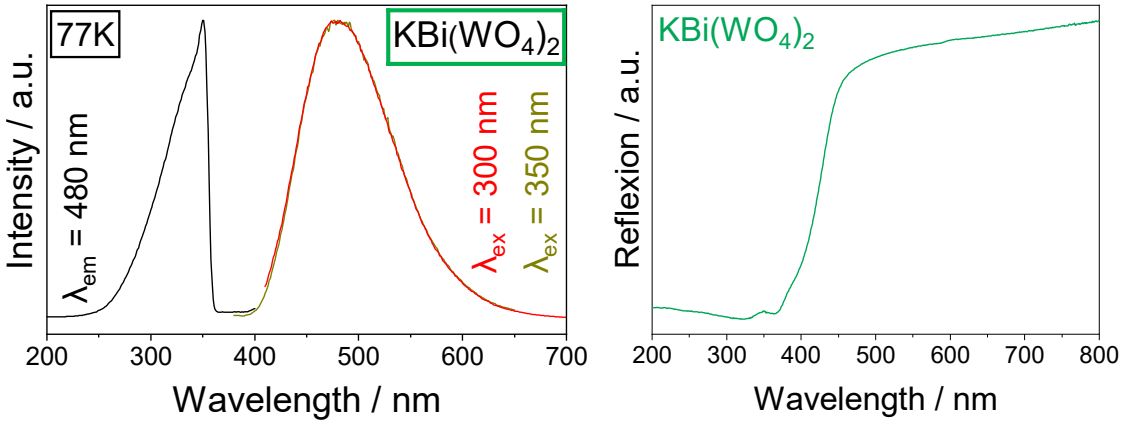

Fig. 5.2.6: Excitation, emission and powder reflectance spectra of $KBi(WO_4)_2$: The colour code for the box around the sum formulae is the same as in Figures 5.2.1 and 5.2.2, i.e. green for the $KY(WO_4)_2$ structure type; the results from fluorescence spectroscopy are shown on the left and the ones from UV-Vis spectroscopy on the right.

Pr^{3+} Luminescence

Both $LiPr(WO_4)_2$-I and $LiPr(WO_4)_2$-II show deep red emission due to f-f transitions according to the spectra in Figure 5.2.7. The assignment of excitation and emission bands is analogous to $Na_5Pr(WO_4)_4$ discussed above (Figure 5.1.9 and table B.1.12). No significant emission from the $^1D_2$ state is observed. This is in line with the discussion above and results on other tungstates.[309–312] Consequently, the Pr-O and Pr-W distances are still large enough to prevent relaxation. The results for $LiPr(WO_4)_2$-II agree with reports for isotypic $NaGd(WO_4)_2$:Pr^{3+}.[309] The emission around 620 nm due to the $^3P_0 \rightarrow {}^3H_6$ is more intense in $LiPr(WO_4)_2$-II due to the higher site symmetry of Pr^{3+}.[xvi] Besides using the three f-f transitions between 440 and 490 nm, excitation is also possible via the broad band in the UV region.[xvii] The maximum for this band is located at 310 nm and 285 nm for $LiPr(WO_4)_2$-I and $LiPr(WO_4)_2$-II, respectively. The relative intensity with respect to the f-f transitions is larger in the former. This can be explained by efficient Pr^{3+}-W^{6+} IVCT in the former. This band is overlapping the O^{2-}-W^{6+} LMCT. The location of the IVCT band can be estimated to be around 330 nm using the empirical equation developed by Boutinaud et al.[310,312] and the praseodymium to tungsten distances from the Rietveld refinement - in good agreement with the excitation spectrum. For $LiPr(WO_4)_2$-II, the excitation band in the UV comprises only the LMCT since the IVCT are located at higher energies. The reason for that can be found in the smaller coordination number of tungsten and the larger Pr-W distances compared to $LiPr(WO_4)_2$-I.

[xvi] The site symmtery is 1 in $LiPr(WO_4)_2$-I and $\bar{4}$ in $LiPr(WO_4)_2$-II. It is also $\bar{4}$ in $Na_5Pr(WO_4)_4$ (Figure 5.1.9).

[xvii] The data is qualitatively equal to the emissions when exciting at 467 nm. However, these are not shown due to the much worse signal-to-noise ratio for these emissions being very weak.

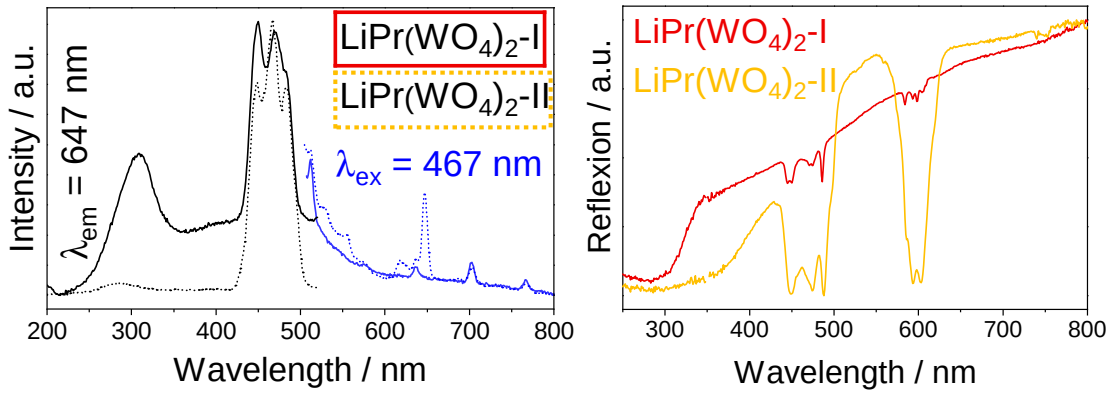

Fig. 5.2.7: Excitation and emission spectra of $LiPr(WO_4)_2$-I (solid) and $LiPr(WO_4)_2$-II (dotted) on the left and the diffusive reflectance spectra of both sample on the right: The colour code for the box around the sum formulae on the left and for the formulae themselves is the same as in Figures 5.2.1 and 5.2.2, i.e. red for the $CuLa(WO_4)_2$ and yellow for the *scheelite* structure type; due to the small signal-to-noise ratio related to the weak intensity of the emission the non-corrected excitation spectra are shown; consequently, the intensity of the charge transfer excitation can be expected to be underestimated.

The diffusive reflectance spectra (Figure 5.2.7) are in line with the brown and green powders of $LiPr(WO_4)_2$-I and $LiPr(WO_4)_2$-II, respectively. The latter shows pronounced f-f transitions resulting in the green colour. These are assigned in Table B.2.4. They are also present in $LiPr(WO_4)_2$-I. However, they are much weaker. The colour is dominated by absorption over almost the whole visible range. This can be explained by the existence of Pr^{4+} cations within this sample and the resulting Pr^{4+}-Pr^{3+} CT transitions causing this absorption. This is plausible in the light of result on isotypic $CuTb(WO_4)_2$ indicating the partial presence of W^{5+} instead of W^{6+} in this structure.[347] Such behaviour is not possible in the high-temperature polymorph $LiPr(WO_4)_2$-II adapting the significantly more symmetric *scheelite* structure type.

Tb^{3+} Luminescence

The luminescent properties of the solid solutions $LiY_{1-x}Tb_x(WO_4)_2$-I, $LiY_{1-x}Tb_x(WO_4)_2$-II, $NaY_{1-x}Tb_x(WO_4)_2$ and $KY_{1-x}Tb_x(WO_4)_2$ were investigated by fluorescence spectroscopy. The results are shown extensively in [121, 279, 280]. An exemplary selection of $NaY_{1-x}Tb_x(WO_4)_2$ is depicted in Figure 5.2.8.All solid solution exhibit typical fluorescence due to f-f transition of Tb^{3+} cations.[145,348] The energy levels of the f states of Tb^{3+} are sketched in Figure 5.1.14. The characteristic green luminescence of Tb^{3+} is caused by the emission from $^5D_4$ to ^7F_J states with $J = 6, 5, 4, 3$. Additional transitions towards $J = 2, 1, 0$ occurring as orange-red emissions are very weak compared to the green ones. Moreover, additional blue emissions from the energetically higher lying excited state $^5D_3$ are possible as well. The intensity of these blue emissions depends on the phenomenon of cross-relaxation. It describes the energy transfer from

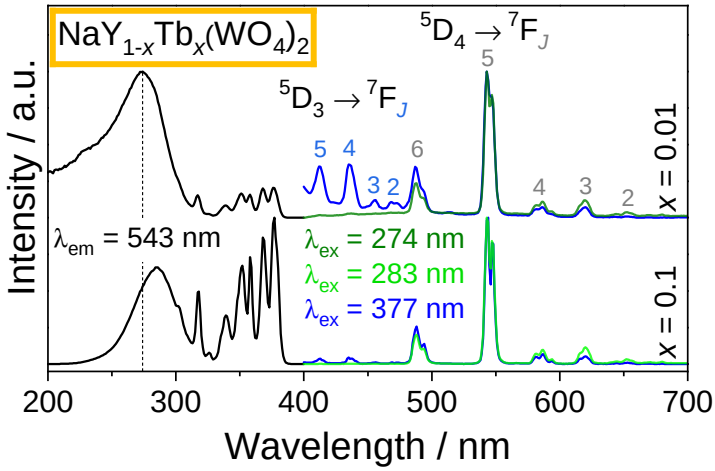

Fig. 5.2.8: Excitation and emission spectra of $NaY_{0.99}Y_{0.01}(WO_4)_2$ (top) and $NaY_{0.9}Y_{0.1}(WO_4)_2$ (bottom): The colour code for the box around the sum formula is the same as in Figures 5.2.1 and 5.2.2, i.e. yellow for the *scheelite* structure type; the respective emissions are labelled; the excitation spectra were corrected with respect to the lamp intensity.

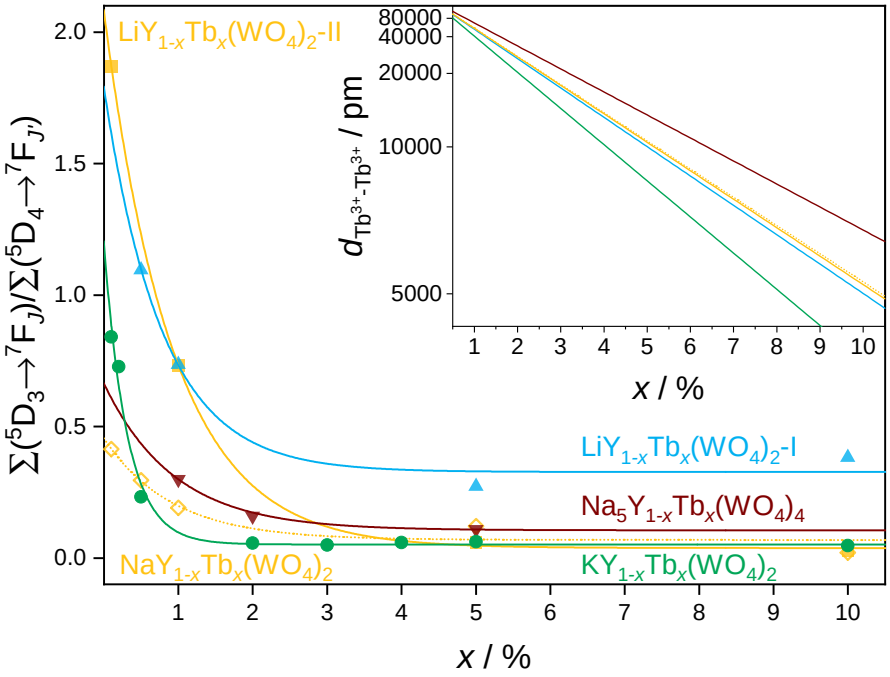

Fig. 5.2.9: Intensity ratio of emissions ${}^5D_3 \rightarrow {}^7F_J$ and ${}^5D_4 \rightarrow {}^7F_J$ in $LiY_{1-x}Tb_x(WO_4)_2$-I, $LiY_{1-x}Tb_x(WO_4)_2$-II, $NaY_{1-x}Tb_x(WO_4)_2$, $KY_{1-x}Tb_x(WO_4)_2$ and $Na_5Y_{1-x}Tb_x(WO_4)_4$ with respect to the terbium content x; the colour code is the same as in Figures 5.2.1 and 5.2.2; the dotted yellow line and open diamonds are $NaY_{1-x}Tb_x(WO_4)_2$, the solid yellow line and closed squares are $LiY_{1-x}Tb_x(WO_4)_2$-II, blue triangles $LiY_{1-x}Tb_x(WO_4)_2$-I, green circles $KY_{1-x}Tb_x(WO_4)_2$, brown triangles pointing downwards $Na_5Y_{1-x}Tb_x(WO_4)_4$; the lines represent exponential fits of the experimental data discussed in the main text; the inset on the right top shows the decrease of $d_{Tb^{3+}\text{-}Tb^{3+}}$ with the terbium content x estimated by $d_{Tb^{3+}\text{-}Tb^{3+}} = \frac{d_{Y^{3+}\text{-}Y^{3+}}}{x}$; the ordinate is scaled reciprocally in order to discriminate the curves.

one excited Tb^{3+} cation to another in the ground state:

$$^5D_3(Tb^{3+}) + {}^7F_6(Tb^{3+}) \rightarrow {}^5D_4(Tb^{3+}) + {}^7F_0(Tb^{3+})$$

This process is mainly governed by the distance between adjacent Tb^{3+} cations, which in turn depends on the terbium concentration, i.e. the x value, in the present solid solutions. Consequently, inefficient cross-relaxation at low terbium concentrations inducing large average terbium to terbium distances results in high intensities for the blue emissions from the $^5D_3$ state relatively to the green emission from the $^5D_4$ state. However, the process of cross-relaxation also depends on the host material and the efficiency of the energy transfer between the two terbium cations involved.[xviii] In line with the discussion above (page 92, Figures 5.1.14 and 5.2.5), the blue emission originating from the $^5D_3$ state is absent when exciting the samples at the LMCT. The energy transmitted by the LMCT emission is not sufficient to reach the $^5D_3$ state states. In the following, the efficiency of the cross-relaxation process in the present solid solutions is investigated via the dependence of the integrated intensity ratios of the emissions $^5D_3 \rightarrow {}^7F_J$ and $^5D_4 \rightarrow {}^7F_J$ with respect to the value for x.[xix] $Na_5Y_{1-x}Tb_x(WO_4)_4$ showing similar behaviour (Figure 5.1.15) was included into the consideration. The excitation spectra can be divided into two regions (Figure 5.2.8): Between 300 and 400 nm f-f transitions occur.[xx] Below 300 nm, a broad excitation band formed by the overlap of O^{2-}-W^{6+} LMCT, Tb^{3+} d-f transitions and Tb^{3+}-W^{6+} IVCT.[349] The relative intensity of the latter two with respect to the LMCT increases with the terbium content. This leads to a shift of this broad excitation band with x discussed in detail in [121]. The IVCT appears to be most efficient in $LiY_{1-x}Tb_x(WO_4)_2$-I - similar to the discussion above for $LiPr(WO_4)_2$-I and $LiPr(WO_4)_2$-II with the former comprising tungstate octahedra and exhibiting significant IVCT. Now, the focus is shifted to the emission spectra. The average terbium to terbium distance $d_{Tb^{3+}\text{-}Tb^{3+}}$ was estimated - assuming statistical distribution of terbium atoms on yttrium sites - to be

$$d_{Tb^{3+}\text{-}Tb^{3+}} = \frac{d_{Y^{3+}\text{-}Y^{3+}}}{x}$$

with $d_{Y^{3+}\text{-}Y^{3+}}$ being the distance of adjacent yttrium compounds in the respective compounds for $x = 0$.[xxi] Consequently, $d_{Tb^{3+}\text{-}Tb^{3+}}$ decreases with x (inset of figure 5.2.9).

[xviii] The intensity of emissions from the $^5D_3$ states is for example weaker in borates compared to phosphates or silicates.[145] For host materials with rather weak coordination strengths such as borosulfates or fluorides, cross-relaxation appears to be less efficient enabling the observation of blue emissions up to Tb^{3+} concentrations of several percent, while the maximum for these typically lies around 1% in oxides.[95,145]

[xix] This ratio was determined using the program OriginPro (OriginLab Corporation) by the division of the respective integrated areas below the emission spectra after baseline fitting. Note that this intensity ratio does not scale with the general intensity of luminescence.

[xx] They were already assigned in Figure 5.1.13 and table B.1.12.

[xxi] This data was taken from the single-crystal structure determinations. Naturally, the approximate equation is only valid for small values of x since for larger values the respective distances should be

Analogously, the intensity ratio of the emissions $^5D_3 \rightarrow {}^7F_J$ and $^5D_4 \rightarrow {}^7F_J$ decreases with x. The respective data, shown in Figure 5.2.9, could be fitted using an exponential fit:

$$f(x) = y_0 + A\exp(R_0 x).$$

Tab. 5.2.2: Fitting results for the solid solutions $LiY_{1-x}Tb_x(WO_4)_2$-I, $LiY_{1-x}Tb_x(WO_4)_2$-II, $NaY_{1-x}Tb_x(WO_4)_2$, $KY_{1-x}Tb_x(WO_4)_2$ and $Na_5Y_{1-x}Tb_x(WO_4)_4$ and the values corrected for the yttrium to yttrium distance in the $x = 0$ compounds ($R_S = \frac{R_0}{d_{Y^{3+}\text{-}Y^{3+}}}$); the standard deviations are given in parentheses; they are zero for $Na_5Y_{1-x}Tb_x(WO_4)_4$ since only three data point were included for this solid solution resulting in a "perfect" exponential fit.

Solid solution	R_0	$d_{Y^{3+}\text{-}Y^{3+}}$ / pm	R_S
$LiY_{1-x}Tb_x(WO_4)_2$-I	1.28(46)	500.4(1)	0.26(9)
$LiY_{1-x}Tb_x(WO_4)_2$-II	1.08(3)	515.87(1)	0.21(1)
$NaY_{1-x}Tb_x(WO_4)_2$	1.1(3)	520.90(2)	0.21(6)
$KY_{1-x}Tb_x(WO_4)_2$	3.22(5)	406.11(2)	0.79(1)
$Na_5Y_{1-x}Tb_x(WO_4)_4$	1.06	638.23(1)	0.17

The value R_0 tabulated in Table 5.2.2 describes the decrease in the intensity ratio. Large R_0 values indicate efficient cross-relaxation. However, this value is still highly dependent on the interatomic distance between two neighbouring terbium atoms, which take part in the cross-relaxation process. It was corrected via division by $d_{Y^{3+}\text{-}Y^{3+}}$ yielding the standardised value R_S. Since the coordination behaviour of all tungstate host materials can be expected to be similar, R_S depends only on the structure type. The results show the most efficient cross-relaxation in $KY_{1-x}Tb_x(WO_4)_2$. Further, it appears to become less efficient in the order $LiY_{1-x}Tb_x(WO_4)_2$-I, $LiY_{1-x}Tb_x(WO_4)_2$-II, $NaY_{1-x}Tb_x(WO_4)_2$, $Na_5Y_{1-x}Tb_x(WO_4)_4$. This trend can be explained by the crystal structures and possible energy transfer pathways within them, i.e. the chemical situation between two neighbouring terbium cations interacting with each other during the cross-relaxation process. Relevant details are illustrated in Figures 5.1.5 and 5.2.10. The energy transfer is most likely to occur via the Förster mechanism.[xxii]

The five solid solutions differ in the pathways to get from one terbium cation to another. In $KY_{1-x}Tb_x(WO_4)_2$, energy transfer between adjacent terbium atoms located on the yttrium sites is easily possible due to edge-sharing distorted square antiprisms. The tungstate anion has not to be involved in this process. This explains the significantly more efficient cross-relaxation in this structure type. In $LiY_{1-x}Tb_x(WO_4)_2$-I, energy transfer via the WO_6 chains might occur. This is more efficient than via non-condensed WO_4 tetrahedra in the remaining two structures - presumably due to electrostatic reasons.

taken from the 100% terbium compounds. Further, it is only valid for $x \neq 0$. For $x = 0$, there are no terbium cations and therefore, no $d_{Tb^{3+}\text{-}Tb^{3+}}$.

[xxii] Förster mechanism depends on electric dipole transitions and the interatomic distance r with the energy transfer efficiency E defined as $E = \frac{R_F^6}{R_F^6 + r^6}$ with R_F being the Förster distance.[350]

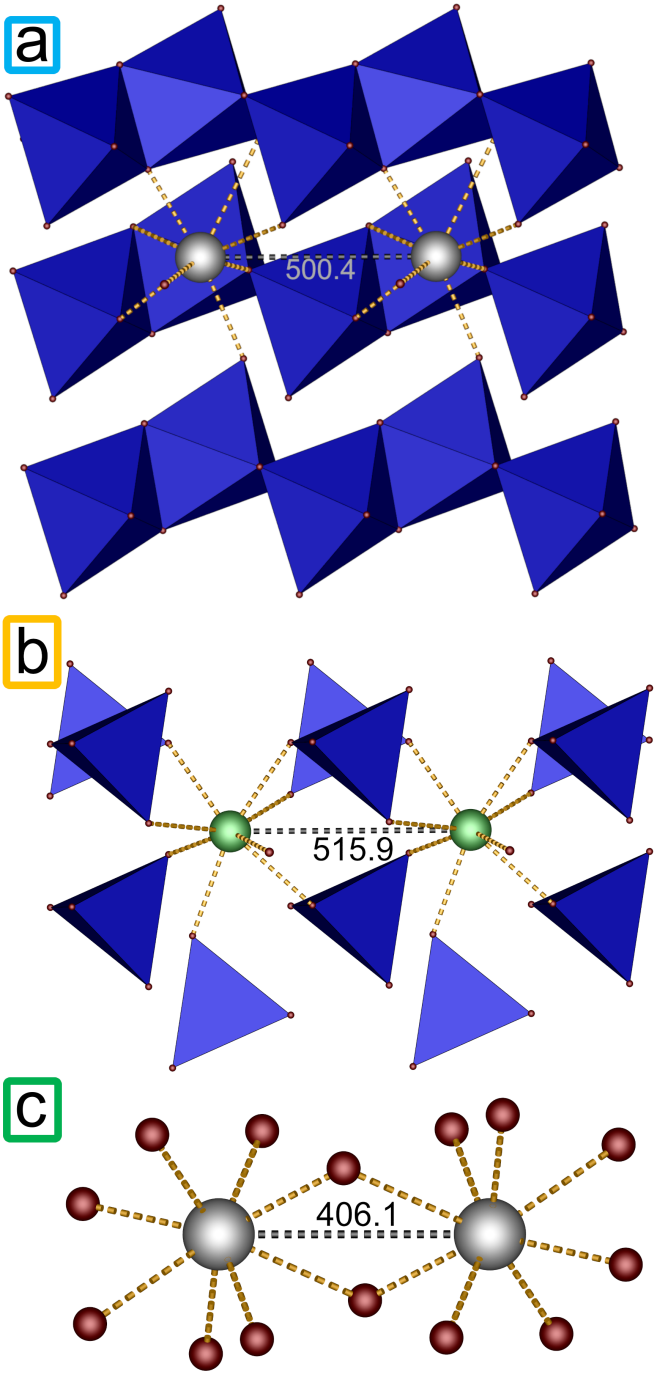

Fig. 5.2.10: Coordination environment of yttrium atoms in (a) $LiY(WO_4)_2$-I, (b) $LiY(WO_4)_2$-II and (c) $KY(WO_4)_2$; the colour code for the box is the same as in Figures 5.2.1 and 5.2.2; for all three structure types, the two yttrium sites with the shortest distance (labelled in pm) is shown; yttrium atoms grey, yttrium atoms disordered with lithium light green, oxygen atoms red, tungsten polyhedra blue; a similar depiction for $Na_5Eu(WO_4)_4$ is shown in Figure 5.1.5; the situation is equal to (b) for isotypic $NaY(WO_4)_2$; for both $LiY(WO_4)_2$-II and $NaY(WO_4)_2$ not the first, but the second next neighbours were considered assuming an alternating occupation of A^+ and Y^{3+} cations; this is plausible due to electrostatic reasons.

Moreover, the very efficient Tb^{3+}-W^{6+} IVCT might also contribute to the efficient cross-relaxation in $LiY_{1-x}Tb_x(WO_4)_2$-I. Interestingly, the R_S values of the isotypic $LiY_{1-x}Tb_x(WO_4)_2$-II and $NaY_{1-x}Tb_x(WO_4)_2$ are very similar. This indicates that these values are indeed dominantly depending on the structure type. Cross-relaxation is even less efficient in $Na_5Y_{1-x}Tb_x(WO_4)_4$ compared to the *scheelite* structure type. In both cases, the energy transfer includes tungstate tetrahedra separating neighbouring terbium cations. The difference can be found in the number of involved WO_4 moieties. While there are three of them offering possible energy transfer pathways in the *scheelite* type, there are only two in the $Na_5Y_{1-x}Tb_x(WO_4)_4$.

Energy Transfer Mechanism in $AM(WO_4)_2$

To conclude, there are two options to excite the $AM(WO_4)_2$ phosphors: Firstly, excitation is possible via the LMCT of the tungstate moiety acting as a sensitiser. Similar to $Na_5M(WO_4)_4$ discussed above, the energy transfer is governed by the luminescence emission of the W^{6+}-O^{2-} LMCT. Secondly, the activator ions M^{3+} can be excited directly via f-f transitions. The emission from the f states is influenced by the distance of the activators and the chemical situation surrounding them. This was demonstrated for Pr^{3+} and Tb^{3+} emission. For the compounds containing trivalent terbium, the diverging efficiency of Tb^{3+}-Tb^{3+} cross-relaxation can be explained by the different structure types - independent from the distances - in the sense of structure-property relations. Further, there is only weak concentration quenching in $AM(WO_4)_2$. However, it is - in line with the shorter M^{3+}-M^{3+} distances - not absent in contrast to $Na_5M(WO_4)_4$.

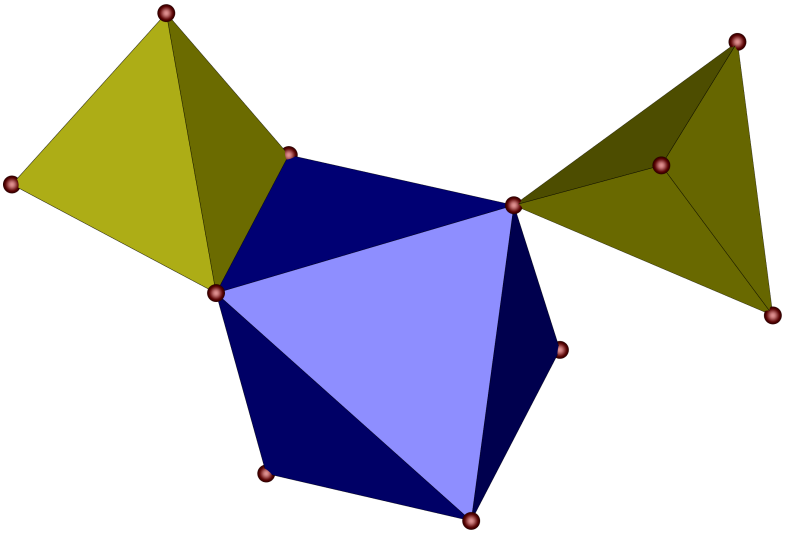

SULFATOTUNGSTATES

6 The First Caesium Sulfatotungstate $Cs_6[(WO_2)_2O(SO_4)_4]$

As demonstrated in the previous chapter, tungstates are good phosphor host materials due to the antenna effect. Moreover, sulfates exhibit interesting optical properties due to the weak coordination behaviour of the non π-conjugated tetrahedral $SO_4{}^{2-}$ groups lacking inversion symmetry. This is discussed in detail in the next chapter. Consequently, sulfatotungstates - combining the material classes tungstates and sulfates - appear to be a promising material class for optical application. Prior to this work, solely four compounds belonging to this material class were reported as already discussed in section 1.4. The optical properties were not investigated for any of these. Herein, $Cs_6[(WO_2)_2O(SO_4)_4]$ is added to this young and small material class and characterised fully with respect to its optical properties by IR and UV-Vis spectroscopy.
The results presented in this chapter originate from the master thesis of Katja Kreß.[279]

Synthesis

$Cs_6[(WO_2)_2O(SO_4)_4]$ was prepared by crystallisation from the melt. Firstly, 2.263 mmol $CsOH \cdot H_2O$ (Acros organics, >99.5%), 0.12 ml (≈ 2.263 mmol) oleum (VWR, 65% SO_3) and 1 ml H_2O were mixed in a nitrogen flushed Schlenk flask and heated at 200°C for 30 min. The temperature was increased to 300°C until a dry and colourless precipitate was obtained. PXRD showed this to be a mixture of predominantly $CsHSO_4$ and the side phase $Cs_2S_2O_7$ (Figure C.0.1). 0.1393 g of the as-prepared mixture was ground together with 0.204 mmol Cs_2SO_4 (Chempur, >99.5%) and 0.203 mmol WO_3 (Alfa Aesar, >99.8%) and filled into a silica glass ampoule (outer diameter: 1.2 cm, wall thickness: 0.1 cm) which was evacuated and sealed. Subsequently, the following temperature program was applied: Heating to 500°C with 200 Kh^{-1}, holding the temperature for 10 h, cooling with 5 Kh^{-1} to 300°C and cooling with 200 Kh^{-1} to room temperature. The synthesis yielded a colourless powder containing single-crystals. Phase purity was confirmed by Rietveld refinement (Figure C.0.2 and table C.0.1). However, it also indicates the existence of a significant amorphous fraction in the sample.

Crystal Structure

$Cs_6[(WO_2)_2O(SO_4)_4]$ crystallises in a new structure type in the monoclinic crystal system with space group $P2_1/c$ (no. 14) and two formula units per unit cell (Tables C.0.2 to C.0.4).

The unit cell is shown in Figure 6.0.1. There are three independent sites for the caesium cations. Cs1 and Cs2 are coordinated by ten and Cs3 is coordinated by nine oxygen atoms.[i] The resulting polyhedra shown in Figure C.0.3 are connected via two or three corners, respectively. Consequently, a Cs-O network is formed. The Cs–O distances ranging between 302 and 361 pm are in agreement with the sum of ionic radii (313 and 316 pm).[216] As commonly observed for alkali metals due to their variety of possible coordinations, Pauling's fifth rule is violated.[351]

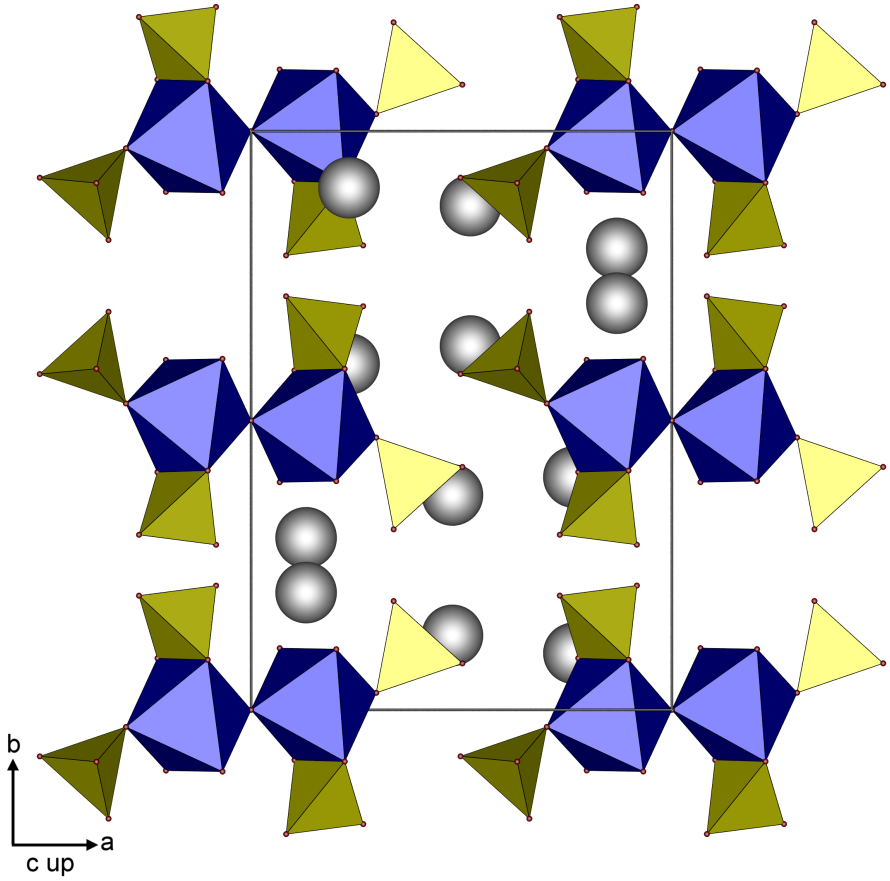

Fig. 6.0.1: Unit cell of $Cs_6[(WO_2)_2O(SO_4)_4]$ viewed along [001]; tungsten octahedra blue, sulfate tetrahedra yellow, caesium atoms grey.

The anionic substructure comprises non-condensed complex $[(WO_2)_2O(SO_4)_4]^{6-}$ anions, depicted in Figure 6.0.2, filling the gaps in the Cs-O network. The anions are formed by two tungstate octahedra sharing one common edge with each other coordinated by two monodentate and two bidentate sulfate tetrahedra each. Up to date - and to the best of my knowledge -, the only edge sharing of sulfate and tungstate polyhedra in solid state is reported for $WO(SO_4)_2$[42] with pentagonal bipyramidal coordination of

[i] Notably, the coordination of Cs3 can also be described as 9+2 in the light of the MAPLE calculations discussed in the following.

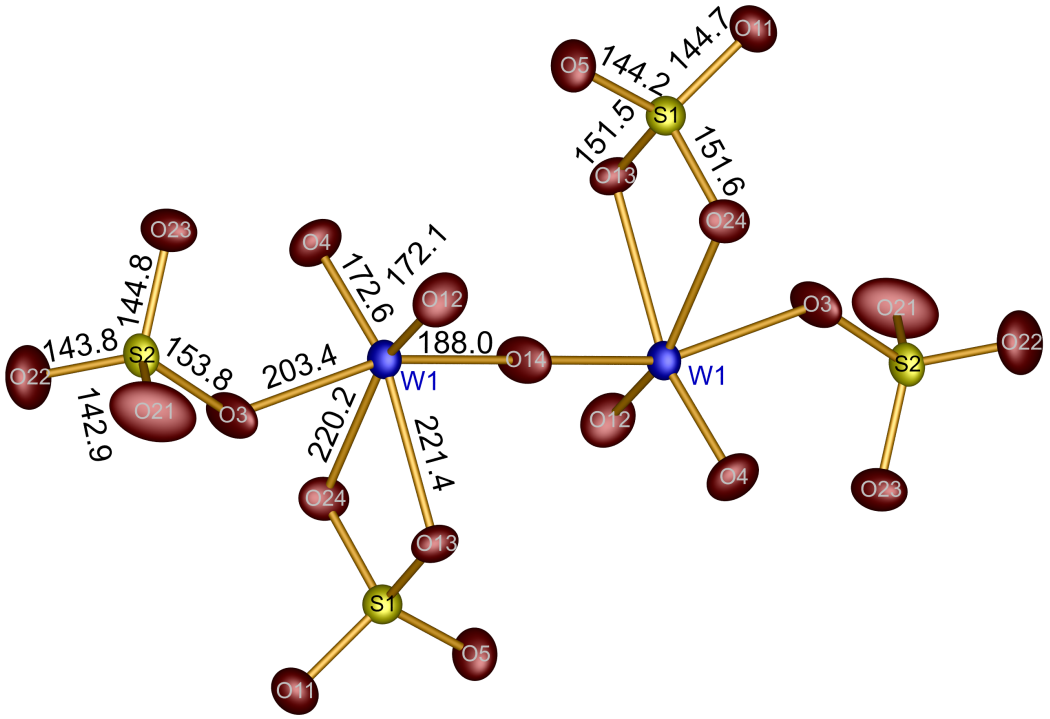

Fig. 6.0.2: The $[(WO_2)_2O(SO_4)_4]^{6-}$ anion in $Cs_6[(WO_2)_2O(SO_4)_4]$: tungsten atoms blue, sulfur atoms yellow, oxygen atoms red; ellipsoids are shown at 60 % probability;

the tungsten atom compared to the octahedra in $Cs_6[(WO_2)_2O(SO_4)_4]$. Further, the existence of anions comprising edge-sharing WO_6 and SO_4 building units in the melt is proposed based on Raman spectra of WO_3-$K_2S_2O_7$-K_2SO_4 melts.[352] Within the anion, two tungsten atoms are connected via a bridging oxygen atom with an unusual W–O–W angle of 180°. Additional low temperature single-crystal XRD measurements confirmed this angle (Table C.0.2).[ii] This is in contrast to $R_2[W_2O_3(SO_4)_6]$ (R = Sm, Eu, Gd, Ho). There, adjacent WO_6 octahedra also share one corner, but the W-O-W angle amounts to 147°.[49] The W-O distances range from 172 to 221 pm (sum of ionic radii: 195 pm[216]), while the S-O distances vary from 143 to 154 pm (sum of ionic radii: 147 pm[216]). As expected, the distance to bridging oxygen atoms is significantly longer compared to the distance to terminally bound oxygen atoms (Figure 6.0.2). For both O-W-O and O-S-O angles ranging from 63.3° to 105.1° and from 99.8° to 112.8°, respectively, the smallest angles can be found where tungstate octahedra and sulfate tetrahedra share common edges. All sulfate tetrahedra can be classified as regular with deviations of 0.08% and 0.39%. The WO_6 octahedron deviates slightly from the octahedral symmetry with Δ_{octa} = 1.3% with a large centroid deviation of 33 pm (ϵ = 0.17), due to the electrostatic repulsion between adjacent S^{6+} and W^{6+}, and W^{6+} and W^{6+} cations. The tungsten

[ii] No indications justifying structure solution in a less symmetric space group were found at 150 K.

atoms are stronger influenced by this repulsion than the sulfur atoms with $R_c = 5.9\,\text{pm}$ and 7.7 pm, and $\epsilon = 0.04$ and 0.05, respectively. The reason for this can be found in the larger coordination number of the former, constituting a larger degree of freedom to react to the electrostatic repulsion for the tungstate anion compared to the sulfate anion. All coordination numbers and the electrostatic plausibility of the crystal structure were confirmed by MAPLE calculations (Table C.0.5).

Optical Properties

Infrared Spectroscopy

The infrared spectrum of $Cs_6[(WO_2)_2O(SO_4)_4]$ shown in Figure 6.0.1 (full spectrum in Figure C.0.4) confirms the crystal structure determined by SC-XRD. The bands in the range of $1200 - 1100\,\text{cm}^{-1}$ and the absorption at $1042\,\text{cm}^{-1}$ can be assigned to the symmetric stretching mode of S-O in sulfate tetrahedra, while the bands between $620\,\text{cm}^{-1}$ and $580\,\text{cm}^{-1}$ are the corresponding bending modes.[353] The bands between $930\,\text{cm}^{-1}$ and $640\,\text{cm}^{-1}$ correspond to the symmetric and asymmetric stretching modes of W-O in the tungstate octahedra. The related bending modes are located below $520\,\text{cm}^{-1}$. The characteristic absorption for the W-O-W stretching can be found at $772\,\text{cm}^{-1}$ and $473\,\text{cm}^{-1}$.[354,355]

UV-Vis Spectroscopy

The powder reflectance spectrum of $Cs_6[(WO_2)_2O(SO_4)_4]$ is shown in Figure 6.0.1. It is governed by the O^{2-}-W^{6+} LMCT centred around 280 nm and thus, in the same region as for other tungstates comprising an octahedral coordination of tungsten by oxygen.[356] Consequently, this result indicates that this sulfatotungstate is suited as a phosphor host due to the antenna effect. However, this could not be demonstrated by

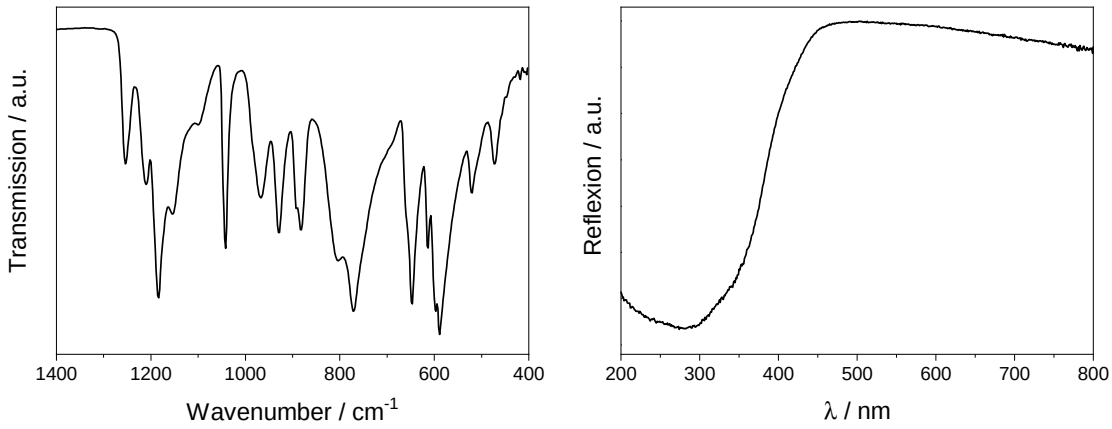

Fig. 6.0.1: FT-IR spectrum on the left and UV-Vis spectrum of $Cs_6[(WO_2)_2O(SO_4)_4]$ on the right

fluorescence spectroscopy due to the lack of an activator in $Cs_6[(WO_2)_2O(SO_4)_4]$. Better suited compounds should contain e.g. rare earth cations. Surprisingly, the luminescent behaviour was not studied for $R_2[W_2O_3(SO_4)_6]$ (R = Sm, Eu, Gd, Ho).[49]

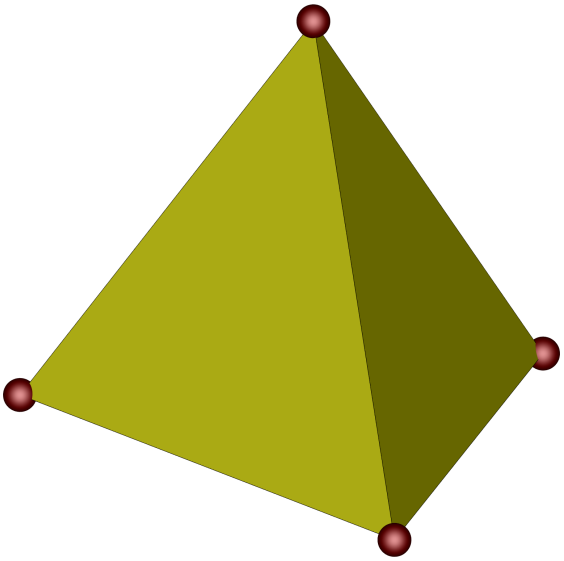

SULFATES

7 Tin and Bismuth Sulfates

In contrast to the sulfatotungstates discussed in the previous chapter, a much greater variety of sulfate compounds have been studied by solid-state chemists. However, in the light of sulfuric acid being one of the most used chemicals both in industry and in research, the knowledge of its compounds is still limited despite significant advancements in recent years.[357–359] Consequently, the results presented in following fill gaps left by past research regarding the cations tin and bismuth.
The compounds presented in this chapter all resulted from syntheses aiming for tin or bismuth borosulfates, respectively. While a tin borosulfates still awaits its discovery – despite attempts in our group for several years[360] – and all syntheses yielded one of the three sulfates investigated in section 7.1, four bismuth borosulfates could be prepared and investigated. These are detailed in chapter 8. The three bismuth sulfates discussed in section 7.2 were, at first, obtained either as side phases or as thermal decomposition products of these borosulfates. Thus, the ternary or quaternary systems Sn-S-O, Bi-S-O and Bi-S-O-H were examined in detail yielding new phases, new crystal structures and insights in the stereochemical activity of the two s^2 cations Sn^{2+} and Bi^{3+} along with the optical and thermal properties of all studied compounds.
The results presented in this chapter were published in part in the journals *Dalton Transactions*[361] and *Inorganic Chemistry*.[362]

7.1 $Sn(SO_4)_2$ and $Sn_2(SO_4)_3$

There is twofold motivation for the following research: On the one hand, compounds comprising s^2 cations like Sn^{2+} are promising candidates for various applications such as rare earth metal free phosphors based on s-p transitions[363,364] or NLO materials with large SHG effects due to stereochemically active lone pairs.[106–108] Recent examples for the latter are the first tin fluorooxoborate $Sn[B_2O_3F_2]$[103,109] or the first tin fluoride borate $Sn_3[B_3O_7]F$.[110] On the other hand, sulfates in general show multiple interesting properties like ionic conductivity[365] and catalytic properties,[366] and are suited as phosphor hosts and NLO materials due to their non π-conjugated tetrahedral SO_4^{2-} groups lacking inversion symmetry.[111,112] Consequently, the combination of both – tin cations and sulfate anions - might yield promising compounds. On the other hand, - prior to our work[361] - only three crystalline members were known for the ternary system Sn-S-O, i.e. $Sn_2(S_2O_4)_2$,[367] Sn_2OSO_4[368] and $SnSO_4$.[369] Despite the first report on the syntheses of tin sulfates or stannous sulfates in 1931[370] $SnSO_4$ was - prior to our work - the only pure tin sulfate with known crystal structure reported by Donaldson and

Puxley in 1972.[369] It adopts a highly distorted variant of the *barite* structure comprising pyramidal SnO_3 units. Broadening the view beyond pure sulfates and considering the quaternary Sn-S-O-H system, only three tin hydroxide oxide sulfates $Sn_3O(OH)_2SO_4$,[371,372] $Sn_6O_4(SO_4)(OH)_2$[373] and $Sn_7(OH)_{12}(SO_4)_2$[374] had been reported. Notably, there are no reports on any homovalent Sn^{4+} compounds comprising sulfate groups - without further cations like in $Ca_3Sn(SO_4)_2(OH)_6(H_2O)_3$[375] or $A_2[Sn(S_2O_7)_3]$ (A = Na, K, Ag, NH_4).[358,376] No crystal structure was reported for tetravalent tin sulfate $Sn(IV)(SO_4)_2$ despite multiple mentions.[377–384] Within their extensive study on the syntheses of various solid compounds prepared from Sn and H_2SO_4, Ahmed et al. proposed a polymorphism of $Sn(SO_4)_2$ and obtained unit cell parameters by indexing powder patterns for two polymorphs.[377] So far, all crystal structures of tetravalent metal sulfates $M(SO_4)_2$ (M = Ce, Zr, U, Th) adopt either the $Ce(SO_4)_2$ or the $Zr(SO_4)_2$ structure type.[385–387]
Heterovalent oxidic tin compounds – crystallographically ordered in contrast to partially oxidised systems[169] – appear to be rare. Apart from the heterovalent tin sulfate hydroxide $Sn(II)_6Sn(IV)(OH)_{12}(SO_4)_2$[374] Ahmed et al. reported the tin oxide sulfate $Sn(II)_2Sn(IV)_4O(SO_4)_9$ merely based on thermogravimetric data.[377] Further, heterovalency is found in $Sn(II)_2Sn(IV)O_4$,[388] $Fe_4Si_2Sn(II)_6Sn(IV)O_{16}$[389] and in $[Sn(II)_3Sn(IV)_3O_{15}]^{12-}$ clusters in polyoxometalates.[390] All these structures comprise condensed $Sn(II)O_x$ (x = 3 or 4) and $Sn(IV)O_6$ polyhedra. Sn^{2+} may exhibit stereochemical activity due to the lone pair effect, thus, occurring in different surroundings, e.g. distorted tetrahedral SnO_3E or distorted trigonal bipyramids SnO_4E – both are present in the structures discussed above. In contrast, tetravalent tin prefers octahedral coordination.
In this section, the crystal structures of two polymorphs of $Sn(SO_4)_2$ are elucidated and the first heterovalent tin sulfate $Sn_2(SO_4)_3 = Sn(II)Sn(IV)(SO_4)_3$ is reported. The optical and thermal properties of these compounds are characterised and compared – also with the known $SnSO_4$.

Syntheses

$Sn_2(SO_4)_3$ Crystalline $Sn_2(SO_4)_3$ was prepared solvothermally. 5 mmol $B(OH)_3$ (Merck, 99.5%) and 5 ml H_2SO_4 (Merck, 95-97%) were mixed inside a nitrogen flushed Schlenk flask at 200°C for 1 h. After natural cooling to 100°C, 0.3 ml oleum (VWR, 65% SO_3) and 1 mmol SnO (Aldrich, >99%) were added and the mixture was stirred for 1 h without further heating. Afterwards, it was transferred into a silica-glass ampoule, which was subsequently fused and placed in a muffle furnace applying the following temperature program: heating to 180°C with 100 Kh^{-1}, holding the temperature for 60 h, and cooling down to room temperature with 100 Kh^{-1}. After opening, decantation and washing (as detailed in section 2.6), a colourless powder containing single-crystals was obtained and phase purity was confirmed by Rietveld analysis depicted in Figure 7.1.1 and table D.1.1. The addition of $B(OH)_3$ proved to be crucial for the crystallisation under these conditions since an analogous sample without boric acid did not crystallise yielding clear solutions

at synthesis temperatures of 180, 250 and 300°C (temperature hold for 60 h each time). However, after furnace treatment at 400°C, single-crystals of $Sn(SO_4)_2$-I were formed indicating thermal conversion from $Sn_2(SO_4)_3$ to $Sn(SO_4)_2$.

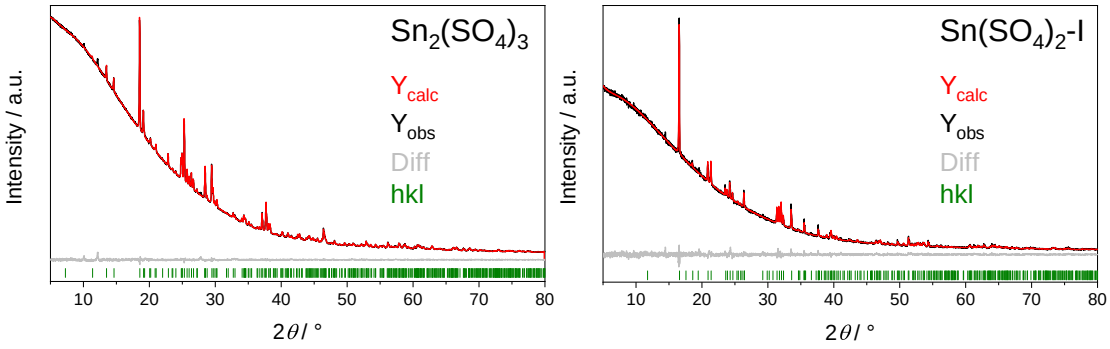

Fig. 7.1.1: Rietveld refinement of phase-pure $Sn_2(SO_4)_3$ (left) and $Sn(SO_4)_2$-I (right).

$Sn(SO_4)_2$ Single-crystals of both polymorphs $Sn(SO_4)_2$-I and $Sn(SO_4)_2$-II were obtained solvothermally and were used for structure determination. 3.2 mmol tin (Alfa Aesar, >99.5%) was mixed with 3.4 ml H_2SO_4 inside a nitrogen flushed Schlenk flask at 200°C and stirred for 1 h, prior to transfer into a silica-glass ampoule, which was fused, placed in a muffle furnace and heated to 400°C for 24 h (heating and cooling ramps 100 Kh^{-1}). The ampoule was opened after cooling with liquid nitrogen and – after decantation of excess sulfuric acid – placed inside a muffle furnace preheated to 150°C and heated at 300°C for 60 h. Afterwards, the dry product was taken out of the furnace at a temperature of 150°C and transferred to an argon filled glovebox. Rietveld analysis revealed a phase composition in this sample of 70% $Sn(SO_4)_2$-I and 30% $Sn(SO_4)_2$-II (Figure D.1.1 and table D.1.2). Phase-pure $Sn(SO_4)_2$-I was prepared by solvothermal synthesis mixing 1.6 mmol SnO_2 and 1.7 ml H_2SO_4 inside a nitrogen flushed Schlenk flask at 200°C under constant stirring for 1 h before transfer into a silica-glass ampoule. Subsequently, the same steps were applied as for the mixed sample detailed above. Phase purity was confirmed by Rietveld analysis (Figure 7.1.1 and table D.1.3). All $Sn(SO_4)_2$ samples were obtained in the form of pale grey powders.

$SnSO_4$ was synthesised similar to the procedure described by Ahmed et al.[377] via room temperature precipitation of 2.33 mmol $SnCl_2 \cdot 2\,H_2O$ (Merck, >96%) in 5 ml H_2SO_4 inside a nitrogen flushed Schlenk flask under constant stirring. The precipitate was washed with 5 ml anhydrous acetonitrile using a frit in a Schlenk line under nitrogen atmosphere. $SnSO_4$ was obtained as a colourless and phase pure powder (Figure D.1.2).
With the exception $SnSO_4$, all products are sensitive towards moisture and hence were stored under inert conditions for further investigations. The stability of $SnSO_4$ at ambient conditions explains why it was the only tin sulfate investigated thoroughly prior to our work.

Crystal Structures

Tab. 7.1.1: Crystal data and structure refinements of $Sn(SO_4)_2$-I, $Sn(SO_4)_2$-II and $Sn_2(SO_4)_3$; $Sn(SO_4)_2$-I was refined as a two-component twin (HKLF 5); the respective standard deviations are given in parentheses; more details are available by the depository numbers and in the original publication.[361]

	$Sn(SO_4)_2$-I	$Sn(SO_4)_2$-II	$Sn_2(SO_4)_3$
CSD number	2081698	2081699	2081697
M / g mol^{-1}	310.81	310.81	525.56
Crystal size / mm^3	0.30 × 0.18 × 0.12	0.14 × 0.07 × 0.06	0.07 × 0.04 × 0.03
Temperature / K	200(2)	286(2)	250(2)
Crystal system	monoclinic	monoclinic	triclinic
Space group	$P2_1/c$ (no. 14)	$P2_1/n$ (no. 14)	$P\bar{1}$ (no. 2)
a / pm	504.34(3)	753.90(3)	483.78(9)
b / pm	1065.43(6)	802.39(3)	809.9(2)
c / pm	1065.47(6)	914.47(3)	1210.7(2)
α / °	90	90	89.007(7)
β / °	91.991(2)	92.496(2)	86.381(7)
γ / °	90	90	73.344(7)
Volume / 10^6 pm^3	572.17(6)	552.66(4)	453.55(14)
Z	4	4	2
ρ_{calcd} / g cm^3	3.61	3.74	3.85
Absorption coefficient μ / mm$^{\smile 1}$	5.2	5.4	6.3
$F(000)$ / e	584	584	488
Radiation; wavelength λ / Å		Mo-K_α; 0.71073	
Diffractometer		Bruker D8 Venture	
Θ range / °	2.704-39.997	3.379-42.496	2.625-24.992
Absorption correction		multi-scan	
Transmission (min; max)	0.490; 0.749	0.415; 0.750	0.544; 0.752
Index range $h \mid k \mid l$	±9 | 0/19 | 0/19	±14 | ±15 | ±17	±5 | ±9 | −12/14
Reflections collected	5940	41984	5982
Independent reflections	4617	3970	1602
Obs. reflections [$I > 2\sigma(I)$]	3961	3585	1326
Refined parameters	104	101	152
BASF	0.497(1)		
R_{int}	0.019	0.041	0.052
R_1	0.050	0.021	0.048
wR_2	0.096	0.033	0.0589
GOF	1.146	1.064	1.066
Residual electron density (max; min) / e^- Å^{-3}	2.77; -3.78	0.88; -0.64	0.78; -0.84

$Sn(SO_4)_2$-I The polymorph $Sn(SO_4)_2$-I crystallises in a new structure type in the monoclinic crystal system with space group $P2_1/c$ (no. 14) and four formula units per unit cell (Table 7.1.1). The unit cell is depicted in Figure 7.1.2 a, in which the sulfate tetrahedra – represented by the sulfur atoms – form a distorted cubic closest packing with the tin atoms being situated in half of all octahedral voids. Essentially, the tin-sulfur substructure forms chains of edge-sharing SnS_6 octahedra and thus, adopts the topology as found in the *rutile* type (Figure 7.1.2 b).

The oxygen atoms of those sulfate anions coordinate the tin ions octahedrally (Figure D.1.3). Out of the four oxygen atoms of each sulfate anion, only three are coordinating tin atoms with the remaining one as expected showing slightly larger atomic displacement parameters (O14 and O21) and significantly shorter S–O bonds (Table D.1.4). Both SO_4

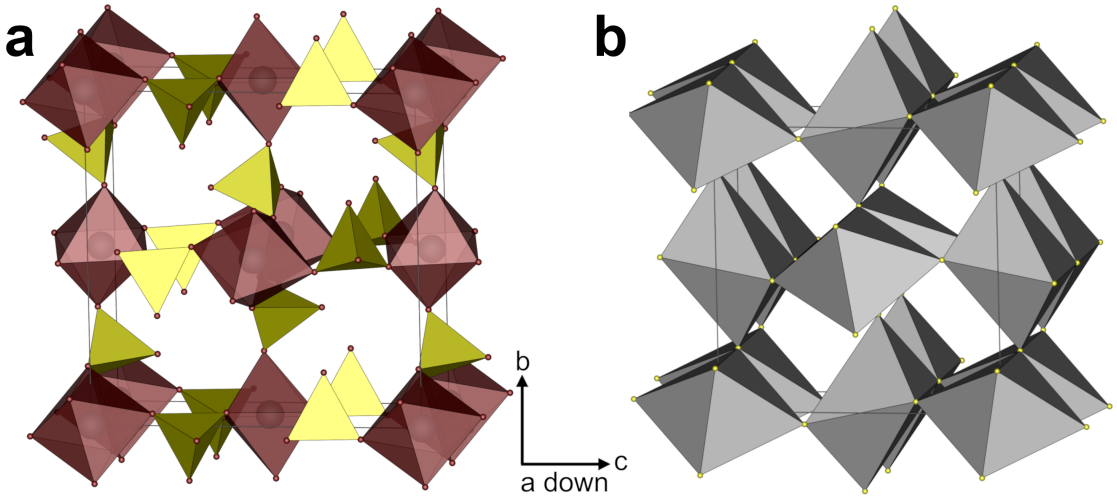

Fig. 7.1.2: (a) Unit cell of $Sn(SO_4)_2$-I viewed along [100]; sulfate tetrahedra yellow, tin cations grey, oxygen atoms red, SnO_6 octahedra pale red; (b) unit cell of Sn(SO4)2-I neglecting the oxygen atoms showing the tin-sulfur substructure comprising SnS_6 octahedra in a *rutile* like arrangement (grey).

tetrahedra can be considered regular with deviations from tetrahedral symmetry of 0.37% and 0.25%. The two SnO_6 octahedra show small deviations from the ideal symmetry of 3.08% and 2.92%. All interatomic distances are in good agreement with the sum of the respective ionic radii (Table D.1.4).[216] The crystal structure of $Sn(SO_4)_2$-I was refined using data measured on a twinned specimen. This twinning is not surprising since the unit cell is close to tetragonal symmetry nicely reflecting its close relation to the *rutile* type. This unit cell coincides with the one reported by Ahmed et al. from indexing for the low temperature polymorph of $Sn(SO_4)_2$-I.[377]

$Sn(SO_4)_2$-II Not surprisingly, the topology of the tin-sulfur network in $Sn(SO_4)_2$-II resembles the high-pressure phase TiO_2-II adapting the α-PbO_2 structure type,[391] while polymorph I was described based on *rutile*. Here, the sulfate anions form a distorted hexagonal closest packing with tin in half of the octahedral voids. As a whole however, $Sn(SO_4)_2$-II crystallises in a new structure type in the monoclinic crystal system with space group $P2_1/n$ (no. 14) and four formula units per unit cell (Figure 7.1.3 a and Table 7.1.1). Again, the oxygen atoms coordinate the tin atoms octahedrally (Figure D.1.4). Analogously to $Sn(SO_4)_2$-I, each sulfate anion coordinates three cation octahedra leaving one oxygen atom per sulfate group non-coordinated. This results in one significantly shorter S-O bond (Table D.1.5). The impression of a denser packing of the SnO_6 and SO_4 polyhedra in $Sn(SO_4)_2$-II in comparison to $Sn(SO_4)_2$-I just by viewing both unit cells agrees with the higher density of $Sn(SO_4)_2$-II. It follows the trend of the underlying structure types. *Rutile* undergoes a first-order phase transition to the denser TiO_2-II upon pressure.[391] In both $Sn(SO_4)_2$ structures, the $Sn(SO_4)_6$ octahedra share two edges with neighbouring octahedra, in *rutile*-like $Sn(SO_4)_2$-I rods and in TiO_2-II-like

$Sn(SO_4)_2$-II zig-zag chains form with the latter wriggling allowing to pack the chains denser (Figure 7.1.3 b and c). Also in $Sn(SO_4)_2$-II, the two distinct SO_4 tetrahedra can be considered regular with deviations from the tetrahedral symmetry of 0.15% each. The deviation of the SnO_6 octahedron from octahedral symmetry amounts to 3.26%. Again, all interatomic distances are in good agreement with the sum of the ionic radii (Table D.1.5).[216]

$Sn_2(SO_4)_3$ crystallises in the triclinic crystal system with space group $P\bar{1}$ (no. 2) and two formula units per unit cell (Figure 7.1.4 and table 7.1.1). The cationic substructure consists of two distinct non-condensed $Sn(IV)O_6$ octahedra (Sn1 and Sn2) and $Sn(II)O_6$ non-condensed pentagonal pyramids (Sn3). These can also be viewed as distorted pentagonal bipyramidal SnO_6E in the light of the VSEPR concept (Figure 7.1.5). With $R_c = 46\,\text{pm}$ and $\epsilon = 0.167$ for the Sn^{2+} cation, the lone pair effect is clearly expressed. This lone pair activity requires space yielding respective vacant regions within the crystal structure. The anion comprises three different SO_4 tetrahedra connecting the $Sn(IV)O_6$ and $Sn(II)O_6$ polyhedra forming a network. The sulfate ions coordinate two Sn(IV) and two Sn(II) cations each. Consequently, there is no non-coordinating oxygen atom. Therefore, the network can be described as $(Sn(IV)O_{6/2})(Sn(II)O_{6/2})(SO_{4/2})_{12/4} \mathrel{\hat{=}} Sn_2(SO_4)_3$. The three sets of sulfate tetrahedra can be considered regular with deviations of 0.05%, 0.10% and 0.11%, respectively. The $Sn(IV)O_6$ octahedra show small deviations of 2.47% and 0.96%. Selected interatomic distances and angles are tabulated in Table D.1.6. The distances are in good agreement with the respective sum of ionic radii.[216,265] The angles inside the $Sn(II)O_6$ pentagonal pyramid deviate from the ideal values of 90° from top to base and 72° inside the base of the pentagonal pyramid as expected from the VSEPR model due to electrostatic reasons. This is not surprising since the centroid deviation in Figure 7.1.5 shows that the stereochemical activity is less symmetric than expected by the VSEPR model. The crystal structure of $Sn_2(SO_4)_3$ comprises alternating layers within the *ac* plane with exclusive Sn(IV) or Sn(II) cations, respectively. These layers are connected via common sulfate anions forming the $Sn_2(SO_4)_3$ network. Consequently, the crystal structure of $Sn_2(SO_4)_3$ can be described as a combination of alternating layers with $SnSO_4$ and $Sn(SO_4)_2$ stoichiometry along the [010] direction. This *AB* stacking scheme is depicted in Figure 7.1.6 a. The $Sn(SO_4)_2$ layers comprise *rutile*-like rods of edge-sharing octahedra (Figure 7.1.6 b). Further, the layers are stacked in such a way that the space requirements of the stereochemical activity of the Sn^{2+} cation are met (Figures 7.1.6 and D.1.5). In contrast to $SnSO_4$, there are more oxygen atoms coordinating the Sn^{2+} cation due to the presence of adjacent layers containing $Sn(IV)O_6$ octahedra forcing the stereochemical activity to occur inside the layer instead of in between adjacent layers as in $SnSO_4$.

Consequently, $Sn_2(SO_4)_3$ is the first heterovalent tin sulfate and the first compound comprising separated $Sn(II)O_x$ ($x = 6$) and $Sn(IV)O_6$ polyhedra. There are no Sn(II)-O-Sn(IV) bonds. Furthermore, $Sn_2(SO_4)_3$ represents the first example for the $Sn(II)O_6E$

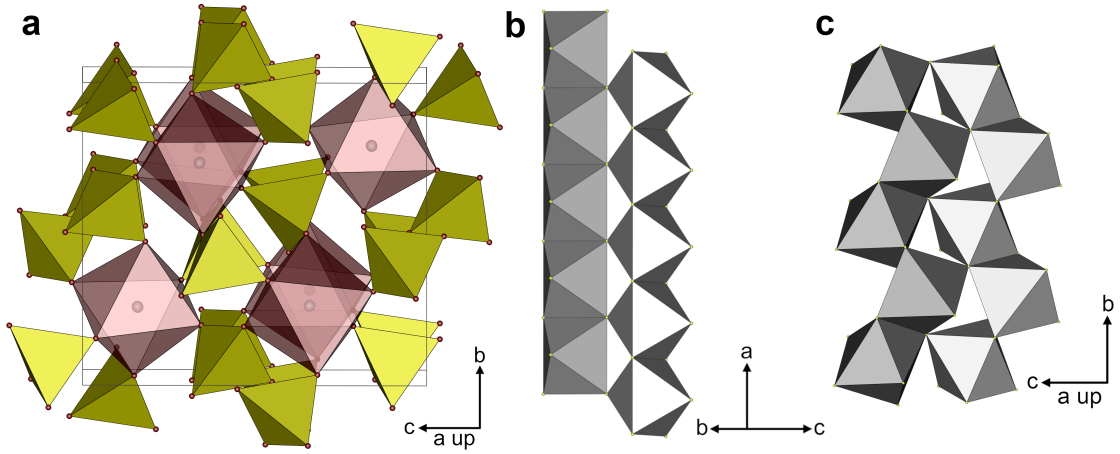

Fig. 7.1.3: (a) Unit cell of $Sn(SO_4)_2$-II viewed along [100]; sulfate tetrahedra yellow, tin cations grey, oxygen atoms red, SnO_6 octahedra pale red; in (b) and (c) the SnS_6 octahedra (grey) chains via common edges in $Sn(SO_4)_2$-I (b) and $Sn(SO_4)_2$-II (c) are compared resembling the connection pattern of *rutile* and TiO_2-II, respectively; oxygen atoms are omitted for clarity.

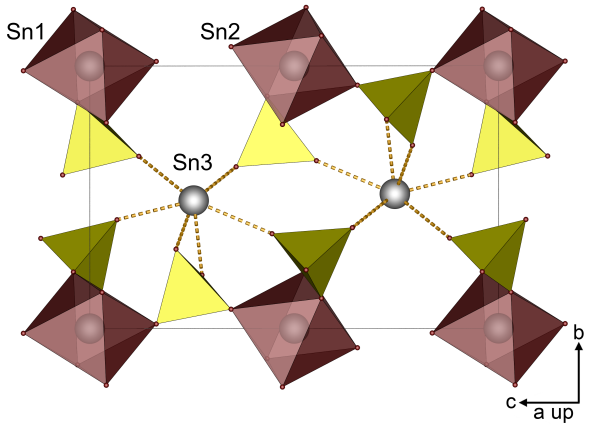

Fig. 7.1.4: Unit cell of $Sn_2(SO_4)_3$ viewed along [100]; sulfate tetrahedra yellow, tin cations grey, oxygen atoms red, SnO_6 octahedra pale red.

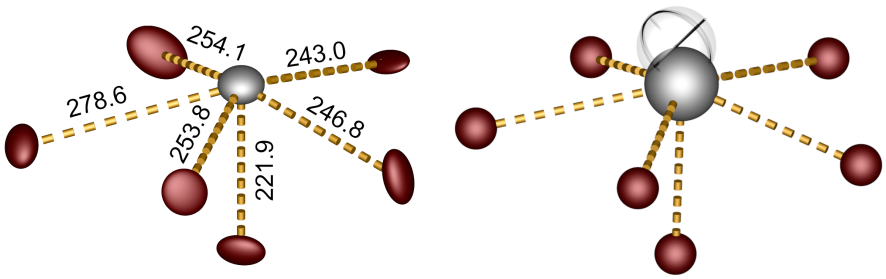

Fig. 7.1.5: $Sn(II)O_6$ polyhedron in $Sn_2(SO_4)_3$: On the left the respective bond lengths are given in pm; in the light of the VSEPR model the lone pair of the SnO_6E stereochemistry can be expected to point towards the top of this representation. tin grey, oxygen red, ellipsoids are shown at 80% probability; on the right the $Sn(II)O_6$ polyhedron is shown including the centroid (semi-transparent octant); tin grey, oxygen red.

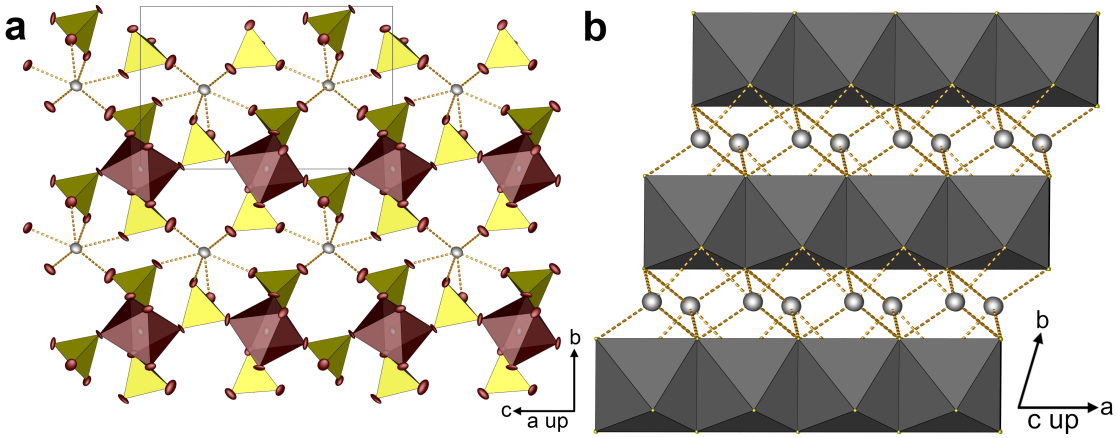

Fig. 7.1.6: Layered structure of $Sn_2(SO_4)_3$ viewed along [100] in (a); sulfate tetrahedra yellow, tin cations grey, oxygen atoms red, SnO_6 octahedra pale red; ellipsoids are shown at 80% probability; and viewed along (001) in (b) displaying the *rutile*-like rods of SnS_6 octahedra (dark grey); oxygen atoms are omitted for clarity.

distorted pentagonal bipyramidal stereochemistry. In all structures discussed at the beginning of this section, the $Sn(II)O_x$ ($x = 3$ or 4) and $Sn(IV)O_6$ polyhedra are condensed and the Sn^{2+} cations are fourfold coordinated at maximum.
In conclusion, all three crystal structures discussed represent new structure types. In the case of $Sn(SO_4)_2$-I and $Sn(SO_4)_2$-II, the range of $M(SO_4)_2$ structure types is expanded beyond $Zr(SO_4)_2$ and $Ce(SO_4)_2$. Mainly, this appears to be due to the high stability of the sixfold coordination of Sn(IV) requiring $Sn(SO_4)_2$-I and $Sn(SO_4)_2$-II to adapt a less symmetric structure than the other two structure types with coordination numbers for M of seven and eight, respectively.

Electrostatic calculations

The electrostatic reasonability of the crystal structures was confirmed by calculations based on the MAPLE concept. The MAPLE values for $Sn(SO_4)_2$-I, $Sn(SO_4)_2$-II and $Sn_2(SO_4)_3$ from single-crystal data were calculated and compared to the respective sum of SnO_2, $SnSO_4$ and SO_3 (Table D.1.7). The deviations are well below 1% for all structures. Moreover, all coordination numbers were confirmed by the calculations (Tables D.1.8 to D.1.10). Especially, the calculated effective coordination numbers (Table D.1.10) confirm that in fact six oxygen atoms coordinate the Sn^{2+} cation in $Sn_2(SO_4)_3$ resulting in the distorted pentagonal bipyramidal SnO_6E discussed above.

Optical Properties

Infrared Spectroscopy

The infrared spectra of $Sn(SO_4)_2$-I and $Sn_2(SO_4)_3$ are shown in Figure 7.1.7 in the region of $1600 - 400\,cm^{-1}$ (full spectra in Figure D.1.6). In accordance with reports in

literature,[384,392,393] the observed absorptions can be attributed to various S–O vibrations. Peaking at 1377 cm^{-1} and 1344 cm^{-1}, the S-O stretching vibrations of non-coordinating oxygen atoms can be found. Consequently, these bands are only present for $Sn(SO_4)_2$-I, since in $SnSO_4$ and $Sn_2(SO_4)_3$ all oxygen atoms are coordinating. Further, they form a doublet due to the two distinct sets of sulfate tetrahedra in $Sn(SO_4)_2$-I. Below down to 800 cm^{-1}, the remaining S-O stretching vibrations of coordinating oxygen atoms are located. Between 700 cm^{-1} and 400 cm^{-1}, the S–O bending modes occur. At the lower end of the spectra, an overlap by Sn–O vibrations cannot be ruled out.[394] The splitting of the respective bands, i.e. the total number of vibrations increases from $SnSO_4$ over $Sn(SO_4)_2$-I to $Sn_2(SO_4)_3$ since the compounds comprise one, two and three distinct SO_4 groups, respectively. Further, the spectrum of $Sn_2(SO_4)_3$ shows the discrimination between S-O stretching vibrations next to Sn(II)-O bonds above 1100 cm^{-1} and Sn(IV)-O bonds below that value. The same increase in the number of bands can be observed for the bending modes - on top of the effect of the higher number of distinct SO_4 tetrahedra.

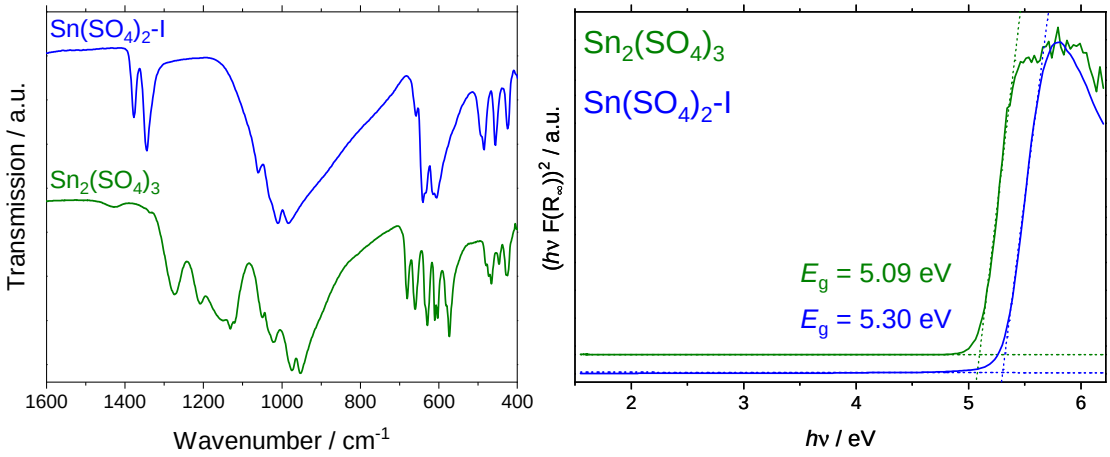

Fig. 7.1.7: Infrared spectra of $Sn(SO_4)_2$-I and $Sn_2(SO_4)_3$ on the left; the full spectra can be found in Figure D.1.6; Tauc-plots calculated from the UV-Vis spectra of $Sn(SO_4)_2$-I and $Sn_2(SO_4)_3$ on the right.

UV-Vis Spectroscopy

The powder reflectance spectra of $Sn(SO_4)_2$-I and $Sn_2(SO_4)_3$ are shown in Figure D.1.7 in the range from 200 to 800 nm. In accordance with the colourless to pale grey powders no absorption in the visible region is observed. For both, the fundamental absorption due to the bandgap of the samples occur in the UV regime. The bandgap energies E_g could be estimated using Tauc plots depicted in Figure 7.1.7. The resulting E_g values are 5.30(1) eV and 5.09(1) eV for $Sn(SO_4)_2$-I and $Sn_2(SO_4)_3$, respectively. The smaller bandgap observed for $Sn_2(SO_4)_3$ might originate from the Sn^{2+} cations. According to earlier reports,[364] $SnSO_4$ shows an absorption in the UV region due to s-p transitions of

Sn^{2+} cations at 230 nm. Such a distinct band is not observed for $Sn_2(SO_4)_3$ despite it also containing Sn^{2+} cations.

Fluorescence Spectroscopy

The well-known self-trapped exciton emission of $SnSO_4$[364] due to s-p transitions could be reproduced as shown in Figure D.1.8. However, no emission originating from the Sn^{2+} cations could be observed for $Sn_2(SO_4)_3$ - in line with the absence of s-p transitions in the UV-Vis spectrum. Apparently, non-radiative energy transfer pathways are very effective here.

Mößbauer Spectroscopy

The experimental and simulated ^{119}Sn Mößbauer spectra of the $Sn(SO_4)_2$-I, $Sn_2(SO_4)_3$ and $SnSO_4$ samples are shown in Figure 7.1.8 and the corresponding fitting parameters are summarised in Table D.1.11. The $Sn(SO_4)_2$-I spectrum was well reproduced with a single signal at an isomer shift of $\delta = -0.259\,\mathrm{mm\,s^{-1}}$, confirming tetravalent tin. The weak quadrupole splitting parameter accounts for a deviation of the site symmetry from cubic (site symmetry $\bar{1}$). $SnSO_4$ shows much higher quadrupole splitting as a consequence of the Sn(II) lone pair. The divalent tin is confirmed through a large isomer shift value of $\delta = 3.969\,\mathrm{mm\,s^{-1}}$. The ^{119}Sn data of our $Sn(SO_4)_2$-I and $SnSO_4$ samples are in good agreement with literature data.[395]
The $Sn_2(SO_4)_3$ sample shows two signals with a Sn(II) to Sn(IV) ratio of 58:42, confirming the SC-XRD data.[i] Again, the Sn(II) sub-signal shows the slightly higher quadrupole splitting parameter.

Thermal Analyses

The thermal decomposition was investigated by TGA under nitrogen atmosphere and TPXRD inside sealed argon filled glass capillaries. The studied tin sulfates decompose according to the following reaction equations:

$$Sn_2(SO_4)_3 \longrightarrow 2\,SnO_2 + 3\,SO_2 + O_2$$
$$Sn(SO_4)_2 \longrightarrow SnO_2 + 2\,SO_2 + O_2$$

The expected mass losses for these processes depicted in Figure 7.1.9 agree well with the observed values, caused by the release of gaseous SO_3, which in turn decomposes to SO_2 and O_2 at these temperatures. The residual powder was investigated by PXRD confirming the formation of SnO_2 (Figure D.1.9). For $Sn(SO_4)_2$, the temperature region of the thermal decomposition is in agreement with earlier reports.[377,383]
As previously introduced, Ahmed et al. reported high temperature polymorphism of $Sn(SO_4)_2$ with a transition temperature of 500°C.[377] Consequently, $Sn(SO_4)_2$-I was

[i] The lower signal-to-noise ratio of the $Sn_2(SO_4)_3$ spectrum is due to the small sample quantity.

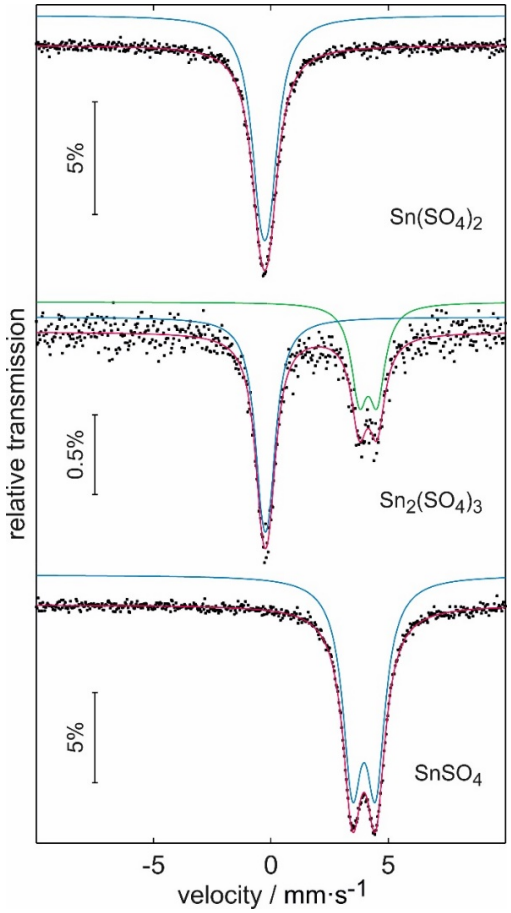

Fig. 7.1.8: Experimental (data points) and simulated (continuous line) ^{119}Sn Mößbauer spectra (78 K data) of $Sn(SO_4)_2$-I, $Sn_2(SO_4)_3$ and $SnSO_4$; the measuring time was one day for the tin(II) and tin(IV) sulfates and five days for the mixed valence sulfate (small sample quantity).

investigated by TPXRD confirming the decomposition towards SnO_2 above 500°C, again. The results are shown in Figure D.1.10. The merging of some reflections is observed at 400°C. This could indicate the existence of a tetragonal or orthorhombic high temperature polymorph. However, Rietveld analysis on this pattern starting from $Sn(SO_4)_2$-I was successful yielding an increased unit cell which is even closer to an orthorhombic cell than the unit cell from SC-XRD data. Details are shown in Figure D.1.11 and table D.1.3. On the other hand, indexing on this measurement yielded an orthorhombic cell similar to the one found by Ahmed et al. Yet, a Pawley fit using this cell (*Pnnn* (no. 48), $a = 758.97(7)$ pm, $b = 757.47(7)$ pm, $c = 507.68(3)$ pm, $R_{\mathrm{Bragg}} = 0.004$, $R_{\mathrm{wp}} = 0.049$, 122 parameters, Figure D.1.12) achieved worse fitting than the Rietveld refinement with the monoclinic $Sn(SO_4)_2$-I structure. Possibly, this unit cell enlargement is the effect observed by Ahmed et al. by DTA and attributed to a phase transformation. Interestingly, equivalent $Sn(SO_4)_2$-I as observed at 400°C could be prepared via precipitation as a pale

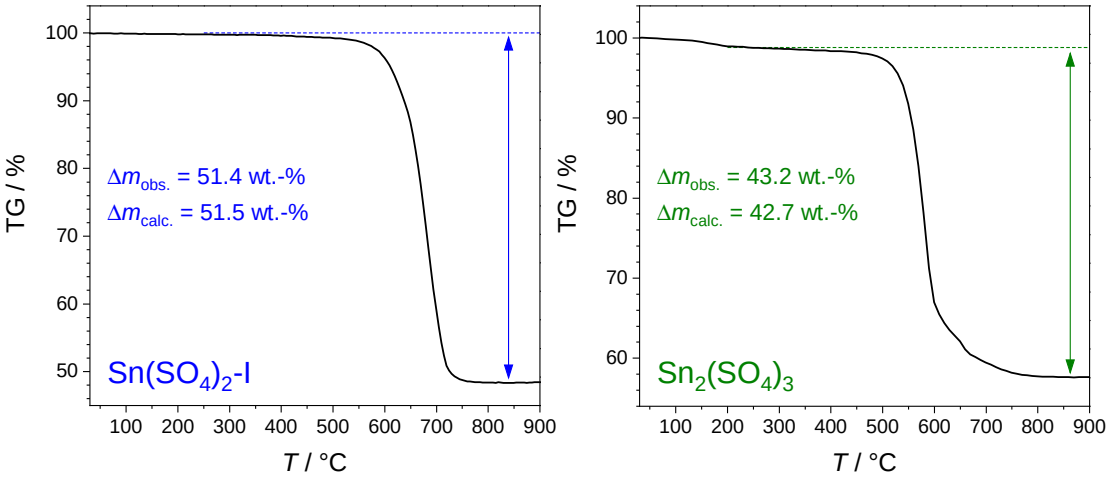

Fig. 7.1.9: Thermogravimetric analyses of $Sn(SO_4)_2$–I (left) and $Sn_2(SO_4)_3$ (right).

grey powder without any single-crystals, starting from 3.2 mmol tin mixed with 5 ml H_2SO_4 inside a nitrogen flushed Schlenk flask and stirred at 300°C for 1 h. The resulting precipitate was washed with 5 ml anhydrous acetonitrile using a frit in a Schlenk line under N_2 atmosphere. Afterwards, the product was transferred to an argon filled glovebox. The Rietveld refinement of this p-$Sn(SO_4)_2$-I, detailed in Figure D.1.13 and table D.1.3, yielded the same enlarged unit cell as above. Further, the infrared spectra of both $Sn(SO_4)_2$-I samples - prepared via precipitation or solvothermal synthesis - displayed in Figure D.1.6 are almost identical confirming the results from Rietveld refinement that both compounds are indeed $Sn(SO_4)_2$-I with differing unit cell parameters. The TGA of the sample prepared by precipitation showed the same one step decomposition towards SnO_2. The decomposition starts at slightly lower temperatures compared to $Sn(SO_4)_2$-I from solvothermal synthesis (Figure D.1.14). The reason for this might be the higher crystallinity of the latter sample. TPXRD performed on the $Sn(SO_4)_2$-I sample prepared by precipitation showed no change of the pattern before decomposition and confirmed the formation of SnO_2 (Figure D.1.15). A possible explanation for the enlarged unit cell of $Sn(SO_4)_2$-I observed both at 400°C and via the preparation by precipitation are kinetic effects. This is underlined by the PXRD pattern depicted in Figure D.1.16 of a $Sn(SO_4)_2$-I sample heated at 500°C for 1 h in inert atmosphere inside the TGA instrument indicating the reversibility of the unit cell enlargement at high temperatures. In the case of $Sn_2(SO_4)_3$, the reaction towards a mixture of $SnSO_4$ and $Sn(SO_4)_2$ prior to the decomposition step towards SnO_2 is conceivable – and consistent with the TGA results since this reaction would not be accompanied by any mass loss. However, heating a sample of $Sn_2(SO_4)_3$ inside the TGA instrument in inert atmosphere up to 450°C, holding the temperature for 1 h and subsequent cooling yielded an unchanged PXRD (Figure D.1.17). However, experiments in an open system, i.e. a corundum crucible inside a muffle furnace at 300°C at air for 24 h as well as inside a sealed glass ampoule in presence

of excess H_2SO_4[ii] showed a transformation from $Sn_2(SO_4)_3$ to $Sn(SO_4)_2$-I (Figure D.1.18). Further, the thermogravimetric data on $Sn_6O(SO_4)_9$ reported by Ahmed et al.[377] and the measurement on $Sn_2(SO_4)_3$ appear to coincide. Thus, it can be concluded that the $Sn_6O(SO_4)_9$ prepared by Ahmed et al. was in reality $Sn_2(SO_4)_3$.
All these thermal processes could be confirmed by the DTA results in Figure D.1.19.

[ii] See syntheses without the addition of $B(OH)_3$ detailed above.

7.2 $Bi(H_3O)(SO_4)_2$, $Bi(HSO_4)_3$ and $Bi_2(SO_4)_3$

Bismuth-based materials can be used in various applications ranging from NLO materials using the SHG effect[106,107] over photonics[396] to phosphors[397,398] – also long persistent ones – or even cosmetics.[399] Largely, these properties are related to the Bi^{3+} cations and their electronic configuration of $6s^2$. Bismuth compounds behave often chemically similar to rare earth compounds due to a similar charge-to-radius ratio.[400] So, they adopt similar crystal structures and an analogous crystal chemistry. However, in contrast to respective rare earth ions, Bi^{3+} cations feature a possibly stereochemically active lone pair due to their electronic configuration of $6s^2$. Depending on the counter-anions this may result in structural distortions caused by the lone pair effect[70] - as already discussed in the introduction (page 7).
In spite of over a century of research,[401–409] crystal structures are still rare in the $Bi_2O_3-SO_3-H_2SO_4$ or $Bi_2O_3-SO_3-H_2O$ system. In 1937, Škramovský and Vondrášek reported the title compound $Bi(H_3O)(SO_4)_2$ as $BiH(SO_4)_2 \cdot H_2O$ based on thermogravimetric data, but not reporting the crystal structure.[402] The crystal structures of the related compounds $(H_3O)Nd(SO_4)_2$ and $(H_3O)Sb(SO_4)_2$ were reported but never discussed with regard to a lone-pair activity.[410,411] Similarly, $Bi(HSO_4)_3$ was reported by Fujioka and Cady in 1957 as a white precipitate formed from Bi(III) trifluoroacetate in sulfuric acid, also without determining the crystal structure.[404] Earlier, Schäfer and Hein had published spectroscopic data associated with $Bi(HSO_4)_3$.[401] In 1938, $Bi_2(SO_4)_3$ was reported for the first time by Hanawalt et al.[403] Despite various reports on the thermal decomposition of this so-called "commercial $Bi_2(SO_4)_3$",[406–408] no crystal structure was reported to date. In 2014, Subban et al. described another $Bi_2(SO_4)_3$ polymorph crystallising in space group $C2/c$,[409] but did not conduct a further investigation of "commercial $Bi_2(SO_4)_3$". They only report the formation of a "poorly crystallized second phase" different to both the $C2/c$ polymorph and "commercial $Bi_2(SO_4)_3$".
In this section, the crystal structure and the optical and thermal properties of $Bi(H_3O)(SO_4)_2$, $Bi(HSO_4)_3$ and $Bi_2(SO_4)_3$ are elucidated. The three compounds offer the opportunity to investigated lone pair-crystal structure relationship to gain further insight in the lone pair activity. In this regard, a link is searched between simple geometrical parameters deduced from the crystal structure (using the method detailed in section 3.6.2) and the lone pair activity proven by DFT and ELF calculations (as detailed in section 3.6.3). This may prove the reliability of the geometric calculations and enable the assessment of the presence and significance of lone pair activity in any oxidic compound containing Bi^{3+} cations by these geometrical parameters only.

Syntheses

$Bi(H_3O)(SO_4)_2$, $Bi(HSO_4)_3$ and $Bi_2(SO_4)_3$ were prepared via solvothermal syntheses in the form of colourless powders containing single-crystals. The products are sensitive towards moisture and hence were stored under inert conditions for further investigations.

$Bi(H_3O)(SO_4)_2$ 1.25 ml H_2SO_4 (Merck, 95-97%) were heated inside a nitrogen flushed Schlenk flask at 200°C for 1 h. After natural cooling to 100°C, 0.15 ml oleum (VWR, 65% SO_3) and 0.5 mmol dehydrated[iii] $Bi(NO_3)_3 \cdot 5\,H_2O$ (AlfaAesar, >99.999%) were added and the mixture was stirred for 1 h without further heating. The mixture was transferred into a silica-glass ampoule (length 15 cm, outer diameter: 1.2 cm, wall thickness: 0.1 cm). Subsequently, the ampoule was fused and placed in a muffle furnace applying the following temperature program: heating to 180°C with $100\,K\,h^{-1}$, holding the temperature for 60 h, and cooling down to room temperature with $5\,K\,h^{-1}$. The ampoule was opened, the sample washed as detailed in section 2.6 and transferred to the glovebox.
$Bi(H_3O)(SO_4)_2$ was obtained phase-pure according to the Rietveld analysis in figure 7.2.1 and table D.2.1.

$Bi(HSO_4)_3$ Single-crystals were prepared by a synthesis identical to the one for $Bi(H_3O)(SO_4)_2$ with the only variation of further addition of 1.25 ml H_2SO_4 after the addition of all other educts followed by stirring for 1 h before transferring the mixture into the ampoule. However, samples prepared this way contained significant amounts of at least 20% $Bi(H_3O)(SO_4)_2$ as side-phase despite synthesis optimisation. The synthesis of bulk $Bi(HSO_4)_3$ was achieved starting from elemental bismuth (Aldrich, 99%). Firstly, 5 ml H_2SO_4 were heated inside a nitrogen flushed Schlenk flask to 200°C and 2 ml oleum were added. After 15 min stirring, 1 mmol Bi was added and the mixture stirred for 1 h at 200°C; then, the mixture was further stirred for 30 min without heating. The greyish mixture was transferred into a silica-glass ampoule, which was fused and placed into a muffle furnace applying the following temperature program: heating to 300°C with $100\,K\,h^{-1}$, holding the temperature for 60 h and cooling down to room temperature with $100\,K\,h^{-1}$. Subsequently, the ampoule was opened, the sample was washed and transferred to the glovebox.
$Bi(HSO_4)_3$ was obtained comprising a 5 wt.-% side phase of $Bi(H_3O)(SO_4)_2$ according to Rietveld analysis (figure 7.2.1 and table D.2.1)

$Bi_2(SO_4)_3$ 2.5 ml H_2SO_4 were heated inside a nitrogen flushed Schlenk flask to 200°C, the temperature held for 30 min, the heating turned off and 0.3 ml oleum (65% SO_3) were added. Then, 0.5 mmol $Bi(NO_3)_3 \cdot 5\,H_2O$ - dehydrated as described above - were added and the mixture stirred for 1 h. Subsequently, the mixture was transferred into a silica-glass ampoule which was fused and placed in a muffle furnace applying the following temperature program: heating to 300°C with $100\,K\,h^{-1}$, holding the temperature for 15 h, and cooling to room temperature with $100\,K\,h^{-1}$. The ampoule was opened after cooling with liquid nitrogen. After decantation of the excess sulfuric acid, the sample was placed inside a muffle furnace preheated to 150°C and heated at 300°C for 20 h with ramps of

[iii] The $Bi(NO_3)_3 \cdot 5\,H_2O$ had been dehydrated in a porcelain crucible in a muffle furnace at 250°C overnight. It was taken out at 250°C and directly added to the mixture.

$100\,K\,h^{-1}$. Afterwards, the dry product was taken out of the furnace at a temperature of 150°C and immediately transferred to the glovebox.
$Bi_2(SO_4)_3$ was obtained as a phase-pure powder according to the Rietveld analysis in figure 7.2.1 and table D.2.1. No indication for the polymorph prepared by Subban et al.[409] or the $Bi_2(SO_4)_3$ phase reported by Hanawalt et al.[403] were found (Figure D.2.1). This is presumably due to the solvothermal conditions preferring only the herein described polymorph. It is possible that the compound prepared here is related to the "poorly crystallized second phase" described by Subban et al.[409]
It is worth noticing that the results of the $Bi_2(SO_4)_3$ syntheses do not differ when using Bi or Bi_2O_3 as educts. Moreover, both $Bi(H_3O)(SO_4)_2$ and $Bi(HSO_4)_3$ samples dried by evaporation of H_2SO_4 as performed for $Bi_2(SO_4)_3$ inside a muffle furnace at 300°C overnight or inside a compartment dryer at 180°C for more than seven days are converted to $Bi_2(SO_4)_3$. This is a first indication that $Bi_2(SO_4)_3$ is the thermal decomposition product of both $Bi(H_3O)(SO_4)_2$ and $Bi(HSO_4)_3$.

Crystal Structures

$Bi(H_3O)(SO_4)_2$ crystallises in the monoclinic crystal system with space group $P2_1/c$ (no. 14) and four formula units per unit cell homeotypic to $(H_3O)Nd(SO_4)_2$. The unit cell is depicted in Figure 7.2.2a.
The quality of the single-crystal structure determination (Table 7.2.1) is of limited quality due to the highly hygroscopic nature of the compound. However, the crystal structure could be confirmed by Rietveld refinement (Figure 7.2.1 and table D.2.1). The crystal structure of $Bi(H_3O)(SO_4)_2$ features two crystallographically distinct sulfate anions; both can be considered regular tetrahedra with deviations of 0.3% and 0.2%. The trivalent bismuth ions are coordinated by five monodentate and two bidentate sulfate tetrahedra forming BiO_9 polyhedra (Figure D.2.2a). The oxonium ions are connected via hydrogen bonds to four oxygen atoms with distances between 254 and 278 pm and to seven further ones with distances between 309 and 339 pm.[iv] The BiO_9 tricapped trigonal prisms depicted in Figure 7.2.2b are connected to three other BiO_9 polyhedra each via common edges as shown in Figure D.2.2b yielding corrugated double layers parallel to the *bc* plane. The $S(2)O_4$ tetrahedra are situated in these layers bridging five BiO_9 polyhedra; contrary, the $S(1)O_4$ tetrahedra coordinate one bismuth cation monodentately and one bidentately – leaving one terminal oxygen atom which forms a moderately strong hydrogen bond with a donor acceptor distance of 262(2) pm to the oxonium ions present in the voids of the aforementioned layers (Figure D.2.3). Both S-O and Bi-O distances agree well with the respective sum of the ionic radii (Table D.2.2).
Although $Bi(H_3O)(SO_4)_2$ crystallises homeotypical to $(H_3O)Nd(SO_4)_2$,[410] both structures are not isotypical due to a smaller width of the double layers in the latter and differing orientations of the sulfate anions. The related higher symmetric $(H_3O)Sb(SO_4)_2$ – reported as $(H_3O)_2Sb_2(SO_4)_4$[411] and crystallising in space group $Pbc2_1$ (no. 29) –

[iv] These values should be treated with caution due to the limited data quality.

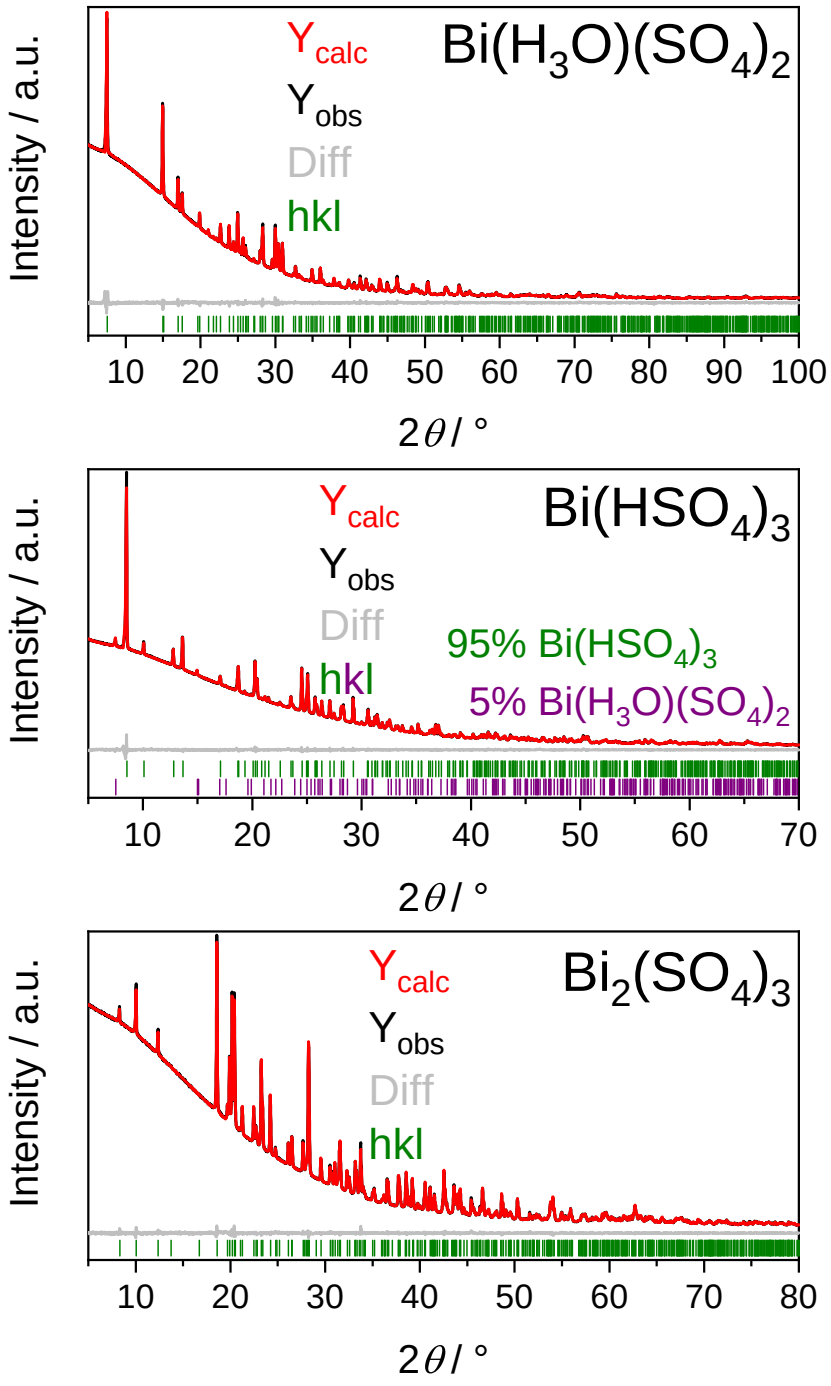

Fig. 7.2.1: Rietveld refinements of $Bi(H_3O)(SO_4)_2$, $Bi(HSO_4)_3$ and $Bi_2(SO_4)_3$ (from top to bottom)

Tab. 7.2.1: Crystal data and structure refinements of $Bi(H_3O)(SO_4)_2$, $Bi(HSO_4)_3$ and $Bi_2(SO_4)_3$ determined from SC-XRD: the respective standard deviations are given in parentheses; more details are available by the depository numbers and in the original publication.[362]

	$Bi(H_3O)(SO_4)_2$	$Bi(HSO_4)_3$	$Bi_2(SO_4)_3$
CSD number.	2118043	2118044	2118045
M / g mol^{-1}	420.12	500.18	706.14
Crystal size / mm^3	0.10 × 0.05 × 0.01	0.34 × 0.12 × 0.06	0.3 × 0.2 × 0.1
Temperature / K		200(2)	
Crystal system	monoclinic	triclinic	monoclinic
Space group	$P2_1/c$ (no. 14)	$P\bar{1}$ (no. 2)	$P2_1/n$ (no. 14)
a / pm	1203.5(4)	492.04(7)	1308.03(7)
b / pm	682.9(2)	910.83(13)	473.25(3)
c / pm	821.2(2)	1040.8(2)	1452.61(8)
α / °	90	85.443(5)	90
β / °	102.988(9)	86.897(5)	100.886(2)
γ / °	90	74.542(4)	90
Volume / 10^6 pm^3	657.7(3)	447.9(1)	883.02(9)
Z	4	2	4
ρ_{calcd} / g cm^3	4.24 3.71 5.31		
Absorption coefficient μ / mm$^{\smile 1}$	27.46	20.45	40.58
$F(000)$ / e	760	460	1240
Radiation; wavelength λ / Å		Mo-K_α; 0.71073	
Diffractometer		Bruker D8 Venture	
Θ range / °	3.452-22.486	2.325-32.494	2.325-32.493
Absorption correction		multi-scan	
Transmission (min; max)	0.3798; 0.7449	0.2972; 0.7491	0.4165; 0.7482
Index range $h \mid k \mid l$	±12 | ±7 | −8/7	±7 | ±13 | ±15	±19 | ±7 | ±21
Reflections collected	4774	14120	28718
Independent reflections	861	3227	3189
Obs. reflections [$I > 2\sigma(I)$]	683	3098	2944
Refined parameters / restraints	88 / 4	154 / 3	155 / 0
R_{int}	0.097	0.034	0.055
R_1	0.070	0.020	0.019
wR_2	0.144	0.048	0.031
GOF	1.024	1.067	1.071
Residual electron density (max; min) / e^-Å^{-3}	3.53; -3.40	1.42; -2.09	1.48; -1.03

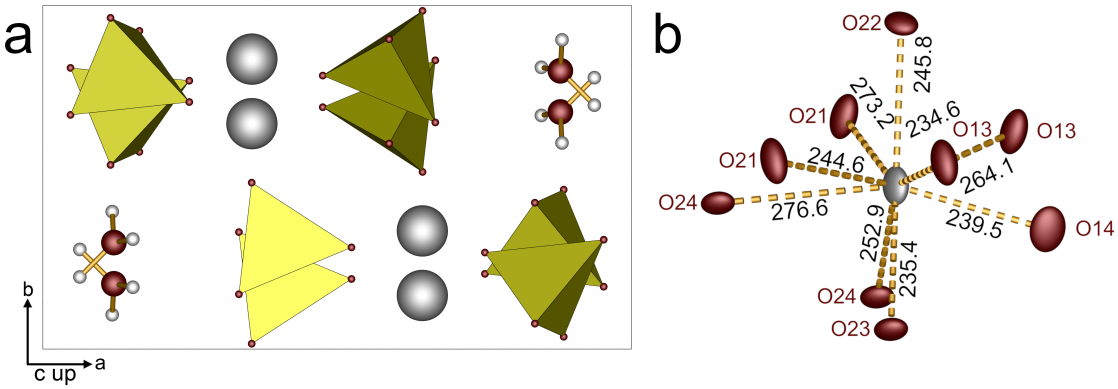

Fig. 7.2.2: (a) Unit cell of $Bi(H_3O)(SO_4)_2$ viewed along $[00\bar{1}]$ and (b) the coordination environment of Bi^{3+} cations with the Bi-O distances labelled in pm; the site symmetry of the bismuth atom is 1; sulfate tetrahedra yellow, bismuth cations grey, oxygen atoms red, hydrogen atoms white; ellipsoids are shown at 80% probability (in (b)).

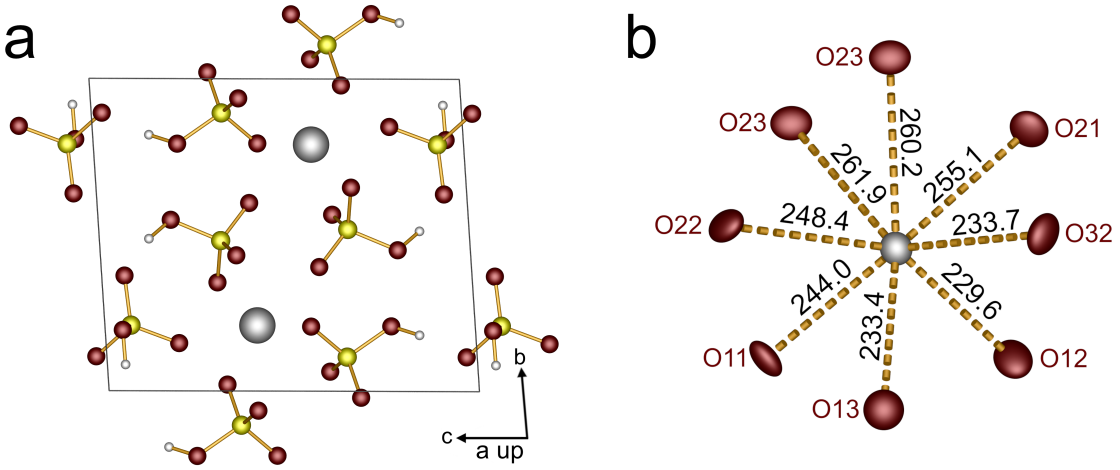

Fig. 7.2.3: (a) Unit cell of $Bi(HSO_4)_3$ viewed along $[\bar{1}00]$ and (b) the coordination environment of Bi^{3+} cations with the Bi-O distances labelled in pm; the site symmetry of the bismuth atom is 1; sulfate tetrahedra yellow, bismuth cations grey, oxygen atoms red, hydrogen atoms white; ellipsoids are shown at 80% probability (in (b)).

comprises distinct SbO_3E and SbO_4E units. The structural motif of the stacked double layers is preserved, but there are no Sb-O-Sb bridges, i.e. the double layers are merely built by the connection via sulfate anions. However, these sulfate anions are orientated similarly to $Bi(H_3O)(SO_4)_2$, which can therefore be treated as an intermediate between lone pair effect-free $(H_3O)Nd(SO_4)_2$ and $(H_3O)Sb(SO_4)_2$ showing large stereochemical activity.

$Bi(HSO_4)_3$ crystallises in a new structure type in the triclinic crystal system with space group $P\bar{1}$ (no. 2) and two formula units per unit cell (Figure 7.2.3a). An irregular packing of three crystallographically distinct HSO_4 tetrahedra hosts trivalent bismuth atoms eight-fold coordinated by oxygen atoms yielding a bicapped trigonal prismatic coordination (Figure 7.2.3b and Figure D.2.4a). The Bi-O distances of 230-262 pm are in good agreement with the sum of the respective ionic radii (252-253 pm) (Table D.2.3).[216] The BiO_8 polyhedra form dimers via shared edges and are primitively packed in the crystal structure. Each dimer shares two hydrogensulfate anions (Figure D.2.4b). Naturally, the protonated oxygen atoms do not contribute to the coordination sphere of bismuth. Between the HSO_4^- ions, medium strong hydrogen bonds are formed – the donor-acceptor distances amount to 260.5(3) and 263.7(4) pm and are similar to those reported for other hydrogensulfates.[412,413] All three hydrogensulfate tetrahedra can be classified as regular with deviations of 0.1%. The interatomic distances are in agreement with the sum of the ionic radii (Table D.2.3) and with other hydrogensulfates.[412–415] The location of the hydrogen atom was clearly indicated by the larger distances from the central sulfur atom to the respective protonated oxygen atom.

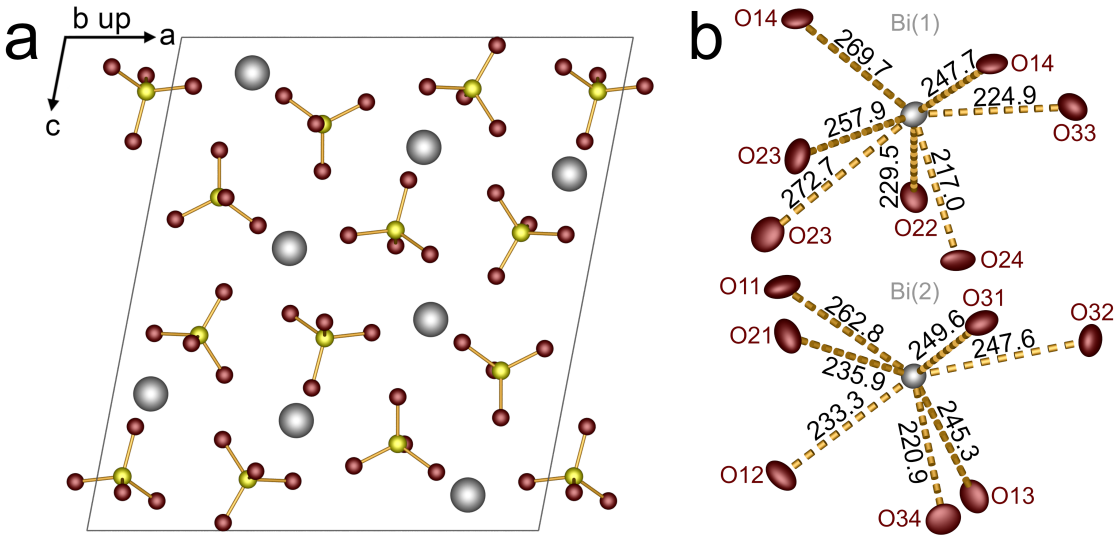

Fig. 7.2.4: (a) Unit cell of $Bi_2(SO_4)_3$ viewed along $[0\bar{1}0]$ and (b) the coordination environment of Bi^{3+} cations with the Bi-O distances labelled in pm; there are two crystallographically distinct bismuth sites: Bi(1) and Bi(2); the site symmetry of both bismuth atoms is 1; sulfate tetrahedra yellow, bismuth cations grey, oxygen atoms red, hydrogen atoms white; ellipsoids are shown at 80% probability (in (b)).

$Bi_2(SO_4)_3$ The new $Bi_2(SO_4)_3$ polymorph crystallises in the monoclinic crystal system with space group $P2_1/n$ (no. 14) and four formula units per unit cell isotypic to $Sb_2(SO_4)_3$.[416] The unit cell is depicted in Figure 7.2.4a. However, $Sb_2(SO_4)_3$ was described in the different setting $P2_1/c$. The anion consists of three crystallographically distinct sulfate tetrahedra. Further, there are two different bismuth sites coordinated by seven oxygen atoms each (Figure 7.2.4b). The Bi-O distances of 217-273 pm are in good agreement with the sum of the respective ionic radii (252-253 pm) (Table D.2.4).[216] The $Bi(1)O_7$ polyhedra can be described as monocapped trigonal prisms. They are coordinated by one bidentate and five monodentate sulfate anions (Figure D.2.5a) and shares corners with three neighbouring $Bi(1)O_7$ yielding zigzag chains along the b axis (Figure D.2.6). The non-condensed $Bi(2)O_7$ polyhedra are coordinated by seven monodentate sulfate anions (Figure D.2.5b). However, the $Bi(2)O_7$ polyhedra are connected via two shared sulfate anions yielding layers in the ab plane. In between these layers, the $Bi(1)O_7$ chains are located (Figure D.2.7). For the anions, the deviations from the tetrahedral symmetry amount to 0.1%, 0.2% and 0.3%, respectively and thus, all three sulfate tetrahedra can be considered regular. The S-O distances agree with the sum of the ionic radii (Table D.2.4).

Electrostatic Calculations

The electrostatic reasonability of the crystal structures of $Bi(H_3O)(SO_4)_2$, $Bi(HSO_4)_3$ and $Bi_2(SO_4)_3$ and all coordination numbers were confirmed by calculations based on

the MAPLE concept (Tables D.2.5 to D.2.8). The effective coordination numbers are discussed with the stereochemical activity in the following.

DFT Calculations

Quantum chemical calculations at the level of DFT were performed for $Bi(H_3O)(SO_4)_2$, $Bi(HSO_4)_3$ and $Bi_2(SO_4)_3$. The structures were each optimized with VASP and ELF was calculated. The optimised lattice parameters (Table D.2.9) and atomic positions agree with the experimentally refined crystal structures. Analysing the DOS, shown in Figure D.2.8, obtained using HSE06, support that all three compositions are insulators with indirect band gaps of approximately 6 eV (Table D.2.10). The DOS indicates that the states at the top of valence band are primarily composed of oxygen 2p states, while the conduction band is composed of the bismuth 6p mixed with the empty oxygen 2p states.

Stereochemical Activity and Lone Pair Effect

The stereochemical activity of Bi^{3+} cations in $Bi(H_3O)(SO_4)_2$, $Bi(HSO_4)_3$ and $Bi_2(SO_4)_3$ is assessed using the centroid deviation and eccentricity from the geometric calculation by the method of Balić-Žunić and Makovicky (section 3.6.2), employing the VSEPR concept based on the Bi-O distances and analysing the results from DFT and ELF calculations (section 3.6.3). An overview is given in Figure 7.2.5. At first, the stereochemical activity is discussed for each individual compound. Afterwards, the results are compared and discussed together.

$Bi(H_3O)(SO_4)_2$ Compared with homeotypic $(H_3O)Nd(SO_4)_2$,[410] the influence of the lone pair effect in $Bi(H_3O)(SO_4)_2$ becomes obvious. The distance of the bismuth atom from the centroid of the BiO_9 polyhedron R_c of 23 pm in $Bi(H_3O)(SO_4)_2$ ($\epsilon = 0.088$) (Rietveld data: $R_c = 20$ pm and $\epsilon = 0.072$) is significantly larger than $R_c = 3.6$ pm ($\epsilon = 0.014$) in $(H_3O)Nd(SO_4)_2$. According to the centroid deviation, the asymmetric electron density is located between the two longest Bi-O bonds, approximately along [010]. This rather simple model is in very good agreement with the more detailed ELF calculations, which confirm both this location and the stereochemical activity (Figure 7.2.5 top).
Employing the VSEPR concept, the coordination of the Bi^{3+} ion can be described as distorted octahedron BiO_5E considering the bond lengths (Figure 7.2.2b) and the effective coordination numbers (Table D.2.6). The O-Bi-O angles of 67.4(5)°, 76.3(5)°, 77.3(4)°, 77.9(5)°, 80.3(4)°, 82.9(5)° and 101.1(4)° deviate from the ideal value of 90° due to repulsion by oxygen atoms with larger Bi-O distances. The angles for the three oxygen atoms with the shortest distances to the bismuth atom (O13, O23, O14) are close to 90° (76.3° − 77.9°) indicating the p-character of the bonding interaction.

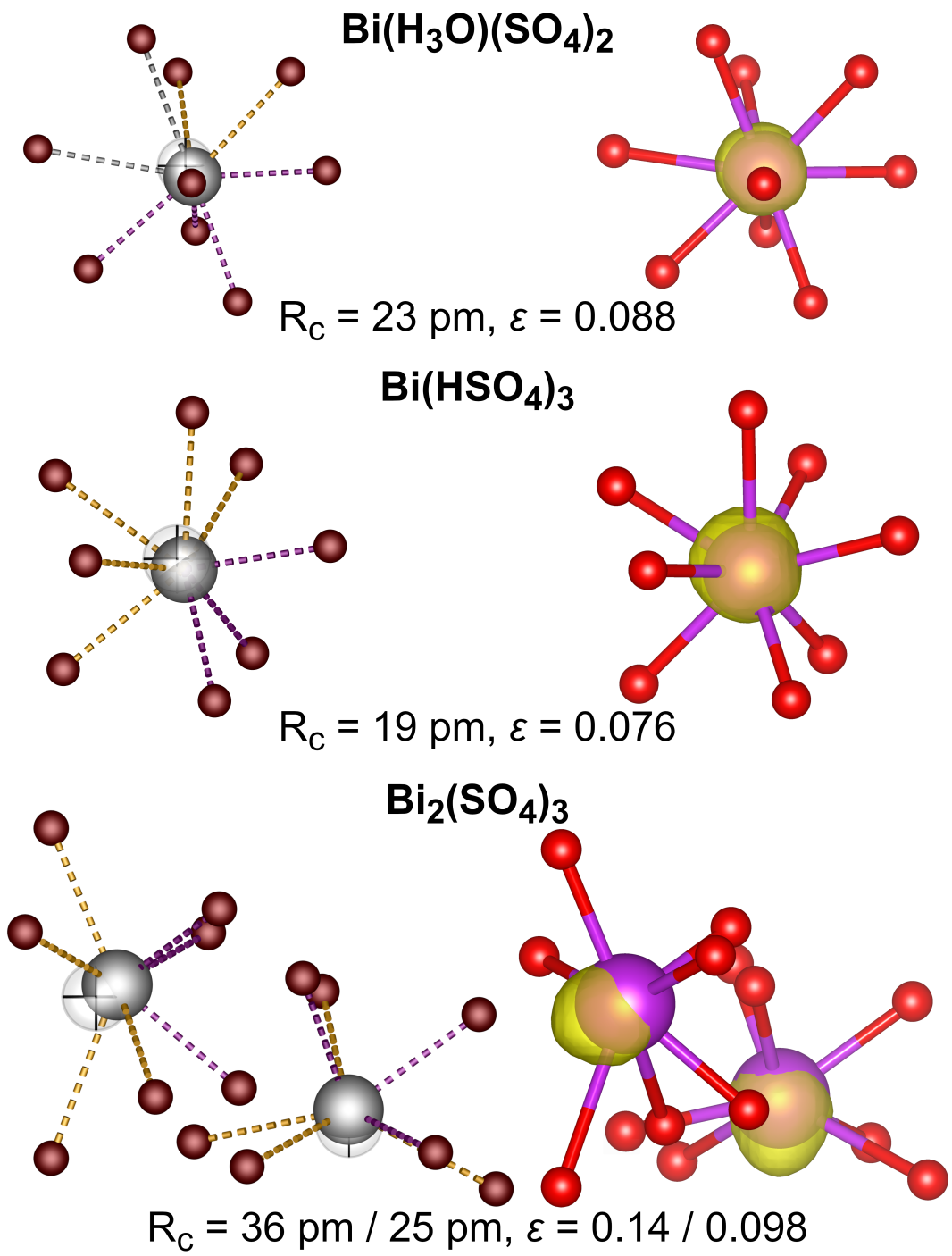

Fig. 7.2.5: Stereochemical activity of the Bi^{3+} cations in $Bi(H_3O)(SO_4)_2$, $Bi(HSO_4)_3$ and $Bi_2(SO_4)_3$ (from top to bottom): On the left the respective BiO_9, BiO_8 and BiO_7 polyhedra are shown including the centroid (semi-transparent octant); the shortest bonds that are part of the BiO_5E distorted octahedron or BiO_3E distorted tetrahedra, respectively, are violet, residual bonds yellow, additionally, the longest bonds towards shared edges in [100] direction in $Bi(H_3O)(SO_4)_2$ are shown in grey; bismuth atoms grey, oxygen red; on the right side, respective details of the ELF showing the same BiO_9, BiO_8 and BiO_7 polyhedra are depicted; the results for the full unit cells of $Bi(H_3O)(SO_4)_2$ and $Bi(HSO_4)_3$ are shown in Figures D.2.9 and D.2.10.

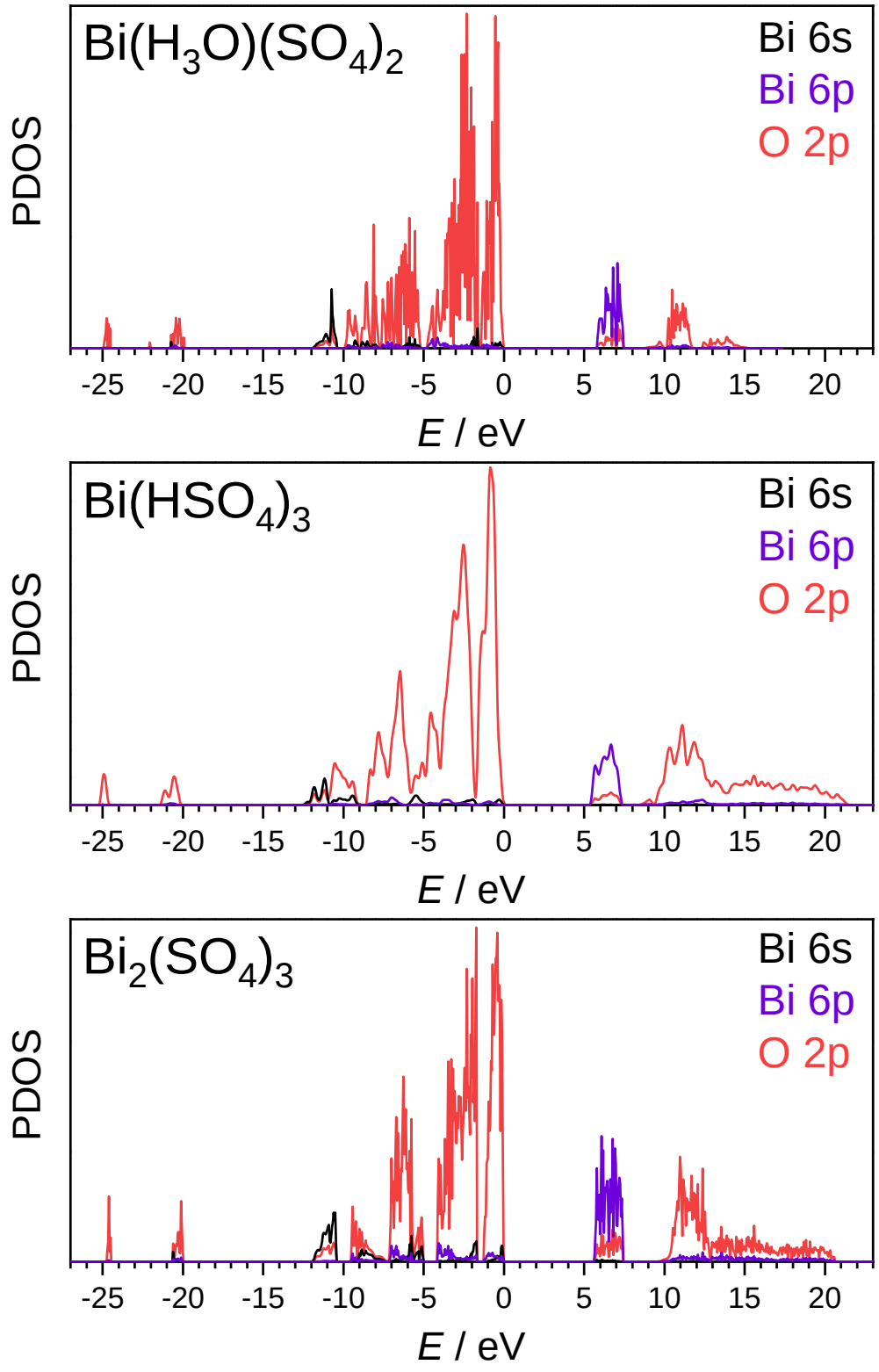

Fig. 7.2.6: Partial density of states of $Bi(H_3O)(SO_4)_2$, $Bi(HSO_4)_3$ and $Bi_2(SO_4)_3$ shown in black, violet and red for the Bi 6s, Bi 6p and O 2p orbitals, respectively.

$Bi(HSO_4)_3$ Rare earth hydrogensulfates similar to $Bi(HSO_4)_3$ are known with both RO_9, e.g. $Ce(HSO_4)_3$,[415] and RO_8 polyhedra, e.g. $Er(HSO_4)_3$.[414] However, in these compounds these polyhedra are non-condensed. R_c of the BiO_8 polyhedron amounts to 19 pm in $Bi(HSO_4)_3$ ($\epsilon = 0.076$). This is significantly larger than 1.7 pm ($\epsilon = 0.007$) and 5.7 pm ($\epsilon = 0.023$) for ErO_8 in $Er(HSO_4)_3$-I and $Er(HSO_4)_3$-II, respectively. Consequently, this indicates the stereochemical activity of the Bi^{3+} cation. As depicted in Figures 7.2.5, D.2.4 and D.2.10, the deviation occurs for each Bi^{3+} ion away from the next Bi^{3+}, with whom it is forming the dimer. Consequently, the presence of electron density pointing towards the shared edge within the dimer is conceivable. The ELF results confirm this assumption coinciding with the direction indicated by the centroid (Figure 7.2.5 middle).

Regarding the VSEPR concept, the coordination of the Bi^{3+} cation can be described as distorted tetrahedron BiO_3E considering the bond lengths (Figure 7.2.3b) and the effective coordination numbers (Table D.2.7). The Bi-O distances can be divided in three groups: three short distances as part of the BiO_3E (230-234 pm, O12, O13, O32), three intermediate distances (244-255 pm, O11, O21, O22) and two long contacts to oxygen atoms shared with another Bi^{3+} in a dimer (260-262 pm, both to O23). In agreement with the earlier discussion, the lone pairs of two adjacent Bi^{3+} cations point towards each other in this consideration, too. Yet, the exact direction of the asymmetric electron density from the ELF results differs from the prediction by the VSEPR model. The O-Bi-O angles of 76.4(1)°, 79.2(1)° and 81.0(1)° deviate from the ideal value of 109.5° due to repulsion effects by other oxygen atoms with larger Bi-O distances. However, these angles are close to 90° indicating the p-character of the bonding interactions – in coincidence with the ELF showing bulges exactly opposite the Bi-O bonds to O12, O13 and O32.

$Bi_2(SO_4)_3$ To compare with, several analogous rare earth sulfates, e.g. $Eu_2(SO_4)_3$, $Er_2(SO_4)_3$ and $Nd_2(SO_4)_3$, are known.[414,417,418] However, in none of them the cations are coordinated by seven oxygen atoms preventing the direct comparison with the crystal structure of $Bi_2(SO_4)_3$. Nevertheless, the coordination environments of both bismuth atoms in $Bi_2(SO_4)_3$ unambiguously indicate an influence of the lone pair effect. Large R_c values of 36 pm ($\epsilon = 0.136$) and 25 pm ($\epsilon = 0.098$) were obtained for Bi(1) and Bi(2), respectively. In comparison to isotypic $Sb_2(SO_4)_3$, weaker lone pair activity can be expected for $Bi_2(SO_4)_3$ due to lower relativistic stabilisation of the 5s electrons compared to the 6s electrons.[70] This results in more diffuse shaped 5s than 6s orbitals. Consequently, stereochemical activity can be expressed easier for the former. Accordingly, Sb(1) and Sb(2) in $Sb_2(SO_4)_3$ show larger values for both Rc of 59 pm and 48 pm and ϵ of 0.219 and 0.193, respectively.

According to the VSEPR concept the coordination of both Bi(1) and Bi(2) can be described as distorted tetrahedral BiO_3E considering the three significantly shorter distances for both bismuth positions (Figure 7.2.4b). The respective O-Bi-O angles of

77.5(1)°, 78.7(1)° and 80.9(1)° for Bi(1) and 74.5(1)°, 74.9(1)° and 93.1(1)° for Bi(2) deviate from the tetrahedral angle of 109.5° due to repulsion by the other oxygen atoms with larger Bi-O distances. This is in accordance with the MAPLE calculations mentioned above. As a rule of thumb, the respective stereochemistries in the VSEPR model can be accessed by the former taking all oxygen atoms into account with effective coordination numbers close to or above one. However, the angles are close to 90° indicating the p-character of the bonding interactions, again. The ELF results (Figure 7.2.5 bottom) coincide with the direction of the asymmetric electron density indicated by the centroid. Moreover, this shows the limitation of accessing the stereochemistry by the VSEPR model, only. The BiO_3E is distorted strongly by the influence of the residual four oxygen atoms, i.e. the lone pair is not pointing where the BiO_3E would suggest. In contrast, the method of calculating the centroid deviation is taking this into account. Consequently, this method is apparently better suited to explain the direction of the stereochemical activity.

Tab. 7.2.2: Geometric parameters calculated for the structures from single-crystal data (SC-XRD) or from the VASP optimisation for $Bi(H_3O)(SO_4)_2$, $Bi(HSO_4)_3$ and $Bi_2(SO_4)_3$; the average Bi-O distance $(Bi{-}O)_{average}$ is calculated for the three shortest bonds linked to the tripod formed by the metal p-orbitals, only; all distances are given in pm.

	R_c (SC-XRD)	R_c (VASP)	ϵ (SC-XRD)	ϵ (VASP)	CN	$(Bi{-}O)_{average}$
$Bi(H_3O)(SO_4)_2$	23	13	0.088	0.051	9	237
$Bi(HSO_4)_3$	19	20	0.076	0.079	8	232
$Bi_2(SO_4)_3$ Bi(1)	36	39	0.14	0.142	7	224
$Bi_2(SO_4)_3$ Bi(2)	25	23	0.098	0.090	7	230

Discussion of the Lone Pair Effect As detailed in the introduction (page 7), smaller energetic gaps between the metal s states and the ligands p states cause stronger urge for expressed stereochemical activity. According to the partial densities of states shown in Figure 7.2.6, the energy levels of bismuth and oxygen do not differ significantly among the three compounds in discussion. As expected,[70,72] the bismuth s states are situated near the bottom end of the valence band for all samples - independently from the expression of the lone-pair effect. On the other hand, the strength of the ligand (p-type) – metal (s) interaction may be scaled via the width and energetic localisation of the metal s band.[71] The width of bands, which should scale with increasing metal-ligand orbital overlap, shows a clear trend. The most pronounced expression of the lone-pair effect is found for $Bi_2(SO_4)_3$, in which the smallest coordination number is found and also geometrically as well as via ELF calculations the highest eccentricities were determined. The remaining compounds show – according to the eccentricity and the ELF results – decreasing stereochemical lone pair activity from $Bi(HSO_4)_3$ to $Bi(H_3O)(SO_4)_2$. The direction and extent of the expression of the lone-pair effect determined by the simple geometric calculation via the eccentricity, summarised in Table 7.2.2, coincides very well with the ELF calculations.

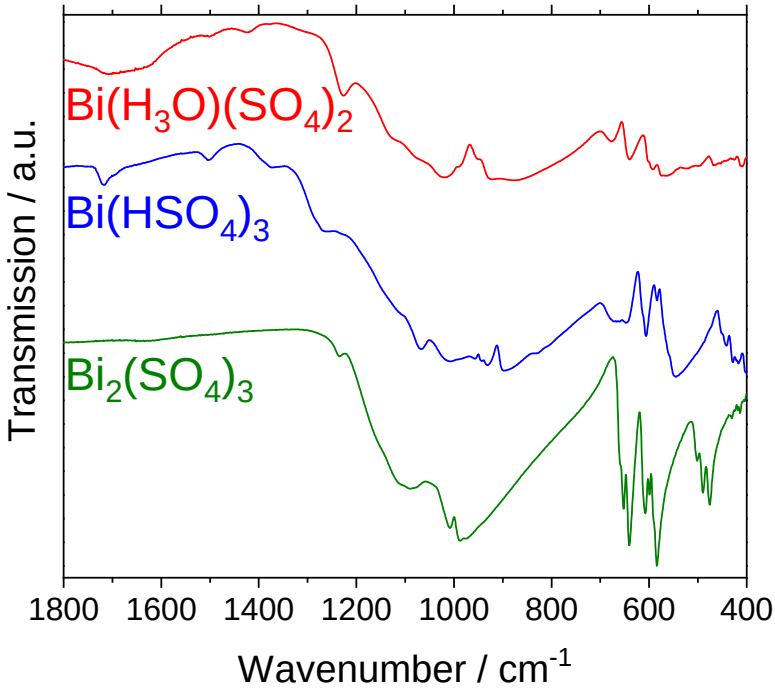

Fig. 7.2.7: Infrared spectra of $Bi(H_3O)(SO_4)_2$, $Bi(HSO_4)_3$ and $Bi_2(SO_4)_3$: The full spectra can be found in Figure D.2.11.

Similar to the eccentricity, the average bond length of the three shortest Bi-O bonds with angles close to 90° associated with the tripod formed by the metal p orbitals can be used a measure for the strength of the lone pair effect for the three title compounds (Table 7.2.2). Smaller Bi-O distances are associated with a stronger lone pair activity. However, this is not possible for compounds with ambiguous coordination environment around bismuth. The best example for this is $Bi_2[B_2(SO_4)_6]$ discussed in section 8.1.

Optical Properties

Infrared Spectroscopy

The infrared spectra of $Bi(H_3O)(SO_4)_2$, $Bi(HSO_4)_3$ and $Bi_2(SO_4)_3$ are shown in Figure 7.2.7 in the regime $1800 - 400\,cm^{-1}$ (full spectra in Fig. S23). The broad absorption around $2800\,cm^{-1}$ due to the O-H symmetric stretching vibration is present for $Bi(H_3O)(SO_4)_2$ and $Bi(HSO_4)_3$, only.[419] However, in both cases it is overlapped by vibrations presumably originating in the formation of sulfuric acid on the surface of the samples reacting with ambient moisture.[420] The absence of these for $Bi_2(SO_4)_3$ can be explained by the more effective drying by furnace treatment compared to the washing with acetonitrile. Additionally, the asymmetric O-H stretching occurs around $1720\,cm^{-1}$.[419,420] Below, the spectra are dominated by S-O vibrations with the respective stretching modes between $1300\,cm^{-1}$ and $800\,cm^{-1}$ and the bending modes below

700 cm^{-1}.[112,421,422] The band peaking at 1227 cm^{-1} for $Bi(H_3O)(SO_4)_2$ is related to the S-O stretching mode of non-coordinating oxygen atoms located at higher energies than the respective vibrations of coordinating oxygen atoms. Similarly, $Bi(HSO_4)_3$ shows an absorption around 1373 cm^{-1} related to the S-O stretching vibrations involving the two oxygen atoms interacting merely with hydrogen atoms, but coordinating no bismuth atoms. Further, the O-H bending and the characteristic S-OH stretching modes can be found at 1262 cm^{-1} and at 897 cm^{-1}, respectively. The S-O stretching vibrations region in $Bi_2(SO_4)_3$ is broad due to the presence of both oxygen atoms with coordination number two and three differing in energy. At energies close to 400 cm^{-1} an overlap by Bi-O vibrations cannot be ruled out.[271]

UV-Vis Spectroscopy

As already seen in chapter 5, Bi^{3+} compounds show absorptions due to s-p transitions between the ground state ($6s^2$) $^1S_0$ and the excited states ($6s^16p^1$) $^3P_0$, $^3P_1$, $^3P_2$ and $^1P_1$. The dipole transition $^1S_0 \rightarrow {}^1P_1$ is spin-allowed. The transitions from $^1S_0$ to $^3P_1$ and $^3P_2$ are partially allowed due to spin orbit coupling and vibronic mixing, respectively. The $^1S_0 \rightarrow {}^3P_0$ transitions are strictly forbidden. Consequently, the three relevant absorptions are commonly labelled A, B and C with increasing energy, i.e. $^1S_0 \rightarrow {}^3P_1$, $^3P_2$ and $^1P_1$.[396,398] Often, only the A band is clearly resolved in UV-Vis spectra. For example, it is present as a shoulder in $Na_5Bi(WO_4)_4$ around 370 nm.[278] Using the experimentally determined relationship $\frac{E_{free}}{E_{crystal}} = 1 + k\,E_{free}$,[v] the location of the B and C band can be estimated, anyway.[398,424]

The powder reflectance spectra of $Bi(H_3O)(SO_4)_2$, $Bi(HSO_4)_3$ and $Bi_2(SO_4)_3$ are shown in Figure 7.2.8 in the range from 200 to 800 nm. In accordance with the colourless powders, no absorption in the visible region is observed. Starting around 400 nm strong absorption occurs in the UV-region. Here, the s-p transitions of the Bi^{3+} cation and the fundamental absorption of the sample are overlapped. For $Bi(HSO_4)_3$ and $Bi_2(SO_4)_3$, the shoulder between 300 and 400 nm could be fitted using a Gaussian fit (Figure D.2.12). In the case of $Bi(H_3O)(SO_4)_2$, the absorption is too weak for proper fitting. This shoulder can be attributed to the A band. Consequently, the B and C band energies were calculated using the equation discussed above. The A, B and C bands are located at 266 nm (4.66 eV), 238 nm (5.22 eV) and 221 nm (5.60 eV) for $Bi(HSO_4)_3$ and 299 nm (4.14 eV), 271 nm (4.57 eV) and 255 nm (4.87 eV) $Bi_2(SO_4)_3$, respectively. Due to the overlap with these transitions, the band gap determined by DFT calculations in Table D.2.10 could not be confirmed by the UV-Vis data using Tauc plots. The energies of the A, B and C bands estimated here can be expected to be underestimated since the latter is usually reported in the vacuum UV region.[425] However, the approximate localisation of the bands enables the sufficient explanation of the experimental data.

[v] The energies of free Bi^{3+} E_{free} for the A, B and C bands are 9.41 eV, 11.96 eV and 14.21 eV, respectively.[398,423]

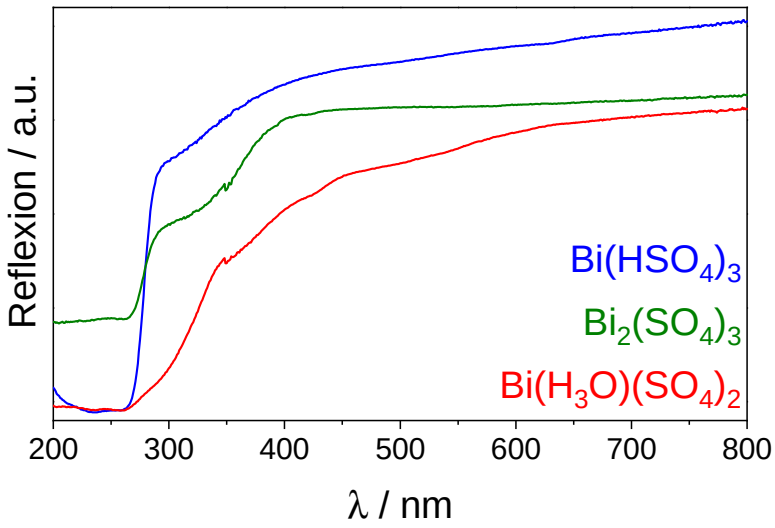

Fig. 7.2.8: Diffusive powder UV-Vis spectra of $Bi(H_3O)(SO_4)_2$, $Bi(HSO_4)_3$ and $Bi_2(SO_4)_3$: The artefact around 350 nm is due to lamp change during the measurement.

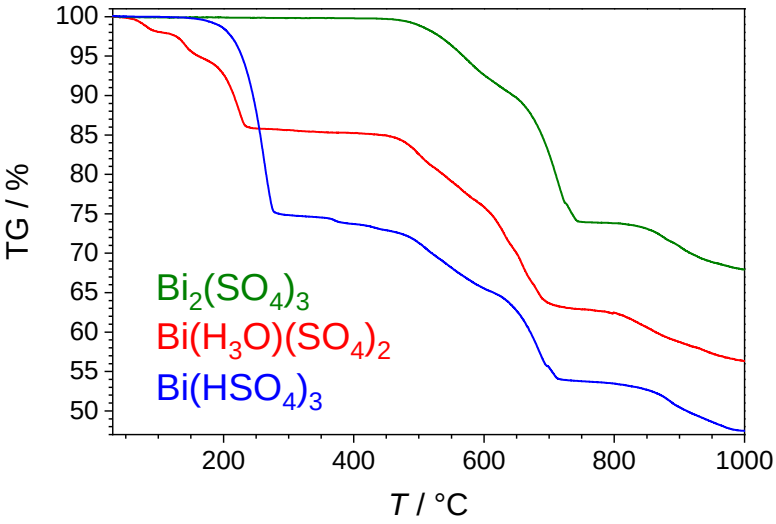

Fig. 7.2.9: TGA of $Bi(H_3O)(SO_4)_2$, $Bi(HSO_4)_3$ and $Bi_2(SO_4)_3$ under nitrogen atmosphere.

Thermal Properties

The thermal decomposition of $Bi(H_3O)(SO_4)_2$, $Bi(HSO_4)_3$ and $Bi_2(SO_4)_3$ was investigated by TGA under nitrogen atmosphere. The respective TG curves are displayed in Figure 7.2.9. Both $Bi(H_3O)(SO_4)_2$ and $Bi(HSO_4)_3$ decompose in a first step to $Bi_2(SO_4)_3$. Subsequently, $Bi_2(SO_4)_3$ decomposes in a four-step process towards Bi_2O_3 releasing SO_3 and O_2. In accordance with literature,[406–408] the intermediates could be identified gravimetrically as $Bi_2O(SO_4)_2$, $Bi_{26}O_{27}(SO_4)_{12}$ and $Bi_{14}O_{16}(SO_4)_5$. The formation of the first is confirmed by PXRD of a $Bi_2(SO_4)_3$ sample decomposed at 500°C (Figure D.2.13). For all three samples, the expected mass losses agree well with the observed values (Table D.2.11). Moreover, the final step towards Bi_2O_3 appears to be not completely finished at 1000°C.

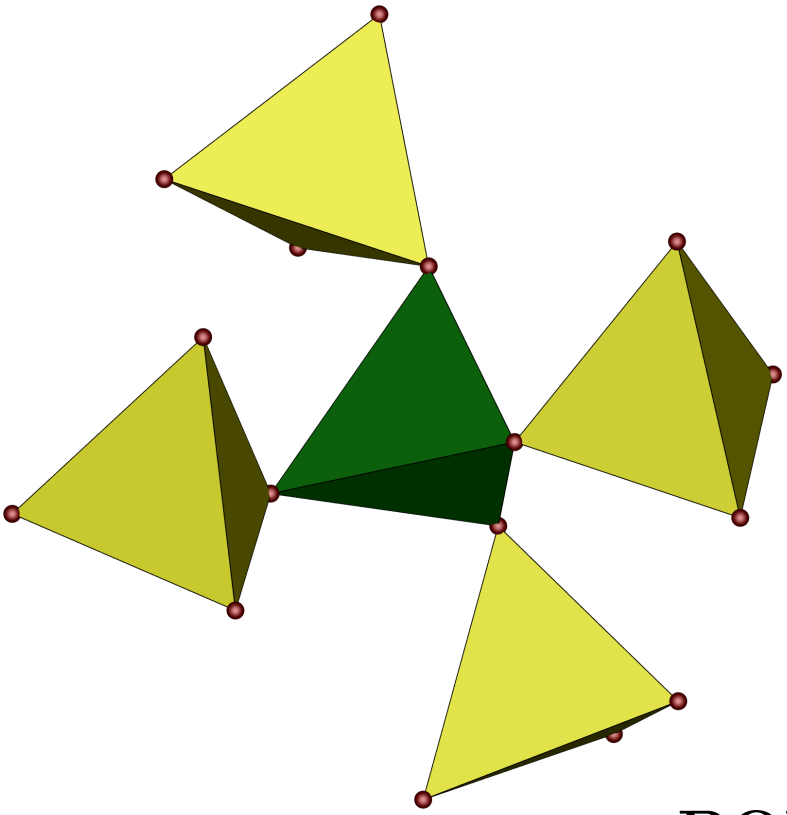

BOROSULFATES

8 Main Group Metal Borosulfates

Prior to this work, $Pb[B_2O(SO_4)_3]$[91] and $Pb[B_2(SO_4)_4]$[87] were the only main group cation borosulfates beyond alkali and alkali earth metals.[i] Within this chapter, the range is expanded by five new borosulfates, four with bismuth and one with antimony as cation. In both cases, the preparation was complicated by the stability of concurring crystallising sulfates described for the bismuth compounds in the previous chapter.
The results presented in the following were partly published in the journal *Angewandte Chemie*.[427] Other parts originate from the master thesis of Erich Turgunbajew.[428]

8.1 $Bi_2[B_2(SO_4)_6]$

As previously discussed, bismuth compounds often behave chemically similar to respective rare-earth compounds as both comprise similarly sized trivalent cations and thus, also adopt crystal structures found for the latter. Consequently, the existence of a bismuth borosulfate isotypic or related to the rare-earth borosulfates $R_2[B_2(SO_4)_6]$[92,95] was conceivable. In this section, the preparation, crystal structure and optical and thermal characterisation of this compound, $Bi_2[B_2(SO_4)_6]$, are reported.

Synthesis

Firstly, $Bi_2[CO_3]O_2$ was synthesised hydrothermally as a precursor according to the procedure reported by Huang et al.[429] 1 mmol $Bi(NO_3)_3 \cdot 5\,H_2O$ (Alfa Aesar, >98%) and 1.6 mmol $CO(NH_2)_2$ (Merck, >99.5%) were dissolved in 10 ml H_2O, transferred into 30 ml PTFE pressure digestion vessels[119] and heated in a compartment dryer at 200°C for six days. After the vessels naturally cooled to room temperature, the precipitates were separated and washed by centrifugation at 4000 rpm for 10 min with deionised water and ethanol and subsequently dried in a compartment dryer at 65°C for 24 h. Phase purity was confirmed by PXRD (Figure E.1.1). Then, 0.25 mmol $Bi_2[CO_3]O_2$ and 1.6 mmol $B(OH)_3$ were loaded into a silica glass ampoule (outer diameter: 1.2 cm, wall thickness: 0.1 cm) together with 0.5 ml oleum (VWR, 65% SO_3) and 0.5 ml H_2SO_4 (Merck, 95-97%). Subsequently, the ampoule was fused and - without further aging - placed in a muffle furnace applying the following temperature program: heating to 180°C with 100 K h^{-1}, holding the temperature for 36 h, and cooling down to room temperature

[i] Up to date, there are 21 alkali and 12 alkali earth metal cation borosulfates with reported crystal structures. This huge variety is due to their stability explained by the respective binary oxides being strong bases stabilising the strong acids SO_3 and B_2O_3 according to the Lux-Flood concept.[426]

with $6\,K\,h^{-1}$. After opening the ampoule previously frozen in liquid nitrogen, the sample was washed with acetonitrile (as detailed in section 2.6) and transferred into the glovebox. The product is sensitive towards moisture and hence was stored under inert conditions. $Bi_2[B_2(SO_4)_6]$ was obtained phase-pure according to the Rietveld refinement shown in Figure E.1.2 and table E.1.1 in the form of a colourless powder containing single-crystals.

Crystal Structure

$Bi_2[B_2(SO_4)_6]$ crystallises in the monoclinic crystal system with space group $C2/c$ (no. 15) and four formula units per unit cell in the $Gd_2[B_2(SO_4)_6]$ structure type and thus, isotypically to $R_2[B_2(SO_4)_6]$ (R =Y, La–Nd, Sm–Lu).[92,95] The unit cell is depicted in Figure 8.1.1a. Details can be found in Tables E.1.1 to E.1.3. The borosulfate anion depicted in Figure 8.1.2a is formed by a *vierer* ring of alternating corner-sharing borate and sulfate tetrahedra with the former further saturated by two sulfate tetrahedra. The BO_4, $S1O_4$ and $S2O_4$ tetrahedra can be considered regular with deviations from the tetrahedral symmetry of 0.3%, 0.3% and 0.1%, respectively. The borosulfate anion can be considered cyclosilicate-analogous - with a similar structural motif found for the mineral *eakerite* (Figure 1.1.2) - and alternatively described by a dimer of edge sharing $B(SO_4)_4$ supertetrahedra (Figure 8.1.2b), i.e. sorosilicate-analogous. The trivalent bismuth atoms are coordinated monodentately by eight sulfate groups - six of them are terminal ones and two are part of the *vierer* ring of the borosulfate anion. The Bi-O distances range between 233.9(2) and 257.3(2) pm resulting in a slightly distorted square antiprismatic coordination environment (Figure E.1.3). No influence of the stereochemical activity of the Bi^{3+} ion due to the lone pair effect is indicated by the ambiguous Bi-O distances (Figure 8.1.1b). However, the R_c value of 16 pm ($\epsilon = 0.064$) is significantly larger than the ones in the isotypic $R_2[B_2(SO_4)_6]$ of 7 ± 1 pm ($\epsilon = 0.03$) as shown in Figure E.1.4, thus, clearly indicating a stereochemical influence of the Bi^{3+} ion. In contrast to the compounds discussed in section 7.2, the assessment of this stereochemical activity based on the Bi-O distances is not possible showcasing the strength of the method of Balić-Žunić and Makovicky to quantify the lone pair effect. Further, the direction of the stereochemical activity indicated by the calculated location of the centroid coincides with the ELF results (Figure 8.1.3). The stereochemical activity is smaller than for $Bi(H_3O)(SO_4)_2$, $Bi(HSO_4)_3$ and $Bi_2(SO_4)_3$ - according to the eccentricity and the ELF results (Table 7.2.2 and Figure 7.2.5). The respective orbital overlap in the PDOS in Figure E.1.5 is in line with that.

The electrostatic reasonability of the crystal structure and all coordination numbers were confirmed by calculations based on the MAPLE concept (Tables E.1.4 and E.1.5).

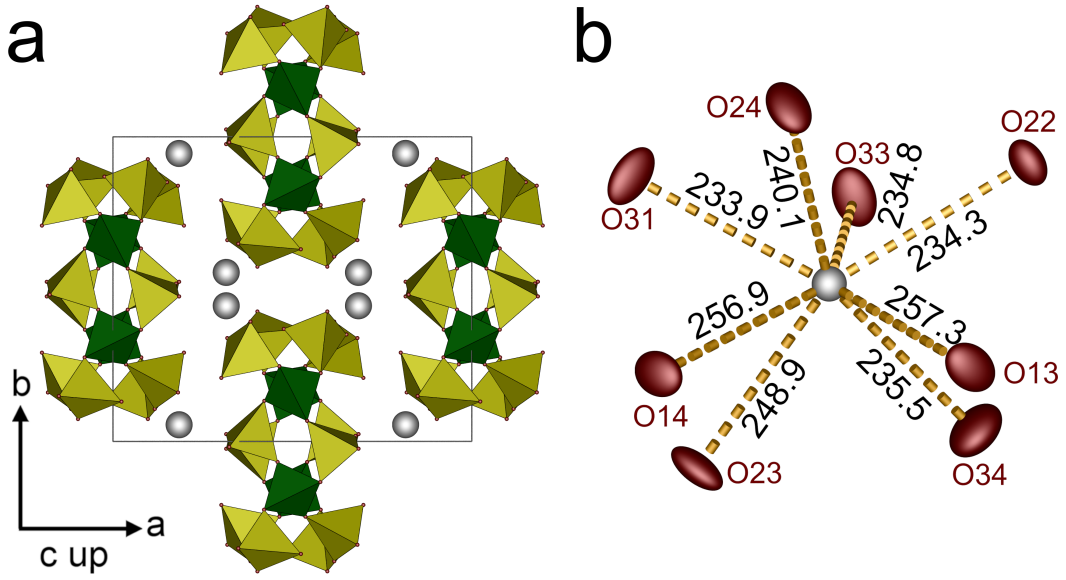

Fig. 8.1.1: (a) Unit cell of $Bi_2[B_2(SO_4)_6]$ and (b) the coordination environment of Bi^{3+} cations with the Bi-O distances labelled in pm: borate and sulfate tetrahedra are shown in green and yellow; oxygen atoms red, bismuth atoms grey; ellipsoids are shown at 80% probability (in (b)).

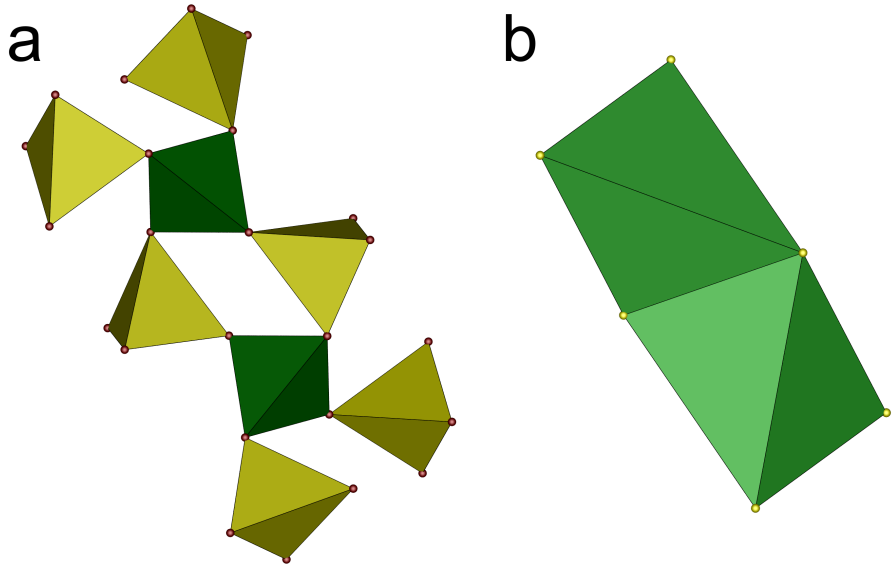

Fig. 8.1.2: The cyclosilicate-analogous borosulfate anion in $Bi_2[B_2(SO_4)_6]$ shown in (a) and the supertetrahedra representation in (b) showing edge sharing dimers of supertetrahedra (light green); borate and sulfate tetrahedra green and yellow; oxygen atoms red.

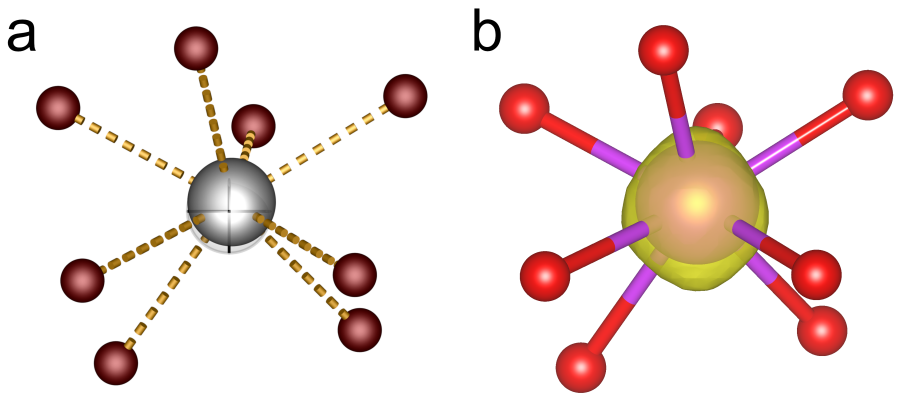

Fig. 8.1.3: The lone pair activity of $Bi_2[B_2(SO_4)_6]$ viewed along (100): In (a) the BiO_8 polyhedron including the centroid (semi-transparent octant) is shown; bismuth grey, oxygen red; in (b) the ELF results for $Bi_2[B_2(SO_4)_6]$ are depicted showing the same BiO_8 polyhedron; oxygen red, bismuth violet; the site symmetry of the Bismuth atom is 1.

Optical Properties

Infrared Spectroscopy

The IR spectrum of $Bi_2[B_2(SO_4)_6]$ depicted in Figure E.1.6 is in excellent agreement with the spectra reported for the isotypic rare-earth compounds $R_2[B_2(SO_4)_6]$.[95] Thus, the absorption bands of borate and sulfate tetrahedra occurring between 1400 and 400 cm^{-1} are not discussed in detail, here.

UV-Vis Spectroscopy

The powder reflectance spectrum of $Bi_2[B_2(SO_4)_6]$ is shown in Figure E.1.7 in the range from 200 to 800 nm. In accordance with the colourless powders, no absorption in the visible region is observed. Analogous to the analysis on page 153, the shoulder attributed to the A band was fitted using a Gaussian fit also shown in Figure E.1.7. Using this fit and the relationship of the s-p transitions of Bi^{3+} discussed on page 153, the A, B and C bands are located at 268 nm (4.63 eV), 240 nm (5.17 eV) and 223 nm (5.55 eV) for $Bi_2[B_2(SO_4)_6]$. According to the DFT calculations $Bi_2[B_2(SO_4)_6]$ exhibits a direct band gap with $E_g = 5.902$ eV. The total DOS is shown in Figure E.1.8. Due to the overlap of the s-p transitions and the fundamental absorption of the sample, this value could not be experimentally probed using a Tauc plot.

Thermal Analyses

According to the TGA result depicted in Figure 8.1.4, $Bi_2[B_2(SO_4)_6]$ decomposes above 370°C to $Bi_2(SO_4)_3$ and B_2O_3 in a first step and Bi_2O_3 and B_2O_3 in a second step accompanied by evaporation of SO_3 or SO_2, respectively. The experimental mass losses

noted in the graph agree to the expected ones.[ii] Similar to the three compounds in section 7.2, several processes appear to overlap between the first and the second step probably related to the formation of the intermediates $Bi_2O(SO_4)_2$, $Bi_{26}O_{27}(SO_4)_{12}$ and $Bi_{14}O_{16}(SO_4)_5$. No PXRD could be measured of the residue after the TGA measurement due to it being baked into the crucible. Taking the results presented in section 8.2 into account, this is presumably related to glass formation at these temperatures.

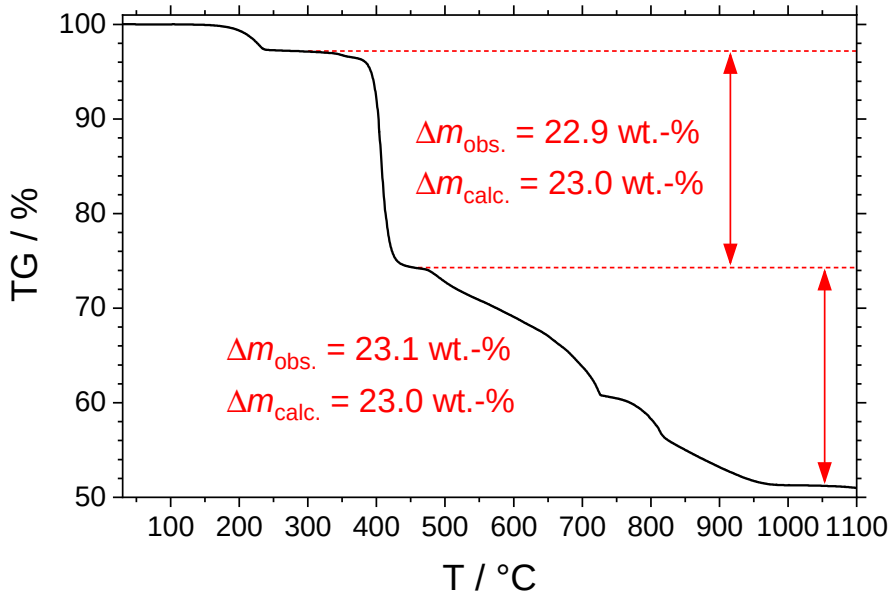

Fig. 8.1.4: Thermogravimetric analysis of $Bi_2[B_2(SO_4)_6]$

[ii] The step prior to this decomposition between 170°C and 240°C responsible for a mass loss of 2.9 wt.-% is due to the evaporation of excess sulfuric acid and thus, not related to the $Bi_2[B_2(SO_4)_6]$ sample.

8.2 BiX[B(SO$_4$)$_2$]$_4$ (X = H$_3$O$^+$, NO$_2^+$ and NH$_4^+$)

As already noted in section 1.6 and Figure 1.6.2, prior to this work, the only tectosilicate-analogous borosulfate with known crystal structure was Li[B(SO$_4$)$_2$].[79] It can be prepared by the thermal decomposition of the precursor Li[B(S$_2$O$_7$)$_2$]. The latter can be classified as unconventional 0D borosulfate comprising S-O-S bridges. In contrast to that, the four tectosilicate-analogous borosulfates presented in this and the next section were prepared directly, i.e. without a precursor, via solvothermal syntheses. Further, they comprise the higher charged Bi^{3+} and Sb^{3+} cations and larger X^+ cations (X = H$_3$O$^+$, NO$_2^+$ and NH$_4^+$) instead of the small and monovalent Li^+ cation in Li[B(SO$_4$)$_2$]. This is a first indication toward the high stability of this novel tectosilicate-analogous borosulfate anionic substructure present in MX[B(SO$_4$)$_2$]$_4$ (M = Bi, Sb, X = H$_3$O$^+$, NO$_2^+$ and NH$_4^+$.[iii] Additionally, CsK$_4$[B(SO$_4$)$_4$], Cs$_3$Na$_2$[B(SO$_4$)$_4$], and Cs$_3$Li$_2$[B(SO$_4$)$_4$] were the only borosulfates containing two different cations, prior to this work.[12] They all exhibit the same charge. Consequently, MX[B(SO$_4$)$_2$]$_4$ are the first borosulfates comprising two differently charged cations. Moreover, the crystal structure of the previously only tectosilicate-analogous borosulfate Li[B(SO$_4$)$_2$] comprising exclusively tetrahedral building units is closely related to *β-tridymite*. Accordingly, the borosulfates detailed in the following are the first tectosilicate-analogous representatives with non-tetrahedrally coordinated cations.

Syntheses

All three compounds, Bi(H$_3$O)[B(SO$_4$)$_2$]$_4$, Bi(NO$_2$)[B(SO$_4$)$_2$]$_4$ and Bi(NH$_4$)[B(SO$_4$)$_2$]$_4$, were synthesised solvothermally in the form of colourless powders containing single-crystals. The samples are phase-pure according to Figure E.2.1.

For Bi(H$_3$O)[B(SO$_4$)$_2$]$_4$, 0.123 mmol Bi$_2$[CO$_3$]O$_2$ - prepared as detailed above (page 159) - and 2.95 mmol B(OH)$_3$ (Merck, >99.5%) were ground together and - together with 1 ml oleum (VWR, 65% SO$_3$) - filled into a silica glass ampoule (length 15 cm, outer diameter: 1.2 cm, wall thickness: 0.1 cm), which was subsequently fused and – without further aging – placed in a muffle furnace applying the following temperature program: heating to 180°C with 50 K h^{-1}, holding the temperature for 10 h, and cooling down to room temperature with 6.25 K h^{-1}.

For Bi(NO$_2$)[B(SO$_4$)$_2$]$_4$, 0.234 mmol Bi(NO$_3$) · 5 H$_2$O (AlfaAesar, >99.999%)[iv] and 1.4 mmol B$_2$O$_3$ (Sigma–Aldrich, > 99%)[v] were ground together and filled into a silica glass ampoule. Then, 1 ml oleum (65% SO$_3$) were added. Subsequently, the ampoule

[iii] The sum formulae of the bismuth representatives are written as in the section's title. In general, multiple cations are ordered alphabetically according to the IUPAC recommendation.[430] Consequently, the monovalent cation is placed in front of the trivalent one in (NH$_4$)Sb[B(SO$_4$)$_2$]$_4$ in the next section.

[iv] In contrast to the syntheses in section 7.2, the educt was not dehydrated.

[v] Due to the hydration of B$_2$O$_3$ at ambient conditions resulting in a significant B(OH)$_3$ side phase, the B$_2$O$_3$ educt was stored in a porcelain crucible inside a compartment dryer at 180°C for several days prior to usage. This is valid throughout this thesis whenever B$_2$O$_3$ was used.

was fused and – without further aging – placed in a muffle furnace applying the following temperature program: heating to 180°C with 50 K h^{-1}, holding the temperature for 10 h, and cooling down to room temperature with 6.25 K h^{-1}.
For Bi(NH$_4$)[B(SO$_4$)$_2$]$_4$, 0.12 mmol Bi$_2$O$_3$ (> 99.5%, Riedel-de Haën), 0.24 mmol (NH$_4$)$_2$SO$_4$ (> 99.5%, Merck) and 1.44 mmol B$_2$O$_3$ were ground together and filled into a silica glass ampoule. Then, 1 ml oleum (65% SO$_3$) was added. The ampoule was fused and – without further aging – placed in a muffle furnace applying the following temperature program: heating to 180°C with 50 K h^{-1}, holding the temperature for 24 h, and cooling down to room temperature with 6.25 K h^{-1}.
Finally, after opening the ampoules previously frozen in liquid nitrogen, all samples were washed with acetonitrile (as detailed in section 2.6) and transferred into the glovebox. The products are sensitive towards moisture and hence, were stored under inert conditions.

Crystal Structures

Bi(H$_3$O)[B(SO$_4$)$_2$]$_4$, Bi(NO$_2$)[B(SO$_4$)$_2$]$_4$ and Bi(NH$_4$)[B(SO$_4$)$_2$]$_4$ all crystallise homeotypically in the tetragonal crystal system with space group $I\bar{4}$ (no. 82) and two formula units per unit cell representing a new structure type each (Figure 8.2.1). More information on the crystal structures can be found in Tables 8.2.1 and E.2.1 to E.2.6.

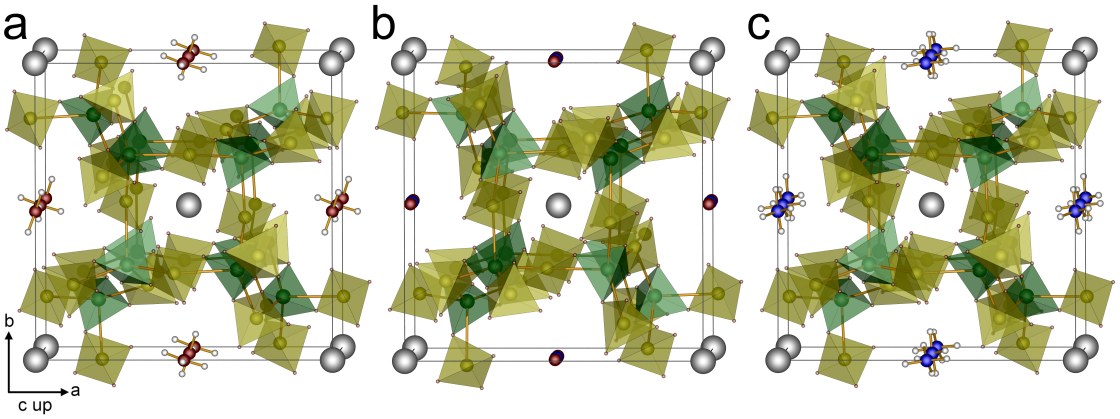

Fig. 8.2.1: Unit cells of (a) Bi(H$_3$O)[B(SO$_4$)$_2$]$_4$, (b) Bi(NO$_2$)[B(SO$_4$)$_2$]$_4$ and (c) Bi(NH$_4$)[B(SO$_4$)$_2$]$_4$: bismuth atoms grey, oxygen atoms red, boron atoms green, sulfur atoms yellow, nitrogen atoms blue, hydrogen atoms white; for the anionic substructure both the borate and sulfate and the B(SO$_4$)$_4$ supertetrahedra are shown simultaneously.

The anion consists of TX_4 supertetrahedra (T = B, X = SO$_4$) sharing all four corners with neighbouring ones yielding a network. Thus, BiX[B(SO$_4$)$_2$]$_4$ (X = H$_3$O$^+$, NO$_2^+$ and NH$_4^+$) can be considered tectosilicate-analogous. *Vierer* and *achter* rings perpendicular to unit cell axis c are formed giving rise for channels along c as depicted in Figure 8.2.2.[vi] The *vierer* ring channels host the bismuth, the *achter* ring channels the X^+ cations. The

[vi] To be precisely, the network can also be described by *achter* rings only. Each ring is connected to two further rings per spatial direction. The *vierer* rings are created by this connection.

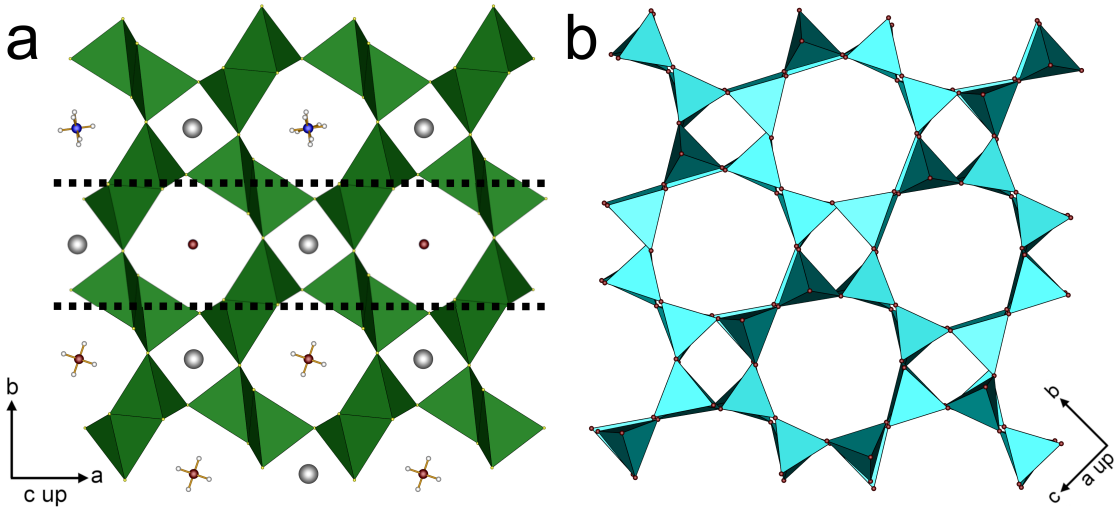

Fig. 8.2.2: (a) Channels of supertetrahedra (light green) shown as fragments from bottom to top for $Bi(H_3O)[B(SO_4)_2]_4$, $Bi(NO_2)[B(SO_4)_2]_4$ and $Bi(NH_4)[B(SO_4)_2]_4$ formed by *vierer* and *achter* rings compared to the analogous structural feature in the mineral *harmotome* $Ba_2Al_4Si_{12}O_{32} \cdot 12\,H_2O$[18] comprising AlO_4/SiO_4 tetrahedra (light blue) in (b): bismuth atoms grey, oxygen atoms red, sulfur atoms yellow, nitrogen atoms blue, hydrogen atoms white; oxygen atoms that are not part of the oxonium or nitronium ion are neglected in (a) while the barium cations are omitted in (b) for clarity.

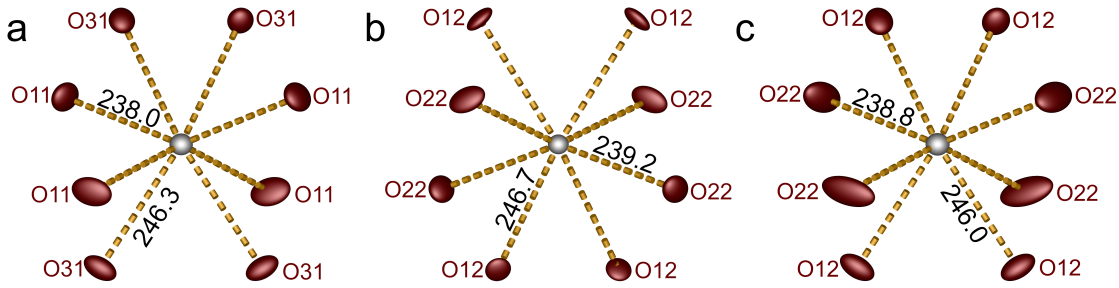

Fig. 8.2.3: Coordination environment of Bi^{3+} cations in (a) $Bi(H_3O)[B(SO_4)_2]_4$, (b) $Bi(NO_2)[B(SO_4)_2]_4$ and (c) $Bi(NH_4)[B(SO_4)_2]_4$ with the Bi-O distances labelled in pm; bismuth atoms grey, oxygen atoms red; ellipsoids are shown at 80% probability.

Tab. 8.2.1: Crystal data and structure refinements of Bi(H$_3$O)[B(SO$_4$)$_2$]$_4$, Bi(NO$_2$)[B(SO$_4$)$_2$]$_4$ and Bi(NH$_4$)[B(SO$_4$)$_2$]$_4$; the respective standard deviations are given in parentheses

	Bi(H$_3$O)[B(SO$_4$)$_2$]$_4$	Bi(NO$_2$)[B(SO$_4$)$_2$]$_4$	Bi(NH$_4$)[B(SO$_4$)$_2$]$_4$
CSD number	2025944		
M / g mol^{-1}	1039.72	1066.71	1038.74
Crystal size / mm^3	0.10 × 0.09 × 0.03	0.11 × 0.11 × 0.06	0.09 × 0.05 × 0.04
Temperature / K	200(2)	200(2)	250(2)
Crystal system		tetragonal	
Space group		$I\bar{4}$ (no. 82)	
a / pm	1185.7(1)	1190.81(1)	1187.5(1)
c / pm	814.86(9)	811.60(2)	813.6(1)
Volume / 10^6 pm^3	1145.7(3)	1150.87(4)	1147.2(2)
Z		2	
ρ_{calcd} / g cm^3	3.01	3.08	3.01
Absorption coefficient μ / mm^{-1}	8.58	8.55	8.57
F(000) / e	996	1020	996
Radiation; wavelength λ / Å		Mo-K_α; 0.71073	
Diffractometer		Bruker D8 Venture	
Θ range / °	2.429-32.489	2.419-34.968	2.426-39.982
Absorption correction		multi-scan	
Transmission (min; max)	0.3717; 0.4981	0.5954; 0.7493	0.6280; 0.7192
Index range h | k | l	±17 | ±17 | ±12	±19 | ±19 | ±13	±21 | ±21 | ±14
Reflections collected	11849	18890	28989
Independent reflections	1947	2382	3487
Obs. reflections [$I > 2\sigma(I)$]	1939	2362	3438
Refined parameters / restraints	111 / 3	109 / 0	113 / 12
R_{int}	0.039	0.043	0.074
R_1	0.017	0.016	0.020
wR_2	0.037	0.036	0.033
GOF	0.962	0.87	0.81
Residual e$^-$ density (max; min) / e^-Å^{-3}	1.36; -0.59	0.44; -0.49	0.90; -0.47

formed network TX_2 resembles the composition of tectosilicates such as SiO$_2$ and features found in naturally occurring silicates: adjacent *vierer* and *achter* rings – however in a different ratio – are known for pure silica *chabazite* prepared via a template-based synthesis with the sum formula SiO$_2$.[431] The mineral *harmotome* Ba$_2$Al$_4$Si$_{12}$O$_{32}$ · 12 H$_2$O[18] - already shown in Figure 1.1.2 - exhibits a network of AlO$_4$/SiO$_4$ tetrahedra comprising channels of adjacent *vierer* and *achter* rings resembling the topology found for the B(SO$_4$)$_4$ supertetrahedra in BiX[B(SO$_4$)$_2$]$_4$ (Figure 8.2.2).

When viewing the borate and sulfate tetrahedra individually, *achter* and 16*er* rings are formed. Each borate group shares four corners with sulfate groups which in turn share two corners with borate tetrahedra. All borate and sulfate tetrahedra can be considered regular with deviations of 0.34%, 0.35% and 0.31% for BO$_4$, 0.31%, 0.26% and 0.27% for S1O$_4$ and 0.17%, 0.15% and 0.13% for S2O$_4$ in Bi(H$_3$O)[B(SO$_4$)$_2$]$_4$, Bi(NO$_2$)[B(SO$_4$)$_2$]$_4$ and Bi(NH$_4$)[B(SO$_4$)$_2$]$_4$, respectively.

Charge compensation is achieved by trivalent bismuth cations coordinated by eight oxygen atoms stemming from monodentate sulfate tetrahedra resulting in distorted square antiprismatic coordination environments depicted in Figures 8.2.3 and E.2.2 as well as monovalent oxonium, nitronium and ammonium cations, respectively. The

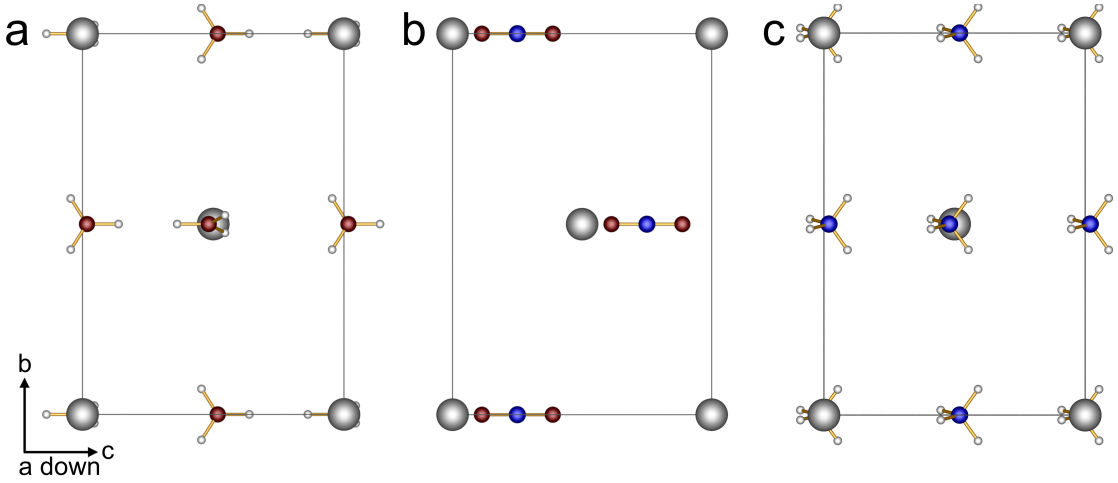

Fig. 8.2.4: Location of the oxonium, nitronium and ammonium cations in the unit cells of (a) Bi(H$_3$O)[B(SO$_4$)$_2$]$_4$, (b) Bi(NO$_2$)[B(SO$_4$)$_2$]$_4$ and (c) Bi(NH$_4$)[B(SO$_4$)$_2$]$_4$: The borosulfate anion is omitted for clarity; bismuth atoms grey, oxygen atoms red, nitrogen atoms blue, hydrogen atoms white; the figure shows the unit cell perpendicular to the viewing direction in Figure 8.2.1 in [100]; the respective occupation of the cation sites is discussed in the main text.

coordination environment of the bismuth cations is very similar to the one found in Bi$_2$[B$_2$(SO$_4$)$_6$] (Figures 8.1.1 and E.1.3). They occupy Wyckoff site 2a with site symmetry $\bar{4}$. Thus, the bismuth substructure can be described as distorted body-centred cubic (bcc) (Figures 8.2.1 and 8.2.4). In Bi(H$_3$O)[B(SO$_4$)$_2$]$_4$, the H$_3$O$^+$ ions are equally distributed with an occupation of 50% on site 4f along the channels (Figure 8.2.4a). Hence, the H$_3$O$^+$ cations are situated in two thirds of the octahedral voids of the bcc packing by the bismuth atoms, thus, achieving maximal distance between the two cation types. Two different orientations regarding the hydrogen atoms due to the local $\bar{4}$ symmetry are observed. The oxonium ions are held in place via medium strong hydrogen bonds[130] to two monodentate sulfate tetrahedra shown in Figure E.2.3a with a donor acceptor distance of 284(1) pm, longer than that reported for H$_3$O[B(SO$_4$)$_2$] (272 pm).[432]

In Bi(NO$_2$)[B(SO$_4$)$_2$]$_4$, the NO$_2^+$ cations located on the 2d sites do not show disorder. Their relative position towards the bismuth substructure can be described as a superimposed distorted bcc arrangement of nitrogen atoms shifted by a vector of $(\frac{1}{2}, 0, \frac{1}{4})$ with respect to the bismuth atoms. The interaction of the nitronium cations with the rest of the crystal structure can be considered to be purely ionic.

In Bi(NH$_4$)[B(SO$_4$)$_2$]$_4$, similar disorder is found for the NH$_4^+$ cations as for H$_3$O$^+$ in Bi(H$_3$O)[B(SO$_4$)$_2$]$_4$ with nitrogen and oxygen occupying equivalent sites - also with an occupation of 50%. There are no differing orientations for NH$_4^+$ due to its tetrahedral symmetry. The ammonium cations form two medium strong and two weak hydrogen bonds[130] to four monodentate sulfate groups as shown in Figure E.2.3b with donor acceptor distances of 297(1) and 329(1) pm. This is longer than for NH$_4$[B(SO$_4$)$_2$] (288-

294 pm)[80] and $(NH_4)_3[B(SO_4)_3]$ (276-299 pm)[85] both exhibiting four hydrogen bonds of moderate strength.

In all three crystal structures, the interatomic distances listed in Table E.2.7 are in good agreement with the sum of the respective ionic radii.[216] Especially, the Bi-O distances do not indicate any stereochemical influence of the lone pair effect (Figure 8.2.3). Further, both R_c and ϵ amount to 0 for all three compounds. Therefore, the lone pair effect can be considered to be quenched in these compounds. Comparing this to the very similar eightfold coordination environment of bismuth in $Bi_2[B_2(SO_4)_6]$ - clearly showing stereochemical activity as discussed above - the reason for the quenching in BiX[B(SO$_4$)$_2$]$_4$ might be found in the rigidity of the tectosilicate-analogous anionic substructure. Alternatively, this might be a symmetry effect due to the $\bar{4}$ site symmetry. Consequently, the structure either lacks the respective degrees of freedom for the lone pair effect or pseudo Jahn-Teller effect to take shape or the hypothetic energy gain from the distortion is outweighed by the energetic losses related to this distortion on the anionic side. In compliance to the discussions in sections 7.2 and 8.1, this is also confirmed by the ELF results shown in Figure E.2.4 and the merely fractional overlap of the bismuth 6s and the oxygen 2p states in the PDOS in Figure E.2.5. Both were calculated for Bi(H$_3$O)[B(SO$_4$)$_2$]$_4$ only. However, no significant differences for the two homeotypic compounds are expected. The VASP optimised structure shows slight changes for Bi(H$_3$O)[B(SO$_4$)$_2$]$_4$ compared to the SC-XRD structure determination. The bismuth atom is no longer occupying the special Wyckoff position 2a (0 0 0) but the 4e position (0 0 0.0028). Similar behaviour is reported for the lead chalcogenides showing locally distorted variants of the rock-salt structure instead of the undistorted variant as previously believed.[71,433] The VASP optimised structure exhibits R_c and ϵ values of 3 pm and 0.012, respectively. Consequently, the quenched lone pair effect is the result of the rigid 3D anion and not of the site symmetry.

The electrostatic reasonability of all three crystal structures and all coordination numbers were confirmed by calculations based on the MAPLE concept (Table E.2.8). In line with the previous discussion, the effective coordination numbers show no stereochemical influence of the Bi^{3+} lone pair effect with all values being close to one (Tables E.2.9 to E.2.11).

Optical Properties

Infrared Spectroscopy

The FT-IR spectra of Bi(H$_3$O)[B(SO$_4$)$_2$]$_4$, Bi(NO$_2$)[B(SO$_4$)$_2$]$_4$ and Bi(NH$_4$)[B(SO$_4$)$_2$]$_4$ are shown in Figure 8.2.5. The bands associated with the borosulfate anion are found in the range from 1400 to 400 cm^{-1}. There, all three measurements coincide. Above, the characteristic absorptions of the H$_3$O$^+$, NO$_2^+$ and NH$_4^+$ cations could be recorded. For oxonium, the O-H vibrations (centred at 2800 cm^{-1} and 1700 cm^{-1}) overlap with broad absorptions from sulfuric acid on the surface of the samples formed by the reaction

with ambient moisture.[419,420] However, the characteristic absorptions of nitronium at 2368 cm^{-1} (asymmetric stretching mode)[434] and ammonium at 3282 cm^{-1} (asymmetric stretching mode) and 1435 cm^{-1} (asymmetric deformation mode)[435] are well suited to distinguish the three compounds. This distinction is easier than by PXRD since their pattern show stark resemblance (Figure E.2.1). At lower wavenumbers, the ν_{asym}(S-O) around 1350 cm^{-1} appear. In accordance with the different set of S-O distances determined via SC-XRD tabulated in Table E.2.7, this vibration is split into two due to the different distances to bridging and terminal oxygen atoms. The broader range of distances in $Bi(H_3O)[B(SO_4)_2]_4$ and $Bi(NH_4)[B(SO_4)_2]_4$ due to oxygen atoms forming hydrogen bonds leads to a broadening of the respective bands in contrast to $Bi(NO_2)[B(SO_4)_2]_4$. They are followed by ν_{asym}(B-O) between 1190 and 1140 cm^{-1}, ν_{sym}(B-O) from 1040 to 990 cm^{-1} and ν_{sym}(S-O) at 920 – 830 cm^{-1}. Below, the bending vibrations δ_{asym}(O-S-O, O-B-O, S-O-B) occur. An overlap by Bi-O vibrations close to 400 cm^{-1} cannot be ruled out.

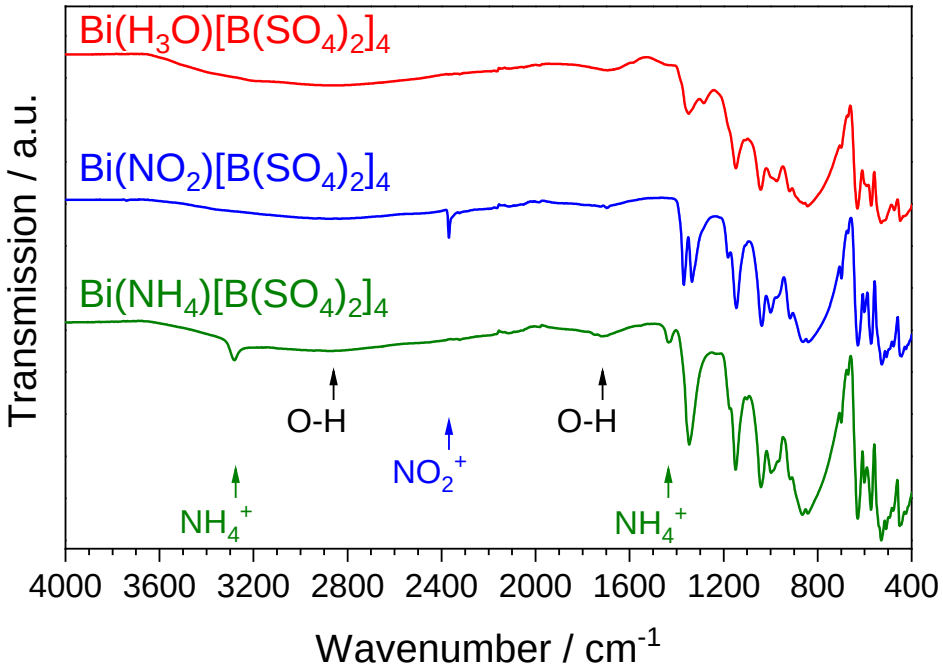

Fig. 8.2.5: Infrared spectra of $Bi(H_3O)[B(SO_4)_2]_4$, $Bi(NO_2)[B(SO_4)_2]_4$ and $Bi(NH_4)[B(SO_4)_2]_4$: The characteristic absorptions of the monovalent cations are marked.

UV-Vis Spectroscopy

The powder reflectance spectra of $Bi(H_3O)[B(SO_4)_2]_4$, $Bi(NO_2)[B(SO_4)_2]_4$ and $Bi(NH_4)[B(SO_4)_2]_4$ shown in Figure E.2.6 are in line with the colourless powders. Below 400 nm, the fundamental absorption due to the band gap of the compounds and the s-p transitions of trivalent bismuth overlap - as seen for the Bi^{3+} compounds in sections 7.2 and 8.1. The band gap of $Bi(H_3O)[B(SO_4)_2]_4$ was calculated using DFT to

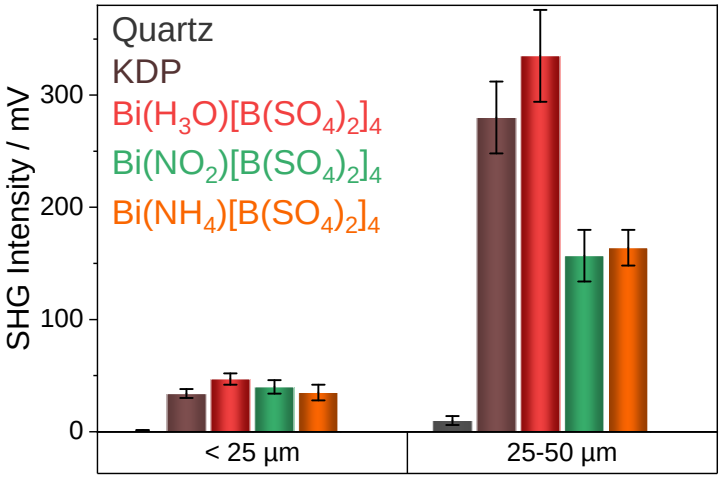

Fig. 8.2.6: Results of the SHG measurements on $Bi(H_3O)[B(SO_4)_2]_4$, $Bi(NO_2)[B(SO_4)_2]_4$ and $Bi(NH_4)[B(SO_4)_2]_4$ compared to quartz and KDP: the standard deviations are given in the form of error bars; control experiments with empty glass capillaries and centrosymmetric Al_2O_3 and $Bi_2[B_2(SO_4)_6]$ yielded 0 mV SHG intensities.

be indirect with an E_g value of 6.74 eV. The respective DOS is depicted in Figure E.2.8. For $Bi(NO_2)[B(SO_4)_2]_4$, the A band appearing as a shoulder could be fitted using a Gaussian fit - as shown above. Consequently, the A, B and C bands are located at 259 nm (4.78 eV), 231 nm (5.36 eV) and 215 nm (5.77 eV). Thus, the band gap energy cannot be experimentally confirmed due to the overlap with these s-p transition, again.

Nonlinear Optical Properties

$Bi(H_3O)[B(SO_4)_2]_4$, $Bi(NO_2)[B(SO_4)_2]_4$ and $Bi(NH_4)[B(SO_4)_2]_4$ were investigated using the powder SHG method. The results are shown in Figure 8.2.6 with respect to the particle size.[vii] On the one hand, these proved the absence of an inversion centre in accordance with the crystal structure determination by SC-XRD. On the other hand, all three compounds exhibit high SHG intensities comparable or even higher than the benchmark material KDP. The larger value for $Bi(H_3O)[B(SO_4)_2]_4$ can be explained by small side phases of centrosymmetric $Bi_2[B_2(SO_4)_6]$ in the other two samples reducing the overall SHG response.[160] Other works indicate that the SHG effect of borosulfates is dominated by the anion with the respective contributions decreasing from BO_3 over SO_4 to BO_4 building units.[77,436] In line with that the monovalent cations appear to have little influence on the SHG intensity.
At the time of the original publication,[427] $Bi(H_3O)[B(SO_4)_2]_4$ was the first SHG active borosulfate.

[vii] The respective fractions were prepared using 25 µm and 50 µm sieves inside the glovebox. Due to problems with the sieving, not the phase-pure samples of $Bi(NO_2)[B(SO_4)_2]_4$ and $Bi(NH_4)[B(SO_4)_2]_4$ used for all other characterisations could be utilised, but other samples containing small (< 5 wt.-%) $Bi_2[B_2(SO_4)_6]$ side phases.

Thermal Properties

The thermal decomposition of Bi(H$_3$O)[B(SO$_4$)$_2$]$_4$, Bi(NO$_2$)[B(SO$_4$)$_2$]$_4$ and Bi(NH$_4$)[B(SO$_4$)$_2$]$_4$ investigated by both TGA and TPXRD can be described by the following reaction equations:

$$\mathrm{Bi(H_3O)[B(SO_4)_2]_4} \longrightarrow \frac{1}{2}\,\mathrm{Bi_2[B_2(SO_4)_6]} + \frac{3}{2}\,\mathrm{B_2O_3} + \mathrm{H_2O(g)} + 5\,\mathrm{SO_3(g)} + \frac{5}{2}\,\mathrm{O_2(g)}$$

$$\mathrm{Bi(NO_2)[B(SO_4)_2]_4} \longrightarrow \frac{1}{2}\,\mathrm{Bi_2[B_2(SO_4)_6]} + \frac{3}{2}\,\mathrm{B_2O_3} + \mathrm{NO(g)} + 5\,\mathrm{SO_3(g)} + 3\,\mathrm{O_2(g)}$$

$$\mathrm{Bi(NH_4)[B(SO_4)_2]_4} \longrightarrow \frac{1}{2}\,\mathrm{Bi_2[B_2(SO_4)_6]} + \frac{3}{2}\,\mathrm{B_2O_3} + \mathrm{NH_3(g)} + 5\,\mathrm{SO_3(g)} + + \frac{9}{4}\,\mathrm{O_2(g)} + \frac{1}{2}\,\mathrm{H_2O\,(g)} \qquad \text{(I)}$$

$$\frac{1}{2}\,\mathrm{Bi_2[B_2(SO_4)_6]} \longrightarrow \frac{1}{2}\,\mathrm{Bi_2(SO_4)_3} + 2\,\mathrm{B_2O_3} + 1.5\,\mathrm{SO_3(g)} \qquad \text{(II)}$$

$$\frac{1}{2}\,\mathrm{Bi_2(SO_4)_3} + 2\,\mathrm{B_2O_3} \longrightarrow \frac{1}{2}\,\mathrm{Bi_2O(SO_4)_2} + 2\,\mathrm{B_2O_3} + \frac{1}{2}\,\mathrm{SO_3(g)} \qquad \text{(III)}$$

$$\frac{1}{2}\,\mathrm{Bi_2O(SO_4)_2} + 2\,\mathrm{B_2O_3} \longrightarrow \frac{1}{2}\,\mathrm{Bi_2O_3} + 2\,\mathrm{B_2O_3} + \mathrm{SO_3(g)} \qquad \text{(IV)}$$

Similar to the earlier discussion in sections 7.2 and 8.1, sulfuric acid on the surface of the sample is evaporated around 200°C prior to the first step. Between the last two reactions, the formation of the intermediates Bi$_{26}$O$_{27}$(SO$_4$)$_{12}$ and Bi$_{14}$O$_{16}$(SO$_4$)$_5$ are expected to overlap. The formation of Bi$_2$[B$_2$(SO$_4$)$_6$], Bi$_2$(SO$_4$)$_3$ and Bi$_2$O(SO$_4$)$_2$ could be confirmed by TPXRD in Figure 8.2.8 for Bi(NO$_2$)[B(SO$_4$)$_2$]$_4$. At higher temperatures, a loss of crystallinity presumably due to glass formation was observed. Again, this prevented the investigation of the residue from the TGA by PXRD. For Bi(NH$_4$)[B(SO$_4$)$_2$]$_4$, the experimental and expected mass losses during the TG measurement match well (Figure 8.2.7 and table E.2.12). Accordingly, Bi(NH$_4$)[B(SO$_4$)$_2$]$_4$ decomposes around 250°C. Similar decomposition temperatures can be expected for Bi(H$_3$O)[B(SO$_4$)$_2$]$_4$ and Bi(NO$_2$)[B(SO$_4$)$_2$]$_4$. For the latter, the decomposition can be placed between 170°C and 290°C according to the TPXRD.

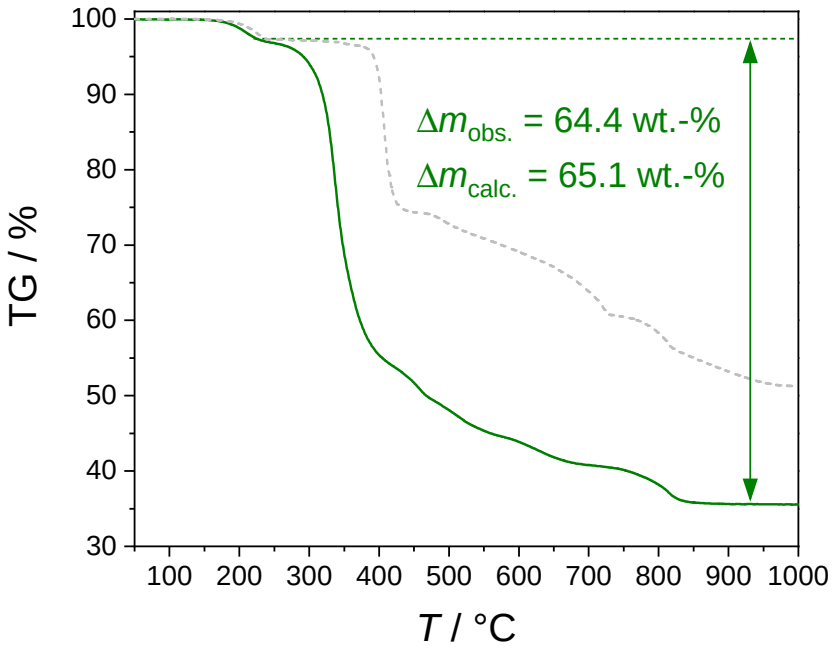

Fig. 8.2.7: Thermogravimetric analysis of $Bi(NH_4)[B(SO_4)_2]_4$: The experimental and expected mass loss is shown for the total decomposition towards Bi_2O_3 and B_2O_3; additionally, the TG signal of $Bi_2[B_2(SO_4)_6]$ is shown in dotted grey in order to show the coincidence at temperatures larger than 400°C emphasising the formation and decomposition of $Bi_2[B_2(SO_4)_6]$ in this temperature regime; the detailed mass losses are tabulated in Table E.2.12.

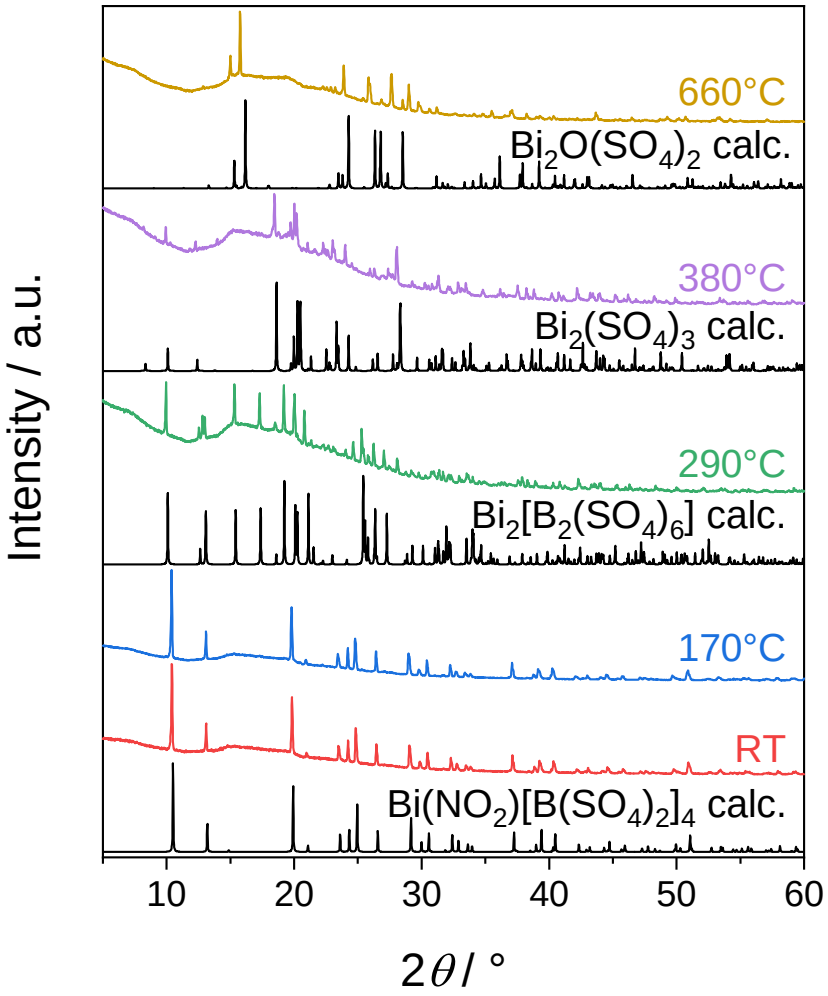

Fig. 8.2.8: TPXRD patterns of $Bi(NO_2)[B(SO_4)_2]_4$ compared to calculated patterns for $Bi_2[B_2(SO_4)_6]$ (section 8.1), $Bi_2(SO_4)_3$ (section 7.2) and $Bi_2O(SO_4)_2$.[408]

8.3 $(NH_4)Sb[B(SO_4)_2]_4$

In this section, the elemental diversity of borosulfates is expanded by the addition of another post-transition metal main group metal: antimony. Sb^{3+} and Bi^{3+} being both s^2 ions can behave very similar with the former most commonly exhibiting more expressed stereochemical activity related to the lone pair effect - as already seen for isotypic $Sb_2(SO_4)_3$ and $Bi_2(SO_4)_3$ (page 150). This leads to the question whether similar tectosilicate-analogous borosulfates might be possible when substituting Bi^{3+} by Sb^{3+}. Consequently, the first antimony borosulfate $(NH_4)Sb[B(SO_4)_2]_4$, its synthesis, its crystal structure and its optical properties are presented.

Synthesis

$(NH_4)Sb[B(SO_4)_2]_4$ was prepared solvothermally in the form of a colourless powder containing single-crystals. 0.13 mmol Sb_2O_3 (> 99%, ABCR), 0.26 mmol $(NH_4)_2SO_4$ and 1.58 mmol B_2O_3 were ground together and filled into a silica glass ampoule. Then, 1 ml oleum (65% SO_3) was added. The ampoule was fused and – without further aging – placed in a muffle furnace applying the following temperature program: heating to 180°C with 50 K h^{-1}, holding the temperature for 24 h, and cooling down to room temperature with 6.25 K h^{-1}. After opening the ampoules previously frozen in liquid nitrogen, the sample was washed with acetonitrile (as detailed in section 2.6) and transferred into an argon filled glovebox. The product is sensitive towards moisture and hence was stored under inert conditions. Phase-purity was confirmed by PXRD shown in Figure E.3.1.

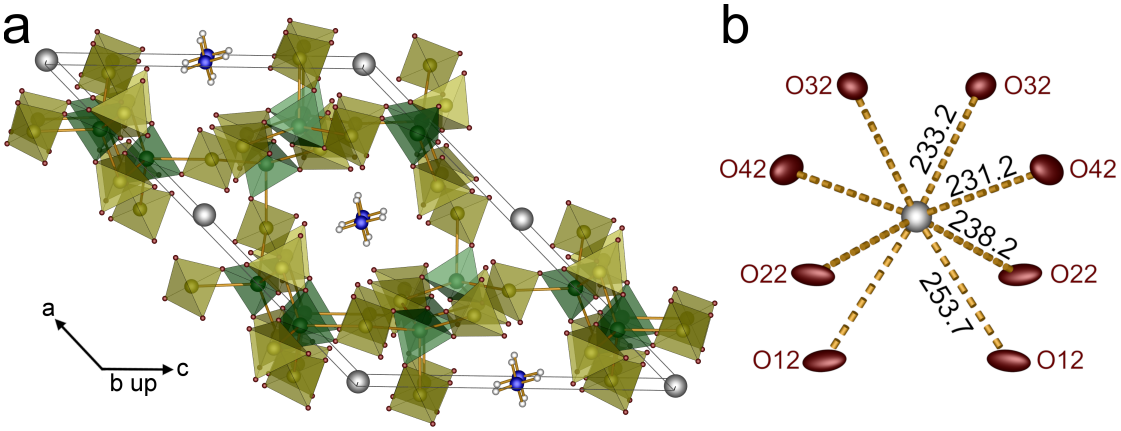

Fig. 8.3.1: (a) Unit cell of $(NH_4)Sb[B(SO_4)_2]_4$ viewed along $(0\bar{1}0)$ and (b) coordination environment of Sb^{3+} cations with Sb-O distances labelled in pm; the site symmetry of the antimony atom is 2; antimony atoms grey, oxygen atoms red, borate tetrahedra green, sulfate tetrahedra yellow, nitrogen atoms blue, hydrogen atoms white; for the anionic substructure both the borate and sulfate and the $B(SO_4)_4$ supertetrahedra are shown, simultaneously; ellipsoids are shown at 80% probability (in (b)).

Tab. 8.3.1: Crystal data and structure refinements of $(NH_4)Sb[B(SO_4)_2]_4$; the respective standard deviations are given in parentheses

M / g mol^{-1}	951.51
Crystal size / mm^3	0.08 × 0.07 × 0.03
Temperature / K	200(2)
Crystal system	monoclinic
Space group	$C2$ (no. 5)
a / pm	1667.82(7)
b / pm	811.40(3)
c / pm	1182.48(9)
β / °	134.793(1)
Volume / 10^6 pm^3	1135.60(11)
Z	2
ρ_{calcd} / g cm^3	2.78
Absorption coefficient μ / mm$^{\check{}}1$	2.11
F (000) / e	932
Radiation; wavelength λ / Å	Mo-K_α; 0.71073
Diffractometer	Bruker D8 Venture
Θ range / °	2.442-28.996
Absorption correction	multi-scan
Transmission (min; max)	0.6083; 0.6925
Index range h | k | l	±22 | −10/11 | ±16
Reflections collected	20608
Independent reflections	3023
Obs. reflections [$I > 2\sigma(I)$]	3005
Refined parameters / restraints	212 / 11
R_{int}	0.031
R_1	0.034
wR_2	0.092
GOF	1.36
Residual electron density (max; min) / e^-Å^{-3}	0.97; -1.26

Crystal Structure

$(NH_4)Sb[B(SO_4)_2]_4$ crystallises in a new structure type in the monoclinic crystal system with space group $C2$ (no. 5) and two formula units per unit cell (Figure 8.3.1). More details are found in Tables 8.3.1, E.3.1 and E.3.2. The tectosilicate-analogous borosulfate anion in $(NH_4)Sb[B(SO_4)_2]_4$ is very similar to the one in $Bi(NH_4)[B(SO_4)_2]_4$ also comprising *vierer* and *achter* rings of $[B(SO_4)_4]$ supertetrahedra forming channels along [010] that host the trivalent antimony and monovalent ammonium cations (Figure 8.3.2a). The sulfate and borate tetrahedra can be considered regular with deviations of 0.1 to 0.3% and 0.3%, respectively. Sb^{3+} - located on Wyckoff site 2*a* with site symmetry 2 - is distorted square antiprismatically coordinated by eight oxygen atoms stemming from monodentate sulfate groups. The coordination environment is depicted in Figures 8.3.1 and E.3.2. In contrast to $Bi(NH_4)[B(SO_4)_2]_4$, there are four sets of Sb-O distances - compared to only two for the Bi-O distances - ranging from 231 to 252 pm (sum of ionic radii: 228 pm,[265] Table E.3.3). This indicates stereochemical activity and is confirmed - as shown in Figure E.3.3 - by the significantly larger R_c of 13 pm and $\epsilon = 0.053$ ($R_c = 0$, $\epsilon = 0$ for $Bi(NH_4)[B(SO_4)_2]_4$) as well as the effective coordination numbers in Table E.3.5 in line with the discussion in section 7.2. Thus, the lone pair effect is

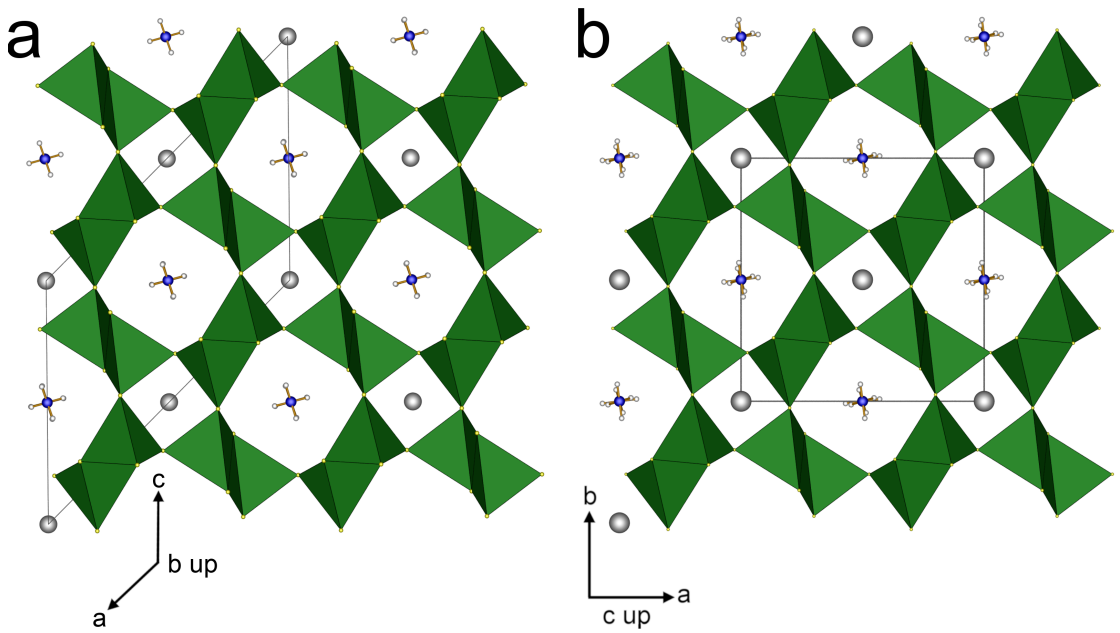

Fig. 8.3.2: Comparison of supertetrahedra channels in (a) $(NH_4)Sb[B(SO_4)_2]_4$ and (b) $Bi(NH_4)[B(SO_4)_2]_4$ including the respective unit cells indicating the group-subgroup relationship detailed in the main text; antimony and bismuth atoms grey, sulfur yellow, supertetrahedra light green, nitrogen atoms blue, hydrogen atoms white.

clearly expressed for $(NH_4)Sb[B(SO_4)_2]_4$ in contrast to the quenched lone pair effect in $Bi(NH_4)[B(SO_4)_2]_4$. Sb^{3+} is a $5s^2$ ion and Bi^{3+} a $6s^2$ ion. Therefore, the lone pair effect is usually more pronounced in the former - as already seen for $Sb_2(SO_4)_3$ and $Bi_2(SO_4)_3$ on page 150 - due to lower relativistic stabilisation of the s electrons.[70] However, it is small in $(NH_4)Sb[B(SO_4)_2]_4$ compared to $Sb_2(SO_4)_3$. This might originate from the rigid tectosilicate-analogous framework of the borosulfate anion. Further charge balance is achieved by monovalent ammonium cations. There is positional disorder of two NH_4^+ sites with occupation factors of 82% and 18%, respectively. The larger value for the $N1H_4^+$ group can be explained by the hydrogen bonding situation shown in Figure E.3.4. All hydrogen bonds occur towards monodentate sulfate groups. Both ammonium groups form two medium strong and two weak hydrogen bonds[130] each with donor-acceptor distances of 294(1) and 327(1) pm for $N1H_4^+$, and 296(2) and 336(3) pm for $N2H_4^+$. Consequently, there is slightly stronger bonding interaction between the borosulfate anion and $N1H_4^+$, thus, explaining the larger occupancy for this variant. The reason for this can be found in the stereochemical activity of the Sb^{3+} cation affecting the borosulfate anion and therefore, resulting in two differently bonded ammonium positions within the crystal structure. In other words, $N1H_4^+$ experiences stronger and $N2H_4^+$ weaker hydrogen bonding than the ammonium cation in $Bi(NH_4)[B(SO_4)_2]_4$, in which positional disorder with 50% occupation was found. The interatomic distances listed in Table E.3.3 are in good agreement with the sum of the respective ionic radii.[216,265] The electrostatic

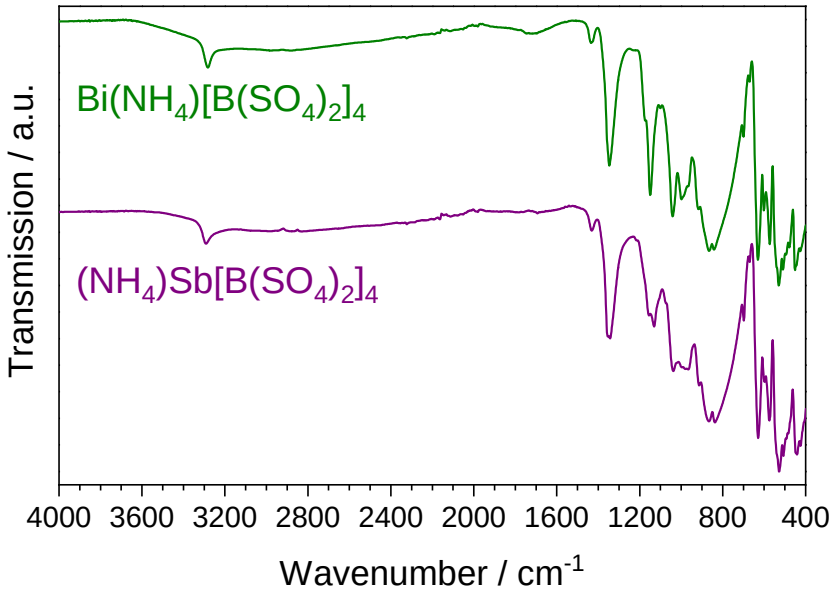

Fig. 8.3.3: Infrared spectrum of $(NH_4)Sb[B(SO_4)_2]_4$ compared to $Bi(NH_4)[B(SO_4)_2]_4$.

reasonability and all coordination numbers were confirmed by calculations based on the MAPLE concept (Tables E.3.4 and E.3.5).
The crystallographic relationship between $Bi(NH_4)[B(SO_4)_2]_4$ and $(NH_4)Sb[B(SO_4)_2]_4$ - the approximate coincidence of both crystal structures becomes obvious by comparing the channels of supertetrahedra displayed in Figure 8.3.2 - can be described by a group-subgroup relation. The lower symmetric (hettotype) $(NH_4)Sb[B(SO_4)_2]_4$ can be derived by a symmetry reduction of the aristotype $Bi(NH_4)[B(SO_4)_2]_4$ via the *translationsgleiche* transition $(t2)$ $-\mathbf{a}-\mathbf{b}$, $\mathbf{c}$, $\mathbf{b}$ including the change of centring from I to C following the Bärnighausen formalism (Figure E.3.5).[298,299] This symmetry decent provides the necessary additional degrees of freedom for the lone pair or pseudo Jahn-Teller effect to take shape by reducing the local symmetry of $\bar{4}$ for bismuth to 2 for antimony as discussed above.

Optical Properties

Infrared Spectroscopy

The infrared spectrum of $(NH_4)Sb[B(SO_4)_2]_4$ is shown in Figure 8.3.3 in comparison to $Bi(NH_4)[B(SO_4)_2]_4$. Both spectra are very similar. Again, the presence of the ammonium cation is confirmed by the presence of the characteristic bands at 3290 and 1433 cm^{-1}.[435] The assignment of the absorption bands related to the borosulfate anion between 1400 and 400 cm^{-1} for $Bi(NH_4)[B(SO_4)_2]_4$ on page 169 can be adopted. Due to the overlap of the related bands close to 400 cm^{-1}, the influence of the shorter Sb-O compared to the Bi-O distances cannot be seen in the spectra.

Nonlinear Optical Properties

$(NH_4)Sb[B(SO_4)_2]_4$ was also investigated with the powder SHG method. In line with the non-centrosymmetric space group determined by SC-XRD, the results in Figure 8.3.4 prove the absence of an inversion centre. Further, SHG intensities comparable to the benchmark KDP could be measured. In contrast to $Bi(NH_4)[B(SO_4)_2]_4$, the $(NH_4)Sb[B(SO_4)_2]_4$ sample shows a larger SHG response. This might be related to the stereochemical activity of Sb^{3+} causing less symmetric SbO_8 building units.[viii] The positive effect of s^2 cations and their lone pair effect on the SHG effect is well known.[106,108] The SHG activity of the borosulfate anion - presumably dominating the total SHG signal - can be expected to be almost equal for $Bi(NH_4)[B(SO_4)_2]_4$ and $(NH_4)Sb[B(SO_4)_2]_4$ since their anions differ only slightly.

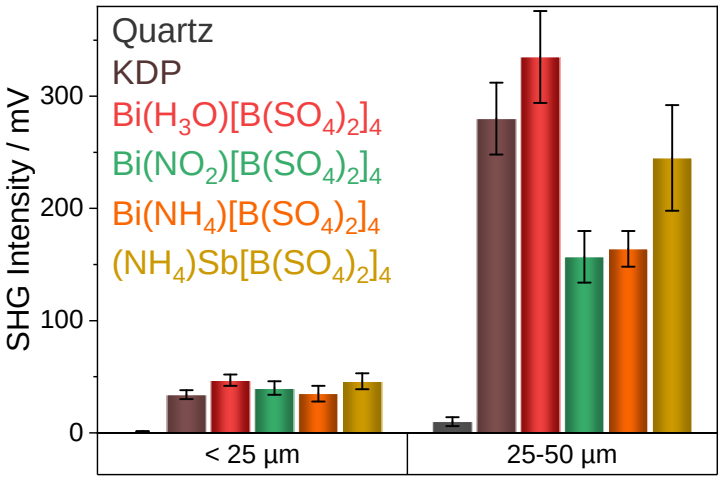

Fig. 8.3.4: Results of the SHG measurement on $(NH_4)Sb[B(SO_4)_2]_4$ compared to quartz KDP, $Bi(H_3O)[B(SO_4)_2]_4$, $Bi(NO_2)[B(SO_4)_2]_4$ and $Bi(NH_4)[B(SO_4)_2]_4$: the standard deviations are given in the form of error bars; control experiments with empty glass capillaries and centrosymmetric Al_2O_3 yielded 0 mV SHG intensities.

[viii] However, the presence of the SHG inactive side phase $Bi_2[B_2(SO_4)_6]$ in the $Bi(NH_4)[B(SO_4)_2]_4$ sample prevents the exact comparison. The values for $Bi(NH_4)[B(SO_4)_2]_4$ can be expected to be underestimated.

9 Transition Metal Borosulfates

Multiple borosulfates with the general sum formula $M[B_2(SO_4)_4]$ are known. As early as 1962, Schott and Kibbel reported the existence of $M[B_2(SO_4)_4]$ (M = Mg, Ca, Sr, Ba, Mn, Co, Ni, Cu, Zn, Cd, Hg)[73] - however, without any structural investigation. Recently, the polymorphism of these compounds, namely for $M[B_2(SO_4)_4]$ (M = Mg, Co, Ni, Zn) was investigated by Netzsch et al.[83] and Pasqualini et al.[89] either both experimentally and based on quantum chemical calculations or merely the latter, respectively. Up to date, four structure types were reported for these compounds. All comprise phyllosilicate-analogous borosulfate anions formed by adjacent *zwölfer* and *vierer* rings. $Ca[B_2(SO_4)_4]$ crystallises in its own structure type.[84] All compounds showing polymorphism adapt both a structure type described as "cation between layer" crystallising in space group $C2/c$ and another one denoted "cation within layer" crystallising in space group $P2_1/n$. An example is depicted in Figure 9.0.1. To be precisely, the latter can be distinguished into two homeotypic structure types merely differing in the orientation of one sulfate tetrahedron (Figure F.0.1). In contrast, the borosulfates $Sr[B_2(SO_4)_4]$ and $Ba[B_2(SO_4)_4]$ comprise inosilicate-analogous anions.[85,86] Based on the data by Netzsch et al.[83] and Pasqualini et al.,[89] Figure 9.0.2 was created showing the polymorphism, the respective structure types and the stability of the polymorphs with respect to each other for $M[B_2(SO_4)_4]$ (M = Co, Mg, Ni, Zn, Mn, Ca).
Parts of the results presented in this chapter were published in the journal *Dalton Transactions*.[437]

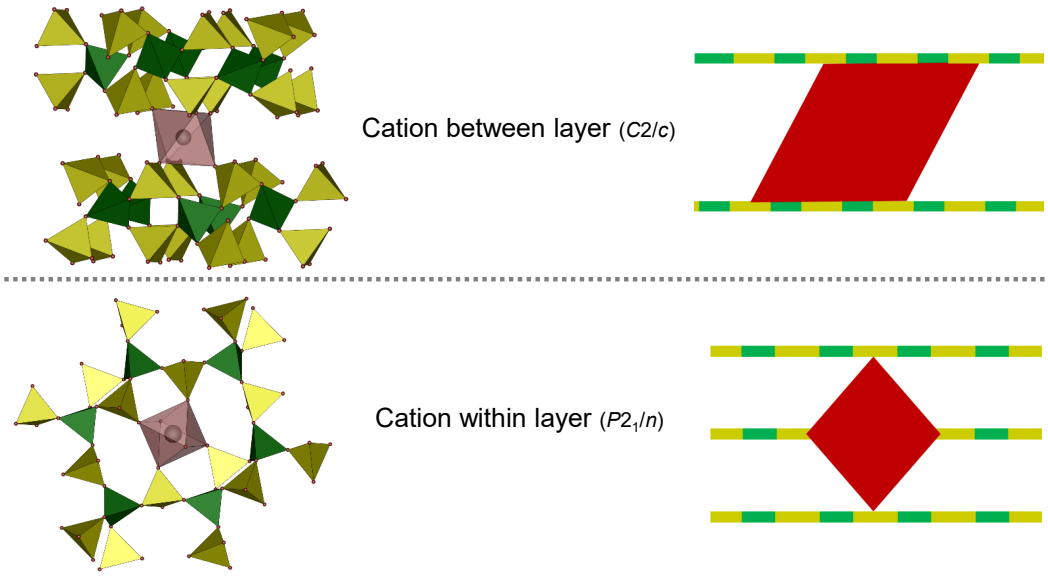

Fig. 9.0.1: Examples for the "cation between layer" and the "cation within layer" structure types of $M[B_2(SO_4)_4]$ borosulfates: This graph is the legend for Figure 9.0.2; as examples for both structure types depicted as pictograms on the right α-Co$[B_2(SO_4)_4]$ and β-Co$[B_2(SO_4)_4]$ taken from [83] are shown on the left.

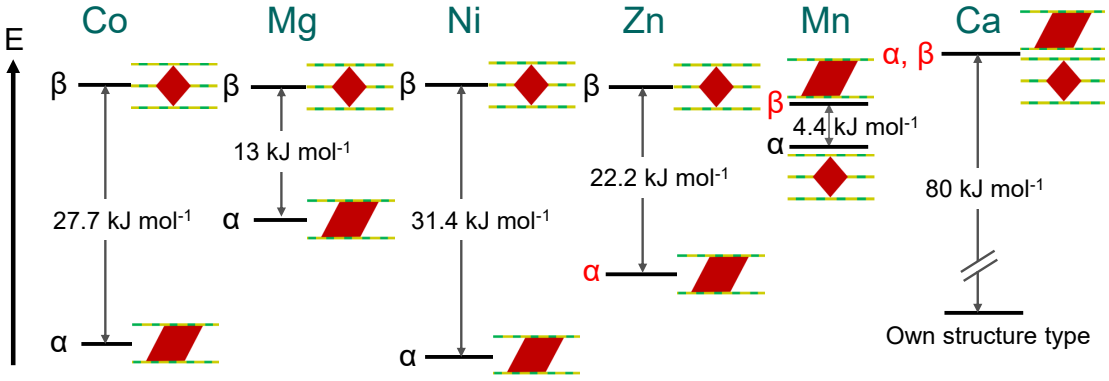

Fig. 9.0.2: Polymorphism of the borosulfates with the general formula $M[B_2(SO_4)_4]$: The metals M are given on top. Below the differences in total electronic energies are displayed as they can be found in literature.[83,89] In all cases, the polymorphs were labelled α and β with decreasing stability. Black letters symbolise experimental crystal structures,[82–84,88,89,438] red indicate that these phases were predicted by DFT, but not yet experimentally found. The pictograms explained in Figure 9.0.1 indicate if either the "cation between layer" or "cation within layer" structure is adapted. The further discrimination between the homeotypic "cation within layer" structure types is neglected.

9.1 $Cd[B_2(SO_4)_4]$

In the commonly used 18-column version of the periodic table, cadmium is nominally a member of the group of transition metals. However, its properties are very often similar to the ones of main group metals due to the filled d orbital, i.e. the lack of valence d electrons.[439] This ambiguity is best reflected by Sanderson's double-appendix periodic table,[440] shown in Figure 9.1.1, placing the zinc group including cadmium in the second main group. Therefore, $Cd[B_2(SO_4)_4]$ is the perfect borosulfate to link the unambiguous main group compounds discussed in the previous chapter and the unambiguous transition metal copper compounds that are following below.
The existence of $Cd[B_2(SO_4)_4]$ was reported as early as 1962.[73] However, up to date, the crystal structure of this compound was not known raising the question whether $Cd[B_2(SO_4)_4]$ adapts a structure type similar to the respective borosulfates of the neighbour zinc or a main group metal like lead or magnesium.

Synthesis

$Cd[B_2(SO_4)_4]$ was synthesised solvothermally starting from 0.5 mmol CdO (Fluka, > 99%) and 1.25 mmol B_2O_3 (Sigma–Aldrich, > 99%) and grinding the educts together, loading them into a silica glass ampoule (length 15 cm, outer diameter: 1.2 cm, wall thickness: 0.1 cm) together with 1 ml oleum (VWR, 65% SO_3). Subsequently, the ampoule was fused and placed in a muffle furnace applying the following temperature program: heating to 300°C with 100 K h^{-1}, holding the temperature for 60 h, and cooling down to room temperature with 100 K h^{-1}. The sample was washed (as detailed in section 2.6) and was transferred into the glovebox. The product is sensitive towards moisture and hence was stored under inert conditions. Even minimal quantities of H_2O lead to a degradation of $Cd[B_2(SO_4)_4]$ towards $CdSO_4 \cdot H_2O$ (Figure F.1.1).[i] The PXRD and Rietveld refinement confirmed the presence of phase-pure $Cd[B_2(SO_4)_4]$ (Figure 9.1.2 and table F.1.1). Further, colourless crystals were obtained (Figure F.1.2). Reducing the SO_3 content by the use of 0.5 ml H_2SO_4 and 0.5 ml oleum (65% SO_3) also yielded single-crystals of $Cd[B_2(SO_4)_4]$ with a simultaneous drastic reduction of the yield. Further, the decrease of the synthesis temperature to 180°C or 250°C yielded $Cd[B_2(SO_4)_4]$ alongside a yet unidentified side phase according to PXRD (Figure F.1.3). Interestingly, the sample prepared at 180°C contained single-crystals of both $Cd[B_2(SO_4)_4]$ and $Cd[S_2O_7]$.[441] However, after washing the side phase in the PXRD is not $Cd[S_2O_7]$.

Crystal Structure

$Cd[B_2(SO_4)_4]$ crystallises in the monoclinic crystal system with space group $P2_1/n$ (no. 14) and two formula units per unit cell in the $Mn[B_2(SO_4)_4]$ structure type (Ta-

[i] For example, such minimal water intake could be adhesive moisture on the polymer lids used to cover the glass sample tubes inside the glovebox. Consequently, the sample tubes were covered using Parafilm stored inside the glovebox.

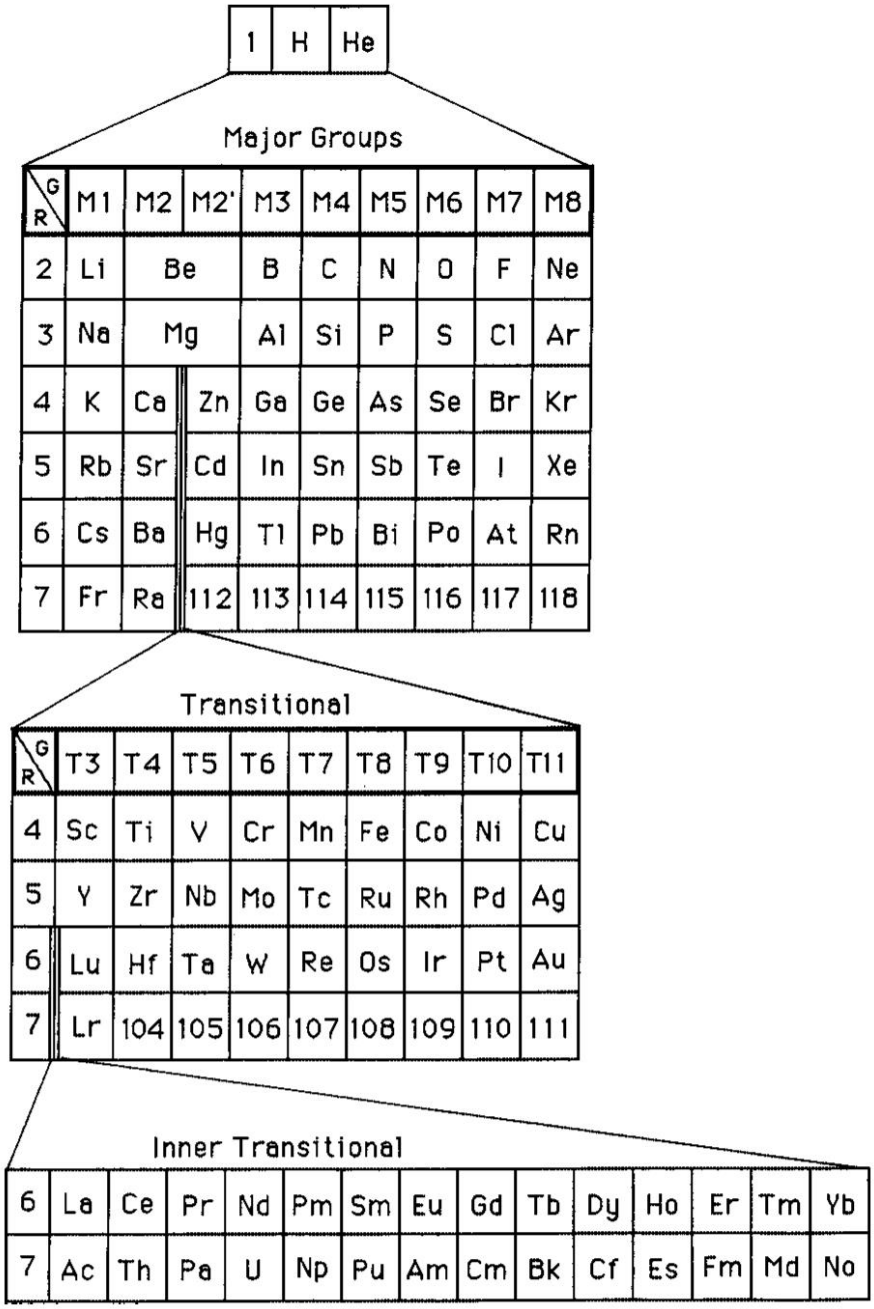

Fig. 9.1.1: An updated version of Sanderson's double-appendix periodic table[440] taken from [439] showing the insertion of the d block and f block elements into the "classical" 8-column version of the periodic table as two appendices and the proper location of the Zinc group below Magnesium.

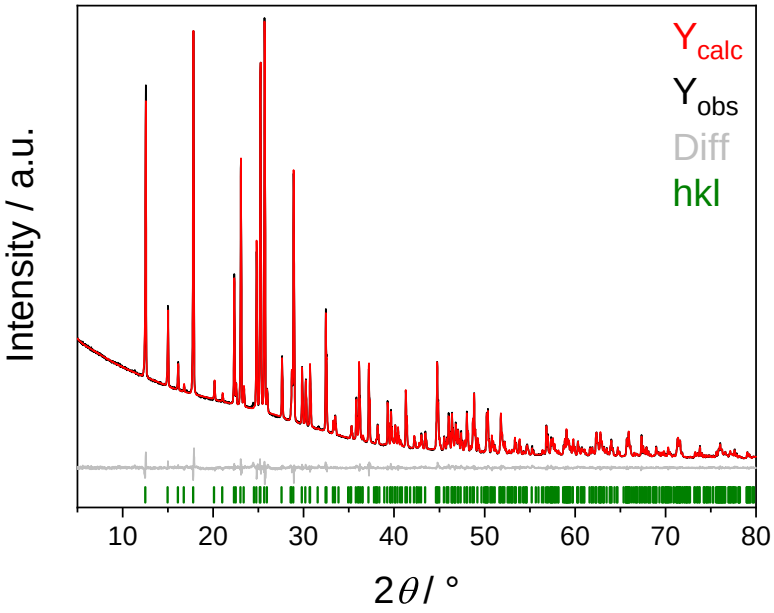

Fig. 9.1.2: Rietveld refinement on $Cd[B_2(SO_4)_4]$.

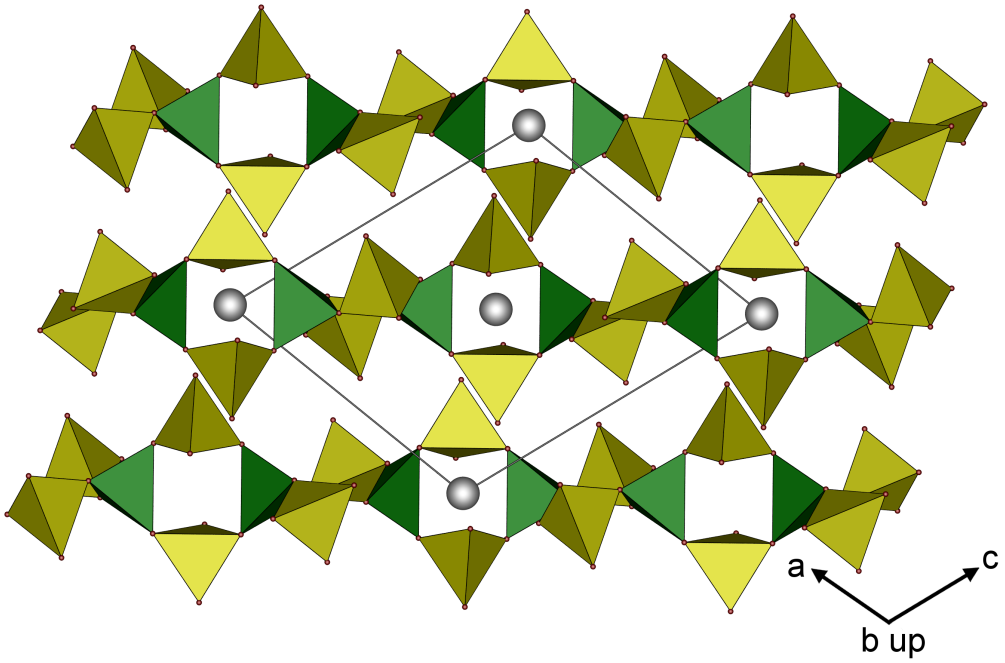

Fig. 9.1.3: Unit cell of $Cd[B_2(SO_4)_4]$ viewed along $[010]$; borate tetrahedra green, sulfate tetrahedra yellow, cadmium cations grey, oxygen atoms red; the $^{2}_{\infty}[B(SO_4)_{4/2}]^-$ anion layers are shown in side view.

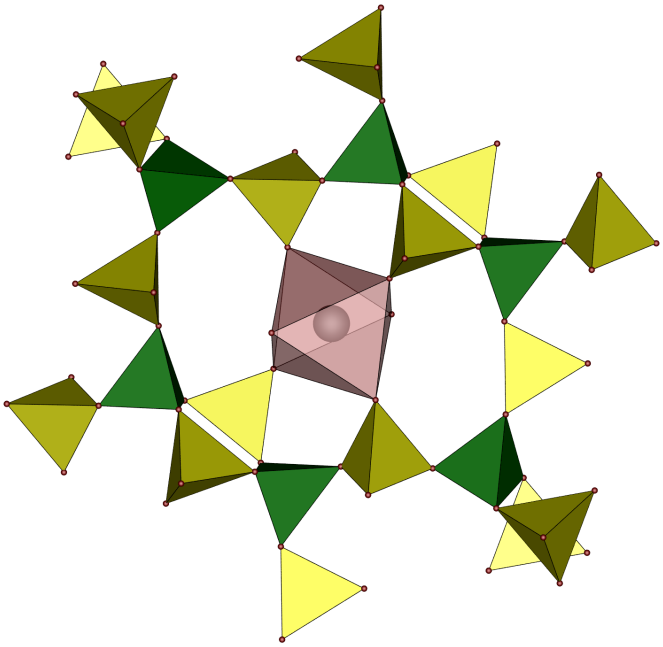

Fig. 9.1.4: Octahedral coordination environment of the Cd^{2+} cations (grey) in $Cd[B_2(SO_4)_4]$ and the location in the *zwölfer* ring; the two additional oxygen atoms belong to the anion layers above and below, respectively; borate tetrahedra green, sulfate tetrahedra yellow, oxygen atoms red; the fact that $Cd[B_2(SO_4)_4]$ crystallises isotypic to $Mn[B_2(SO_4)_4]$ can be seen in comparison to Figure F.0.1.

bles F.1.2 to F.1.4 and Figure 9.1.3). The borosulfate anion forms exclusively $B(SO_4)_4$ supertetrahedra. The supertetrahedra share alternately edges and corners forming *sechser* rings and dimers (Figure F.1.4). Consequently, the anion can be classified as phyllosilicate-analogous. More precisely, the anion is described by the Niggli formula $\{^2_\infty[B(SO_4)_{2/2}{}^e\, B(SO_4)_{2/2}{}^c]^-\}$[ii] by considering the supertetrahedron $B(SO_4)_4$ as building unit.[83] By looking at the individual tetrahedra, the layers comprise *zwölfer* and *vierer* rings. Each *zwölfer* ring is connected to four other *zwölfer* rings directly and to another two via *vierer* rings. The silicate-analogy can be demonstrated by the comparison to the mineral *manganpyrosmalite* (Figure 1.1.2) comprising an anionic substructure formed by *zwölfer* and *vierer* rings as well as additional *sechser* rings. So far, no anion comprising exclusively *zwölfer* and *vierer* rings has been observed in silicates.

The Cd^{2+} cation is octahedrally coordinated by six oxygen atoms, i.e. monodentately by six sulfate tetrahedra (Figure 9.1.4). Four sulfate moieties belong to one anion layer with the cation inside the *zwölfer* ring and the residual two belong to the layers above and below, respectively. Consequently, a network is formed. The borate and sulfate tetrahedra can all be classified as regular with deviations from the tetrahedral symmetry of 0.46%, 0.13% and 0.57% for $B1O_4$, $S1O_4$ and $S2O_4$, respectively. The Cd-O distances ranging from 222.9(3) to 230.0(2) pm are reasonably close to the sum of ionic radii (220 pm).[216]

[ii] e = edge sharing, c = corner sharing

The deviation from the octahedral symmetry amounts to 6.1%. This value differs not significantly from isotypic $Mn[B_2(SO_4)_4]$ ($\Delta_{octa} = 7.9\%$) or homeotypic $Zn[B_2(SO_4)_4]$ ($\Delta_{octa} = 5.8\%$). The electrostatic calculations based on the MAPLE concept confirming the electrostatic reasonability of the crystal structure (Table F.1.5) yielded similar effective coordination numbers as the isotypic and homeotypic compounds (Tables F.1.6 and F.1.7, see also [83]).
As discussed above, polymorphism is frequently found for transition metal borosulfates $M[B_2(SO_4)_4]$. Interestingly, no indication for such behaviour was found for $Cd[B_2(SO_4)_4]$ despite synthesis variations, i.e. aging or reduction of the SO_3 content. Similarly, only one polymorph could be prepared for the isotypic $Mn[B_2(SO_4)_4]$ so far.[88,438]

Optical Properties

Infrared Spectroscopy

The infrared spectrum of $Cd[B_2(SO_4)_4]$ is shown in Figure F.1.5. The spectrum agrees with those of the homeotypic α-$Co[B_2(SO_4)_4]$ and β-$Mg[B_2(SO_4)_4]$.[83] A detailed discussion is given for the isotypic β-$Cu[B_2(SO_4)_4]$ on page 197.

UV-Vis Spectroscopy

The powder reflectance spectrum of $Cd[B_2(SO_4)_4]$ is shown in Figure F.1.6. It is governed by the fundamental absorption due to the bandgap of the sample in the UV regime since there are - as discussed above - no valence d electrons in Cd^{2+}. The optical band gap was estimated using the Tauc plot in Figure 9.1.5 with an experimental value of 4.76(1) eV.

Thermal Analyses

The thermal decomposition was investigated by TGA under nitrogen atmosphere and TPXRD inside sealed argon filled glass capillaries. According to the results of the former (Figure 9.1.6, $Cd[B_2(SO_4)_4]$ decomposes above 330°C via a two step process. Priorly, an amorphous side phase accounting to 1.9 wt.-% is decomposed at 210°C and adhesive sulfuric acid evaporates around 280°C ($\approx$ 2 wt.-%). After the first step, $CdSO_4$ is formed together with amorphous B_2O_3 which in turn decomposes starting at 850°C to CdO. These steps are accompanied by the evaporation of 3 SO_3 and 1 SO_3, respectively. The last step is in accordance with earlier reports on the thermal decomposition of $CdSO_4$.[442] Additionally, the decomposition process was investigated by TPXRD shown in Figure F.1.7 confirming the formation of $CdSO_4$ and showing the formation of CdB_4O_7 at 800°C - by the reaction of CdO and B_2O_3. This behaviour is well-known for borosulfates.[82,95] Gravimetrically, it is not possible to discriminate between mixtures of CdO and B_2O_3, and of CdO and CdB_4O_7. Measurements at higher temperatures close to the melting point of CdB_4O_7 (976°C)[443] resulted in a loss of crystallinity presumably accompanied by glass formation. This would also explain why no PXRD could be measured using

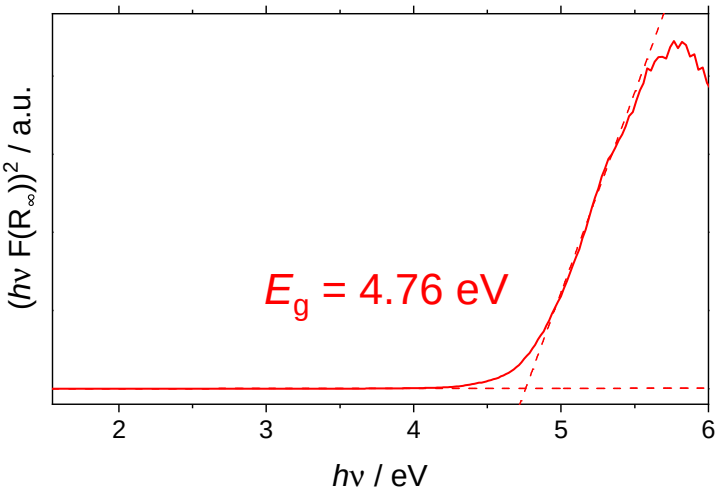

Fig. 9.1.5: Tauc plot calculated from the UV-Vis spectrum of $Cd[B_2(SO_4)_4]$.

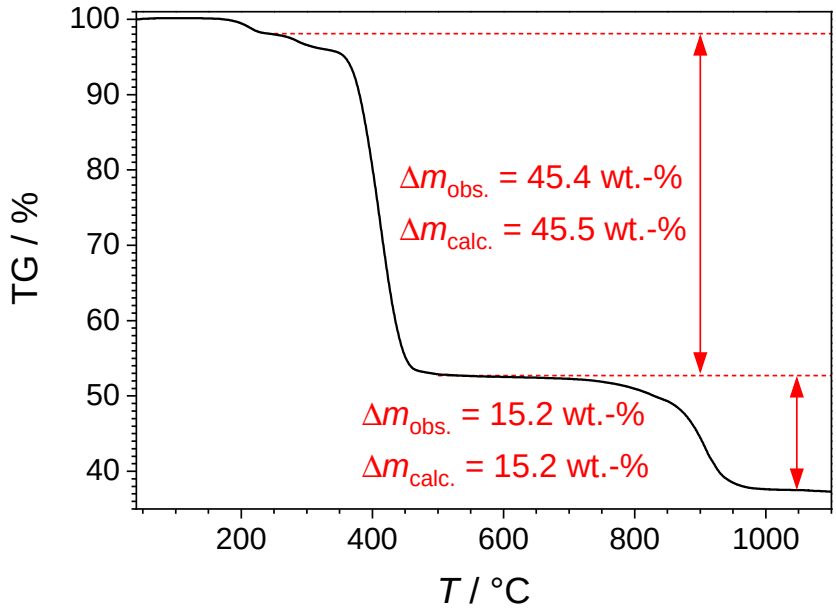

Fig. 9.1.6: Thermogravimetric analysis of $Cd[B_2(SO_4)_4]$.

the residue from the TGA measurement.[iii] Interestingly, at 300°C a novel pattern was observed (Figure F.1.7). This could be assigned to $Cd[B_2O(SO_4)_3]$ in spite of the fact that no mass loss was observed for this temperature regime in TGA. However, this investigation is beyond the scope of this thesis and covered elsewhere.[444]

[iii] Additionally, a sample of $Cd[B_2(SO_4)_4]$ heated for 10 h at 1000°C in a corundum crucible inside a tube furnace could not be separated from the crucible after the heat treatment - presumably, also due to either glass formation or the melting of CdB_4O_7.

9.2 $Cu[B_2(SO_4)_4]$

Besides the polymorphism of the borosulfates $M[B_2(SO_4)_4]$ detailed in the previous section, polymorphism appears to be rare in borosulfate chemistry. There are only three more examples, namely $Na_5[B(SO_4)_4]$ with two nesosilicate-analogous polymorphs,[79] the unconventional 0D borosulfates $Mg_4[B_2O(SO_4)_6]$ comprising B-O-B bonds[82] and $Mg_3[H_2O{\rightarrow}B(SO_4)_3]_2$ forming a Lewis acid base adduct with water.[76] Remarkably, in all cases the dimensionality of the anionic substructure is the same for both polymorphs. In 2018, the first two copper borosulfates $Cu[B_2(SO_4)_4]$ and $Cu[B(SO_4)_2(HSO_4)]$ were reported crystallising with inosilicate-analogous and cyclosilicate-analogous borosulfate anions, respectively. Besides the crystal structures, only the magnetic properties of both compounds had been investigated. Notably, no phase pure samples could only be prepared for both $Cu[B(SO_4)_2(HSO_4)]$ and $Cu[B_2(SO_4)_4]$. The latter was obtained solely in mixtures with $Cu[B(SO_4)_2(HSO_4)]$ and a maximum content of 22 wt.-% $Cu[B_2(SO_4)_4]$.[90] Most commonly, Cu^{2+} oxo salt compounds feature CuO_6 polyhedra.[445] Due to the $[Ar]3d^9$ electronic ground state of the Cu^{2+} cation, the octahedral coordination environment is affected strongly by Jahn-Teller distortion[60] usually resulting in a (4+2) coordination with four – equatorial – Cu-O distances (R_{eq}) being shorter and two – apical – ones (R_{ap}) being longer. Nevertheless, the formation of a compressed octahedron with (2+4) coordination is equally likely according to the first order Jahn-Teller distortion – however, this is rarely found.[61,445–447] The reason for this might be found in the fact that four instead of two elongated distances are necessary for this coordination requiring more energetic effort and degrees of freedom.[196]

This section investigates the polymorphism of $Cu[B_2(SO_4)_4]$. The phase pure synthesis of the already reported $Cu[B_2(SO_4)_4]$ – more precisely α-$Cu[B_2(SO_4)_4]$ according to DFT calculations described in the following – and the new polymorph β-$Cu[B_2(SO_4)_4]$, the elucidation of the crystal structures and the nature of the polymorphism, as well as the investigation of their optical, magnetic and thermal properties are presented. The relative stability of the polymorphs as well as the possible existence of a third polymorph analogous to the "cation between layer" modification in other $M[B_2(SO_4)_4]$ borosulfates as discussed before were investigated by DFT calculations. For the sake of completeness and comparison, $Cu[B(SO_4)_2(HSO_4)]$ was also characterised with respect to its optical and thermal properties since no such characterisation was carried out in the original publication.[90]

Syntheses

Both α-$Cu[B_2(SO_4)_4]$ and β-$Cu[B_2(SO_4)_4]$ were synthesised solvothermally at 180°C from 0.25 mmol $Cu_2[(OH)_2CO_3]$ (Alfa Aesar, >55% Cu) and 2 mmol $B(OH)_3$ (Merck, >99.5%) in pure oleum (1 ml, VWR, 65% SO_3) or in a mixture of 0.5 ml H_2SO_4 (Merck, 95-97%) and 0.5 ml oleum, respectively. The educts were loaded into a silica glass ampoule (length 15 cm, outer diameter: 1.2 cm, wall thickness: 0.1 cm) which was subsequently fused and

– without further aging – placed in a muffle furnace applying the following temperature program: heating to 180°C with $100\,K\,h^{-1}$, holding the temperature for 36 h, and cooling down to room temperature with $6\,K\,h^{-1}$. The syntheses yielded colourless powders containing large single-crystals shown in Figure F.2.1. Judging by the morphology of the crystals two different kinds were observed in the β-$Cu[B_2(SO_4)_4]$ sample and only a single one in α-$Cu[B_2(SO_4)_4]$. The phase composition was checked by PXRD after washing the products (as detailed in section 2.6). According to the Rietveld analysis depicted in Figure 9.2.1 and table F.2.1, β-$Cu[B_2(SO_4)_4]$ was obtained with a 7 wt.-% side phase of α-$Cu[B_2(SO_4)_4]$, while α-$Cu[B_2(SO_4)_4]$ could be prepared as phase pure powder. This agrees with the morphology differences observed by light microscopy showing two different single-crystal species in the former.

During handling the highly hygroscopic nature of $Cu[B_2(SO_4)_4]$ was observed. The colourless compound reacts with moisture from air readily to forming $CuSO_4 \cdot xH_2O$ (Figure F.2.2). Consequently, the decomposition via hydrolysis is accompanied by an instant colour change to light blue occurring within less than one minute when handling the powder under non-inert conditions.[iv]

In contrast to earlier reports by Bruns et al.,[90] the formation of $Cu[B(SO_4)_2(HSO_4)]$ was not observed for both syntheses. The selective synthesis of a polymorph is governed by the SO_3 content. However, the SO_3 content and the synthesis temperature appear to be complementary parameters. Bruns et al.[90] prepared $Cu[B(SO_4)_2(HSO_4)]$ containing an unidentified side phase from Cu_2O with 20% SO_3 at 180°C, while herein $Cu[B(SO_4)_2(HSO_4)]$ could be synthesised using 65% SO_3 and at 130°C from 0.25 mmol $Cu_2[(OH)_2CO_3]$, 1.6 mmol $B(OH)_3$, 0.5 ml oleum and 0.5 ml H_2SO_4 by the same procedure as above solely changing the furnace temperature as an almost colourless very pale blueish powder. Rietveld refinement revealed the presence of a 2 wt.-% side phase of $CuSO_4$ (Figure F.2.3 and table F.2.2).

Crystal Structures

α-$Cu[B_2(SO_4)_4]$ crystallises in the triclinic crystal system with space group $P\bar{1}$ (no. 2) with and one formula unit per unit cell (Figure 9.2.2a)[v]. The borosulfate anion forms exclusively $B(SO_4)_4$ supertetrahedra consisting of tetrahedrally coordinated sulfate and borate anions. The borate and sulfate tetrahedra can all be classified regular with deviations from the tetrahedral symmetry of 0.7%, 1.2% and 1.8% for $B1O_4$, $S1O_4$ and $S2O_4$, respectively. The inosilicate-analogous anion forms loop branched *vierer* single chains with the Niggli formula $^1_\infty\left[B(SO_4)_{4/2}\right]^-$ and can therefore be described as a

[iv] From time to time, this effect was also observed during the washing step and the transfer into the glovebox. However, the decomposition appeared to affect the surface of the powder, only. Thus, a colourless powder could be obtained after grinding. Compared to $Cd[B_2(SO_4)_4]$, $Cu[B_2(SO_4)_4]$ appears to be slightly less hygroscopic.

[v] The crystal structure of α-$Cu[B_2(SO_4)_4]$ was described by Bruns et al. from SC-XRD data[90] and is redetermined herein using a Rietveld refinement.

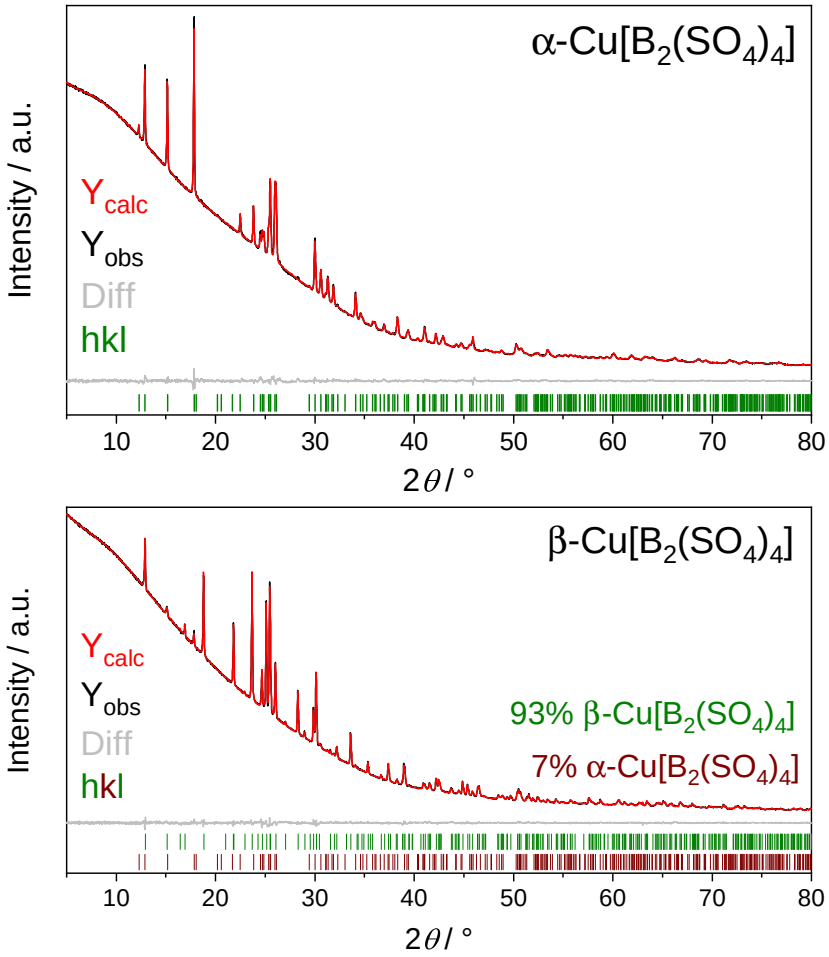

Fig. 9.2.1: Rietveld refinement of α-$Cu[B_2(SO_4)_4]$ confirming the phase purity (top) and β-$Cu[B_2(SO_4)_4]$ showing contents of 93 wt.-% for the main phase β-$Cu[B_2(SO_4)_4]$ and 7 wt.-% for the side phase α-$Cu[B_2(SO_4)_4]$ (bottom); further details can be found in Table F.2.1.

chain of edge sharing supertetrahedra (Figure 9.2.2b). The Cu^{2+} cation is octahedrally coordinated by six oxygen atoms. Six sulfate units coordinate in a monodentate fashion stemming from four different anion chains, i.e. two chains provide two oxygen atoms and two provide one (Figure 9.2.2c). Jahn-Teller distortion leads to enlarged apical Cu-O distances. This is towards the anion chains coordinating by one sulfate anion, only. The Cu-O distances are reasonably close to the sum of ionic radii (Table F.2.3) with a (2+2+2) coordination, a subclass of the (4+2) coordination introduced earlier.[445] As expected, the CuO_6 octahedra deviate significantly from the ideal symmetry with $\Delta_{\mathrm{octa}} = 22\%$ with the Cu^{2+} cation only 0.0(1) pm away from the centroid of the octahedron. Consequently, the Jahn-Teller distortion being a ligand field effect influences the shape of the octahedron and not the location of the Cu^{2+} cation.

According to the TX formalism introduced in section 1.6, the B:S ratio of 1:2 in

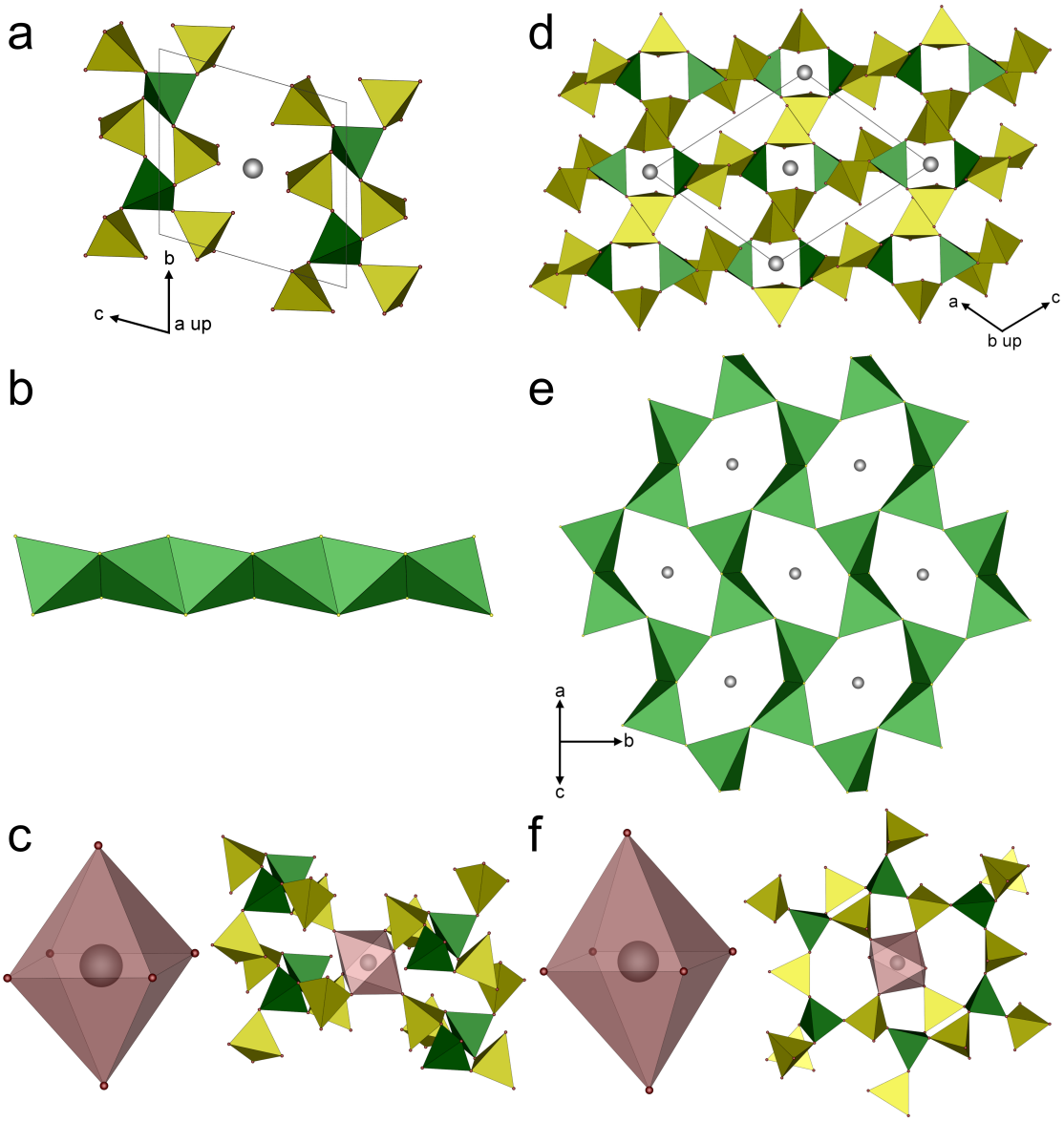

Fig. 9.2.2: The following colour code has been used: copper atoms are grey, borate tetrahedra green, sulfate tetrahedra yellow, oxygen atoms red and $B(SO_4)_4$ supertetrahedra light green; (a) Unit cell of α-$Cu[B_2(SO_4)_4]$ viewed along [100]; (b) the $^{1}_{\infty}\left[B(SO_4)_{4/2}\right]^{-}$ anion chain in α-$Cu[B_2(SO_4)_4]$ depicted as edge sharing $B(SO_4)_4$ supertetrahedra (c) octahedral coordination environment of the Cu^{2+} cations in α-$Cu[B_2(SO_4)_4]$ (left) and the location of those octahedra between four anion chains (right); (d) unit cell of β-$Cu[B_2(SO_4)_4]$ viewed along $[010]$; the $^{2}_{\infty}\left[B(SO_4)_{4/2}\right]^{-}$ anion layers are shown in side view; (e) the layers in β-$Cu[B_2(SO_4)_4]$ formed by corner and edge sharing supertetrahedra $B(SO_4)_4$ resulting in *sechser* rings with the Cu^{2+} cations located inside and corner sharing dimers of supertetrahedra; (f) octahedral coordination environment of the Cu^{2+} cations in β-$Cu[B_2(SO_4)_4]$ (left) and the location of those octahedra in the *zwölfer* ring (right); the two additional oxygen atoms belong to the anion layers above and below, respectively.

α-Cu[$B_2(SO_4)_4$] indicates a three-dimensional anion. However, α-Cu[$B_2(SO_4)_4$] shows exclusively the connection pattern of SiS_2[78] resulting in the one-dimensional anion.

β-Cu[B$_2$(SO$_4$)$_4$] crystallises in the monoclinic crystal system with space group $P2_1/n$ (no. 14) with and two formula units per unit cell (Figure 9.2.2d) isotypically to Cd[$B_2(SO_4)_4$] described above in the Mn[$B_2(SO_4)_4$] structure type (Tables F.2.4 to F.2.6). Again, the borosulfate anion forms exclusively $B(SO_4)_4$ supertetrahedra sharing alternately edges and corners (Figure 9.2.2e). By looking at the individual borate and sulfate tetrahedra, they form $^2_\infty\left[B(SO_4)_{4/2}\right]^-$ layers comprising of *zwölfer* and *vierer* rings. Thus, the anion is phyllosilicate-analogous. It was described in detail for Cd[$B_2(SO_4)_4$] (page 183). The borate and sulfate tetrahedra can all be classified regular with deviations of 0.4%, 0.2% and 0.7% for $B1O_4$, $S1O_4$ and $S2O_4$, respectively.The Cu^{2+} cation is octahedrally coordinated by six oxygen atoms, i.e. monodentately by six sulfate tetrahedra. Four sulfate moieties belong to one anion layer with the Cu^{2+} cation inside the *zwölfer* ring and the residual two belong to the layers above and below, respectively (Figure 9.2.2f). The Cu-O distances are reasonably close to the sum of ionic radii (Table F.2.7). Further, Jahn-Teller distortion leads to elongation of the apical Cu-O distances. Again, the coordination of the Cu^{2+} cation can be described as (2+2+2). However, the difference between the two sets of equatorial distances is much smaller than they differ from the apical ones. The CuO_6 octahedra deviate significantly from the ideal symmetry with $\Delta_{\mathrm{octa}} = 35\%$ with the Cu^{2+} cation 0.0(1) pm away from the centroid. This is larger than for isotypic Cd[$B_2(SO_4)_4$] (6.1%, section 9.1) and for α-Cu[$B_2(SO_4)_4$] ($\Delta_{\mathrm{octa}} = 22\%$, dev. from centroid: 0.0(1) pm). Further, the elongation of the apical Cu-O distances is smaller in α-Cu[$B_2(SO_4)_4$], too. Thus, the Jahn-Teller distortion in β-Cu[$B_2(SO_4)_4$] is more pronounced compared to α-Cu[$B_2(SO_4)_4$] with tetragonalities T[448] of 0.82 and 0.89, respectively.[vi] This can be explained by different cooperative effects[61] between the anionic substructure and the Cu^{2+} cation. This effect appears to be stronger in β-Cu[$B_2(SO_4)_4$] and can be explained by the more rigid phyllosilicate-analogous anion. The anionic substructure of β-Cu[$B_2(SO_4)_4$] is affected by the Jahn-Teller distortion. Apparently, this distortion of the anionic substructure enhances a larger Jahn-Teller distortion due to cooperative effects. On the other hand, such cooperative effects are apparently much weaker for α-Cu[$B_2(SO_4)_4$] and its anionic chains.

According to the sum formula and the TX formalism introduced in section 1.6, the B:S ratio of 1:2 indicates a three-dimensional anion, again. However, the alternation of edge and corner sharing supertetrahedra combines both connecting patterns of three-dimensional networks like in SiO_2[449] and the one-dimensional chain like in SiS_2[78] resulting in the layered two-dimensional anion.

[vi] The tetragonality $T = \frac{R_{\mathrm{eq}}}{R_{\mathrm{ap}}}$ is discussed in detail with the optical properties in the following.

Cu[B(SO$_4$)$_2$(HSO$_4$)] The crystal structure of Cu[B(SO$_4$)$_2$(HSO$_4$)] was reported by Bruns et al. from single-crystal data at 173 K.[90] Once again, the Cu^{2+} cation is coordinated by six oxygen atoms forming a Jahn-Teller distorted octahedron with elongated apical Cu-O distances. The octahedra deviate significantly from the ideal symmetry with deviations of 37% and 39% for Cu1 and Cu2, respectively. The cyclosilicate-analogous borosulfate anion comprises non-condensed dimers of edge sharing supertetrahedra – similar to the ones found in M_2[B$_2$(SO$_4$)$_6$] (M = Y, La–Nd, Sm–Lu, Bi)[92,95,427] (see also section 8.1) - with additional hydrogen atoms at opposing terminal corners.

Electrostatic Calculations

The electrostatic reasonability of the crystal structures of α-Cu[B$_2$(SO$_4$)$_4$] and β-Cu[B$_2$(SO$_4$)$_4$] was confirmed by calculations of the MAPLE values of the two Cu[B$_2$(SO$_4$)$_4$] polymorphs compared to the sum of the MAPLE values of CuSO$_4$, B$_2$S$_2$O$_9$, B$_2$O$_3$ and SO$_3$, respectively (Table F.2.8). The deviations are well below 1%. Furthermore, the calculations confirm all coordination numbers discussed earlier (Tables F.2.9 to F.2.11). The effective coordination numbers also show the influence of the Jahn-Teller distortion – especially in comparison to isotypic Cd[B$_2$(SO$_4$)$_4$] and Mn[B$_2$(SO$_4$)$_4$] (Tables F.1.6 and F.1.7) as well as homeotypic β-M[B$_2$(SO$_4$)$_4$] (M = Mg, Co).[83] Additionally, these calculations confirm the stronger effect of the Jahn-Teller distortion in β-Cu[B$_2$(SO$_4$)$_4$] compared to α-Cu[B$_2$(SO$_4$)$_4$].

DFT Calculations

Quantum chemical calculations were performed in order to investigate the relative stabilities of the Cu[B$_2$(SO$_4$)$_4$] polymorphs. β-Cu[B$_2$(SO$_4$)$_4$] crystallises isotypically to Mn[B$_2$(SO$_4$)$_4$] (and Cd[B$_2$(SO$_4$)$_4$]) and homeotypically – differing in the orientation of one sulfate tetrahedron, only – to Zn[B$_2$(SO$_4$)$_4$],[88] β-Mg[B$_2$(SO$_4$)$_4$] and β-Co[B$_2$(SO$_4$)$_4$].[83,89] Further, the borosulfates α-Mg[B$_2$(SO$_4$)$_4$][82] and α-Co[B$_2$(SO$_4$)$_4$][83,89] exhibit analogous sum formulae and similar structures comprising also phyllosilicate-analogous anions formed by *zwölfer* and *vierer* rings. The structures deviate in the position of the respective cation being located above and underneath the *zwölfer* rings and thus, in between two layers instead inside the rings in β-Cu[B$_2$(SO$_4$)$_4$]. This configuration – "cation between layers" in contrast to "cation within layers" – appears to be less stable for Cu[B$_2$(SO$_4$)$_4$] since no such borosulfate was observed during all syntheses. This might be due to the Jahn-Teller distortion requiring two different sets of four short equatorial and two long apical Cu-O distances. The equatorial and apical cation oxygen distances deviate only slightly from each other in α-Mg[B$_2$(SO$_4$)$_4$][82] (205-206 pm, 203 pm, $\sum$ IR = 207 pm)[216] and α-Co[B$_2$(SO$_4$)$_4$][83] (209 pm, 204 pm, $\sum$ IR = 210 pm).[216] If the cations are hosted between two layers, their coordination is influenced by these two, while in β-Cu[B$_2$(SO$_4$)$_4$] in total three layers contribute to the coordination sphere of the cations. Consequently, there is little freedom for the Jahn-Teller distortion to take

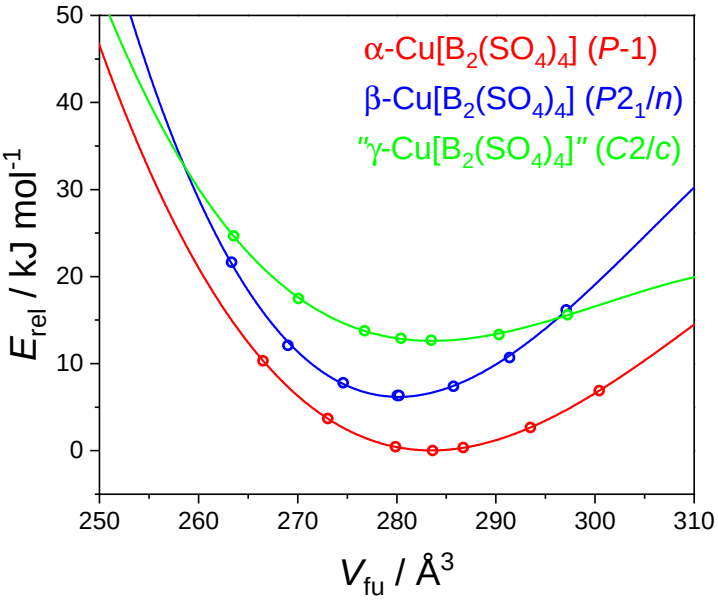

Fig. 9.2.3: Energy versus volume plots for α-Cu[B$_2$(SO$_4$)$_4$] ($P\bar{1}$), β-Cu[B$_2$(SO$_4$)$_4$] ($P2_1/n$, "cation within layer") and γ-Cu[B$_2$(SO$_4$)$_4$] ($C2/c$, "cation between layer")

shape in the former, whereas the higher number of anion layers involved in the Cu^{2+} coordination in β-Cu[B$_2$(SO$_4$)$_4$] provides more flexibility for the distortion. This was discussed under the term cooperative effects above and is confirmed by DFT calculations including a hypothetical structure denoted as "γ-Cu[B$_2$(SO$_4$)$_4$]" where the cations are localised between the anionic layers isotypic to α-Co[B$_2$(SO$_4$)$_4$] in the monoclinic crystal system with space group $C2/c$ (no. 15). According to the optimised structures from DFT, whose lattice parameters and cell volumes are tabulated in Table F.2.12, the α-modification is the most stable of the three investigated models.[vii] It is favoured over β-Cu[B$_2$(SO$_4$)$_4$] by 6.3 kJ mol^{-1}. The hypothetical γ-Cu[B$_2$(SO$_4$)$_4$] is further 6.6 kJ mol^{-1} above the β-polymorph (Figure 9.2.3). In γ-Cu[B$_2$(SO$_4$)$_4$], the CuO$_6$ octahedra in a fully relaxed structural model exhibit shorter apical than equatorial Cu-O distances, therefore being compressed ($T = 1.04$) instead of elongated as found for the α- and β-polymorphs (Figure 9.2.4). This rather unusual (2+4) coordination environment for Cu^{2+}, which is found for example in the two nesosilicate-analogous compounds Cu$_3$Mo$_2$O$_9$($T = 1.19$)[447] and Cu$_3$Cr$_4$(PO$_4$)$_6$($T = 1.18$)[446] can be understood as the consequence of the dilemma described above with the rigid borosulfate anion preventing a significant elongation of the CuO$_6$ octahedra. A tendency towards compressed octahedra is also present in α-Mg[B$_2$(SO$_4$)$_4$] ($T = 1.01$) and α-Co[B$_2$(SO$_4$)$_4$] ($T = 1.02$). Due to the rather small energetic difference of the hypothetical "cation between layer"-model γ-Cu[B$_2$(SO$_4$)$_4$] to β-Cu[B$_2$(SO$_4$)$_4$], the existence of this third polymorph of Cu[B$_2$(SO$_4$)$_4$] with a rare Cu^{2+} coordination can be predicted.

[vii] This result led to the denomination of α-Cu[B$_2$(SO$_4$)$_4$] and β-Cu[B$_2$(SO$_4$)$_4$].

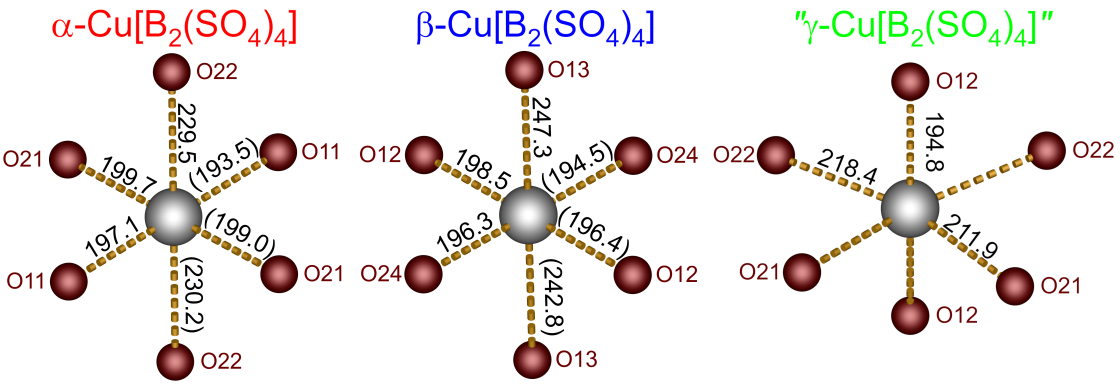

Fig. 9.2.4: CuO_6 octahedra in the DFT optimised structures of α-$Cu[B_2(SO_4)_4]$, β-$Cu[B_2(SO_4)_4]$ and γ-$Cu[B_2(SO_4)_4]$; the Cu-O distances are given in pm from the DFT calculations and from the SC-XRD data (in parentheses, α-$Cu[B_2(SO_4)_4]$: [90], β-$Cu[B_2(SO_4)_4]$: this work); the tetragonality $T = \frac{R_{eq}}{R_{ap}}$ amounts to 0.86, 0.80 and 1.04 for α-$Cu[B_2(SO_4)_4]$, β-$Cu[B_2(SO_4)_4]$ and γ-$Cu[B_2(SO_4)_4]$, respectively.

Optical Properties

Infrared Spectroscopy

The infrared spectra of α-$Cu[B_2(SO_4)_4]$ and β-$Cu[B_2(SO_4)_4]$ are shown in Figure 9.2.5a from 1600 to 400 cm^{-1} (full spectra in Figure F.2.4). The spectrum of β-$Cu[B_2(SO_4)_4]$ agrees well with those of the homeotypic β-$Co[B_2(SO_4)_4]$ and β-$Mg[B_2(SO_4)_4]$[83] and the calculations for the former.[89] The asymmetric stretching modes ν_{asym}(S-O) appear at 1371 cm^{-1}, 1339 cm^{-1}, 1193 cm^{-1} and 1183 cm^{-1}. The subsequent bands between 1160 cm^{-1} and 970 cm^{-1} can be assigned to $\nu_{asym/sym}$(B-O) and are followed by ν_{sym}(S-O) at 870 cm^{-1}. Below, the spectrum is governed by bending vibrations, namely the asymmetric bending vibrations δ_{asym}(O-S-O, O-B-O, S-O-B) between 720 cm^{-1} and 550 cm^{-1} and δ_{asym}(O-S-O, S-O-Cu) below. For α-$Cu[B_2(SO_4)_4]$, calculated IR modes were reported by Bruns et al.[90] They agree roughly with the experimental ones. The asymmetric stretching modes ν_{asym}(S-O) at 1338 cm^{-1} and 1147 cm^{-1} are followed by $\nu_{asym/sym}$(B-O) between 1030 cm^{-1} and 937 cm^{-1} and the symmetric stretching vibrations ν_{sym}(S-O) at 884 cm^{-1} and 855 cm^{-1}. Then, δ(O-S-O, O-B-O, S-O-B) appear between 724 cm^{-1} and 602 cm^{-1}. The deformation modes of the CuO_6 octahedra are overlapped by further δ(O-S-O) vibrations at 529 cm^{-1}, 503 cm^{-1} and 417 cm^{-1}.

Further, the IR spectrum of $Cu[B(SO_4)_2(HSO_4)]$ depicted in Figure 9.2.5a is in good agreement with the calculated one reported by Bruns et al.[90] In contrast to $Cu[B_2(SO_4)_4]$, the asymmetric O-H stretching and the asymmetric and symmetric S-O-H bending modes are present at 2435 cm^{-1}, 1340 cm^{-1} and 1230 cm^{-1}, respectively. They are followed by the asymmetric S-O stretching modes at 1265 cm^{-1} and 1146 cm^{-1} as well as the symmetric one at 1164 cm^{-1}. The three bands at 1045 cm^{-1}, 1014 cm^{-1} and 940 cm^{-1} can be assigned to the asymmetric B-O stretching vibrations. Below, the spectrum is again

governed by bending vibrations like the δ(S-O-H) at 891 cm^{-1}, δ(O-B-O) at 820 cm^{-1}, δ(O-S-O, S-O-B) between 660 cm^{-1} and 550 cm^{-1} and δ(O-S-O, S-O-Cu) below.

UV-Vis-NIR Spectroscopy

The powder reflectance spectra of α-Cu[$B_2(SO_4)_4$] and β-Cu[$B_2(SO_4)_4$] are shown in Figure 9.2.5b in the range from 200 to 1500 nm. Besides the fundamental absorption due to the bandgap of the samples in the UV regime, a broad absorption band between 700 and 1300 nm can be found. The latter can be attributed to the d-d transitions of the Cu^{2+} cation. The spectra are in line with colourless powders. According to ligand field theory and the Jahn-Teller effect three possible d-d transitions may be recorded in Cu[$B_2(SO_4)_4$]:[450,451]

$$\begin{aligned} a_{1g} &\rightarrow b_{1g} \\ b_{2g} &\rightarrow b_{1g} \\ e_g &\rightarrow b_{1g}. \end{aligned}$$

The respective energy scheme is sketched in Figure 9.2.6. The simplification of assuming D_{4h} symmetry, i.e. a (4+2) coordination of Cu^{2+} is legitimate since the further splitting of states due to the actual (2+2+2) coordination can be expected to be too small to influence the resulting reflectance spectra significantly. Consequently, the ligand field splitting energy Δ and the Jahn-Teller energy E_{JT} can be derived directly from the spectra. The transitions could be located at 1.07 eV (1163 nm), 1.38 eV (900 nm) and 1.65 eV (752 nm) for α-Cu[$B_2(SO_4)_4$] and 1.08 eV (1147 nm), 1.39 eV (895 nm) and 1.61 eV (769 nm) for β-Cu[$B_2(SO_4)_4$] using three Gaussian fits of the measured spectra, respectively (Figures F.2.5 and F.2.6). Hence, there are ligand field splitting energies Δ of 11116 cm^{-1} and 11171 cm^{-1} and Jahn-Teller energies E_{JT} of 2149 cm^{-1} and 2179 cm^{-1} for α-Cu[$B_2(SO_4)_4$] and β-Cu[$B_2(SO_4)_4$], respectively. These values are compared to other Cu^{2+} compounds from literature in Table 9.2.1. Borosulfates are known to show weak ligand field splitting.[82,83] Consequently, the ligand field splitting energies are smaller than for the hexaaqua complex Cu(II)[$(OH_2)_6$]$^{2+}$ (13000 cm^{-1})[59,448] and larger than for respective fluorides or sulfates (9100 cm^{-1}).[452] E_{JT} is – in agreement with the crystallographic and electrostatic discussion above – larger for β-Cu[$B_2(SO_4)_4$] compared to α-Cu[$B_2(SO_4)_4$] confirming a stronger Jahn-Teller effect. The comparison with other Cu^{2+} compounds using Δ_{octa} appears to be not straightforward (Table 9.2.1). The tetragonality T[448] – roughly following E_{JT} – appears to be better suited to compare the 'strength' of the Jahn-Teller distortion using crystallographic data (Table 9.2.1). However, this analysis emphasises the strength of spectroscopy in examining the Jahn-Teller effect. The same holds for Cu[$B(SO_4)_2(HSO_4)$] (Figure 9.2.5b) with its three transitions located at 1.21 eV (1022 nm), 1.53 eV (809 nm) and 1.74 eV (714 nm) (Figure F.2.7). The large energy of the last transition explains the pale blue appearance of the measured powder – especially in comparison to colourless Cu[$B_2(SO_4)_4$]. The large E_{JT} of 2447 cm^{-1} can

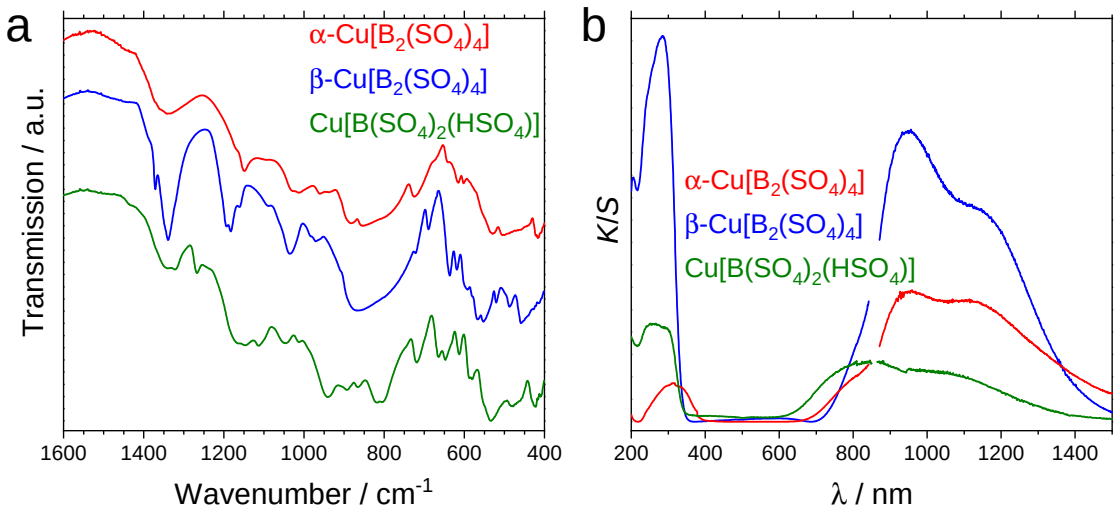

Fig. 9.2.5: (a) Infrared spectra of α-$Cu[B_2(SO_4)_4]$, β-$Cu[B_2(SO_4)_4]$ and $Cu[B(SO_4)_2(HSO_4)]$: The full spectra can be found in Figure F.2.4; (b) powder reflectance UV-Vis-NIR spectra of α-$Cu[B_2(SO_4)_4]$, β-$Cu[B_2(SO_4)_4]$ and $Cu[B(SO_4)_2(HSO_4)]$: The spectra are broken around 850 nm due to the change of detector within the measuring device.

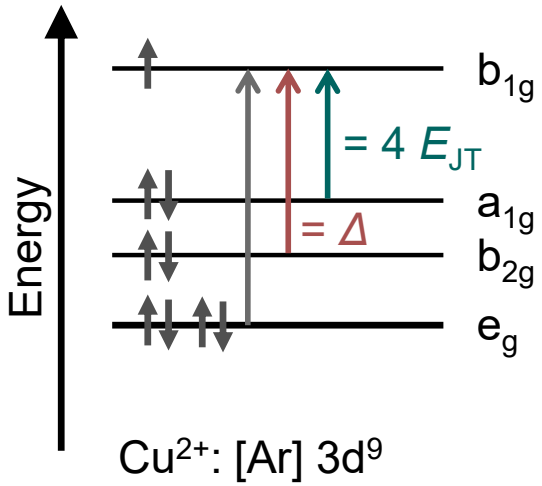

Fig. 9.2.6: Cu^{2+} energy scheme in D_{4h} symmetry showing the three possible d-d transitions of Cu^{2+} and the related parameters according to classical ligand field theory (Δ: ligand field splitting energy, E_{JT}: Jahn-Teller energy).

be explained by the small tetragonality T both indicating a strong Jahn-Teller effect (Table 9.2.1). The ligand field splitting energy of 12355 cm^{-1} is larger than the one for both polymorphs of Cu[B$_2$(SO$_4$)$_4$] but still smaller than for the hexaaqua complex (13000 cm^{-1}).[59,448]

All three spectra show transitions from the valence to the conduction band in the UV region. The band gaps were estimated using Tauc plots shown in Figures F.2.8 to F.2.10 with experimental values of 3.33(1) eV, 3.82(1) eV and 3.76(1) eV for α-Cu[B$_2$(SO$_4$)$_4$], β-Cu[B$_2$(SO$_4$)$_4$] and Cu[B(SO$_4$)$_2$(HSO$_4$)], respectively.

Although Cu^{2+} near infrared luminescence is known for Cu^{2+} containing silicates,[453,454] no emission could be observed for both α-Cu[B$_2$(SO$_4$)$_4$] and β-Cu[B$_2$(SO$_4$)$_4$] up to 1500 nm.

Tab. 9.2.1: Comparison of relevant parameters derived from the UV-Vis-NIR spectra of Cu[B$_2$(SO$_4$)$_4$] and Cu[B(SO$_4$)$_2$(HSO$_4$)] with other Cu^{2+} compounds from literature: The Jahn-Teller energy E_{JT} describes the strength of the Jahn-Teller effect, Δ is the ligand field splitting energy, Δ_{octa} the deviation from the octahedral symmetry and T the tetragonality.

Compound	E_{JT} / cm^{-1}	Δ / cm^{-1}	Δ_{octa} / %	$T = \frac{R_{eq}}{R_{ap}}$	Reference
α-Cu[B$_2$(SO$_4$)$_4$]	2149	11116	22 / 28[i]	0.89 / 0.85[i]	this work / [90]
β-Cu[B$_2$(SO$_4$)$_4$]	2179	11171	33 / 35[i]	0.82 / 0.81[i]	this work
Cu[B(SO$_4$)$_2$(HSO$_4$)]	2447	12355	44 / 34[ii]	0.79	this work[iii]
CuSO$_4$	1830	9100	26	0.84	[452, 455]
CuWO$_4$	2319	11136	32	0.82	[451]
CsCuCl$_3$	2076	10000	26	0.83	[456]
K$_2$CuF$_4$	1950	9200	25	0.87	[457, 458]
Cu(II)[(OH$_2$)$_6$]$^{2+}$	≈2000	≈13000	-	-	[59, 448]

[i] Results using Rietveld on the left and single-crystal data on the right. [ii] There are two crystallographically distinct CuO$_6$ polyhedra in Cu[B(SO$_4$)$_2$(HSO$_4$)]. [iii] Δ_{octa} and T were calculated using the single-crystal data reported by Bruns et. al.[90]

Magnetic Properties

The temperature dependent magnetic susceptibilities (χ) and the inverse (χ^{-1}) of α-Cu[B$_2$(SO$_4$)$_4$] and β-Cu[B$_2$(SO$_4$)$_4$] are shown in Figure 9.2.7. The inverse susceptibilities were fitted in the temperature range from 50-300 K via the Curie-Weiss law, using the corrected data. The effective magnetic moments of $\mu_{eff} = 1.76(1)\,\mu_B$ for α-Cu[B$_2$(SO$_4$)$_4$] and $\mu_{eff} = 1.74(1)\,\mu_B$ for β-Cu[B$_2$(SO$_4$)$_4$] are in excellent agreement with the calculated effective magnetic moment of $1.73\,\mu_B$ for Cu^{2+} (d^9). In line with the absence of magnetic ordering, the Weiss constants are $\Theta_P = -3.5(1)$ K (α-Cu[B$_2$(SO$_4$)$_4$]) and $\Theta_P = -0.9(1)$ K (β-Cu[B$_2$(SO$_4$)$_4$]) indicating only very weak (antiferro)magnetic interactions in the paramagnetic temperature regime. Due to the mixed composition of the samples, the calculation of both μ_B and Θ_P was not possible during the first report of α-Cu[B$_2$(SO$_4$)$_4$] by Bruns et al.[90]

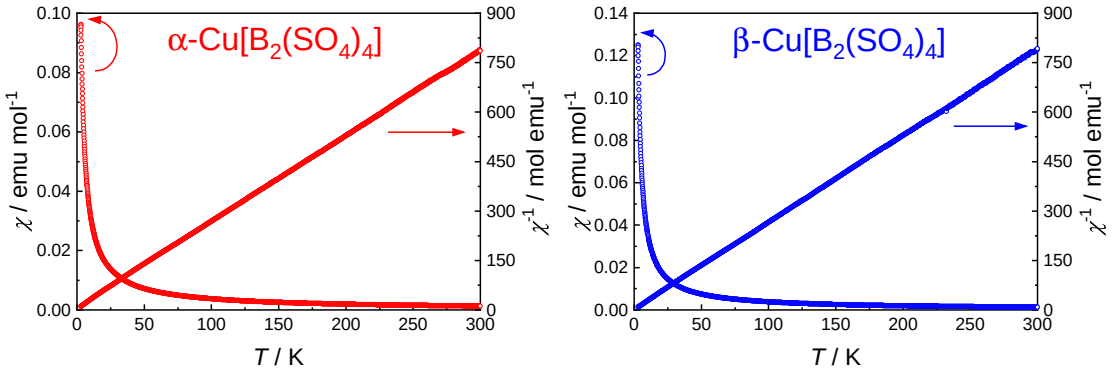

Fig. 9.2.7: Magnetic properties (χ and χ^{-1} data) of α-$Cu[B_2(SO_4)_4]$ (left) and a mixture of 93 wt.-% β-$Cu[B_2(SO_4)_4]$ and 7 wt.-% α-$Cu[B_2(SO_4)_4]$ (right).

Thermal Analyses

The thermal decomposition of $Cu[B_2(SO_4)_4]$ was investigated by TGA, DTA both displayed in Figure 9.2.8 under nitrogen atmosphere and TPXRD inside sealed argon filled glass capillaries (Figure F.2.11). Additionally, a sample of β-$Cu[B_2(SO_4)_4]$ was heated for 10 h inside corundum crucibles at at 300°C in nitrogen atmosphere with 70 ml min^{-1} flow. The residual powder was investigated by PXRD (Figure F.2.12).

Both α-$Cu[B_2(SO_4)_4]$ and β-$Cu[B_2(SO_4)_4]$ decompose at 190°C following these reaction equation:

$$Cu[B_2(SO_4)_4] \longrightarrow CuSO_4 + B_2O_3 + 3\,SO_3(g)$$

The expected mass losses for this process agree well with the observed values (Table F.2.13). SO_3 is released while $CuSO_4$ (Figures F.2.11 and F.2.12) is formedThe further decomposition from $CuSO_4$ on is detailed in the original publication.[437] For β-$Cu[B_2(SO_4)_4]$, an additional decomposition step occurs prior to the formation of $CuSO_4$ indicating the evaporation of 2.5 SO_3 (Figure 9.2.8). In principle, this could indicate the formation of the hypothetical unconventional borosulfate $Cu_4[B_2O(SO_4)_6]$ analogous to the respective magnesium, manganese, cobalt, nickel, and zinc compounds[82] comprising B-O-B bonds following the reaction equation:

$$Cu[B_2(SO_4)_4] \longrightarrow \frac{1}{4}\,Cu_4[B_2O(SO_4)_6] + \frac{3}{4}\,B_2O_3 + 2.5\,SO_3(g)$$

The observed mass loss of 43.8 wt.-% and the expected value of 42.6 wt.-% agree roughly. However, both TPXRD (Figure F.2.11) and powder diffraction on a sample heated at 300°C (Figure F.2.12) revealed only the presence of $CuSO_4$ in this temperature regime and no diffraction pattern related to the additional phase indicated by TG. Additionally, syntheses analogous to the ones employed for $M_4[B_2O(SO_4)_6]$ (M = Mg, Mn, Co, Ni, Zn)[82] with Cu, CuO or $Cu_2[(OH)_2CO_3]$ as starting materials resulted in the sole formation of $CuSO_4$, too. The Jahn-Teller distortion might make the formation of a

dimer analogous to the M_2O_9 building unit in $M_4[B_2O(SO_4)_6]$ comprising two face-sharing CuO_6 octahedra highly unlikely or at least thermodynamically instable. Moreover, both polymorphs of $Cu[B_2(SO_4)_4]$ do not differ in their thermal stability. Generally, a decrease in thermal stability of borosulfates is reported for higher condensed networks.[82,83,95] The reason, why this is not the case for $Cu[B_2(SO_4)_4]$, might again be found in the Jahn-Teller distortion and the cooperative effects.

For the sake of completeness, the thermal decomposition of $Cu[B(SO_4)_2(HSO_4)]$ was investigated, too. According to Figure 9.2.8, it decomposes above 160°C via a similar process as $Cu[B_2(SO_4)_4]$ to $CuSO_4$. The experimental and the expected mass losses in Table F.2.14 match as well as the temperature ranges of both $Cu[B(SO_4)_2(HSO_4)]$ and $Cu[B_2(SO_4)_4]$.

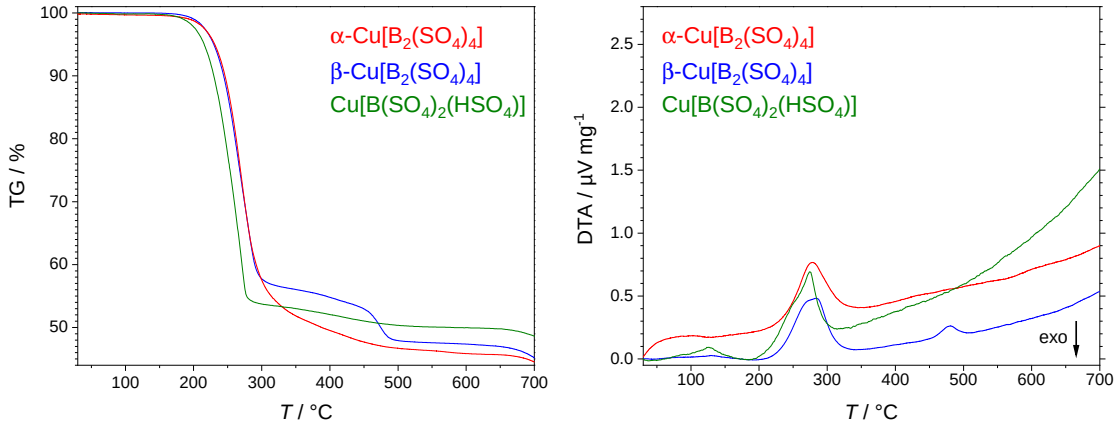

Fig. 9.2.8: Thermogravimetric analyses (left) and differential thermal analyses (right) of α-$Cu[B_2(SO_4)_4]$, β-$Cu[B_2(SO_4)_4]$ and $Cu[B(SO_4)_2(HSO_4)]$ measured simultaneously.

10 Summary

Carbon-based Precursor Compounds

$Sr_3(C_6H_5O_7)_2 \cdot H_2O$

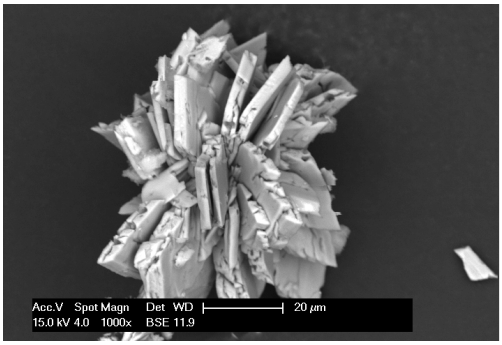

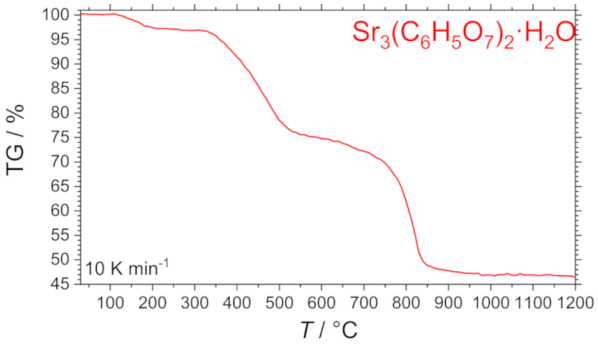

$Sr_3(C_6H_5O_7)_2 \cdot H_2O$ was prepared for the first time via microwave-assisted hydrothermal synthesis. It was characterised using SC-XRD, EDX spectroscopy, PXRD, IR spectroscopy and TGA. $Sr_3(C_6H_5O_7)_2 \cdot H_2O$ represents a new structure type. Two distinct citrate groups differ in the hydrogen bonding situation and the coordination towards the strontium atoms. Orientational disorder of one citrate ligand results in one strontium cation being disordered over two lattice sites. The crystal structure is formed by the combination of two interpenetrating Sr-O and citrate-crystal water networks. The compound may be used as a precursor. As a proof of principle, this was demonstrated for $SrWO_4$.

$Ln[CO_3][OH]$ (Ln=La, Pr, Nd, Sm, Eu, Gd, Tb)

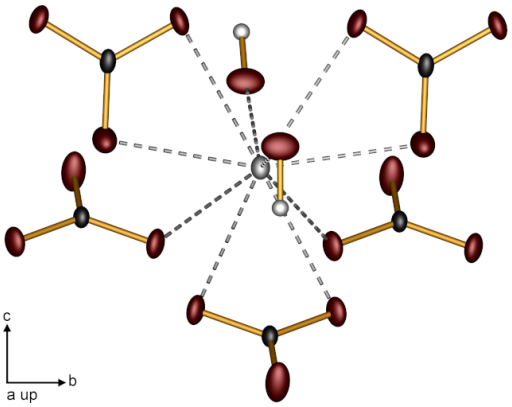

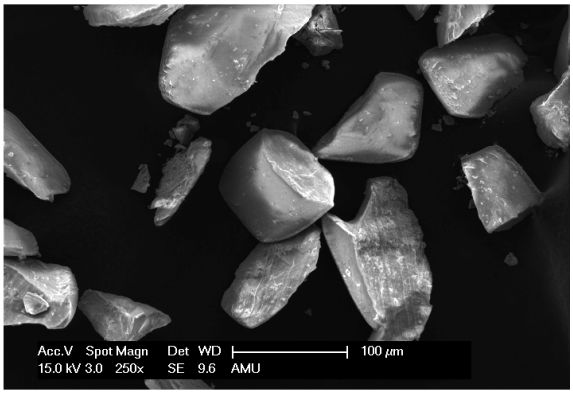

The compounds $Ln[CO_3][OH]$ (Ln = La, Pr, Nd, Sm, Eu, Gd) were prepared via hydrothermal syntheses using ambient CO_2 as carbonate source, thus, resembling the natural formation of the minerals *ancylite* or *kozoite*. Further, $Tb[CO_3][OH]$ was synthesised with urea as carbonate source. Employing a combination of SC-XRD and powder SHG measurements, the ongoing discussion in literature could be clarified. $Ln[CO_3][OH]$ crystallises in space group $Pnma$ (no. 62) for Ln = La-Gd and in space group $P2_12_12_1$ (no. 19) for Ln = Tb-Lu. Further, unequivocal localisation of hydrogen was possible. Moreover, it was shown - on the basis of chemical and crystallographic argumentations - that compounds reported as $Ln_2O(CO_3)_2 \cdot H_2O$ are apparently identical with $Ln[CO_3][OH]$. This includes several minerals such as *ancylite*. Finally, the application of the carbonate hydrates as precursors for the corresponding carbonate oxides and the pure oxides was demonstrated.

Tungstates

$Na_5M(WO_4)_4$ (M = Y, La-Nd, Sm-Lu, Bi)

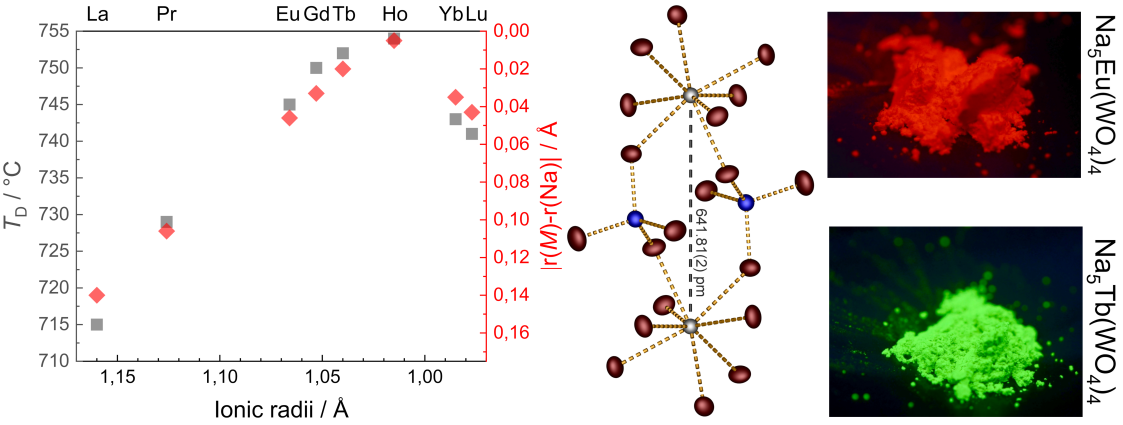

The pentasodium rare earth metal tetratungstates were investigated extensively with respect to crystal structures, crystallographic relationships as well as thermal, magnetic, ^{151}Eu Mößbauer spectroscopic and luminescent properties. Firstly, improved flux syntheses reduced the $NaM(WO_4)_2$ side phases. The crystallographic relationship of $Na_5M(WO_4)_4$ to $NaM(WO_4)_2$ was described by a group-subgroup relation. This explains the competitive crystallisation of both compounds. Further, $Na_5M(WO_4)_4$ decomposes while simultaneously melting to $NaM(WO_4)_2$ and Na_2WO_4. There is a maximum in the melting and decomposition temperature for $Na_5Ho(WO_4)_4$. This can be explained by the ionic radii difference in $Na_5M(WO_4)_4$ taking into account the existence of domains within the crystal structure related to the decomposition products, a behaviour also known as *chemical twinning*. Further, the temperature dependent miscibility gap in $Na_5Y_{1-x}Eu_x(WO_4)_4$ and $Na_5Y_{1-y}Tb_y(WO_4)_4$ was identified and characterised. Solid solutions are formed irreversibly above a threshold temperature of 660°C to 700°C.
$Na_5M(WO_4)_4$ is a promising class of phosphors due to the possible O^{2-}-W^{6+} LMCT excitation and the large M-M distances yielding in special properties such as the lack of concentration quenching or the absence of cross-relaxation of neighbouring Sm^{3+} ions. Fluorescence spectroscopy showed that the energy transfer from WO_4^{2-} to M^{3+} is governed by the W^{6+}-O^{2-} LMCT emission.
The oxidation states +6 of tungsten and +3 of europium were confirmed by the magnetic properties of $Na_5Bi(WO_4)_4$ and the ^{151}Eu Mößbauer spectrum of $Na_5Eu(WO_4)_4$, respectively. Finally, the temperature dependent measurement of the magnetic susceptibility showed no onset of any magnetic interactions in agreement with the large M-M distances.

$AM(WO_4)_2$ (A = Li, Na, K; M = Y, La, Pr, Tb, Bi

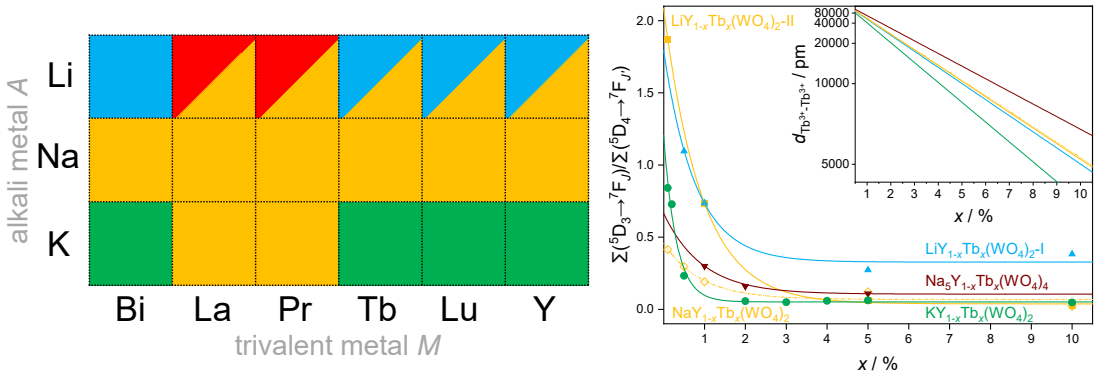

The material class of alkali rare earth metal double tungstates exhibits structural variety with four structure types relevant for the studied compounds. The crystal structures were (re)determined by SC-XRD or Rietveld refinement in order to clarify ambiguities in literature. All structure types were ascribed to differing distortion variants of the *scheelite* structure type. The ionic radii of the respective A^+ and M^{3+} cations govern the adapted structure type. Beyond that, the compounds were investigated with respect to their thermal and optical properties. The latter are relevant for the application of $AM(WO_4)_2$ powders as phosphors. Energy transfer from the tungstate moiety to the activator is caused by the W^{6+}-O^{2-} LMCT emission. Further, structure-property relations were established for the differently efficient Tb^{3+}-Tb^{3+} cross-relaxation beyond simple distance arguments.

The First Cesium Sulfatotungstate $Cs_6[(WO_2)_2O(SO_4)_4]$

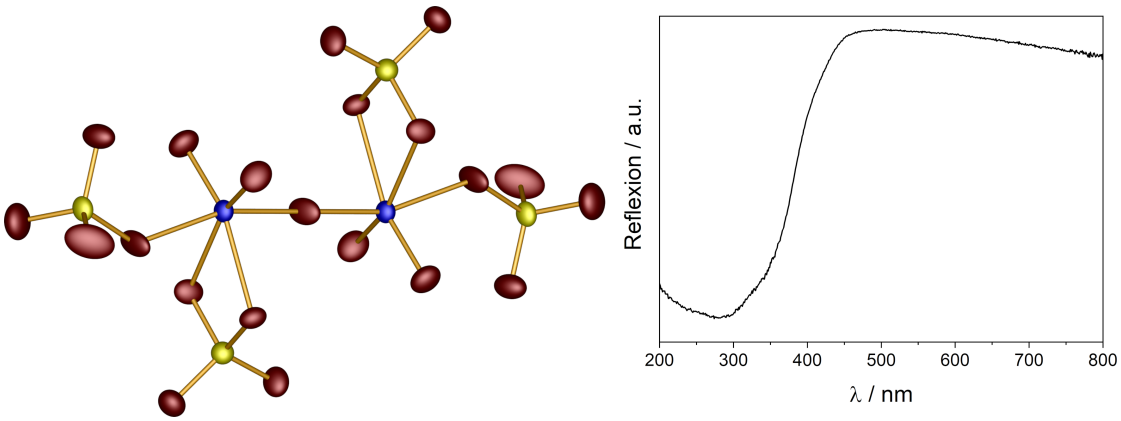

The crystal structure of $Cs_6[(WO_2)_2O(SO_4)_4]$ prepared via crystallisation from the melt inside an evacuated ampoule was determined via SC-XRD. It comprises an unprecedented $[(WO_2)_2O(SO_4)_4]^{6-}$ anion featuring - for the first time - edge-sharing WO_6 octahedra and SO_4 tetrahedra. Further, the full characterisation of its optical properties - for the first time for any sulfatotungstate - showed the LMCT of the tungstate moiety. This underlines the promising prospects of this young and small material class with respect to the use as luminescent materials.

Sulfates

$Sn(SO_4)_2$ and $Sn_2(SO_4)_3$

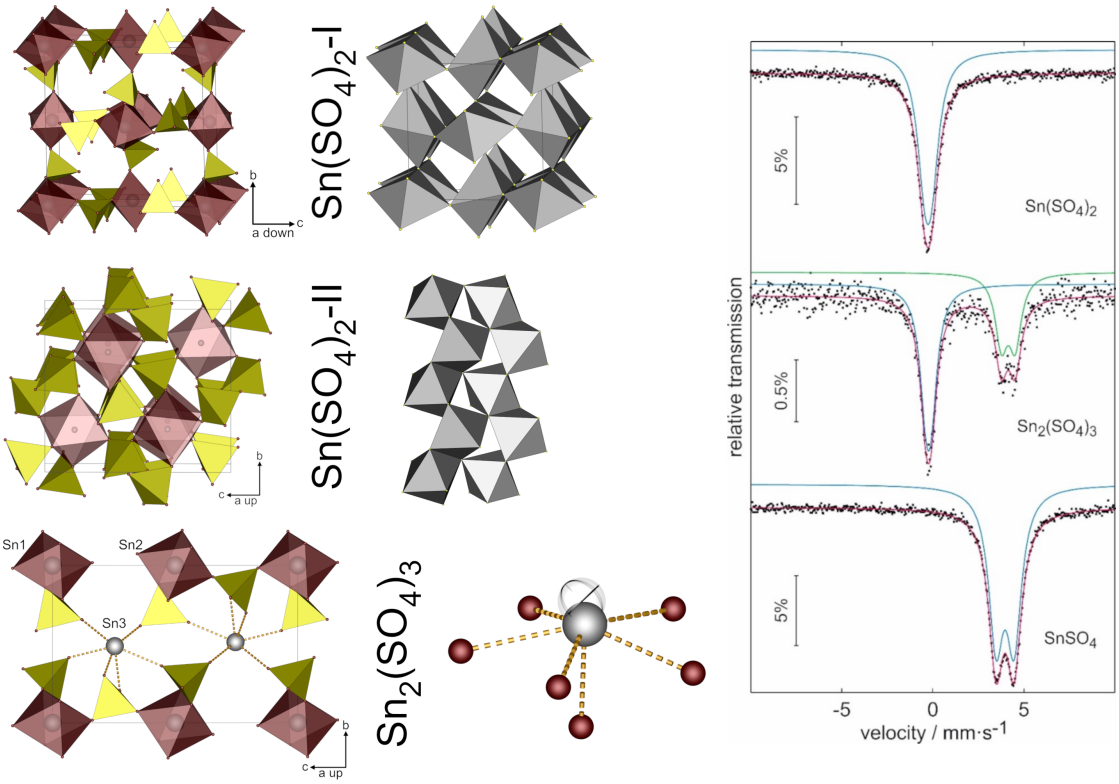

The crystal structures of $Sn(SO_4)_2$-I, $Sn(SO_4)_2$-II and $Sn_2(SO_4)_3$ were elucidated for the first time representing three new structure types. The latter is the first heterovalent pure tin sulfate and for the first time the coexistence of both Sn^{2+} and Sn^{4+} cations within one crystal structure without Sn^{2+}-O-Sn^{4+} bridges is reported. Further, it comprises alternating layers with $Sn(SO_4)_2$ and $SnSO_4$ stoichiometry. The Sn^{2+} cations show an expressed lone pair effect. Interestingly, the two $Sn(SO_4)_2$ polymorphs can be traced back to the simple structure types *rutile* for $Sn(SO_4)_2$-I and TiO_2-II/α-PbO_2 for $Sn(SO_4)_2$-II. The optical and thermal properties of these tin sulfates were investigated and compared to $SnSO_4$ – the only tin sulfate with already known crystal structure. Infrared and ^{119}Sn Mößbauer spectroscopy could confirm the structure determination, i.e. the various connection patterns and oxidation states of tin. The band gaps of the compounds could be estimated by UV-Vis spectroscopy. Moreover, the thermal decomposition process towards SnO_2 was explored in detail including possible conversion pathways from one tin sulfate to another. $Sn_2(SO_4)_3$ can be converted to $Sn(SO_4)_2$-I in oxidising conditions.

$Bi(H_3O)(SO_4)_2$, $Bi(HSO_4)_3$ and $Bi_2(SO_4)_3$

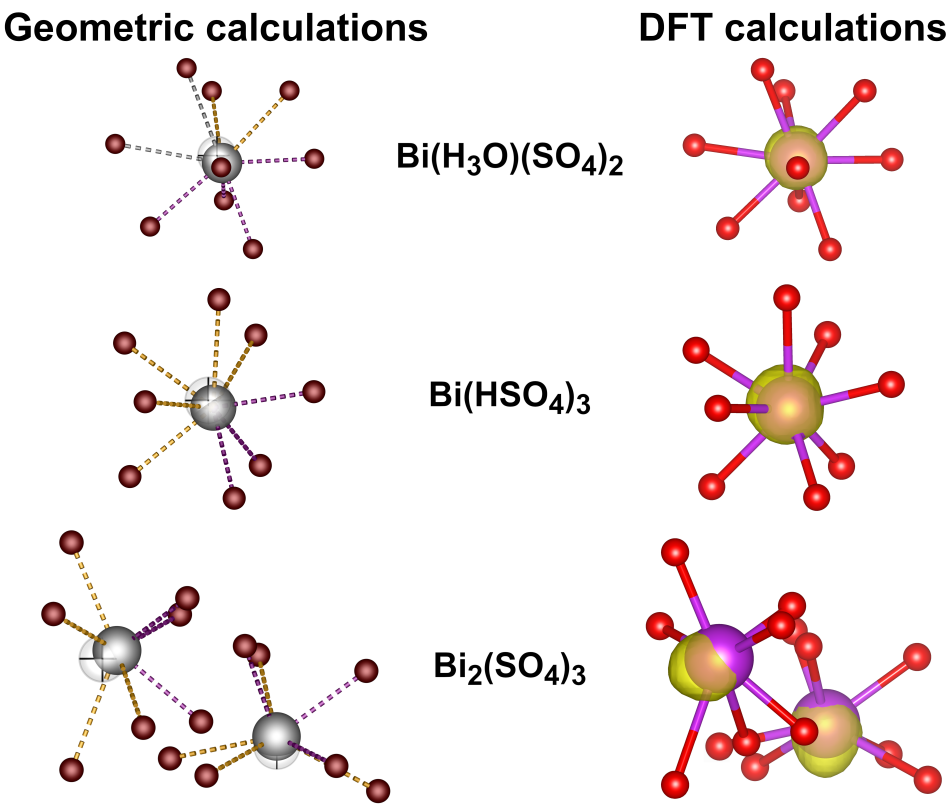

$Bi(H_3O)(SO_4)_2$, $Bi(HSO_4)_3$ and $Bi_2(SO_4)_3$ were synthesised solvothermally and characterised using SC-XRD, Rietveld refinements, DFT calculations, IR and UV-Vis spectroscopy and TGA. The three compounds comprise BiO_9, BiO_8 and BiO_7 polyhedra, respectively, and show stereochemical activity of the Bi^{3+} cations. The nature of the lone pair effect is investigated by both geometrical considerations based on structural data and DFT calculations employing ELF. Coincidence of both methods is achieved and a trend in the lone pair activity is found. It was shown that the geometrical calculations of the distance of the Bi^{3+} cation from the centroid of the respective polyhedron and the eccentricity by the method of Balić-Žunić and Makovicky are powerful tools both to investigate the direction of the lone pair effect and to quantify the strength of the stereochemical activity. Consequently, this method can be applied to any oxidic compound containing ns^2 cations, e.g. Bi^{3+} or Sn^{2+}, yielding insights of similar quality as accessible by ELF calculations using structural data, only.

Main Group Borosulfates

$Bi_2[B_2(SO_4)_6]$

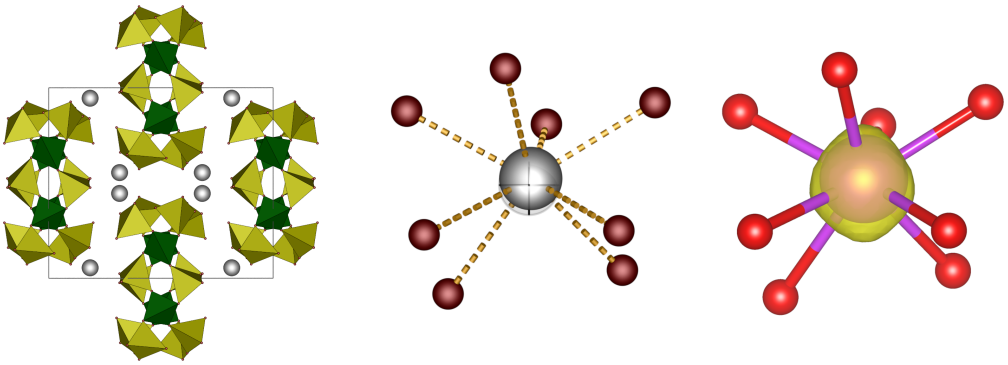

The first bismuth borosulfate $Bi_2[B_2(SO_4)_6]$ was synthesised solvothermally and characterised by SC-XRD, Rietveld refinement, DFT, IR and UV-Vis spectroscopy and TGA. It crystallises isotypic to $R_2[B_2(SO_4)_6]$ (R = Y, La-Nd, Sm-Lu) with a cyclosilicate-analogous borosulfate anion. However, in contrast to the rare earth representatives, stereochemical activity due to the lone pair effect of the bismuth cations was found. This was confirmed by both geometrical and ELF calculations. $Bi_2[B_2(SO_4)_6]$ decomposes thermally via $Bi_2(SO_4)_3$ to Bi_2O_3.

$Bi\boldsymbol{X}[B(SO_4)_2]_4$ ($\boldsymbol{X}$ = H_3O^+, NO_2^+ and NH_4^+)

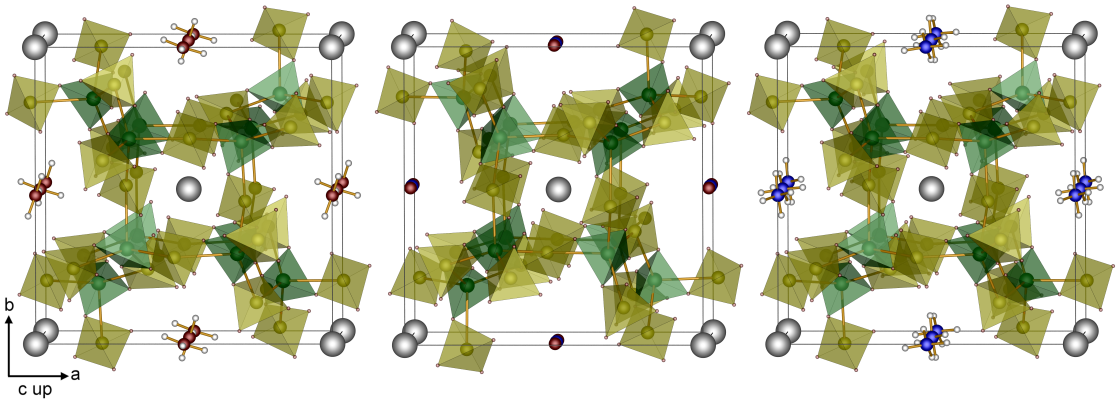

The further three bismuth borosulfates $Bi(H_3O)[B(SO_4)_2]_4$, $Bi(NO_2)[B(SO_4)_2]_4$ and $Bi(NH_4)[B(SO_4)_2]_4$ comprise - for the first time in borosulfate chemistry - two differently charged cations, i.e. the trivalent bismuth cation and the monovalent molecular cation, as well as tectosilicate-analogous borosulfate anions. Priorly, only one tectosilicate-analogous borosulfate was known, which could only be prepared via decomposition of a precursor. The three compounds were synthesised directly by solvothermal syntheses, i.e. without a precursor, and investigated using SC-XRD, PXRD, DFT, IR and UV-Vis spectroscopy, the powder SHG method and TGA as well as TPXRD. All three crystallise homeotypic, i.e. with the same three-dimensional borosulfate anion. Further, the lone pair effect is quenched confirmed by geometrical and ELF calculations. This appears to be related to the rigidity of the anionic substructure and the resulting lack of degrees of freedom. $Bi(H_3O)[B(SO_4)_2]_4$ is the first SHG active borosulfate and all three compounds exhibit SHG signals comparable to the benchmark KDP. Thermally, all three decompose to $Bi_2[B_2(SO_4)_6]$.

$(NH_4)Sb[B(SO_4)_2]_4$

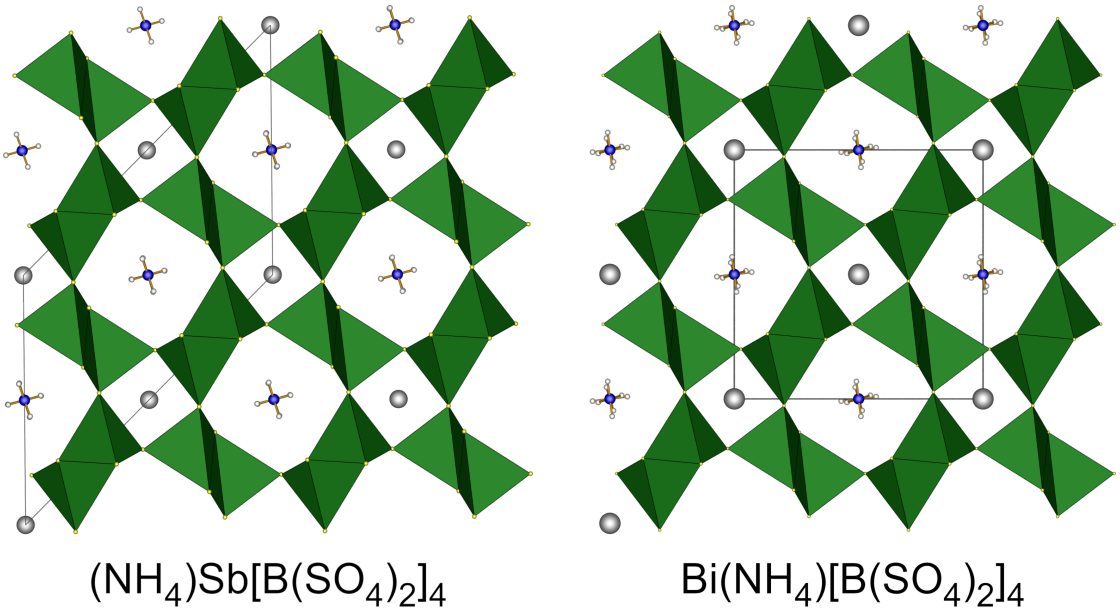

The first antimony borosulfate $(NH_4)Sb[B(SO_4)_2]_4$ comprises a tectosilicate-analogous borosulfate anion and crystallises in a new structure type. It was synthesised solvothermally and characterised using SC-XRD, PXRD, IR spectroscopy and the powder SHG method. The crystallographic relationship between $Bi(NH_4)[B(SO_4)_2]_4$ and $(NH_4)Sb[B(SO_4)_2]_4$ was described by a group-subgroup relation. In contrast to the aristotype, the lone pair effect is expressed in the hettotype $(NH_4)Sb[B(SO_4)_2]_4$. The lower symmetric crystal structure is a result of the additional degrees of freedom that the stereochemical activity needs to take shape. The tectosilicate-analogous borosulfate anion is merely insignificantly affected by the symmetry reduction. Again, a SHG signal comparable to the benchmark KDP could be measured.

Transition Metal Borosulfates

$Cd[B_2(SO_4)_4]$

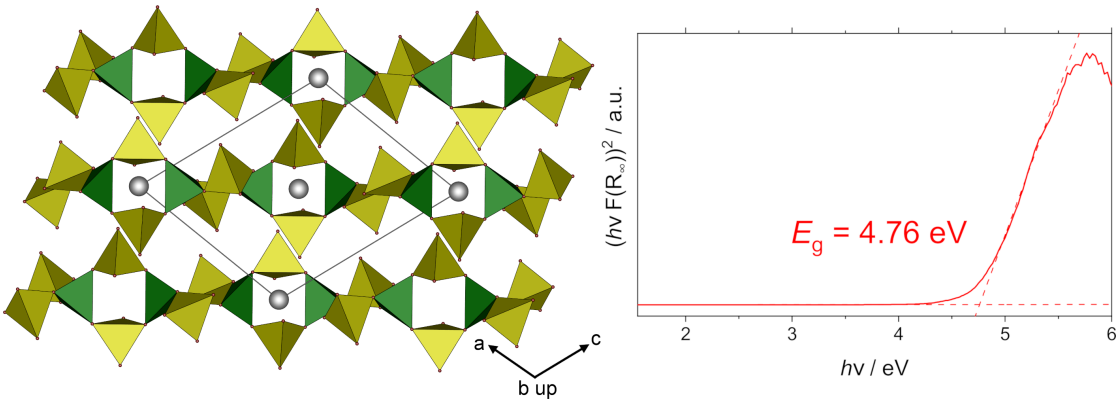

The first cadmium borosulfate $Cd[B_2(SO_4)_4]$ was prepared via solvothermal synthesis and investigated by SC-XRD, Rietveld refinement, IR and UV-Vis spectroscopy and TGA as well as TPXRD. It crystallises in the $Mn[B_2(SO_4)_4]$ structure type and thus, only homeotypic to $Zn[B_2(SO_4)_4]$ and comprises a phyllosilicate-analogous borosulfate anion. In contrast to other borosulfates with the general formula $M[B_2(SO_4)_4]$, no indication for synthesis dependent polymorphism was observed. The optical band gap was estimated using a Tauc plot and the thermal decomposition over $CdSO_4$ and CdB_4O_7 to CdO was elucidated. The thermal analysis indicated the existence of another cadmium borosulfate.

$Cu[B_2(SO_4)_4]$

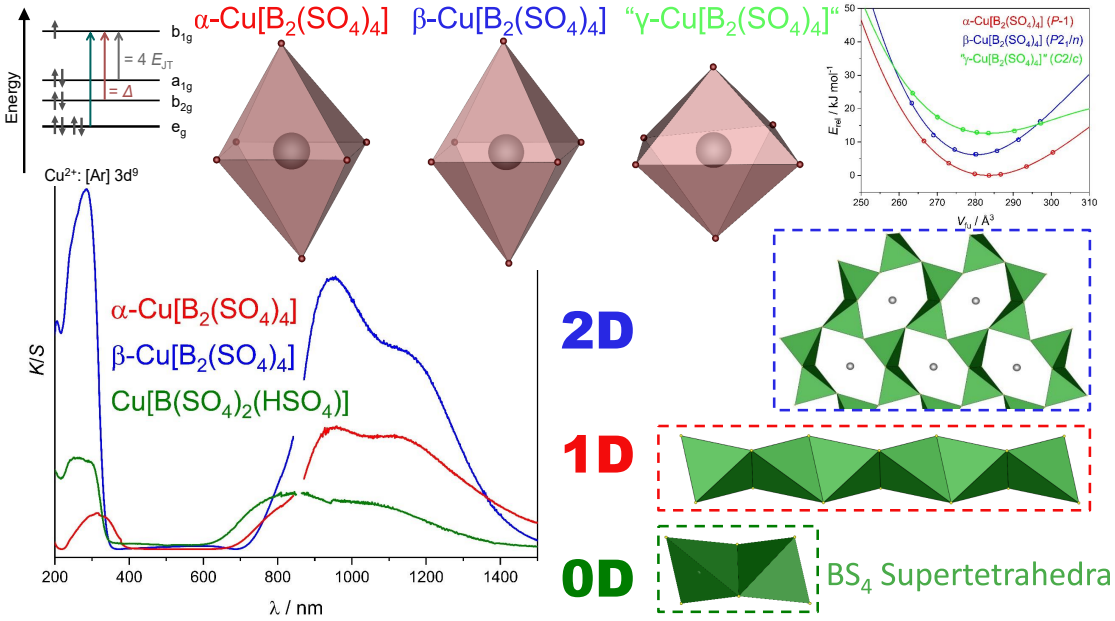

The two polymorphs α-$Cu[B_2(SO_4)_4]$ and β-$Cu[B_2(SO_4)_4]$ as well as the third copper borosulfate $Cu[B(SO_4)_2(HSO_4)]$ were prepared via selective solvothermal syntheses. Their crystal structure was (re)determined. In both inosilicate-analogous α-$Cu[B_2(SO_4)_4]$ and phyllosilicate-analogous β-$Cu[B_2(SO_4)_4]$ (crystallising isotypically to $Cd[B_2(SO_4)_4]$), the Cu^{2+} cation is octahedrally coordinated showing Jahn-Teller distortion resulting in elongated octahedra. The stability of the two polymorphs α-$Cu[B_2(SO_4)_4]$ and β-$Cu[B_2(SO_4)_4]$ was compared based on DFT. A third polymorph with a hypothetical structure isotypic to α-$Co[B_2(SO_4)_4]$ ("cation between layers") energetically close to the known structures is predicted. This γ-$Cu[B_2(SO_4)_4]$ model features rather unusual compressed CuO_6 octahedra.

The optical, magnetic and thermal properties of both $Cu[B_2(SO_4)_4]$ polymorphs and $Cu[B(SO_4)_2(HSO_4)]$ were characterised extensively. The Cu^{2+} cations confirmed by magnetic measurements govern the UV-Vis-NIR spectra with three distinct d-d transitions revealing the weak coordination behaviour of the borosulfate anion. Thermally, $Cu[B_2(SO_4)_4]$ and $Cu[B(SO_4)_2(HSO_4)]$ decompose above 190°C and 160°C, respectively. Hence, there are three borosulfates for one cation, namely copper, with either cyclo- (0D), ino- (1D) or phyllosilicate-analogous (2D) anions. Additionally, $Cu[B_2(SO_4)_4]$ is the first example in borosulfate chemistry of polymorphism with two polymorphs differing in the dimensionality of their borosulfate anions.

11 Conclusion and Outlook

Finally, conclusion are drawn based on the results presented in this thesis. They are roughly grouped by the material classes despite many aspects going beyond a single material class. Thus, these are discussed over the whole range of this work. Moreover, brief outlooks are given on further expansion and prospects.

Precursors

The research on carbon-based precursor materials yielded two main facets: On the one hand, new precursors can always be found especially when using additional synthesis methods. Firstly, the microwave-assisted hydrothermal synthesis yielded $Sr_3(C_6H_5O_7)_2 \cdot H_2O$. Apparently, the compound can only be prepared by this special method enabling the cheap and fast preparation. Secondly, the hydrothermal syntheses of $Ln[CO_3][OH]$ are the first using solely CO_2 from air as carbonate source resembling the geological formation of minerals such as *ancylite* or *kozoite*. $Sr_3(C_6H_5O_7)_2 \cdot H_2O$ and $Ln[CO_3][OH]$ were obtained in the form of plate-like and block-shaped crystals, respectively. Controlled morphology is crucial for precursors since it may be passed on to the final product. Works on other precursors showed that the morphology can be fine-tuned, e.g. by adjusting the pH value or adding further templating agents.[20] Such optimisation is expected to be also easily possible with the two precursors presented herein.

On the other hand, it was shown on the example of $Ln[CO_3][OH]$ that the powder SHG method is a powerful tool to clarify ambiguity with respect to crystal structures due to its ability to distinguish between centrosymmetric and non-centrosymmetric space groups. Consequently, the powder SHG method being a relatively easy experiment should gain more importance in crystallography. Still, crystal structure discussion are most commonly limited to diffraction experiments. Especially, when reporting crystal structures with a non-centrosymmetric space group, confirmation of this result by a powder SHG measurement should become the norm.

On a side note, the preparation of crystalline anhydrous strontium citrate remains the objective of further investigations. FT-IR data showed the successful dehydration of the respective hydrates. With more careful dehydration methods, this might be possible without losing long range order.

Tungstates

The tungstates containing both alkali and rare earth metals studied in this work are an excellent example for the fact that research is never finished nor completed. Despite over a century of past research, it was still possible to add new insights to these material groups. The straightforward explanation of the melting point and decomposition temperature of $Na_5M(WO_4)_4$ not following the lanthanide contraction based on the difference in ionic radii and *chemical twinning* shows that the properties of rare earth containing compounds are often, but not always, governed by the lanthanide contraction. Thus, it is worth to investigate such compounds over the whole range of lanthanides. For the phenomenon of cross-relaxation, structure-property relations were established beyond simple distance considerations. These await testing on other material classes. Further, the energy barrier between the ground and the first excited state of Sm^{3+} was determined from magnetic measurements for the first time for any ionic compound on the example $Na_5Sm(WO_4)_4$. This emphasises the suitability of these tungstates as probes to study fundamental properties due to their simple syntheses, excellent long-term stability and the feasibility to prepare large single-crystals.

Sulfatotungstates

Only the fifth member was added to the small material class of sulfatotungstates. However, they are promising materials for optical applications. In addition to the weak coordination behaviour of the sulfate moieties, the tungstate group acting as an antenna might foster interesting optical properties. Thus, the next step is the incorporation of an activator into these structures. Since their syntheses dependent on the melt formation, double sulfatotungstates comprising both alkali as well as rare earth metals are conceivable if the rare earth metals are added in the form of sulfates. Further, the rare earth representatives known in literature were prepared solvothermally from rare earth oxides, $WOCl_4$ and oleum. The combination of both methods might yield further expansion of this material class. An excess of the SO_x educts should be helpful to suppress the formation of the double tungstates also studied in this work. Further, preliminary experiments revealed that the extraordinary stability of alkaline earth sulfates is a major obstacle for the preparation of respective sulfatotungstates.[279]

Sulfates

The same consideration as for the tungstates holds for the tin and bismuth sulfates. In spite of 90 years of research, new compounds and new crystal structures could be added to the ternary or quaternary systems Sn-S-O, Bi-S-O and Bi-S-O-H. This highlights that it can be worth to revisit well-known regions of solid-state chemistry employing not yet extensively used methods like the solvothermal syntheses in sulfuric acid utilised herein.

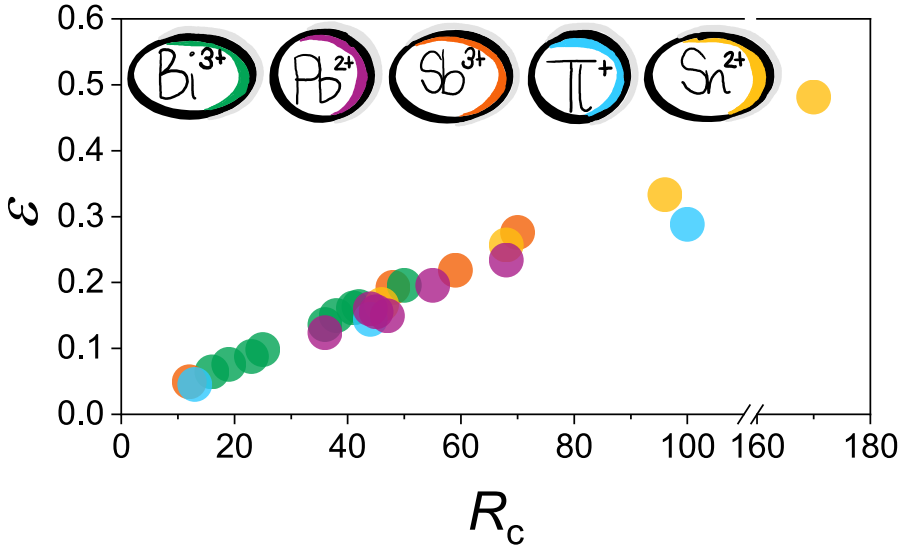

Fig. 11.0.1: Colour-coded values for the distance from the centroid R_c and the eccentricity ϵ for various oxidic compounds from this work and from literature: The colours represent the stereoactive ns^2 ions with the legend given at the top of the figure; the data used for this graph can be found in Table G.0.1.

Future work on sulfates could be dedicated to non-centrosymmetric structures comprising Sn^{2+}. This might be fostered by the introduction of halogen ions.[107,108] Additionally, the experiences from the tin sulfates might be helpful for the preparation of the first tin borosulfate which still awaits its discovery. Moreover, $Bi_2O(SO_4)_2$ is present in this work as thermal decomposition product of $Bi_2(SO_4)_3$. It is reported both from geological orgin[i] and synthetically. Its temperature-dependent polymorphism was so far only poorly studied.[459] The selective syntheses of both polymorphs and the redetermination of their crystal structures are desirable[189] to further enrich and elucidate the Bi-S-O system.

Furthermore, the sulfates are excellent model systems. With the help of quantum chemical calculations of the electron localisation function (ELF), it could be shown that the stereochemical activity of ns^2 cations can be assessed by simple geometric calculations by the method of Balić-Žunić and Makovicky.[182,183] The ELF and the geometric calculations coincide very well. Thus, crystal structures can be quantified exclusively by these geometric calculations. Figure 11.0.1 shows respective results for various oxidic compounds from this work and from literature. In principle, there is no reason why this method should not work for non-oxidic compounds. It is a great way to check if a certain crystal structure shows an expressed or quenched lone pair effect - especially in the case of ambiguous coordination environments.[ii]

In contrast to the lone pair effect being an effect of the central atom of the respective polyhedra and thus, affecting the eccentricity, the Jahn-Teller effect is a ligand field effect

[i] In form of the mineral *balićžunićite*.[189]

[ii] Naturally, the method stops working for coordination numbers smaller than four. However, in these cases, the stereochemical activity is obvious and the method unnecessary.

that effects the shape of the polyhedron and not the eccentricities. Thus, large polyhedra deviations, but small eccentricities are found. Consequently, the calculations can also be used to distinguish between various effects distorting the coordination environments within the studied crystal structure from an ideal symmetric arrangement. For example, the sulfatotungstates showed large eccentricities, but small polyhedra deviations due to electrostatic repulsion governed by the charges of the central atoms. To summarise, the geometrical calculations are generally suited to quantify the influence of both the Jahn-Teller and the pseudo Jahn-Teller effect on crystal structures. Consequently, they are very helpful to assess crystal structures since these two effects are the only sources of distortions away from high-symmetry configurations.[58]

Borosulfates

The elemental diversity of borosulfates could be enriched by three elements, namely bismuth, antimony and cadmium. Thus, there are 34 cations incorporated in borosulfates with reported crystal structures excluding molecular cations such as NH_4^+ or H_3O^+, up to date. Beyond that, novel structure types comprising tectosilicate-analogous anions could be found. Prior to this work, only one tectosilicate-analogous borosulfate was known. Four new ones were added (Figure 11.0.1). Certainly, there are many more to be added in the near future. The Bi^{3+}-R^{3+} analogy works both ways: While $Bi_2[B_2(SO_4)_6]$ crystallising isotypically to $R_2[B_2(SO_4)_6]$ was presented herein, the borosulfates $RX[B(SO_4)_2]_4$ ($X = H_3O^+$, NO_2^+ and NH_4^+) crystallise isotypically to the bismuth representatives. Multiple of these borosulfates could be synthesised and are further investigated.[428,438] They merit the study of their luminescent properties with potential insights into the influence of the anion's dimensionality on its coordination strength. Additionally, solid solutions $(Y_{1-x}Tb_x)_2[B_2(SO_4)_6]$ and $Y_{1-x}Tb_xX[B(SO_4)_2]_4$ could be suited to test the cross-relaxation structure-property relations established for the tungstates herein.

Despite prior research indicating a decrease in thermal and overall stability of borosulfate with increasing dimensionality of its anion, the tectosilicate-analogous anion in $BiX[B(SO_4)_2]_4$ and $(NH_4)Sb[B(SO_4)_2]_4$ appears to be surprisingly stable and flexible stabilising both trivalent cations with quenched and expressed lone pair effects. The incorporation of monovalent silver cations into this network can be expected to be possible. Further, the fact that two differently charged cations are present in these borosulfates indicate the existence of much more borosulfates with two cations. The low valent cations appear to stabilise the high charged cations. Future research should be dedicated to identify and optimise the synthesis conditions at which the incorporation of two cations instead of one is favoured. Particularly, tetravalent metal cations, e.g. Sn^{4+} or Ti^{4+}, might be stabilised in combination with monovalent cations like in $A_2[Sn(S_2O_7)_3]$ (A = NH_4, Ag).[358]

Moreover, these tectosilicate-analogous borosulfates are SHG active. Their construction of tetrahedral building units lacking inversion symmetry makes them interesting SHG

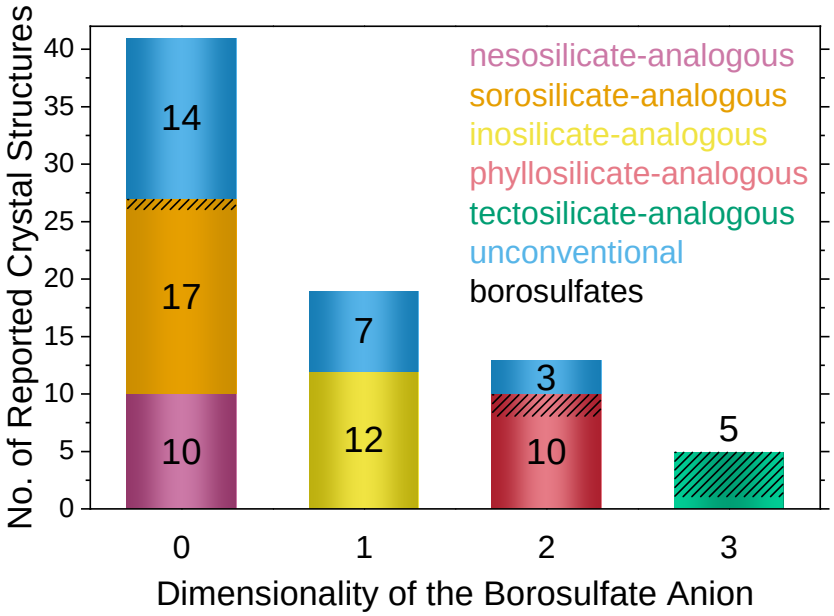

Fig. 11.0.1: Number of reported borosulfates shown with respect to the dimensionality of their borosulfate anion, i.e. the connection of supertetrahedra: The respective silicate-analogies are colour coded; unconventional borosulfates comprise either S-O-S or B-O-B, or trigonal planar BO_3 building units; in contrast to Figure 1.6.2, the borosulfates presented in this work are included; the respective differences are hatched; seven new crystal structures were added.

materials. Further improvement of the SHG coefficients can be expected for a borosulfate comprising divalent tin or by the integration of trigonal planar BO_3 building units. The former is complicated by the stability of the tin sulfates presented herein. One possibility - besides the already mentioned incorporation of stabilising monovalent cations - might be the reduction of the SO_3 content by the use of the method reported by Pasqualini et al.[460] The insertion of trigonal BO_3 moieties appears to be only possible for huge boron to sulfur ratios[77] that cannot be realised in solvothermal synthesis. However, many new borosulfates await their discovery in this ever-expanding and fascinating material class. There are still four compounds reported by Schott and Kibbel in 1962[73] that were - so far - not reproduced in order to determine their crystal structures. Namely, these are $Cs[B(SO_4)_2]$, $Tl[B(SO_4)_2]$, $Hg[B_2(SO_4)_4]$ and $Ca[B_2O(SO_4)_3]$. Additionally, it is possible that a whole new - boron-rich - subgroup of borosulfates is only accessible via chemical vapour deposition.[77]

In addition to these optical properties, silicate-analogous materials are frequently suited as solid-state ion conductors.[461] In particular, the borosulfate $NH_4[B(SO_4)_2]$ is a promising electrolyte for solid acid fuel cells due to its high proton conductivity.[462] Similarly, the proton conductivity of the two borosulfates $Bi(NH_4)[B(SO_4)_2]_4$ and $(NH_4)Sb[B(SO_4)_2]_4$ should be worth investigating since the disordered ammonium groups indicate high proton mobility.

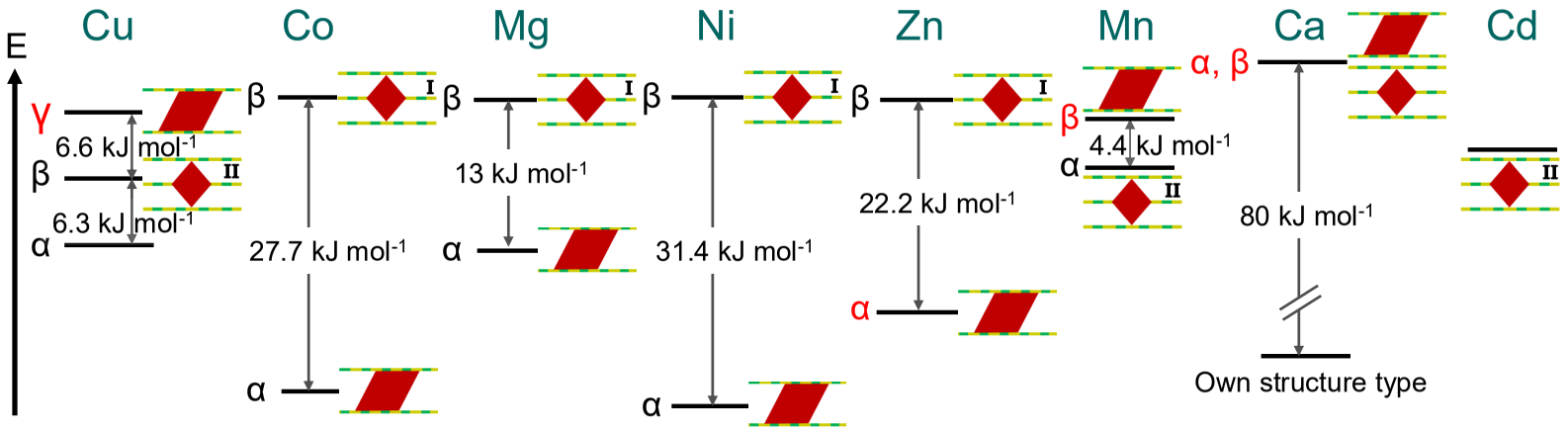

Fig. 11.0.2: Polymorphism of the borosulfates with the general formula $M[B_2(SO_4)_4]$: The metals M are given on top. Below the differences in total electronic energies are displayed as they can be found in literature.[83,89] In all cases, the polymorphs were labelled α and β with decreasing stability. Black letters symbolise experimental crystal structures,[82–84,88,89,438] red indicate that these phases were predicted by DFT, but not yet experimentally found. The pictograms explained in Figure 9.0.1 indicate if either the "cation between layer" or "cation within layer" is adapted. The further discrimination between the homeotypic "cation within layer" structure types is given by little Roman numbers with "I" representing the $Zn[B_2(SO_4)_4]$ and "II" the $Mn[B_2(SO_4)_4]$ structure type, respectively. In contrast to Figure 9.0.2 the results on $Cd[B_2(SO_4)_4]$ and $Cu[B_2(SO_4)_4]$ were added.

Lastly, the importance of synthesis in borosulfate chemistry is - once more - underlined by the synthesis-dependent polymorphism for the transition metal borosulfates with the general formula $M[B_2(SO_4)_4]$. An overview over this group including the results from this work is given in Figure 11.0.2. There are still several polymorphs predicted by DFT that have not been prepared and characterised experimentally. Remarkably, so far, the two polymorphs ("cation between layer" and "cation within layer") could only be prepared for borosulfates with the latter crystallising in the $Zn[B_2(SO_4)_4]$ structure type and not for the ones adapting the $Mn[B_2(SO_4)_4]$ structure type - with the exception of $Cu[B_2(SO_4)_4]$. More data is needed to reveal the underlying trend for this. However, the exceptional behaviour of $Cu[B_2(SO_4)_4]$ is clearly related to the strong Jahn-Teller effect. This observation might reveal the limitations of solvothermal synthesis, again. Moreover, the phenomena synthesis and temperature[76] dependent polymorphism imply that polymorphism has probably been overlooked for various borosulfates. It is worth revisiting some borosulfates that were only studied incompletely - especially to investigate their thermal decomposition.[86,96]

In conclusion, it was shown that the vast structural diversity of both naturally occurring and synthetic silicates can even be topped by the substitution variants tungstates, sulfatotungstates, sulfates and borosulfates. These silicate-analogous materials show interesting optical properties like the absence of concentration quenching facilitating 100% phosphors or large SHG intensities. Structure-property relations were established between the 27 new and 22 redetermined crystal structures reported herein - including 11 new structure types - and optical, magnetic and thermal properties. In particular, for the double substituted material classes of sulfatotungstates and borosulfates, further expansion is expected possibly yielding promising applications as phosphors or SHG materials - similar to other also double substituted silicate-analogous variants like oxonitridosilicates and flurooxoborates for whom these special optical properties are already well-known.[8,103]

Bibliography

[1] F. Liebau, *Structural Chemistry of Silicates*, Springer, Heidelberg, **1985**.

[2] F. Liebau, *Angew. Chem. Int. Ed.* **1999**, *38*, 1733–1737; *Angew. Chem.* **1999**, *111*, 1845–1850.

[3] K. H. Wedepohl, *Geochemistry*, Holt, Rinehart and Winston, New York, **1971**.

[4] F. C. Hawthorne, R. Oberti, G. E. Harlow, W. V. Maresch, R. F. Martin, J. C. Schumacher, M. D. Welch, *Amer. Min.* **2012**, *97*, 2031–2048.

[5] N. Morimoto, *Miner. Petrol.* **1988**, *39*, 55–76.

[6] P. Ptáček in *Apatites and their Synthetic Analogues - Synthesis, Structure, Properties and Applications*, (Ed.: P. Ptáček), IntechOpen, **2016**.

[7] Y. Li, L. Li, J. Yu, *Chem* **2017**, *3*, 928–949.

[8] M. Zeuner, S. Pagano, W. Schnick, *Angew. Chem. Int. Ed.* **2011**, *50*, 7754–7775; *Angew. Chem.* **2011**, *123*, 7898–7920.

[9] R. Mueller-Mach, G. Mueller, M. R. Krames, H. A. Höppe, F. Stadler, W. Schnick, T. Juestel, P. Schmidt, *Phys. Stat. Sol. (a)* **2005**, *202*, 1727–1732.

[10] B. Ewald, Y.-X. Huang, R. Kniep, *Z. Anorg. Allg. Chem.* **2007**, *633*, 1517–1540.

[11] M. Zhang, J. Wang, W. Ding, Q. Zhang, Q. Su, *Appl. Phys. B* **2007**, *86*, 647–651.

[12] J. Bruns, H. A. Höppe, M. Daub, H. Hillebrecht, H. Huppertz, *Chem. Eur. J.* **2020**, *26*, 7966–7980.

[13] G. A. Lager, F. K. Ross, F. J. Rotella, J. D. Jorgensen, *J. Appl. Crystallogr.* **1981**, *14*, 137–139.

[14] L. Pauling, *Z. Kristallogr.* **1933**, *84*, 442–452.

[15] A. A. Kossiakoff, P. B. Leavens, *Amer. Min.* **1976**, *61*, 956–962.

[16] J. Zussman, *Acta Crystallogr.* **1959**, *12*, 309–312.

[17] T. Kato, Y. Takeuchi, *Can. Mineral.* **1983**, *21*, 1–6.

[18] R. Sadanaga, F. Marumo, Y. Takéuchi, *Acta Crystallogr.* **1961**, *14*, 1153–1163.

[19] C. Sanchez, L. Rozes, F. Ribot, C. Laberty-Robert, D. Grosso, C. Sassoye, C. Boissiere, L. Nicole, *C. R. Chim.* **2010**, *13*, 3–39.

[20] A. M. Kaczmarek, K. van Hecke, R. van Deun, *Chem. Soc. Rev.* **2015**, *44*, 2032–2059.

[21] A. M. Kaczmarek, R. van Deun, *Chem. Soc. Rev.* **2013**, *42*, 8835–8848.

[22] C. S. Riccardi, R. C. Lima, M. L. dos Santos, P. R. Bueno, J. A. Varela, E. Longo, *Solid State Ionics* **2009**, *180*, 288–291.

[23] Z. Xu, S. Bian, J. Wang, T. Liu, L. Wang, Y. Gao, *RSC Adv.* **2013**, *3*, 1410–1419.

[24] P. Gross, H. A. Höppe, *Chem. Mater.* **2019**, *31*, 8052–8061.

[25] A. G. Högbom, *Öfvers. Akad. Stockholm* **1885**, *42*.

[26] F. R. M. Hitchcock, *J. Am. Chem. Soc.* **1895**, *17*, 483–494.

[27] E. D. Desi, *J. Am. Chem. Soc.* **1897**, *19*, 213–242.

[28] M. Gärtner, D. Abeln, A. Pring, M. Wilde, A. Reller, *J. Solid State Chem.* **1994**, *111*, 128–133.

[29] T. Gressling, H. Müller-Buschbaum, *Z. Naturforsch. B* **1995**, *50*, 1513–1516.

[30] M. Weil, B. Stöger, L. Aleksandrov, *Acta Crystallogr. E* **2009**, *65*, i45.

[31] D. H. Templeton, A. Zalkin, **1963**, *16*, 762–766.

[32] S. Rong, W. Cong, W. Tianmin, D. Cheng, C. X. Long, L. J. Kui, *Rare Met.* **2003**, *22*, 49–54.

[33] S. Han, Y. Wang, Q. Jing, H. Wu, S. Pan, Z. Yang, *Dalton Trans.* **2015**, *44*, 5810–5817.

[34] J. M. Serres, P. Loiko, V. Jambunathan, X. Mateos, V. Vitkin, A. Lucianetti, T. Mocek, M. Aguiló, F. Díaz, U. Griebner, V. Petrov, **2018**, *43*, 218–221.

[35] T. Guo, Y. Lin, W.-J. Zhang, J.-S. Hong, R.-H. Lin, X.-P. Wu, J. Li, C.-H. Lu, H.-H. Yang, **2018**, *10*, 1607–1612.

[36] S. M. Martinussen, R. N. Frentrop, M. Dijkstra, F. Segerink, V. Tormo-Márquez, J. Olivares, S. M. Garcia-Blanco, *Opt. Mater. Express* **2019**, *9*, 3371.

[37] M. Laguna, A. Escudero, N. O. Núñez, A. I. Becerro, M. Ocaña, *Dalton Trans.* **2017**, *46*, 11575–11583.

[38] Y. Liu, G. Liu, J. Wang, X. Dong, W. Yu, *Inorg. Chem.* **2014**, *53*, 11457–11466.

[39] T. Schustereit, P. Netzsch, H. A. Höppe, I. Hartenbach, *Z. Anorg. Allg. Chem.* **2018**, *101*, 11.

[40] Z. Han, A. Golev, M. Edraki, *Minerals* **2021**, *11*, 701.

[41] T. Betz, R. Hoppe, *J. Less-Common Met.* **1985**, *105*, 87–104.

[42] U. Betke, M. S. Wickleder, *Inorg. Chem.* **2011**, *50*, 858–872.

[43] M. I. Kay, B. C. Frazer, I. Almodovar, *J. Chem. Phys.* **1964**, *40*, 504–506.

[44] D. Ülkü, *Z. Kristallogr.* **1967**, *124*, 192–219.

[45] H. Cid-Dresdner, C. Escobar, *Z. Kristallogr.* **1968**, *127*, 61–72.

[46] S. Azuma, T. Kadoguchi, Y. Eguchi, H. Hirabaru, H. Ota, M. Sadakane, K. Yanagisawa, T. Hasegawa, T. Ueda, *Dalton Trans.* **2020**, *49*, 2766–2770.

[47] S. J. C. Schäffer, R. W. Berg, *Acta Crystallogr. E* **2005**, *61*, i49–i51.

[48] K. Ståhl, R. W. Berg, *Acta Crystallogr. E* **2009**, *65*, i88.

[49] U. Betke, M. S. Wickleder, *Eur. J. Inorg. Chem.* **2011**, *2011*, 4400–4413.

[50] S. Boghosian, *J. Catal.* **1989**, *119*, 121–134.

[51] F. Borup, R. W. Berg, K. Nielsen, M. Trætteberg, H. Yamada, B. Långström, T. Tokii, *Acta Chem. Scand.* **1990**, *44*, 328–331.

[52] T. Noerbygaard, R. W. Berg, K. Nielsen, *ECS PV* **1998**, *1998-11*, 553–573.

[53] R. W. Berg, N. Thorup, *Inorg. Chem.* **2005**, *44*, 3485–3493.

[54] R. W. Berg, I. M. Ferré, S. J. C. Schäffer, *Vib. Spectrosc.* **2006**, *42*, 346–352.

[55] L. Pauling, *J. Am. Chem. Soc.* **1929**, *51*, 1010–1026.

[56] L. V. Schindler, A. Becker, M. Wieckhusen, T. Klüner, M. S. Wickleder, *Angew. Chem. Int. Ed.* **2016**, *55*, 16165–16167; *Angew. Chem.* **2016**, *128*, 16399–16401.

[57] B. A. Maksimov, V. P. Kalinin, B. V. Merinov, V. V. Ilyukhin, N. V. Belov, *Dokl. Akad. Nauk SSSR* **1980**, *252*, 875–879.

[58] I. B. Bersuker, *Chem. Rev.* **2013**, *113*, 1351–1390.

[59] B. N. Figgis, M. A. Hitchman, *Ligand field theory and its applications*, Wiley-VCH, New York, NY, **2000**.

[60] H. A. Jahn, E. Teller, *Proc. R. Soc. Lond. A* **1937**, *161*, 220–235.

[61] F. C. Hawthorne, M. A. Cooper, *Mineral. mag.* **2013**, *77*, 2901–2912.

[62] U. Öpik, M. H. L. Pryce, *Proc. R. Soc. Lond. A* **1957**, *238*, 425–447.

[63] R. J. Gillespie, *J. Chem. Soc.* **1963**, 4672–4678.

[64] R. J. Gillespie, *J. Chem. Educ.* **1963**, *40*, 295–301.

[65] R. J. Gillespie, *Coord. Chem. Rev.* **2008**, *252*, 1315–1327.

[66] S. Andersson, A. Åström, J. Galy, G. Meunier, *J. Solid State Chem.* **1973**, *6*, 187–190.

[67] J. Galy, G. Meunier, S. Andersson, A. Åström, *J. Solid State Chem.* **1975**, *13*, 142–159.

[68] L. E. Orgel, *J. Chem. Soc.* **1959**, 3815–3819.

[69] M. Atanasov, D. Reinen, *J. Am. Chem. Soc.* **2002**, *124*, 6693–6705.

[70] A. Walsh, D. J. Payne, R. G. Egdell, G. W. Watson, *Chem. Soc. Rev.* **2011**, *40*, 4455–4463.

[71] W. G. Zeier, A. Zevalkink, Z. M. Gibbs, G. Hautier, M. G. Kanatzidis, G. J. Snyder, *Angew. Chem. Int. Ed.* **2016**, *55*, 6826–6841; *Angew. Chem.* **2016**, *128*, 6938–6954.

[72] D. J. Payne, R. G. Egdell, A. Walsh, G. W. Watson, J. Guo, P.-A. Glans, T. Learmonth, K. E. Smith, *Phys. Rev. Lett.* **2006**, *96*, 157403.

[73] G. Schott, H. U. Kibbel, *Z. Anorg. Allg. Chem.* **1962**, *314*, 104–112.

[74] R. J. Gillespie, E. A. Robinson, *Can. J. Chem.* **1962**, *40*, 784–787.

[75] H. A. Höppe, K. Kazmierczak, M. Daub, K. Förg, F. Fuchs, H. Hillebrecht, *Angew. Chem. Int. Ed.* **2012**, *51*, 6255–6257; *Angew. Chem.* **2012**, *124*, 6359–6362.

[76] P. Netzsch, R. Stroh, F. Pielnhofer, I. Krossing, H. A. Höppe, *Angew. Chem. Int. Ed.* **2021**, *60*, 10643–10646; *Angew. Chem.* **2021**, *133*, 10738–10741.

[77] Z. Li, W. Jin, F. Zhang, Z. Chen, Z. Yang, S. Pan, *Angew. Chem. Int. Ed.* **2022**, *61*, e202112844.

[78] J. Peters, B. Krebs, *Acta Crystallogr. B* **1982**, *38*, 1270–1272.

[79] M. Daub, K. Kazmierczak, P. Gross, H. A. Höppe, H. Hillebrecht, *Inorg. Chem.* **2013**, *52*, 6011–6020.

[80] M. Daub, H. A. Höppe, H. Hillebrecht, *Z. Anorg. Allg. Chem.* **2014**, *640*, 2914–2921.

[81] J. Bruns, M. Podewitz, M. Schauperl, K. R. Liedl, O. Janka, R. Pöttgen, H. Huppertz, *Eur. J. Inorg. Chem.* **2017**, 3981–3989.

[82] P. Netzsch, P. Gross, H. Takahashi, H. A. Höppe, *Inorg. Chem.* **2018**, *57*, 8530–8539.

[83] P. Netzsch, F. Pielnhofer, R. Glaum, H. A. Höppe, *Chem. Eur. J.* **2020**, *26*, 14745–14753.

[84] J. Bruns, M. Podewitz, M. Schauperl, B. Joachim, K. R. Liedl, H. Huppertz, *Chem. Eur. J.* **2017**, *23*, 16773–16781.

[85] P. Netzsch, H. A. Höppe, *Z. Anorg. Allg. Chem.* **2020**, *646*, 1563–1569.

[86] P. Netzsch, F. Pielnhofer, H. A. Höppe, *Inorg. Chem.* **2020**, *59*, 15180–15188.

[87] S. Schönegger, J. Bruns, B. Gartner, K. Wurst, H. Huppertz, *Z. Anorg. Allg. Chem.* **2018**, *644*, 1702–1706.

[88] L. C. Pasqualini, H. Huppertz, J. Bruns, *Inorganics* **2019**, *7*, 145.

[89] L. C. Pasqualini, O. Janka, S. Olthof, H. Huppertz, K. R. Liedl, R. Pöttgen, M. Podewitz, J. Bruns, *Chem. Eur. J.* **2020**, *26*, 17405–17415.

[90] J. Bruns, M. Podewitz, K. R. Liedl, O. Janka, R. Pöttgen, H. Huppertz, *Angew. Chem. Int. Ed.* **2018**, *57*, 9548–9552.

[91] P. Netzsch, P. Gross, H. Takahashi, S. Lotfi, J. Brgoch, H. A. Höppe, *Eur. J. Inorg. Chem.* **2019**, 3975–3981.

[92] P. Gross, A. Kirchhain, H. A. Höppe, *Angew. Chem. Int. Ed.* **2016**, *55*, 4353–4355; *Angew. Chem.* **2016**, *128*, 4426–4428.

[93] M. Daub, Dissertation, Albert-Ludwigs-Universität Freiburg im Breisgau, **2015**.

[94] P. Netzsch, Dissertation, Universität Augsburg, **2021**.

[95] P. Netzsch, M. Hämmer, P. Gross, H. Bariss, T. Block, L. Heletta, R. Pöttgen, J. Bruns, H. Huppertz, H. A. Höppe, *Dalton Trans.* **2019**, *48*, 4387–4397.

[96] P. Netzsch, H. A. Höppe, *Inorg. Chem.* **2020**, *59*, 18102–18108.

[97] W. Loewenstein, *Amer. Min.* **1954**, *39*, 92–96.

[98] S. Nakamura, T. Mukai, M. Senoh, *Appl. Phys. Lett.* **1994**, *64*, 1687–1689.

[99] S. Nakamura, *Angew. Chem. Int. Ed.* **2015**, *54*, 7770–7788.

[100] M. Hämmer, Master Thesis, Universität Augsburg, **2016**.

[101] H. A. Höppe, *Angew. Chem. Int. Ed.* **2009**, *48*, 3572–3582; *Angew. Chem.* **2009**, *121*, 3626–3636.

[102] P. A. Franken, A. E. Hill, C. W. Peters, G. Weinreich, *Phys. Rev. Lett.* **1961**, *7*, 118–119.

[103] S. G. Jantz, M. Dialer, L. Bayarjargal, B. Winkler, L. van Wüllen, F. Pielnhofer, J. Brgoch, R. Weihrich, H. A. Höppe, *Adv. Opt. Mater.* **2018**, *7*, 1800497.

[104] Y. Liu, X. Liu, S. Liu, Q. Ding, Y. Li, L. Li, S. Zhao, Z. Lin, J. Luo, M. Hong, *Angew. Chem. Int. Ed.* **2020**, *59*, 7793–7796.

[105] P. Huber, *Opt. Commun.* **1975**, *15*, 196–200.

[106] R. Cong, Y. Wang, L. Kang, Z. Zhou, Z. Lin, T. Yang, *Inorg. Chem. Front.* **2015**, *2*, 170–176.

[107] K. Chen, Y. Yang, G. Peng, S. Yang, T. Yan, H. Fan, Z. Lin, N. Ye, *J. Mater. Chem. C* **2019**, *7*, 9900–9907.

[108] X. Dong, L. Huang, C. Hu, H. Zeng, Z. Lin, X. Wang, K. M. Ok, G. Zou, *Angew. Chem. Int. Ed.* **2019**, *58*, 6528–6534.

[109] M. Luo, F. Liang, Y. Song, D. Zhao, N. Ye, Z. Lin, *J. Am. Chem. Soc.* **2018**, *140*, 6814–6817.

[110] S. Schönegger, S. G. Jantz, A. Saxer, L. Bayarjargal, B. Winkler, F. Pielnhofer, H. A. Höppe, H. Huppertz, *Chem. Eur. J.* **2018**, *24*, 16036–16043.

[111] Y. Li, F. Liang, S. Zhao, L. Li, Z. Wu, Q. Ding, S. Liu, Z. Lin, M. Hong, J. Luo, *J. Am. Chem. Soc.* **2019**, *141*, 3833–3837.

[112] P. Netzsch, H. Bariss, L. Bayarjargal, H. A. Höppe, *Dalton Trans.* **2019**, *48*, 16377–16383.

[113] I. Zelenina, P. Simon, I. Veremchuk, X. Wang, M. Bobnar, W. Lu, C. H. Liebscher, Y. Grin, *Commun. Mater.* **2021**, *2*, 526.

[114] A. R. West, *Solid State Chemistry and its Applications*, 2. ed., Wiley, Hoboken, **2014**.

[115] L. Smart, E. A. Moore, *Solid state chemistry: An introduction*, 3rd ed., Taylor and Francis, Boca Raton, **2005**.

[116] A. D. Smigelskas, E. O. Kirkendall, *Trans. AIME* **1947**, *171*, 130–142.

[117] M. Daub, A. J. Lehner, H. A. Höppe, *Dalton Trans.* **2012**, *41*, 12121–12128.

[118] K. Byrappa, M. Yoshimura, *Handbook of hydrothermal technology*, 2. ed., Elsevier/Andrews, Amsterdam, **2013**.

[119] H. Heinrichs, H.-J. Brumsack, N. Loftfield, N. König, *Z. Pflanzenernaehr. Bodenk.* **1986**, *149*, 350–353.

[120] W. Massa, *Kristallstrukturbestimmung*, 5., überarb. Aufl., Teubner, Wiesbaden, **2007**.

[121] V. Wessels, Master Thesis, Universität Augsburg, **2021**.

[122] W. Clegg, *X-ray crystallography*, 2. ed., Oxford Univ. Press, Oxford, **2015**.

[123] G. Taylor, *Acta Crystallogr. D* **2003**, *59*, 1881–1890.

[124] H. Hauptman, *Angew. Chem.* **1986**, *98*, 600–610.

[125] A. L. Patterson, *Z. Kristallogr.* **1935**, *90*, 517–542.

[126] G. M. Sheldrick, *Acta Crystallogr. C* **2015**, *71*, 3–8.

[127] Bruker AXS, APEX3, Version 2016.9-0, Madison, Wisconsin, USA, **2016**.

[128] Bruker AXS, SADABS, Madison, Wisconsin, USA, **2001**.

[129] G. M. Sheldrick, *Acta Crystallogr. A* **2008**, *64*, 112–122.

[130] T. Steiner, *Angew. Chem. Int. Ed.* **2002**, *41*, 48–76; *Angew. Chem.* **2002**, *114*, 50–80.

[131] G. Will, *Powder diffraction: The Rietveld method and the two-stage method to determine and refine crystal structures from powder diffraction data*, Springer, Berlin and New York, **2006**.

[132] H. M. Rietveld, *Acta Crystallogr.* **1967**, *22*, 151–152.

[133] H. M. Rietveld, *J. Appl. Crystallogr.* **1969**, *2*, 65–71.

[134] H. M. Rietveld, *Z. Kristallogr.* **2010**, *225*, 545–547.

[135] R. A. Young, *The Rietveld method*, Repr, Oxford Univ. Press, Oxford, **2002**.

[136] R. W. Cheary, A. Coelho, *J. Appl. Crystallogr.* **1992**, *25*, 109–121.

[137] R. W. Cheary, A. A. Coelho, J. P. Cline, *J. Res. Natl. Inst. Stand. Technol.* **2004**, *109*, 1–25.

[138] R. J. Hill, C. J. Howard, *J. Appl. Crystallogr.* **1987**, *20*, 467–474.

[139] Bruker AXS, Topas V5, General profile and structure analysis software for powder diffraction data. User's Manual, Karlsruhe, Germany, **2014**.

[140] R. S. Czernuszewicz, T. G. Spiro in *Methodology*, (Eds.: E. I. Solomon, A. B. P. Lever), Inorganic electronic structure and spectroscopy, Wiley, New York, **1999**, pp. 353–441.

[141] K. Nakamoto, *Infrared and Raman spectra of inorganic and coordination compounds*, 6th ed., Wiley-Blackwell, Oxford, **2008**.

[142] H. Günzler, H.-U. Gremlich, *IR spectroscopy: An introduction*, Wiley-VCH, Weinheim, **2002**.

[143] A. Jabłoński, *Z. Physik* **1935**, *94*, 38–46.

[144] J. R. Lakowicz, *Principles of fluorescence spectroscopy*, Third edition, corrected at 4. printing, Springer, New York, NY, **2010**.

[145] *Phosphor handbook*, 2nd ed., (Eds.: H. Yamamoto, S. Shionoya, W. M. Yen), Taylor & Francis distributor, Boca Raton, Fla and London, **2007**.

[146] P. Kubelka, F. Munk, *Z. Techn. Phys.* **1931**, *12*, 593–601.

[147] P. Kubelka, *J. Opt. Soc. Am.* **1948**, *38*, 448–457.

[148] G. Kortüm, W. Braun, G. Herzog, *Angew. Chem. Int. Ed.* **1963**, *2*, 333–341; *Angew. Chem.* **1963**, *75*, 653–661.

[149] P. Makuła, M. Pacia, W. Macyk, *J. Phys. Chem. Lett.* **2018**, *9*, 6814–6817.

[150] J. Tauc, R. Grigorovici, A. Vancu, *Phys. Stat. Sol. (b)* **1966**, *15*, 627–637.

[151] G. H. Dieke, *Spectra and Energy Levels of Rare Earth Ions in Crystals*, Wiley Interscience, New York, **1968**.

[152] W. T. Carnall, P. R. Fields, B. G. Wybourne, *J. Chem. Phys.* **1965**, *42*, 3797–3806.

[153] W. T. Carnall, P. R. Fields, K. Rajnak, *J. Chem. Phys.* **1968**, *49*, 4412–4423.

[154] W. T. Carnall, P. R. Fields, K. Rajnak, *J. Chem. Phys.* **1968**, *49*, 4424–4442.

[155] W. T. Carnall, P. R. Fields, K. Rajnak, *J. Chem. Phys.* **1968**, *49*, 4443–4446.

[156] W. T. Carnall, P. R. Fields, K. Rajnak, *J. Chem. Phys.* **1968**, *49*, 4447–4449.

[157] W. T. Carnall, P. R. Fields, K. Rajnak, *J. Chem. Phys.* **1968**, *49*, 4450–4455.

[158] R. W. Boyd, *Nonlinear optics*, 3. ed., Elsevier/Academic Press, Amsterdam, **2008**.

[159] S. K. Kurtz, T. T. Perry, *J. Appl. Phys.* **1968**, *39*, 3798–3813.

[160] J. P. Dougherty, S. K. Kurtz, *J. Appl. Crystallogr.* **1976**, *9*, 145–158.

[161] L. Bayarjargal, B. Winkler, E. Haussühl, R. Boehler, *Appl. Phys. Lett.* **2009**, *95*, 061907.

[162] P. J. Goodhew, F. J. Humphreys, R. Beanland, *Electron microscopy and analysis*, Third edition, CRC Press, Taylor & Francis Group, Boca Raton, **2001**.

[163] A. J. Garratt-Reed, D. C. Bell, *Energy-dispersive X-ray analysis in the electron microscope*, BIOS, Oxford, **2003**.

[164] R. L. Mößbauer, *Z. Physik* **1958**, *151*, 124–143.

[165] R. L. Mößbauer, *Naturwissenschaften* **1958**, *45*, 538–539.

[166] R. L. Mößbauer, *Z. Naturforsch. A* **1959**, *14*, 211–216.

[167] P. Gütlich, E. Bill, A. X. Trautwein, *Mössbauer Spectroscopy and Transition Metal Chemistry*, Springer-Verlag, Berlin, Heidelberg, **2011**.

[168] P. Gütlich, J. Ensling in *Methodology*, (Eds.: E. I. Solomon, A. B. P. Lever), Inorganic electronic structure and spectroscopy, Wiley, New York, **1999**, pp. 161–212.

[169] D. J. Stewart, O. Knop, R. E. Meads, W. G. Parker, *Can. J. Chem.* **1973**, *51*, 1041–1049.

[170] G. J. Long, T. E. Cranshaw, G. Langsworth, *Moessbauer Eff. Ref. Data J.* **1983**, *216*.

[171] R. A. Brand, WINNORMOS for IGOR6, version for IGOR6.2 or above: 22/02/2017, (Ed.: Universität Duisburg), Duisburg, Germany, **2017**.

[172] H.-J. Meyer in *Moderne anorganische Chemie*, (Eds.: E. Riedel, R. Alsfasser), de Gruyter, Berlin, **2007**.

[173] K. Kopitzki, P. Herzog, *Einführung in die Festkörperphysik*, 4., überarbeitete Auflage, Vieweg+Teubner Verlag, Wiesbaden, **2002**.

[174] J. H. van Vleck, *The Theory Of Electric And Magnetic Susceptibilities*, Oxford At The Clarendon Press, **1932**.

[175] Y. Takikawa, S. Ebisu, S. Nagata, *J. Phys. Chem. Solids* **2010**, *71*, 1592–1598.

[176] G. A. Bain, J. F. Berry, *J. Chem. Educ.* **2008**, *85*, 532–536.

[177] P. Haines, P. G. Laye, S. B. Warrington, T. M. Group, G. R. Heal, D. M. Price, R. Wilson, *Principles of Thermal Analysis and Calorimetry*, Royal Society of Chemistry, Cambridge, **2002**.

[178] R. Hoppe, *Angew. Chem.* **1966**, *78*, 52–63.

[179] R. Hoppe, *Angew. Chem. Int. Ed.* **1970**, *9*, 25–34.

[180] R. Hübenthal, MAPLE: Program for the Calculation of the Madelung Part of Lattice Energy, Gießen, **1993**.

[181] R. Hoppe, *Z. Kristallogr.* **1979**, *150*, 23–52.

[182] T. Balić Žunić, E. Makovicky, *Acta Crystallogr.* **1996**, *B52*, 78–81.

[183] E. Makovicky, T. Balić-Žunić, *Acta Crystallogr.* **1998**, *B54*, 766–773.

[184] L. A. Olsen, J. López-Solano, A. García, T. Balić-Žunić, E. Makovicky, *J. Solid State Chem.* **2010**, *183*, 2133–2143.

[185] A. G. Christy, S. J. Mills, *Acta Crystallogr. B* **2013**, *69*, 446–456.

[186] A. Friedrich, E. A. Juarez-Arellano, E. Haussühl, R. Boehler, B. Winkler, L. Wiehl, W. Morgenroth, M. Burianek, M. Mühlberg, *Acta Crystallogr. B* **2010**, *66*, 323–337.

[187] L. F. Lundegaard, E. Makovicky, T. Boffa-Ballaran, T. Balic-Zunic, *Phys Chem Minerals* **2005**, *32*, 578–584.

[188] A. L. J. Pereira, J. A. Sans, R. Vilaplana, O. Gomis, F. J. Manjón, P. Rodríguez-Hernández, A. Muñoz, C. Popescu, A. Beltrán, *J. Phys. Chem. C* **2014**, *118*, 23189–23201.

[189] D. Pinto, A. Garavelli, T. Balić-Žunić, *Mineral. mag.* **2015**, *79*, 597–611.

[190] H. A. Höppe, *J. Solid State Chem.* **2009**, *182*, 1786–1791.

[191] J. Cumby, J. P. Attfield, *Nat. Commun.* **2017**, *8*, 14235.

[192] D. Stoiber, R. Niewa, *Z. Kristallogr.* **2019**, *234*, 201–209.

[193] P. Hohenberg, W. Kohn, *Phys. Rev.* **1964**, *136*, B864–B871.

[194] A. D. Becke, K. E. Edgecombe, *J. Chem. Phys.* **1990**, *92*, 5397–5403.

[195] A. Savin, J. Flad, H. Preuß, O. Jepsen, O. K. Anderson, H. G. von Schnering, *Angew. Chem.* **1992**, *104*, 186–188.

[196] U. Müller, *Anorganische Strukturchemie*, 6., aktualisierte Aufl., unveränd. Nachdr, Vieweg + Teubner, Wiesbaden, **2009**.

[197] G. Kresse, J. Furthmüller, *Phys. Rev. B* **1996**, *54*, 11169–11186.

[198] G. Kresse, D. Joubert, *Phys. Rev. B* **1999**, *59*, 1758–1775.

[199] P. E. Blöchl, *Phys. Rev. B* **1994**, *50*, 17953–17979.

[200] R. Dovesi, V. R. Saunders, C. Roetti, R. Orlando, C. M. Zicovich-Wilson, Pascale F., B. Civalleri, K. Doll, N. M. Harrison, I. J. Bush, P. D'Arco, M. Llunell, M. Causà, J. Noël, L. Maschio, A. Erba, A. Rerat, S. Casassa, CRYSTAL17 User's Manual, Torino, **2017**.

[201] R. Dovesi, A. Erba, R. Orlando, C. M. Zicovich-Wilson, B. Civalleri, L. Maschio, M. Rérat, S. Casassa, J. Baima, S. Salustro, B. Kirtman, *WIREs Comput Mol Sci* **2018**, *8*, e1360.

[202] J. P. Perdew, K. Burke, M. Ernzerhof, *Phys. Rev. Lett.* **1996**, *77*, 3865–3868.

[203] S. Grimme, J. Antony, S. Ehrlich, H. Krieg, *J. Chem. Phys.* **2010**, *132*, 154104.

[204] S. Grimme, S. Ehrlich, L. Goerigk, *J. Comput. Chem.* **2011**, *32*, 1456–1465.

[205] S. Grimme, A. Hansen, J. G. Brandenburg, C. Bannwarth, *Chem. Rev.* **2016**, *116*, 5105–5154.

[206] M. Hämmer, V. Wessels, R. Ettlinger, H. A. Höppe, *Z. Anorg. Allg. Chem.* **2021**, *647*, 204–209.

[207] M. Hämmer, H. A. Höppe, *Z. Naturforsch. B* **2019**, *74*, 59–70.

[208] S. Guillemet-Fritsch, H. Coradin, A. Barnabé, C. Calmet, P. Tailhades, A. Rousset, *MRS Proc.* **2001**, *674*, 127.

[209] E. Herdtweck, T. Kornprobst, R. Sieber, L. Straver, J. Plank, *Z. Anorg. Allg. Chem.* **2011**, *637*, 655–659.

[210] J. A. Kaduk, *Powder Diffr.* **2018**, *33*, 98–107.

[211] D. E. Zacharias, J. P. Glusker, *Acta Crystallogr. C* **1993**, *49*, 1732–1735.

[212] B. Sheldrick, *Acta Crystallogr. B* **1974**, *30*, 2056–2057.

[213] C. K. Johnson, *Acta Crystallogr.* **1965**, *18*, 1004–1018.

[214] K. Byrappa, T. Adschiri, *Prog. Cryst. Growth Charact. Mater.* **2007**, *53*, 117–166.

[215] L.-Y. Meng, B. Wang, M.-G. Ma, K.-L. Lin, *Mater. Today Chem.* **2016**, *1-2*, 63–83.

[216] R. D. Shannon, *Acta Crystallogr. A* **1976**, *32*, 751–767.

[217] H. A. Höppe, M. Daub, M. C. Bröhmer, *Chem. Mater.* **2007**, *19*, 6358–6362.

[218] M. J. Schäfer, S. G. Jantz, H. A. Höppe, *Z. Naturforsch. B* **2020**, *75*, 143–148.

[219] A. Rammohan, J. A. Kaduk, *Acta Crystallogr. B* **2018**, *74*, 239–252.

[220] J. P. Glusker, J. A. Minkin, A. L. Patterson, *Acta Crystallogr. B* **1969**, *25*, 1066–1072.

[221] P. Tarakeshwar, S. Manogaran, *Spectrochim. Acta Part A* **1994**, *50*, 2327–2343.

[222] A. Drzewiecka-Antonik, A. E. Koziol, P. Rejmak, K. Lawniczak-Jablonska, L. Nittler, T. Lis, *Polyhedron* **2017**, *132*, 1–11.

[223] M. Matzapetakis, N. Karligiano, A. Bino, M. Dakanali, C. P. Raptopoulou, V. Tangoulis, A. Terzis, J. Giapintzakis, A. Salifoglou, *Inorg. Chem.* **2000**, *39*, 4044–4051.

[224] Y. Gao, P. Zhang, J. Li, W. Cao, X. Lai, L. Zhong, *Micro Nano Lett.* **2015**, *10*, 419–421.

[225] S. A. Mansour, *Thermochim. Acta* **1994**, *233*, 243–256.

[226] S. A. Mansour, *Thermochim. Acta* **1994**, *233*, 231–242.

[227] M. M. Barbooti, D. A. Al-Sammerrai, *Thermochim. Acta* **1986**, *98*, 119–126.

[228] A. Srivastava, P. Singh, V. G. Gunjikar, C. I. Jose, *Thermochim. Acta* **1984**, *76*, 249–254.

[229] R. Dinescu, M. Preda, *J. Therm. Anal.* **1973**, *5*, 465–473.

[230] L. G. Sillén, A. L. Nylander, *Arkiv Kemi Miner. Geol.* **1943**, *17A*.

[231] E. Gürmen, E. Daniels, J. S. King, *J. Chem. Phys.* **1971**, *55*, 1093–1097.

[232] R. Gopal, J. Manam, *Mater. Today: Proc.* **2020**, *518*, 249.

[233] Z. Ju, R. Wei, X. Gao, W. Liu, C. Pang, *Opt. Mater.* **2011**, *33*, 909–913.

[234] J. Liao, B. Qiu, H. Wen, J. Chen, W. You, L. Liu, *J. Alloys Compd.* **2009**, *487*, 758–762.

[235] M. Fait, H.-J. Lunk, M. Feist, M. Schneider, J. N. Dann, T. A. Frisk, *Thermochim. Acta* **2008**, *469*, 12–22.

[236] G. J. French, F. R. Sale, *J. Mater. Sci.* **1981**, *16*, 3427–3436.

[237] W. Pannhorst, J. Löhn, *Z. Kristallogr.* **1970**, *131*, 455–459.

[238] P. M. Woodward, A. W. Sleight, T. Vogt, *J. Phys. Chem. Solids* **1995**, *56*, 1305–1315.

[239] A. M. Kaczmarek, L. Miermans, R. van Deun, *Dalton Trans.* **2013**, *42*, 4639–4649.

[240] M.-H. Lee, W.-S. Jung, *Bull. Korean Chem. Soc.* **2013**, *34*, 3609–3614.

[241] B. Pan, Q. Xie, H. Wang, J. Zhu, Y. Zhang, W. Su, X. Wang, *J. Mater. Chem. A* **2013**, *1*, 6629–6634.

[242] Y.-C. Chen, L. Qin, Z.-S. Meng, D.-F. Yang, C. Wu, Z. Fu, Y.-Z. Zheng, J.-L. Liu, R. Tarasenko, M. Orendáč, J. Prokleška, V. Sechovský, M.-L. Tong, *J. Mater. Chem. A* **2014**, *2*, 9851–9858.

[243] J. M. Calderon-Moreno, V. G. Pol, S.-H. Suh, H.-K. Shin, M. Popa, *J. Nanosci. Nanotech.* **2014**, *14*, 5473–5479.

[244] L. D'Assunção, I. Giolito, M. Ionashiro, *Thermochim. Acta* **1989**, *137*, 319–330.

[245] P. Jeevanandam, Y. Koltypin, O. Palchik, A. Gedanken, *J. Mater. Chem.* **2001**, *11*, 869–873.

[246] Y. Zhang, Z. Xu, X. Yin, Z. Fang, W. Zhu, H. He, *Cryst. Res. Technol.* **2010**, *45*, 1183–1188.

[247] S. Huang, D. Wang, Y. Wang, L. Wang, X. Zhang, P. Yang, *J. Alloys Compd.* **2012**, *529*, 140–147.

[248] Y. Zhang, L. Jin, K. Sterling, Z. Luo, T. Jiang, R. Miao, C. Guild, S. L. Suib, *Green Chem.* **2015**, *17*, 3600–3608.

[249] H. A. Höppe, G. Kotzyba, R. Pöttgen, W. Schnick, *J. Solid State Chem.* **2002**, *167*, 393–401.

[250] T. Tahara, I. Nakai, R. Miyawaki, S. Matsubara, *Z. Kristallogr.* **2007**, *222*, 326–334.

[251] A. N. Christensen, G. Sundström, C. A. Wachtmeister, J. Songstad, A. H. Norbury, C.-G. Swahn, *Acta Chem. Scand.* **1973**, *27*, 2973–2982.

[252] T. Doert, O. Rademacher, J. Getzschmann, *Z. Kristallogr.* **1999**, *214*, 11–12.

[253] K. Michiba, T. Tahara, I. Nakai, R. Miyawaki, S. Matsubara, *Z. Kristallogr.* **2011**, *226*, 314.

[254] C. Heinrichs, Dissertation, Universität zu Köln, **2013**.

[255] G. W. Beall, W. O. Milligan, S. Mroczkowski, *Acta Crystallogr. B* **1976**, *32*, 3143–3144.

[256] R. J. C. Dixey, P. J. Saines, *Inorg. Chem.* **2018**, *57*, 12543–12551.

[257] H.-S. Sheu, W.-J. Shih, W.-T. Chuang, I.-F. Li, C.-S. Yeh, *Jnl Chinese Chemical Soc* **2010**, *57*, 938–945.

[258] Z. Li, J. Zhang, J. Du, H. Gao, Y. Gao, T. Mu, B. Han, *Mater. Lett.* **2005**, *59*, 963–965.

[259] A. dal Negro, G. Rossi, V. Tazzoli, *Amer. Min.* **1975**, *60*, 280–284.

[260] R. Miyawaki, S. Matsubara, K. Yokoyama, S. Iwano, K. Hamasaki, I. Yukinori, *J. Miner. Petr. Sci.* **2003**, *98*, 137–141.

[261] R. Miyawaki, S. Matsubara, K. Yokoyama, K. Takeuchi, Y. Terada, I. Nakai, *Amer. Min.* **2000**, *85*, 1076–1081.

[262] T. Zhang, G. Xu, J. Puckette, F. D. Blum, *J. Phys. Chem. C* **2012**, *116*, 11626–11634.

[263] C. Pan, D. Zhang, L. Shi, *J. Solid State Chem.* **2008**, *181*, 1298–1306.

[264] P. Schmidt, Habilitationsschrift, Technische Universität Dresden, **2007**.

[265] A. A. B. Baloch, S. M. Alqahtani, F. Mumtaz, A. H. Muqaibel, S. N. Rashkeev, F. H. Alharbi, *Phys. Rev. Mater.* **2021**, *5*, 1080.

[266] S. A. Mohitkar, J. Nuss, H. A. Höppe, C. Felser, M. Jansen, *Dalton Trans.* **2018**, *47*, 5968–5976.

[267] S. A. Morozov, *Russ. J. Gen. Chem.* **2003**, *73*, 37–42.

[268] P. Orlandi, M. Pasero, G. Vezzalini, *Eur. J. Miner.* **1990**, *2*, 413–418.

[269] F. A. Andersen, L. Brečević, G. Beuter, D. B. Dell'Amico, F. Calderazzo, N. J. Bjerrum, A. E. Underhill, *Acta Chem. Scand.* **1991**, *45*, 1018–1024.

[270] A. L. Spek, *Acta Crystallogr. D* **2009**, *65*, 148–155.

[271] N. T. McDevitt, W. L. Baun, *Spectrochim. Acta* **1964**, *20*, 799–808.

[272] S. Ni, T. Li, X. Yang, *J. Alloys Compd.* **2011**, *509*, 7874–7876.

[273] R. F. Klevtsova, La Glinskaya, L. P. Kozeeva, P. V. Klevtsov, *Sov. Phys. Crystallography* **1972**, *17*, 672–676.

[274] P. V. Klevtsov, R. F. Klevtsova, *J. Struct. Chem.* **1977**, *18*, 339–355.

[275] R. F. Klevtsova, L. Kharchenko, S. V. Borisov, V. A. Efremov, P. V. Klevtsov, *Sov. Phys. Crystallography* **1979**, *24*, 258–263.

[276] H.-P. Hong, K. Dwight, *Mater. Res. Bull* **1974**, *9*, 775–780.

[277] V. A. Efremov, V. K. Trunov, T. A. Berezina, *Kristallografiya* **1982**, *27*, 134–139.

[278] M. Hämmer, O. Janka, J. Bönnighausen, S. Klenner, R. Pöttgen, H. A. Höppe, *Dalton Trans.* **2020**, *49*, 8209–8225.

[279] K. Kreß, Master Thesis, Universität Augsburg, **2020**.

[280] F. Becker, Bachelor Thesis, Universität Augsburg, **2022**.

[281] L. Yao, *Zhongguo Jiguang* **1989**, *16*, 123–125.

[282] I. Hartenbach, B. Marchetti, T. Schleid, *Z. Kristallogr. Suppl. Issue* **2007**, *25*, 22.

[283] D. C. Huang, Y. F. Zhou, W. T. Xu, Z. F. Yang, M. C. Hong, Y. H. Lin, J. C. Yu, *AMR* **2012**, *624*, 244–247.

[284] G. Q. Wang, Y. P. Lin, R. Ye, Y. N. Feng, L. Y. Li, *J. Alloys Compd.* **2019**, *779*, 41–48.

[285] D. Qin, W. Tang, *RSC Adv.* **2016**, *6*, 45376–45385.

[286] J. Pan, L.-z. Yau, L.-g. Chen, G.-w. Zhao, G.-e. Zhou, C.-x. Guo, *J. Lumin.* **1988**, *40-41*, 856–857.

[287] J. van Vliet, G. Blasse, *J. Solid State Chem.* **1990**, *85*, 56–64.

[288] Z. Xia, Q. Liu, *Prog. Mater Sci.* **2016**, *84*, 59–117.

[289] G. Blasse, A. Bril, *J. Chem. Phys.* **1966**, *45*, 2350–2355.

[290] S. I. Weissman, *J. Chem. Phys.* **1942**, *10*, 214–217.

[291] N. Saito, N. Sonoyama, T. Sakata, *BCSJ* **1996**, *69*, 2191–2194.

[292] D. Huang, Y. Zhou, W. Xu, Z. Yang, M. Hong, J. Yu, *J. Lumin.* **2012**, *132*, 2788–2793.

[293] J. Zhang, Z. Q. Chen, C. H. Wang, A. M. Li, H. Yin, Z. Li, *AMR* **2013**, *787*, 281–285.

[294] J. Wang, J. You, M. Wang, L. Lu, A. A. Sobol, S. Wan, *J Raman Spectrosc* **2018**, *49*, 1693–1705.

[295] N. J. Stedman, A. K. Cheetham, P. D. Battle, *J. Mater. Chem.* **1994**, *4*, 707–711.

[296] D. Zhao, W.-D. Cheng, H. Zhang, S.-P. Huang, M. Fang, W.-L. Zhang, S.-L. Yang, *J. Mol. Struct.* **2009**, *919*, 178–184.

[297] C.-H. Chiu, C.-H. Liu, S.-B. Huang, T.-M. Chen, *J. Electrochem. Soc.* **2008**, *155*, J71–J77.

[298] H. Bärnighausen, *MATCH Communications in Mathematical Chemistry* **1980**, *9*, 139–175.

[299] U. Müller, *Z. Anorg. Allg. Chem.* **2004**, *630*, 1519–1537.

[300] J. Liao, S. Zhang, H. You, H.-R. Wen, J.-L. Chen, W. You, *Opt. Mater.* **2011**, *33*, 953–957.

[301] A. D. Fortes, *Acta Crystallogr. E* **2015**, *71*, 592–596.

[302] S. Seidel, R. Pöttgen, *Z. Kristallogr.* **2020**, *235*, 29–39.

[303] S. Andersson, *Angew. Chem. Int. Ed.* **1983**, *22*, 69–81; *Angew. Chem.* **1983**, *95*, 67–80.

[304] J. Kim, *Inorg. Chem.* **2017**, *56*, 8078–8086.

[305] L. Vegard, *Z. Physik* **1921**, *5*, 17–26.

[306] D. L. Dexter, *J. Chem. Phys.* **1953**, *21*, 836–850.

[307] T. Förster, *Z. Elektrochem. Angew. Phys. Chem.* **1949**, *53*, 93–99.

[308] T. Förster, *Radiat. Res. Suppl.* **1960**, *2*, 326–339.

[309] F. B. Xiong, Z. W. Zhang, H. F. Lin, L. J. Wang, Y. C. Xu, W. Z. Zhu, *Opt. Mater.* **2015**, *42*, 394–398.

[310] P. Boutinaud, R. Mahiou, E. Cavalli, M. Bettinelli, *J. Lumin.* **2007**, *122-123*, 430–433.

[311] E. Pinel, P. Boutinaud, R. Mahiou, *J. Alloys Compd.* **2004**, *374*, 165–168.

[312] P. Boutinaud, M. Bettinelli, F. Diaz, *Opt. Mater.* **2010**, *32*, 1659–1663.

[313] A. Durairajan, D. Balaji, K. Kavi Rasu, S. Moorthy Babu, M. A. Valente, D. Thangaraju, Y. Hayakawa, *J. Lumin.* **2016**, *170*, 743–748.

[314] K. Li, R. van Deun, *Dalton Trans.* **2018**, *47*, 6995–7004.

[315] G. Blasse, *J. Solid State Chem.* **1972**, *4*, 52–54.

[316] K. Binnemans, *Coord. Chem. Rev.* **2015**, *295*, 1–45.

[317] H. E. Hoefdraad, *J. Solid State Chem.* **1975**, *15*, 175–177.

[318] P. Dorenbos, *J. Lumin.* **2005**, *111*, 89–104.

[319] W.-W. Wang, X. Xu, J.-T. Kong, J.-G. Mao, *Inorg. Chem.* **2018**, *57*, 163–174.

[320] J. Huang, J. Loriers, P. Porcher, G. Teste de Sagey, P. Caro, C. Levy–Clement, *J. Chem. Phys.* **1984**, *80*, 6204–6209.

[321] G. Blasse, B. C. Grabmeier, *Luminescent Materials*, Springer-Verlag, Berlin, Heidelberg, **1994**.

[322] A. Durairajan, D. Thangaraju, M. Valente, S. Moorthy Babu, *J. Electron. Mater.* **2015**, *44*, 4199–4206.

[323] J. Liao, B. Qiu, H. Lai, *J. Lumin.* **2009**, *129*, 668–671.

[324] J. Han, F. Pan, M. S. Molokeev, J. Dai, M. Peng, W. Zhou, J. Wang, *ACS Appl. Mater. Interfaces* **2018**, *10*, 13660–13668.

[325] R. M. Bozorth, J. H. van Vleck, *Phys. Rev.* **1960**, *118*, 1493–1498.

[326] H. C. Hamaker, L. D. Woolf, H. B. MacKay, Z. Fisk, M. B. Maple, *Solid State Commun.* **1979**, *32*, 289–294.

[327] F. Stegemann, T. Block, S. Klenner, O. Janka, *Chem. Eur. J.* **2019**, *25*, 3505–3509.

[328] A. M. Stewart, *Phys. Rev. B* **1972**, *6*, 1985–1998.

[329] A. M. Stewart, *Phys. Rev. B* **1993**, *47*, 11242–11246.

[330] S. Seidel, O. Niehaus, S. F. Matar, O. Janka, B. Gerke, U. C. Rodewald, R. Pöttgen, *Z. Naturforsch. B* **2014**, *69*, 1105–1118.

[331] W. M. Yuhasz, N. A. Frederick, P.-C. Ho, N. P. Butch, B. J. Taylor, T. A. Sayles, M. B. Maple, J. B. Betts, A. H. Lacerda, P. Rogl, G. Giester, *Phys. Rev. B* **2005**, *71*, 104402.

[332] B. Anke, S. Hund, C. Lorent, O. Janka, T. Block, R. Pöttgen, M. Lerch, *Z. Anorg. Allg. Chem.* **2017**, *643*, 1824–1830.

[333] P. Pues, S. Schwung, D. Rytz, L. Schubert, S. Klenner, F. Stegemann, R. Pöttgen, T. Jüstel, *J. Lumin.* **2019**, *215*, 116653.

[334] J. M. Postema, W. T. Fu, D. IJdo, *J. Solid State Chem.* **2011**, *184*, 2004–2008.

[335] R. F. Klevtsova, P. V. Klevtsov, *Kristallografiya* **1970**, *15*, 953–958.

[336] R. F. Klevtsova, L. P. Solov'eva, V. A. Vinokurov, P. V. Klevtsov, *Kristallografiya* **1975**, *20*, 270–275.

[337] B. Rekik, M. Derbal, K. Lebbou, M. Benammar, *J. Cryst. Growth* **2016**, *452*, 101–104.

[338] M. Tyagi, S. G. Singh, Sangeeta, R. Prasad, S. Auluck, D. J. Singh, *Phys. B* **2010**, *405*, 3267–3271.

[339] H. Xie, D. Shen, C. Xie, X. Wang, G. Shen, *Cryst. Res. Technol.* **2006**, *41*, 961–966.

[340] A. Boehlke, H. Müller-Buschbaum, *J. Less-Common Met.* **1990**, *162*, 141–147.

[341] H. Weitzel, H. Schröcke, *Z. Kristallogr.* **1980**, *152*, 69–82.

[342] D. Errandonea, F. J. Manjón, M. Somayazulu, D. Häusermann, *J. Solid State Chem.* **2004**, *177*, 1087–1097.

[343] R. M. Hazen, L. W. Finger, J. W. Mariathasan, *J. Phys. Chem. Solids* **1985**, *46*, 253–263.

[344] A. A. Maier, M. V. Provotorov, V. A. Balashov, *Russ. Chem. Rev.* **1973**, *42*, 822–833.

[345] V. K. Trunov, A. Evdokimov, *Kristallografiya* **1974**, *19*, 994–97.

[346] W. Barendswaard, J. H. van der Waals, *Mol. Phys.* **1986**, *59*, 337–353.

[347] H. Mller-Buschbaum, H. Szillat, *Z. Anorg. Allg. Chem.* **1994**, *620*, 642–646.

[348] F. S. Richardson, *Chem. Rev.* **1982**, *82*, 541–552.

[349] P. Boutinaud, P. Putaj, R. Mahiou, E. Cavalli, A. Speghini, M. Bettinelli, *Spectrosc. Lett.* **2007**, *40*, 209–220.

[350] *FRET - Förster resonance energy transfer: From theory to applications*, (Eds.: I. Medintz, N. Hildebrandt), Wiley-VCH Verlag GmbH & Co. KGaA, Weinheim, **2014**.

[351] J. George, D. Waroquiers, D. Di Stefano, G. Petretto, G.-M. Rignanese, G. Hautier, *Angew. Chem. Int. Ed.* **2020**, *59*, 7569–7575.

[352] A. L. Paulsen, A. G. Kalampounias, R. W. Berg, S. Boghosian, *J. Phys. Chem. A* **2011**, *115*, 4214–4222.

[353] R. M. Atkins, K. A. Gingerich, *Chem. Phys. Lett.* **1978**, *53*, 347–349.

[354] P. Ropuszyńska-Robak, P. E. Tomaszewski, L. Kępiński, L. Macalik, *RSC Adv.* **2018**, *8*, 2632–2641.

[355] H. Wang, Y. Li, Z. Ning, L. Huang, C. Zhong, C. Wang, M. Liu, X. Lai, D. Gao, J. Bi, *J. Lumin.* **2018**, *201*, 364–371.

[356] S. Schwung, D. Enseling, V. Wesemann, D. Rytz, B. Heying, U. C. Rodewald, B. Gerke, O. Niehaus, R. Pöttgen, T. Jüstel, *J. Lumin.* **2015**, *159*, 251–257.

[357] M. S. Wickleder, *Z. Anorg. Allg. Chem.* **2001**, *627*, 2112–2114.

[358] C. Logemann, D. Gunzelmann, T. Klüner, J. Senker, M. S. Wickleder, *Chem. Eur. J.* **2012**, *18*, 15495–15503.

[359] J. Bruns, M. Hänsch, M. S. Wickleder, *Inorg. Chem.* **2015**, *54*, 5681–5690.

[360] P. Netzsch, Master Thesis, Universität Augsburg, **2016**.

[361] M. Hämmer, P. Netzsch, S. Klenner, K. Neuschulz, M. Struckmann, M. S. Wickleder, M. Daub, H. Hillebrecht, R. Pöttgen, H. A. Höppe, *Dalton Trans.* **2021**, *50*, 12913–12922.

[362] M. Hämmer, J. Brgoch, P. Netzsch, H. A. Höppe, *Inorg. Chem.* **2022**, *61*, 4102–4113.

[363] X. Zhang, W. Jiang, Q. Pan, G. Yuan, H. J. Seo, *Mater. Lett.* **2014**, *128*, 89–92.

[364] H. Donker, W. M. A. Smit, G. Blasse, *Phys. Stat. Sol. (b)* **1988**, *148*, 413–419.

[365] S. M. Haile, D. A. Boysen, C. R. Chisholm, R. B. Merle, *Nature* **2001**, *410*, 910–913.

[366] C. Cascales, B. G. Lor, E. G. Puebla, M. Iglesias, M. A. Monge, C. R. Valero, N. Snejko, *Chem. Mater.* **2004**, *16*, 4144–4149.

[367] A. Magnusson, L.-G. Johansson, *Acta Chem. Scand.* **1982**, *36a*, 429–433.

[368] G. Lundren, G. Wernfors, T. Yamaguchi, *Acta Crystallogr. B* **1982**, *38*, 2357–2361.

[369] J. D. Donaldson, D. C. Puxley, *Acta Crystallogr. B* **1972**, *28*, 864–867.

[370] F. C. Mathers, H. S. Rothrock, *Ind. Eng. Chem.* **1931**, *23*, 831–832.

[371] S. Grimvall, S. Husebye, Å. Rolandsen, A. F. Andresen, P. Fischer, *Acta Chem. Scand.* **1975**, *29a*, 590–598.

[372] C. G. Davies, J. D. Donaldson, D. R. Laughlin, R. A. Howie, R. Beddoes, *J. Chem. Soc. Dalton Trans.* **1975**, 2241.

[373] A. J. Locock, R. A. Ramik, M. E. Back, *Can. Mineral.* **2006**, *44*, 1457–1467.

[374] S. Grimvall, *Acta Chem. Scand.* **1982**, *36a*, 361–364.

[375] I. V. Pekov, E. V. Sereda, N. V. Zubkova, V. O. Yapaskurt, N. V. Chukanov, S. N. Britvin, I. S. Lykova, D. Y. Pushcharovsky, *Eur. J. Mineral.* **2018**, *30*, 375–382.

[376] C. Logemann, J. Witt, D. Gunzelmann, J. Senker, M. S. Wickleder, *Z. Anorg. Allg. Chem.* **2012**, *638*, 2053–2061.

[377] M. A. K. Ahmed, H. Fjellvåg, A. Kjekshus, L. V. Vilkov, R. Sillanpää, G. Bernáth, J. Szúnyog, B. Långström, *Acta Chem. Scand.* **1998**, *52*, 305–311.

[378] M. S. Wickleder, C. Logemann in *Handbook of Chalcogen Chemistry: New Perspectives in Sulfur, Selenium and Tellurium (2)*, *Vol. 1*, The Royal Society of Chemistry, **2013**, pp. 307–345.

[379] R. C. Ropp, *Encyclopedia of the alkaline earth compounds*, Elsevier, Oxford, **2013**.

[380] E. G. Rochow, E. W. Abel, *The Chemistry of Germanium: Tin and Lead*, Pergamon Press, Oxford, **1973**.

[381] G. Brauer, *Handbuch der Präparativen Anorganischen Chemie*, Ferdinand Enke Verlag, Stuttgart, **1975-1981**.

[382] C. H. Brubaker, *J. Am. Chem. Soc.* **1954**, *76*, 4269–4271.

[383] K. H. Stern, *High temperature properties and thermal decomposition of inorganic salts with oxyanions*, CRC Press, Boca Raton, Fla, **2001**.

[384] I. J. Dijs, R. de Koning, J. W. Geus, L. W. Jenneskens, *Phys. Chem. Chem. Phys.* **2001**, *3*, 4423–4429.

[385] I. J. Bear, W. G. Mumme, *Acta Crystallogr. B* **1970**, *26*, 1140–1145.

[386] U. Betke, M. S. Wickleder, *Eur. J. Inorg. Chem.* **2012**, *2012*, 306–317.

[387] D. L. Rogachev, M. A. Porai-Koshits, V. Y. Kuznetsov, L. M. Dikareva, *J. Struct. Chem.* **1974**, *15*, 397–401.

[388] T. A. White, M. S. Moreno, P. A. Midgley, *Z. Kristallogr.* **2010**, *225*, 274.

[389] T. Söhnel, P. Böttcher, W. Reichelt, F. E. Wagner, *Z. Anorg. Allg. Chem.* **1998**, *624*, 708–714.

[390] K. Suzuki, T. Hanaya, R. Sato, T. Minato, K. Yamaguchi, N. Mizuno, *Chem. Commun.* **2016**, *52*, 10688–10691.

[391] S. K. Filatov, N. A. Bendeliani, B. Albert, J. Kopf, T. I. Dyuzheva, L. M. Lityagina, *Dokl. Phys.* **2007**, *52*, 195–199.

[392] E. E. Platero, M. P. Mentruit, *Catal Lett* **1995**, *30*, 31–39.

[393] J. Weidlein, U. Müller, K. Dehnicke, *Schwingungsfrequenzen*, Thieme, Stuttgart, **1981**.

[394] R. S. Katiyar, P. Dawson, M. M. Hargreave, G. R. Wilkinson, *J. Phys. C: Solid State Phys.* **1971**, *4*, 2421–2431.

[395] J. K. Lees, P. A. Flinn, *J. Chem. Phys.* **1968**, *48*, 882–889.

[396] H.-T. Sun, J. Zhou, J. Qiu, *Prog. Mater. Sci.* **2014**, *64*, 1–72.

[397] G. Blasse, A. Bril, *J. Chem. Phys.* **1968**, *48*, 217–222.

[398] A. Krasnikov, E. Mihokova, M. Nikl, S. Zazubovich, Y. Zhydachevskyy, *Crystals* **2020**, *10*, 208.

[399] G. Zaccariello, M. Back, M. Zanello, P. Canton, E. Cattaruzza, P. Riello, A. Alimonti, A. Benedetti, *ACS Appl. Mater. Interfaces* **2017**, *9*, 1913–1921.

[400] J. R. Sorg, T. Wehner, P. R. Matthes, R. Sure, S. Grimme, J. Heine, K. Müller-Buschbaum, *Dalton Trans.* **2018**, *47*, 7669–7681.

[401] K. Schaefer, F. Hein, *Z. Anorg. Allg. Chem.* **1917**, *100*, 249–303.

[402] S. Škramovský, O. Vondrášek, *Collect. Czech. Chem. Commun.* **1937**, *9*, 329–344.

[403] J. D. Hanawalt, H. W. Rinn, L. K. Frevel, *Ind. Eng. Chem. Anal. Ed.* **1938**, *10*, 457–512.

[404] G. S. Fujioka, G. H. Cady, *J. Am. Chem. Soc.* **1957**, *79*, 2451–2454.

[405] L. Gmelin, *Bismuth: = Gmelins Handbuch der anorganischen Chemie*, 8th ed., Verlag Chemie, Weinheim, **1964**.

[406] R. Matsuzaki, A. Sofue, H. Masumizu, Y. Saeki, *Chem. Lett.* **1974**, *3*, 737–740.

[407] B. Aurivillius, *Acta Chem. Scand.* **1987**, *41a*, 415–422.

[408] B. Aurivillius, *Acta Chem. Scand.* **1988**, *42a*, 95–110.

[409] C. V. Subban, G. Rousse, M. Courty, P. Barboux, J.-M. Tarascon, *Solid State Sci.* **2014**, *38*, 25–29.

[410] Z. Zhang, Z. Zhang, *Acta Crystallogr. C* **2010**, *66*, i9–11.

[411] R. Mercier, J. Douglade, P. G. Jones, G. M. Sheldrick, *Acta Crystallogr. C* **1983**, *39*, 145–148.

[412] M. S. Wickleder, *Z. Anorg. Allg. Chem.* **1999**, *625*, 1707–1711.

[413] M. S. Wickleder, *Z. Anorg. Allg. Chem.* **2000**, *626*, 621–622.

[414] M. S. Wickleder, *Z. Anorg. Allg. Chem.* **1998**, *624*, 1347–1354.

[415] M. S. Wickleder, *Z. Anorg. Allg. Chem.* **1998**, *624*, 1583–1587.

[416] R. Mercier, J. Douglade, J. Bernard, *Acta Crystallogr. B* **1976**, *32*, 2787–2791.

[417] S. P. Sirotinkin, V. A. Efremov, L. M. Kovba, A. N. Pokrovskij, *Kristallografiya* **1977**, *22*, 1272–1273.

[418] Y. Denisenko, A. S. Aleksandrovsky, V. V. Atuchin, A. S. Krylov, M. S. Molokeev, A. S. Oreshonkov, N. P. Shestakov, O. V. Andreev, *J. Ind. Eng. Chem.* **2018**, *68*, 109–116.

[419] K. L. Nash, K. J. Sully, A. B. Horn, *J. Phys. Chem. A* **2001**, *105*, 9422–9426.

[420] A. B. Horn, K. Jessica Sully, *Phys. Chem. Chem. Phys.* **1999**, *1*, 3801–3806.

[421] C. Postmus, J. R. Ferraro, *J. Chem. Phys.* **1968**, *48*, 3605–3611.

[422] L. Wrobel, L. Miersch, M. Schlesinger, T. Rüffer, H. Lang, M. Mehring, *Z. Anorg. Allg. Chem.* **2014**, *640*, 1431–1436.

[423] *Landolt-Börnstein Zahlenwerte und Funktionen, I Band, Atom- und Molekularphysik, I Teil, Atome und Ionen: p. 439*, (Ed.: A. Eucken), Springer, Berlin, **1950**.

[424] N. E. Lushchik, C. B. Lushchik, *Sov. Phys. Opt. Spectrosc.* **1960**, *8*, 839–846.

[425] M. Back, J. Ueda, J. Xu, K. Asami, L. Amidani, E. Trave, S. Tanabe, *J. Phys. Chem. C* **2019**, *123*, 14677–14688.

[426] D. W. Smith, *J. Chem. Educ.* **1987**, *64*, 480.

[427] M. Hämmer, L. Bayarjargal, H. A. Höppe, *Angew. Chem. Int. Ed.* **2021**, *60*, 1503–1506; *Angew. Chem.* **2021**, *133*, 1525–1529.

[428] E. Turgunbajew, Master Thesis, Universität Augsburg, **2021**.

[429] H. Huang, N. Tian, S. Jin, Y. Zhang, S. Wang, *Solid State Sci.* **2014**, *30*, 1–5.

[430] N. G. Connelly, *Nomenclature of inorganic chemistry: IUPAC recommendations 2005*, RSC Publ, Cambridge, **2005**.

[431] M.-J. Díaz-Cabañas, P. A. Barrett, *Chem. Commun.* **1998**, 1881–1882.

[432] M. Daub, K. Kazmierczak, H. A. Höppe, H. Hillebrecht, *Chem. Eur. J.* **2013**, *19*, 16954–16962.

[433] S. Kastbjerg, N. Bindzus, M. Søndergaard, S. Johnsen, N. Lock, M. Christensen, M. Takata, M. A. Spackman, B. Brummerstedt Iversen, *Adv. Funct. Mater.* **2013**, *23*, 5477–5483.

[434] J. W. Nebgen, A. D. McElroy, H. F. Klodowski, *Inorg. Chem.* **1965**, *4*, 1796–1799.

[435] A. Théorêt, C. Sandorfy, *Can. J. Chem.* **1964**, *42*, 57–62.

[436] Y. Li, Z. Zhou, S. Zhao, F. Liang, Q. Ding, J. Sun, Z. Lin, M. Hong, J. Luo, *Angew. Chem. Int. Ed.* **2021**, *60*, 11457–11463.

[437] M. Hämmer, F. Pielnhofer, O. Janka, H. Takahashi, P. Gross, R. Pöttgen, H. A. Höppe, *Dalton Trans.* **2022**, *51*, 3104–3115.

[438] J. Müller, Master Thesis, Universität Augsburg, **2022**.

[439] W. B. Jensen, *J. Chem. Educ.* **2003**, *80*, 952.

[440] R. T. Sanderson, *J. Chem. Educ.* **1964**, *41*, 187.

[441] M. A. Simonov, S. V. Shkovrov, S. I. Troyanov, *Kristallografiya* **1988**, *33*, 502–503.

[442] H. Tagawa, K. Kawabe, *Thermochim. Acta* **1990**, *158*, 293–300.

[443] T. N. Khamaganova, T. G. Khumaeva, A. K. Subanakov, A. V. Perevalov, *Inorg. Mater.* **2017**, *53*, 81–85.

[444] M. Hämmer, H. A. Höppe, *in preparation.*

[445] P. C. Burns, F. C. Hawthorne, *Can. Mineral.* **1996**, *34*, 1089–1105.

[446] M. Gruß, R. Glaum, *Z. Kristallogr.* **1997**, *212*, 2647.

[447] U. Steiner, W. Reichelt, *Acta Crystallogr. C* **1997**, *53*, 1371–1373.

[448] M. A. Hitchman, T. D. Waite, *Inorg. Chem.* **1976**, *15*, 2150–2154.

[449] R. W. G. Wyckoff, *Am. J. Sci.* **1925**, *s5-9*, 448–459.

[450] R. Valiente, F. Rodríguez, *Phys. Rev. B* **1999**, *60*, 9423–9429.

[451] J. Ruiz-Fuertes, M. N. Sanz-Ortiz, J. González, F. Rodríguez, A. Segura, D. Errandonea, *J. Phys.: Conf. Ser.* **2010**, *215*, 012048.

[452] M. Wildner, G. Giester, M. Kersten, K. Langer, *Phys Chem Minerals* **2014**, *41*, 669–680.

[453] G. Pozza, D. Ajò, G. Chiari, F. de Zuane, M. Favaro, *J. Cult. Herit.* **2000**, *1*, 393–398.

[454] G. Accorsi, G. Verri, M. Bolognesi, N. Armaroli, C. Clementi, C. Miliani, A. Romani, *Chem. Commun.* **2009**, 3392–3394.

[455] M. Wildner, G. Giester, *Miner. Petrol.* **1988**, *39*, 201–209.

[456] R. Laiho, M. Natarajan, M. Kaira, *Phys. Stat. Sol. (a)* **1973**, *15*, 311–317.

[457] D. Oelkrug, *Structure and Bonding* **1971**, *9*, 1.

[458] M. Hidaka, K. Inoue, I. Yamada, P. J. Walker, *Phys. B+C* **1983**, *121*, 343–350.

[459] W. M. Jones, *J. Chem. Phys.* **1984**, *80*, 3408–3419.

[460] L. C. Pasqualini, H. Huppertz, M. Je, H. Choi, J. Bruns, *Angew. Chem. Int. Ed.* **2021**, *60*, 19740–19743; *Angew. Chem.* **2021**, *133*, 19892–19896.

[461] J. C. Bachman, S. Muy, A. Grimaud, H.-H. Chang, N. Pour, S. F. Lux, O. Paschos, F. Maglia, S. Lupart, P. Lamp, L. Giordano, Y. Shao-Horn, *Chem. Rev.* **2016**, *116*, 140–162.

[462] M. D. Ward, B. L. Chaloux, M. D. Johannes, A. Epshteyn, *Adv. Mater.* **2020**, *32*, 2003667.

[463] W. Gerlach, *Z. Physik* **1922**, *9*, 184–192.

[464] B. C. Chakoumakos, G. A. Lager, J. A. Fernandez-Baca, *Acta Crystallogr. C* **1992**, *48*, 414–419.

[465] K. A. Denault, J. Brgoch, S. D. Kloss, M. W. Gaultois, J. Siewenie, K. Page, R. Seshadri, *ACS Appl. Mater. Interfaces* **2015**, *7*, 7264–7272.

[466] L. Huang, X. Chen, Q. Li, *J. Mater. Chem.* **2001**, *11*, 610–615.

[467] E. Kümmerle, G. Heger, *J. Solid State Chem.* **1999**, *147*, 485–500.

[468] G. Schiller, Dissertation, Universität Karlsruhe, **1985**.

[469] A. Goto, T. Hondoh, S. Mae, *J. Chem. Phys.* **1990**, *93*, 1412–1417.

[470] T. Pilati, F. Demartin, C. M. Gramaccioli, *Acta Crystallogr. A* **1998**, *54*, 515–523.

[471] I. Oftedal, *Z. Phys. Chem.* **1927**, *128U*, 154–158.

[472] H. C. R. Wolf, R. Hoppe, *Z. Anorg. Allg. Chem.* **1985**, *529*, 61–64.

[473] A. Saiki, N. Ishizawa, N. Mizutani, M. Kato, *J. Ceram. Soc. Japan* **1985**, *93*, 649–654.

[474] M. Gasgnier, G. Schiffmacher, P. Caro, L. Eyring, *J. Less-Common Met.* **1986**, *116*, 31–42.

[475] J. Attfield, G. Férey, *J. Solid State Chem.* **1989**, *82*, 132–138.

[476] A. F. Andreeva, I. Gil'man, M. Gamarnik, V. I. Dekhtyaruk, *Inorg. Mater.* **1987**, *22*, 1320–1325.

[477] V. Petříček, M. Dušek, L. Palatinus, *Z. Kristallogr.* **2014**, *229*, 345–352.

[478] I. Kutlu, G. Meyer, *Z. Anorg. Allg. Chem.* **1999**, *625*, 402–406.

[479] A. N. Christensen, S. E. Rasmussen, E. Kvamme, R. Ohlson, A. Shimizu, *Acta Chem. Scand.* **1970**, *24*, 2440–2446.

[480] H. Kohlmann, C. Hein, R. Kautenburger, T. C. Hansen, C. Ritter, S. Doyle, *Z. Kristallogr.* **2016**, *231*, 517–523.

[481] D. Zhao, F. Li, W. Cheng, H. Zhang, *Acta Crystallogr. E* **2009**, *66*, i2.

[482] E. Zintl, A. Harder, B. Dauth, *Z. Elektrochem. Angew. Phys. Chem.* **1934**, *40*, 558–593.

[483] A. Aird, M. C. Domeneghetti, F. Mazzi, V. Tazzoli, E. K. H. Salje, *J. Phys.: Condens. Matter* **1998**, *10*, L569–L574.

[484] B. Antic, M. Mitric, D. Rodic, *J. Magn. Magn. Mater.* **1995**, *145*, 349–356.

[485] T. Schleid, G. Meyer, *J. Less-Common Met.* **1989**, *149*, 73–80.

[486] S. Hull, S. T. Norberg, M. G. Tucker, S. G. Eriksson, C. E. Mohn, S. Stølen, *Dalton Trans.* **2009**, 8737–8745.

[487] C. W. F. T. Pistorius, *J. Chem. Phys.* **1966**, *44*, 4532–4537.

[488] D. Huang, Y. Zhou, W. Xu, Z. Yang, Z. Liu, M. Hong, Y. Lin, J. Yu, *J. Alloys Compd.* **2013**, *554*, 312–318.

[489] P. Dorenbos, *J. Phys.: Condens. Matter* **2003**, *15*, 8417–8434.

[490] H. Li, G. Hong, S. Yue, *Zhongguo Xitu Xuebao* **1990**, *8*, 37–41.

[491] E. Salje, K. Viswanathan, *Acta Crystallogr. A* **1975**, *31*, 356–359.

[492] J. B. Forsyth, C. C. Wilson, T. M. Sabine, *Acta Crystallogr. A* **1989**, *45*, 244–247.

[493] T. Fukami, *IRJPAC* **2014**, *4*, 621–637.

[494] K. Ståhl, R. W. Berg, K. M. Eriksen, R. Fehrmann, *Acta Crystallogr. B* **2009**, *65*, 551–557.

[495] A. G. Nord, S. L. Holt, F. Cavalito, K. J. Watson, M. Sandström, *Acta Chem. Scand.* **1976**, *30a*, 198–202.

[496] R. Diehl, G. Brandt, E. Salje, *Acta Crystallogr. B* **1978**, *34*, 1105–1111.

[497] R. Pascard, C. Pascard-Billy, *Acta Crystallogr.* **1965**, *18*, 830–834.

[498] S. M. Antao, *Powder Diffr.* **2012**, *27*, 179–183.

[499] W. H. Baur, A. A. Khan, *Acta Crystallogr. B* **1971**, *27*, 2133–2139.

[500] C. G. Davies, J. D. Donaldson, *J. Chem. Soc. A* **1967**, 1790.

[501] G. E. Gurr, P. W. Montgomery, C. D. Knutson, B. T. Gorres, *Acta Crystallogr. B* **1970**, *26*, 906–915.

[502] E. Grison, K. Eriks, J. L. de Vries, *Acta Crystallogr.* **1950**, *3*, 290–294.

[503] R. Boese, N. Niederprüm, D. Bläser, A. Maulitz, M. Y. Antipin, P. R. Mallinson, *J. Phys. Chem. B* **1997**, *101*, 5794–5799.

[504] C. Theppitak, K. Chainok, *Acta Crystallogr. E* **2015**, *71*, i8–i9.

[505] K. Aurivillius, C. Stålhandske, *Z. Kristallogr.* **1980**, *153*, 121–129.

[506] M. Ihara, J. Krogh-Moe, *Acta Crystallogr* **1966**, *20*, 132–134.

[507] G. Giester, *Miner. Petrol.* **1988**, *38*, 277–284.

[508] C. Logemann, M. S. Wickleder, *Angew. Chem. Int. Ed.* **2013**, *52*, 14229–14232.

[509] R. Westrik, C. H. Mac Gillavry, *Recl. Trav. Chim. Pays-Bas* **1941**, *60*, 794–810.

[510] A. D. Rae, J. G. Thompson, R. L. Withers, *Acta Crystallogr. B* **1991**, *47*, 870–881.

[511] R. Fröhlich, L. Bohatý, J. Liebertz, *Acta Crystallogr. C* **1984**, *40*, 343–344.

[512] W.-L. Zhang, Z.-Z. He, T.-L. Xia, Z.-Z. Luo, H. Zhang, C.-S. Lin, W.-D. Cheng, *Inorg. Chem.* **2012**, *51*, 8842–8847.

[513] S. G. Jantz, F. Pielnhofer, M. Dialer, H. A. Höppe, *Z. Anorg. Allg. Chem.* **2017**, *643*, 2031–2037.

[514] T.-T. Ruan, W.-W. Wang, C.-L. Hu, X. Xu, J.-G. Mao, *J. Solid State Chem.* **2018**, *260*, 39–45.

[515] K. Okada, J. Ossaka, S. Iwai, *Acta Crystallogr. B* **1979**, *35*, 2189–2191.

[516] M. Touboul, E. Bétourné, G. Nowogrocki, *J. Solid State Chem.* **1997**, *131*, 370–373.

[517] G. Sohr, L. Perfler, H. Huppertz, *Z. Naturforsch. B* **2014**, *69*, 1260–1268.

[518] M. J. Schäfer, S. G. Jantz, F. Pielnhofer, H. A. Höppe, *Dalton Trans.* **2019**, *48*, 10398–10402.

A Supplementary Material to Chapter 4

A.1 $Sr_3(C_6H_5O_7)_2 \cdot H_2O$

Tab. A.1.1: Crystal data and structure refinements of $Sr_3(C_6H_5O_7)_2 \cdot H_2O$ determined from powder X-ray diffraction data via Rietveld refinement using the majority variant from our SC-XRD as model; the Rietveld refinement provides a slightly different set of lattice parameters founded on better statistics than the single crystal measurement; the respective standard deviations are given in parentheses.

M / g × mol^{-1}	659.08
Temperature / K	300(2)
Space group	$P\bar{1}$ (No. 2)
a / pm	1010.33(4)
b / pm	1014.08(5)
c / pm	1083.32(6)
α / °	89.853(4)
β / °	67.164(3)
γ / °	62.033(3)
Volume / 10^6 pm^3	881.24(9)
Z	2
ρ_{calcd} / g cm^3	2.48
Radiation; wavelength λ / Å	Cu$K\alpha$; 1.54184
Diffractometer	Bruker D8 Advance
Θ range / °	2.5-35
Observed reflections	773
Refined parameters	57
R_{Bragg}	0.0028
R_{p}	0.0045
R_{wp}	0.0065
GOF	1.53

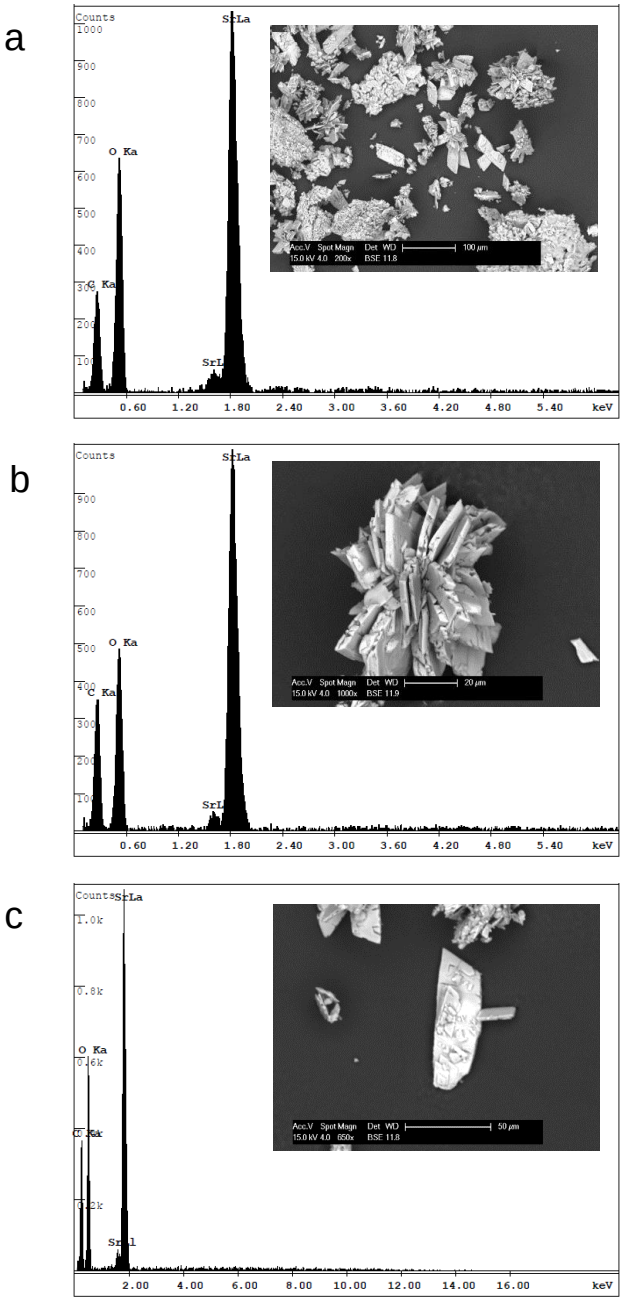

Fig. A.1.1: EDX spectra of $Sr_3(C_6H_5O_7)_2 \cdot H_2O$ (a-c) and as insets the respective SEM image taken right before the EDX measurement.

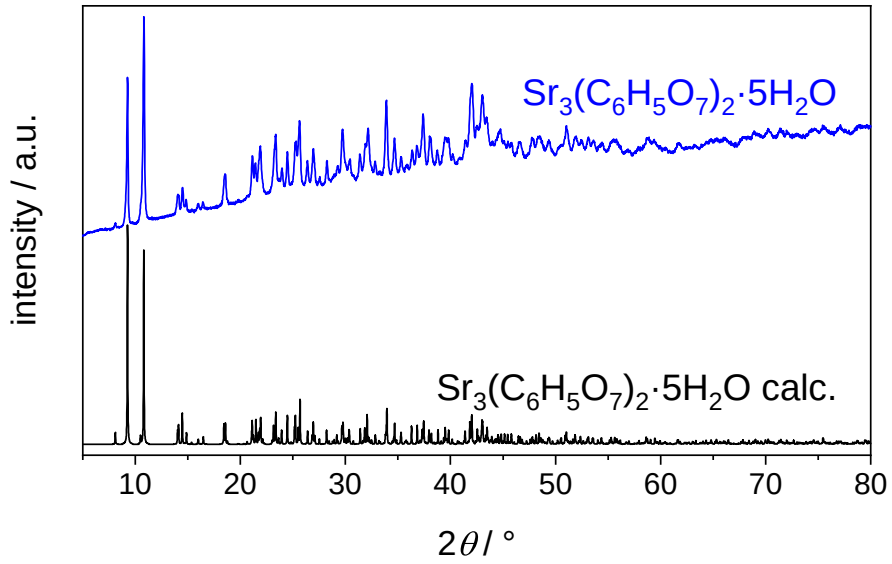

Fig. A.1.2: PXRD pattern of as prepared $Sr_3(C_6H_5O_7)_2 \cdot 5\,H_2O$ compared to a calculated pattern of $Sr_3(C_6H_5O_7)_2 \cdot 5\,H_2O$.[211]

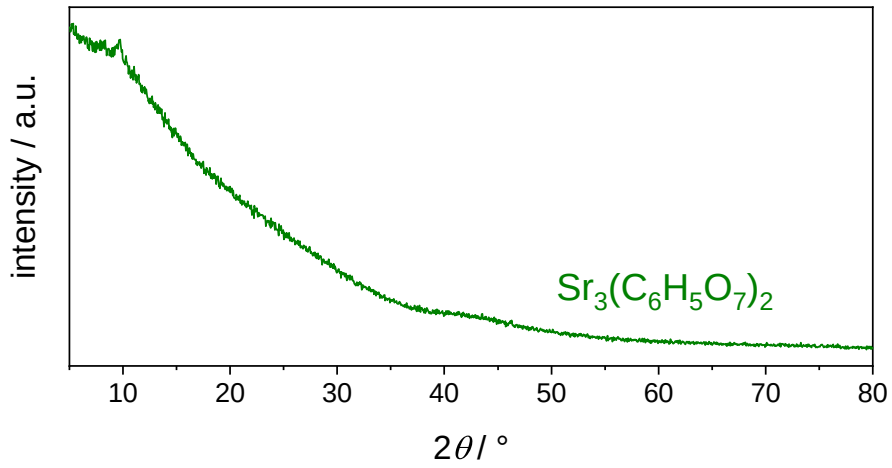

Fig. A.1.3: PXRD pattern of dehydrated $Sr_3(C_6H_5O_7)_2 \cdot 5\,H_2O$ showing no crystallinity.

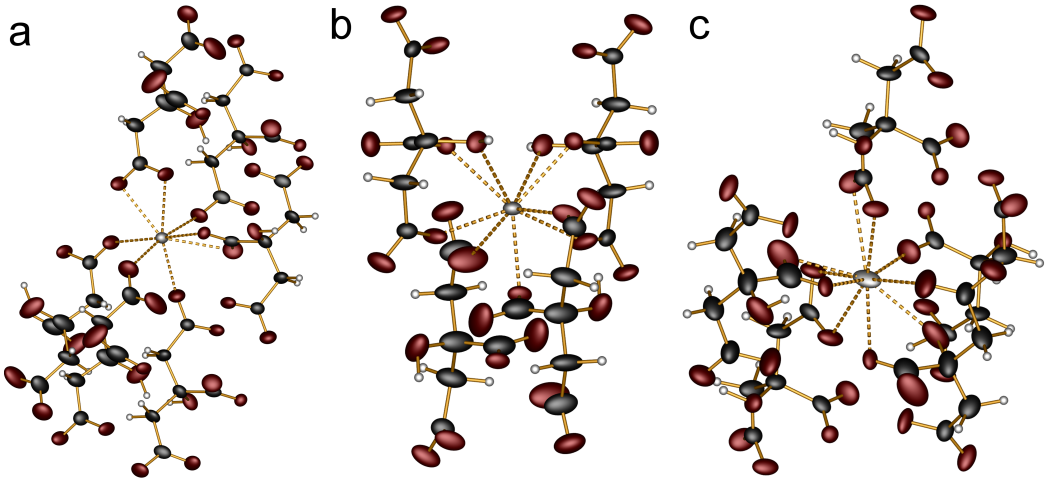

Fig. A.1.4: Coordination environments of the Sr^{2+} cations in $Sr_3(C_6H_5O_7)_2 \cdot H_2O$ including the citrate groups: (a) Sr(1), (b) Sr(2), (c) Sr(3); displacement ellipsoids are set to 60% probability and hydrogen atoms are shown as simple spheres; the majority components are shown, only.

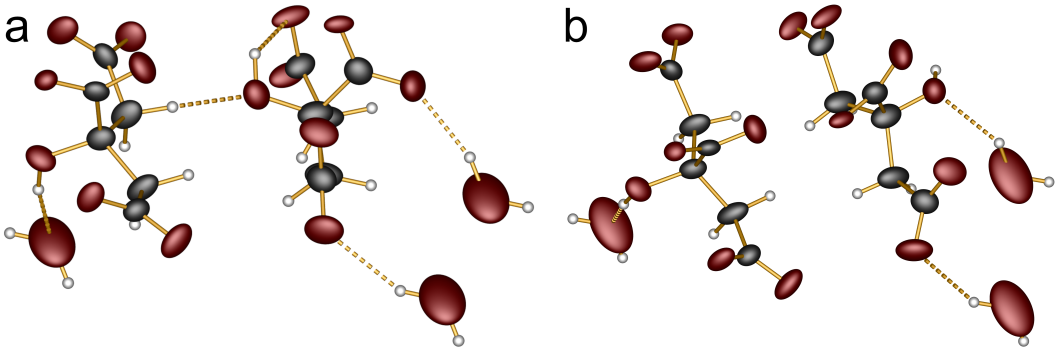

Fig. A.1.5: Hydrogen bonding in $Sr_3(C_6H_5O_7)_2 \cdot H_2O$ showing the majority components in (a) and the minority components in (b): The two citrate groups are shown together with adjacent crystal water molecules; carbon is shown in black, oxygen in red and hydrogen in white; the displacement ellipsoids are set to 60% probability and hydrogen atoms are shown as simple spheres.

Tab. A.1.2: Experimental and theoretically predicted mass losses in wt.-% for the thermal analysis of $Sr_3(C_6H_5O_7)_2 \cdot H_2O$ depicted in Figure 4.1.7

Decomposition Step	exp.	calc.
$Sr_3(C_6H_5O_7)_2 \cdot H_2O \longrightarrow Sr_3(C_6H_5O_7)_2$	3.0	2.7
$Sr_3(C_6H_5O_7)_2 \longrightarrow Sr_3(C_6H_3O_6)_2$	8.5	8.2
$Sr_3(C_6H_3O_6)_2 \longrightarrow 3\,SrCO_3$	27.8	32.8
$3\,SrCO_3 \longrightarrow 3\,SrO$	53.3	52.8

Tab. A.1.3: Experimental and theoretically predicted mass losses in wt.-% for the thermal analysis of $Sr_3(C_6H_5O_7)_2 \cdot 5\,H_2O$ depicted in Figure 4.1.7

Decomposition Step	exp.	calc.
$Sr_3(C_6H_5O_7)_2 \cdot 5\,H_2O \longrightarrow Sr_3(C_6H_5O_7)_2$	10.2	12.3
$Sr_3(C_6H_5O_7)_2 \longrightarrow Sr_3(C_6H_3O_6)_2$	17.1	17.3
$Sr_3(C_6H_3O_6)_2 \longrightarrow 3\,SrCO_3$	30.7	39.4
$3\,SrCO_3 \longrightarrow 3\,SrO$	49.6	57.5

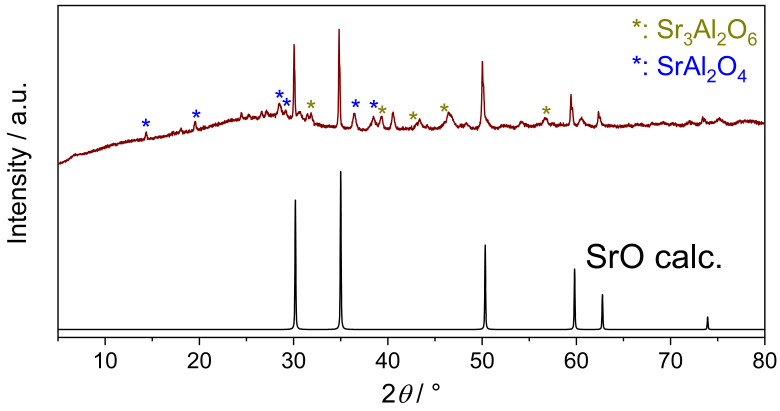

Fig. A.1.6: PXRD pattern of decomposed $Sr_3(C_6H_5O_7)_2 \cdot 5\,H_2O$ (10 h at 1200°) compared to a calculated pattern for SrO:[463] Additionally, Sr3Al2O6[464] and SrAl2O4[465] could be found as side phases presumably due to reaction with the corundum crucible.

A.2 *Ln*[CO_3][OH] (*Ln*=La, Pr, Nd, Sm, Eu, Gd)

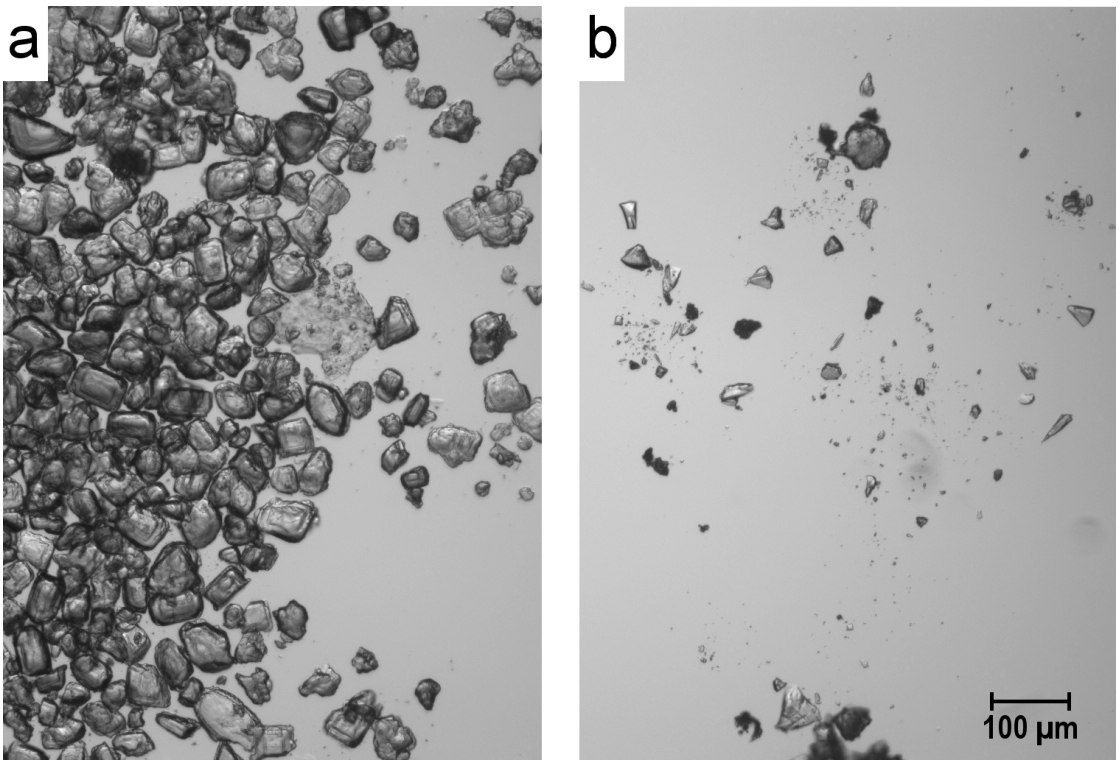

Fig. A.2.1: Optical microscope pictures of (a) La[CO_3][OH] synthesised in the reported way and (b) La[CO_3][OH] synthesised equally but without CTAB.

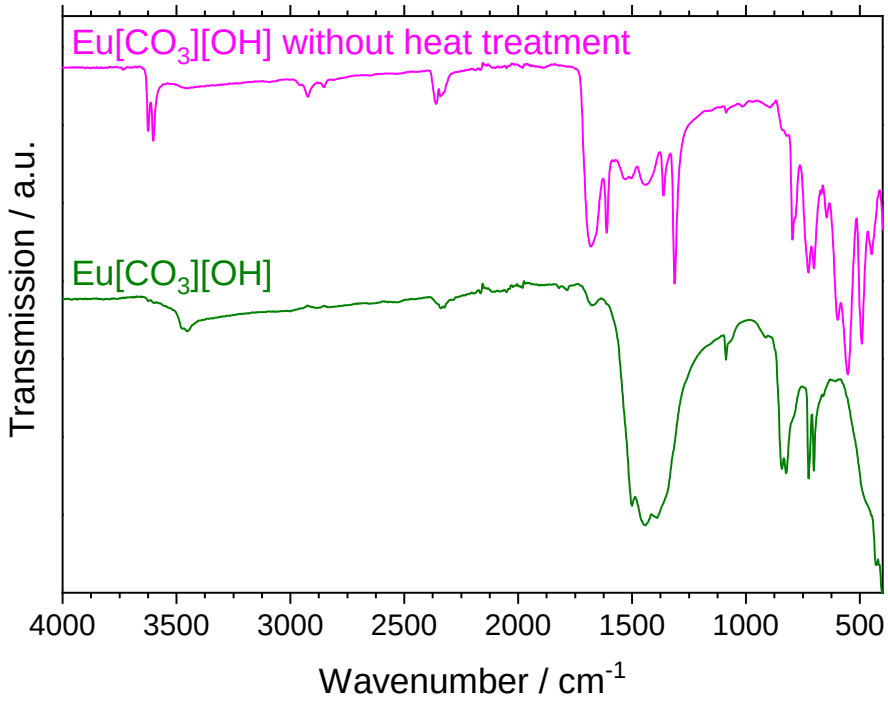

Fig. A.2.2: Infrared spectra of Eu[CO_3][OH] prepared as reported (bottom) and without the final heat treatment (top): The presence of CTAB is apparent from the characteristic absorption bands at $2956\,\mathrm{cm}^{-1}$ (CH_3 asymmetrical stretching), $2924\,\mathrm{cm}^{-1}$ (CH_2 asymmetrical stretching) and $2853\,\mathrm{cm}^{-1}$ (CH_3 symmetrical stretching).[466]

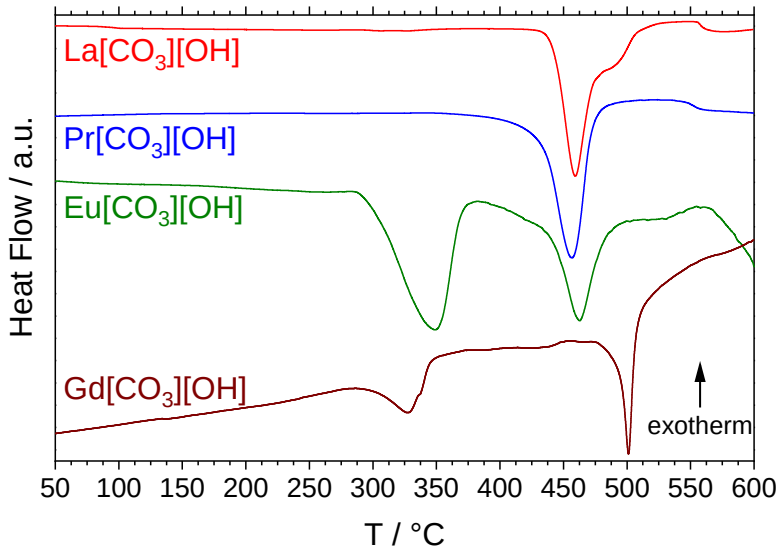

Fig. A.2.3: DSC signal of La[CO_3][OH], Pr[CO_3][OH], Eu[CO_3][OH] and Gd[CO_3][OH]: The latter two show the decomposition of the side phase around 350 and 330°, respectively. For all samples, non-heat treated powders were used. The second endothermic peak relates to the transition of *Ln*[CO_3][OH] to *Ln*[CO_3]O_2 detailed in section 4.2.

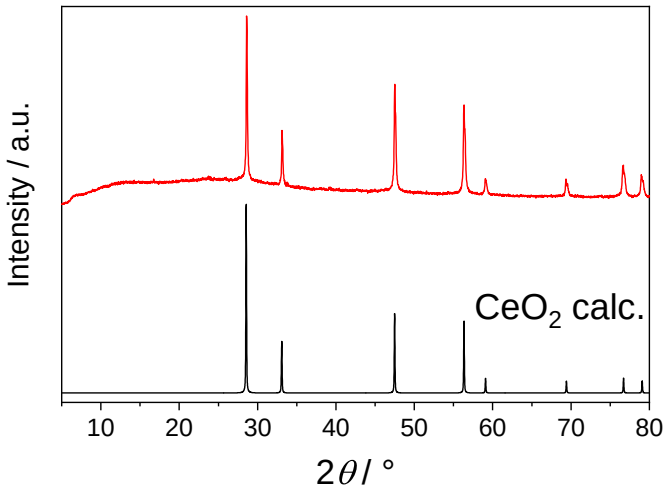

Fig. A.2.4: PXRD pattern of the approach using the reported synthesis for *Ln*[CO_3][OH] with $Ce(NO_3)_3 \cdot 5\,H_2O$ as starting material (top) compared to a calculated pattern calculated from single-crystal data of CeO_2 (bottom).[467]

Tab. A.2.1: Electrostatic calculations for the rare earth carbonate hydroxides *Ln*[CO_3][OH] (*Ln* = La, Pr, Eu, Gd) in space group $Pnma$.

$La[CO_3][OH]$	$\frac{1}{2}\ La_2O_3^{[468]} + H_2O^{[469]} + CaCO_3^{[470]} - CaO^{[471]}$
$MAPLE = 27016\ kJ\,mol^{-1}$	$MAPLE = 27084\ kJ\,mol^{-1}$
	$\Delta = 0.25\%$
$Pr[CO_3][OH]$	$\frac{1}{2}\ Pr_2O_3^{[472]} + H_2O^{[469]} + CaCO_3^{[470]} - CaO^{[471]}$
$MAPLE = 27336\ kJ\,mol^{-1}$	$MAPLE = 27201\ kJ\,mol^{-1}$
	$\Delta = 0.49\%$
$Eu[CO_3][OH]$	$\frac{1}{2}\ Eu_2O_3^{[473]} + H_2O^{[469]} + CaCO_3^{[470]} - CaO^{[471]}$
$MAPLE = 27520\ kJ\,mol^{-1}$	$MAPLE = 27448\ kJ\,mol^{-1}$
	$\Delta = 0.26\%$
$Gd[CO_3][OH]$	$\frac{1}{2}\ Gd_2O_3^{[473]} + H_2O^{[469]} + CaCO_3^{[470]} - CaO^{[471]}$
$MAPLE = 27571\ kJ\,mol^{-1}$	$MAPLE = 27483\ kJ\,mol^{-1}$
	$\Delta = 0.32\%$

Tab. A.2.2: Electrostatic calculations for Eu[CO_3][OH] in $Pnma$ and $P2_12_12_1$

$Eu[CO_3][OH]\ (Pnma)$	$\frac{1}{2}\ Eu_2O_3[473] + H_2O[469] + CaCO_3[470] - CaO[471]$
$MAPLE = 27520\ kJ\,mol^{-1}$	$MAPLE = 27448\ kJ\,mol^{-1}$
	$\Delta = 0.26\%$
$Eu[CO_3][OH]\ (P2_12_12_1)$	$\frac{1}{2}\ Eu_2O_3[473] + H_2O[469] + CaCO_3[470] - CaO[471]$
$MAPLE = 27535\ kJ\,mol^{-1}$	$MAPLE = 27448\ kJ\,mol^{-1}$
	$\Delta = 0.32\%$

Tab. A.2.3: Coordination numbers from MAPLE calculations for Eu[CO_3][OH] in space groups $Pnma$ and $P2_12_12_1$: For Eu^{3+}, a CN of 10 is found for both space groups. This disagrees to the reported structure in $P2_12_12_1$ with CN = 9.

$Pnma$	$P2_12_12_1$	
Eu	10	10
O1	4	4
O2	3	3
O3[i]	-	3
C	3	3
OW	1	3
H	1	1

[i] The position O3 is absent in the solution in $Pnma$ due to inversion symmetry.

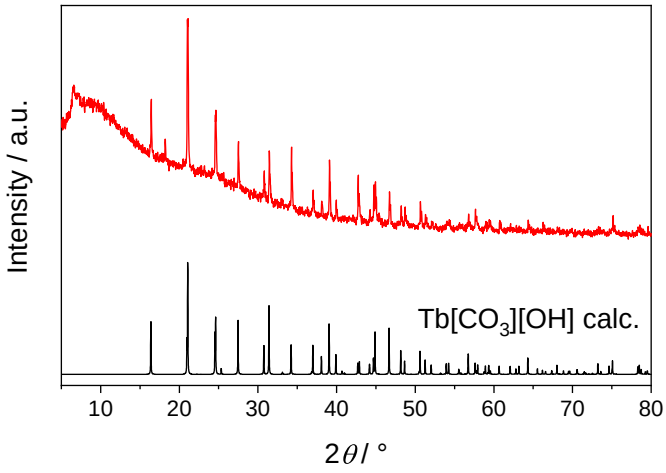

Fig. A.2.5: PXRD pattern of Tb[CO_3][OH] compared to a calculated pattern from the SC-XRD.

Tab. A.2.4: Electrostatic calculations for Tb[CO_3][OH]

$Tb[CO_3][OH]$	$\frac{1}{2}\ Tb_2O_3[474] + H_2O[469] + CaCO_3[470] - CaO[471]$
MAPLE = 27596 kJ mol^{-1}	MAPLE = 27539 kJ mol^{-1}
	$\Delta = 0.21\%$

Tab. A.2.5: Absorption band assignment of the IR spectra of *Ln*[CO_3][OH] (*Ln* = La, Pr, Nd, Sm, Eu, Gd) displayed in Figure 4.2.5; all values are given in cm^{-1}.

Band (La)	Band (Pr)	Band (Nd)	Band (Sm)	Band (Eu)	Band (Gd)	Assignment
3440	3435	3444	3446	3454	3483	OH stretching
1677	1628	1634	1680	1677	1670	OH stretching
1483	1489	1493	1481	1500	1508	$\nu_3\left(CO_3^{2-}\right)$
1423	1435	1439	1427	1441	1448	$\nu_3\left(CO_3^{2-}\right)$
1319	1319	1347	1315	1390	1388	OH bending
1074	1078	1080	1086	1087	1090	$\nu_1\left(CO_3^{2-}\right)$
856	854	854	856	843	845	$\nu_2\left(CO_3^{2-}\right)$
796	810	816	818	824	827	CO_3^{2-} deformation
723	725	727	725	725	727	$\nu_4\left(CO_3^{2-}\right)$
694	696	698	700	702	704	$\nu_4\left(CO_3^{2-}\right)$
472	478	480	463	474	440	Ln-O
400	400	400	400	400	400	Ln-O

Tab. A.2.6: Experimental and theoretically predicted mass losses in wt.-% for the thermal analysis of La[CO_3][OH], Pr[CO_3][OH] and Eu[CO_3][OH] depicted in Figure 4.2.8.

Decomposition Step	$Ln[CO_3][OH] \longrightarrow Ln_2[CO_3]O_2 + CO_2 + H_2O$	$Ln_2[CO_3]O_2 \longrightarrow Ln_2O_3 + CO_2$
exp. (La[CO_3][OH])	16.2	10.0
calc. (La[CO_3][OH])	14.4	10.2
exp. (Pr[CO_3][OH])	17.3	9.3
calc. (Pr[CO_3][OH])	14.2	10.1
exp. (Eu[CO_3][OH])	9.7	8.7
calc. (Eu[CO_3][OH]))	13.5	9.6

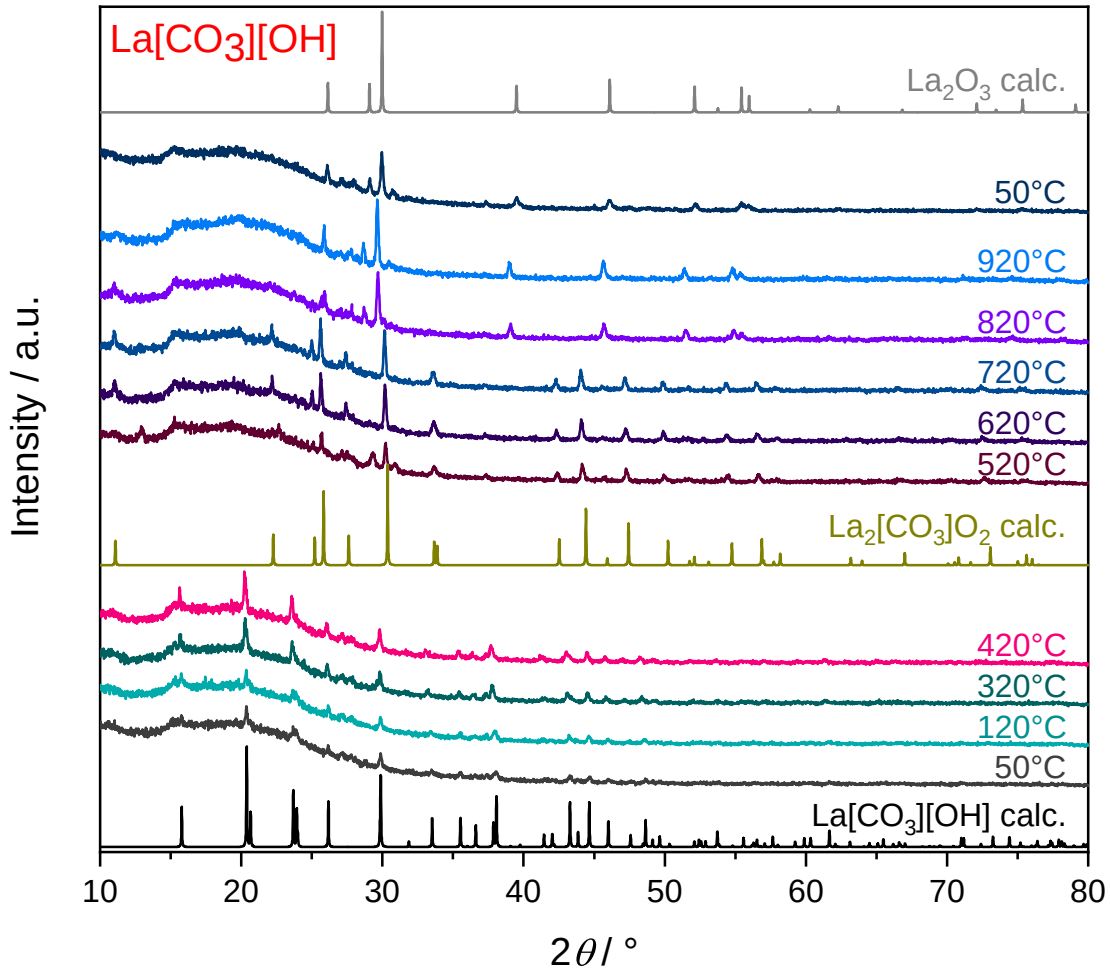

Fig. A.2.6: TPXRD patterns of La[CO_3][OH] compared to theoretical patterns calculated from the SC-XRD data for La[CO_3][OH] and literature for $La_2[CO_3]O_2$ [475] and La_2O_3.[468]

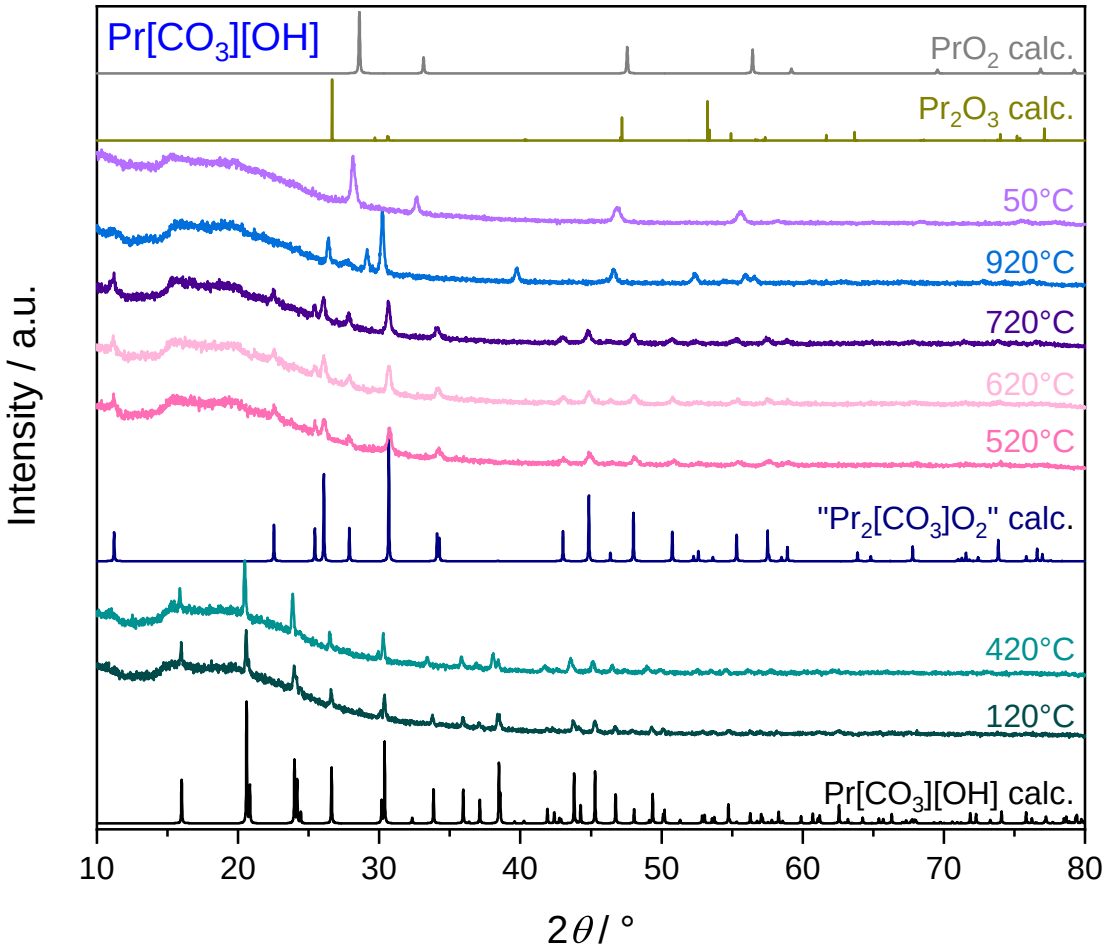

Fig. A.2.7: TPXRD patterns of Pr[CO_3][OH] compared to theoretical patterns calculated from the SC-XRD data for Pr[CO_3][OH], refined data for Pr_2[CO_3]O_2 (given in quotation marks due to the mere refinement of the lattice parameters without further structure refinement), and literature for Pr_2O_3 [472] and PrO_2;[476] the lattice parameters of the intermediate product Pr_2[CO_3]O_2 ($a = 4.0388$, $c = 15.7651$ Å) could be determined using the high-temperature PXRD measurement at 720°C with the crystal structure of La_2[CO_3]O_2 ($a = 4.0755, c = 15.957$ Å, space group $P63/mmc$ (no. 194)) as a model.[475]; the refinement based on the CIF data of the lanthanum compound was carried out using the program JANA2006; $R_1 = 7.11$, $R_2 = 6.40$, GOF = 1.05;[477] the refined lattice parameters are in agreement with the reported structures of Nd_2[CO_3]O_2, Gd_2[CO_3]O_2 and Dy_2[CO_3]O_2 taking into account the lanthanide contraction;[257, 478, 479].

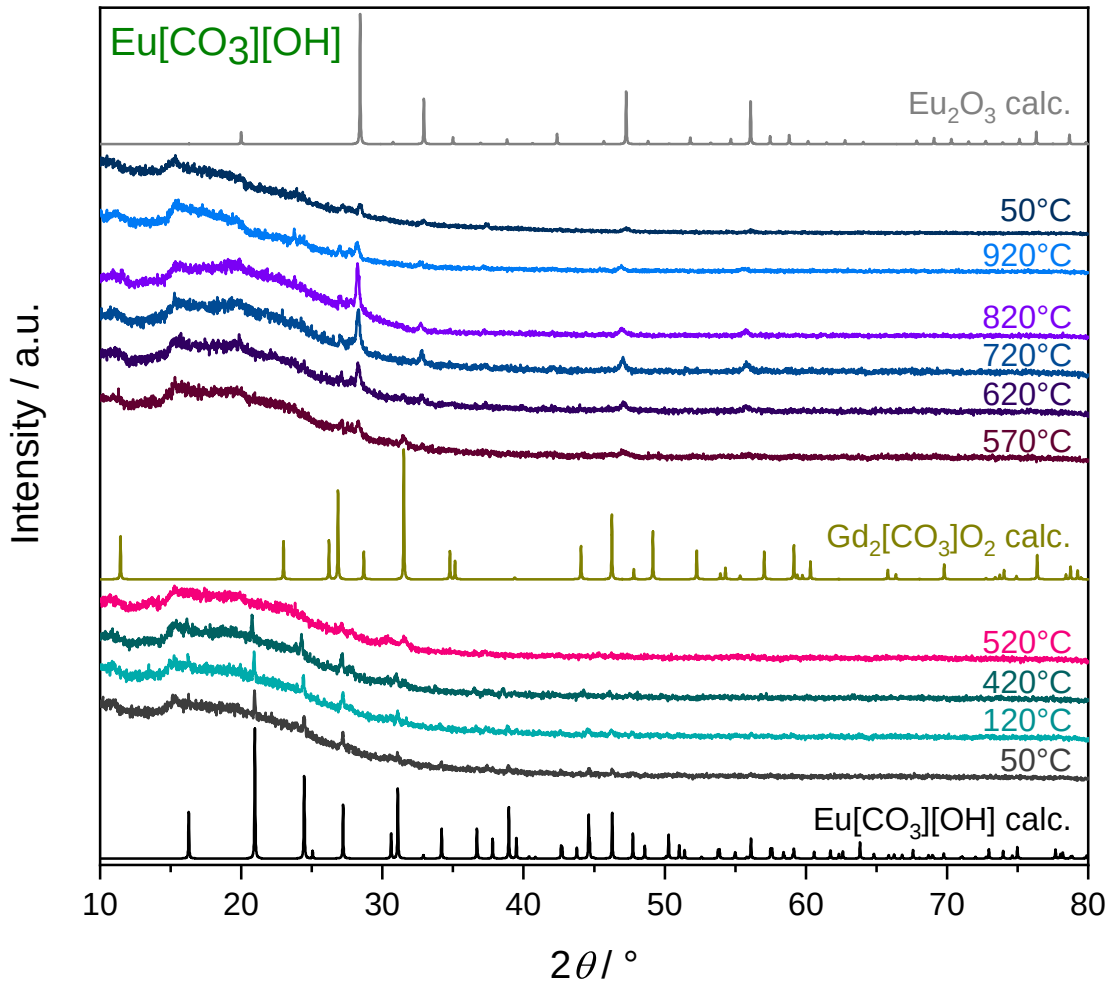

Fig. A.2.8: TPXRD patterns of $Eu[CO_3][OH]$ compared to theoretical patterns calculated from the SC-XRD data for $Eu[CO_3][OH]$ and literature for $Gd_2[CO_3]O_2$ [257] - since there is no data for $Eu_2[CO_3]O_2$ in literature - and Eu_2O_3.[480]

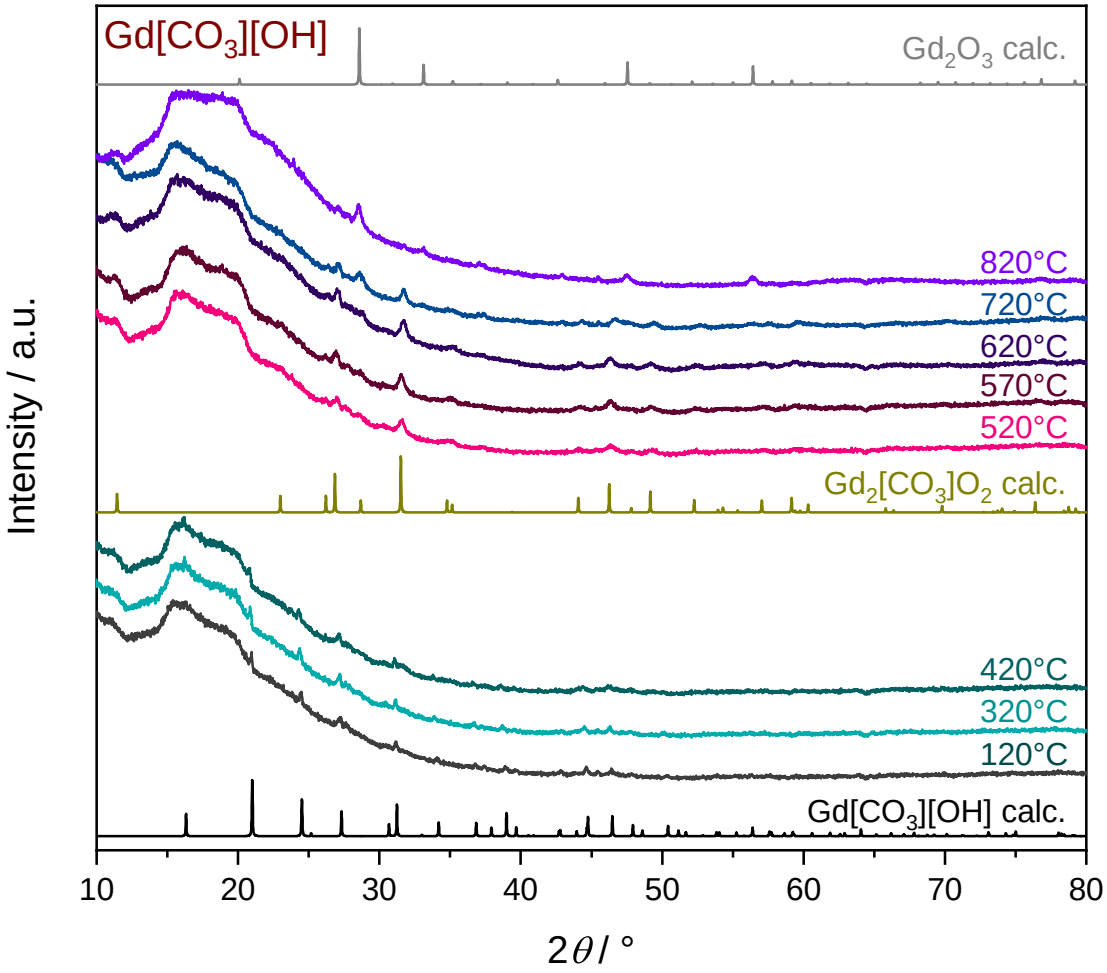

Fig. A.2.9: TPXRD patterns of Gd[CO$_3$][OH] compared to theoretical patterns calculated from the SC-XRD data for Gd[CO$_3$][OH] and literature data for Gd$_2$[CO$_3$]O$_2$ [257] and Gd$_2$O$_3$;[473] the strong background between $12.5^\circ < 2\Theta < 30^\circ$ is due to the used furnace attachment.

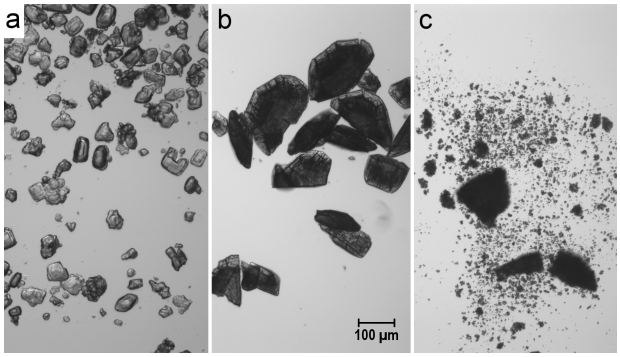

Fig. A.2.10: Optical microscope pictures of (a) La[CO_3][OH], (b) $La_2[CO_3]O_2$ and (c) La_2O_3 showing the inheritance of morphology from the precursor during the decomposition; (a) shows the as synthesised sample, for (b) it was heated in corundum crucibles for 10 h at 470°C (heating ramps $200\,\mathrm{K\,h^{-1}}$) and (c) represents the product of the TG analysis.

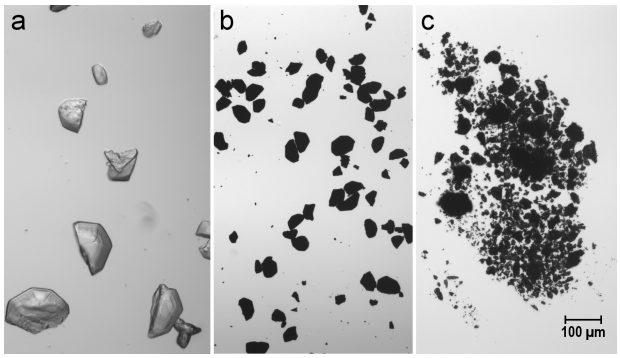

Fig. A.2.11: Optical microscope pictures of (a) Pr[CO_3][OH], (b) $Pr_2[CO_3]O_2$ and (c) Pr_2O_3 showing the inheritance of morphology from the precursor during the decomposition; (a) shows the as synthesised sample, for (b) it was heated in corundum crucibles for 10 h at 460°C (heating ramps $200\,\mathrm{K\,h^{-1}}$) and (c) represents the product of the TG analysis.

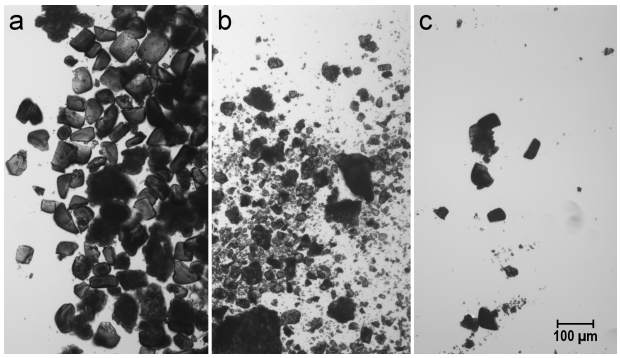

Fig. A.2.12: Optical microscope pictures of (a) Eu[CO_3][OH], (b) $Eu_2[CO_3]O_2$ and (c) Eu_2O_3 showing the inheritance of morphology from the precursor during the decomposition; (a) shows the as synthesised sample, for (b) it was heated in corundum crucibles for 10 h at 500°C (heating ramps $200\,\mathrm{K\,h^{-1}}$) and (c) represents the product of the TG analysis.

B Supplementary Material to Chapter 5

B.1 $Na_5M(WO_4)_4$

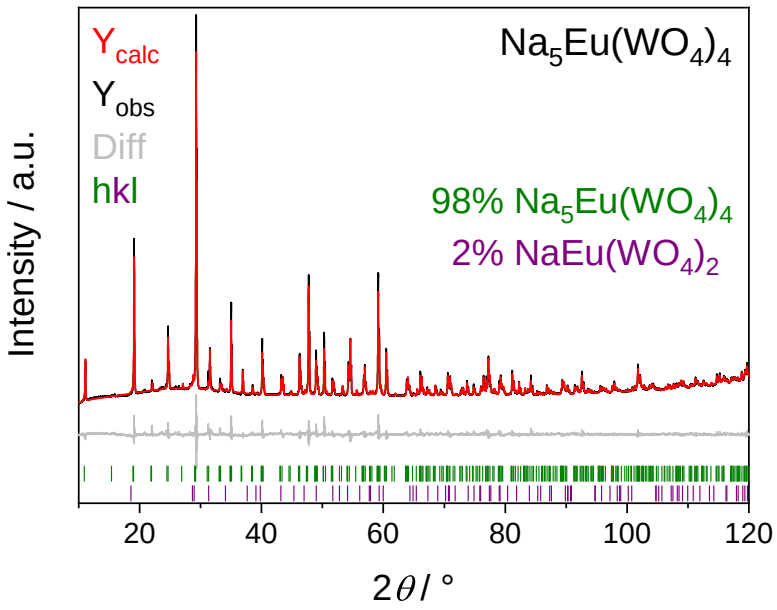

Fig. B.1.1: Rietveld-Refinement of $Na_5Eu(WO_4)_4$ prepared by flux synthesis; further details can be found in Table B.1.3.

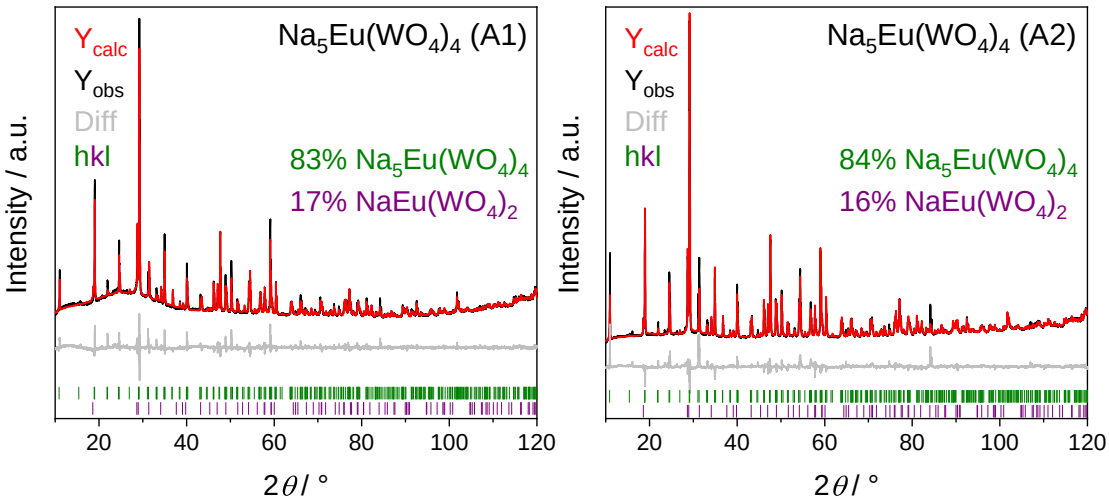

Fig. B.1.2: Rietveld refinements of $Na_5Eu(WO_4)_4$ prepared by standard solid state reaction at 600°C (A1) (left) and 700°C (A2) (right): the refinements yielded in R_{wp} of 2.24% and 4.23%, R_{Bragg} of 1.29% and 2.91% for $Na_5Eu(WO_4)_4$ and 0.72% and 1.77% for $NaEu(WO_4)_2$, respectively.

Tab. B.1.1: Crystal data and structure refinements of $NaEu(WO_4)_2$ and $Na_5M(WO_4)_4$ (M = Ce, Pr, Nd, Sm, Eu) determined from single-crystal data; the respective standard deviations are given in parentheses.

	$NaEu(WO_4)_2$	$Na_5Ce(WO_4)_4$	$Na_5Pr(WO_4)_4$	$Na_5Nd(WO_4)_4$	$Na_5Sm(WO_4)_4$	$Na_5Eu(WO_4)_4$
CSD-No.	1986866	1986870	1986859	1986871	1986862	1986865
M / g mol^{-1}	670.65	1246.47	1247.26	1250.59	1256.70	1258.31
Crystal size / mm^3	0.04 × 0.04 × 0.03	0.07 × 0.03 × 0.03	0.04 × 0.04 × 0.04	0.04 × 0.04 × 0.03	0.04 × 0.04 × 0.02	0.10 × 0.06 × 0.03
Temperature / K	300(3)					
Space group	$I4_1/a$ (No. 88)					
a / pm	526.24(1)	1158.57(3)	1157.65(2)	1155.89(4)	1151.61(4)	1149.98(4)
c / pm	1140.78(3)	1152.47(4)	1147.97(2)	1147.22(4)	1142.31(4)	1140.61(4)
Volume / 10^6 pm^3	316.07(3)	1546.94(10)	1538.46(6)	1532.78(12)	1514.94(12)	1508.40(12)
Z	2			4		
ρ_{calcd} / g cm^3	7.05	5.35	5.39	5.42	5.51	5.54
Absorption coefficient μ / mm^{-1}	46.2	32.7	33.1	33.5	34.3	34.7
$F(000)$ / e	572	2148	2152	2156	2164	2168
Radiation; wavelength λ / Å	Mo-K_α; 0.71073					
Diffractometer	Bruker D8 Venture					
Absorption correction	multi-scan					
Transmission (min; max)	0.6338; 0.7503	0.6678; 0.7478	0.6011; 0.7488	0.5281; 0.7472	0.5921; 0.7479	0.6001; 0.7483
Index range h | k | l	±9 | ±9 | ±21	−14/16 | −15/16 | ±15	−19/21 | ±21 | ±20	−17/16 | −16/17 | ±17	−18/19 | ±19 | ±19	±20 | −15/20 | ±20
Θ range / °	4.265-41.863	2.493-29.415	2.499-40.487	2.501-33.497	2.511-36.979	2.515-39.996
Reflections collected	21433	9235	26586	13470	18168	16901
Independent reflections	546	1062	2455	1504	1937	2337
R_{int}	0.0284	0.0325	0.0504	0.056	0.0403	0.0406
Obs. reflections [$I > 2\sigma(I)$]	472	1008	2191	1277	1722	2025
Refined parameters / restraints	16	59	60	60	60	60
R_1 (all data)	0.018	0.0321	0.024	0.0322	0.023	0.0258
wR_2 (all data)	0.034	0.0719	0.0298	0.0362	0.0321	0.0356
GOF	1.12	1.342	1.076	1.038	1.038	1.026
Residual electron density (max; min) / e^-Å^{-3}	2.08; -1.51	2.16; -2.13	1.16; -1.22	1.08; -1.18	1.56; -1.10	1.41; -1.18

Tab. B.1.2: Crystal data and structure refinements of $Na_5M(WO_4)_4$ (M = Gd, Tb, Ho, Tm, Yb, Bi) determined from single-crystal data; the respective standard deviations are given in parentheses.

	$Na_5Gd(WO_4)_4$	$Na_5Tb(WO_4)_4$	$Na_5Ho(WO_4)_4$	$Na_5Tm(WO_4)_4$	$Na_5Yb(WO_4)_4$	$Na_5Bi(WO_4)_4$
CSD-No.	1986868	1986861	1986869	1986863	1986867	1986858
M / g mol^{-1}	1263.60	1265.27	1271.28	1275.28	1279.39	1315.33
Crystal size / mm^3	0.06 × 0.04 × 0.04	0.08 × 0.04 × 0.03	0.06 × 0.06 × 0.04	0.08 × 0.05 × 0.04	0.05 × 0.05 × 0.04	0.08 × 0.04 × 0.03
Temperature / K	300(3)					
Space group	$I4_1/a$ (No. 88)					
a / pm	1147.96(4)	1146.90(5)	1143.99(4)	1139.99(6)	1139.65(10)	1154.33(4)
c / pm	1137.79(4)	1137.91(6)	1134.69(5)	1129.85(6)	1129.32(11)	1141.36(4)
Volume / 10^6 pm^3	1499.39(12)	1496.78(15)	1484.98(12)	1468.33(17)	1466.8(3)	1520.84(12)
Z	4					
ρ_{calcd} / g cm^3	5.60	5.61	5.69	5.77	5.79	5.75
Absorption coefficient μ / mm$^{\breve{}1}$	35.2	35.5	36.4	37.4	37.8	41.9
$F(000)$ / e	2172	2176	2184	2192	2196	2248
Radiation; wavelength λ / Å	Mo-K_α; 0.71073					
Diffractometer	Bruker D8 Venture					
Absorption correction	multi-scan					
Transmission (min; max)	0.5701; 0.7492	0.5804; 0.7479	0.4945; 0.7489	0.5591; 0.7506	0.4954; 0.7477	0.6549; 0.7459
Index range h | k | l	−20/16 | ±20 | ±20	±19 | −19/14 | ±19	±19 | −19/13 | ±19	±20 | −20/18 | ±20	−12/19 | −18/19 | ±18	±15 | ±15 | ±15
Θ range / °	2.520-40.496	2.521-37.475	2.528-37.999	2.538-39.496	2.539-36.400	2.510-29.246
Reflections collected	23034	15674	15782	18502	13271	12840
Independent reflections	2397	1961	2021	2215	1795	1040
R_{int}	0.0459	0.044	0.0378	0.0449	0.0468	0.0521
Obs. reflections [$I > 2\sigma(I)$]	2116	1718	1795	1940	1533	912
Refined parameters	60	60	60	60	60	60
R_1 (all data)	0.0243	0.0282	0.0252	0.0266	0.03	0.025
wR_2 (all data)	0.0349	0.04	0.0354	0.0363	0.0391	0.0307
GOF	1.081	1.095	1.086	1.076	1.049	1.069
Residual electron density (max; min) / e^-Å^{-3}	2.05; -1.12	1.99; -1.21	1.45; -1.19	1.43; -1.30	1.28; -1.50	1.11; -0.84

Tab. B.1.3: Crystal data and structure refinements of $Na_5M(WO_4)_4$ (M = La, Pr, Sm, Eu, Gd, Tb) determined from PXRD data via Rietveld refinement using the structure of $Na_5Ho(WO_4)_4$ from the SC-XRD and the structure of $NaGd(WO_4)_2$[481] as starting models; the respective standard deviations are given in parentheses; the $NaM(WO_4)_2$ side phase was not refined under a fraction of 1 wt.-%.

	$Na_5La(WO_4)_4$	$Na_5Pr(WO_4)_4$	$Na_5Sm(WO_4)_4$	$Na_5Eu(WO_4)_4$	$Na_5Gd(WO_4)_4$	$Na_5Tb(WO_4)_4$
CSD-No.	1986874					
M / g mol^{-1}	1245.21	1247.21	1256.66	1258.26	1263.55	1265.23
Temperature / K				300(3)		
Space group				$I4_1/a$ (No. 88)		
a / pm	1163.319(11)	1158.140(15)	1152.270(14)	1150.503(12)	1149.044(13)	1147.108(14)
c / pm	1154.299(13)	1148.516(17)	1142.453(16)	1140.722(14)	1139.496(15)	1137.197(16)
Volume / 10^6 pm^3	1562.13(3)	1540.49(5)	1516.86(4)	1509.92(4)	1504.48(4)	1496.39(4)
Z				4		
ρ_{calcd} / g cm^3	5.30	5.38	5.50	5.54	5.58	5.62
R_{Bragg} / %	2.23	1.973	1.527	1.203	1.252	0.951
Radiation; wavelength λ / Å				Cu$K\alpha$; 1.54184		
Diffractometer				Seifert 3003 TT		
Θ range / °				2.5-60		
Observed reflections	714	703	692	692	688	682
Refined parameters	49	49	49	49	49	49
R_{wp}	0.0375	0.0366	0.0382	0.0253	0.029	0.02257
Side phase	$NaLa(WO_4)_2$	$NaPr(WO_4)_2$	$NaSm(WO_4)_2$	$NaEu(WO_4)_2$	$NaGd(WO_4)_2$	$NaTb(WO_4)_2$
Fraction of side phase / wt.-%	4	3	4	2	1	1
Space group				$I4_1/a$ (No. 88)		
a / pm	535.799(18)	531.45(3)	527.10(2)	525.72(4)	524.80(8)	523.09(11)
c / pm	1165.51(7)	1154.88(13)	1143.46(10)	1140.84(17)	1137.1(3)	1135.0(5)
Volume / 10^6 pm^3	334.60(3)	326.19(6)	317.70(4)	315.31(7)	313.16(13)	310.58(19)
Z				2		
R_{Bragg} / %	1.233	1.211	1.135	0.689	1.099	0.895

Tab. B.1.4: Crystal data and structure refinements of $Na_5M(WO_4)_4$ (M = Dy, Ho, Er, Lu, Y) determined from PXRD data via Rietveld refinement using the structure of $Na_5Ho(WO_4)_4$ from the SC-XRD and the structure of $NaGd(WO_4)_2$[481] as starting models; the respective standard deviations are given in parentheses; the $NaM(WO_4)_2$ side phase was not refined under a fraction of 1 wt.-%.

	$Na_5Dy(WO_4)_4$	$Na_5Ho(WO_4)_4$	$Na_5Er(WO_4)_4$	$Na_5Lu(WO_4)_4$	$Na_5Y(WO_4)_4$
CSD-No.			1986873	1986876	1986875
M / g mol^{-1}	1268.80	1271.23	1273.56	1281.27	1195.21
Temperature / K			300(3)		
Space group			$I4_1/a$ (No. 88)		
a / pm	1145.626(15)	1143.999(12)	1142.573(13)	1138.701(12)	1143.616(11)
c / pm	1135.742(17)	1134.018(14)	1132.408(14)	1128.231(13)	1134.047(12)
Volume / 10^6 pm^3	1490.61(4)	1484.13(4)	1478.33(4)	1462.91(3)	1483.17(3)
Z			4		
ρ_{calcd} / g cm^3	5.66	5.69	5.72	5.82	5.35
R_{Bragg} / %	1.52	1.32	1.6	1.63	1.69
Radiation; wavelength λ / Å			Cu$K\alpha$; 1.54184		
Diffractometer			Seifert 3003 TT		
Θ range / °			2.5-60		
Observed reflections	562	556	553	661	554
Refined parameters	46	46	46	49	46
R_{wp}	0.0375	0.0322	0.0394	0.036	0.0371
Side phase	-	-	-	$NaLu(WO_4)_2$	-
Fraction of side phase / wt.-%	-	-	-	3	-
Space group	-	-	-	$I4_1/a$ (No. 88)	-
a / pm	-	-	-	516.39(3)	-
c / pm	-	-	-	1117.20(11)	-
Volume / 10^6 pm^3	-	-	-	297.91(4)	-
Z	-	-	-	2	-
R_{Bragg} / %	-	-	-	1.93	-

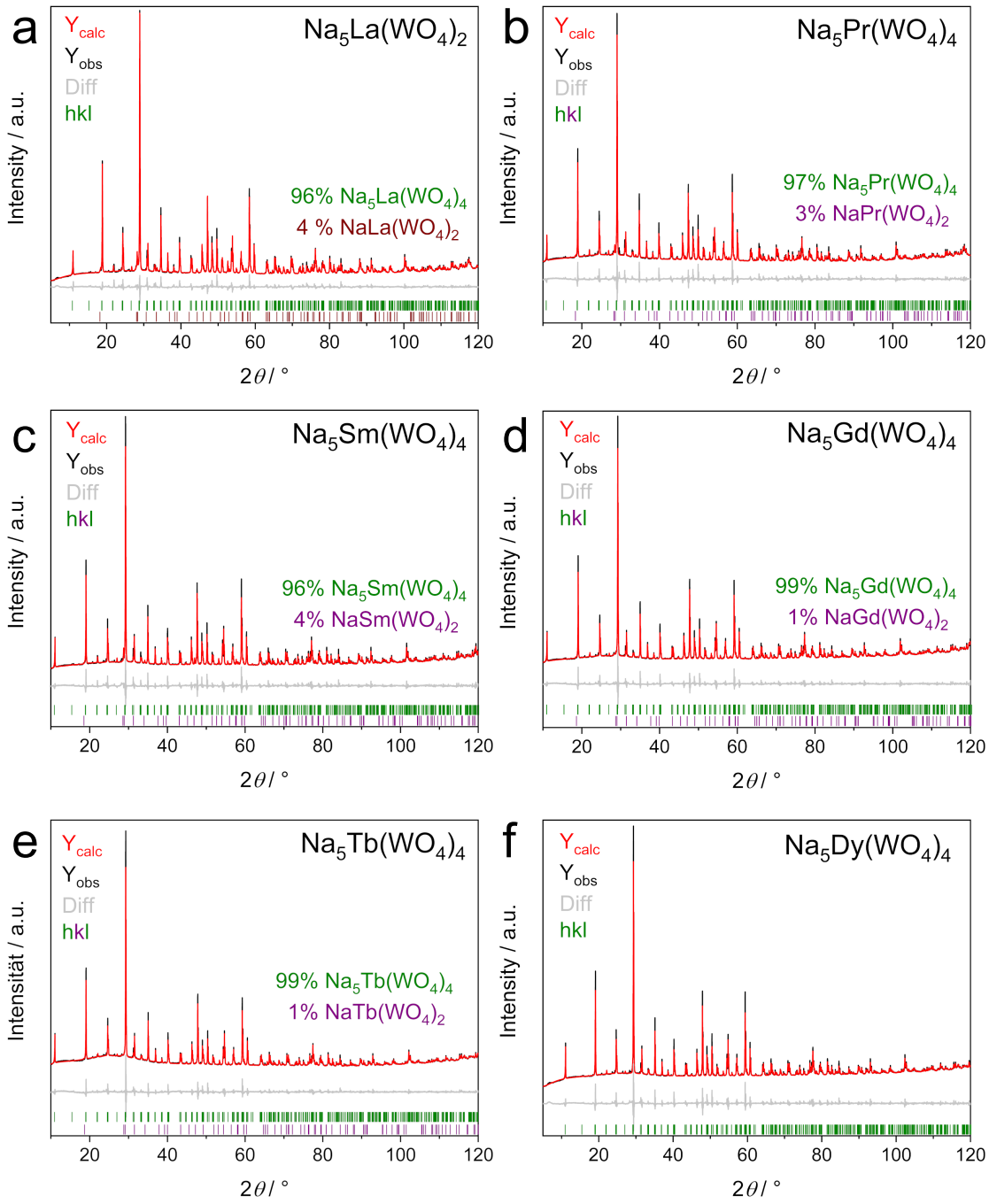

Fig. B.1.3: Rietveld refinements of (a) $Na_5La(WO_4)_4$, (b) $Na_5Pr(WO_4)_4$, (c) $Na_5Sm(WO_4)_4$, (d) $Na_5Gd(WO_4)_4$, (e) $Na_5Tb(WO_4)_4$ and (f) $Na_5Dy(WO_4)_4$ prepared by flux synthesis; further details can be found in Tables S3 and S4.

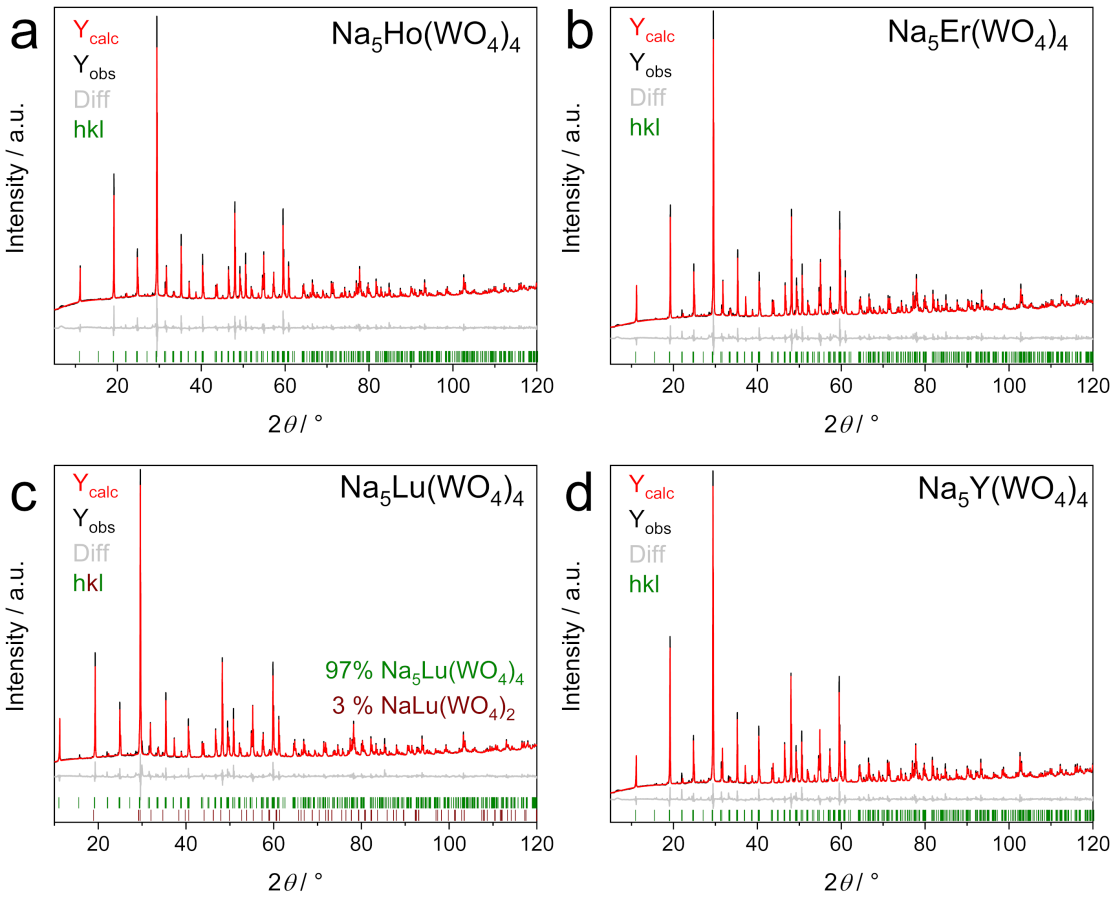

Fig. B.1.4: Rietveld refinements of (a) $Na_5Ho(WO_4)_4$, (b) $Na_5Er(WO_4)_4$, (c) $Na_5Lu(WO_4)_4$ and (d) $Na_5Y(WO_4)_4$ prepared by flux synthesis; further details can be found in Table S4.

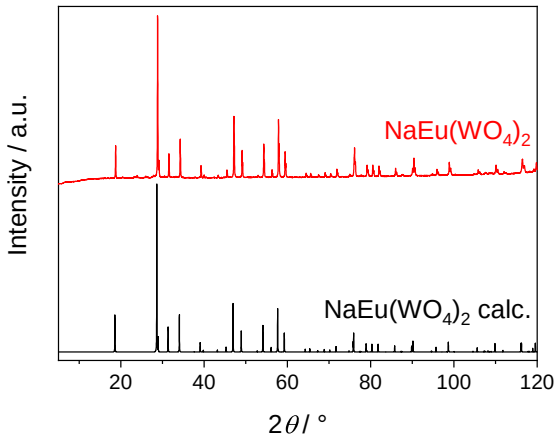

Fig. B.1.5: PXRD pattern of polycrystalline $NaEu(WO_4)_2$ compared to a pattern calculated from single crystal data showing phase purity.

Tab. B.1.5: Selected interatomic distances (in pm) and angles (in °) of $NaEu(WO_4)_2$; the respective standard deviations are given in parentheses.

Na/Eu-O[i]	245.71(18); 247.67(18)
$\sum$ IR (Na/Eu-O)[216] [ii]	248
Na/Eu-Na/Eu	388.03(1)
W-O	178.97(18)
$\sum$ IR (W-O)[216]	178
O-W-O	107.13(6); 114.26(12)

[i] There are two groups of four oxygen in different distances to cation; [ii] The average value of Na^+ and Eu^{3+} was used for the sum of ionic radii.

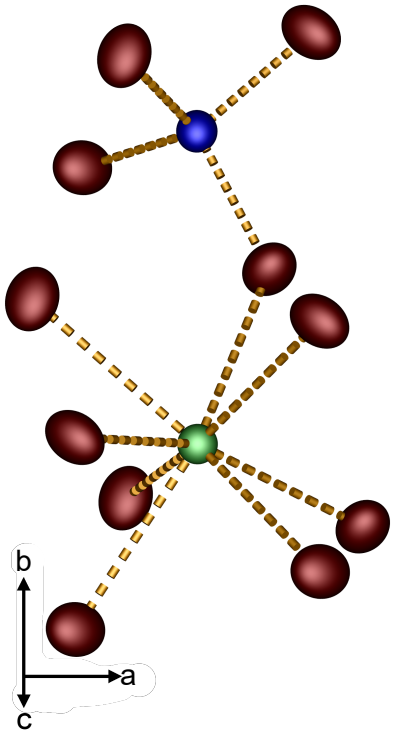

Fig. B.1.6: Coordination environments of Na^+/Eu^{3+}(green) and W^{6+}(blue) in $NaEu(WO_4)_2$: The former form $[(Na/Eu)O_8]$ dodecahedra and the latter WO_4 tetrahedra; oxygen is depicted in red; the ellipsoids are shown at 90% probability

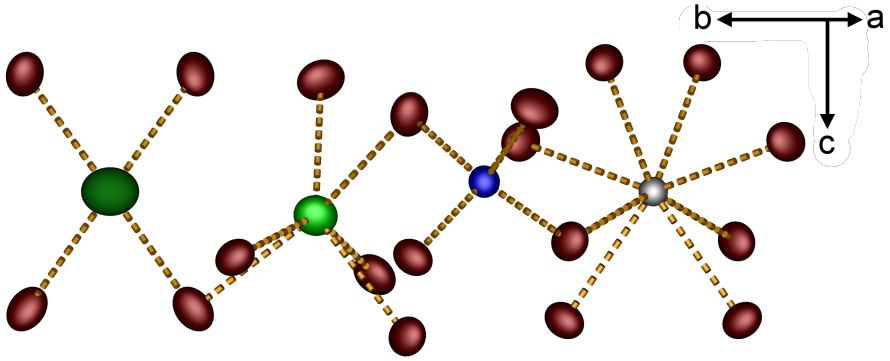

Fig. B.1.7: Coordination environments of Na^+ (light green Na(1) and dark green Na(2)) Eu^{3+}(grey) and W^{6+}(blue) in $Na_5Eu(WO_4)_4$: they form Na(1) O_6 trigonal prisms, Na(2) O_4 tetrahedra, WO_4 tetrahedra and EuO_8 dodecahedra together with oxygen (red), respectively; the ellipsoids are shown at 90% probability.

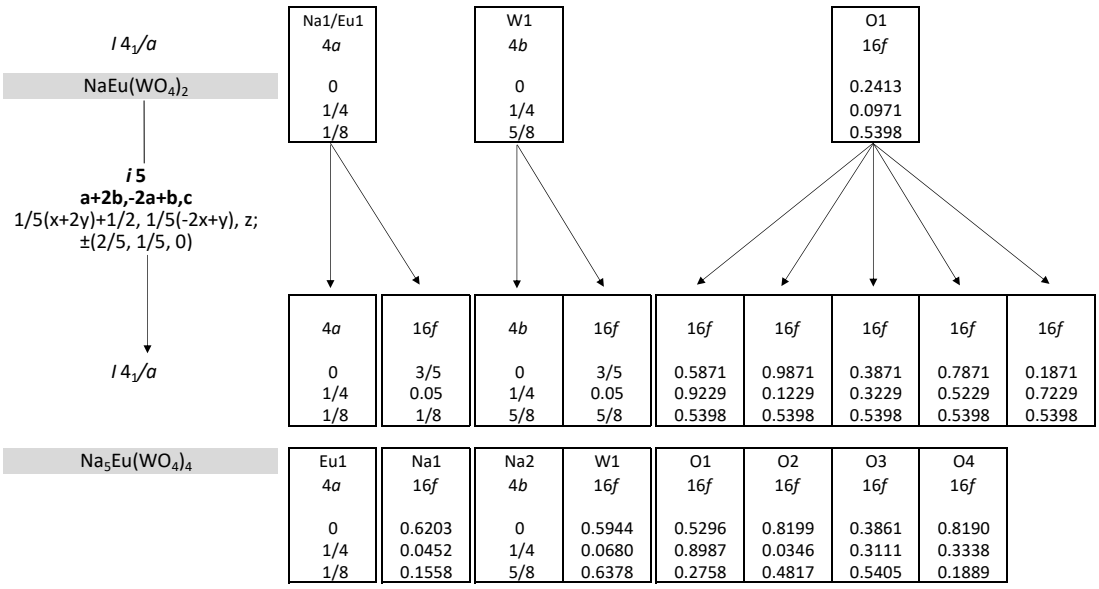

Fig. B.1.8: Group–subgroup scheme in the Bärnighausen formalism[298,299] showing the symmetry relation between $Na_5Eu(WO_4)_4$ and $NaEu(WO_4)_2$.

Tab. B.1.6: Selected interatomic distances (in pm), angles (in °) and the deviation from the ideal symmetry Δ_{octa} or Δ_{tetr} (in %) of $Na_5M(WO_4)_4$ (M = La, Ce, Pr, Nd, Sm); the respective standard deviations are given in parentheses.

	$Na_5La(WO_4)_4$	$Na_5Ce(WO_4)_4$	$Na_5Pr(WO_4)_4$	$Na_5Nd(WO_4)_4$	$Na_5Sm(WO_4)_4$
Data	Rietveld	SC-XRD	SC-XRD	SC-XRD	SC-XRD
M-O[i]	238(1)-247(1)	246.3(7)-247.1(7)	245.4(2)-245.8(2)	244.5(3)-244.7(3)	241.4(2)-241.9(2)
$\sum$ IR (M-O)[216]	252	250.3	248.6	246.9	243.9
M-M	649.31(1)	646.98(1)	646.07(1)	645.20(2)	642.73(2)
Na(1)-O	217(1)-275(1)	228.2(8)-257.7(9)	228.7(2)-255.8(2)	229.1(3)-255.2(3)	228.7(2)-253.1(2)
$\sum$ IR (Na(1)-O)[216] ii			238; 240		
Δ_{octa}(Na(1) O_6)[iii]		2	2.14	2.34	2.79
Na(2)-O	239(1)	247.6(8)	246.3(2)	246.4(3)	245.5(2)
$\sum$ IR (Na(2)-O)[216]			237		
Δ_{tetr}(Na(2) O_4)[iii]		7.39	7.18	7.33	7.4
W-O	170(1)-191(1)	176.5(7)-180.2(7)	175.6(2)-180.5(2)	175.6(3)-180.0(3)	175.9(2)-180.6(2)
$\sum$ IR (W-O)[216] ii			178; 180		
O-W-O	103.0(6)-116.2(5)	106.5(3)-113.3(3)	106.2(1)-113.4(1)	105.9(1)-113.5(1)	105.9(1)-113.7(1)
$\Delta_{tetr}(WO_4)$[iii]		0.45	0.56	0.6	0.63
M-O-W	130.9(6)-137.0(6)	129.1(3)-130.4(4)	129.3(1)-130.2(1)	129.4(2)-130.3(1)	129.3(1)-130.3(1)

[i] There are two distinct pairs of M-O distances; [ii] Different sums of ionic radii due to oxygen with both CN = 3 and 4;
[iii] The deviation of the NaO6 octahedra, NaO4 tetrahedra and WO4 tetrahedra from the ideal symmetry Δ_{octa} or Δ_{tetr} was calculated for all structures derived from single-crystal XRD data.

Tab. B.1.7: Selected interatomic distances (in pm), angles (in °) and the deviation from the ideal symmetry Δ_{octa} or Δ_{tetr} (in %) of $Na_5M(WO_4)_4$ (M = Eu, Gd, Tb, Dy, Ho); the respective standard deviations are given in parentheses.

	$Na_5Eu(WO_4)_4$	$Na_5Gd(WO_4)_4$	$Na_5Tb(WO_4)_4$	$Na_5Dy(WO_4)_4$	$Na_5Ho(WO_4)_4$
Data	SC-XRD	SC-XRD	SC-XRD	Rietveld	SC-XRD
M-O[i]	240.3(2)-240.7(2)	239.2(2)-239.2(2)	238.2(3)-238.8(3)	222(2)-238(2)	236.0(2)-237.1(2)
$\sum$ IR (M-O)[216]	242.6	241.3	240	238.7	237.5
M-M	641.81(2)	640.20(2)	640.13(2)	639.32(1)	638.47(2)
Na(1)-O	229.3(2)-252.3(2)	228.9(2)-251.2(3)	229.6(3)-250.7(3)	226(2)-265(2)	229.6(3)-249.6(3)
$\sum$ IR (Na(1)-O)[216] [ii]			238; 240		
$\Delta_{octa}(Na(1)O_6)$[iii]	2.97	3.33	3.78		3.97
Na(2)-O	245.0(2)	245.0(2)	244.9(3)	242(2)	243.9(2)
$\sum$ IR (Na(2)-O)[216]			237		
$\Delta_{tetr}(Na(2)O_4)$[iii]	7.53	7.48	7.67		7.81
W-O	175.6(2)-180.7(2)	175.6(2)-181.0(2)	175.4(3)-180.6(3)	170(2)-191(2)	175.6(2)-180.6(2)
$\sum$ IR (W-O)[216] [ii]			178; 180		
O-W-O	105.6(1)-113.8(1)	107.1(1)-113.7(1)	105.5(1)-113.8(1)	97.7(9)-115.9(8)	105.3(1)-114.0(1)
$\Delta_{tetr}(WO_4)$[iii]	0.71	0.75	0.73		0.79
M-O-W	129.4(1)-130.1(1)	129.4(1)-130.0(1)	129.5(1)-130.2(1)	133(1)-133.5(9)	129.5(1)-130.0(1)

[i] There are two distinct pairs of M-O distances; [ii] Different sums of ionic radii due to oxygen with both CN = 3 and 4;
[iii] The deviation of the NaO6 octahedra, NaO4 tetrahedra and WO4 tetrahedra from the ideal symmetry Δ_{octa} or Δ_{tetr} was calculated for all structures derived from single-crystal XRD data.

Tab. B.1.8: Selected interatomic distances (in pm), angles (in °) and the deviation from the ideal symmetry Δ_{octa} or Δ_{tetr} (in %) of $Na_5M(WO_4)_4$ (M = Er, Tm, Yb, Lu, Y, Bi); the respective standard deviations are given in parentheses.

	$Na_5Er(WO_4)_4$	$Na_5Tm(WO_4)_4$	$Na_5Yb(WO_4)_4$	$Na_5Lu(WO_4)_4$	$Na_5Y(WO_4)_4$	$Na_5Bi(WO_4)_4$
Data	Rietveld	SC-XRD	SC-XRD	Rietveld	Rietveld	SC-XRD
M-O[i]	232(1)-243(1)	233.5(2)-234.8(2)	233.3(3)-234.7(3)	226(1)-238(1)	228(1)-243(1)	243.7(4)-244.5(4)
$\sum$ IR (M-O)[216]	236.4	235.4	234.5	233.7	237.9	234.5
M-M	637.59(1)	636.14(3)	635.93(5)	635.39(1)	638.23(1)	643.85(2)
Na(1)-O	208(1)-264(2)	228.9(3)-247.7(3)	229.6(3)-247.2(3)	212(2)-269(2)	218(1)-258(2)	228.8(4)-253.4(4)
$\sum$ IR (Na(1)-O)[216] [ii]			238; 240			
$\Delta_{octa}(Na(1)O_6)$[iii]		4.53	4.37			2.17
Na(2)-O	228(2)	243.1(2)	243.5(3)	237(2)	242(1)	245.8(4)
$\sum$ IR (Na(2)-O)[216]			237			
$\Delta_{tetr}(Na(2)O_4)$[iii]		7.77	8.01			7.49
W-O	170(1)-191(2)	175.3(2)-181.0(2)	175.7(3)-181.0(3)	172(1)-190(1)	164(1)-189(1)	175.3(4)-180.5(4)
$\sum$ IR (W-O)[216] [ii]			178; 180			
O-W-O	98.6(7)-116.5(7)	105.2(1)-114.1(1)	104.9(1)-114.3(1)	98.5(7)-119.8(6)	99.8(6)-114.6(5)	105.3(2)-114.1(2)
$\Delta_{tetr}(WO_4)$[iii]		0.89	0.92			0.71
M-O-W	130.7(7)-131.7(8)	129.4(1)-129.9(1)	129.3(1)-129.6(1)	130.2(7)-131.2(7)	130.2(6)-135.2(6)	128.5(2)-129.3(2)

[i] There are two distinct pairs of M-O distances; [ii] Different sums of ionic radii due to oxygen with both CN = 3 and 4; [iii] The deviation of the NaO6 octahedra, NaO4 tetrahedra and WO4 tetrahedra from the ideal symmetry Δ_{octa} or Δ_{tetr} was calculated for all structures derived from single-crystal XRD data.

Tab. B.1.9: Electrostatic calculations for $NaEu(WO_4)_2$ and $Na_5M(WO_4)_4$ (M = Pr, Sm, Eu, Tb, Ho, Yb, Bi) from single-crystal data and $Na_5M(WO_4)_4$ (M = La, Ho) from Rietveld data)

$NaEu(WO_4)_2$ (SC-XRD) MAPLE = 59523 kJ mol^{-1}	$\frac{1}{2}\,Eu_2O_3$ [473] + 2 Na_2WO_4 [301] − 1.5 Na_2O [482] MAPLE = 59555 kJ mol^{-1} (Δ = 0.05%)
$Na_5La(WO_4)_4$ (Rietveld) MAPLE = 115590 kJ mol^{-1}	$\frac{1}{2}\,La_2O_3$ [468] + 1.5 WO_3 [483] + 2.5 Na_2WO_4 [301] MAPLE = 116583 kJ mol^{-1} (Δ = 0.86%)
$Na_5Pr(WO_4)_4$ (SC-XRD) MAPLE = 116403 kJ mol^{-1}	$\frac{1}{2}\,Pr_2O_3$ [472] + 1.5 WO_3 [483] + 2.5 Na_2WO_4 [301] MAPLE = 116700 kJ mol^{-1} (Δ = 0.26%)
$Na_5Sm(WO_4)_4$ (SC-XRD) MAPLE = 116571 kJ mol^{-1}	$\frac{1}{2}\,Sm_2O_3$ [473] + 1.5 WO_3 [483] + 2.5 Na_2WO_4 [301] MAPLE = 116905 kJ mol^{-1} (Δ = 0.29%)
$Na_5Eu(WO_4)_4$ (SC-XRD) MAPLE = 116575 kJ mol^{-1}	$\frac{1}{2}\,Eu_2O_3$ [473] + 1.5 WO_3 [483] + 2.5 Na_2WO_4 [301] MAPLE = 116947 kJ mol^{-1} (Δ = 0.32%)
$Na_5Tb(WO_4)_4$ (SC-XRD) MAPLE = 116917 kJ mol^{-1}	$\frac{1}{2}\,Tb_2O_3$ [474] + 1.5 WO_3 [483] + 2.5 Na_2WO_4 [301] MAPLE = 117038 kJ mol^{-1} (Δ = 0.10%)
$Na_5Ho(WO_4)_4$ (SC-XRD) MAPLE = 116787 kJ mol^{-1}	$\frac{1}{2}\,Ho_2O_3$ [484] + 1.5 WO_3 [483] + 2.5 Na_2WO_4 [301] MAPLE = 117106 kJ mol^{-1} (Δ = 0.27%)
$Na_5Ho(WO_4)_4$ (Rietveld) MAPLE = 117448 kJ mol^{-1}	$\frac{1}{2}\,Ho_2O_3$ [484] + 1.5 WO_3 [483] + 2.5 Na_2WO_4 [301] MAPLE = 117106 kJ mol^{-1} (Δ = 0.29%)
$Na_5Yb(WO_4)_4$ (SC-XRD) MAPLE = 116917 kJ mol^{-1}	$\frac{1}{2}\,Yb_2O_3$ [485] + 1.5 WO_3 [483] + 2.5 Na_2WO_4 [301] MAPLE = 117167 kJ mol^{-1} (Δ = 0.29%)
$Na_5Bi(WO_4)_4$ (SC-XRD) MAPLE = 116685 kJ mol^{-1}	$\frac{1}{2}\,Bi_2O_3$ [486] + 1.5 WO_3 [483] + 2.5 Na_2WO_4 [301] MAPLE = 116681 kJ mol^{-1} (Δ = 0.00%)

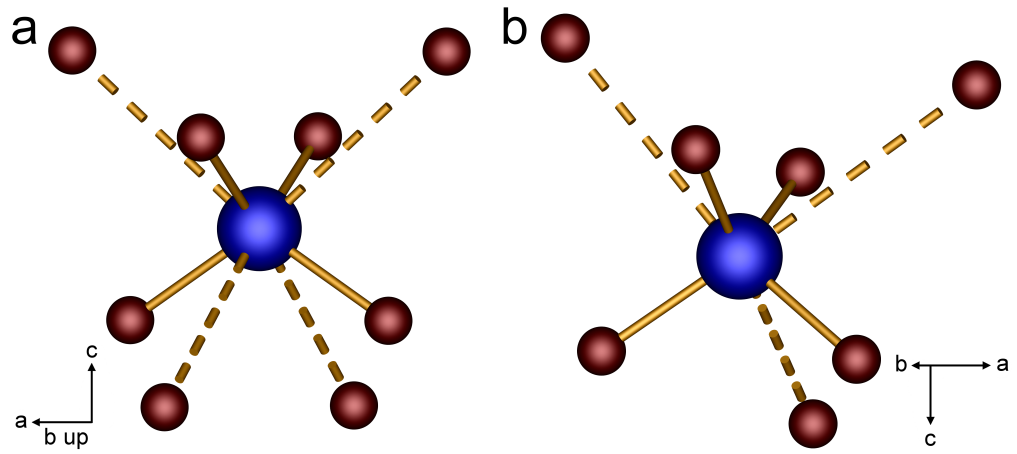

Fig. B.1.9: Coordination environments of W^{6+} in (a) $NaEu(WO_4)_2$ and (b) $Na_5Eu(WO_4)_4$: they differ in the second coordination sphere; the WO_4 tetrahedra in the first coordination sphere are tetracapped and tricapped in the second coordination sphere, respectively; oxygen is depicted in red, tungsten in blue.

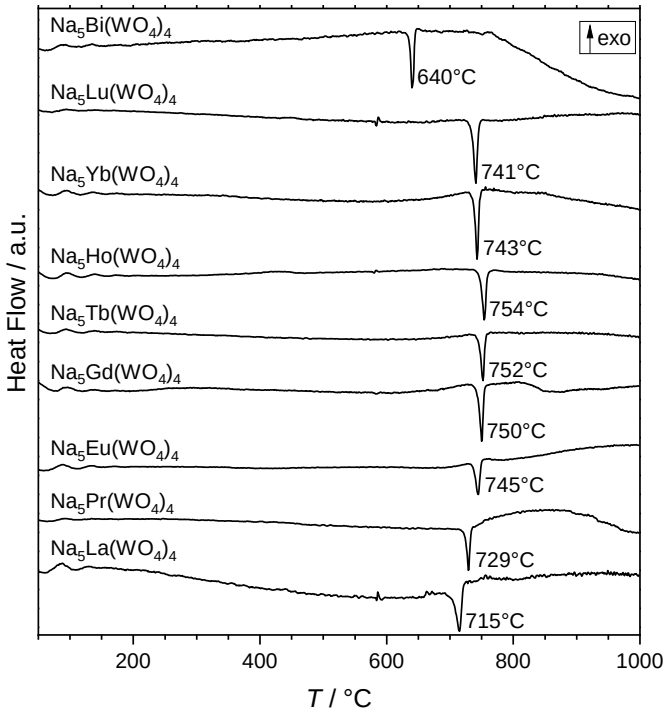

Fig. B.1.10: DSC signals of $Na_5M(WO_4)_4$ (M = La, Pr, Eu, Gd, Tb, Ho, Yb, Lu, Bi): all samples show one endothermic peak related to the simultaneous melting and decomposition point labelled with the temperature of the maxima of the peaks (T_d).

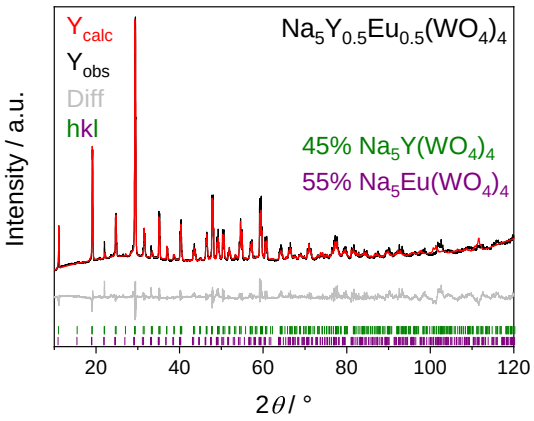

Fig. B.1.11: Rietveld refinement of $Na_5Y_{0.5}Eu_{0.5}(WO_4)_4$ prepared via the flux synthesis with 500% Na_2WO_4 surplus showing a phase mixture of 45% $Na_5Y(WO_4)_4$ and 55% $Na_5Eu(WO_4)_4$: details can be found in Table B.1.10.

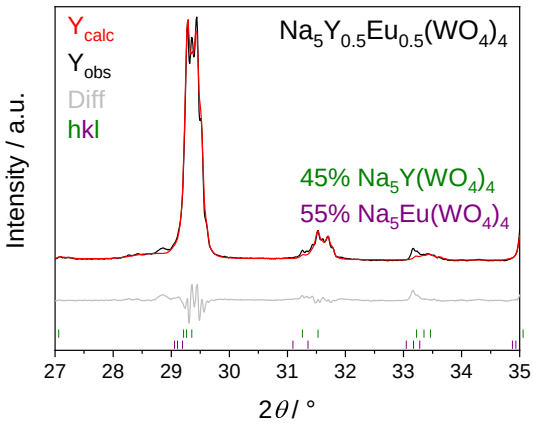

Fig. B.1.12: Enlarged depiction of the Rietveld refinement on the left showing the splitting of the main reflection at $2\theta \approx 29.5°$.

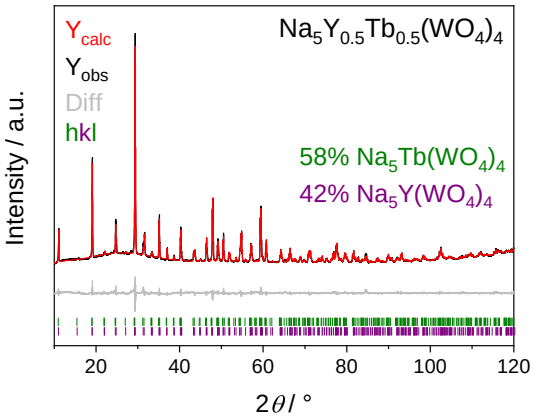

Fig. B.1.13: Rietveld refinement of $Na_5Y_{0.5}Tb_{0.5}(WO_4)_4$ prepared via the flux synthesis with 500% Na_2WO_4 surplus showing a phase mixture of 58% $Na_5Y(WO_4)_4$ and 42% $Na_5Tb(WO_4)_4$: details can be found in Table B.1.10.

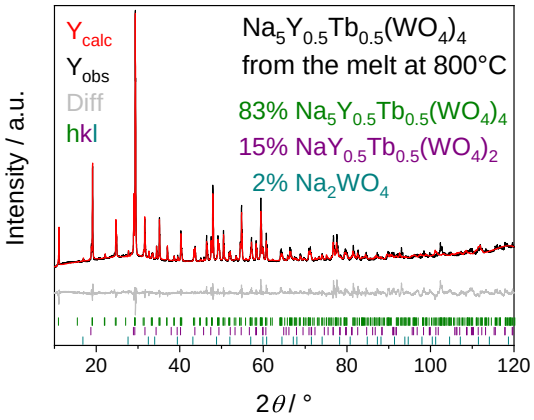

Fig. B.1.14: Rietveld refinement of $Na_5Y_{0.5}Tb_{0.5}(WO_4)_4$ after subsequent melting at 800°C in a Pt crucible showing a phase mixture of 83% $Na_5Y_{0.5}Tb_{0.5}(WO_4)_4$, 15% $NaY_{0.5}Tb_{0.5}(WO_4)_2$ and 2% Na_2WO_4: details can be found in Table B.1.10.

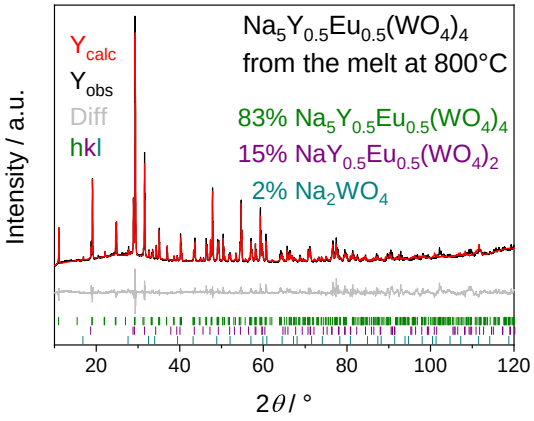

Fig. B.1.15: Rietveld refinement of $Na_5Y_{0.5}Eu_{0.5}(WO_4)_4$ prepared via the flux synthesis with 500% Na_2WO_4 surplus and subsequently melted at 800°C in a Pt crucible showing a phase mixture of 83% $Na_5Y_{0.5}Eu_{0.5}(WO_4)_4$, 15% $NaY_{0.5}Eu_{0.5}(WO_4)_2$ and 2% Na_2WO_4: details can be found in Table B.1.10.

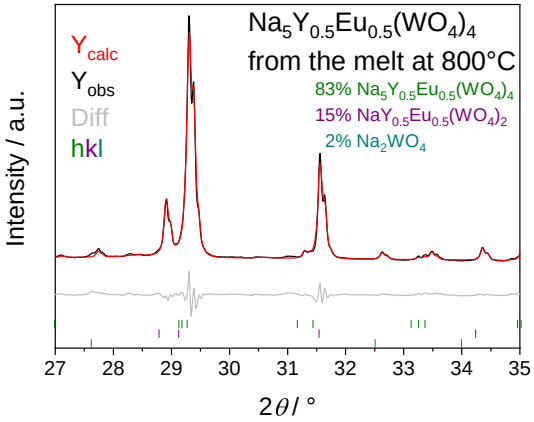

Fig. B.1.16: Enlarged depiction of the Rietveld refinement on the left showing the non-splitting of the main reflection at $2\theta \approx 29.5°$.

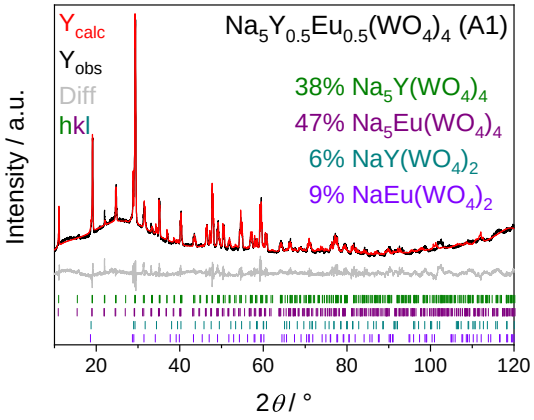

Fig. B.1.17: Rietveld refinement of $Na_5Y_{0.5}Eu_{0.5}(WO_4)_4$ prepared via solid state syntheses A1; details can be found in Table B.1.10.

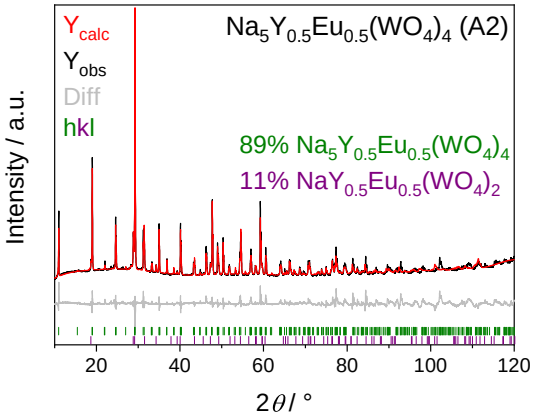

Fig. B.1.18: Rietveld refinement of $Na_5Y_{0.5}Eu_{0.5}(WO_4)_4$ prepared via solid state syntheses A2

Tab. B.1.10: Structural data from the Rietveld refinement on $Na_5Y_{1-x}Eu_x(WO_4)_4$ and $Na_5Y_{1-y}Tb_y(WO_4)_4$; the respective standard deviations are given in parentheses; unless specified differently, all phases crystallise in space group $I4_1/a$ (No. 88) with $Z = 4$ for all $Na_5M(WO_4)_4$ phases and $Z = 2$ for all $NaM(WO_4)_2$ phases, respectively; the suffix M symbolises the samples obtained from the melt at 800°C; Na_2WO_4 crystallises in space group $Fd\bar{3}m$ (No. 227) with $Z = 8$; the structures from the SC-XRD as well as the structure of Na_2WO_4 reported by Fortes[301] were used as starting models.

	$Na_5Y_{0.5}Eu_{0.5}(WO_4)_4$	$Na_5Y_{0.5}Eu_{0.5}(WO_4)_4$ M	$Na_5Y_{0.5}Eu_{0.5}(WO_4)_4$ (A1)	$Na_5Y_{0.5}Eu_{0.5}(WO_4)_4$ (A2)	$Na_5Y_{0.5}Tb_{0.5}(WO_4)_4$	$Na_5Y_{0.5}Tb_{0.5}(WO_4)_4$ M
R_{wp}	0.044	0.04	0.024	0.05	0.02	0.041
Refined parameters	44	42	49	43	45	46
Temperature / K	300(3)					
Radiation; λ / Å	Cu$K\alpha$; 1.54184					
Diffractometer	Seifert 3003 TT					
Θ range / °	2.5-60					
First Phase	$Na_5Y(WO_4)_4$	$Na_5Y_{0.5}Eu_{0.5}(WO_4)_4$	$Na_5Y(WO_4)_4$	$Na_5Y_{0.5}Eu_{0.5}(WO_4)_4$	$Na_5Y(WO_4)_4$	$Na_5Y_{0.5}Tb_{0.5}(WO_4)_4$
Fraction 1st phase / wt.-%	45	83	38	89	42	83
a / pm	1143.70(2)	1146.879(14)	1143.60(2)	1146.315(17)	1143.562(16)	1145.023(18)
c / pm	1134.14(3)	1137.303(15)	1134.40(4)	1138.78(2)	1133.83(2)	1135.50(2)
Volume / 10^6 pm^3	1483.50(7)	1495.93(4)	1483.58(8)	1496.40(6)	1482.75(5)	1488.73(6)
R_{Bragg} / %	2.28	2.26	1.09	3.25	1.04	2.22
Second Phase	$Na_5Eu(WO_4)_4$	$NaY_{0.5}Eu_{0.5}(WO_4)_2$	$Na_5Eu(WO_4)_4$	$NaY_{0.5}Eu_{0.5}(WO_4)_2$	$Na_5Tb(WO_4)_4$	$NaY_{0.5}Tb_{0.5}(WO_4)_2$
Fraction 2nd phase / wt.-%	55	15	47	11	58	15
a / pm	1149.57(2)	523.357(14)	1149.05(2)	522.89(5)	1146.404(15)	521.938(19)
c / pm	1140.25(4)	1133.64(6)	1140.18(4)	1134.2(2)	1136.631(18)	1129.70(8)
Volume / 10^6 pm^3	1506.86(8)	310.51(2)	1505.38(7)	310.10(8)	1493.81(5)	307.75(3)
R_{Bragg} / %	3.03	1.96	1.46	1.99	0.9	1.79
Third phase		Na_2WO_4	$NaY(WO_4)_2$			Na_2WO_4
Fraction 3rd phase / wt.-%		2	6			2
a / pm		912.80(5)	520.67(4)			913.29(7)
c / pm		)	1127.27(15)			
Volume / 10^6 pm^3		760.54(13)	305.60(6)			761.78(17)
R_{Bragg} / %		1.97	1.25			1.54
Forth phase			$NaEu(WO_4)_2$			
Fraction 4th phase / wt.-%			9			
a / pm			525.15(3)			
c / pm			1138.43(11)			
Volume / 10^6 pm^3			313.95(4)			
R_{Bragg} / %			1.03			

Tab. B.1.11: Crystal data and structure refinements of $Na_5Y_{0.49}Eu_{0.51}(WO_4)_4$ and $Na_5Y_{0.49}Tb_{0.51}(WO_4)_4$ determined from single-crystal data; the respective standard deviations are given in parentheses.

	$Na_5Y_{0.49}Eu_{0.51}(WO_4)_4$	$Na_5Y_{0.49}Tb_{0.51}(WO_4)_4$
CSD-No.	1986865	19868560
M / g mol^{-1}	1228.23	1231.29
Crystal size / mm^3	0.05 × 0.02 × 0.02	0.05 × 0.03 × 0.03
Temperature / K	300(3)	
Space group	$I4_1/a$ (No. 88)	
a / pm	1146.81(4)	1146.02(2)
c / pm	1137.59(4)	1136.78(3)
Volume / 10^6 pm^3	1496.13(12)	1493.00(7)
Z	4	
ρ_{calcd} / g cm^3	5.45	5.47
Absorption coefficient μ / mm$^{\check{}}$1	34.9	35.2
$F(000)$ / e	2120	2124
Radiation; wavelength λ / Å	Mo-K_α; 0.71073	
Diffractometer	Bruker D8 Venture	
Absorption correction	multi-scan	
Transmission (min; max)	0.6014; 0.7453	
Index range $h \mid k \mid l$	$\pm20 \mid -20/19 \mid \pm19$	$\pm21 \mid \pm21 \mid \pm21$
Θ range / °	2.522-38.483	2.524-42.492
Reflections collected	26544	20167
Independent reflections	2103	2682
Obs. reflections [$I > 2\sigma(I)$]	1822	2438
Refined parameters / restraints	61	61
R_{int}	0.0633	0.0221
R_1 (all data)	0.027	0.021
wR_2	0.033	0.031
GOF	1.05	1.11
Residual electron density (max; min) / e^-Å^{-3}	1.68; -1.45	1.28; -1.14

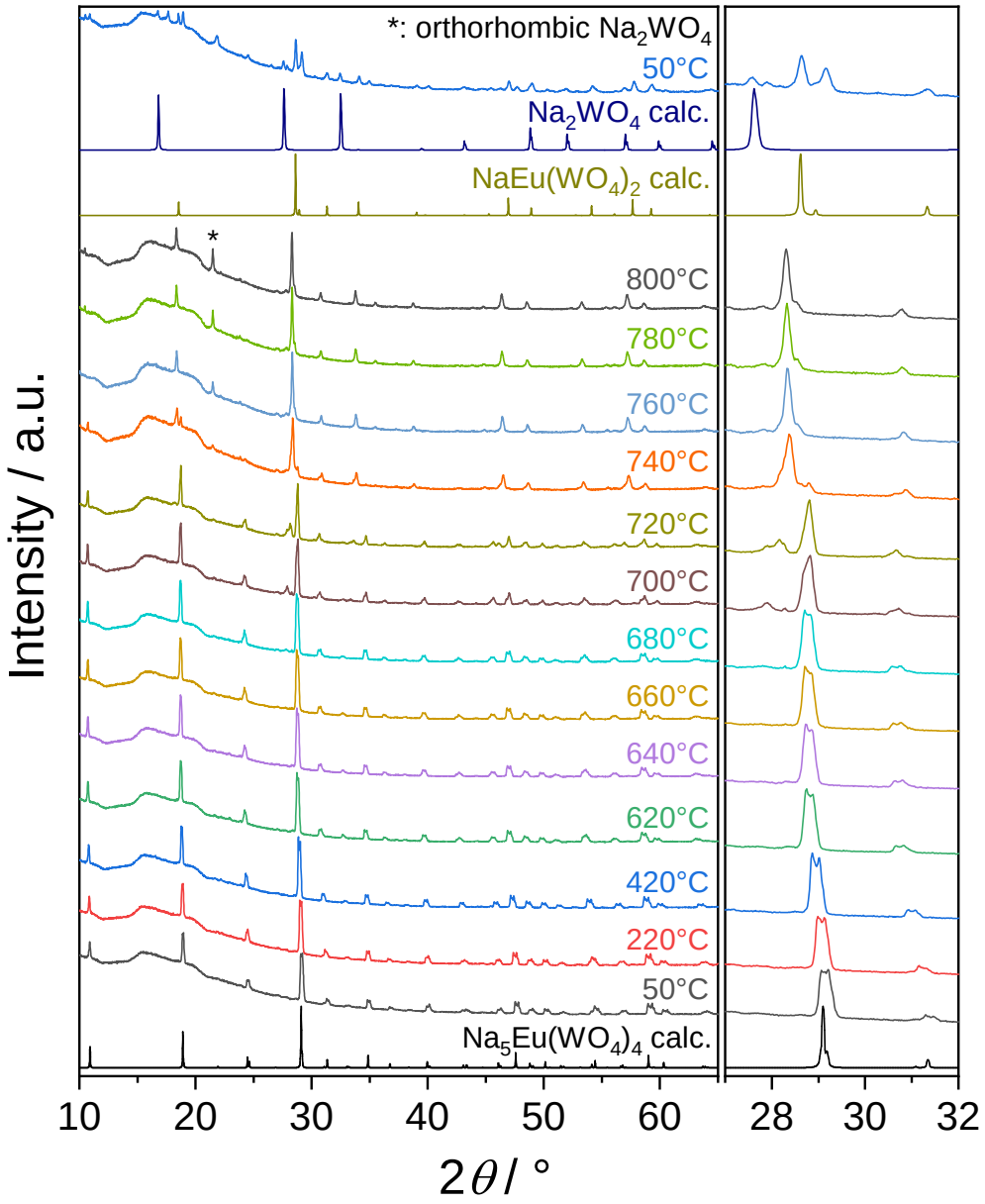

Fig. B.1.19: TPXRD patterns of $Na_5Y_{0.5}Eu_{0.5}(WO_4)_4$ prepared via the flux synthesis with 500% Na_2WO_4 surplus compared to theoretical patterns calculated from the SC-XRD data for $Na_5Eu(WO_4)_4$ and $NaEu(WO_4)_2$ as well as from literature for Na_2WO_4:[301] the pattern show the closing of the miscibility gap between 680°C and 720°C with the double reflection around $2\theta = 29°$ŕ becoming a single reflection as well as the decomposition into $NaY_{0.5}Eu_{0.5}(WO_4)_2$ and Na_2WO_4 starting around 700°C; moreover, the reflexes related to Na_2WO_4 disappear above 720°C due to the melting of this phase; there is an experimental offset between the furnace temperatures displayed in the graph and the actual temperature at the sample of approximately 20°C; the additional reflection at $2\theta = 21.5°$ marked with a black asterisk could be assigned to the orthorhombic high-temperature modification of Na_2WO_4 reported by Pistorius.[487]

Tab. B.1.12: Assignment of emission and excitation peaks in the fluorescence spectra of $Na_5M(WO_4)_4$;[38,154,157,285,292,315–317,488,489] doublets, triplets et cetera are marked by two or three values in the λ column; only the respective energy for the first value is displayed; the two λ values for $Na_5Bi(WO_4)_4$ represent the maxima at both room temperature and 77 K.

$Na_5Pr(WO_4)_4$			
Excitation	Wavelength λ / nm	Energy E / cm^{-1}	Assignment
A	250	40000	O^{2-}-W^{6+} LMCT
B	446	22422	$^3H_4 \rightarrow {}^1I_6$
C	470	21277	$^3H_4 \rightarrow {}^3P_1$
D	484	20661	$^3H_4 \rightarrow {}^3P_0$
Emission	Wavelength λ / nm	Energy E / cm^{-1}	Assignment
	481; 488, 496	20790	$^3P_0 \rightarrow {}^3H_4$
	528	18939	$^3P_1 \rightarrow {}^3H_5$
	546, 553	18315	$^3P_0 \rightarrow {}^3H_5$
	595	16807	$^1D_2 \rightarrow {}^3H_4$
	616	16234	$^3P_0 \rightarrow {}^3H_6$
	646	15480	$^3P_0 \rightarrow {}^3F_2$
	680	14706	$^3P_0 \rightarrow {}^3F_3$
	730	13699	$^3P_0 \rightarrow {}^3F_4$
$Na_5Sm(WO_4)_4$			
Excitation	Wavelength λ / nm	Energy E / cm^{-1}	Assignment
A	240	41667	O^{2-}-W^{6+} LMCT
B	304	32895	$^6H_{\frac{5}{2}} \rightarrow {}^4P_{\frac{5}{2}}$
C	316	31646	$^6H_{\frac{5}{2}} \rightarrow {}^4P_{\frac{3}{2}}$
D	331	30211	$^6H_{\frac{5}{2}} \rightarrow {}^4G_{\frac{9}{2}}$
E	344	29070	$^6H_{\frac{5}{2}} \rightarrow \left({}^4H_{\frac{9}{2}}, {}^4D_{\frac{7}{2}}\right)$
F	362	27624	$^6H_{\frac{5}{2}} \rightarrow {}^4D_{\frac{3}{2}}$
G	375	266667	$^6H_{\frac{5}{2}} \rightarrow {}^6P_{\frac{7}{2}}$
H	390	25641	$^6H_{\frac{5}{2}} \rightarrow {}^4L_{\frac{15}{2}}$
I	403	24814	$^6H_{\frac{5}{2}} \rightarrow {}^4L_{\frac{13}{2}}$
J	417	23981	$^6H_{\frac{5}{2}} \rightarrow \left({}^6P, {}^4P\right)_{\frac{5}{2}}$
K	439	22779	$^6H_{\frac{5}{2}} \rightarrow {}^4G_{\frac{9}{2}}$
L	448	22321	$^6H_{\frac{5}{2}} \rightarrow {}^4F_{\frac{5}{2}}$
M	465	21505	$^6H_{\frac{5}{2}} \rightarrow {}^6I_{\frac{13}{2}}$
N	471	21231	$^6H_{\frac{5}{2}} \rightarrow {}^4I_{\frac{11}{2}}$
O	479	20877	$^6H_{\frac{5}{2}} \rightarrow {}^4M_{\frac{15}{2}}$
P	487	20534	$^6H_{\frac{5}{2}} \rightarrow {}^4I_{\frac{9}{2}}$
Q	497	20121	$^6H_{\frac{5}{2}} \rightarrow {}^4G_{\frac{7}{2}}$
Emission	Wavelength λ / nm	Energy E / cm^{-1}	Assignment
	553; 562	17794	$^4G_{\frac{5}{2}} \rightarrow {}^6H_{\frac{5}{2}}$
	600	16667	$^4G_{\frac{5}{2}} \rightarrow {}^6H_{\frac{7}{2}}$

	645; 664	15504	$^4G_{\frac{5}{2}} \rightarrow {}^6H_{\frac{9}{2}}$
	703	14225	$^4G_{\frac{5}{2}} \rightarrow {}^6H_{\frac{11}{2}}$
	772	12953	$^4G_{\frac{5}{2}} \rightarrow {}^6H_{\frac{13}{2}}$
$Na_5Eu(WO_4)_4$			
Excitation	Wavelength λ / nm	Energy E / cm^{-1}	Assignment
A	270	37037	O^{2-}-W^{6+} LMCT + O^{2-}-Eu^{3+} LMCT
B	285	35088	$^7F_0 \rightarrow \left(^5I, {}^5H\right)_6$
C	293	34130	$^7F_0 \rightarrow {}^5F_5$
D	298	33557	$^7F_0 \rightarrow {}^5F_4$
E	302	33113	$^7F_0 \rightarrow {}^5F_2$
F	305	32787	$^7F_0 \rightarrow {}^3P_0$
G	317	31546	$^7F_0 \rightarrow {}^5H_6$
H	321	31153	$^7F_0 \rightarrow {}^5H_7$
I	326	30675	$^7F_0 \rightarrow {}^5H_3$
J	361	27701	$^7F_0 \rightarrow {}^5D_4$
K	366	27322	$^7F_0 \rightarrow {}^5L_3$
L	375	26667	$^7F_0 \rightarrow {}^5G_6$
M	380	26316	$^7F_0 \rightarrow {}^5L_7$
N	383	26110	$^7F_0 \rightarrow {}^5G_2$
O	393; 396; 399	25445	$^7F_0 \rightarrow {}^5L_6$
P	415	24096	$^7F_0 \rightarrow {}^5D_3$
Q	464; 472, 481, 488	21552	$^7F_0 \rightarrow {}^5D_2$
Emission	Wavelength λ / nm	Energy E / cm^{-1}	Assignment
	535	18692	$^5D_0 \rightarrow {}^7F_0$
	591	16920	$^5D_0 \rightarrow {}^7F_1$
	606; 611; 615	16502	$^5D_0 \rightarrow {}^7F_2$
	653	15314	$^5D_0 \rightarrow {}^7F_3$
	693; 699; 702	14430	$^5D_0 \rightarrow {}^7F_4$
$Na_5Tb(WO_4)_4$			
Excitation	Wavelength λ / nm	Energy E / cm^{-1}	Assignment
A	251	39841	O^{2-}-W^{6+} LMCT + Tb^{3+} 4f $\rightarrow$ 5d
B	284	35211	$^7F_6 \rightarrow {}^5I_8$
C	295	33898	$^7F_6 \rightarrow {}^5H_5$
D	303	33003	$^7F_6 \rightarrow {}^5H_6$
E	317	31546	$^7F_6 \rightarrow {}^5H_7$
F	326	30675	$^7F_6 \rightarrow {}^5D_1$
G	339	29499	$^7F_6 \rightarrow {}^5L_7$
H	351	28490	$^7F_6 \rightarrow {}^5L_9$
I	358	27933	$^7F_6 \rightarrow {}^5G_5$
J	369	27100	$^7F_6 \rightarrow {}^5L_{10}$
K	377	26525	$^7F_6 \rightarrow {}^5G_6$
Emission	Wavelength λ / nm	Energy E / cm^{-1}	Assignment
	487; 493	20534	$^5D_4 \rightarrow {}^7F_6$
	543; 547	18416	$^5D_4 \rightarrow {}^7F_5$
	581; 587	17212	$^5D_4 \rightarrow {}^7F_4$
	616; 620	16234	$^5D_4 \rightarrow {}^7F_3$

	644; 650	15528	$^5D_4 \rightarrow {}^7F_2$
	669	14948	$^5D_4 \rightarrow {}^7F_1$
	679	14728	$^5D_4 \rightarrow {}^7F_0$
$Na_5Bi(WO_4)_4$			
Excitation	Wavelength λ / nm	Energy E / cm^{-1}	Assignment
	250; 258	40000	O^{2-}-W^{6+} LMCT
	273; 275	36630	$^1S_0 \rightarrow {}^1P_1$
	281; 290	35587	$^1S_0 \rightarrow {}^3P_1$
Emission	Wavelength λ / nm	Energy E / cm^{-1}	Assignment
	470	21277	$^3P_1 \rightarrow {}^1S_0$

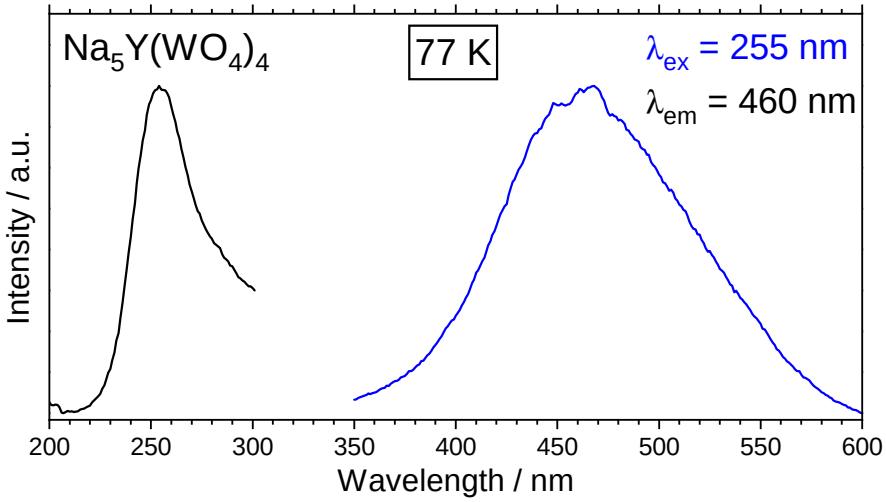

Fig. B.1.20: Excitation and emission spectra of $Na_5Y(WO_4)_4$ measured at 77 K: the compound shows a broad W^{6+}-O^{2-} LMCT emission centred at 460 nm; the excitation spectrum was not corrected with respect to the lamp intensity.

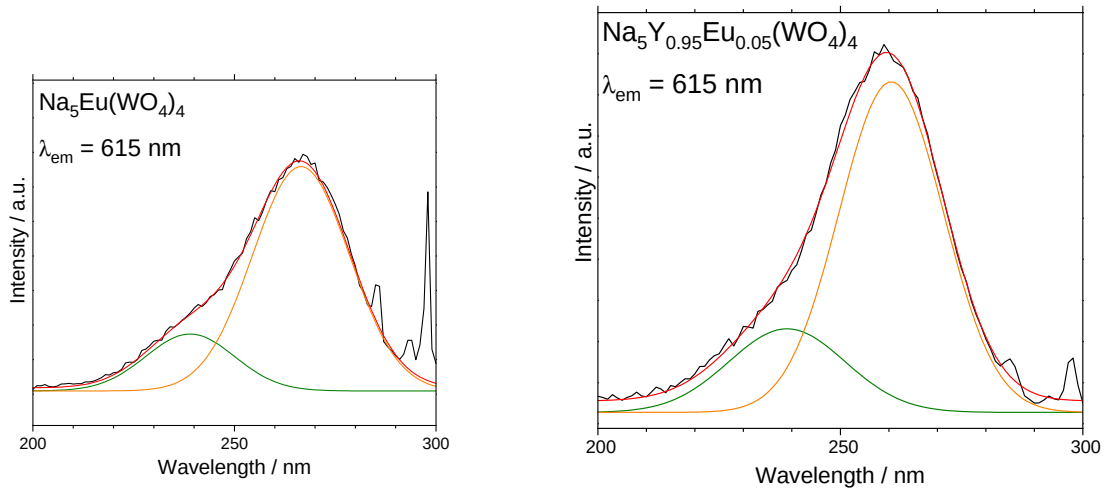

Fig. B.1.21: Gaussian fit of the excitation spectra of $Na_5Eu(WO_4)_4$ (left) and $Na_5Y_{0.95}Eu_{0.05}(WO_4)_4$ (right): they were fitted using two peaks centred at 239 nm (O^{2-}-W^{6+} LMCT) for both spectra and at 266.5 nm (left) and 260.5 nm (right) (O^{2-}-Eu^{3+} LMCT), respectively; the excitation spectra are corrected with respect to the lamp intensity.

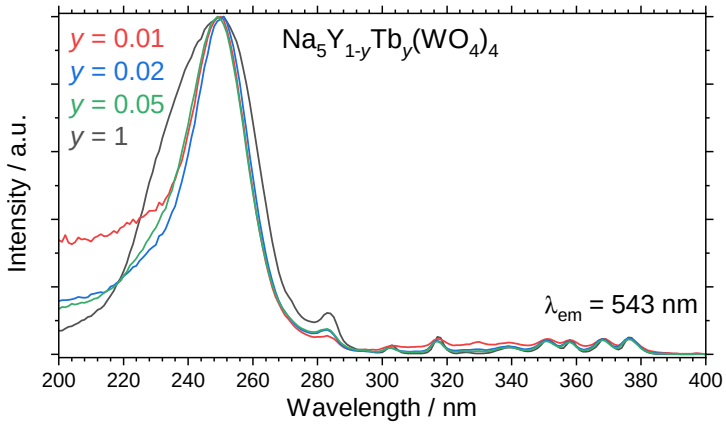

Fig. B.1.22: Excitation spectra of $Na_5Y_{1-y}Tb_y(WO_4)_4$ ($y = 0.01, 0.02, 0.05, 1$) showing an increase of the intensity ratio of the broad LMCT band around 250 nm and the f-f transitions of Tb^{3+} with decreasing terbium content.

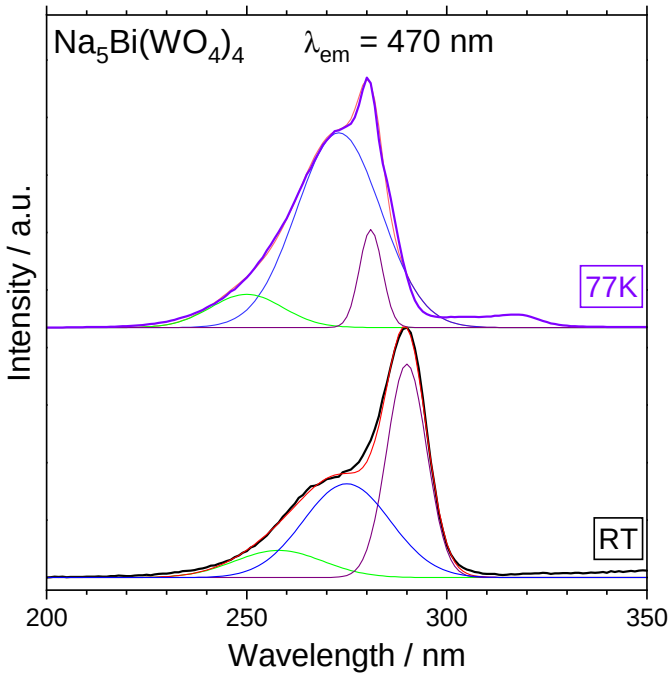

Fig. B.1.23: Gaussian fit of the excitation spectra of $Na_5Bi(WO_4)_4$ at both room temperature and 77 K; the excitation spectra are not corrected with respect to the lamp intensity.

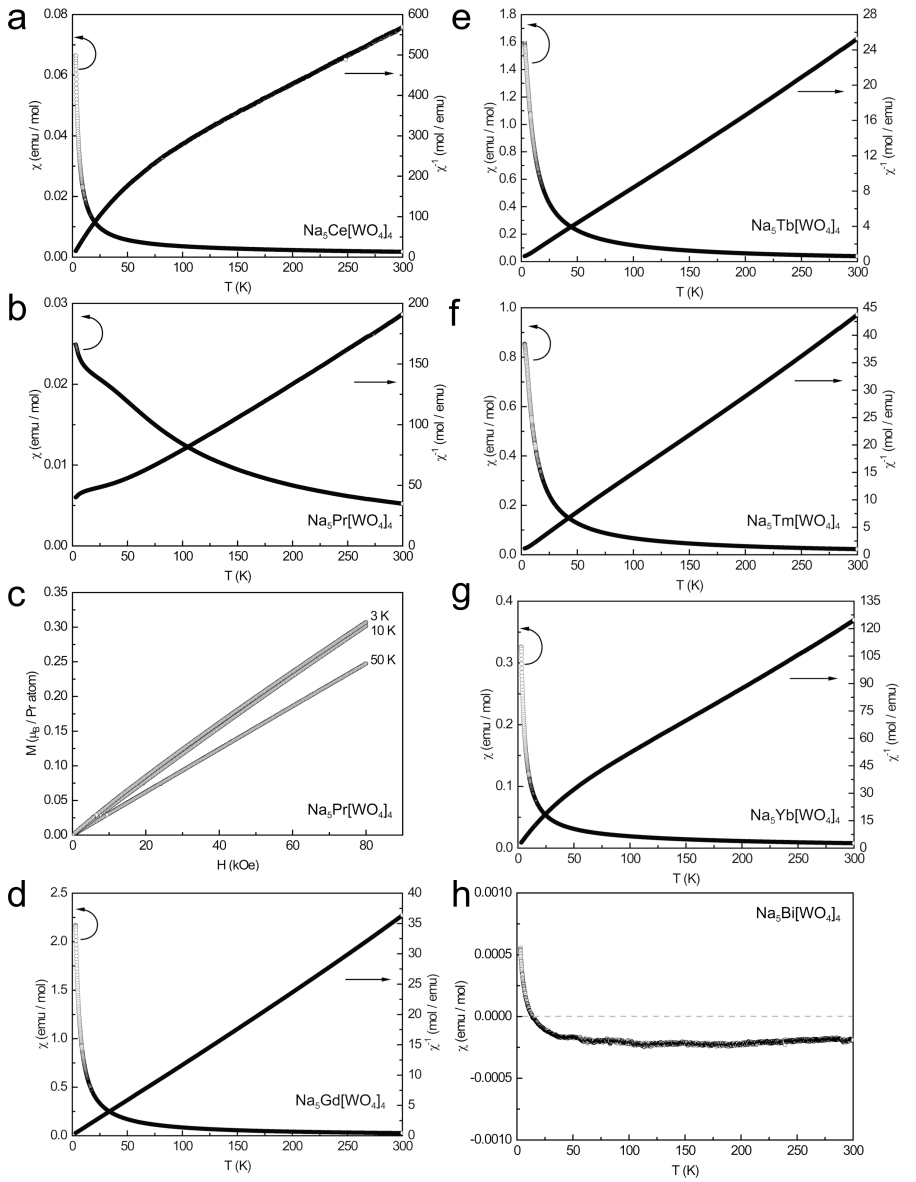

Fig. B.1.24: Magnetic properties of $Na_5M(WO_4)_4$: temperature dependence of the magnetic susceptibility (χ and χ^{-1} data) measured at $10\,\mathrm{kOe}$ of magnetic properties of (a) $Na_5Ce(WO_4)_4$, (b) $Na_5Pr(WO_4)_4$, (d) $Na_5Gd(WO_4)_4$, (e) $Na_5Tb(WO_4)_4$, (f) $Na_5Tm(WO_4)_4$, (g) $Na_5Yb(WO_4)_4$ and (h) $Na_5Bi(WO_4)_4$; (c) magnetic properties of $Na_5Pr(WO_4)_4$ showing the magnetisation isotherms at 3, 10 and 50 K.

B.2 $NaM(WO_4)_2$

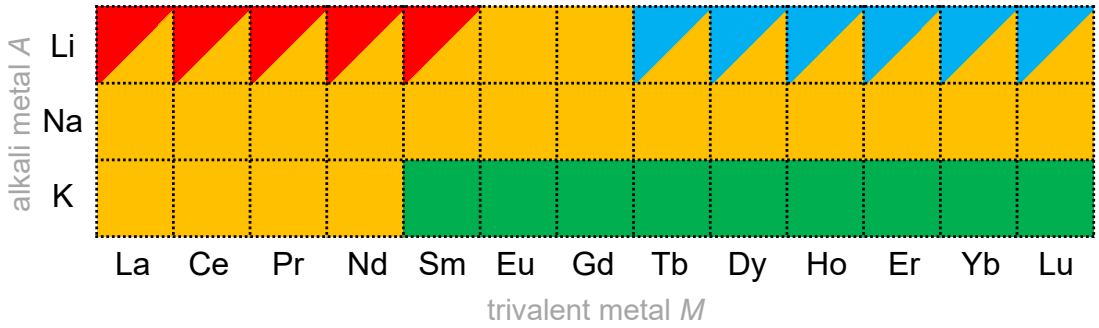

Fig. B.2.1: Overview over the polymorphism of $AM(WO_4)_2$: The respective alkali metal A is given on the left and the respective trivalent metal M on the bottom; the colours represent different structure types with the colour code explained in Figure 5.2.2; for compounds adapting two structure types, the colour in the top left represents the low temperature polymorph - denoted by the suffix -I - and the colour on the bottom right the high temperature form - denoted with the suffix -II.

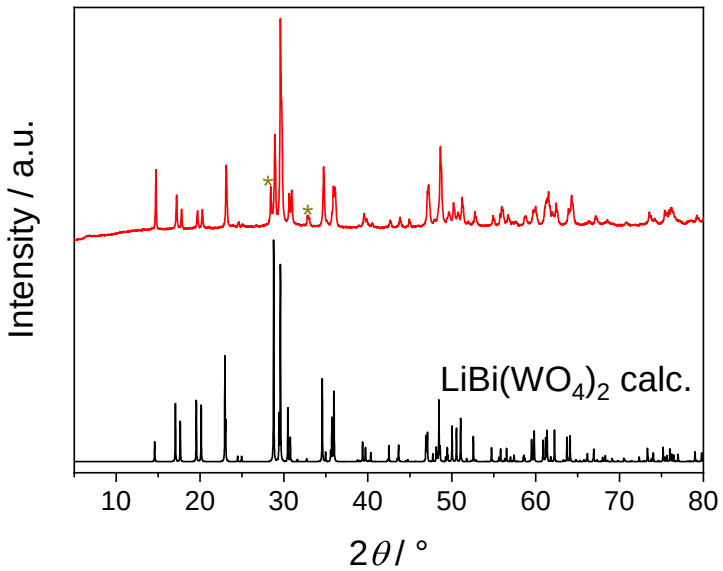

Fig. B.2.2: PXRD of $LiBi(WO_4)_2$ compared to a calculated pattern from SC-XRD; the reflexes marked with asterisks belong to a small Bi_2WO_6 side phase.

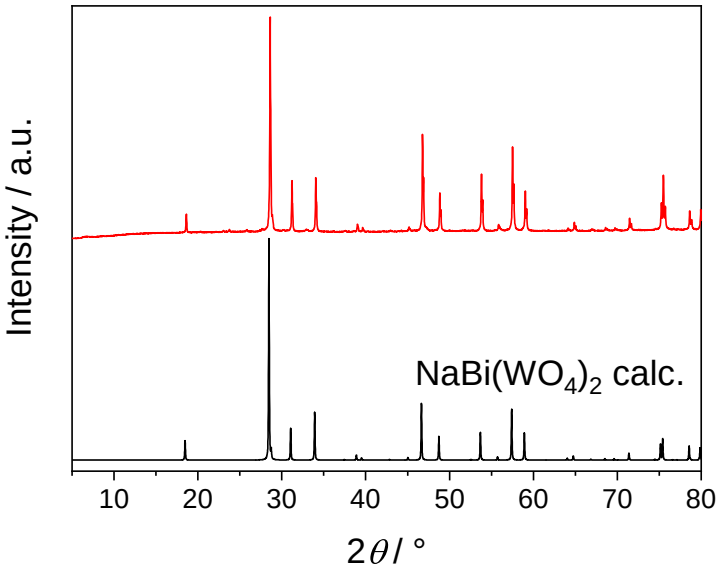

Fig. B.2.3: PXRD of $NaBi(WO_4)_2$ compared to a calculated pattern from SC-XRD.

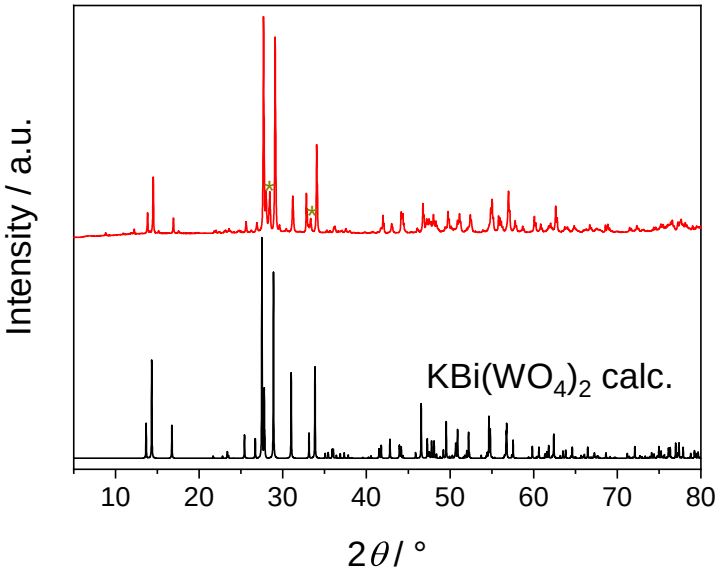

Fig. B.2.4: PXRD of $KBi(WO_4)_2$ compared to a calculated pattern from SC-XRD; the reflexes marked with asterisks belong to a small Bi_2WO_6 side phase.

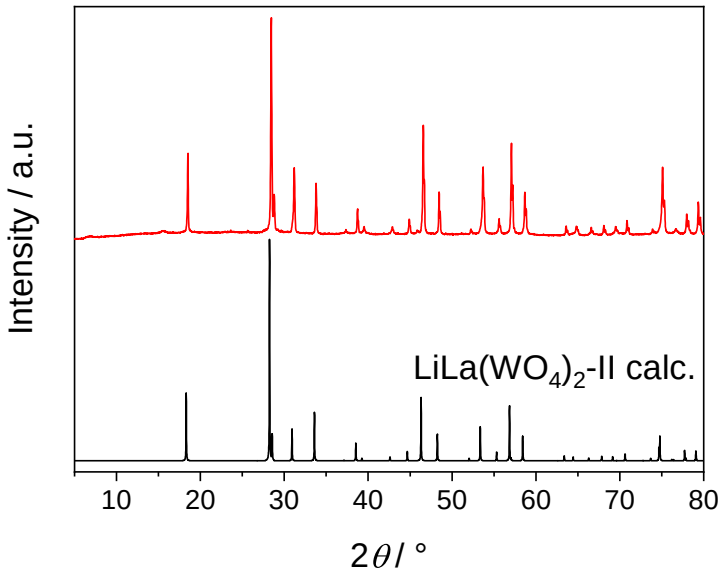

Fig. B.2.5: PXRD of $LiLa(WO_4)_2$-II compared to a calculated pattern from SC-XRD.

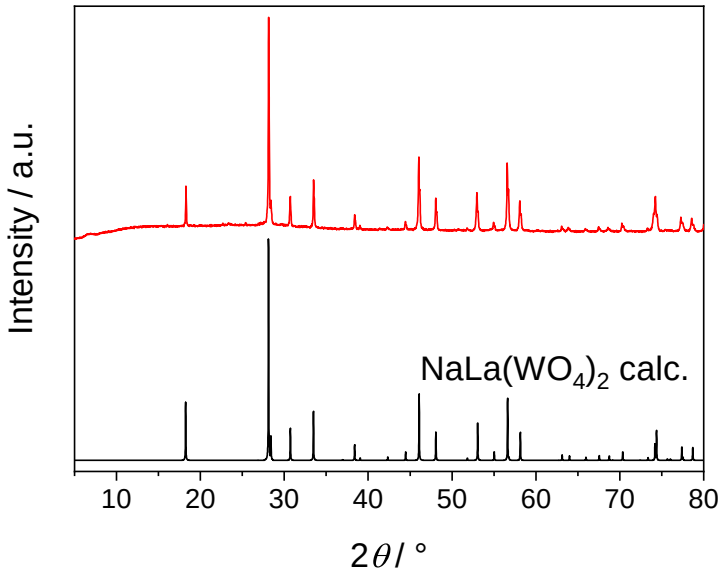

Fig. B.2.6: PXRD of $NaLa(WO_4)_2$ compared to a calculated pattern.[490]

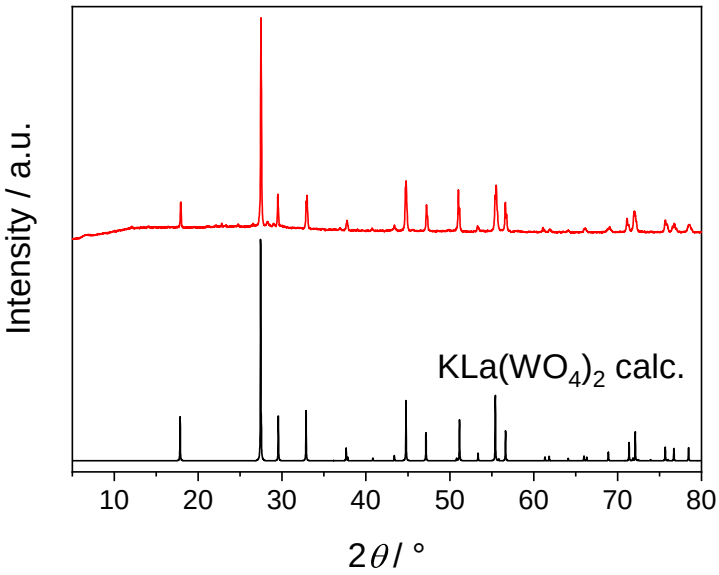

Fig. B.2.7: PXRD of $KLa(WO_4)_2$ compared to a calculated pattern from SC-XRD.

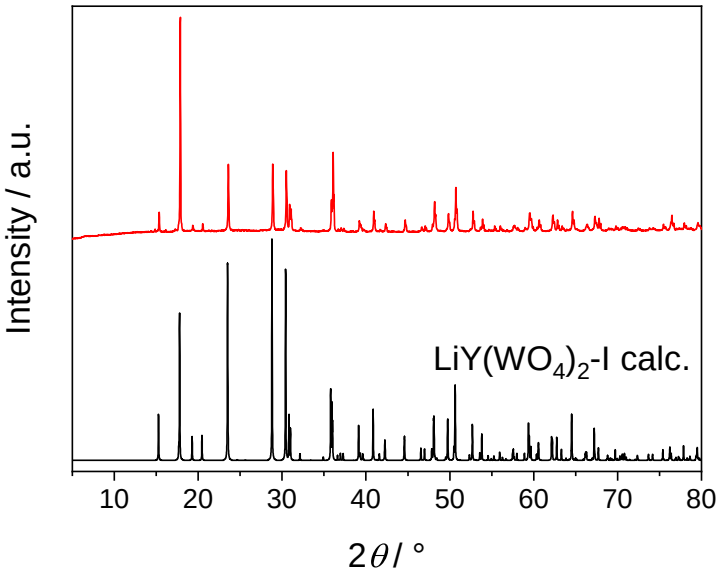

Fig. B.2.8: PXRD of $LiY(WO_4)_2$-I compared to a calculated pattern.[334]

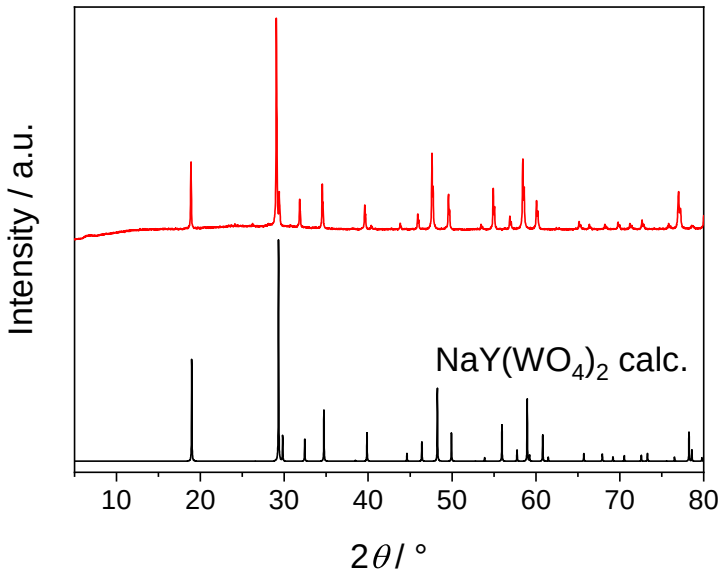

Fig. B.2.9: PXRD of $NaY(WO_4)_2$ compared to a calculated pattern from SC-XRD.

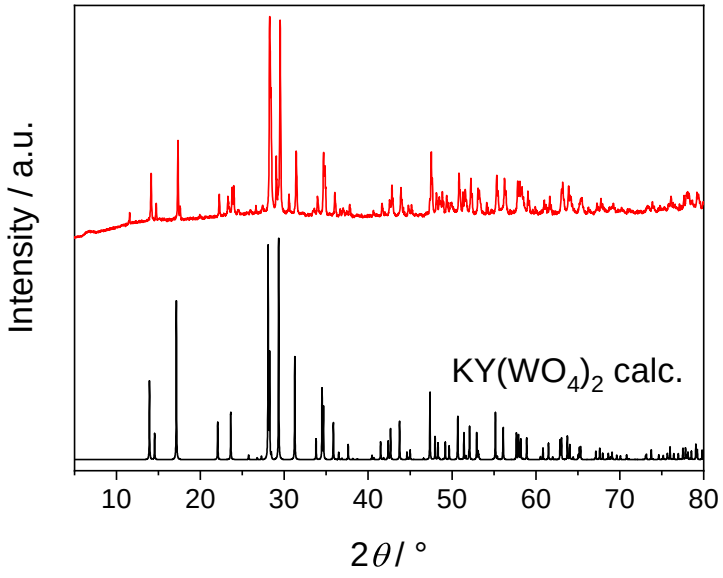

Fig. B.2.10: PXRD of $KY(WO_4)_2$ compared to a calculated pattern from SC-XRD.

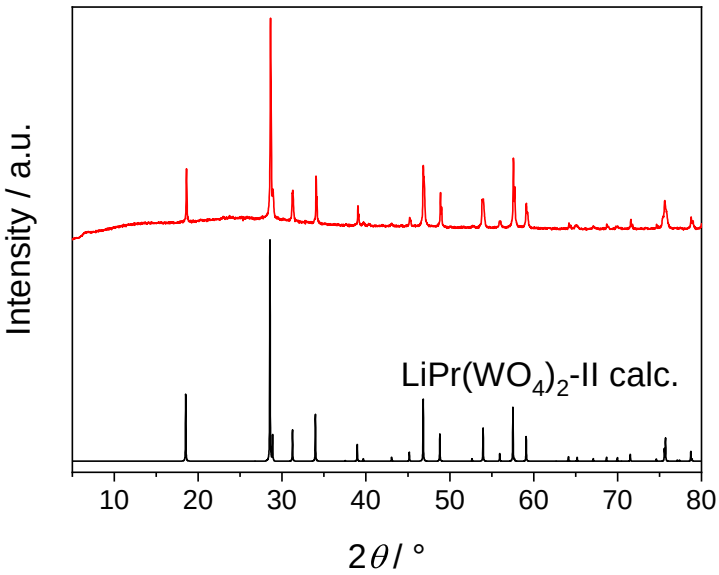

Fig. B.2.11: PXRD of $LiPr(WO_4)_2$-II compared to a calculated pattern from SC-XRD.

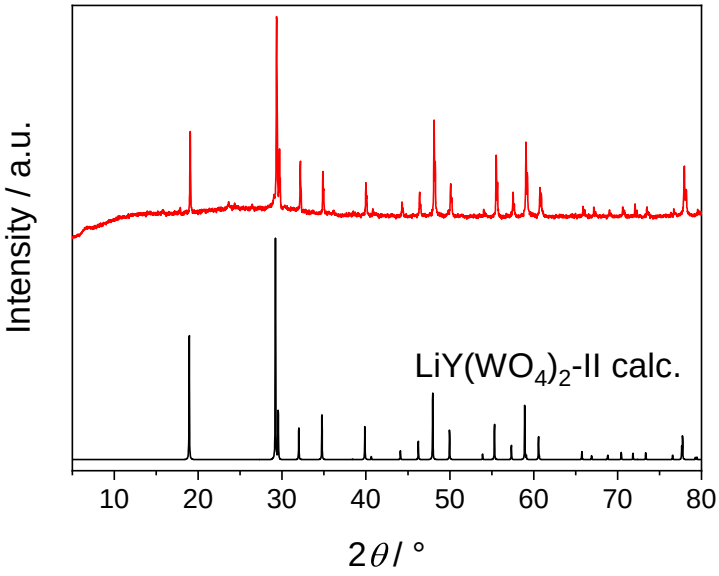

Fig. B.2.12: PXRD of $LiY(WO_4)_2$-II compared to a calculated pattern from SC-XRD.

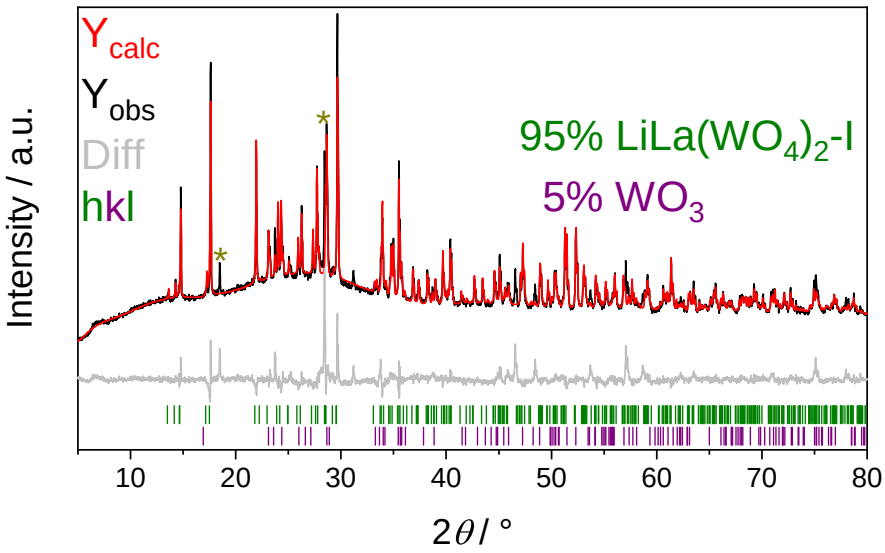

Fig. B.2.13: Rietveld refinement of $LiLa(WO_4)_2$-I revealing a 5 wt.-% WO_3 side phase; the structures reported by Klevtsova et al.[275] and Salje and Viswanathan[491] were used as starting models; the additional reflexes marked with asterisks are related to $LiLa(WO_4)_2$-II.

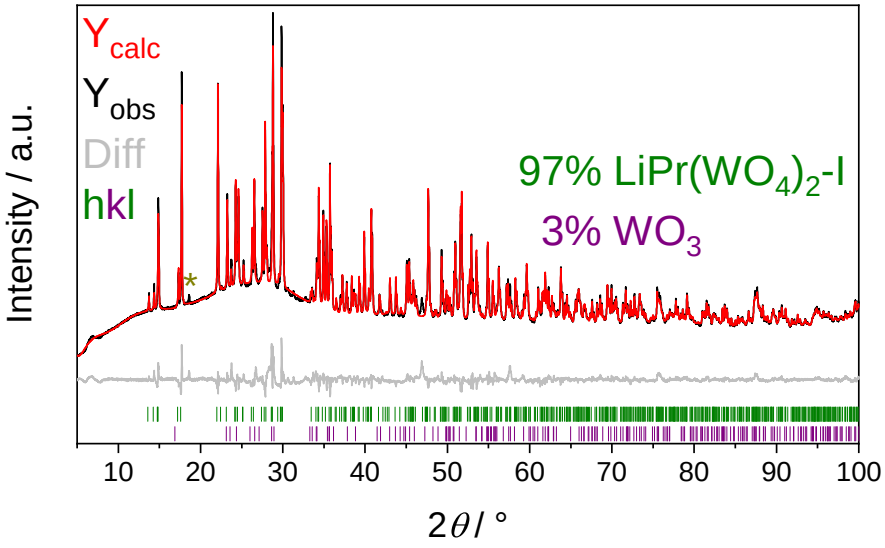

Fig. B.2.14: Rietveld refinement of $LiPr(WO_4)_2$-I revealing a 3 wt.-% WO_3 side phase; the structures reported by Klevtsova et al.[275] and Salje and Viswanathan[491] were used as starting models; the additional reflexes marked with asterisks are related to $LiPr(WO_4)_2$-II.

Tab. B.2.1: Crystal data and structure refinement of LiLa(WO$_4$)$_2$-I and LiPr(WO$_4$)$_2$-I determined from PXRD data via Rietveld refinement using the structure reported by Klevtsova et al.[275] and Salje and Viswanathan[491] as starting model; the respective standard deviations are given in parentheses.

	LiLa(WO$_4$)$_2$-I	LiPr(WO$_4$)$_2$-I
M / g × mol^{-1}	641.52	643.52
Temperature / K	298(2)	
Space group	$P\bar{1}$ (no. 2)	
a / pm	714.03(2)	709.87(1)
b / pm	738.30(3)	735.11(1)
c / pm	755.82(2)	747.46(1)
α / °	114.127(2)	114.367(1)
β / °	115.664(2)	115.562(1)
γ / °	90.944(2)	91.056(1)
Volume / 10^6 pm^3	318.56(2)	311.23(1)
Z	2	
ρ_{calcd} / g cm^3	6.69	6.87
Radiation; wavelength λ / Å	Cu$K\alpha$; 1.54184	
Diffractometer	Bruker D8 Advance	
Θ range / °	2.5.40	2.5-50
Observed reflections	630	510
Refined parameters	49	67
R_{Bragg}	0.026	0.014
R_p	0.031	0.017
R_{wp}	0.051	0.026
GOF	0.34	0.12

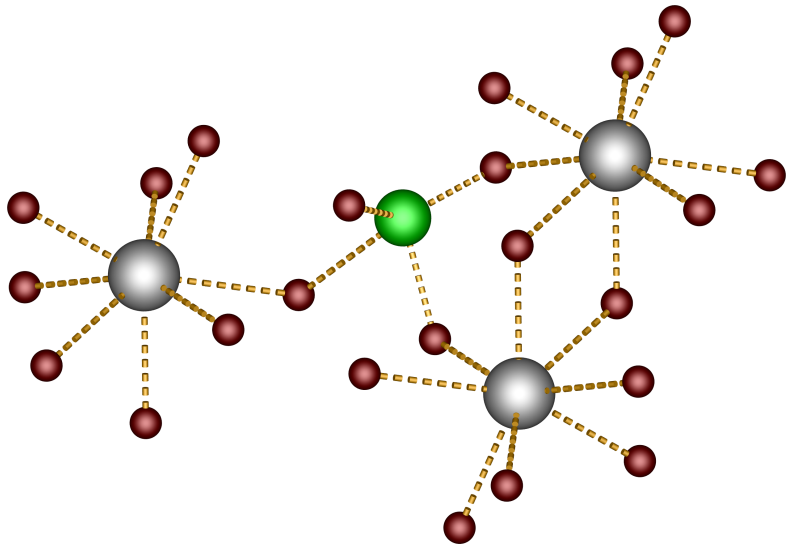

Fig. B.2.15: Coordination environments and connection pattern of the cationic substructure in LiPr(WO$_4$)$_2$-I: oxygen atoms red, lithium atoms light green, praseodymium atoms grey.

Tab. B.2.2: Crystal data and structure refinements $LiBi(WO_4)_2$, $NaBi(WO_4)_2$, $KBi(WO_4)_2$, $LiLa(WO_4)_2$-II, $KLa(WO_4)_2$ and $LiPr(WO_4)_2$-II determined from single-crystal data; the respective standard deviations are given in parentheses.

	$LiBi(WO_4)_2$	$NaBi(WO_4)_2$	$KBi(WO_4)_2$	$LiLa(WO_4)_2$-II	$KLa(WO_4)_2$	$LiPr(WO_4)_2$-II
M / g mol^{-1}	711.62	727.67	743.78	641.55	673.71	643.55
Crystal size / mm^3	0.05 × 0.03 × 0.02	0.06 × 0.04 × 0.03	0.06 × 0.05 × 0.02	0.06 × 0.03 × 0.02	0.06 × 0.03 × 0.02	0.06 × 0.05 × 0.03
Temperature / K	294(2)	298(2)	300(2)	298(2)	300(2)	299(2)
Space group	$P2/n$ (no.13)	$I4_1/a$ (no. 88)	$C2/c$ (no. 15)	$I4_1/a$ (no. 88)	$I4_1/a$ (no. 88)	$I4_1/a$ (no. 88)
a / pm	499.56(3)	528.23(9)	1081.70(4)	533.52(3)	544.42(2)	527.312(3)
b / pm	606.87(4)	528.23(9)	1056.11(4)	533.52(3)	544.42(2)	527.312(3)
c / pm	1005.45(6)	1150.9(2)	760.45(3)	1157.36(8)	1214.06(6)	1144.153(8)
beta / °	92.08(2)	90	130.8497(7)	90	90	90
Volume / 10^6 pm^3	304.62(3)	321.12(12)	657.13(4)	329.44(4)	359.84(3)	318.141(4)
Z	2	2	4	2	2	2
ρ_{calcd} / g cm^3	7.76	5.53	7.52	6.47	6.22	6.72
Absorption coefficient μ / mm$^{\smile 1}$	66.5	63.1	62.3	41.2	38.3	43.6
$F(000)$ / e	596	612	1256	544	576	548
Radiation; wavelength λ / Å	Mo-K_α; 0.71073					
Diffractometer	Bruker D8 Venture					
Absorption correction	multi-scan					
Transmission (min; max)	0.313; 0.749	0.4861; 0.749	0.5701; 0.7479	0.5423; 0.749	0.4672; 0.7516	0.4525; 0.7514
Index range h | k | l	−7/6 | ±8 | −13/14	−8/7 | ±8 | ±18	±17 | ±16 | ±12	±7 | ±7 | ±16	±8 | ±8 | ±18	±7 | ±8 | ±17
Θ range / °	3.357-29.999	4.245-35.978	3.149-34.999	4.206-29.724	4.102-32.962	4.256-33.454
Reflections collected	5674	2286	12151	47796	3076	
Independent reflections	883	383	1450	242	338	319
R_{int}	0.039	0.032	0.041	0.028	0.050	0.023
Obs. reflections [$I > 2\sigma(I)$]	857	320	1301	241	335	294
Refined parameters / restraints	57	16	57	16	16	16
R_1 (all data)	0.019	0.026	0.024	0.052	0.029	0.027
wR_2 (all data)	0.044	0.036	0.032	0.126	0.066	0.053
GOF	1.163	1.044	1.068	1.747	1.491	1.289
Residual electron density (max; min) / e^-Å^{-3}	1.89; -1.89	1.55; -0.89	1.84; -1.63	2.98; -2.77	1.19; -1.50	1.63; -2.03

Tab. B.2.3: Crystal data and structure refinements of $LiY(WO_4)_2$-I, $LiY(WO_4)_2$-II, $NaY(WO_4)_2$ and $KY(WO_4)_2$ determined from single-crystal data; the respective standard deviations are given in parentheses.

	$LiY(WO_4)_2$-I	$LiY(WO_4)_2$-II	$NaY(WO_4)_2$	$KY(WO_4)_2$
M / g mol^{-1}	591.55	591.55	607.60	623.71
Crystal size / mm^3	$0.08 \times 0.04 \times 0.02$	$0.04 \times 0.03 \times 0.02$	$0.02 \times 0.02 \times 0.01$	$0.02 \times 0.01 \times 0.01$
Temperature / K	300(2)	301(2)	300(2)	299(2)
Space group	$P2/n$ (no.13)	$I4_1/a$ (no. 88)	$I4_1/a$ (no. 88)	$C2/c$ (no. 15)
a / pm	500.38(1)	515.87(5)	520.90(2)	1062.45(4)
b / pm	579.93(2)	515.87(5)	520.90(2)	1033.66(4)
c / pm	999.59(3)	1117.99(12)	1129.30(5)	754.97(3)
$beta$ / °	94.185(1)	90	90	130.742(1)
Volume / 10^6 pm^3	289.293(14)	297.52(7)	306.42(3)	628.18(4)
Z	2	2	2	4
ρ_{calcd} / g cm^3	6.79	6.60	6.59	6.60
Absorption coefficient μ / mm$^{\breve{}1}$	49.6	48.2	46.9	41.2
$F(000)$ / e	508	508	524	1080
Radiation; wavelength λ / Å		Mo-K_α; 0.71073		
Diffractometer		Bruker D8 Venture		
Absorption correction		multi-scan		
Transmission (min; max)	0.3308; 0.7503	0.3308; 0.7503	0.6474; 0.749	0.6156; 0.749
Index range $h \mid k \mid l$	$\pm6 \mid \pm7 \mid \pm13$	$\pm7 \mid -6/7 \mid \pm15$	$\pm7 \mid \pm7 \mid \pm16$	$\pm17 \mid \pm16 \mid \pm12$
Θ range / °	3.513-27.976	4.351-29.785	4.309-32.404	3.208-34.962
Reflections collected	6256	1804	2828	9999
Independent reflections	706	215	276	1387
R_{int}	0.034	0.029	0.029	0.037
Obs. reflections [$I > 2\sigma(I)$]	693	201	243	1151
Refined parameters / restraints	57	15	16	57
R_1 (all data)	0.013	0.023	0.017	0.030
wR_2 (all data)	0.031	0.047	0.037	0.039
GOF	1.209	1.382	1.202	1.054
Residual electron density (max; min) / e^-Å^{-3}	1.96; -0.93	1.69; -1.52	1.33; -0.92	1.75; -1.43

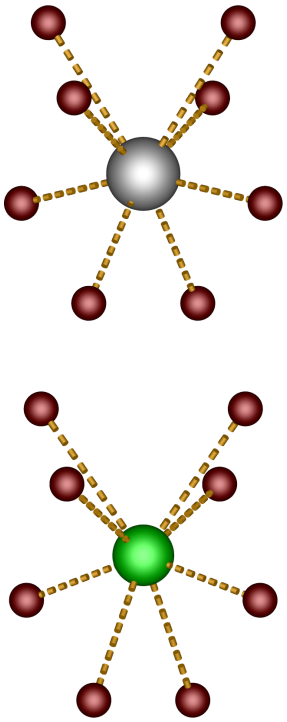

Fig. B.2.16: Coordination environments of the cationic substructure in $LiY(WO_4)_2$-I: oxygen atoms red, lithium atoms light green, yttrium atoms grey.

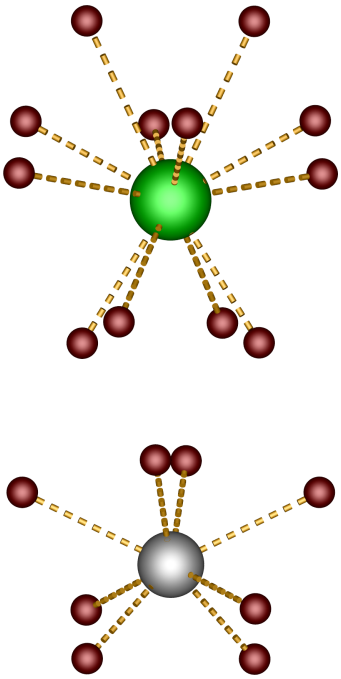

Fig. B.2.17: Coordination environments of the cationic substructure in $KY(WO_4)_2$: oxygen atoms red, potassium atoms light green, yttrium atoms grey.

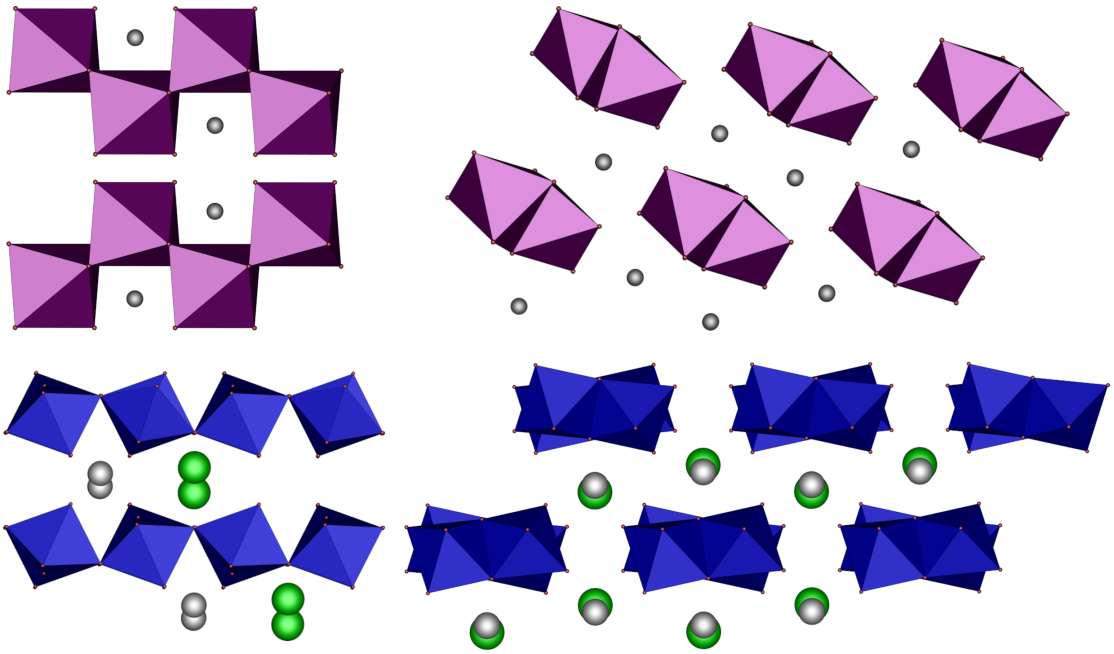

Fig. B.2.18: Relationship of the structures of $YNbO_4$ (top) and $KBi(WO_4)_2$ (bottom): The latter can be considered a distorted variant of the former; yttrium and bismuth atoms grey, potassium green, WO_6 octahedra blue, NbO_6 octahedra violet; the relations and distortion of both structures can be understood by the comparison of these crystal structure depictions.

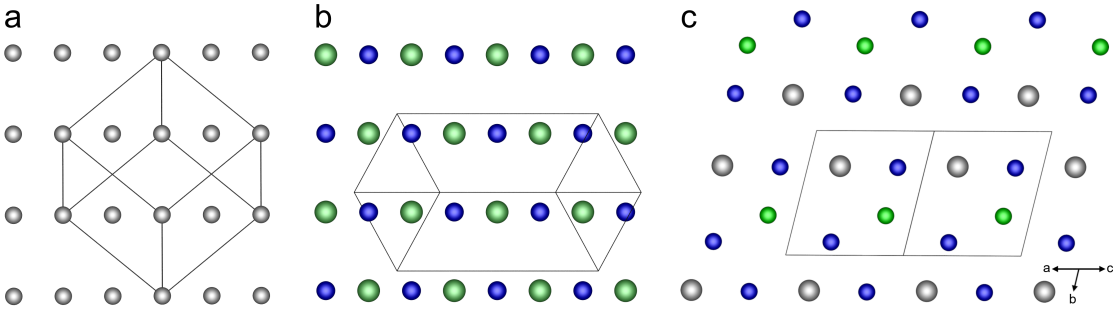

Fig. B.2.19: Relationship of the *fluorite*, *scheelite* and $CuLa(WO_4)_2$ structure type based on the respective cationic sublattice: (a) shows the cation arrangement in SrF_2,[492] (b) in $NaEu(WO_4)_2$ (compare also figures 5.1.2 and 5.1.6 and (c) for $LiPr(WO_4)_2$-I; in the latter case, two translationally not identical layers are formed; these are connected via the inversion centre in this structure; (b) and (c) can be considered variants of (a); (a) and (b) are viewed towards the (112) plane; (c) would show the same plane if transformed into a pseudoorthorhombic setting; details can be found in [275].

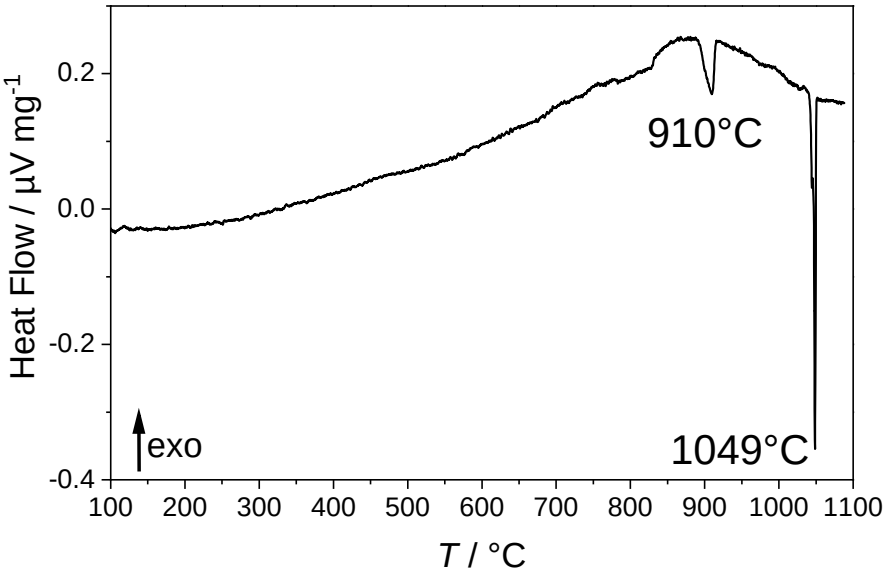

Fig. B.2.20: DSC results for $LiY(WO_4)_2$-I; the endothermic events are labelled with the respective temperatures.

Tab. B.2.4: Assignment of f-f transitions in the reflectance spectrum of $LiPr(WO_4)_2$-II according to [154]

Wavelength λ / nm	Energy E / cm^{-1}	Assignment
449	22272	$^3H_4 \rightarrow {}^1I_6$
474	21097	$^3H_4 \rightarrow {}^3P_1$
488	20492	$^3H_4 \rightarrow {}^3P_0$
586, 593, 603	17065, 16863, 16584	$^3H_4 \rightarrow {}^1D_2$

C Supplementary Material to Chapter 6

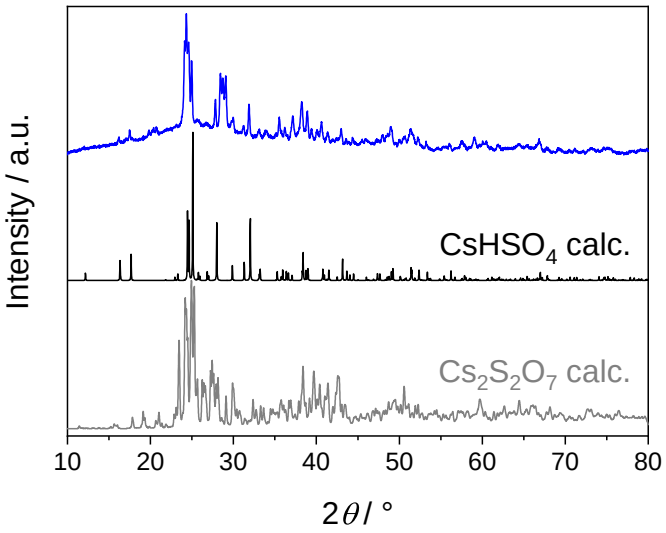

Fig. C.0.1: PXRD of the educt prepared prior to the synthesis of compared to calculated pattern for $CsHSO_4$[493] and $Cs_2S_2O_7$[494]

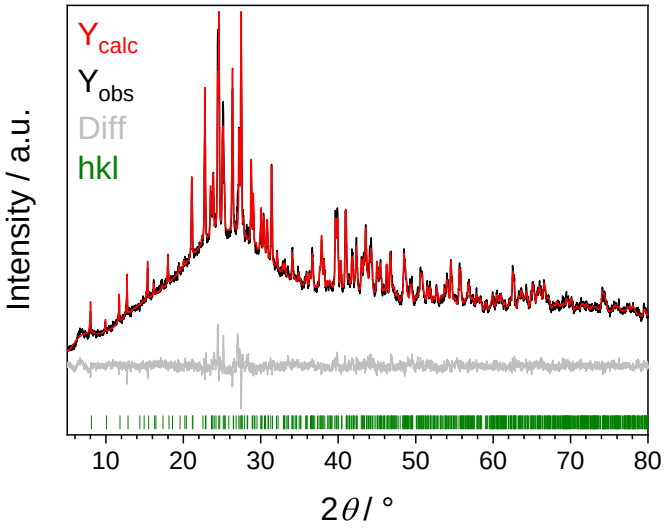

Fig. C.0.2: Rietveld refinement of $Cs_6[(WO_2)_2O(SO_4)_4]$

Tab. C.0.1: Crystal data and structure refinements of $Cs_6[(WO_2)_2O(SO_4)_4]$ determined from powder X-ray diffraction data via Rietveld refinement using the structure from SC-XRD as starting model; the respective standard deviations are given in parentheses.

M / g × mol^{-1}	1629.4
Temperature / K	297(2)
Space group	$P2_1/c$ (no. 14)
a / pm	1087.97(5)
b / pm	1495.58(6)
c / pm	776.69(3)
β / °	92.691(3)
Volume / 10^6 pm^3	1262.4(1)
Z	2
ρ_{calcd} / g cm^3	4.29
Radiation; wavelength λ / Å	Cu$K\alpha$; 1.54184
Diffractometer	Seifert 3003 TT
Θ range / °	2.5-40
Observed reflections	572
Refined parameters	29
R_{Bragg}	0.015
R_p	0.021
R_{wp}	0.028
GOF	0.2

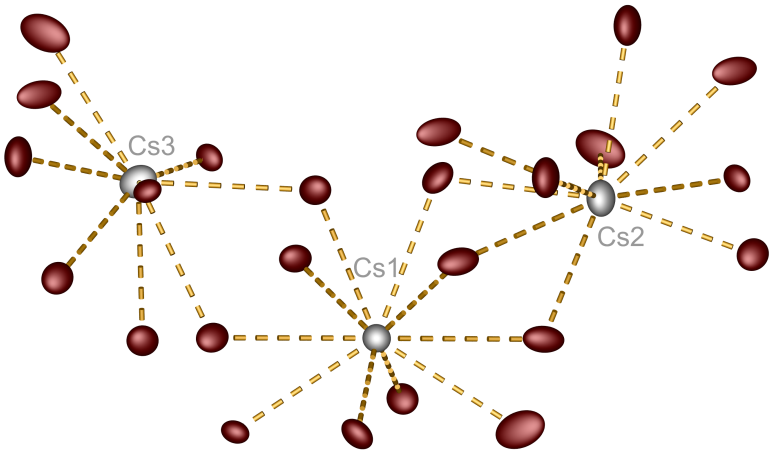

Fig. C.0.3: Coordination environment of caesium atoms (grey) in $Cs_6[(WO_2)_2O(SO_4)_4]$; oxygen atoms red; the ellipsoids are shown at 60% probability.

Tab. C.0.2: Crystal data and structure refinements of $Cs_6[(WO_2)_2O(SO_4)_4]$ determined from SC-XRD both at room temperature and at 149 K; the respective standard deviations are given in parentheses.

M / g mol^{-1}	1629.4	
Crystal size / mm^3	$0.03 \times 0.02 \times 0.02$	
Temperature / K	297(2)	149(2)
Space group	$P2_1/c$ (no. 14)	
a / pm	1087.44(3)	1083.35(16)
b / pm	1494.57(5)	1488.1(2)
c / pm	776.19(3)	772.52(12)
β / °	92.701(1)	92.860(5)
Volume / 10^6 pm^3	1260.10(7)	1243.8(3)
Z	2	
ρ_{calcd} / g cm^3	4.29	4.35
Absorption coefficient μ / mm$^{\smile 1}$	10.57	18.31
$F(000)$ / e	908	1420
Radiation; wavelength λ / Å	Mo-K_α; 0.71073	
Diffractometer	Bruker D8 Venture	
Θ range / °	2.318-27.924	2.327-29.292
Absorption correction	multi-scan	
Transmission (min; max)	0.5892; 0.7456	0.6204; 0.7458
Index range $h \mid k \mid l$	$\pm 14 \mid \pm 19 \mid \pm 10$	$-13/14 \mid \pm 20 \mid \pm 10$
Reflections collected	30493	12626
Independent reflections	3019	3394
Obs. reflections [$I > 2\sigma(I)$]	2490	2419
Refined parameters	152	152
R_{int}	0.066	0.087
R_1	0.040	0.076
wR_2	0.042	0.064
GOF	1.046	1.051
Residual electron density (max; min) / e^- Å^{-3}	1.00; -0.95	1.75; -2.25

Tab. C.0.3: Wyckoff symbols, refined atomic coordinates and isotropic displacement parameters U_{eq} / Å^2 in $Cs_6[(WO_2)_2O(SO_4)_4]$; estimated standard deviations in parentheses.

Atom	Wyckoff position	x	y	z	U_{eq}
W1	4*e*	0.86105(2)	0.53573(2)	0.11767(3)	0.01547(6)
Cs1	4*e*	0.86928(3)	0.79734(3)	0.11093(5)	0.02260(9)
Cs2	4*e*	0.52150(4)	0.62866(3)	-0.14395(6)	0.03193(11)
Cs3	4*e*	1.23286(4)	0.59775(3)	0.37491(5)	0.03110(11)
S1	4*e*	1.16934(13)	0.84707(10)	0.34637(19)	0.0191(3)
O11	4*e*	0.2664(4)	0.6974(3)	-0.2420(6)	0.0310(11)
O12	4*e*	0.9320(4)	0.6066(3)	0.2662(6)	0.0293(10)
O13	4*e*	0.8970(4)	0.4134(3)	0.2728(5)	0.0205(9)
O14	2*c*	1	$\frac{1}{2}$	0	0.0325(16)
S2	4*e*	0.61970(12)	0.89939(10)	-0.17529(19)	0.0185(3)
O21	4*e*	0.6324(5)	0.9105(4)	0.0076(6)	0.0473(14)
O22	4*e*	0.4978(4)	0.5803(4)	0.2559(7)	0.0434(13)
O23	4*e*	0.6612(4)	0.6880(3)	0.2717(6)	0.0349(12)
O24	4*e*	0.775(4)	0.4108(3)	0.0176(5)	0.0223(9)
O3	4*e*	0.7026(4)	0.5295(3)	0.2463(6)	0.0371(12)
O4	4*e*	0.7976(4)	0.6048(3)	-0.0410(6)	0.0302(11)
O5	4*e*	1.0832(4)	0.7853(3)	0.4170(6)	0.0295(10)

Tab. C.0.4: Anisotropic displacement parameters U_{ij} / Å^2 in $Cs_6[(WO_2)_2O(SO_4)_4]$; estimated standard deviations in parentheses.

Atom	U_{11}	U_{22}	U_{33}	U_{12}	U_{13}	U_{23}
W1	0.01351(11)	0.01655(12)	0.01671(12)	-0.00053(10)	0.00441(8)	0.00145(10)
Cs1	0.02296(19)	0.0231(2)	0.02186(19)	0.00026(17)	0.00199(4)	-0.00072(16)
Cs2	0.0225(2)	0.0389(3)	0.0343(2)	0.0022(2)	0.00088(16)	-0.00191(18)
Cs3	0.0386(2)	0.0325(2)	0.0229(2)	0.00197(18)	0.00815(17)	0.00550(18)
S1	0.0175(7)	0.0164(8)	0.0236(8)	-0.0002(6)	0.0022(5)	-0.0003(5)
O11	0.024(2)	0.029(3)	0.040(3)	0.008(2)	0.006(2)	-0.0024(19)
O12	0.034(3)	0.027(3)	0.027(2)	-0.007(2)	-0.0027(19)	0.004(2)
O13	0.025(2)	0.016(2)	0.021(2)	0.0024(18)	-0.0003(17)	0.0025(17)
O14	0.0035(4)	0.024(4)	0.041(4)	0.001(3)	0.026(3)	0.004(3)
S2	0.0147(7)	0.0202(8)	0.0212(7)	0.0018(6)	0.0065(5)	0.0011(6)
O21	0.079(4)	0.044(3)	0.019(3)	0.004(2)	0.006(2)	0.016(3)
O22	0.022(2)	0.047(3)	0.060(3)	0.005(3)	-0.007(2)	-0.002(2)
O23	0.036(3)	0.022(3)	0.048(3)	0.006(2)	0.019(2)	0.002(2)
O24	0.027(2)	0.022(2)	0.017(2)	0.0003(18)	-0.0051(17)	-0.0038(18)
O3	0.031(2)	0.023(3)	0.060(3)	0.003(2)	0.033(2)	0.002(2)
O4	0.031(2)	0.028(3)	0.031(3)	0.008(2)	-0.0017(19)	0.007(2)
O5	0.023(2)	0.024(2)	0.042(3)	0.007(2)	0.008(2)	-0.0026(18))

Tab. C.0.5: Electrostatic calculations for $Cs_6[(WO_2)_2O(SO_4)_4]$: the MAPLE values are compared to the sum of the MAPLE values of Cs_2SO_4, WO_3 and SO_3; a deviation below 1% is the empirical benchmark for electrostatic consistency.

$Cs_6[(WO_2)_2O(SO_4)_4]$	$3\ Cs_2SO_4^{[495]} + 2\ WO_3^{[496]} + SO_3^{[497]}$
MAPLE $= 179610\ \mathrm{kJ\,mol^{-1}}$	MAPLE $= 180135\ \mathrm{kJ\,mol^{-1}}$
	$\Delta = 0.3\%$

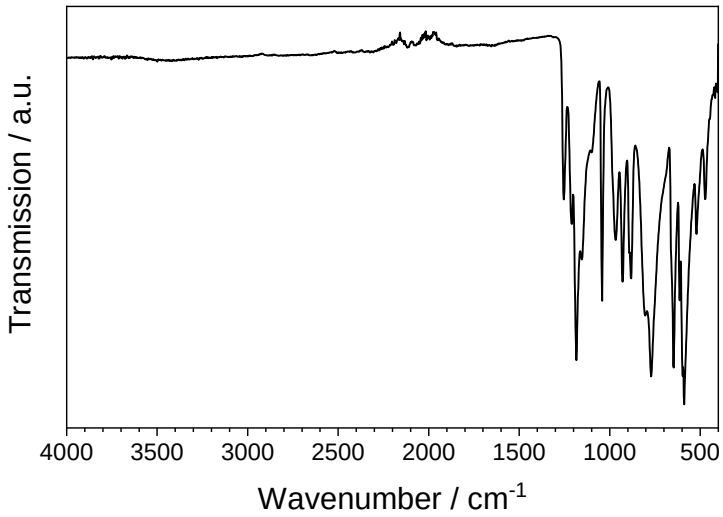

Fig. C.0.4: Full IR spectrum of $Cs_6[(WO_2)_2O(SO_4)_4]$

D Supplementary Material to Chapter 7

D.1 $Sn(SO_4)_2$ and $Sn_2(SO_4)_3$

Tab. D.1.1: Crystal data and structure refinements of $Sn_2(SO_4)_3$ determined from PXRD data via Rietveld refinement using the structure from SC-XRD as starting model; the respective standard deviations are given in parentheses.

M / g × mol^{-1}	525.56
Temperature / K	298(2)
Space group	$P\bar{1}$ (no. 2)
a / pm	484.95(1)
b / pm	811.45(1)
c / pm	1213.51(2)
α / °	88.987(2)
β / °	86.438(2)
γ / °	73.329(1)
Volume / 10^6 pm^3	456.57(1)
Z	2
ρ_{calcd} / g cm^3	3.82
Radiation; wavelength λ / Å	Cu$K\alpha$; 1.54184
Diffractometer	Bruker D8 Advance
Θ range / °	2.5-40
Observed reflections	549
Refined parameters	31
R_{Bragg}	0.004
R_p	0.005
R_{wp}	0.008
GOF	1.44

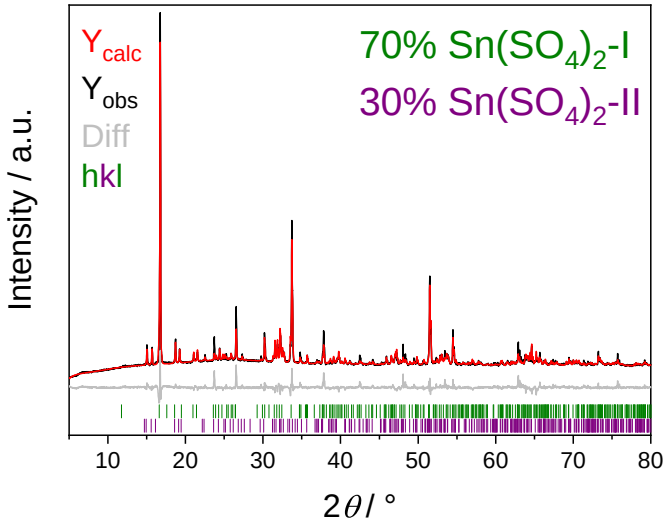

Fig. D.1.1: Rietveld-Refinement of the mixed $Sn(SO_4)_2$ sample.

Tab. D.1.2: Crystal data and structure refinements of mixed $Sn(SO_4)_2$ determined from PXRD data via Rietveld refinement using the structures from SC-XRD as starting models; the respective standard deviations are given in parentheses.

	$Sn(SO_4)_2$-I	$Sn(SO_4)_2$-II
M / g × mol^{-1}	310.81	
Temperature / K	298(2)	
Space group	$P2_1/c$ (no. 14)	$P2_1/n$ (no. 14)
a / pm	504.27(4)	752.95(7)
b / pm	1065.53(7)	801.5(1)
c / pm	1065.76(7)	913.3(1)
β / °	91.954(4)	92.533(4)
Volume / 10^6 pm^3	572.31(7)	550.6(1)
Z	4	
ρ_{calcd} / g cm^3	3.61	3.75
Radiation; wavelength λ / Å	Cu$K\alpha$; 1.54184	
Diffractometer	Seifert 3003 TT	
Θ range / °	2.5-40	
Observed reflections	647	
Refined parameters	42	
R_{Bragg}	0.034	0.030
R_p	0.034	
R_{wp}	0.054	
GOF	0.40	

Tab. D.1.3: Crystal data and structure refinements on $Sn(SO_4)_2$-I determined from PXRD data via Rietveld refinementa; the sample indicated by p was prepared via precipitation starting from tin in H_2SO_4 as a pale grey powder (see text on page 136 for further explanation); the respective standard deviations are given in parentheses; the structure from SC-XRD was used as starting model.

	$Sn(SO_4)_2$-I	$Sn(SO_4)_2$-I	p-$Sn(SO_4)_2$-I
M / g × mol^{-1}		310.81	
Temperature / K	298(2)	673(2)	298(2)
Space group	$P2_1/c$ (no. 14)	$P2_1/c$ (no. 14)	$P2_1/c$ (no. 14)
a / pm	504.68(2)	507.78(2)	502.29(1)
b / pm	1066.29(4)	1073.10(7)	1071.46(4)
c / pm	1066.46(6)	1071.18(8)	1070.53(4)
β / °	91.945(4)	90.04(2)	90.138(3)
Volume / 10^6 pm^3	573.57(4)	583.68(6)	576.14(3)
Z		4	
ρ_{calcd} / g cm^3	3.60	3.54	3.58
Radiation; wavelength λ / Å		Cu$K\alpha$; 1.54184	
Diffractometer		Bruker D8 Advance	
Θ range / °	2.5-40	2.5-30	2.5-40
Observed reflections	328	98	343
Refined parameters	33	33	28
R_{Bragg}	0.019	0.026	0.017
R_p	0.016	0.03	0.009
R_{wp}	0.025	0.044	0.017
GOF	1.35	0.12	3.28

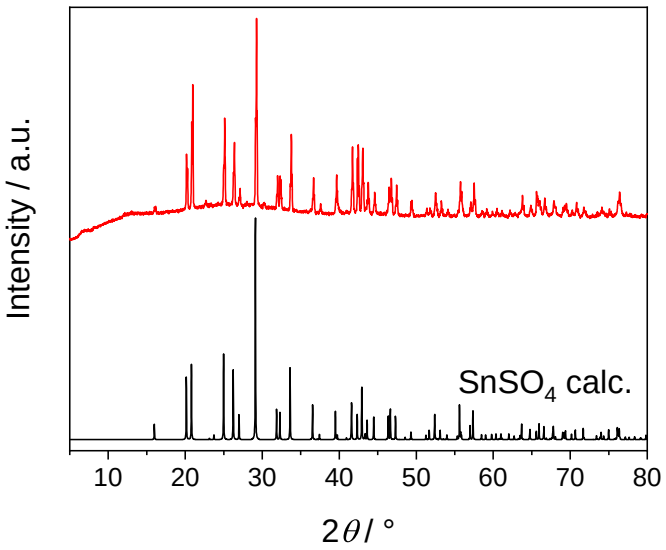

Fig. D.1.2: PXRD pattern of as-prepared $SnSO_4$ compared to a calculated pattern.[498]

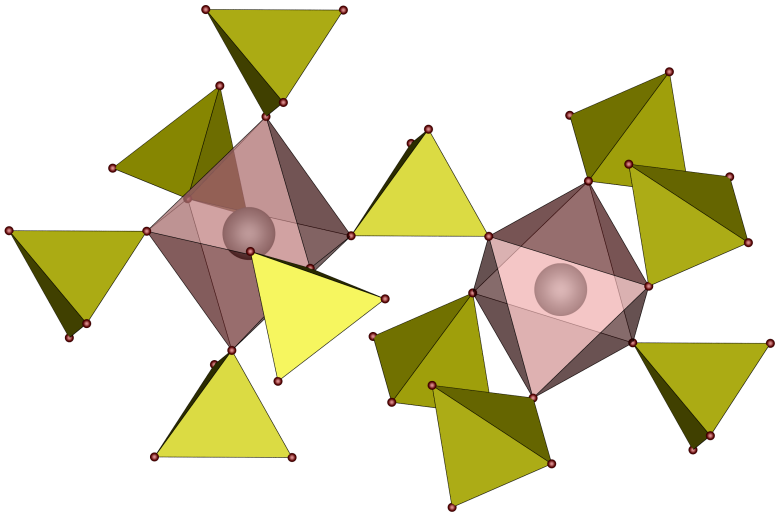

Fig. D.1.3: Coordination environment and connection pattern of Sn^{4+} cations in $Sn(SO_4)_2$-I; Sn grey, O red, sulfate tetrahedra yellow, SnO_6 octahedra pale red.

Tab. D.1.4: Selected interatomic distances (in pm) and angles (in °) in $Sn(SO_4)_2$-I determined by SC-XRD; the respective standard deviations are given in parentheses.

Sn-O	201.6(3)-204.9(3)
$\sum$ IR (Sn-O)[216]	204
S-O_c [i]	149.1(3)-150.9(3)
S-O_{nc} [i]	140.8(3)-141.2(3)
$\sum$ IR (S-O)[216]	147
O-S-O	103.7(2)-115.5(2)

[i] The S-O distances are discriminated between the ones containing oxygen atoms coordinating tin atoms O_c and the ones not coordinating tin atoms O_{nc}.

Tab. D.1.5: Selected interatomic distances (in pm) and angles (in °) in $Sn(SO_4)_2$-II determined by single crystal XRD; the respective standard deviations are given in parentheses.

Sn-O	202.0(1)-204.1(1)
$\sum$ IR (Sn-O)[216]	204
S-O_c [i]	147.7(1)-150.8(1)
S-O_{nc} [i]	141.3(1)-141.4(1)
$\sum$ IR (S-O)[216]	147
O-S-O	104.35(5)-114.88(5)

[i] The S-O distances are discriminated between the ones containing oxygen atoms coordinating tin atoms O_c and the ones not coordinating tin atoms O_{nc}.

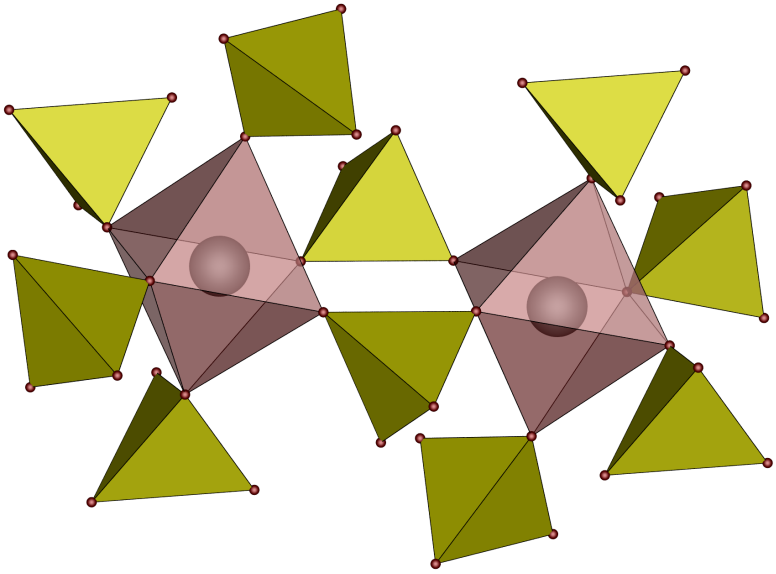

Fig. D.1.4: Coordination environment and connection pattern of Sn^{4+} cations in $Sn(SO_4)_2$-II; Sn grey, O red, sulfate tetrahedra yellow, SnO_6 octahedra pale red.

Tab. D.1.6: Selected interatomic distances (in pm) and angles (in °) in $Sn_2(SO_4)_3$ determined by single crystal XRD; the respective standard deviations are given in parentheses.

Sn(IV)-O	200.2(5)-203.1(5)
$\sum$ IR (Sn(IV)-O)[216]	204
Sn(II)-O	221.8(5)-278.7(5)
$\sum$ IR (Sn(II)-O)[265]	234.9
O-Sn(II)-O[i]	75.3(2)-82.3(2)
O-Sn(II)-O[ii]	67.4(2)-76.2(2)
S-O	142.5(5)-151.5(5)
$\sum$ IR (S-O)[216]	147
O-S-O	104.0(3)-115.4(3)

[i] angle in between the top and the base of the pentagonal pyramid; [ii] angle inside the base of the pentagonal pyramid.

Tab. D.1.7: Electrostatic calculations for $Sn(SO_4)_2$-I, $Sn(SO_4)_2$-II and $Sn_2(SO_4)_3$: the MAPLE values are compared to the sum of the MAPLE values of respective simple compounds; a deviation below 1% is the empirical benchmark for electrostatic consistency.

$Sn(SO_4)_2$-I	SnO_2[499] + 2 SO_3[497]
MAPLE = 73337 kJ mol^{-1}	MAPLE = 72873 kJ mol^{-1}
$\Delta = 0.6\%$	
$Sn(SO_4)_2$-II	SnO_2[499] + 2 SO_3[497]
MAPLE = 73441 kJ mol^{-1}	MAPLE = 72873 kJ mol^{-1}
$\Delta = 0.8\%$	
$Sn_2(SO_4)_3$	$SnSO_4$[498] + $Sn(SO_4)_2$-I
MAPLE = 108366 kJ mol^{-1}	MAPLE = 107721 kJ mol^{-1}
$\Delta = 0.6\%$	

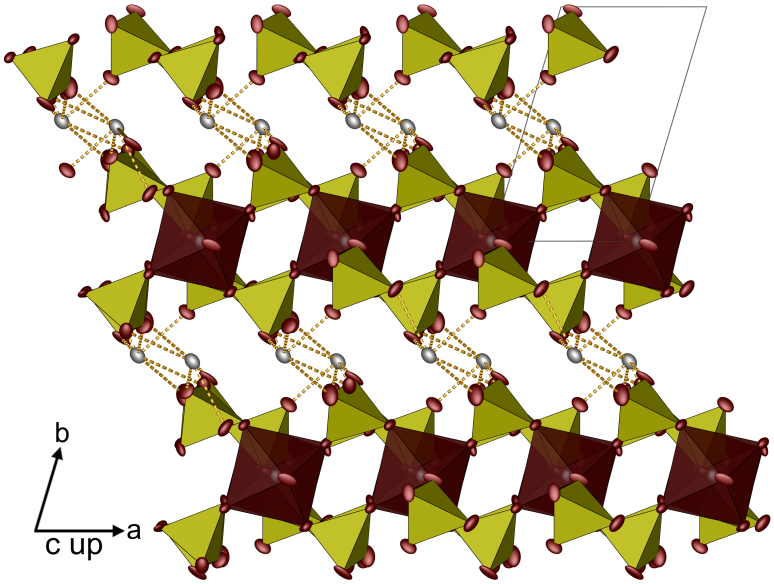

Fig. D.1.5: Layered structure of $Sn_2(SO_4)_3$ viewed along (001); sulfate tetrahedra yellow, tin cations grey, oxygen atoms red, SnO_6 octahedra pale red; ellipsoids are shown at 80% probability.

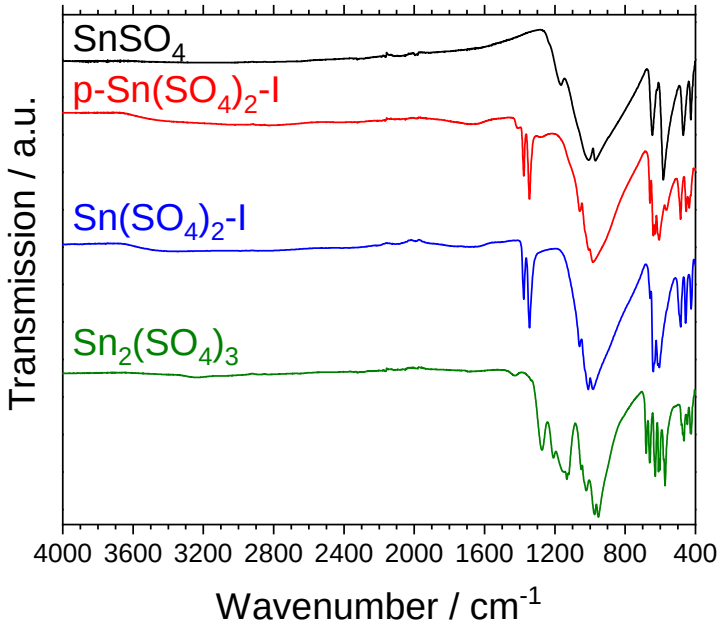

Fig. D.1.6: Full FT-IR spectra of $SnSO_4$, $Sn(SO_4)_2$-I and $Sn_2(SO_4)_3$ as well as $Sn(SO_4)_2$-I prepared via precipitation (p-$Sn(SO_4)_2$-I)

Tab. D.1.8: ECoN derived by MAPLE-calculations for Cd atoms in $Sn(SO_4)_2$-I

Atom	x	y	z	Distance / pm	ECoN(1)	ECoN(3)
Central atom						
Sn1	0	$\frac{1}{2}$	$\frac{1}{2}$			
Ligand						
O22	0.0027	0.5358	0.3141	201.719	1.028	1.028
O22	-0.0027	0.4642	0.6859	201.719	1.028	1.028
O12	-0.3324	0.3991	0.4637	201.757	1.027	1.027
O12	0.3324	0.6009	0.5363	201.757	1.027	1.027
O13	0.2158	0.3396	0.4758	204.72	0.940	0.940
O13	-0.2158	0.6604	0.5242	204.72	0.940	0.940
Next Ligand						
O21	-0.0539	0.3323	0.2111	356.134	0	0
Central atom						
Sn2	$\frac{1}{2}$	$\frac{1}{2}$	0			
Ligand						
O24	0.2965	0.477	0.1575	201.225	1.035	1.035
O24	0.7035	0.523	-0.1575	201.225	1.035	1.035
O11	0.5618	0.3138	-0.0191	201.954	1.013	1.013
O11	0.4382	0.6862	0.0191	201.954	1.013	1.013
O23	0.1567	0.4708	-0.1031	204.183	0.948	0.948
O23	0.8433	0.5292	0.1031	204.183	0.948	0.948
Next Ligand						
O23	-0.1567	0.5292	0.1031	353.916	0	0

Tab. D.1.9: ECoN derived by MAPLE-calculations for Cd atoms in $Sn(SO_4)_2$-II

Atom	x	y	z	Distance / pm	ECoN(1)	ECoN(3)
Central atom						
Sn1	0.4763	0.7656	0.1599			
Ligand						
O22	0.3515	0.8192	0.3453	202.052	1.031	1.031
O12	0.5796	0.9985	0.1499	202.768	1.010	1.010
O14	0.6873	0.6873	0.2869	202.782	1.009	1.009
O23	0.3519	0.543	0.1824	203.226	0.996	0.996
O13	0.2664	0.8593	0.0386	203.68	0.983	0.983
O24	0.5815	0.6905	-0.0313	204.138	0.969	0.969
Next Ligand						
O11	0.883	0.9202	0.0994	337.509	0	0

Tab. D.1.10: ECoN derived by MAPLE-calculations for Cd atoms in $Sn_2(SO_4)_3$

Atom	x	y	z	Distance / pm	ECoN(1)	ECoN(4)
Central atom						
Sn1	0	0	0			
Ligand						
O24	-0.2802	-0.1379	0.0299	200.196	1.043	1.043
O24	0.2802	0.1379	-0.0299	200.196	1.043	1.043
O23	0.3194	-0.2157	-0.0403	201.605	1.001	1.001
O23	-0.3194	0.2157	0.0403	201.605	1.001	1.001
O34	-0.0886	0.0176	-0.1624	203.262	0.952	0.952
O34	0.0886	-0.0176	0.1624	203.262	0.952	0.952
Next Ligand						
O24	0.7198	-0.1379	0.0299	337.937	0	0
Atom	x	y	z	Distance / pm	ECoN(1)	ECoN(4)
Central atom						
Sn2	0	0	$\frac{1}{2}$			
Ligand						
O13	-0.2914	-0.1151	0.5663	202.119	1.014	1.014
O13	0.2914	0.1151	0.4337	202.119	1.014	1.014
O33	0.0528	0.0735	0.6545	202.597	1.000	1.000
O33	-0.0528	-0.0735	0.3455	202.597	1.000	1.000
O14	-0.3096	0.2231	0.4711	203.063	0.986	0.986
O14	0.3096	-0.2231	0.5289	203.063	0.986	0.986
Next Ligand						
O13	0.7086	-0.1151	0.5663	342.848	0	0
Atom	x	y	z	Distance / pm	ECoN(1)	ECoN(4)
Central atom						
Sn3	0.8058	0.5126	0.2540			
Ligand						
O32	1.0562	0.6977	0.2110	221.812	1.424	1.530
O22	0.6609	0.5855	0.0666	243.006	0.889	1.006
O31	0.4412	0.7962	0.2744	246.803	0.797	0.913
O21	1.2085	0.3439	0.1201	253.800	0.637	0.748
O11	0.7864	0.6389	0.4457	253.805	0.637	0.748
O12	1.3222	0.3838	0.3579	278.709	0.214	0.283
Next Ligand						
O12	0.3222	0.3838	0.3579	302.105	0.044	0.069

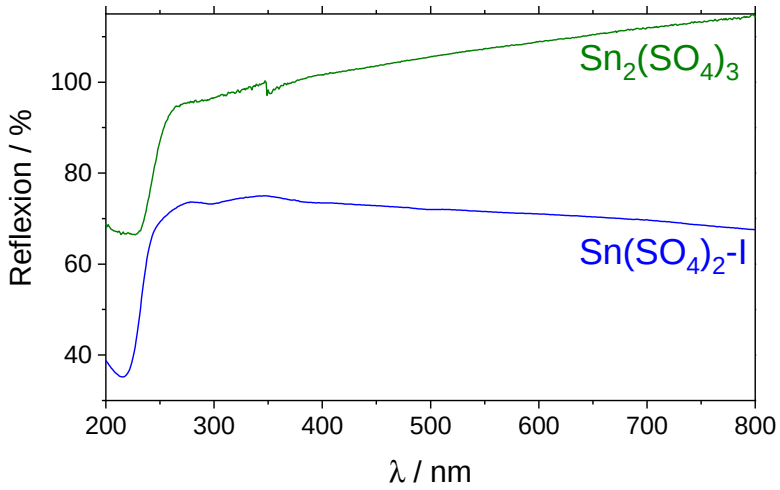

Fig. D.1.7: Diffusive powder UV-Vis spectra of$Sn(SO_4)_2$-I and $Sn_2(SO_4)_3$: The artefact around 350 nm is due to lamp change during the measurement.

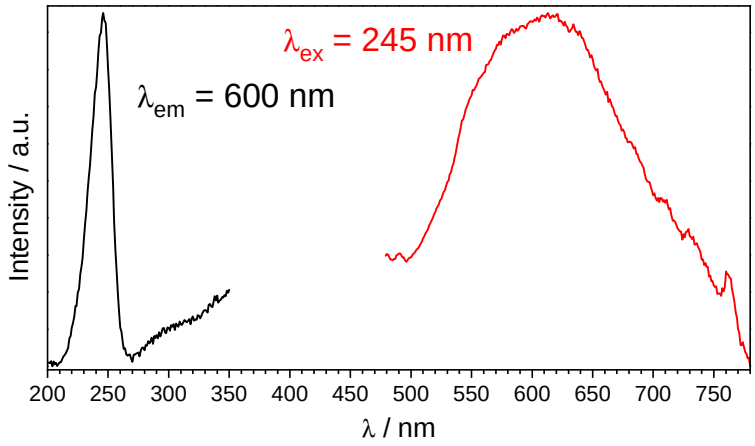

Fig. D.1.8: Fluorescence Spectrum of $SnSO_4$

Tab. D.1.11: Fitting parameters of ^{119}Sn Mößbauer spectroscopic measurements at 78 K for the tin sulfates $Sn(SO_4)_2$-I, $Sn_2(SO_4)_3$ and $SnSO_4$; δ = isomer shift, ΔE_Q = electric quadrupole splitting, Γ = experimental line width; standard deviations are given in parentheses.

Compound	δ / mm s^{-1}	ΔE_Q / mm s^{-1}	Γ / mm s^{-1}	ratio / %
$Sn(IV)(SO_4)_2$-I	-0.259(2)	0.376(14)	0.997(14)	100
$Sn(II)Sn(IV)(SO_4)_3$	-0.231(7)	0.29(4)	0.83(4)	58(2)
	4.146(14)	0.75(2)	0.82(4)	42(2)
$Sn(II)SO_4$	3.969(2)	0.992(3)	0.984(6)	100

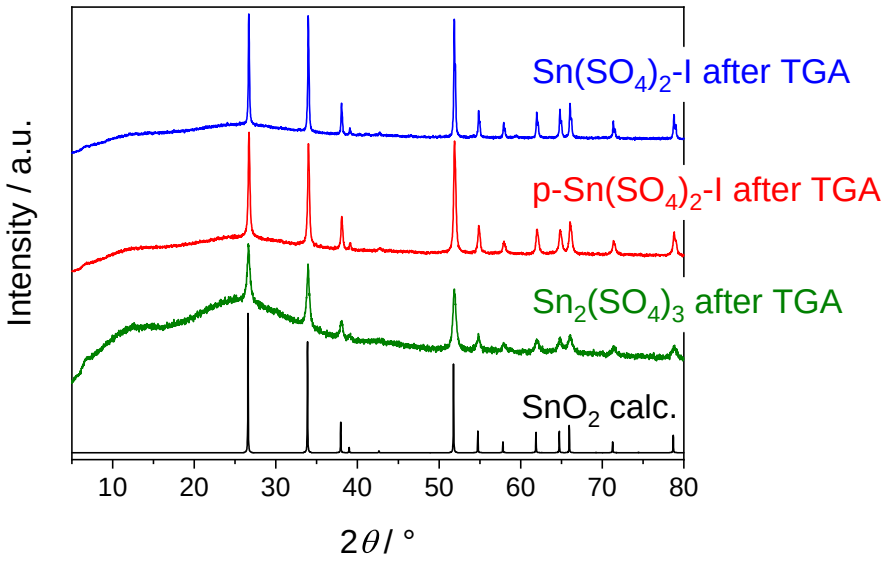

Fig. D.1.9: PXRD patterns of the residues after the TGA measurements compared to a calculated pattern for SnO_2.[499]

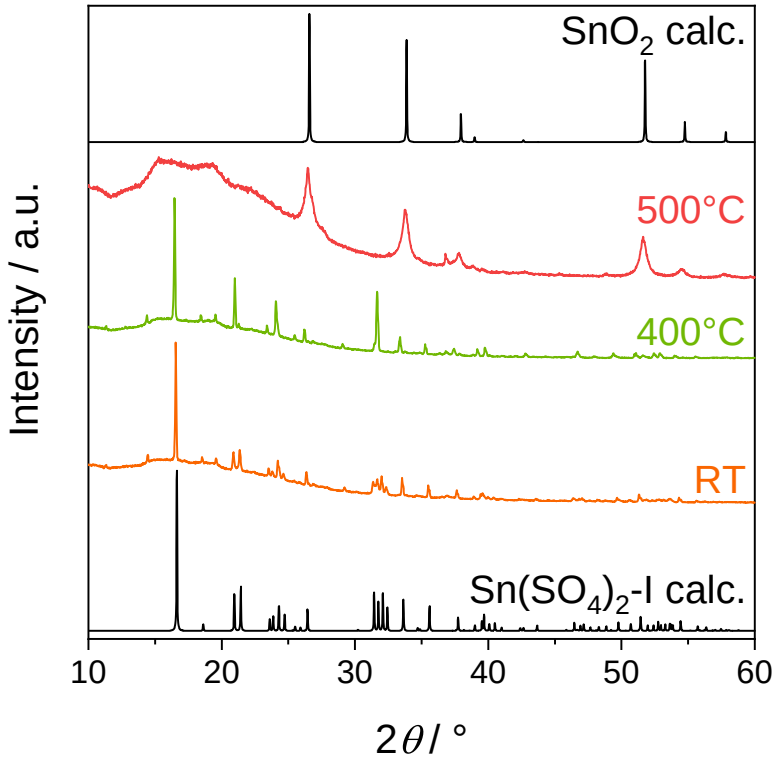

Fig. D.1.10: TPXRD powder patterns of $Sn(SO_4)_2$-I compared to calculated patterns of $Sn(SO_4)_2$-I from the single-crystal XRD and SnO_2.[499]

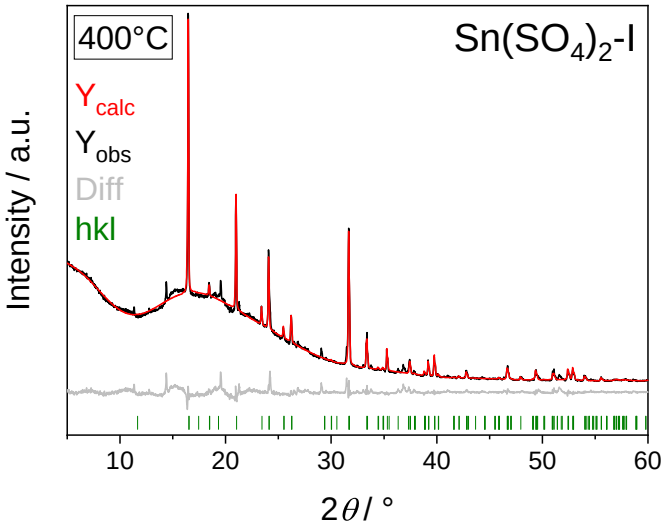

Fig. D.1.11: Rietveld refinement on $Sn(SO_4)_2$-I at 400°C.

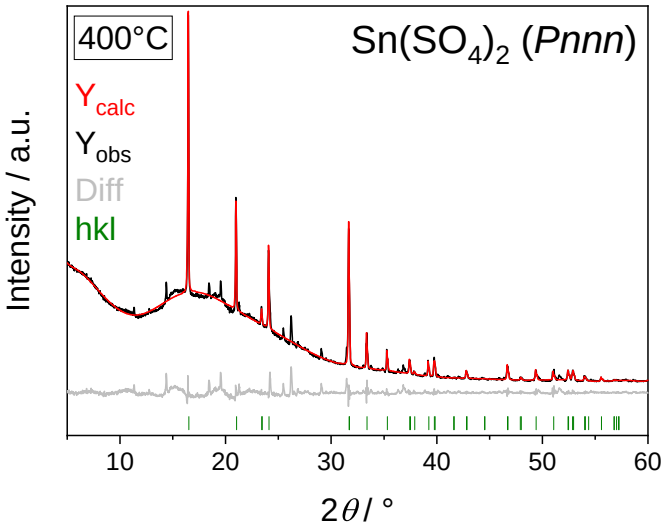

Fig. D.1.12: Pawley fit on $Sn(SO_4)_2$-I at 400°C.

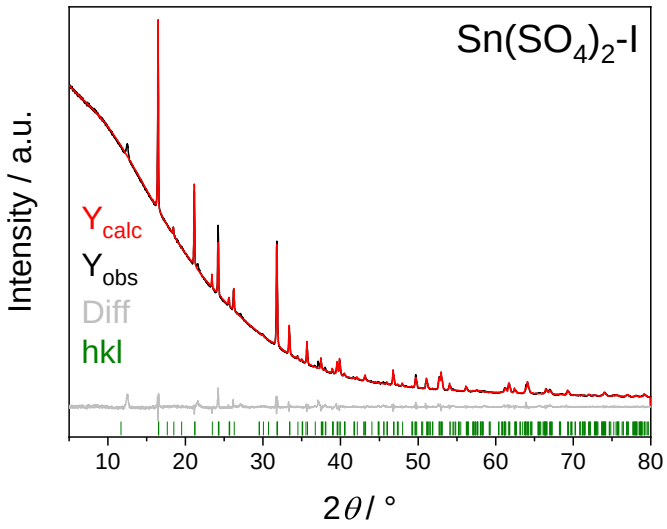

Fig. D.1.13: Rietveld refinement on $Sn(SO_4)_2$-I prepared by precipitation.

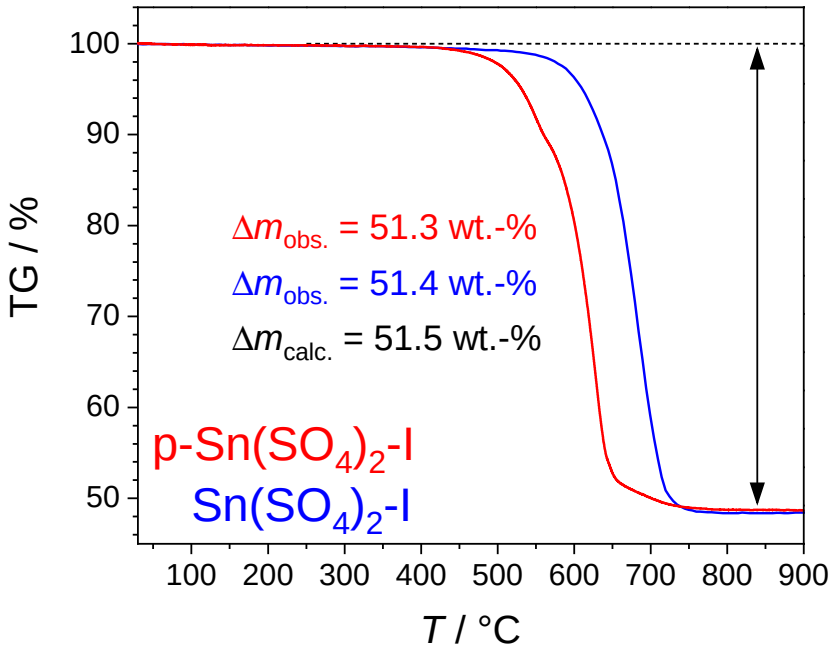

Fig. D.1.14: Thermogravimetric analyses of $Sn(SO_4)_2$-I and the $Sn(SO_4)_2$-I sample prepared via precipitation (p-$Sn(SO_4)_2$-I)

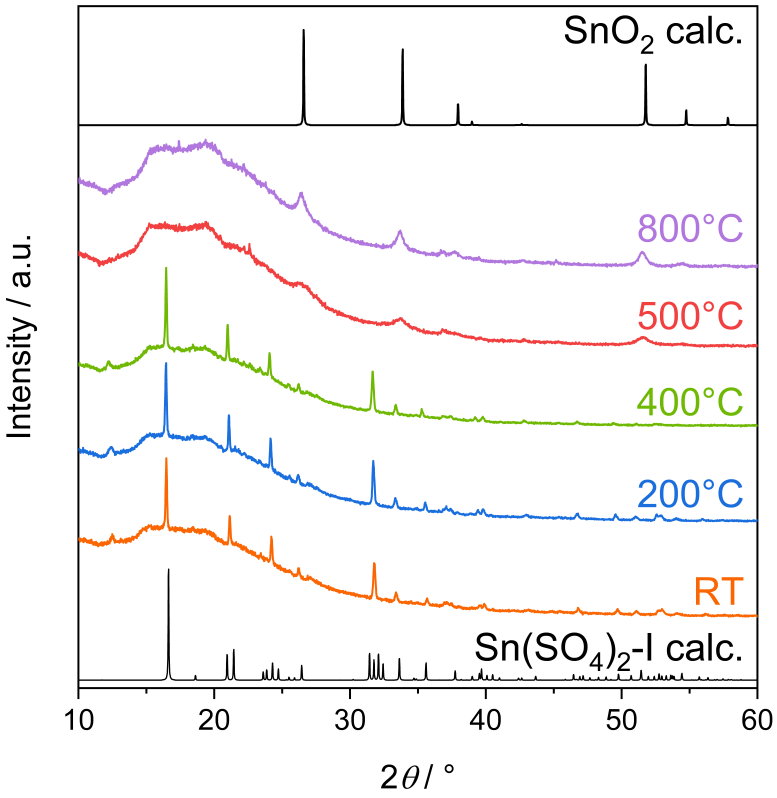

Fig. D.1.15: TPXRD powder patterns of $Sn(SO_4)_2$-I prepared via precipitation compared to calculated patterns of $Sn(SO_4)_2$-I from the single-crystal XRD and SnO_2.[499]

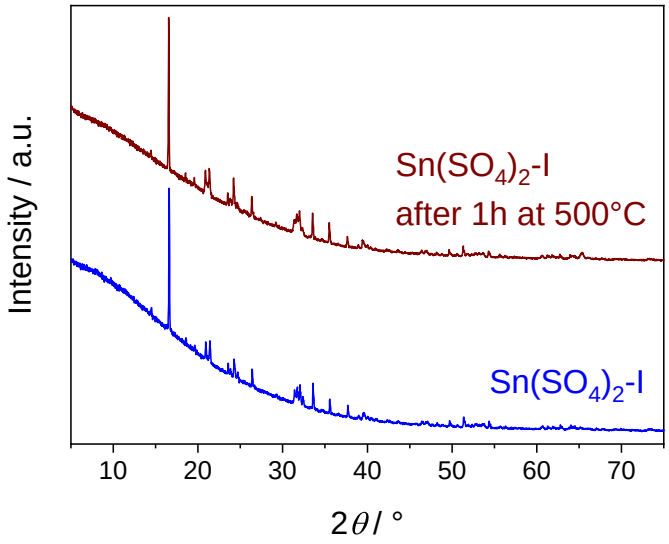

Fig. D.1.16: PXRD patterns comparing as-prepared $Sn(SO_4)_2$-I (bottom) and a sample heat treated at 500°C (top) showing almost no differences between both.

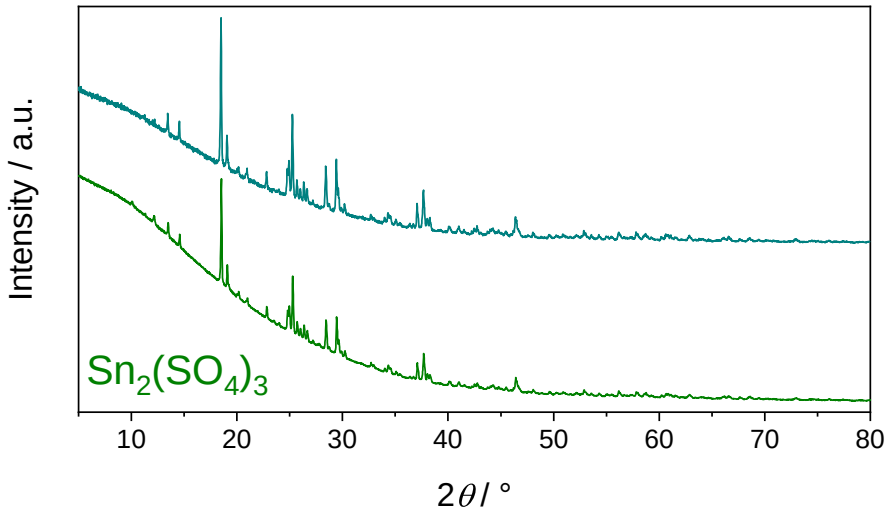

Fig. D.1.17: PXRD patterns comparing as-prepared $Sn_2(SO_4)_3$ (bottom) and a sample heat treated at 450°C (top) showing almost no differences between both.

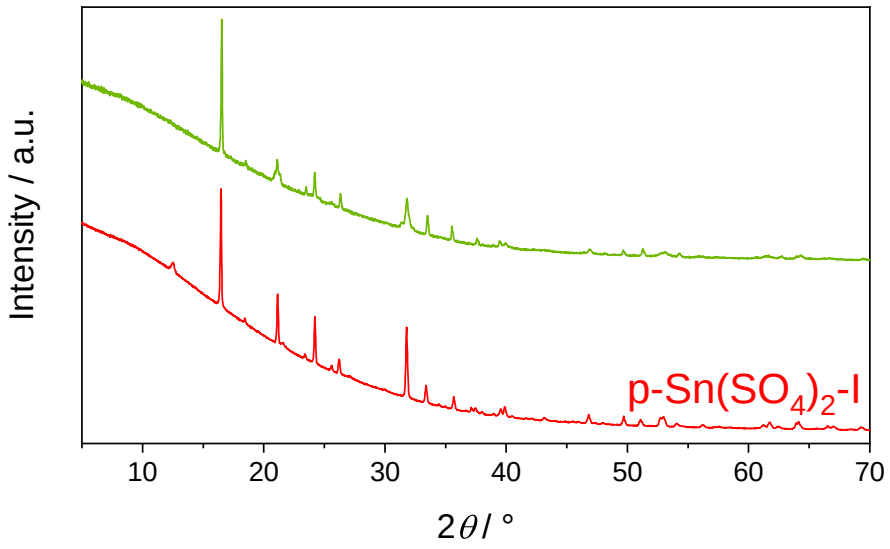

Fig. D.1.18: PXRD patterns comparing as-prepared p-$Sn(SO_4)_2$-I (bottom) and a $Sn_2(SO_4)_3$ sample heated at 300°C in air (top).

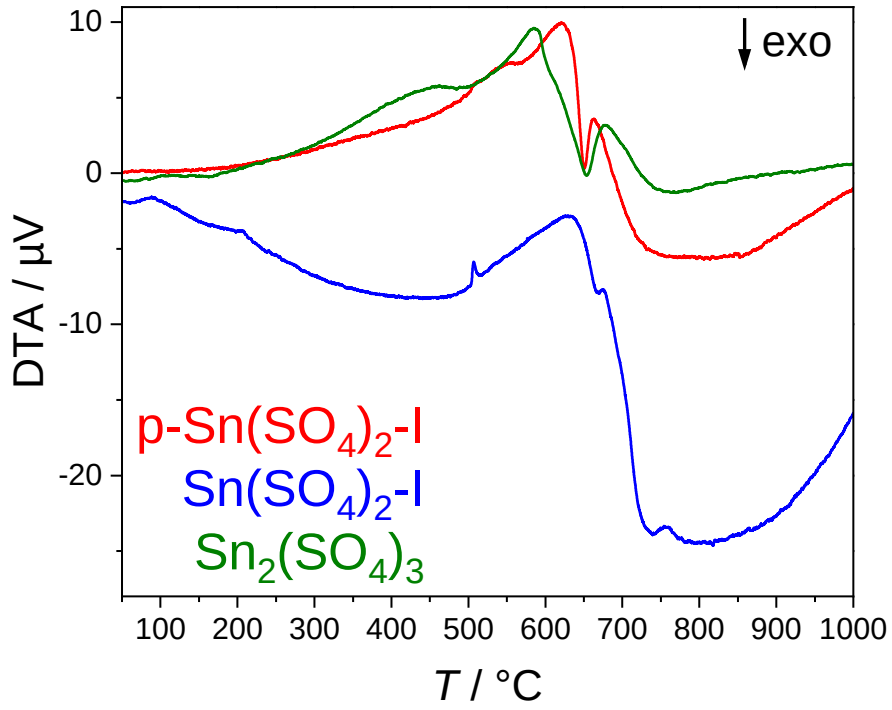

Fig. D.1.19: DTA results for $Sn(SO_4)_2$-I, p-$Sn(SO_4)_2$-I and $Sn_2(SO_4)_3$: The data shows broad endothermic events for the main decomposition step for all three samples centred at 631°, 620° and 585° for $Sn(SO_4)_2$-I, p-$Sn(SO_4)_2$-I and $Sn_2(SO_4)_3$, respectively, which is overlapped by an exothermic event. This can be attributed to the crystallisation of initially amorphous SnO_2.[500] Further, only in the signal of $Sn(SO_4)_2$-I an endothermic event at 507° is observed - in accordance with the data by Ahmed et al..[377] It is related to the unit cell enlargement effect discussed in the main text.

D.2 $Bi(H_3O)(SO_4)_2$, $Bi(HSO_4)_3$ and $Bi_2(SO_4)_3$

Tab. D.2.1: Crystal data and structure refinements of $Bi(H_3O)(SO_4)_2$, $Bi(HSO_4)_3$ and $Bi_2(SO_4)_3$ determined from PXRD data via Rietveld refinements using the structures from SC-XRD as starting models; the respective standard deviations are given in parentheses.

	$Bi(H_3O)(SO_4)_2$	$Bi(HSO_4)_3$[i]	$Bi_2(SO_4)_3$
CSD number	2118042		
M / g × mol^{-1}	420.12	500.18	706.14
Temperature / K		298(2)	
Space group	$P2_1/c$ (no. 14)	$P\bar{1}$ (no. 2)	$P2_1/n$ (no. 14)
a / pm	1205.73(2)	492.820(6)	1311.13(1)
b / pm	683.946(8)	910.22(1)	474.186(3)
c / pm	823.81(1)	1039.89(2)	1454.25(1)
α / °	90	85.593(1)	90
β / °	103.018(1)	86.866(1)	100.861(1)
γ / °	90	74.491(1)	90
Volume / 10^6 pm^3	661.896(17)	447.87(1)	887.94(1)
Z	4	2	4
ρ_{calcd} / g cm^3	4.22	3.71	5.28
Radiation; wavelength λ / Å		Cu$K\alpha$; 1.54184	
Diffractometer		Bruker D8 Advance	
Θ range / °	2.5-50	2.5-35	2.5-40
Observed reflections	585	657	537
Refined parameters	76	81	83
R_{Bragg}	0.01	0.005	0.006
R_p	0.009	0.007	0.006
R_{wp}	0.015	0.012	0.009
GOF	2.74	2.50	1.84

[i] $Bi(HSO_4)_3$ was refined with a 5 wt.-% side phase of $Bi(H_3O)(SO_4)_2$ (R_{Bragg} = 0.006) taking the results of the separate refinement on $Bi(H_3O)(SO_4)_2$ as fixed values.

Tab. D.2.2: Selected interatomic distances (in pm) and angles (in °) in $Bi(H_3O)(SO_4)_2$ determined by both SC-XRD and Rietveld refinement; the respective standard deviations are given in parentheses.

	SC-XRD	Rietveld
Bi-O	235(1)-273(1)	236(2)-286(2)
$\sum$ IR (Bi-O)[216]	252-253	
Bi-Bi	430.2(2)	431.1(2)
S-O	143(1)-150(1)	147(2)-158(2)
$\sum$ IR (S-O)[216]	147-148	
O-S-O	108(1)-114(1)	98(1)-120(1)

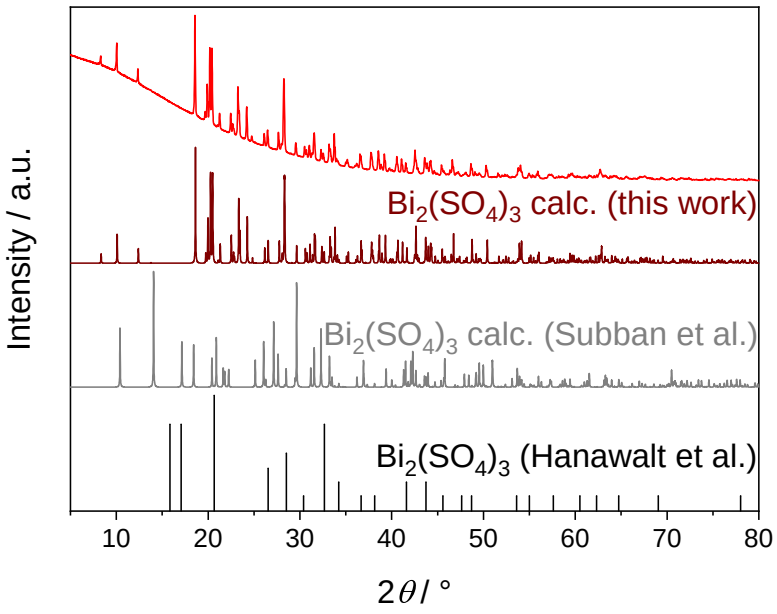

Fig. D.2.1: PXRD pattern of the $Bi_2(SO_4)_3$ sample compared to calculated pattern from the single-crystal structure determination and from the data by Subban et al.[409] as well as the reflex positions and intensities reported by Hanawalt et al.[403]

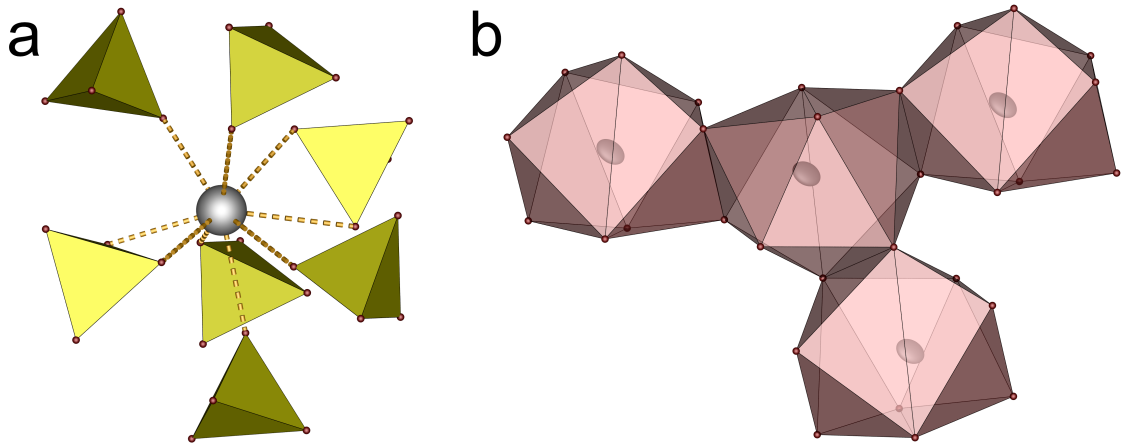

Fig. D.2.2: Coordination environment of the Bi^{3+} cations (grey) in $Bi(H_3O)(SO_4)_2$ showing the coordination by the sulfate anions in (a) and the connection of adjacent BiO_9 tricapped trigonal prisms in (b); sulfate tetrahedra yellow, oxygen atoms red; ellipsoids are shown at 80% probability (for bismuth in (b)).

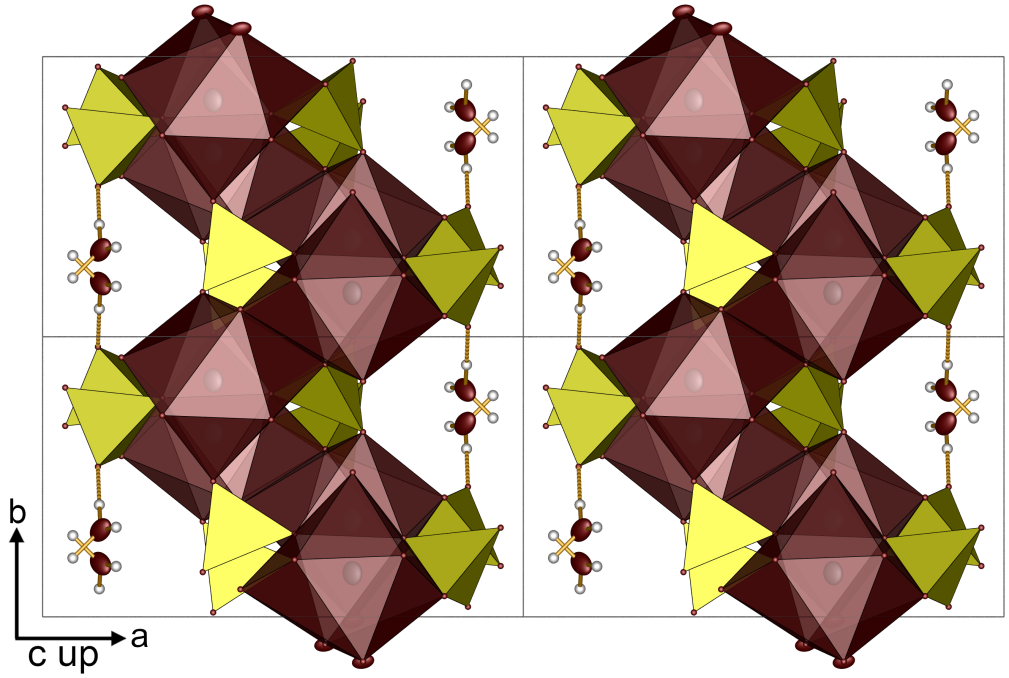

Fig. D.2.3: 2×2 supercell of $Bi(H_3O)(SO_4)_2$ showing formation of the network via the connection of layers in the bc plane by the oxonium ions; hydrogen bonds are displayed as broken lines; Bismuth grey, sulfate tetrahedra yellow, oxygen atoms red; hydrogen white; ellipsoids are shown at 80% probability.

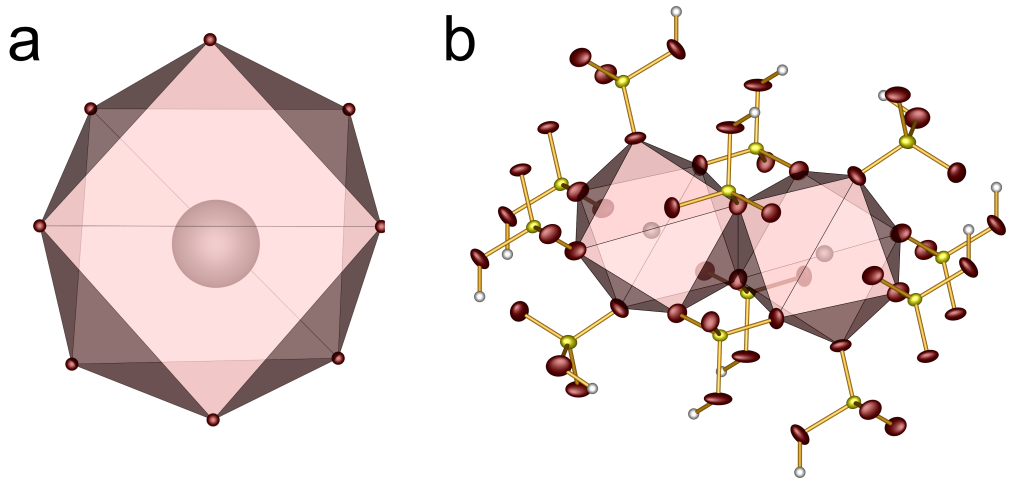

Fig. D.2.4: Coordination environment of the Bi^{3+} cations (grey) in $Bi(HSO_4)_3$ showing a single distorted square antiprism in (a) and the dimers and the coordination of these by HSO_4 groups in (b); sulfur yellow, oxygen atoms red; hydrogen white; ellipsoids are shown at 80% probability in (b).

Tab. D.2.3: Selected interatomic distances (in pm) and angles (in °) in $Bi(HSO_4)_3$; the respective standard deviations are given in parentheses; O_H is the protonated oxygen atom.

Bi-O	229.6(2)-261.8(2)
$\sum$ IR (Bi-O)[216]	252-253
Bi-Bi	423.22(6)
S-O	143.3(2)-148.4(2)
S-O_H	152.4(3)-154.6(3)
$\sum$ IR (S-O)[216]	147-148
O-S-O	105.3(2)-114.7(1)

Tab. D.2.4: Selected interatomic distances (in pm) and angles (in °) in $Bi_2(SO_4)_3$; the respective standard deviations are given in parentheses.

Bi-O	217.0(2)-272.8(3)
$\sum$ IR (Bi-O)[216]	252-253
Bi-Bi	473.25(3)
S-O	145.1(2)-149.7(2)
$\sum$ IR (S-O)[216]	147-148
O-S-O	105.5(1)-113.0(2)

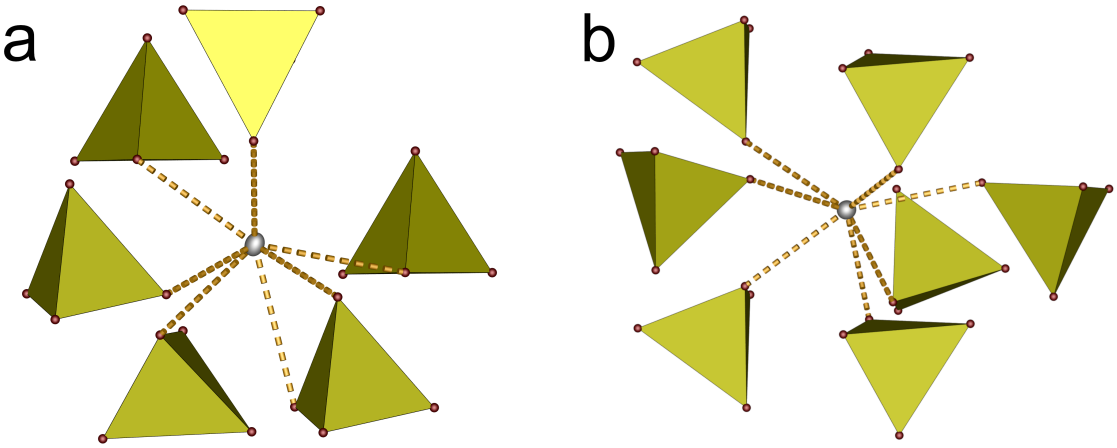

Fig. D.2.5: Coordination of the Bi^{3+} cations (grey) in $Bi_2(SO_4)_3$ by the sulfate groups: (a) Bi(1) and (b) Bi(2); sulfate tetrahedra yellow, oxygen red; ellipsoids of bismuth atoms are shown at 80% probability.

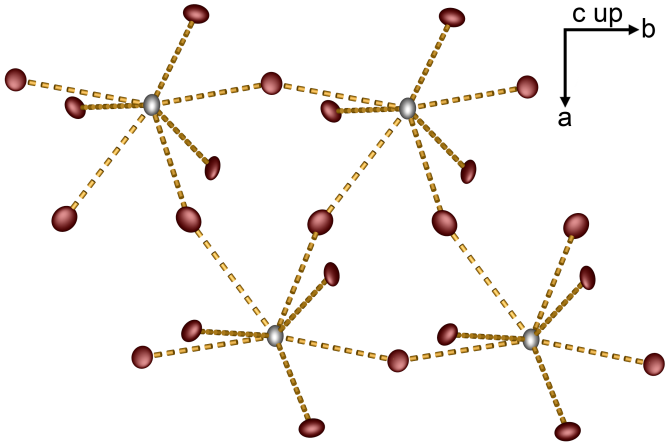

Fig. D.2.6: Connection pattern of the condensed $Bi(1)O_7$ polyhedra in $Bi_2(SO_4)_3$, bismuth grey; oxygen red; ellipsoids are shown at 80% probability.

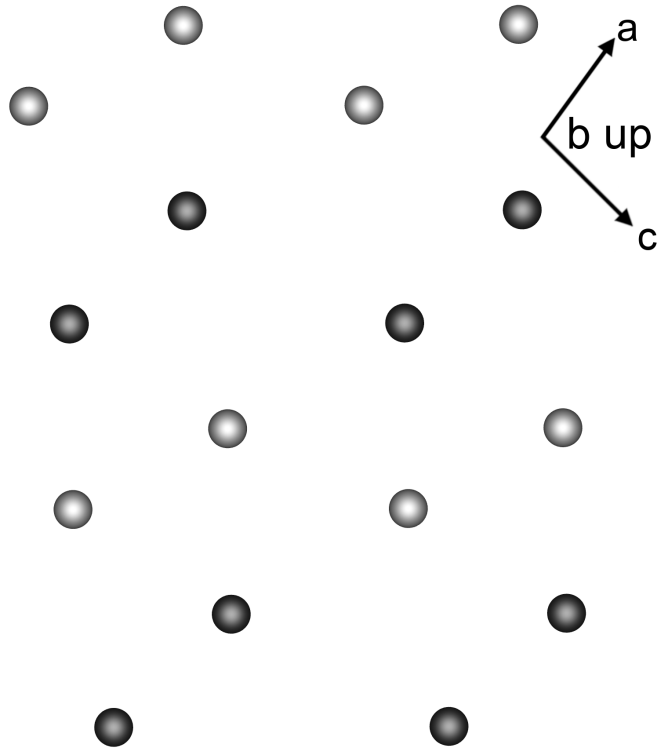

Fig. D.2.7: Layered arrangement of bismuth atoms in $Bi_2(SO_4)_3$: Bi(1) dark grey, Bi(2) light grey.

Tab. D.2.5: Electrostatic calculations for $Bi(H_3O)(SO_4)_2$, $Bi(HSO_4)_3$ and $Bi_2(SO_4)_3$: the MAPLE values are compared to the sum of the MAPLE values of respective simple compounds; a deviation below 1% is the empirical benchmark for electrostatic consistency.

$Bi(H_3O)(SO_4)_2$ (SC-XRD) MAPLE = 75391 kJ mol^{-1}	$\frac{3}{2}\,H_2O^{[469]} + \frac{1}{2}\,Bi_2O_3^{[486]} + 2\,SO_3^{[497]}$ MAPLE = 74575 kJ mol^{-1} $\Delta = 1.1\%$
$Bi(H_3O)(SO_4)_2$ (SC-XRD) MAPLE = 73161 kJ mol^{-1}	$\frac{3}{2}\,H_2O^{[469]} + \frac{1}{2}\,Bi_2O_3^{[486]} + 2\,SO_3^{[497]}$ MAPLE = 74575 kJ mol^{-1} $\Delta = 1.9\%$
$Bi(HSO_4)_3$ (SC-XRD) MAPLE = 105577 kJ mol^{-1}	$\frac{3}{2}\,H_2O^{[469]} + \frac{1}{2}\,Bi_2O_3^{[486]} + 3\,SO_3^{[497]}$ MAPLE = 104506 kJ mol^{-1} $\Delta = 1.0\%$
$Bi_2(SO_4)_3$ (SC-XRD) MAPLE = 105377 kJ mol^{-1}	$Bi_2O_3^{[486]} + 3\,SO_3^{[497]}$ MAPLE = 104171 kJ mol^{-1} $\Delta = 1.0\%$

Tab. D.2.6: ECoN derived by MAPLE-calculations for Bi atoms in $Bi(H_3O)(SO_4)_2$ (SC-XRD)

Atom	x	y	z	Distance / pm	ECoN(1)	ECoN(3)
Central atom						
Bi1	0.6448	0.1561	0.1438			
Ligand						
O13	0.7512	0.2190	0.4152	234.724	1.251	1.283
O23	0.6670	-0.1597	0.2616	235.409	1.234	1.266
O14	0.8361	0.0740	0.1303	239.653	1.129	1.161
O21	0.5246	0.2050	0.3443	244.636	1.005	1.038
O22	0.6452	0.5150	0.1574	245.395	0.987	1.020
O24	0.5884	-0.0980	-0.0835	252.704	0.812	0.844
O13	0.7512	0.2810	-0.0848	264.078	0.563	0.593
O21	0.5246	0.2950	-0.1557	272.806	0.401	0.427
O24	0.4116	0.0980	0.0835	276.633	0.340	0.363
Next Ligand						
O12	0.8851	0.4640	0.3631	370.012	0	0

Tab. D.2.7: ECoN derived by MAPLE-calculations for Bi atoms in $Bi(HSO_4)_3$ (SC-XRD)

Atom	x	y	z	Distance / pm	ECoN(1)	ECoN(3)
Central atom						
Bi1	0.1111	0.7897	0.4117			
Ligand						
O12	-0.1349	0.6524	0.3116	229.492	1.286	1.316
O13	0.4520	0.5655	0.3671	233.247	1.191	1.222
O32	0.2363	0.8471	0.1975	233.676	1.180	1.211
O11	0.0813	0.6023	0.5891	243.903	0.924	0.956
O22	0.4939	0.7930	0.5567	248.401	0.815	0.847
O21	-0.3270	0.9795	0.3208	255.041	0.663	0.693
O23	0.1858	1.0628	0.3996	260.171	0.555	0.583
O23	-0.1858	0.9372	0.6004	261.885	0.520	0.548
Next Ligand						
O22	-0.5061	0.7930	0.5567	331.132	0.003	0.004

Tab. D.2.8: ECoN derived by MAPLE-calculations for Bi atoms in $Bi_2(SO_4)_3$ (SC-XRD)

Atom	x	y	z	Distance / pm	ECoN(1)	ECoN(4)
Central atom						
Bi1	0.5832	0.4208	0.2230			
Ligand						
O24	0.6517	0.6502	0.1203	217.026	1.322	1.432
O33	0.4365	0.5792	0.1311	224.868	1.114	1.230
O22	0.5653	0.1081	0.1002	229.529	0.992	1.109
O14	0.5631	0.8953	0.2892	247.668	0.553	0.660
O23	0.7617	0.5812	0.3155	257.866	0.358	0.448
O14	0.5631	-0.1047	0.2892	269.711	0.191	0.257
O23	0.7383	0.0812	0.1845	272.744	0.159	0.218
Next Ligand						
O11	0.5625	0.5970	0.4225	307.590	0.008	0.015
Central atom						
Bi2	0.1716	0.1454	0.0721			
Ligand						
O34	0.2510	0.5469	0.1186	220.877	1.390	1.453
O12	0.1421	0.4360	-0.0600	233.297	1.072	1.140
O21	0.2982	0.0143	-0.0160	235.897	1.005	1.073
O13	0.0464	0.5078	0.0988	245.269	0.773	0.841
O32	0.1315	0.0475	0.2289	247.585	0.719	0.785
O31	0.3340	-0.0287	0.1751	249.606	0.673	0.738
O11	0.0625	-0.0970	-0.0775	262.770	0.406	0.461
Next Ligand						
O34	0.2510	-0.4531	0.1186	304.837	0.026	0.036

Tab. D.2.9: VASP optimised unit cell parameters of $Bi(H_3O)(SO_4)_2$, $Bi(HSO_4)_3$ and $Bi_2(SO_4)_3$

	$Bi(H_3O)(SO_4)_2$	$Bi(HSO_4)_3$	$Bi_2(SO_4)_3$
a / pm	1205.96	506.66	1347.63
b / pm	688.35	929.66	487.16
c / pm	817.83	1053.62	1474.29
α / °	90	84.586	90
β / °	102.378	86.518	101.334
γ / °	90	73.946	90
Volume / $10^6\,pm^3$	663.13	474.48	949.02

Tab. D.2.10: Band gap information for $Bi(H_3O)(SO_4)_2$, $Bi(HSO_4)_3$ and $Bi_2(SO_4)_3$ determined by DFT calculations

	E_g / eV	Band gap type	k-point of transition
$Bi(H_3O)(SO_4)_2$	5.806	indirect	0.5,0,0 → 0,0.5,0
$Bi(HSO_4)_3$	5.506	indirect	0,0.5,0.5 → 0.5,0.5,0
$Bi_2(SO_4)_3$	5.617	indirect	0.5,0.5,0.5 → 0.5,0,0.5

Tab. D.2.11: Experimental and theoretically predicted mass losses in wt.-% for the thermogravimetric analysis of $Bi(H_3O)(SO_4)_2$, $Bi(HSO_4)_3$ and $Bi_2(SO_4)_3$ depicted in Figure 7.2.9

Decomposition Steps for $Bi(H_3O)(SO_4)_2$	exp.	calc.
$Bi(H_3O)(SO_4)_2] \longrightarrow \frac{1}{2}\,Bi_2(SO_4)_3 + H_2O(g) + \frac{1}{2}\,SO_3(g)$	15.1	15.9
$Bi_2(SO_4)_3 \longrightarrow Bi_2O(SO_4)_2 + SO_3(g)$	24.6	25.5
$Bi_2O(SO_4)_2 \longrightarrow Bi_{26}O_{27}(SO_4)_{12} + SO_3(g) + O_2(g)$	36.1	35.8
$Bi_{26}O_{27}(SO_4)_{12} \longrightarrow Bi_{14}O_{16}(SO_4)_5 + SO_3(g) + O_2(g)$	37.6	37.7
$Bi_{14}O_{16}(SO_4)_5 \longrightarrow Bi_2O_3 + SO_3(g) + O_2(g)$	43.7	44.5
Decomposition Steps for $Bi(HSO_4)_3$	**exp.**	**calc.**
$95\,\%\,Bi(HSO_4)_3 + 5\,\%\,Bi(H_3O)(SO_4)_2 \longrightarrow \frac{1}{2}\,Bi_2(SO_4)_3 + H_2O(g) + SO_3(g)$	27.7	28.8
$Bi_2(SO_4)_3 \longrightarrow Bi_2O(SO_4)_2 + SO_3(g)$	35.7	36.9
$Bi_2O(SO_4)_2 \longrightarrow Bi_{26}O_{27}(SO_4)_{12} + SO_3(g) + O_2(g)$	46.0	45.6
$Bi_{26}O_{27}(SO_4)_{12} \longrightarrow Bi_{14}O_{16}(SO_4)_5 + SO_3(g) + O_2(g)$	47.6	47.3
$Bi_{14}O_{16}(SO_4)_5 \longrightarrow Bi_2O_3 + SO_3(g) + O_2(g)$	52.5	53.0
Decomposition Steps for $Bi_2(SO_4)_3$	**exp.**	**calc.**
$Bi_2(SO_4)_3 \longrightarrow Bi_2O(SO_4)_2 + SO_3(g)$	10.6	11.3
$Bi_2O(SO_4)_2 \longrightarrow Bi_{26}O_{27}(SO_4)_{12} + SO_3(g) + O_2(g)$	23.5	23.6
$Bi_{26}O_{27}(SO_4)_{12} \longrightarrow Bi_{14}O_{16}(SO_4)_5 + SO_3(g) + O_2(g)$	26.1	25.9
$Bi_{14}O_{16}(SO_4)_5 \longrightarrow Bi_2O_3 + SO_3(g) + O_2(g)$	52.5	53.0

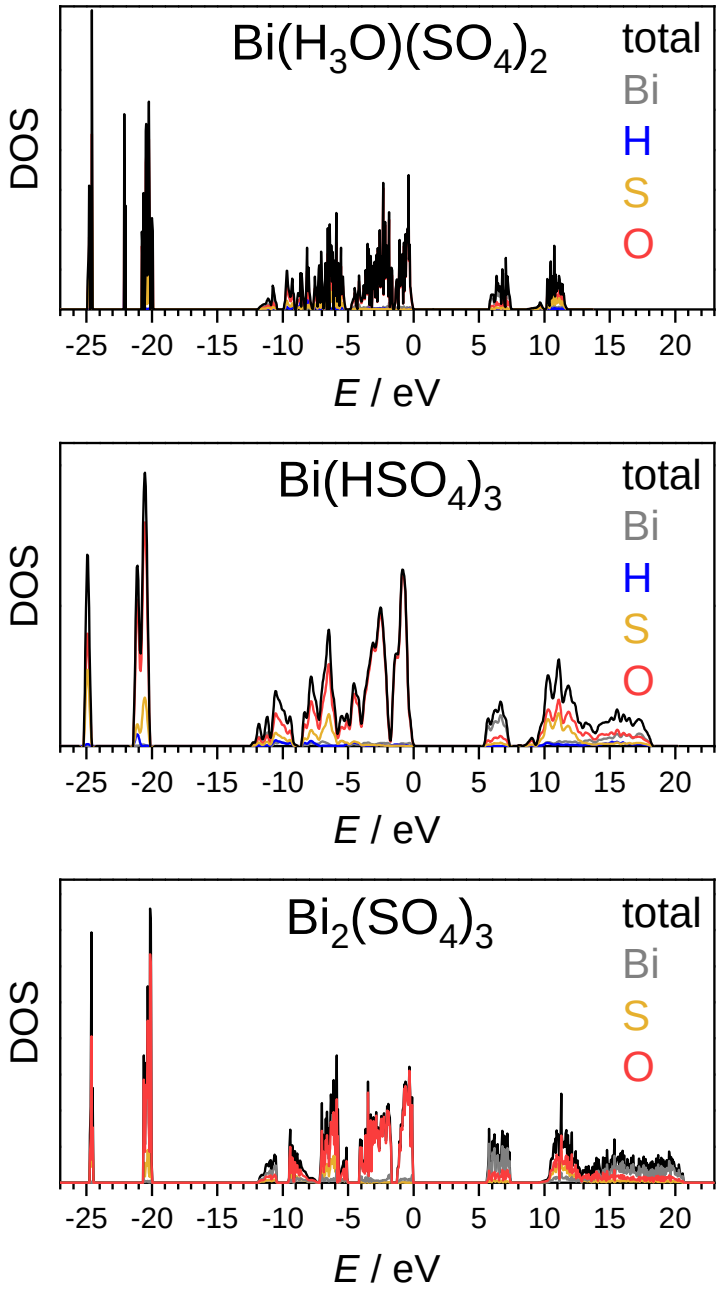

Fig. D.2.8: Total density of states calculated for $Bi(H_3O)(SO_4)_2$, $Bi(HSO_4)_3$ and $Bi_2(SO_4)_3$ (from top to bottom): The total density of states is shown by the black line, while the partial DOS is shown grey, blue, yellow and red for Bi, H, S, and O, respectively; The Fermi level is set to 0 eV.

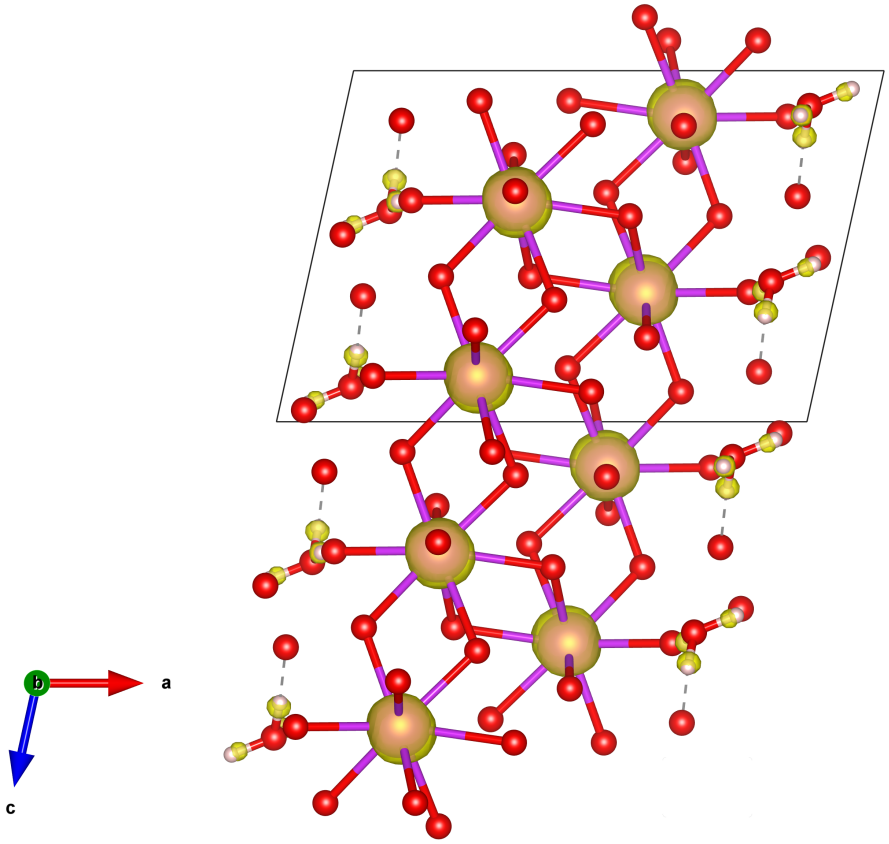

Fig. D.2.9: ELF results for $Bi(H_3O)(SO_4)_2$ showing the excerpt of one Bi-O double layer; oxygen red, bismuth violet, hydrogen white, ELF semi-transparent yellow.

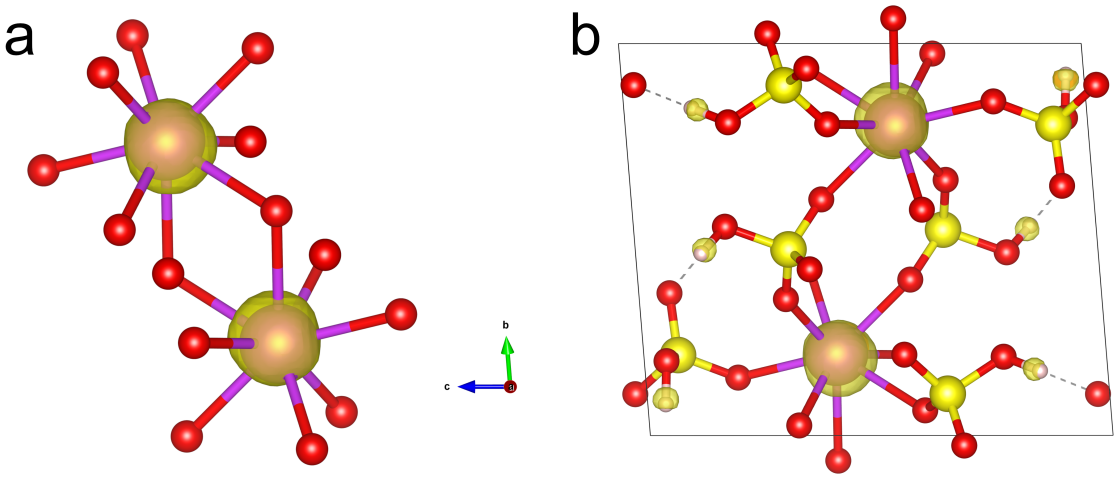

Fig. D.2.10: ELF results for $Bi(HSO_4)_3$ displayed for one dimer of two BiO_8 polyhedra in (a) and for the whole unit cell in (b); oxygen red, bismuth violet, sulfur yellow, hydrogen white, ELF semi-transparent yellow.

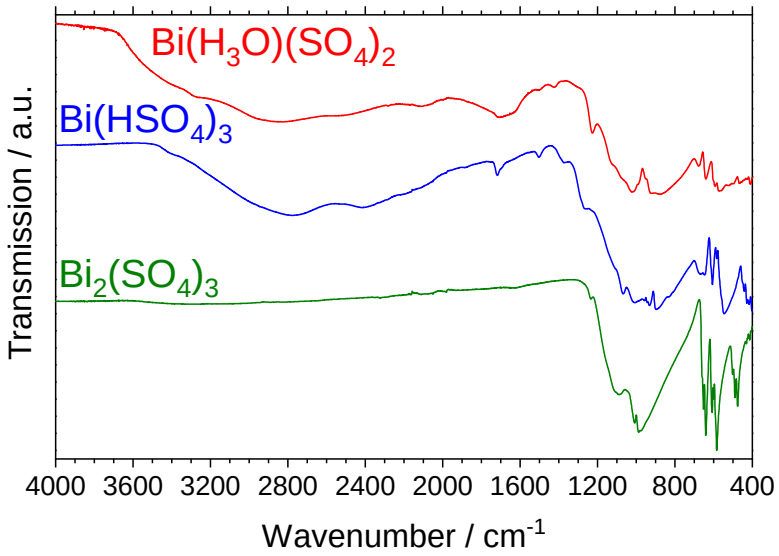

Fig. D.2.11: Full FT-IR spectra of $Bi(H_3O)(SO_4)_2$, $Bi(HSO_4)_3$ and $Bi_2(SO_4)_3$

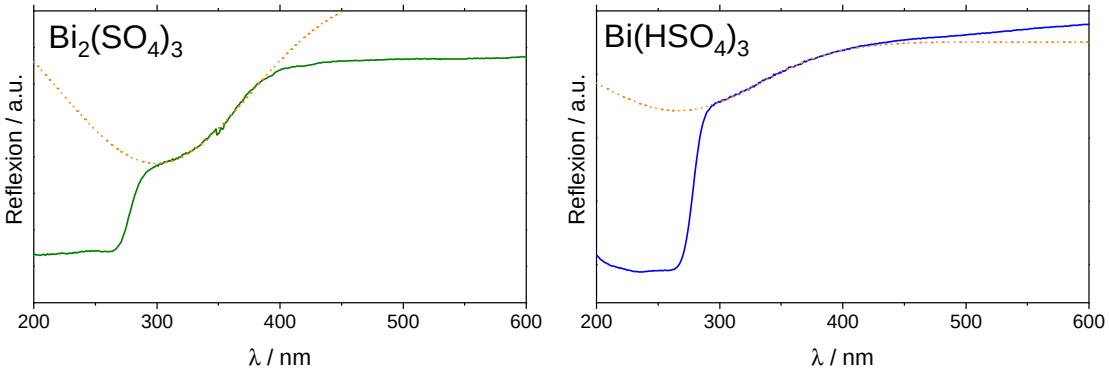

Fig. D.2.12: Gaussian fit of the A band (orange) in the UV-Vis spectra of $Bi(HSO_4)_3$ (left) and $Bi_2(SO_4)_3$ (right).

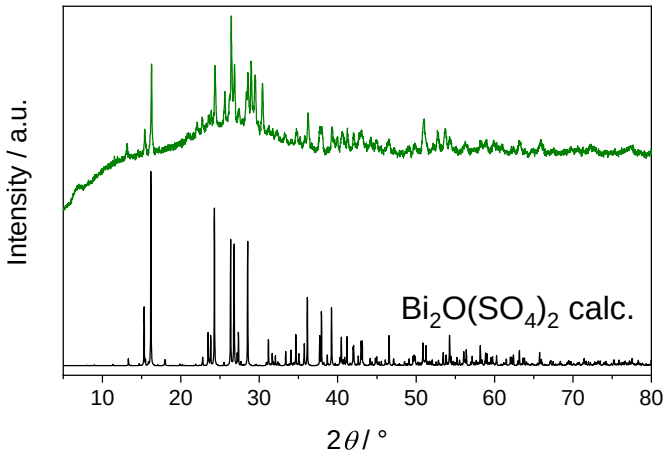

Fig. D.2.13: PXRD pattern of $Bi_2(SO_4)_3$ heated at 500°C for 24 h compared to a calculated pattern for $Bi_2O(SO_4)_2$.[408]

E Supplementary Material to Chapter 8

E.1 $Bi_2[B_2(SO_4)_6]$

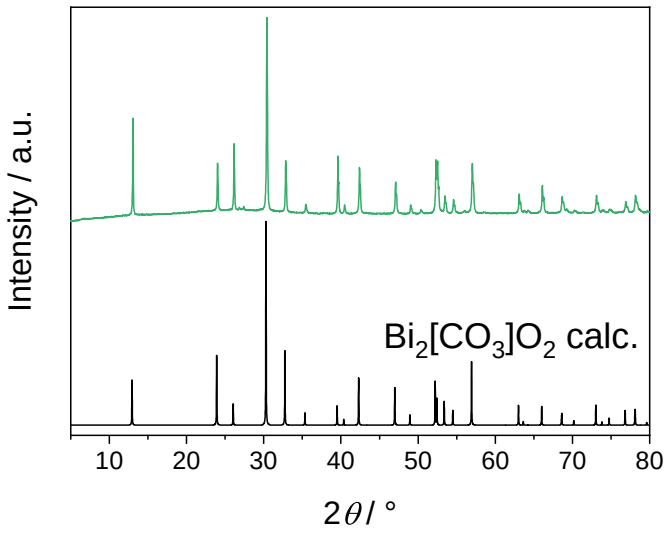

Fig. E.1.1: PXRD pattern of $Bi_2[CO_3]O_2$ (top) compared to a calculated pattern (bottom).[429]

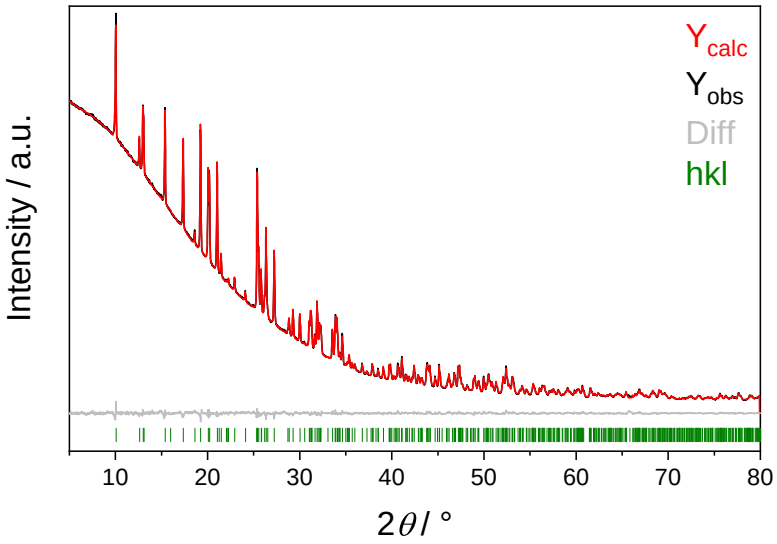

Fig. E.1.2: Rietveld-refinement of $Bi_2[B_2(SO_4)_6]$

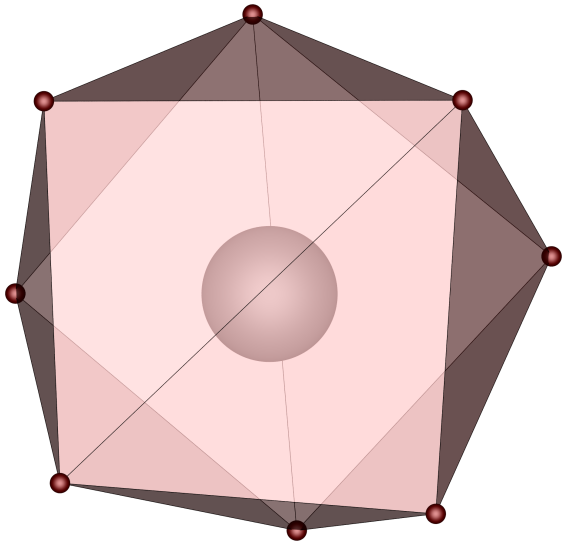

Fig. E.1.3: Slightly distorted square antiprismatic coordination polyhedron BiO_8 in $Bi_2[B_2(SO_4)_6]$

Tab. E.1.1: Crystal data and structure refinements of $Bi_2[B_2(SO_4)_6]$ determined from SC-XRD and PXRD data via Rietveld refinement using the structure from SC-XRD as starting model; the respective standard deviations are given in parentheses.

	SC-XRD	Rietveld
CSD-No.	2025945	
M / g mol^{-1}	659.08	
Crystal size / mm^3	$0.13 \times 0.10 \times 0.05$	
Temperature / K	200(2)	300(2)
Space group	$C2/c$ (No. 15)	
a / pm	1356.87(19)	1361.66(2)
b / pm	1149.04(16)	1149.44(1)
c / pm	1110.61(15)	1108.89(1)
β / °	93.253(6)	93.295(1)
Volume / 10^6 pm^3	1728.8(4)	1732.71(4)
Z	4	
ρ_{calcd} / g cm^3	3.903	3.895
Absorption coefficient μ / mm$^{\check{}}$1	21.19	
$F(000)$ / e	1856	
Radiation; wavelength λ / Å	Mo-K_α; 0.71073	Cu$K\alpha$; 1.54184
Diffractometer	Bruker D8 Venture	Bruker D8 Advance
Θ range / °	2.324-32.491	2.5-40
Absorption correction	multi-scan	
Transmission (min; max)	0.5437; 0.7516	
Index range $h \mid k \mid l$	$\pm20 \mid \pm17 \mid \pm16$	
Reflections collected	34076	
Independent reflections	3127	
Obs. reflections $[I > 2\sigma(I)]$ / $\lvert F_K\rvert^2 > 0$	3038	533
Refined parameters	155	31
R_{int} / R_{Bragg}	0.043	0.008
R_1 / R_p	0.016	0.007
wR_2 / R_{wp}	0.035	0.011
GOF	1.097	2.3
Residual electron density (max; min) / e^-Å^{-3}	1.65; -1.57	

Tab. E.1.2: Wyckoff symbols, refined atomic coordinates and isotropic displacement parameters U_{eq} / Å^2 in $Bi_2[B_2(SO_4)_6]$; estimated standard deviations in parentheses.

Atom	Wyckoff position	x	y	z	U_{eq}
Bi1	$8f$	0.18433(2)	0.05474(2)	0.15481(2)	0.00647(3)
S1	$8f$	0.37337(4)	0.01489(4)	-0.07896(4)	0.00600(8)
S2	$8f$	0.13792(4)	0.20042(4)	-0.14130(4)	0.00535(8)
S3	$8f$	0.07504(4)	0.15046(4)	0.42158(4)	0.00617(8)
O11	$8f$	0.45881(12)	-0.06746(13)	-0.09894(14)	0.0076(3)
O12	$8f$	0.42194(12)	0.13323(13)	-0.06031(14)	0.0097(3)
O13	$8f$	0.32402(13)	-0.01826(15)	0.02692(15)	0.0129(3)
O14	$8f$	0.31557(12)	-0.02404(15)	0.30963(15)	0.0116(3)
O21	$8f$	0.03632(12)	0.25303(14)	-0.12083(14)	0.0097(3)
O22	$8f$	0.18133(12)	0.16077(14)	-0.02552(13)	0.0096(3)
O23	$8f$	0.11666(12)	-0.10666(14)	0.27479(15)	0.0121(3)
O24	$8f$	0.19796(13)	0.29146(15)	-0.19158(14)	0.0130(3)
O31	$8f$	0.15076(12)	0.14891(16)	0.33465(15)	0.0127(3)
O32	$8f$	0.57890(12)	0.22416(14)	-0.03143(15)	0.0107(3)
O33	$8f$	0.02373(12)	0.13069(16)	0.13210(14)	0.0124(3)
O34	$8f$	0.09742(16)	-0.07353(16)	0.02183(17)	0.0181(4)
B1	$8f$	0.50014(16)	0.16862(19)	0.03124(19)	0.0062(3)

Tab. E.1.3: Anisotropic displacement parameters U_{ij} / Å^2 in $Bi_2[B_2(SO_4)_6]$; estimated standard deviations in parentheses.

Atom	U_{11}	U_{22}	U_{33}	U_{23}	U_{13}	U_{12}
Bi1	0.00591(4)	0.00684(4)	0.00673(4)	-0.00006(2)	0.00079(2)	0.00009(2)
S1	0.00508(19)	0.00568(19)	0.00720(18)	-0.00035(14)	-0.00011(14)	0.00072(15)
S2	0.00517(19)	0.00514(18)	0.00581(17)	-0.00027(14)	0.00072(14)	0.00033(14)
S3	0.0062(2)	0.00619(19)	0.00614(18)	-0.00088(14)	0.00089(14)	0.00042(15)
O11	0.0068(6)	0.0072(6)	0.0090(6)	0.0012(5)	0.0023(5)	0.0030(5)
O12	0.0118(7)	0.0049(6)	0.0118(6)	-0.0007(5)	-0.0051(5)	-0.0007(5)
O13	0.0124(7)	0.0133(7)	0.0137(7)	0.0031(5)	0.0074(6)	0.0044(6)
O14	0.0099(7)	0.0117(7)	0.0125(7)	0.0019(6)	-0.0055(5)	-0.0007(6)
O21	0.0065(6)	0.0120(7)	0.0104(6)	-0.0043(5)	-0.0003(5)	0.0034(5)
O22	0.0087(7)	0.0117(7)	0.0083(6)	0.0035(5)	0.0002(5)	0.0015(5)
O23	0.0109(7)	0.0108(7)	0.0147(7)	0.0078(5)	-0.0007(5)	-0.0025(5)
O24	0.0128(7)	0.0145(7)	0.0116(6)	0.0041(5)	-0.0003(5)	-0.0072(6)
O31	0.0083(7)	0.0183(8)	0.0122(7)	-0.0071(6)	0.0052(5)	-0.0020(6)
O32	0.0097(7)	0.0069(6)	0.0162(7)	0.0039(5)	0.0050(5)	0.0007(5)
O33	0.0069(7)	0.0194(8)	0.0111(6)	0.0031(6)	0.0014(5)	0.0051(6)
O34	0.0234(10)	0.0158(8)	0.0152(8)	-0.0061(6)	0.0010(7)	-0.0072(7)
B1	0.0053(8)	0.0052(8)	0.0081(8)	0.0001(6)	0.0013(7)	0.0001(7)

Tab. E.1.4: Electrostatic calculations for $Bi_2[B_2(SO_4)_6]$.

$Bi_2[B_2(SO_4)_6]$	$Bi_2(SO_4)_3 + B_2O_3$[501] +3 SO_3[497]
MAPLE = 218847 kJ mol^{-1}	MAPLE = 217115 kJ mol^{-1}
$\Delta = 0.8\%$	

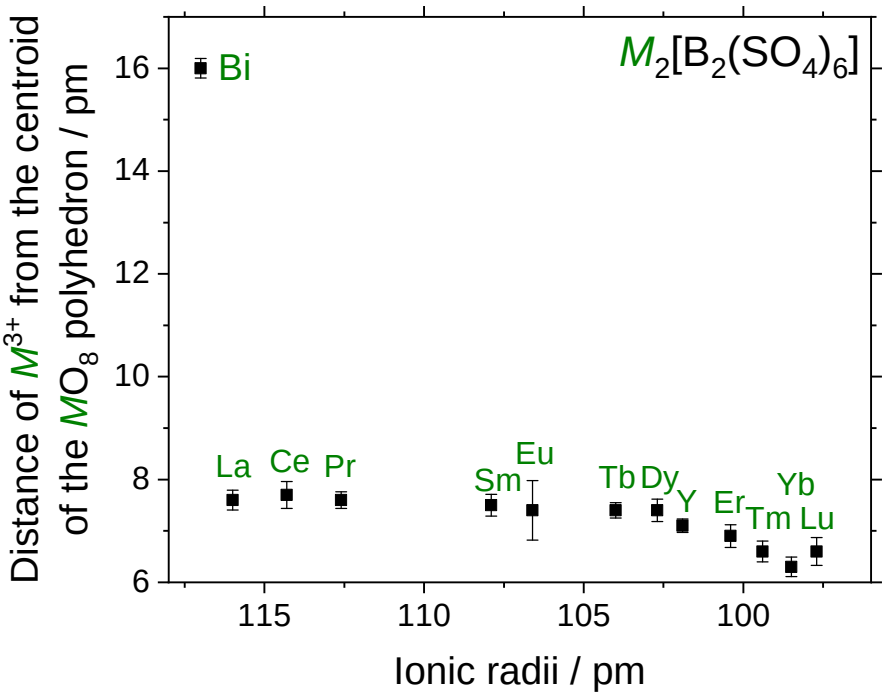

Fig. E.1.4: Distance R_c of the M^{3+} cation from the centroid of the MO_8 polyhedron in $M_2[B_2(SO_4)_6]$ (M = Bi, La, Ce, Pr, Sm, Eu, Tb, Dy, Er, Tm, Yb, Lu, Y)[95] plotted against the ionic radii of M^{3+}: the standard deviation represented as error bars was estimated by the standard deviation of the M-O distances determined by SC-XRD.

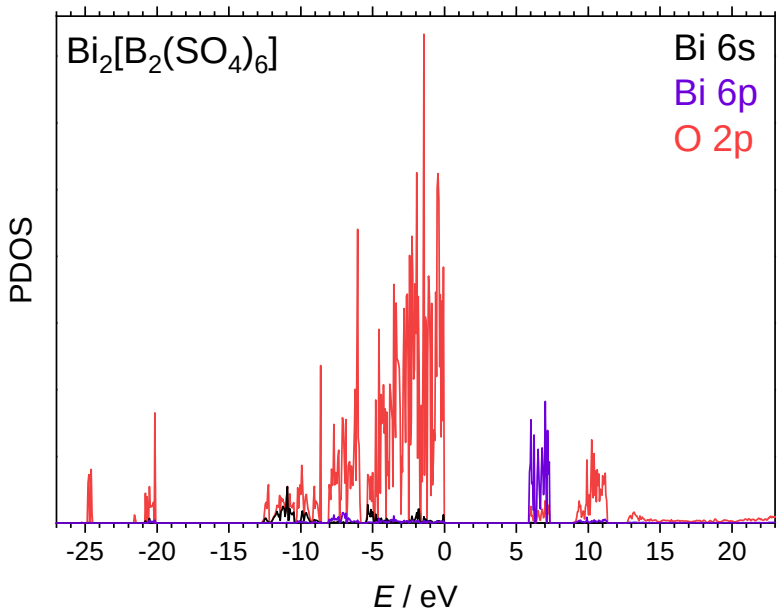

Fig. E.1.5: Partial density of states of $Bi_2[B_2(SO_4)_6]$ shown in black, violet and red for the Bi 6s, Bi 6p and O 2p orbitals, respectively.

Tab. E.1.5: ECoN derived by MAPLE-calculations for Bi atoms in $Bi_2[B_2(SO_4)_6]$

Atom	x	y	z	Distance / pm	ECoN(1)	ECoN(3)
Central atom						
Bi1	0.1843	0.0547	0.1548			
Ligand						
O31	0.1508	0.1489	0.3347	233.899	1.156	1.165
O22	0.1813	0.1608	-0.0255	234.260	1.147	1.155
O33	0.0237	0.1307	0.1321	234.765	1.134	1.143
O34	0.0974	-0.0735	0.0218	235.510	1.115	1.124
O24	0.3020	0.2085	0.1916	240.141	0.998	1.007
O23	0.1167	-0.1067	0.2748	248.935	0.784	0.793
O14	0.3156	-0.0240	0.3096	256.895	0.606	0.614
O13	0.3240	-0.0183	0.0269	257.277	0.598	0.606
Next Ligand						
O33	-0.0237	0.1307	0.3679	388.466	0	0

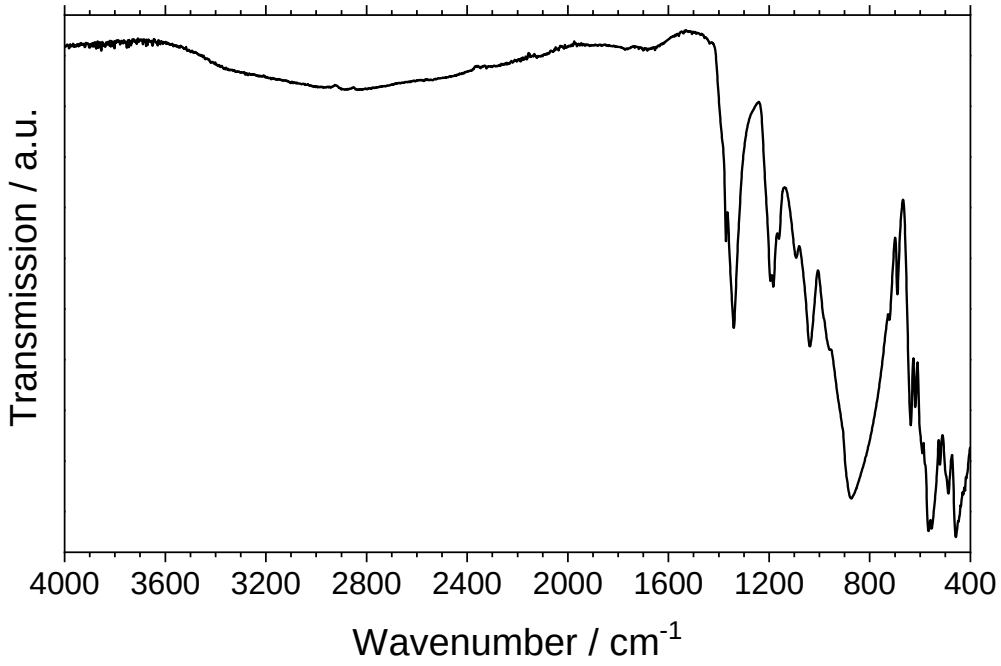

Fig. E.1.6: Infrared spectrum of $Bi_2[B_2(SO_4)_6]$: the broad bands at high wavelength can be assigned to O-H vibrations (centred at $2800\,\mathrm{cm}^{-1}$ and $1700\,\mathrm{cm}^{-1}$) presumably related to the formation of sulfuric acid on the surface of the samples reacting with ambient moisture.[419,420]

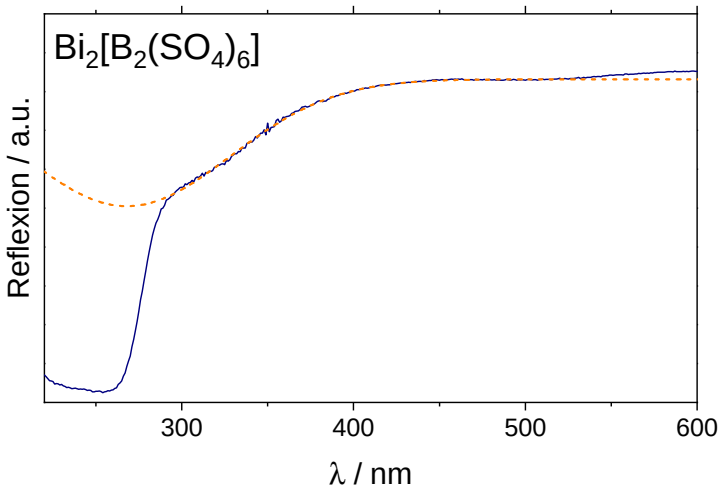

Fig. E.1.7: Gaussian fit of the A band in the UV-Vis spectrum of $Bi_2[B_2(SO_4)_6]$

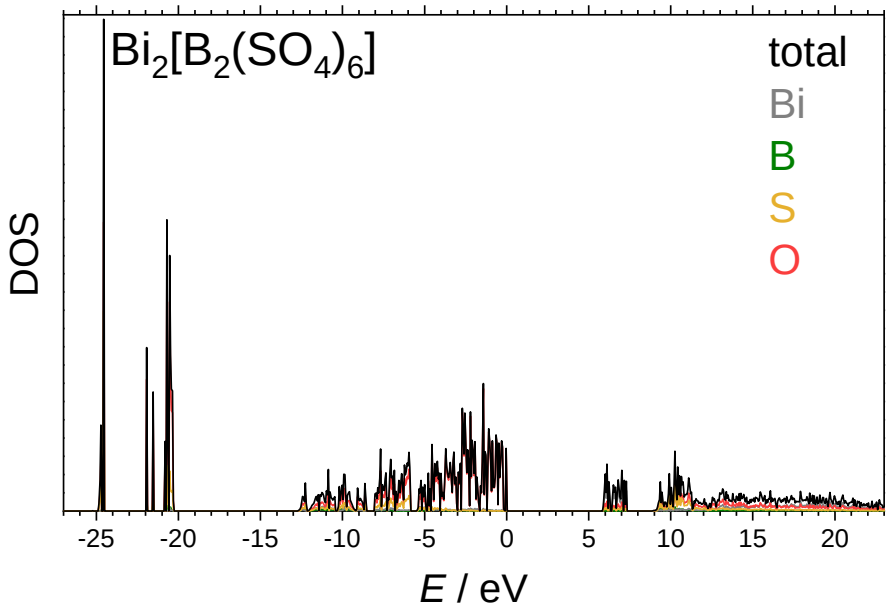

Fig. E.1.8: Total density of states calculated for $Bi_2[B_2(SO_4)_6]$: The total density of states is shown by the black line, while the partial DOS is shown grey, blue, green, yellow and red for Bi, H, B, S, and O, respectively; The Fermi level is set to 0 eV.

E.2 BiX[B(SO$_4$)$_2$]$_4$ (X = H$_3$O$^+$, NO$_2^+$ and NH$_4^+$)

Tab. E.2.1: Wyckoff symbols, refined atomic coordinates and isotropic displacement parameters U_{eq} / Å^2 in Bi(H$_3$O)[B(SO$_4$)$_2$]$_4$; estimated standard deviations in parentheses.

Atom	Wyckoff position	x	y	z	U_{eq}	site occupancy
Bi1	2a	0	0	0	0.00671(6)	
S1	8g	0.73826(7)	0.13323(7)	0.16322(10)	0.00688(14)	1
S3	8g	0.02683(7)	0.20022(7)	0.32063(10)	0.00706(14)	1
O11	8g	0.8486(2)	0.1165(3)	0.0898(3)	0.0138(5)	1
O12	8g	0.6790(3)	0.0346(3)	0.2094(4)	0.0173(6)	1
O13	8g	0.7526(2)	0.2165(2)	0.3059(3)	0.0092(5)	1
O14	8g	0.1992(2)	0.3347(2)	0.9559(3)	0.0084(5)	1
O31	8g	0.0773(2)	0.1056(2)	0.2347(3)	0.0105(5)	1
O32	8g	0.9902(3)	0.2948(3)	0.2274(4)	0.0152(6)	1
O33	8g	0.7561(2)	0.1098(2)	0.5506(3)	0.0092(5)	1
O34	8g	0.9310(2)	0.1475(2)	0.4219(3)	0.0087(5)	1
B1	8g	0.8187(3)	0.1933(3)	0.4556(4)	0.0076(6)	1
O1	4f	0	$\frac{1}{2}$	0.483(2)	0.040(3)	0.5
H1	4f	0	$\frac{1}{2}$	0.362(2)	0.048	0.5
H2	8g	-0.067(3)	0.523(8)	0.545(4)	0.048	0.5

Tab. E.2.2: Anisotropic displacement parameters U_{ij} / Å^2 in Bi(H$_3$O)[B(SO$_4$)$_2$]$_4$; estimated standard deviations in parentheses.

Atom	U_{11}	U_{22}	U_{33}	U_{23}	U_{13}	U_{12}
Bi1	0.00702(7)	0.00702(7)	0.00610(8)	0	0	0
S1	0.0078(3)	0.0071(3)	0.0058(3)	0.0002(3)	-0.0006(3)	0.0017(3)
S3	0.0065(3)	0.0078(3)	0.0069(3)	-0.0006(3)	-0.0006(3)	0.0002(3)
O11	0.0097(12)	0.0207(14)	0.0111(11)	-0.0031(10)	0.0020(9)	0.0066(10)
O12	0.0230(16)	0.0090(13)	0.0199(14)	0.0042(11)	-0.0014(12)	-0.0019(12)
O13	0.0103(11)	0.0110(11)	0.0062(10)	-0.0021(9)	-0.0026(9)	0.0048(9)
O14	0.0095(11)	0.0087(10)	0.0069(10)	-0.0027(8)	-0.0016(8)	-0.0008(8)
O31	0.0090(11)	0.0138(12)	0.0086(10)	-0.0046(9)	0.0005(9)	0.0008(9)
O32	0.0141(14)	0.0123(13)	0.0194(14)	0.0060(11)	-0.0049(12)	0.0002(11)
O33	0.0078(10)	0.0092(11)	0.0107(10)	0.0030(8)	-0.0027(8)	0.0011(8)
O34	0.0055(11)	0.0109(12)	0.0096(11)	0.0012(9)	0.0025(9)	0.0029(9)
B1	0.0073(15)	0.0108(16)	0.0046(13)	0.0009(11)	0.0003(10)	0.0019(12)
O1	0.013(3)	0.032(5)	0.074(10)	0	0	-0.010(3)

Tab. E.2.3: Wyckoff symbols, refined atomic coordinates and isotropic displacement parameters U_{eq} / Å^2 in $Bi(NO_2)[B(SO_4)_2]_4$; estimated standard deviations in parentheses.

Atom	Wyckoff position	x	y	z	U_{eq}
Bi	$2a$	0	0	0	0.00540(4)
S1	$8g$	-0.19685(5)	0.02800(5)	0.32201(6)	0.00462(9)
O11	$8g$	-0.28966(18)	-0.0075(2)	0.2250(2)	0.0101(3)
O12	$8g$	-0.10220(16)	0.07821(17)	0.2382(2)	0.0080(3)
O13	$8g$	-0.24235(15)	0.10997(16)	0.4497(2)	0.0065(3)
O14	$8g$	-0.14729(16)	-0.06889(16)	0.4225(2)	0.0069(3)
S2	$8g$	-0.26083(5)	0.13300(5)	-0.16137(7)	0.00569(9)
O21	$8g$	-0.3180(2)	0.0349(2)	-0.2097(3)	0.0149(4)
O22	$8g$	-0.15159(18)	0.11829(19)	-0.0852(3)	0.0117(3)
O23	$8g$	-0.33488(16)	0.19959(16)	-0.0435(2)	0.0067(3)
O24	$8g$	-0.24527(16)	0.21695(16)	-0.3042(2)	0.0071(3)
B1	$8g$	-0.1804(2)	0.1943(2)	0.5460(3)	0.0060(4)
N1	$2d$	$-\frac{1}{2}$	0	$\frac{1}{4}$	0.0168(9)
O3	$4f$	$-\frac{1}{2}$	0	0.1133(5)	0.0208(6)

Tab. E.2.4: Anisotropic displacement parameters U_{ij} / Å^2 in $Bi(NO_2)[B(SO_4)_2]_4$; estimated standard deviations in parentheses.

Atom	U_{11}	U_{22}	U_{33}	U_{23}	U_{13}	U_{12}
Bi	0.00558(4)	0.00558(4)	0.00503(5)	0	0	0
S1	0.0051(2)	0.0051(2)	0.00362(17)	-0.00031(16)	0.00024(16)	-0.00025(17)
O11	0.0082(8)	0.0126(9)	0.0095(7)	-0.0028(7)	-0.0048(6)	-0.0011(7)
O12	0.0084(7)	0.0086(7)	0.0069(6)	0.0008(6)	0.0049(6)	-0.0010(6)
O13	0.0050(6)	0.0081(7)	0.0065(5)	-0.0038(5)	0.0004(5)	0.0002(5)
O14	0.0078(7)	0.0049(7)	0.0081(7)	0.0027(5)	-0.0021(6)	-0.0015(5)
S2	0.0069(2)	0.0054(2)	0.00482(18)	0.00017(16)	0.00063(17)	0.00191(17)
O21	0.0207(11)	0.0078(8)	0.0163(8)	-0.0055(7)	0.0029(8)	-0.0031(8)
O22	0.0087(8)	0.0166(9)	0.0098(7)	0.0045(7)	-0.0005(6)	0.0055(7)
O23	0.0070(7)	0.0069(7)	0.0062(5)	-0.0014(5)	0.0031(5)	0.0008(6)
O24	0.0096(7)	0.0078(7)	0.0038(6)	0.0008(6)	0.0019(6)	0.0034(6)
B1	0.0065(10)	0.0067(9)	0.0048(7)	-0.0008(7)	-0.0004(7)	0.0013(8)
N1	0.0101(12)	0.0101(12)	0.030(3)	0	0	0
O3	0.0138(14)	0.0216(16)	0.0270(16)	0	0	0.0002(12)

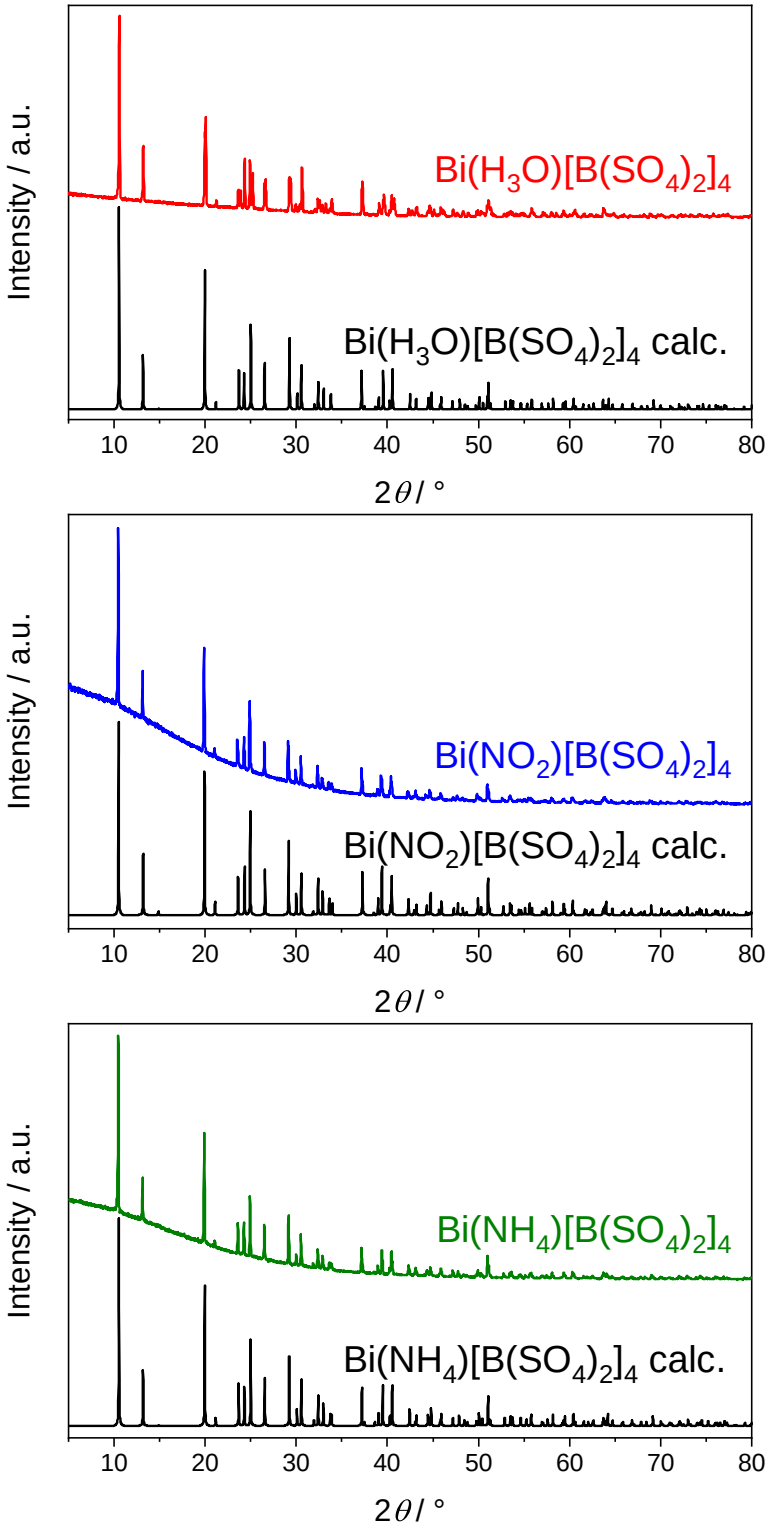

Fig. E.2.1: PXRD pattern of (from top to bottom) $Bi(H_3O)[B(SO_4)_2]_4$, $Bi(NO_2)[B(SO_4)_2]_4$ and $Bi(NH_4)[B(SO_4)_2]_4$ compared to calculated patterns from the respective SC-XRD.

Tab. E.2.5: Wyckoff symbols, refined atomic coordinates and isotropic displacement parameters U_{eq} / Å^2 in $Bi(NH_4)[B(SO_4)_2]_4$; estimated standard deviations in parentheses.

Atom	Wyckoff position	x	y	z	U_{eq}	site occupancy
Bi1	$2a$	$\frac{1}{2}$	$\frac{1}{2}$	$\frac{1}{2}$	0.00721(3)	1
S1	$8g$	0.47272(4)	0.29995(4)	0.82093(6)	0.00850(8)	1
O11	$8g$	0.5091(2)	0.20582(17)	0.7282(2)	0.0178(3)	1
O12	$8g$	0.42346(15)	0.39465(15)	0.73513(19)	0.0119(3)	1
O13	$8g$	0.38886(15)	0.25702(14)	0.94863(18)	0.0113(3)	1
O14	$8g$	0.56799(14)	0.35085(14)	0.92382(19)	0.0102(2)	1
S2	$8g$	0.13362(5)	0.26114(5)	0.83404(6)	0.01152(9)	1
O21	$8g$	0.03625(18)	0.3193(2)	0.7832(3)	0.0229(4)	1
O22	$8g$	0.1167(2)	0.15173(18)	0.9100(2)	0.0226(4)	1
O23	$8g$	0.19850(15)	0.33542(14)	0.95312(19)	0.0115(3)	1
O24	$8g$	0.21840(15)	0.24527(15)	0.69310(18)	0.0114(3)	1
B1	$8g$	0.3052(2)	0.3199(2)	1.0426(3)	0.0100(4)	1
N1	$4f$	0	$\frac{1}{2}$	1.0192(13)	0.0223(16)	0.5
H1	$8g$	0.013(6)	0.4323(15)	1.090(3)	0.027	0.5
H2	$8g$	-0.0674(15)	0.487(6)	0.947(3)	0.027	0.5

Tab. E.2.6: Anisotropic displacement parameters U_{ij} / Å^2 in $Bi(NH_4)[B(SO_4)_2]_4$; estimated standard deviations in parentheses.

Atom	U_{11}	U_{22}	U_{33}	U_{23}	U_{13}	U_{12}
Bi1	0.00751(3)	0.00751(3)	0.00661(4)	0	0	0
S1	0.0108(2)	0.00891(19)	0.00575(16)	-0.00004(13)	0.00026(14)	0.00004(15)
O11	0.0250(10)	0.0142(8)	0.0142(7)	-0.0067(6)	0.0051(7)	-0.0003(7)
O12	0.0103(6)	0.0155(7)	0.0098(6)	0.0058(5)	-0.0009(5)	0.0003(5)
O13	0.0157(7)	0.0091(6)	0.0091(5)	0.0008(4)	0.0036(5)	-0.0022(5)
O14	0.0081(6)	0.0126(6)	0.0099(5)	-0.0023(5)	-0.0027(4)	0.0038(5)
S2	0.0127(2)	0.0150(2)	0.00682(17)	-0.00171(15)	0.00048(15)	-0.00702(17)
O21	0.0125(8)	0.0355(12)	0.0207(8)	-0.0086(8)	-0.0039(7)	-0.0003(8)
O22	0.0368(12)	0.0182(8)	0.0127(7)	-0.0015(6)	0.0083(7)	-0.0170(8)
O23	0.0137(7)	0.0126(7)	0.0082(5)	-0.0029(5)	-0.0023(5)	-0.0028(5)
O24	0.0136(7)	0.0147(7)	0.0061(5)	-0.0024(5)	0.0004(5)	-0.0059(5)
B1	0.0143(10)	0.0100(8)	0.0059(6)	0.0002(6)	0.0007(6)	-0.0049(7)
N1	0.018(2)	0.016(2)	0.033(5)	0	0	0.0045(18)

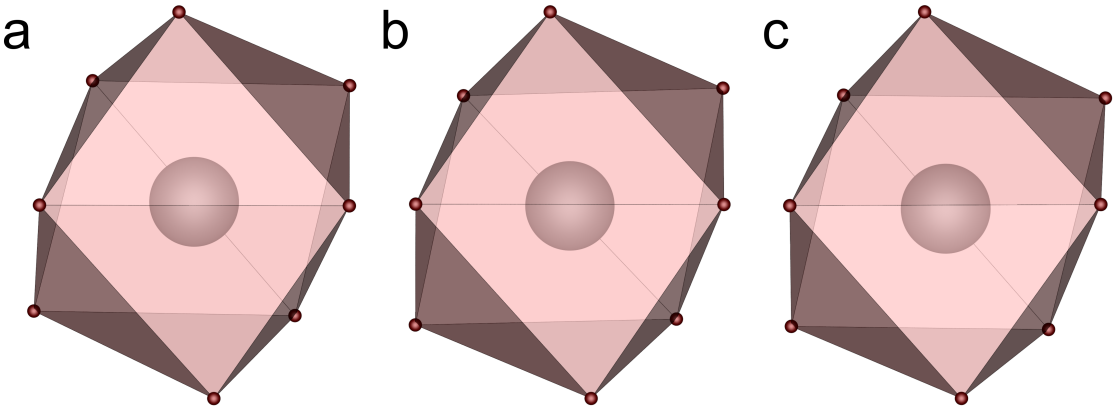

Fig. E.2.2: Distorted square antiprism BiO_8 in (a) $Bi(H_3O)[B(SO_4)_2]_4$, (b) $Bi(NO_2)[B(SO_4)_2]_4$ and (c) $Bi(NH_4)[B(SO_4)_2]_4$: bismuth atoms grey, oxygen atoms red.

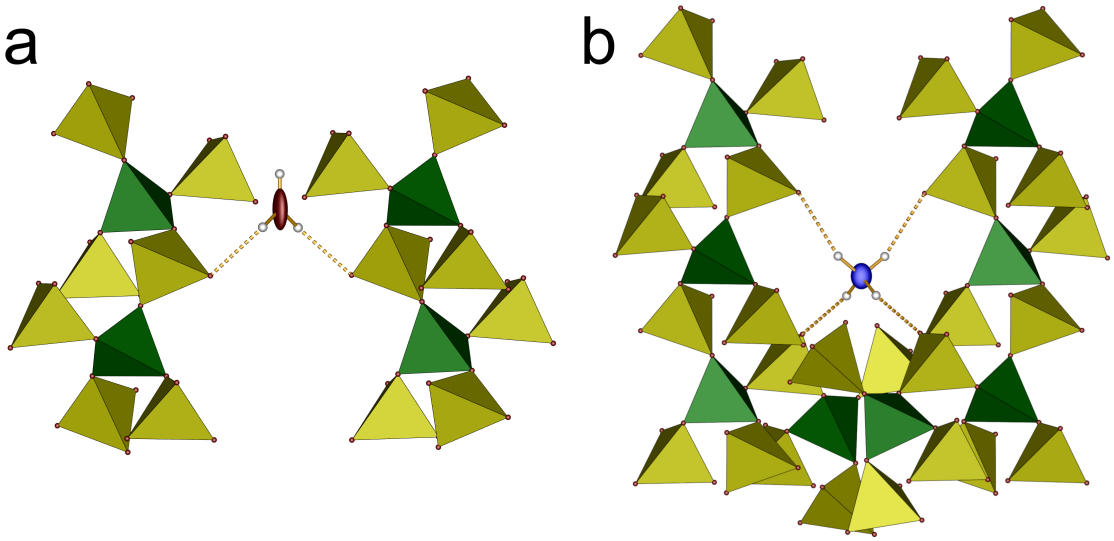

Fig. E.2.3: Hydrogen bonding in (a) $Bi(H_3O)[B(SO_4)_2]_4$ and (b) $Bi(NH_4)[B(SO_4)_2]_4$; borate tetrahedra green, sulfate tetrahedra yellow, oxygen atoms red, nitrogen atoms blue, hydrogen atoms white; ellipsoids for oxygen and nitrogen, respectively, are shown at 80% probability.

Tab. E.2.7: Selected interatomic distances (in pm) and angles (in °) in $Bi(H_3O)[B(SO_4)_2]_4$, $Bi(NO_2)[B(SO_4)_2]_4$ and $Bi(NH_4)[B(SO_4)_2]_4$; the respective standard deviations are given in parentheses.

	$Bi(H_3O)[B(SO_4)_2]_4$	$Bi(NO_2)[B(SO_4)_2]_4$	$Bi(NH_4)[B(SO_4)_2]_4$
Bi-O	237.9(3)-246.3(3)	239.2(2)-246.7(2)	238.8(2)-246.0(2)
$\sum$ IR (Bi-O)[216]		252	
Bi-Bi	814.9(1)	811.60(2)	813.6(1)
S-O_{br}[i]	151.7(3)-153.7(3)	152.3(2)-154.2(2)	152.0(2)-153.8(2)
S-O_{t1}[ii]	145.2(3)	144.6(2)-145.1(2)	144.7(2)-145.3(2)
S-O_{t2}[iii]	141.5(4)		140.9(2)-141.6(2)
S-O_{t3}[iv]	142.3(3)	140.8(3)-142.1(2)	
$\sum$ IR (S-O)[216]		147	
B-O	145.9(4)-147.7(4)	146.4(3)-147.0(3)	145.9(3)-147.5(3)
$\sum$ IR (B-O)[216]		146	
O-S-O	102.5(1)-118.5(2)	101.8(1)-117.9(1)	102.4(1)-118.7(1)
O-B-O	107.1(3)-113.4(3)	106.7(2)-113.8(2)	107.2(2)-113.1(2)

[i] The O_{br} bridging atoms are part of the B-O-S bridges. [ii] The terminal O_{t1} atoms coordinate the bismuth cations. [iii] The terminal O_{t2} atoms form hydrogen bonds with the oxonium and ammonium cations, respectively. [iv] The terminal O_{nc} atoms are non-coordinating.

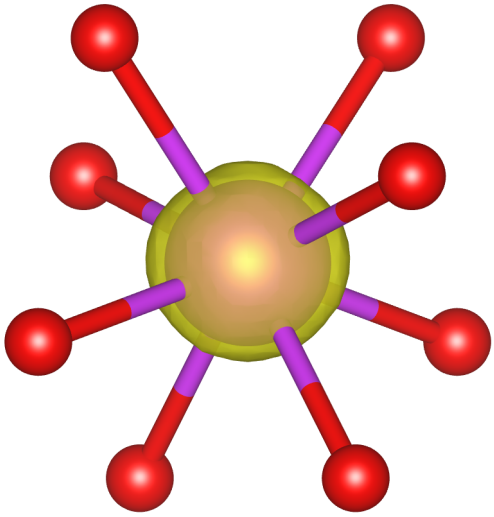

Fig. E.2.4: Detail of the ELF result for $Bi(H_3O)[B(SO_4)_2]_4$ showing the homogeneous electron density distribution around the bismuth atom; note, that the VASP optimised structure is shown; therein, the bismuth atom does no longer occupy the special Wyckoff position $2a$ (0 0 0) but the $4e$ position (0 0 0.0028). Similar behaviour is reported for the lead chalcogenides showing locally distorted variants of the rock-salt structure instead of the undistorted variant as previously believed;[433] this results in a non-zero eccentricity ϵ of 0.01; however, this is to small to have a stereochemical influence in an order of magnitude assessable by single-crystal XRD.

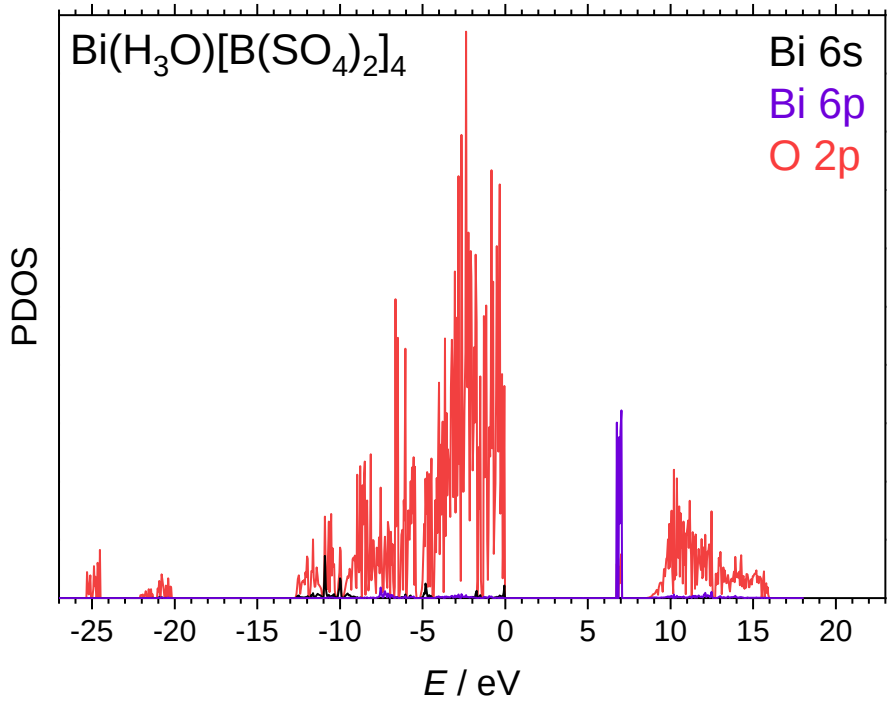

Fig. E.2.5: Partial density of states of $Bi(H_3O)[B(SO_4)_2]_4$ shown in black, violet and red for the Bi 6s, Bi 6p and O 2p orbitals, respectively.

Tab. E.2.8: Electrostatic calculations for $Bi(H_3O)[B(SO_4)_2]_4$, $Bi(NO_2)[B(SO_4)_2]_4$ and $Bi(NH_4)[B(SO_4)_2]_4$.

$Bi(H_3O)[B(SO_4)_2]_4$ MAPLE = 295527 kJ mol^{-1}	$\frac{1}{2}\,Bi_2(SO_4)_3 + 2\,B_2O_3$[501] +6.5 SO_3[497] + $\frac{3}{2}\,H_2O$[469] MAPLE = 298621 kJ mol^{-1} $\Delta = 1\%$
$Bi(NO_2)[B(SO_4)_2]_4$ MAPLE = 315375 kJ mol^{-1}	$\frac{1}{2}\,Bi_2(SO_4)_3 + 2\,B_2O_3$[501] +6.5 SO_3[497] + $\frac{1}{2}\,N_2O_5$[502] MAPLE = 315162 kJ mol^{-1} $\Delta = 0.1\%$
$Bi(NH_4)[B(SO_4)_2]_4$ MAPLE = 307870 kJ mol^{-1}	$\frac{1}{2}\,Bi_2(SO_4)_3 + 2\,B_2O_3$[501] +6.5 SO_3[497] + $\frac{1}{2}\,H_2O$[469] + NH_3[503] MAPLE = 305478 kJ mol^{-1} $\Delta = 0.8\%$

Tab. E.2.9: ECoN derived by MAPLE-calculations for Bi atoms in $Bi(H_3O)[B(SO_4)_2]_4$

Atom	x	y	z	Distance / pm	ECoN(1)	ECoN(2)
Central atom						
Bi1	0	0	0			
Ligand						
O11	-0.1165	-0.1514	-0.0898	238.043	1.091	1.092
O11	0.1514	-0.1165	0.0898	238.043	1.091	1.092
O11	0.1165	0.1514	-0.0898	238.043	1.091	1.092
O11	-0.1514	0.1165	0.0898	238.043	1.091	1.092
O31	-0.1056	0.0773	-0.2347	246.283	0.888	0.888
O31	-0.0773	-0.1056	0.2347	246.283	0.888	0.888
O31	0.1056	-0.0773	-0.2347	246.283	0.888	0.888
O31	0.0773	0.1056	0.2347	246.283	0.888	0.888
Next Ligand						
O34	-0.1475	-0.0690	-0.4219	394.302	0	0

Tab. E.2.10: ECoN derived by MAPLE-calculations for Bi atoms in $Bi(NO_2)[B(SO_4)_2]_4$

Atom	x	y	z	Distance / pm	ECoN(1)	ECoN(2)
Central atom						
Bi1	0	0	0			
Ligand						
O22	-0.1183	-0.1516	0.0852	239.184	1.084	1.085
O22	0.1516	-0.1183	-0.0852	239.184	1.084	1.085
O22	0.1183	0.1516	0.0852	239.184	1.084	1.085
O22	-0.1516	0.1183	-0.0852	239.184	1.084	1.085
O12	-0.0782	-0.1022	-0.2382	246.696	0.899	0.899
O12	0.1022	-0.0782	0.2382	246.696	0.899	0.899
O12	0.0782	0.1022	-0.2382	246.696	0.899	0.899
O12	-0.1022	0.0782	0.2382	246.696	0.899	0.899
Next Ligand						
O11	0.0075	-0.2897	-0.2250	390.388	0	0

Tab. E.2.11: ECoN derived by MAPLE-calculations for Bi atoms in $Bi(NH_4)[B(SO_4)_2]_4$

Atom	x	y	z	Distance / pm	ECoN(1)	ECoN(2)
Central atom						
Bi1	$\frac{1}{2}$	$\frac{1}{2}$	$\frac{1}{2}$			
Ligand						
O22	0.6517	0.3833	0.5900	238.796	1.081	1.081
O22	0.3483	0.6167	0.5900	238.796	1.081	1.081
O22	0.3833	0.3483	0.4100	238.796	1.081	1.081
O22	0.6167	0.6517	0.4100	238.796	1.081	1.081
O12	0.3947	0.5766	0.2649	245.973	0.903	0.904
O12	0.6054	0.4235	0.2649	245.973	0.903	0.904
O12	0.4235	0.3947	0.7351	245.973	0.903	0.904
O12	0.5766	0.6054	0.7351	245.973	0.903	0.904
Next Ligand						
O11	0.4909	0.7942	0.7282	395.770	0	0

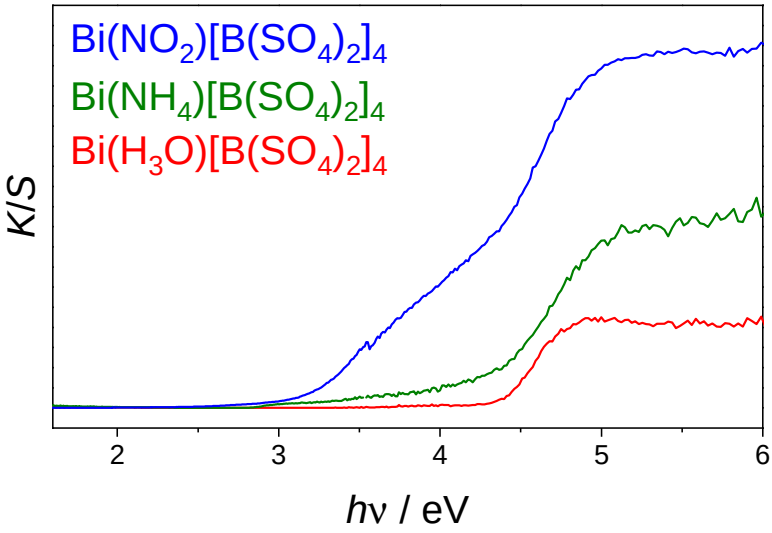

Fig. E.2.6: UV-Vis spectra of $Bi(H_3O)[B(SO_4)_2]_4$, $Bi(NO_2)[B(SO_4)_2]_4$ and $Bi(NH_4)[B(SO_4)_2]_4$

Tab. E.2.12: Experimental and theoretically predicted mass losses in wt.-% for the thermogravimetric analysis of $Bi(NH_4)[B(SO_4)_2]_4$ depicted in Figure 8.2.7

Decomposition Step	exp.	calc.
$Bi(NH_4)[B(SO_4)_2]_4 \longrightarrow \frac{1}{2}\,Bi_2[B_2(SO_4)_6] + \frac{3}{2}\,B_2O_3 + 5\,SO_3(g) + NH_3(g)$	43.3	42.6
$\frac{1}{2}\,Bi_2[B_2(SO_4)_6] + \frac{3}{2}\,B_2O_3 \longrightarrow \frac{1}{2}\,Bi_2(SO_4)_3 + 2\,B_2O_3 + 1.5\,SO_3(g)$	54.2	53.8
$\frac{1}{2}\,Bi_2(SO_4)_3 + 2\,B_2O_3 \longrightarrow \frac{1}{2}\,Bi_2O(SO_4)_2 + 2\,B_2O_3 + \frac{1}{2}\,SO_3(g)$	58.1	57.6
$\frac{1}{2}\,Bi_2O(SO_4)_2 + 2\,B_2O_3 \longrightarrow \frac{1}{2}\,Bi_2O_3 + 2\,B_2O_3 + SO_3(g)$	64.4	65.1

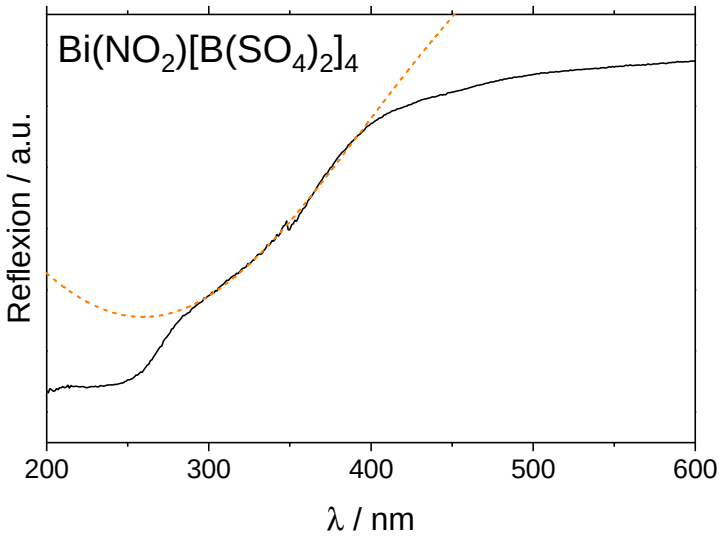

Fig. E.2.7: Gaussian fit of the A band in the UV-Vis spectrum of $Bi(NO_2)[B(SO_4)_2]_4$

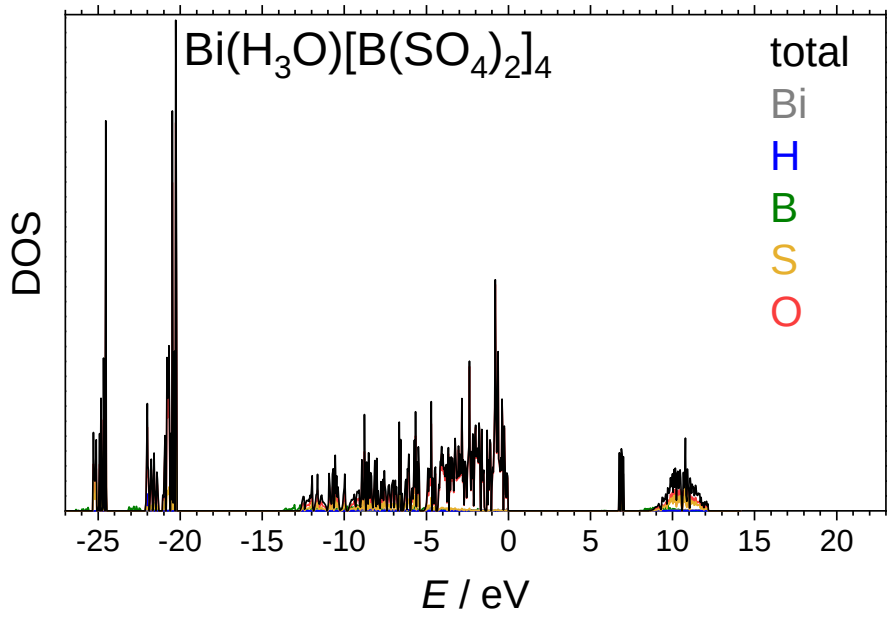

Fig. E.2.8: Total density of states calculated for $Bi(H_3O)[B(SO_4)_2]_4$: The total density of states is shown by the black line, while the partial DOS is shown grey, blue, green, yellow and red for Bi, H, B, S, and O, respectively; The Fermi level is set to 0 eV.

E.3 $(NH_4)Sb[B(SO_4)_2]_4$

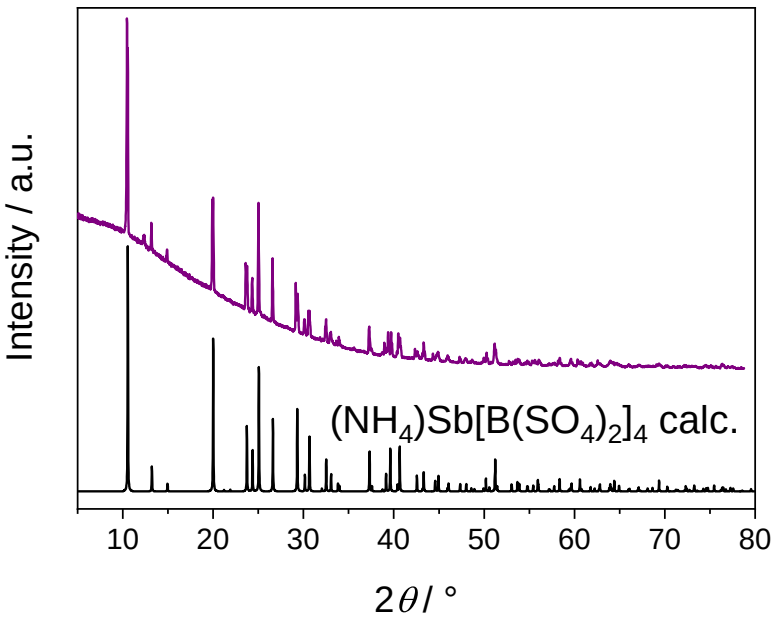

Fig. E.3.1: PXRD of $(NH_4)Sb[B(SO_4)_2]_4$

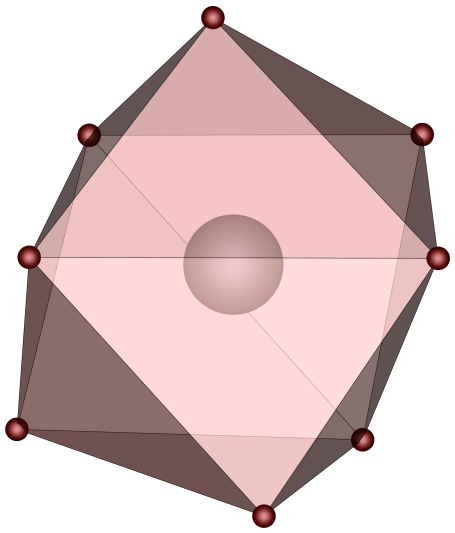

Fig. E.3.2: Distorted square antiprism SbO_8 in $(NH_4)Sb[B(SO_4)_2]_4$: antimony atom grey, oxygen atoms red.

Tab. E.3.1: Wyckoff symbols, refined atomic coordinates and isotropic displacement parameters U_{eq} / Å^2 in $(NH_4)Sb[B(SO_4)_2]_4$; estimated standard deviations in parentheses.

Atom	Wyckoff position	x	y	z	U_{eq}	site occupancy
Sb1	2*a*	0	-0.37877(8)	0	0.0094(2)	1
S1	4*c*	0.20040(15)	0.2873(2)	0.2286(2)	0.0077(3)	1
O11	4*c*	0.2965(5)	0.3775(8)	0.2864(8)	0.0147(12)	1
O12	4*c*	0.1073(5)	0.3766(7)	0.1861(7)	0.0122(8)	1
O13	4*c*	-0.2447(5)	0.1581(6)	-0.3575(6)	0.0083(11)	1
O14	4*c*	0.1481(5)	0.1829(7)	0.0814(7)	0.0087(10)	1
S2	4*c*	0.36724(15)	-0.0550(2)	0.1248(2)	0.0074(4)	1
O21	4*c*	0.4677(5)	-0.1028(8)	0.2811(7)	0.0142(12)	1
O22	4*c*	0.3794(5)	0.0226(7)	0.0265(7)	0.0122(8)	1
O23	4*c*	0.3022(5)	0.0642(7)	0.1367(7)	0.0097(11)	1
O24	4*c*	0.2159(5)	0.3017(7)	-0.0300(7)	0.0102(11)	1
S3	4*c*	0.02693(15)	-0.0727(2)	-0.1724(2)	0.0070(3)	1
O31	4*c*	-0.0082(5)	-0.1707(9)	-0.2999(8)	0.0156(13)	1
O32	4*c*	0.0748(5)	-0.1572(7)	-0.0265(7)	0.0106(11)	1
O33	4*c*	0.1133(5)	0.0531(7)	-0.1297(7)	0.0094(8)	1
O34	4*c*	0.0689(5)	0.0322(7)	0.2197(6)	0.0082(10)	1
S4	4*c*	-0.26206(15)	-0.2267(2)	-0.3927(2)	0.0079(3)	1
O41	4*c*	-0.3228(6)	-0.1742(8)	-0.3565(8)	0.0159(12)	1
O42	4*c*	-0.1514(5)	-0.2991(8)	-0.2612(7)	0.0153(12)	1
O43	4*c*	-0.1670(4)	0.1507(7)	-0.4717(6)	0.0094(8)	1
O44	4*c*	-0.2450(5)	-0.0886(7)	-0.4625(7)	0.0105(11)	1
B1	4*c*	0.1949(7)	0.1529(9)	0.0160(10)	0.0068(15)	1
B2	4*c*	-0.1811(7)	0.0631(11)	-0.3776(10)	0.0088(15)	1
N1	2*b*	$\frac{1}{2}$	0.1311(19)	$\frac{1}{2}$	0.012(2)	0.82(2)
H11	4*c*	0.522(10)	0.204(6)	0.587(7)	0.015	0.82(2)
H12	4*c*	0.565(4)	0.054(6)	0.547(12)	0.015	0.82(2)
N2	2*b*	$-\frac{1}{2}$	-0.411(6)	$-\frac{1}{2}$	0.012(2)	0.18(2)
H21	4*c*	-0.48(3)	-0.339(9)	-0.412(19)	0.015	0.18(2)
H22	4*c*	-0.433(9)	-0.483(9)	-0.45(4)	0.015	0.18(2)

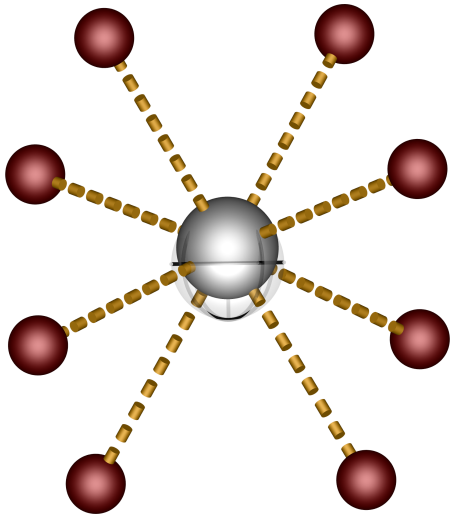

Fig. E.3.3: Stereochemical activity in $(NH_4)Sb[B(SO_4)_2]_4$: the SbO_8 polyhedron including the centroid (semi-transparent octant) is shown; antimony atom grey, oxygen atoms red.

Tab. E.3.2: Anisotropic displacement parameters U_{ij} / Å^2 in $(NH_4)Sb[B(SO_4)_2]_4$; estimated standard deviations in parentheses.

Atom	U_{11}	U_{22}	U_{33}	U_{23}	U_{13}	U_{12}
Sb1	0.0098(3)	0.0103(4)	0.0087(3)	0	0.0067(3)	0
S1	0.0088(8)	0.0073(8)	0.0076(7)	-0.0011(6)	0.0060(7)	-0.0010(7)
O11	0.011(3)	0.016(3)	0.014(3)	-0.006(2)	0.008(2)	-0.009(2)
O12	0.020(2)	0.0053(19)	0.020(2)	-0.0005(15)	0.0175(19)	-0.0018(15)
O13	0.010(2)	0.006(3)	0.009(2)	-0.0018(18)	0.007(2)	0.0004(18)
O14	0.010(2)	0.009(2)	0.010(2)	-0.003(2)	0.008(2)	-0.0005(19)
S2	0.0089(8)	0.0034(8)	0.0108(8)	0.0013(6)	0.0073(7)	0.0011(6)
O21	0.009(3)	0.011(3)	0.013(3)	-0.002(2)	0.005(2)	0.000(2)
O22	0.020(2)	0.0053(19)	0.020(2)	-0.0005(15)	0.0175(19)	-0.0018(15)
O23	0.009(2)	0.010(3)	0.009(2)	-0.002(2)	0.006(2)	0.001(2)
O24	0.009(2)	0.009(3)	0.013(3)	0.002(2)	0.008(2)	0.002(2)
S3	0.0074(7)	0.0055(9)	0.0077(8)	0.0002(6)	0.0052(7)	0.0005(6)
O31	0.015(3)	0.021(3)	0.013(3)	-0.010(2)	0.011(3)	-0.008(3)
O32	0.010(2)	0.008(3)	0.011(2)	0.001(2)	0.006(2)	0.001(2)
O33	0.0101(17)	0.0094(19)	0.0087(16)	0.0012(14)	0.0067(15)	0.0004(14)
O34	0.007(2)	0.006(3)	0.007(2)	-0.0014(19)	0.003(2)	-0.0028(19)
S4	0.0096(8)	0.0061(8)	0.0069(7)	0.0002(6)	0.0054(7)	0.0010(6)
O41	0.026(3)	0.011(3)	0.020(3)	-0.004(2)	0.020(3)	0.000(2)
O42	0.012(3)	0.010(3)	0.010(3)	0.001(2)	0.003(2)	0.002(2)
O43	0.0101(17)	0.0094(19)	0.0087(16)	0.0012(14)	0.0067(15)	0.0004(14)
O44	0.012(2)	0.011(3)	0.009(2)	0.003(2)	0.007(2)	0.001(2)
B1	0.009(3)	0.002(4)	0.011(3)	0.002(3)	0.008(3)	0.003(3)
B2	0.008(4)	0.009(4)	0.007(4)	0.001(3)	0.005(3)	0.002(3)
N1	0.015(5)	0.004(5)	0.012(4)	0	0.007(4)	0
N2	0.015(5)	0.004(5)	0.012(4)	0	0.007(4)	0

Tab. E.3.3: Selected interatomic distances (in pm) and angles (in °) in $(NH_4)Sb[B(SO_4)_2]_4$; the respective standard deviations are given in parentheses.

Sb-O	231.2(5)-253.7(6)
$\sum$ IR (Sb-O)[265]	228
Sb-Sb	927.36(5)
S-O_{br}[i]	151.2(5)-153.9(7)
S-O_{t1}[ii]	144.5(9)-146.4(8)
S-O_{t2}[iii]	142(1)-142.4(8)
$\sum$ IR (S-O)[216]	147
B-O	146(2)-147.4(9)
$\sum$ IR (B-O)[216]	146
O-S-O	102.3(3)-118.7(4)
O-B-O	103.0(7)-114.7(6)

[i] The O_{br} bridging atoms are part of the B-O-S bridges. [ii] The terminal O_{t1} atoms coordinate the bismuth cations. [iii] The terminal O_{t2} atoms form hydrogen bonds with the oxonium and ammonium cations, respectively.

Tab. E.3.4: Electrostatic calculations for $(NH_4)Sb[B(SO_4)_2]_4$.

$(NH_4)Sb[B(SO_4)_2]_4$	$\frac{1}{2}\,Sb_2(SO_4)_3$[416] + $2\,B_2O_3$[501] +6.5 SO_3[497] + $\frac{1}{2}\,H_2O$[469] + NH_3[503]
MAPLE = 307870 kJ mol^{-1}	MAPLE = 305812 kJ mol^{-1}
	$\Delta = 0.7\%$

Tab. E.3.5: ECoN derived by MAPLE-calculations for Bi atoms in $(NH_4)Sb[B(SO_4)_2]_4$

Atom	x	y	z	Distance / pm	ECoN(1)	ECoN(2)
Central atom						
Bi1	$\frac{1}{2}$	0.2965	$\frac{1}{2}$			
Ligand						
O42	0.3894	0.2153	0.2384	231.241	1.157	1.163
O42	0.6106	0.2153	0.7616	231.241	1.157	1.163
O12	0.3985	0.0741	0.4738	234.395	1.076	1.083
O12	0.6015	0.0741	0.5262	234.395	1.076	1.083
O32	0.6474	0.3930	0.5262	239.167	0.956	0.962
O32	0.3526	0.3930	0.4738	239.167	0.956	0.962
O22	0.5793	0.5389	0.6869	252.413	0.641	0.647
O22	0.4207	0.5389	0.3131	252.413	0.641	0.647
Next Ligand						
O11	0.7921	0.0852	0.8003	386.178	0	0

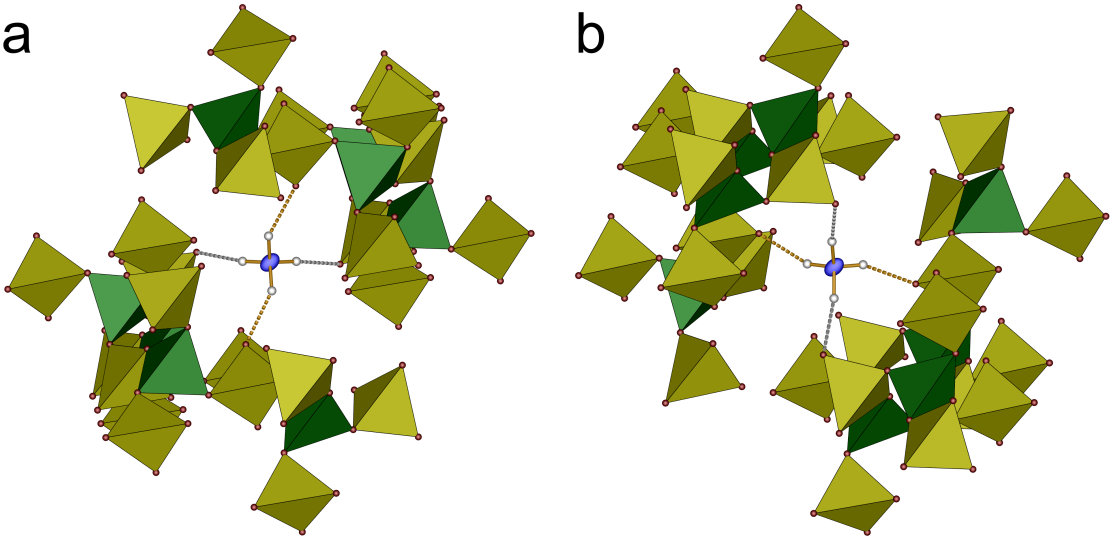

Fig. E.3.4: Hydrogen bonding in $(NH_4)Sb[B(SO_4)_2]_4$ for (a) $N1H_4^+$ and (b) $N2H_4^+$: borate tetrahedra green, sulfate tetrahedra yellow, oxygen atoms red, nitrogen atoms blue, hydrogen atoms white; ellipsoids for and nitrogen are shown at 80% probability.

Fig. E.3.5: Group–subgroup scheme in the Bärnighausen formalism[298,299] showing the symmetry relation between $Bi(NH_4)[B(SO_4)_2]_4$ and $(NH_4)Sb[B(SO_4)_2]_4$: Please note, that the change in centring is already incorporated into the unit cell transformation; further, the coordinates x, y, z and $x \pm \frac{1}{2}$, $y \pm \frac{1}{2}$, z are equivalent due to the symmetry of the space group.

F Supplementary Material to Chapter 9

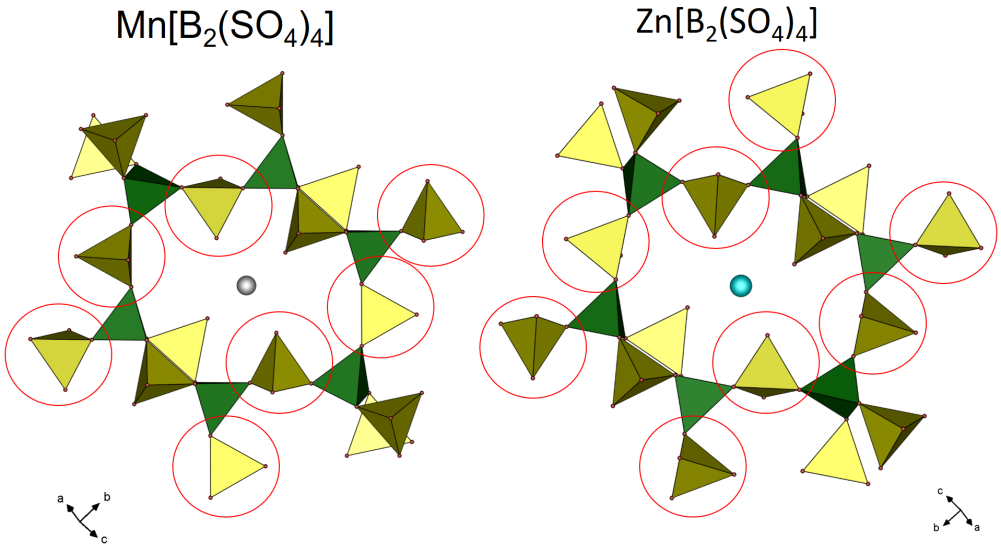

Fig. F.0.1: Comparison of $Mn[B_2(SO_4)_4]$ and $Zn[B_2(SO_4)_4]$[88] showing that there are actually two homeotypic, but not isotypic "cation within layer" structure types for $M[B_2(SO_4)_4]$: The two crystal structures differ in the orientation of one sulfate tetrahedron marked with red circles; please note, that all marked tetrahedra are crystallographically equivalent; further, the two crystal structures are isotypic on the BS_4 supertetrahedra level neglecting the oxygen atoms.

F.1 $Cd[B_2(SO_4)_4]$

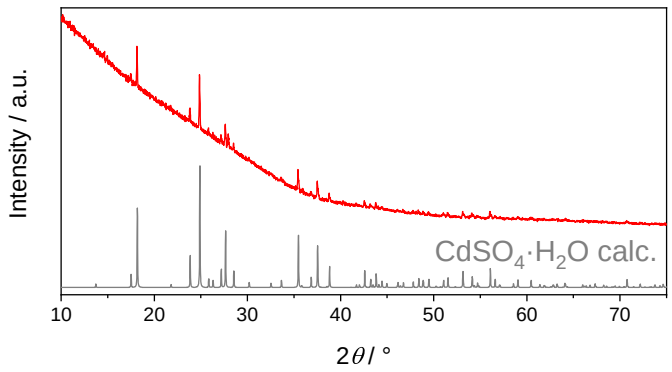

Fig. F.1.1: PXRD pattern of $Cd[B_2(SO_4)_4]$ decomposed due to the presence of moisture compared to a calculated pattern for $CdSO_4 \cdot H_2O$[504]

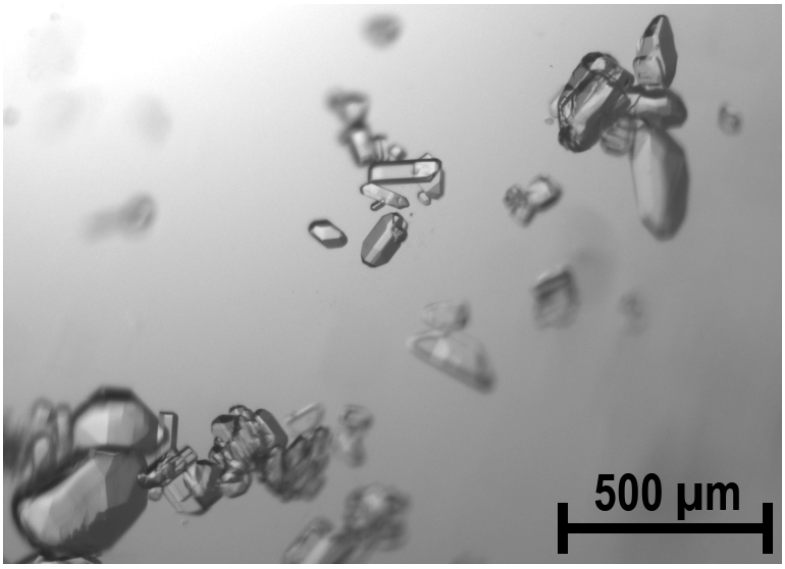

Fig. F.1.2: Optical microscope picture of $Cd[B_2(SO_4)_4]$

Tab. F.1.1: Crystal data and structure refinement of $Cd[B_2(SO_4)_4]$ determined from PXRD data via Rietveld refinement using the structure from SC-XRD as starting model; the respective standard deviations are given in parentheses.

M / g × mol^{-1}	518.26
Temperature / K	298(2)
Space group	$P2_1/n$ (no. 14)
a / pm	809.25(1)
b / pm	797.00(1)
c / pm	938.48(1)
β / °	109.8566(4)
Volume / 10^6 pm^3	569.31(1)
Z	2
ρ_{calcd} / g cm^3	3.02
Radiation; wavelength λ / Å	Cu$K\alpha$; 1.54184
Diffractometer	Bruker D8 Advance
Θ range / °	2.5-40
Observed reflections	350
Refined parameters	67
R_{Bragg}	0.010
R_p	0.014
R_{wp}	0.021
GOF	2.35

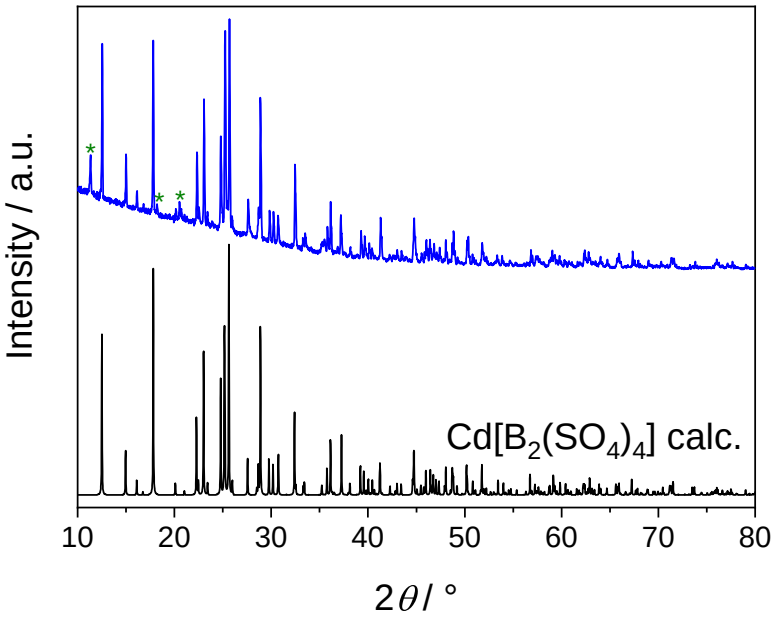

Fig. F.1.3: PXRD pattern of $Cd[B_2(SO_4)_4]$ synthesised at 180°C with a yet unidentified side phase; the related reflexes are labelled with green asterisks; the experimental pattern is compared to a calculated pattern from the SC-XRD.

Tab. F.1.2: Crystal data and structure refinement of $Cd[B_2(SO_4)_4]$ determined from SC-XRD; the respective standard deviations are given in parentheses.

M / g mol^{-1}	518.26
Crystal size / mm^3	$0.05 \times 0.04 \times 0.02$
Temperature / K	250(2)
Space group	$P2_1/n$ (No. 14)
a / pm	807.6(1)
b / pm	797.5(1)
c / pm	939.5(1)
β / °	110.010(7)
Volume / 10^6 pm^3	568.6(2)
Z	2
ρ_{calcd} / g cm^3	3.027
Absorption coefficient μ / mm$^{\breve{}1}$	2.76
$F\,(000)$ / e	500
Radiation; wavelength λ / Å	Mo-K_α; 0.71073
Diffractometer	Bruker D8 Venture
Θ range / °	2.879-33.499
Absorption correction	multi-scan
Transmission (min; max)	0.6554; 0.7488
Index range $h \mid k \mid l$	$\pm11 \mid \pm11 \mid \pm12$
Reflections collected	23626
Independent reflections	2230
Obs. reflections $[I > 2\sigma\,(I)]$	1827
Refined parameters	106
R_{int}	0.082
R_1	0.043
wR_2	0.067
GOF	1.11
Residual electron density (max; min) / e^-Å^{-3}	0.87; -0.86

Tab. F.1.3: Wyckoff symbols, refined atomic coordinates and isotropic displacement parameters U_{eq} / Å^2 in $Cd[B_2(SO_4)_4]$; estimated standard deviations in parentheses.

Atom	Wyckoff position	x	y	z	U_{eq}
Cd1	2*a*	0	0	0	0.00981(7)
S1	4*e*	0.18967(7)	0.41774(7)	0.14024(6)	0.00795(11)
S2	4*e*	-0.29299(8)	0.17394(7)	0.15331(7)	0.01002(11)
O11	4*e*	0.1507(2)	-0.0900(3)	0.2337(2)	0.0170(4)
O12	4*e*	0.1211(2)	0.2612(2)	0.0700(2)	0.0134(3)
O13	4*e*	0.2190(2)	0.5381(2)	0.0247(2)	0.0118(3)
O14	4*e*	0.0544(2)	0.5097(2)	0.1916(2)	0.0116(3)
O21	4*e*	-0.4611(3)	0.2402(3)	0.0757(2)	0.0241(4)
O22	4*e*	-0.2297(3)	0.0485(3)	0.0745(3)	0.0213(4)
O23	4*e*	-0.2759(2)	0.1071(2)	0.3100(2)	0.0153(4)
O24	4*e*	-0.1515(2)	0.3096(2)	0.2069(2)	0.0144(4)
B1	4*e*	-0.1375(4)	0.4715(3)	0.1417(3)	0.0101(5)

Tab. F.1.4: Anisotropic displacement parameters U_{ij} / Å^2 in $Cd[B_2(SO_4)_4]$; estimated standard deviations in parentheses.

Atom	U_{11}	U_{22}	U_{33}	U_{23}	U_{13}	U_{12}
Cd1	0.01152(11)	0.00943(10)	0.00798(11)	-0.00031(9)	0.00269(8)	-0.00072(9)
S1	0.0096(2)	0.0078(2)	0.0064(3)	-0.00082(19)	0.0027(2)	-0.00035(18)
S2	0.0103(2)	0.0118(2)	0.0100(3)	0.0015(2)	0.0060(2)	-0.00038(19)
O11	0.0156(9)	0.0214(9)	0.0104(9)	0.0037(7)	-0.0004(7)	-0.0024(7)
O12	0.0175(8)	0.0077(7)	0.0157(9)	-0.0021(7)	0.0065(7)	-0.0018(6)
O13	0.0168(8)	0.0099(7)	0.0100(8)	-0.0011(6)	0.0064(7)	-0.0042(6)
O14	0.0139(8)	0.0106(7)	0.0124(8)	-0.0038(7)	0.0073(7)	-0.0009(6)
O21	0.0150(9)	0.0285(11)	0.0255(12)	0.0067(9)	0.0029(8)	0.0033(8)
O22	0.0247(10)	0.0208(9)	0.0254(11)	-0.0083(8)	0.0178(9)	-0.0038(8)
O23	0.0182(9)	0.0188(9)	0.0098(9)	0.0014(7)	0.0061(7)	-0.0084(7)
O24	0.0161(8)	0.0126(8)	0.0142(9)	0.0049(7)	0.0049(7)	-0.0029(7)
B1	0.0122(11)	0.0095(12)	0.0106(12)	0.0011(9)	0.0064(10)	-0.0004(8)

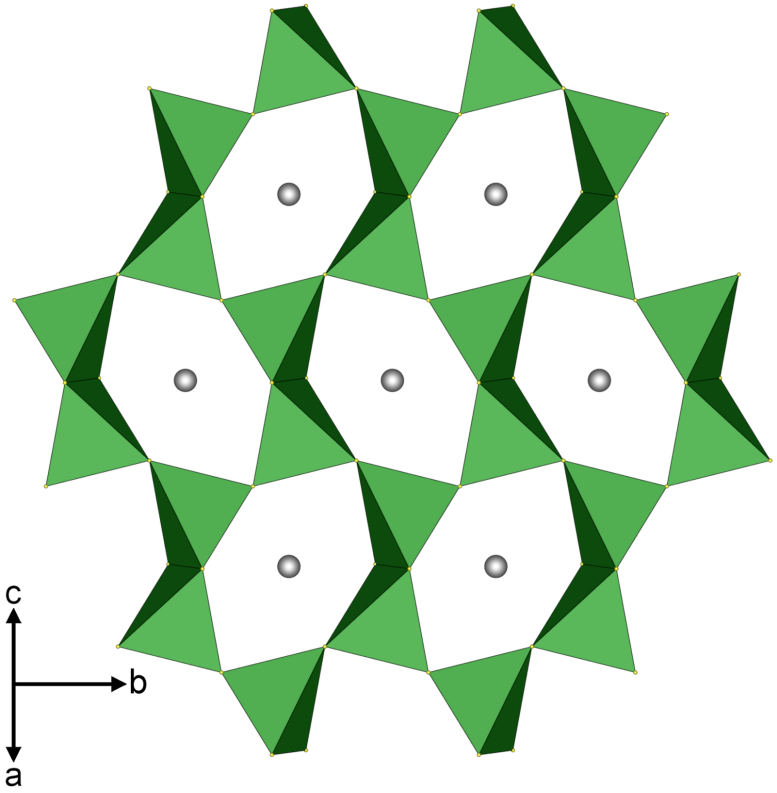

Fig. F.1.4: Layers in $Cd[B_2(SO_4)_4]$ formed by corner and edge sharing supertetrahedra $B(SO_4)_4$ resulting in *sechser* rings with the cations located inside and corner sharing dimers of supertetrahedra; supertetrahedra light green, Cd^{2+} grey, sulfur yellow.

Tab. F.1.5: Electrostatic calculations for $Cd[B_2(SO_4)_4]$.

$Cd[B_2(SO_4)_4]$	$CdSO_4{}^{[505]} + B_2O_3{}^{[501]} + 3\ SO_3{}^{[497]}$
MAPLE $= 146705$ kJ mol^{-1}	MAPLE $= 146270$ kJ mol^{-1}
	$\Delta = 0.3\%$

Tab. F.1.6: ECoN derived by MAPLE-calculations for Cd atoms in $Cd[B_2(SO_4)_4]$

Atom	x	y	z	Distance / pm	ECoN(1)	ECoN(2)
Central atom						
Cd1	0	0	0			
Ligand						
O22	0.2297	-0.0485	-0.0745	222.932	1.059	1.059
O22	-0.2297	0.0485	0.0745	222.932	1.059	1.059
O11	-0.1507	0.0900	-0.2337	223.352	1.047	1.048
O11	0.1507	-0.0900	0.2337	223.352	1.047	1.048
O12	-0.1211	-0.2612	-0.0700	229.949	0.873	0.873
O12	0.1211	0.2612	0.0700	229.949	0.873	0.873
Next Ligand						
O24	0.1515	-0.3096	-0.2069	360.545	0	0

Tab. F.1.7: ECoN derived by MAPLE-calculations for Mn atoms in $Mn[B_2(SO_4)_4]$ calculated using the SC-XRD data from [88]

Atom	x	y	z	Distance / pm	ECoN(1)	ECoN(2)
Central atom						
Mn1	$\frac{1}{2}$	0	$\frac{1}{2}$			
Ligand						
O11	0.2847	-0.0442	0.5791	213.878	1.069	1.070
O11	0.7153	0.0442	0.4209	213.878	1.069	1.070
O22	0.6510	0.0985	0.7226	213.996	1.066	1.067
O22	0.3490	-0.0985	0.2774	213.996	1.066	1.067
O21	0.6168	-0.2549	0.5732	222.767	0.826	0.827
O21	0.3832	0.2549	0.4268	222.767	0.826	0.827
Next Ligand						
O111	0.6540	0.3129	0.2956	360.200	0.000	0.000

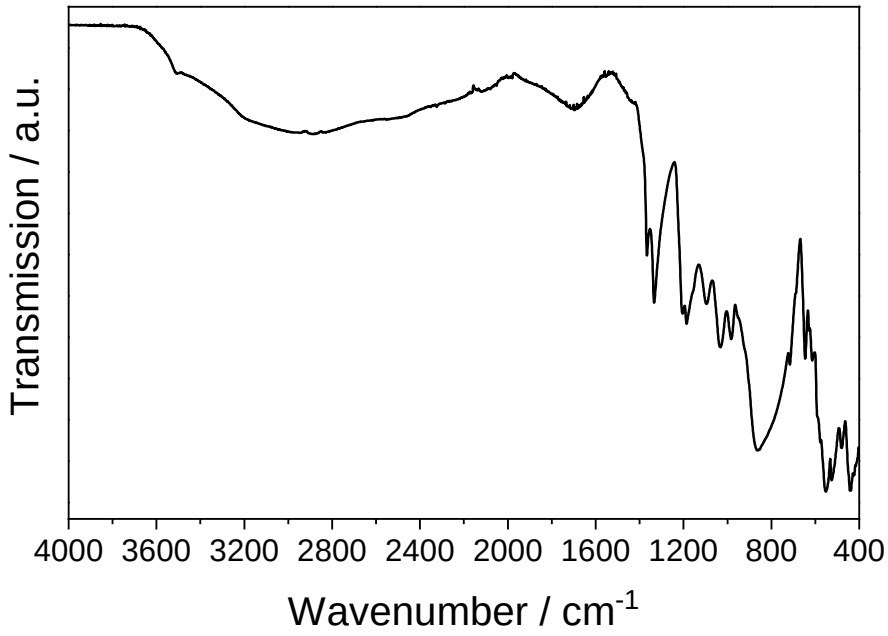

Fig. F.1.5: Full IR spectrum of $Cd[B_2(SO_4)_4]$

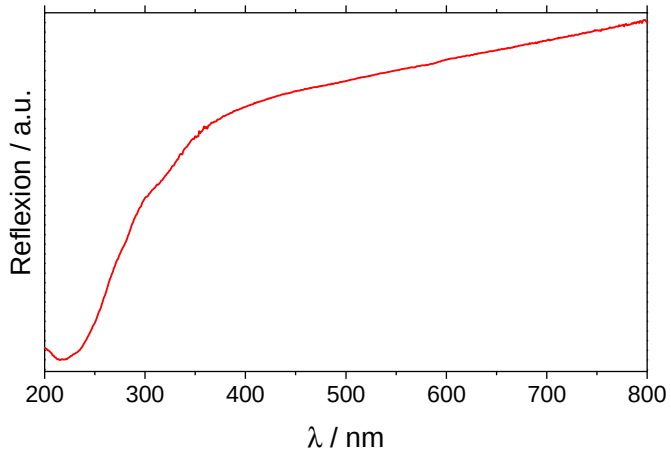

Fig. F.1.6: UV-Vis spectrum of $Cd[B_2(SO_4)_4]$

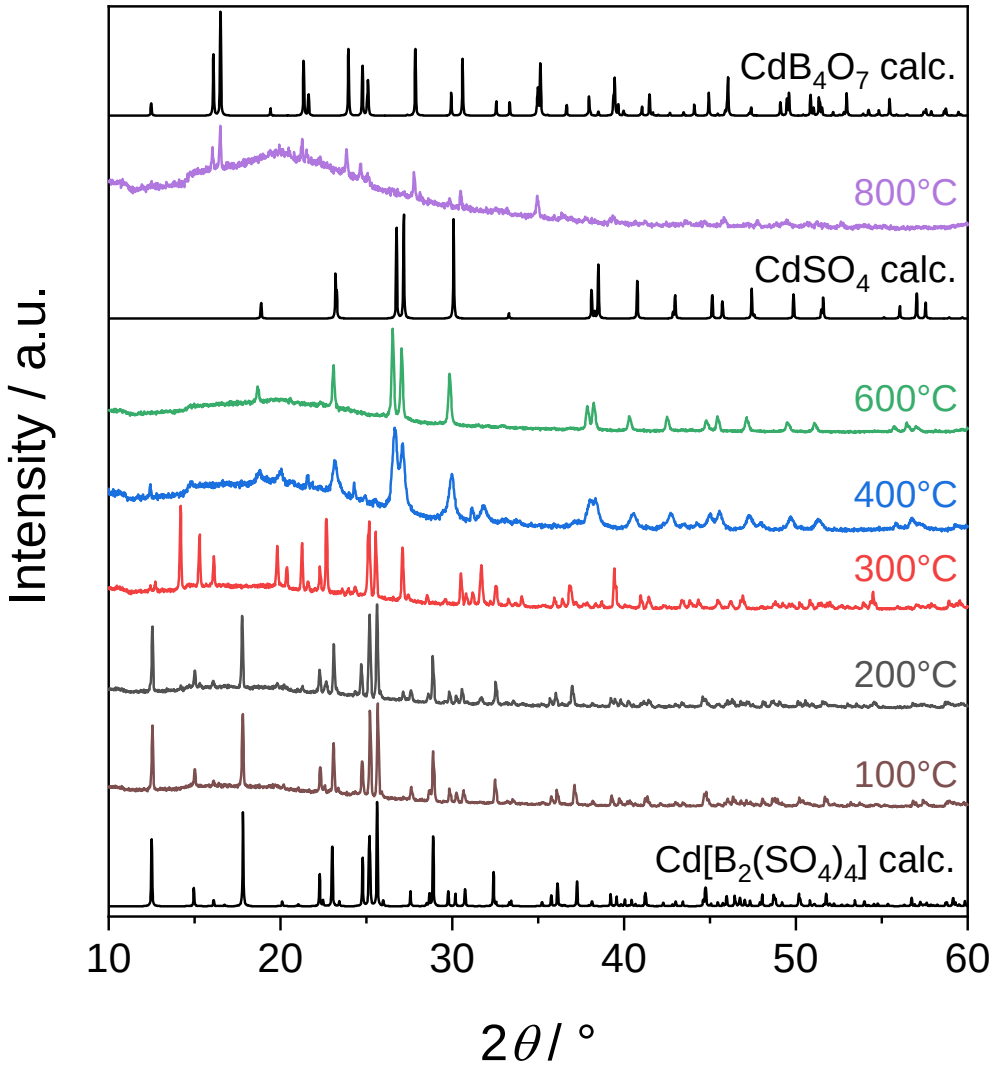

Fig. F.1.7: TPXRD patterns of $Cd[B_2(SO_4)_4]$ compared to calculated patterns for $Cd[B_2(SO_4)_4]$ from SC-XRD, $CdSO_4$[505] and CdB_4O_7;[506] details are discussed in the main text.

F.2 Cu[B$_2$(SO$_4$)$_4$]

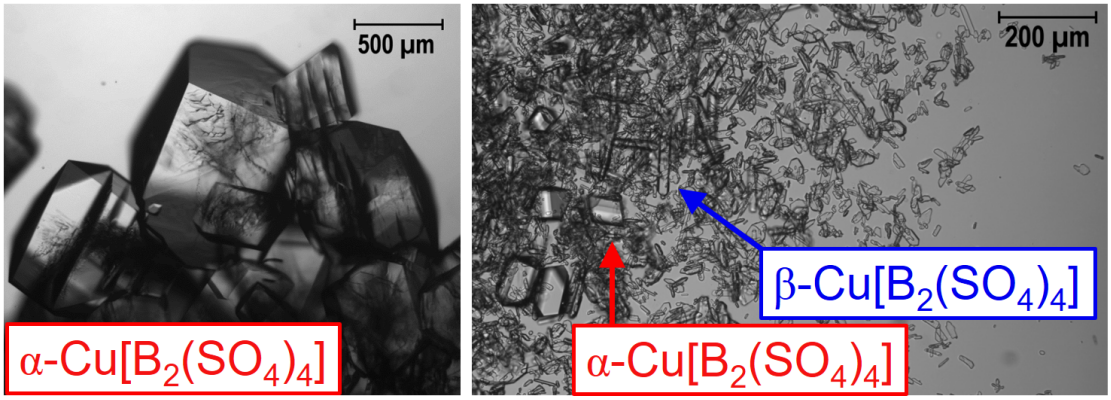

Fig. F.2.1: Microscope pictures of α-Cu[B$_2$(SO$_4$)$_4$] (left, through closed ampoule) and β-Cu[B$_2$(SO$_4$)$_4$] (right, embedded in LV CryoOil) showing the morphology of the crystals.

Tab. F.2.1: Crystal data and structure refinements of β-Cu[B$_2$(SO$_4$)$_4$] and β-Cu[B$_2$(SO$_4$)$_4$] determined from PXRD data via Rietveld refinement; the respective standard deviations are given in parentheses.

	α-Cu[B$_2$(SO$_4$)$_4$][i]	β-Cu[B$_2$(SO$_4$)$_4$][ii]
CSD number	2118182	2118180
M / g × mol^{-1}	469.40	
Temperature / K	298(2)	
Space group	$P\bar{1}$ (no. 2)	$P2_1/n$ (no. 14)
a / pm	526.36(2)	772.63(1)
b / pm	714.49(2)	813.14(1)
c / pm	793.52(2)	906.64(1)
α / °	73.698(2)	90
β / °	70.737(2)	111.132(1)
γ / °	86.677(2)	90
Volume / 10^6 pm^3	270.19(1)	531.30(1)
Z	1	2
ρ_{calcd} / g cm^3	2.885	2.934
Radiation; wavelength λ / Å	Cu$K\alpha$; 1.54184	
Diffractometer	Bruker D8 Advance	
Θ range / °	2.5-40	
Observed reflections	332	663
Refined parameters	65	64
R_{Bragg}	0.005	0.004
R_p	0.006	0.005
R_{wp}	0.009	0.008
GOF	1.99	1.82

[i] The structural model from [90] was used as a starting model for Rietveld analysis. [ii] The structural model from the SC-XRD was used as a starting model for Rietveld analysis. β-Cu[B$_2$(SO$_4$)$_4$] was refined with a 7 wt.-% side phase of α-Cu[B$_2$(SO$_4$)$_4$] (R_{Bragg} = 0.006) taking the results of the refinement on α-Cu[B$_2$(SO$_4$)$_4$] as fixed values.

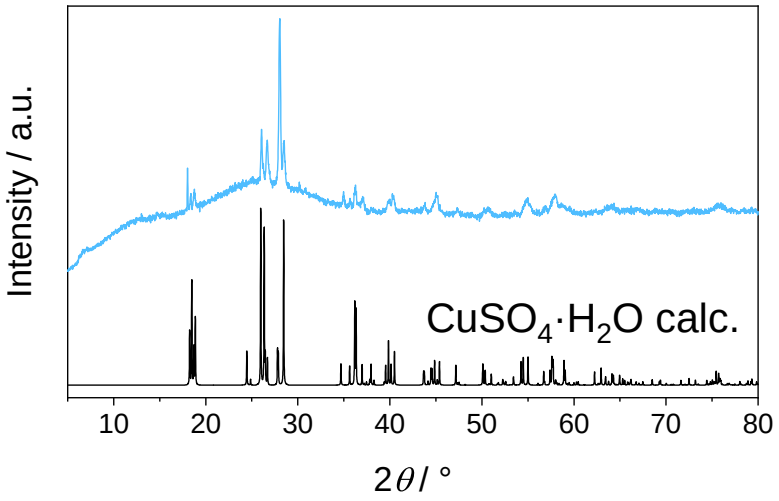

Fig. F.2.2: PXRD pattern of β-$Cu[B_2(SO_4)_4]$ stored at ambient conditions for 30 min compared to a calculated pattern for $CuSO_4 \cdot H_2O$.[507]

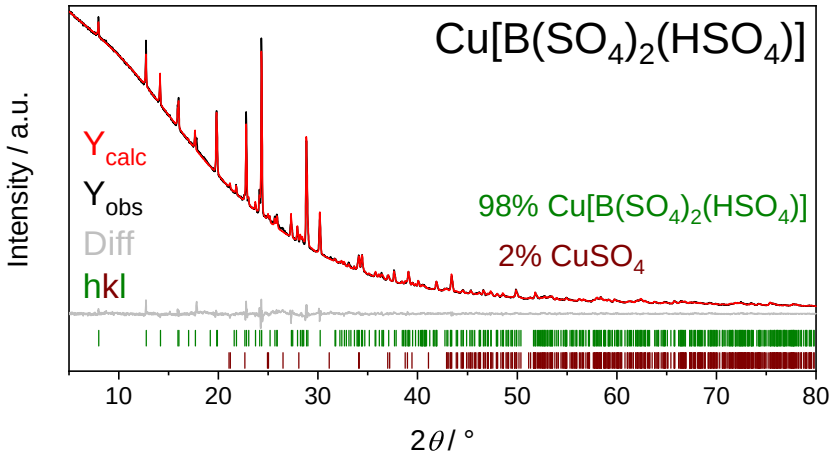

Fig. F.2.3: Rietveld-Refinement of $Cu[B(SO_4)_2(HSO_4)]$ showing contents of 98 wt.-% for the main phase $Cu[B(SO_4)_2(HSO_4)]$ and 2 wt.-% for the side phase $CuSO_4$. Further details can be found in Table F.2.2.

Tab. F.2.2: Crystal data and structure refinements of $Cu[B(SO_4)_2(HSO_4)]$ determined from PXRD data via Rietveld refinement using the structure reported by Bruns et al.[90] as starting model; the respective standard deviations are given in parentheses.

M / g × mol^{-1}	363.54
Temperature / K	300(2)
Space group	$P\bar{1}$ (no. 2)
a / pm	533.32(2)
b / pm	707.36(3)
c / pm	1130.6(1)
α / °	81.271(2)
β / °	80.205(3)
γ / °	81.141(2)
Volume / 10^6 pm^3	411.82(3)
Z	2
ρ_{calcd} / g cm^3	2.932
R_{Bragg}	0.009
Side phase	$CuSO_4$[i]
Fraction of side phase / wt.-%	2
Space group	$Pnma$ (no. 62)
a / pm	842.2(2)
b / pm	672.80(2)
c / pm	482.99(2)
Volume / 10^6 pm^3	273.7(1)
Z	2
Radiation; wavelength λ / Å	Cu$K\alpha$; 1.54184
Diffractometer	Bruker D8 Advance
Θ range / °	2.5-40
Observed reflections	506
Refined parameters	82
R_p	0.008
R_{wp}	0.015
GOF	2.77

[i] The structural model from [455] was used as a starting models for Rietveld analysis.

Tab. F.2.3: Selected interatomic distances (in pm) and angles (in °) in α-Cu[$B_2(SO_4)_4$]; the respective standard deviations are given in parentheses; the data was taken from the Rietveld refinement.

Cu-O11	196.3(9)
Cu-O21	188(1)
Cu-O22[i]	217.1(9)
$\sum$ IR (Cu-O)[216]	208
S1-O	145.7(9)-160(1)
S2-O	147(1)-157(1)
$\sum$ IR (S-O)[216]	150
B-O	143(2)-160(2)
$\sum$ IR (B-O)[216]	149
O-S1-O	100(1)-118.7(7)
O-S2-O	102(1)-122.4(6)
O-B-O	101(1)-120(2)

[i] O22 is part of the anion coordinating Cu^{2+} via one sulfate group, only.

Tab. F.2.4: Crystal data and structure refinement of β-Cu[$B_2(SO_4)_4$] determined from SC-XRD; the respective standard deviations are given in parentheses.

CSD number	2118186
M / g mol^{-1}	469.40
Crystal size / mm^3	$0.19 \times 0.15 \times 0.11$
Temperature / K	250(2)
Space group	$P2_1/n$ (no. 14)
a / pm	771.2(3)
b / pm	814.9(3)
c / pm	909.2(3)
β / °	111.220(11)
Volume / 10^6 pm^3	532.7(4)
Z	2
ρ_{calcd} / g cm^3	2.927
Absorption coefficient μ / mm$^{\breve{}}$1	2.94
F (000) / e	462
Radiation; wavelength λ / Å	Mo-K_α; 0.71073
Diffractometer	Bruker D8 Venture
Θ range / °	2.979-44.998
Absorption correction	multi-scan
Transmission (min; max)	0.6364; 0.7503
Index range $h \mid k \mid l$	$-14;15 \mid \pm 16 \mid \pm -18;17$
Reflections collected	34144
Independent reflections	4392
Obs. reflections [$I > 2\sigma(I)$]	3946
Refined parameters	107
R_{int}	0.034
R_1	0.026
wR_2	0.057
GOF	1.099
Residual electron density (max; min) / e^- Å^{-3}	0.69; -0.72

Tab. F.2.5: Wyckoff symbols, refined atomic coordinates and isotropic displacement parameters U_{eq} / Å^2 in β-Cu[B$_2$(SO$_4$)$_4$]; estimated standard deviations in parentheses.

Atom	Wyckoff position	x	y	z	U_{eq}
Cu1	2*a*	0	0	0	0.00930(3)
S1	4*e*	-0.70341(2)	0.07667(2)	0.35248(2)	0.00705(3)
S2	4*e*	-0.28559(2)	-0.15745(2)	0.14445(2)	0.00767(3)
O11	4*e*	-0.55572(8)	-0.00838(6)	0.30333(7)	0.00960(7)
O12	4*e*	-0.87400(8)	0.07809(8)	0.21717(6)	0.01419(9)
O13	4*e*	-0.64003(8)	0.23124(7)	0.42536(7)	0.01201(8)
O14	4*e*	-0.26681(8)	0.04578(7)	0.53145(6)	0.01036(8)
O21	4*e*	-0.25357(8)	-0.07599(8)	0.30274(7)	0.0139(1)
O22	4*e*	-0.46914(8)	-0.21492(9)	0.06907(8)	0.0169(1)
O23	4*e*	-0.35697(8)	0.20540(7)	0.29374(7)	0.01281(9)
O24	4*e*	-0.21975(9)	-0.04850(9)	0.04959(8)	0.0164(1)
B1	4*e*	-0.3588(1)	0.04135(9)	0.35691(9)	0.0083(1)

Tab. F.2.6: Anisotropic displacement parameters U_{ij} / Å^2 in β-Cu[B$_2$(SO$_4$)$_4$]; estimated standard deviations in parentheses.

Atom	U_{11}	U_{22}	U_{33}	U_{23}	U_{13}	U_{12}
Cu1	0.00893(5)	0.01355(5)	0.00553(4)	-0.00049(3)	0.00273(3)	-0.00231(3)
S1	0.00772(5)	0.00795(5)	0.00516(5)	-0.00063(4)	0.00193(4)	-0.00002(4)
S2	0.00727(5)	0.00943(6)	0.00715(6)	-0.00116(4)	0.00362(4)	-0.00021(4)
O11	0.00943(17)	0.00996(17)	0.01056(2)	-0.0026(1)	0.0050(1)	-0.0006(1)
O12	0.01087(19)	0.0216(3)	0.0071(2)	-0.0026(2)	-0.0003(2)	0.0031(23)
O13	0.0147(2)	0.0082(2)	0.0134(2)	-0.0027(2)	0.0054(2)	-0.0011(2)
O14	0.01372(19)	0.0113(2)	0.0067(2)	-0.0005(1)	0.0044(1)	-0.0035(2)
O21	0.0136(2)	0.0183(2)	0.0096(2)	-0.0048(2)	0.0038(2)	0.0053(2)
O22	0.00930(19)	0.0213(3)	0.0185(2)	-0.0042(2)	0.0032(2)	-0.0041(2)
O23	0.0137(2)	0.0102(2)	0.0128(2)	0.0033(1)	0.0027(2)	-0.0034(2)
O24	0.0137(2)	0.0219(3)	0.0162(2)	0.0082(2)	0.0085(2)	0.0009(2)
B1	0.0101(2)	0.0083(2)	0.0077(2)	-0.0002(2)	0.0047(2)	-0.00002(19)

Tab. F.2.7: Selected interatomic distances (in pm) and angles (in °) in α-Cu[B$_2$(SO$_4$)$_4$]; the respective standard deviations are given in parentheses; both data taken from the SC-XRD and the Rietveld refinement is shown.

	SC-XRD	Rietveld
Cu-O12	196.48(8)	203.6(7)
Cu-O13	242.8(1)	239.4(8)
Cu-O24	195.54(9)	189.5(8)
$\sum$ IR (Cu-O)[216]	208	
S1-O[i]	142.51(7)-153.14(7)	140.0(8)-154.9(9)
S2-O	141.06(8)-152.56(7)	135.7(8)-155.5(8)
$\sum$ IR (S-O)[216]	150	
B-O	145.1(1)-148.5(1)	139(2)-157(2)
$\sum$ IR (B-O)[216]	149	
O-S1-O	102.67(4)-116.35(4)	101.1(5)-117.9(4)
O-S2-O	97.04(4)-114.82(5)	92.6(4)-118.5(5)
O-B-O	105.59(6)-113.36(6)	101(1)-118(1)

[i] $S1O_4$ tetrahedra are forming the *vierer* rings.

Tab. F.2.8: Electrostatic calculations for α-Cu[B$_2$(SO$_4$)$_4$] and β-Cu[B$_2$(SO$_4$)$_4$]

α-Cu[B$_2$(SO$_4$)$_4$] (Rietveld)	$CuSO_4$[455] + $B_2S_2O_9$[508] + SO_3[509]
MAPLE = 142636 kJ mol^{-1}	MAPLE = 142929 kJ mol^{-1}
	$\Delta = 0.2\%$
β-Cu[B$_2$(SO$_4$)$_4$] (SC-XRD)	$CuSO_4$[455] + B_2O_3[501] +3 SO_3[497]
MAPLE = 146610 kJ mol^{-1}	MAPLE = 146832 kJ mol^{-1}
	$\Delta = 0.2\%$
β-Cu[B$_2$(SO$_4$)$_4$] (Rietveld)	$CuSO_4$[455] + B_2O_3[501] +3 SO_3[497]
MAPLE = 146352 kJ mol^{-1}	MAPLE = 146832 kJ mol^{-1}
	$\Delta = 0.3\%$

Tab. F.2.9: ECoN derived by MAPLE-calculations for Cu atoms in α-Cu[B$_2$(SO$_4$)$_4$]

Atom	x	y	z	Distance / pm	ECoN(1)	ECoN(3)
Central atom						
Cu1	$\frac{1}{2}$	$\frac{1}{2}$	$\frac{1}{2}$			
Ligand						
O21	0.5860	0.5668	0.6889	188.520	1.207	1.233
O21	0.4140	0.4332	0.3111	188.520	1.207	1.233
O11	0.4192	0.7705	0.3936	196.331	0.965	0.992
O11	0.5808	0.2295	0.6064	196.331	0.965	0.992
O22	0.0860	0.4721	0.6845	217.099	0.409	0.430
O22	0.9140	0.5279	0.3155	217.099	0.409	0.430
Next Ligand						
O111	0.7301	0.8528	0.0723	348.975	0	0

Tab. F.2.10: ECoN derived by MAPLE-calculations for Cu atoms in β-Cu[B$_2$(SO$_4$)$_4$] (SC-XRD)

Atom	x	y	z	Distance / pm	ECoN(1)	ECoN(2)
Central atom						
Cu1	0	$\frac{1}{2}$	0			
Ligand						
O24	0.2197	0.5485	-0.0496	194.543	1.073	1.082
O24	-0.2197	0.4515	0.0496	194.543	1.073	1.082
O12	-0.1260	0.4219	-0.2172	196.437	1.015	1.024
O12	0.1260	0.5781	0.2172	196.437	1.015	1.024
O13	-0.1400	0.7688	-0.0746	242.760	0.081	0.084
O13	0.1400	0.2312	0.0746	242.760	0.081	0.084
Next Ligand						
O23	0.1430	0.7946	-0.2063	346.336	0	0

Tab. F.2.11: ECoN derived by MAPLE-calculations for Cu atoms in β-Cu[B$_2$(SO$_4$)$_4$] (Rietveld)

Atom	x	y	z	Distance / pm	ECoN(1)	ECoN(2)
Central atom						
Cu1	0	0	0			
Ligand						
O24	0.2120	0.0434	-0.0522	189.484	1.200	1.241
O24	-0.2120	-0.0434	0.0522	189.484	1.200	1.241
O12	-0.1273	-0.0779	-0.2270	203.586	0.773	0.814
O12	0.1273	0.0779	0.2270	203.586	0.773	0.814
O13	-0.1363	0.2664	-0.0714	239.352	0.098	0.112
O13	0.1363	-0.2664	0.0714	239.352	0.098	0.112
Next Ligand						
O23	0.1426	0.2968	-0.2161	352.611	0	0

Tab. F.2.12: DFT optimized lattice parameters and cell volumes per formula unit for α-Cu[B$_2$(SO$_4$)$_4$] ($P\bar{1}$), β-Cu[B$_2$(SO$_4$)$_4$] ($P2_1/n$, "cation within layer") and γ-Cu[B$_2$(SO$_4$)$_4$] ($C2/c$, "cation between layer"); note that space group setting here is $P2_1/c$ for β-Cu[B$_2$(SO$_4$)$_4$]

	a / pm	b / pm	c / pm	α / °	β / °	γ / °	VZ^{-1} / 10^6 pm^3
α-Cu[B$_2$(SO$_4$)$_4$]	5.292	7.359	8.035	73.48	71.05	86.13	283.63
β-Cu[B$_2$(SO$_4$)$_4$]	7.673	8.449	9.647	116.29	280.36		
γ-Cu[B$_2$(SO$_4$)$_4$]	17.662	5.336	14.541	125.06	280.46		

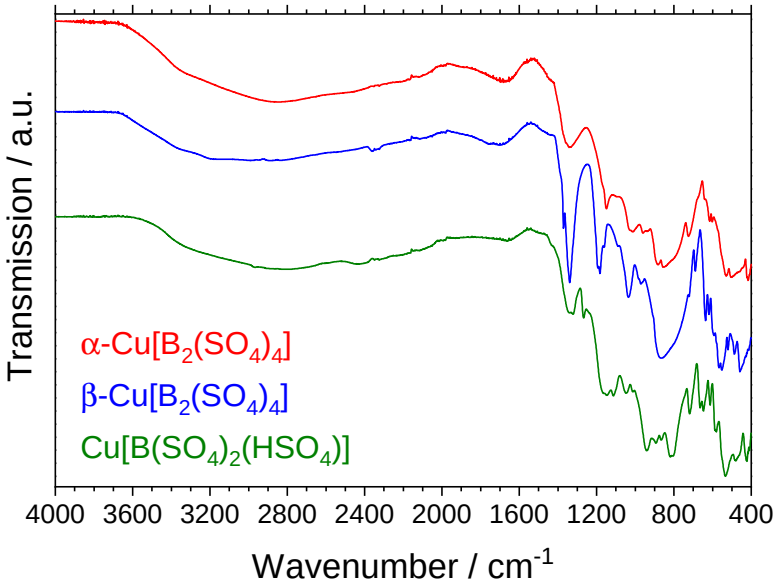

Fig. F.2.4: Full infrared spectra of α-Cu[B$_2$(SO$_4$)$_4$], β-Cu[B$_2$(SO$_4$)$_4$] and Cu[B(SO$_4$)$_2$(HSO$_4$)] including broad bands at high wavelengths that can be assigned to O-H vibrations (centred at $2800\,\mathrm{cm^{-1}}$ and $1700\,\mathrm{cm^{-1}}$) related to the formation of sulfuric acid on the surface of the samples reacting with ambient moisture.[419,420]

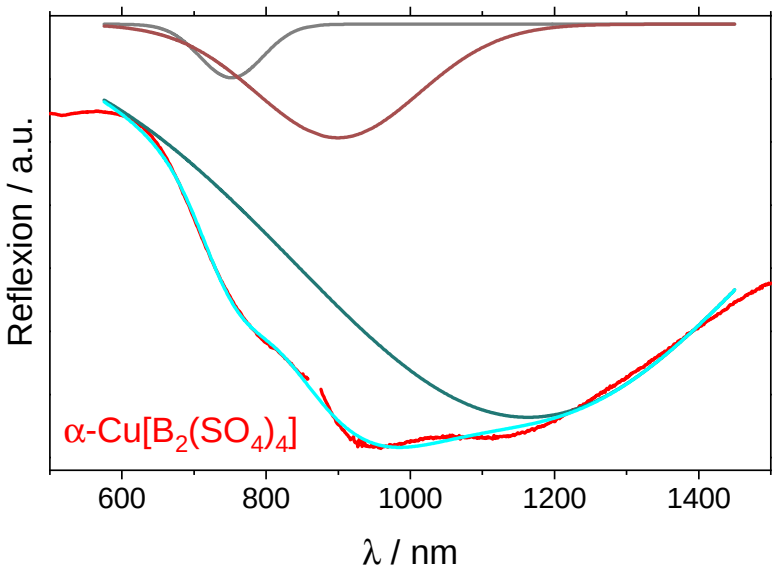

Fig. F.2.5: Gaussian fit of the UV-Vis-NIR spectrum of α-$Cu[B_2(SO_4)_4]$

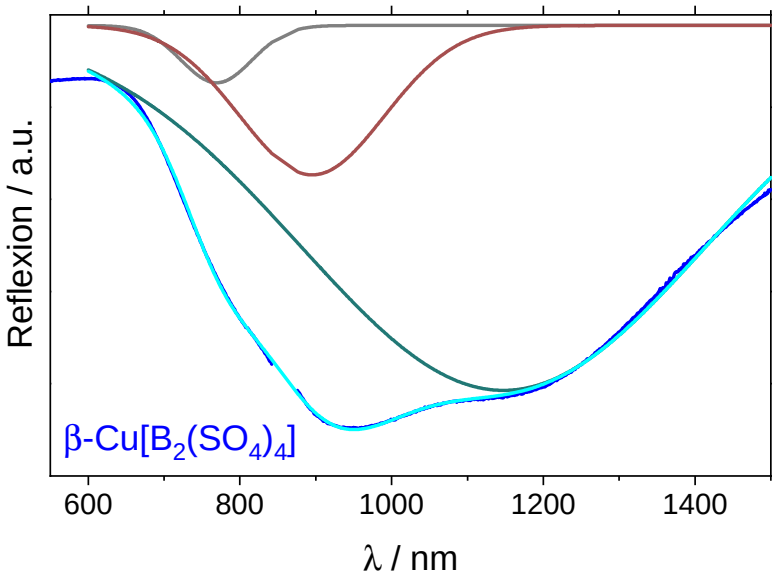

Fig. F.2.6: Gaussian fit of the UV-Vis-NIR spectrum of β-$Cu[B_2(SO_4)_4]$

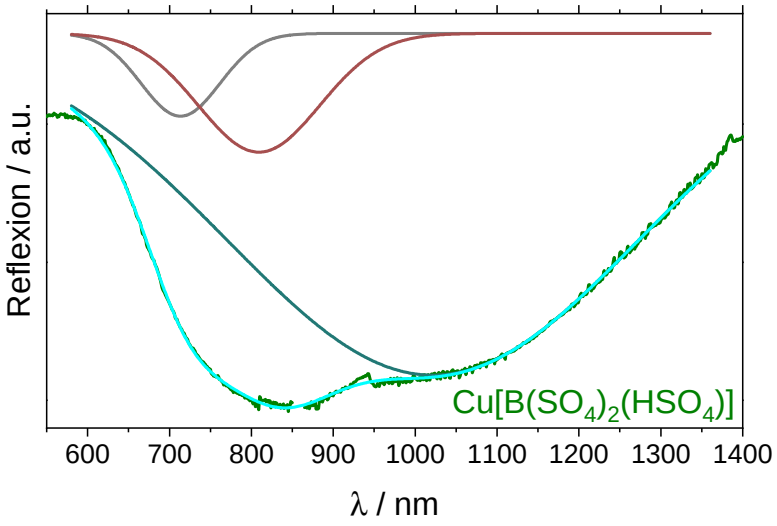

Fig. F.2.7: Gaussian fit of the UV-Vis-NIR spectrum of $Cu[B(SO_4)_2(HSO_4)]$

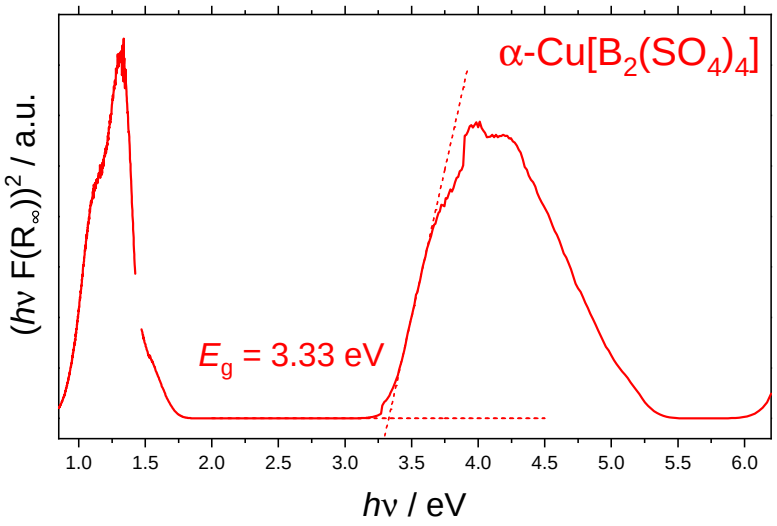

Fig. F.2.8: Tauc plot calculated from the UV-Vis-NIR spectrum of α-$Cu[B_2(SO_4)_4]$

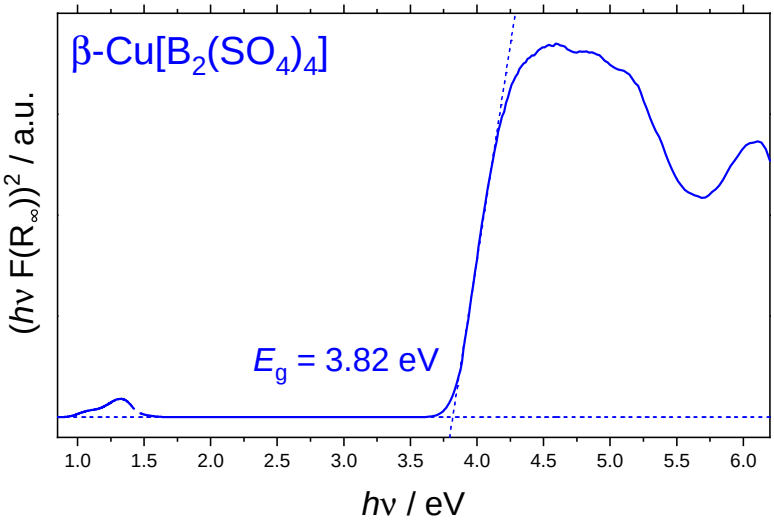

Fig. F.2.9: Tauc plot calculated from the UV-Vis-NIR spectrum of β-$Cu[B_2(SO_4)_4]$

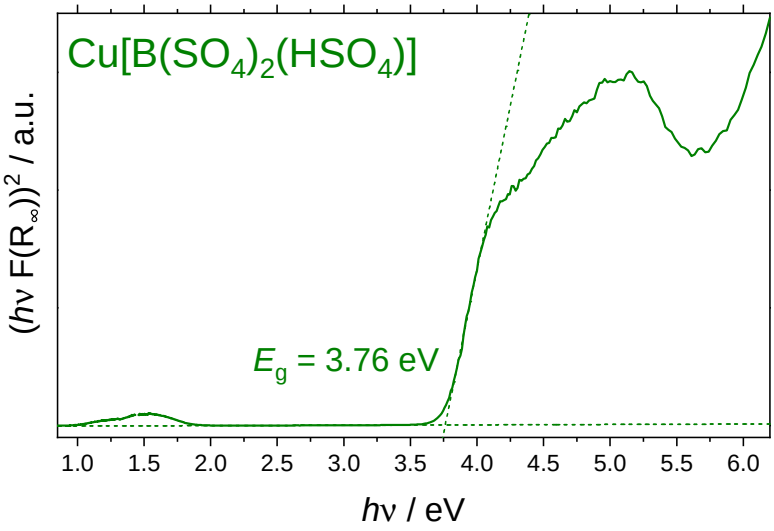

Fig. F.2.10: Tauc plot calculated from the UV-Vis-NIR spectrum of $Cu[B(SO_4)_2(HSO_4)]$

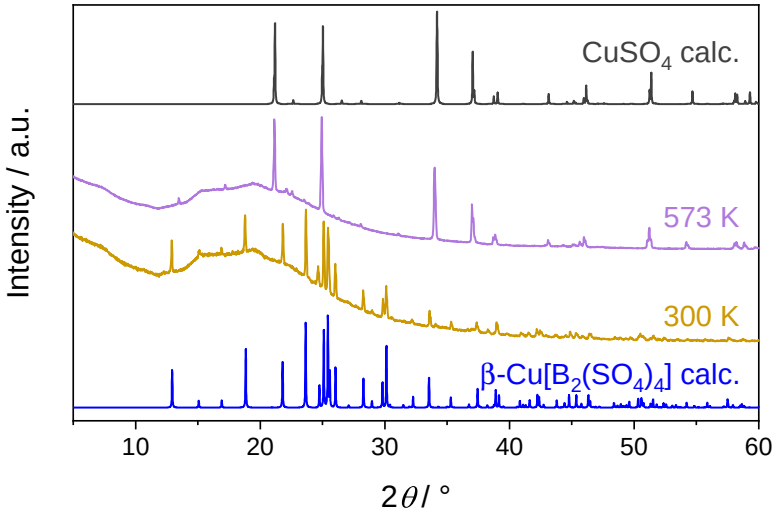

Fig. F.2.11: TPXRD powder pattern of β-$Cu[B_2(SO_4)_4]$ compared to calculated pattern for TPXRD powder pattern of β-$Cu[B_2(SO_4)_4]$ from our single-crystal XRD and $CuSO_4$[455] confirming the latter as decomposition product of the former.

Tab. F.2.13: Experimental and theoretically predicted mass losses in wt.-% for the thermogravimetric analysis of $Cu[B_2(SO_4)_4]$ depicted in Figure 9.2.8

Decomposition Step	exp. (α)	exp. (β)	calc.
$Cu[B_2(SO_4)_4] \longrightarrow CuSO_4 + B_2O_3 + 3\,SO_3(g)$	53.3	52.2	51.2

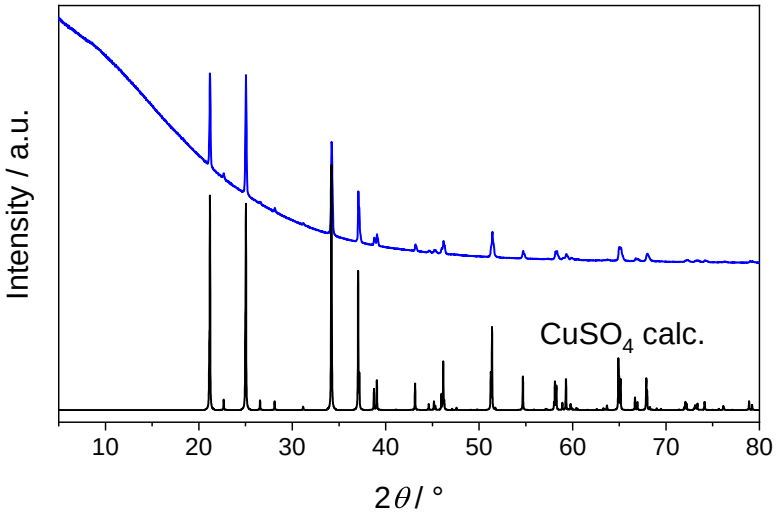

Fig. F.2.12: PXRD pattern of β-$Cu[B_2(SO_4)_4]$ heated at 300°C for 10 h in nitrogen atmosphere compared to a calculated pattern for $CuSO_4$.[455]

Tab. F.2.14: Experimental and theoretically predicted mass losses in wt.-% for the thermogravimetric analysis of $Cu[B(SO_4)_2(HSO_4)]$ depicted in Figure 9.2.8

Decomposition Step	exp.	calc.
$Cu[B(SO_4)_2(HSO_4)] \longrightarrow CuSO_4 + \frac{1}{2}\,B_2O_3 + 2\,SO_3(g) + \frac{1}{2}\,H_2O(g)$	46.5	46.5

G Supplementary Material to Chapter 11

Tab. G.0.1: Results for centroid deviation and eccentricity for various compounds from this work and from work visualised in Figure 11.0.1: For compounds with more than one crystallographic site for the ns^2 ion, they are numbered in the "site" column; the eccentricity ϵ is calculated by the division of the centroid deviation R_c by the radius of the enclosing sphere r_s; all calculations were performed for this work; the used crystallographic data is referenced.

ns^2 ion	Compound	CN	site	R_c / pm	r_s / pm	ϵ	Reference
Bi^{3+}	$Bi(H_3O)(SO_4)_2$	9		23	262.21	0.088	this work
Bi^{3+}	$Bi(HSO_4)_3$	8		19	250.01	0.076	this work
Bi^{3+}	$Bi_2(SO_4)_3$	7	1	36	264.63	0.136	this work
Bi^{3+}	$Bi_2(SO_4)_3$	7	2	25	254.38	0.098	this work
Bi^{3+}	$Bi_2[B_2(SO_4)_6]$	8		16	249.4	0.064	this work
Bi^{3+}	Bi_2WO_6	6	1	38	249.4	0.150	[510]
Bi^{3+}	Bi_2WO_6	6	2	42	256.57	0.164	[510]
Bi^{3+}	BiB_3O_6	6		50	255.64	0.196	[511]
Bi^{3+}	$BiCo_2BP_2O_{10}$	6		41	254.27	0.161	[512]
Pb^{2+}	Pb_2WO_5	8	1	45	289.39	0.156	[513]
Pb^{2+}	Pb_2WO_5	8	2	44	274.59	0.160	[513]
Pb^{2+}	$Pb_4(BO_3)_2(SO_4)$	8	1	47	314.8	0.149	[514]
Pb^{2+}	$Pb_4(BO_3)_2(SO_4)$	7	2	36	290.46	0.124	[514]
Pb^{2+}	$Pb_4(BO_3)_2(SO_4)$	7	3	55	281.23	0.196	[514]
Pb^{2+}	$Pb_4(BO_3)_2(SO_4)$	6	4	68	290.26	0.234	[514]
Sb^{3+}	$Sb_2(SO_4)_3$	7	1	59	269.57	0.219	[416]
Sb^{3+}	$Sb_2(SO_4)_3$	7	2	48	248.88	0.193	[416]
Sb^{3+}	SbB_3O_6	6		70	253.45	0.276	[104]
Tl^{+}	Tl_2WO_4	7		100	346.95	0.288	[515]
Tl^{+}	TlB_3O_5	4		44	304.92	0.144	[516]
Tl^{+}	TlB_3O_5 (high pressure)	5		13	286.58	0.045	[517]
Sn^{2+}	$Sn_2(SO_4)_3$	6		46	275.85	0.167	this work
Sn^{2+}	$Sn_3B_4O_9$	4	1	68	264.53	0.257	[518]
Sn^{2+}	$Sn_3B_4O_9$	4	2	96	288.02	0.333	[518]
Sn^{2+}	$Sn_3B_4O_9$	4	3	170	353.06	0.482	[518]

H Lists of Publications and Contributions

Publications With Results Presented in This Thesis

1. Matthias Hämmer, Henning A. Höppe, "Crystalline orthorhombic *Ln*[CO_3][OH] (*Ln*=La, Pr, Nd, Sm, Eu, Gd) compounds hydrothermally synthesised with CO_2 from air as carbonate source" *Zeitschrift für Naturforschung B* **2019**, *74*, 59-70.

2. Matthias Hämmer, Oliver Janka, Judith Bönnighausen, Steffen Klenner, Rainer Pöttgen, Henning A. Höppe, "On the phosphors $Na_5M(WO_4)_4$ (M = Y, La–Nd, Sm–Lu, Bi) – crystal structures, thermal decomposition, and optical and magnetic properties" *Dalton Transactions* **2020**, *49*, 8209-8225.

3. Matthias Hämmer, Vivien Wessels, Romy Ettlinger, Henning A. Höppe, "Microwave-Assisted Hydrothermal Synthesis, Crystal Structure, and Thermal Decomposition of Strontium Citrate Monohydrate $Sr_3(C_6H_5O_7)_2 \cdot H_2O$" *Zeitschrift für anorganische und allgemeine Chemie* **2021**, *647*, 204-209.

4. Matthias Hämmer, Lkhamsuren Bayarjargal, Henning A. Höppe, "The First Bismuth Borosulfates Comprising Oxonium and a Tectosilicate-Analogous Anion" *Angewandte Chemie International Edition* **2021**, *60*, 1503-1506; *Angewandte Chemie* **2021**, *133*, 1525–1529.

5. Matthias Hämmer, Philip Netzsch, Steffen Klenner, Kai Neuschulz, Mona Struckmann, Mathias S. Wickleder, Michael Daub, Harald Hillebrecht, Rainer Pöttgen, Henning A. Höppe, "The tin sulfates $Sn(SO_4)_2$ and $Sn_2(SO_4)_3$: Crystal structures, optical and thermal properties" *Dalton Transactions* **2021**, *50*, 12913-12922.

6. Matthias Hämmer, Florian Pielnhofer, Oliver Janka, Hirotaka Takahashi, Peter Gross, Rainer Pöttgen, Henning A. Höppe, "Polymorphism and Optical, Magnetic and Thermal Properties of the either Phyllo- or Inosilicate-analogous Borosulfate $Cu[B_2(SO_4)_4]$" *Dalton Transactions* **2022**, *51*, 3104-3115.

7. Matthias Hämmer, Jakoah Brgoch, Philip Netzsch, Henning A. Höppe, "The Role of the Bi^{3+} Lone Pair in $Bi(H_3O)(SO_4)_2$, $Bi(HSO_4)_3$ and $Bi_2(SO_4)_3$" *Inorganic Chemistry* **2022**, *61*, 4102-4113.

8. Matthias Hämmer, Leonard C. Pasqualini, Sean S. Sebastian, Hubert Huppertz, Henning A. Höppe, Jörn Bruns "$Cd[B_2(SO_4)_4]$ and $H_2[B_2(SO_4)_4]$ – A phyllosilicate analogue borosulfate and its homeotypic heteropolyacid" *in preparation.*

Publications Beyond This Thesis

1. Matthias Hämmer, Brendan Roycroft, Mahbub Akhter, Duc V. Dinh, Zhiheng Quan, Jian Zhao, Peter J. Parbrook, Brian Corbett, "Size-Dependent Bandwidth of Semipolar $(11\bar{2}2)$ Light-Emitting-Diodes" *IEEE Photonics Technology Letters* **2018**, *30*, 439-442.

2. Matthias Hämmer, Andrea Gassmann, Armin Reller, Heinz von Seggern, Oliver Gutfleisch, Rudolf Stauber, Jörg Zimmermann, "Recyclable Phosphor Films: Three Water-Soluble Binder Systems Enabling the Recovery of Phosphor Powders in White LEDs" *Journal of Electronic Materials* **2019**, *48*, 2294-2300.

3. Matthias Hämmer, Andrea Gassmann, Armin Reller, Heinz von Seggern, Oliver Gutfleisch, Rudolf Stauber, Jörg Zimmermann, "Recyclable phosphor sheet based on polyvinyl alcohol for LED lighting using remote phosphor technology" *Materials Technology* **2019**, *34*, 178-183.

4. Philip Netzsch, Matthias Hämmer, Peter Gross, Harijs Bariss, Theresa Block, Lukas Heletta, Rainer Pöttgen, Jörn Bruns, Hubert Huppertz, Henning A. Höppe, "$RE_2B_2(SO_4)_6$ (RE = Y, La-Nd, Sm, Eu, Tb-Lu): A silicate-analogous host structure with weak coordination behaviour" *Dalton Transactions* **2019**, *48*, 4387-4397.

5. Philip Netzsch, Matthias Hämmer, Thomas P. van Swieten, Erich Turgunbajew, Andries Meijerink, Henning A. Höppe, Markus Suta, "Distance control and selection rules of non-radiative thermalization rates to widen the dynamic range of luminescent thermometers" *Advanced Optical Materials* **2022**, *10*, 2200059.

6. Matthias Hämmer, Henning A. Höppe, "New Insights on Alkali Metal Tungstates: The High Temperature Polymorphism of Na_2WO_4, the New Polymorph Li_2WO_4-V and the Redetermined Crystal Structure of $Li_2W_2O_7$" *Zeitschrift für anorganische und allgemeine Chemie* **2022**, *648*, e202100373.

7. Matthias Hämmer, Henning A. Höppe, "The unconventional cadmium borosulfates $Cd[B_2O(SO_4)_3]$ and $Cd_4[B_2O(SO_4)_6]$" *in preparation.*

Contributions to Conferences and Seminars

1. Matthias Hämmer, "On the Way to Borotungstates" **Presentation**, AK Höppe Mitarbeiterseminar, Augsburg, 20.06.2018.

2. Philip Netzsch, Matthias Hämmer, Peter Gross, Harijs Bariss, Henning A. Höppe, "The Borosulfates $RE_2[B_2(SO_4)_6]$ (RE = Y, La-Nd, Eu-Lu): Hoststructures for Phosphors" **Poster**, 19. Vortragstagung für Anorganische Chemie, Regensburg, 24.-27.09.2018.

3. Matthias Hämmer, "Rare-Earth Carbonate Hydroxides And Pentasodium Rare-Earth Tetratungstates" **Presentation**, AK Höppe Mitarbeiterseminar, Augsburg, 05.12.2018.

4. Matthias Hämmer, "Silicate-Analogous Materials: New Borosulfates And Pentasodium Rare-Earth Tetratungstates" **Presentation**, 48. Hirschegg-Seminar Festkörperchemie, Hirschegg, 21.06.2019.

5. Matthias Hämmer "New Borosulfates of Bismuth and Copper plus something completely different" **Presentation**, AK Höppe Mitarbeiterseminar, Augsburg, 11.12.2019.

6. Matthias Hämmer, "TOPAS - Praxis der Strukturverfeinerung" **Presentation**, AK Höppe Mitarbeiterseminar, Augsburg, 06.02.2020.

7. Matthias Hämmer, "New Horizons in Borosulfate Chemistry" **Virtual Presentation**, AK Höppe Mitarbeiterseminar, Augsburg, 29.07.2020.

8. Matthias Hämmer, Lkhamsuren Bayarjargal, Henning A. Höppe, "$(H_3O)Bi[B(SO_4)_2]_4$ - The First Bismuth (III) Borosulfate Comprising Oxonium and a Tectosilicate Analogous Anion" **Virtual Poster** (Poster Prize), Online-Vortragstagung für Anorganische Chemie der Fachgruppen Wöhler-Vereinigung und Festkörperchemie und Materialforschung, 29.-30.09.2020.

9. Matthias Hämmer "Copper, Bismuth and Tin Borosulfates and Sulfates", **Virtual Presentation**, AK Höppe Mitarbeiterseminar, Augsburg, 09.12.2020.

10. Matthias Hämmer, Erich Turgunbajew, Henning A. Höppe, "Tectosilicate-analogous Borosulfates $Bi(H_3O)[B(SO_4)_2]_4$, $Bi(NO_2)[B(SO_4)_2]_4$, and $Bi(NH_4)[B(SO_4)_2]_4$" **Virtual Poster and Poster Video**, ACS Spring 2021, 05.-30.04.2021.

11. Matthias Hämmer "Lone Pair Effect and Crystal Structure", **Virtual Presentation**, AK Höppe Mitarbeiterseminar, Augsburg, 19.05.2021.

12. Matthias Hämmer, Jakoah Brgoch, Philip Netzsch, Henning A. Höppe, "The Bi^{3+} Lone Pair Effect in $(H_3O)Bi(SO_4)_2$, $Bi(HSO_4)_3$ and $Bi_2(SO_4)_3$" **Virtual Poster and Poster Video**, SCS Fall Meeting 2021, 10.09.2021.

I Acknowledgements

Zuallererst gilt mein Dank Prof. Dr. Henning Höppe für die Möglichkeit, diese Promotion in seinem Arbeitskreis am Lehrstuhl für Festkörperchemie der Universität Augsburg durchzuführen, das spannende und breite Thema, die intensive Betreuung und die vielen Besprechungen, aber auch die Freiheit, selbst die Schwerpunkte meiner Forschung wählen zu können.

Prof. Dr. Leo van Wüllen danke ich für die freundliche und unkomplizierte Übernahme des Zweitgutachtens.

Meinen Masterand*innen Katja Kress, Vivien Wessels, Erich Turgunbajew und Julian Müller danke ich für die gute Zusammenarbeit, ihre Beharrlichkeit und die vielen Stunden im Labor sowie das Verzeihen mancher fruchtlosen Idee meinerseits. Vielen Dank für eure tollen Ergebnisse, die zum Teil auch den Weg in diese Arbeit gefunden haben.

Dr. Florian Pielnhofer und Prof. Dr. Jakoah Brgoch danke ich für Durchführung, Auswertung und Interpretation der DFT-Rechnungen.

Bei Steffen Klenner, PD Dr. Oliver Janka, Judith Bönnighausen und Prof. Dr. Rainer Pöttgen möchte ich mich für die mößbauerspektroskopischen und die magnetischen Messungen sowie deren Auswertung bedanken.

Besonderer Dank gilt auch Dr. Lkhamsuren Bayarjargal für die vielen SHG-Messungen in dieser Arbeit.

Mein Dank gilt zudem Dr. Romy Ettlinger aber auch Ralph Freund und Marcel Hirrle für die EDX- und ESEM-Messungen - insbesondere auch die vielen, die es nicht in diese Arbeit geschafft haben.

Prof. Dr. Oliver Clemens danke ich für den äußerst hilfreichen TOPAS-Workshop.

Ich bedanke mich zudem bei allen Kolleg*innen am Lehrstuhl für Festkörperchemie für das kollegiale Klima, die gute Zusammenarbeit, die Schafkopfrunden und den Kuchen. Hervorzuheben ist Andreas Kalytta-Mewes für seine technische Expertise und die Reparatur zahlreicher Geräte, ohne die deutlich weniger schöne Messungen den Weg in diese Arbeit gefunden hätten.

Außerdem gilt mein Dank den Mitgliedern des AK Höppe, Dr. Stephan Jantz, Peter Gross, Martin Schäfer und Dr. Philip Netzsch für das angenehme Arbeits- und Büroklima, fachliche Diskussionen sowie die Beantwortung vieler Fragen.

Ich danke Dr. Romy Ettlinger, Dr. Philip Netzsch und Marcel Vöst für die unterhaltsamen Mittagspausen, Verdauungsspaziergänge, die „Motivationsteams“ und die schönen Jahre auch außerhalb der Universität.

Explizit danke ich auch erneut Dr. Philip Netzsch für die Beantwortung und Diskussion vieler fachlicher Fragen sowie insbesondere für den Tipp, mich doch einfach mal im AK Höppe zu bewerben.

Bewusst zuletzt danke ich meiner Familie: Meinen Eltern vielen Dank für die Unterstützung und Geduld während des Studiums und der Promotion.

Meiner Ehefrau Selina danke ich für ihr Verständnis, das geduldige Zuhören und ihre Liebe! Und meiner Tochter Mathilda für ganz viele ganz neue Perspektiven!